

# Short-Lived Radionuclides in Chemistry and Biology

In Short-Lived Radionuclides in Chemistry and Biology; Root, J., et al.;  
Advances in Chemistry; American Chemical Society: Washington, DC, 1982.



# Short-Lived Radionuclides in Chemistry and Biology

**John W. Root**, EDITOR

*University of California, Davis*

**Kenneth A. Krohn**, EDITOR

*University of California, Davis*

Based on a symposium  
cosponsored by the Divisions of  
Nuclear Chemistry and Technology  
and Physical Chemistry and  
jointly sponsored by the  
Division of Biological Chemistry  
at the 178th Meeting of the  
American Chemical Society,  
Washington, D.C.,  
September 10–13, 1979.

ADVANCES IN CHEMISTRY SERIES

197

**AMERICAN CHEMICAL SOCIETY**  
**WASHINGTON, D. C. 1981**



Library of Congress  Data

**Short-lived radionuclides in chemistry and biology.**

(Advances in chemistry series, ISSN 0065-2393; 197)

Includes bibliographies and index.

1. Radioisotopes—Congresses. 2. Radiobiology—Congresses.

I. Root, John W., 1935—. II. Krohn, Kenneth A., 1945—. III. American Chemical Society. Division of Nuclear Chemistry and Technology. IV. American Chemical Society. Division of Physical Chemistry. V. American Chemical Society. Division of Biological Chemistry. VI. Series.

QD1.A355 no. 197 [QD601.A1] 540s [574.19'283]  
ISBN 0-8412-0603-1 81-19148 AACR2  
ADC SAJ 197 1-548 1981

Copyright © 1981

American Chemical Society

All Rights Reserved. The appearance of the code at the bottom of the first page of each article in this volume indicates the copyright owner's consent that reprographic copies of the article may be made for personal or internal use or for the personal or internal use of specific clients. This consent is given on the condition, however, that the copier pay the stated per copy fee through the Copyright Clearance Center, Inc. for copying beyond that permitted by Sections 107 or 108 of the U.S. Copyright Law. This consent does not extend to copying or transmission by any means—graphic or electronic—for any other purpose, such as for general distribution, for advertising or promotional purposes, for creating new collective work, for resale, or for information storage and retrieval systems.

The citation of trade names and/or names of manufacturers in this publication is not to be construed as an endorsement or as approval by ACS of the commercial products or services referenced herein; nor should the mere reference herein to any drawing, specification, chemical process, or other data be regarded as a license or as a conveyance of any right or permission, to the holder, reader, or any other person or corporation, to manufacture, reproduce, use, or sell any patented invention or copyrighted work that may in any way be related thereto.

PRINTED IN THE UNITED STATES OF AMERICA  
**American Chemical  
Society Library**  
1155 16th St., N.W.  
Washington, D.C. 20036

# Advances in Chemistry Series

**M. Joan Comstock, *Series Editor***

## *Advisory Board*

David L. Allara

Robert Baker

Donald D. Dollberg

Robert E. Feeney

Brian M. Harney

W. Jeffrey Howe

James D. Idol, Jr.

Herbert D. Kaesz

Marvin Margoshes

Robert Ory

Leon Petrakis

Theodore Provder

Charles N. Satterfield

Dennis Schuetzle

Davis L. Temple, Jr.

Gunter Zweig

# FOREWORD

**ADVANCES IN CHEMISTRY SERIES** was founded in 1949 by the American Chemical Society as an outlet for symposia and collections of data in special areas of topical interest that could not be accommodated in the Society's journals. It provides a medium for symposia that would otherwise be fragmented, their papers distributed among several journals or not published at all. Papers are reviewed critically according to ACS editorial standards and receive the careful attention and processing characteristic of ACS publications. Volumes in the **ADVANCES IN CHEMISTRY SERIES** maintain the integrity of the symposia on which they are based; however, verbatim reproductions of previously published papers are not accepted. Papers may include reports of research as well as reviews since symposia may embrace both types of presentation.

## PREFACE

**I**n organizing the symposium upon which this book is based, we brought together a diverse group of scientists whose common bond was an interest in radiochemistry, primarily with short-lived nuclides of carbon, nitrogen, oxygen, and the halogen elements.

One of the great strengths of radiochemistry is that it can be applied to a wide range of problems in the biological and physical sciences. At the same time this diversity also represents a potential weakness, because the activities of radiochemists cannot be identified with a single traditional discipline. Increasing numbers of radiochemists are working outside the confines of chemistry and physics. Radiotracer techniques are now being used with success in such diverse areas as biochemistry, medicine, physiology, microbiology, geochemistry, and agricultural and environmental science.

The principal goals of the symposium and of this book have been to illustrate the scope of recent radiotracer research within both traditional and nontraditional settings. Roughly equal emphasis has been given to biological and environmental research on the one hand and to pure chemistry and chemical kinetics on the other. This volume represents the first compendium of applications of radiochemistry to such a broad spectrum of disciplines in chemistry and the biological sciences. Although this is not a textbook, we hope that the level of background information and technical detail presented in the various chapters is sufficient to encourage new practitioners of this type of research. We also hope that the book will stimulate the exchange of ideas and information relating to new problems and possible methods of solving them between an expanded audience of biological, physical, and nuclear chemists.

In focusing the symposium on short-lived isotopes, we have emphasized experiments in which the investigator has to produce the tracer on site at the time that it is to be used. Because of this time constraint, the experimental demands of working with short-lived radiotracers are often severe. Even so, hot atom chemists have been using such species for many years to develop the mechanistic chemistry and chemical kinetics of isolated atomic reactions. Pioneering research by M. D. Kamen, J. E. Varner, and C. P. Wolk, among others, has extended this methodology to biological research. A recurring theme of this book is

that the scientific rewards will justify the additional demands inherent in radiotracer methods when novel or uniquely precise results are achieved.

To provide a balanced technical overview and to suggest directions for future research, selected topics involving other nuclear techniques and longer-lived  $^3\text{H}$  and  $^{14}\text{C}$  radionuclides have been included. These latter chapters reflect the potential of such methods for obtaining mechanistic and kinetic information of extraordinary precision and accuracy.

We wish to thank the symposium participants and each author who contributed to this book. Our special appreciation goes to Dr. Darleane C. Hoffman, who served as chairperson of the Division of Nuclear Chemistry and Technology during the meeting, for her support and encouragement in this endeavor.

**JOHN W. ROOT**  
Department of Chemistry  
University of California  
Davis, CA 95616

**KENNETH A. KROHN**  
Department of Radiology  
University of California Medical Center  
Sacramento, CA 95817

September 8, 1981



# Recoil Chemistry and Mechanistic Studies with Polyvalent Atoms

PETER P. GASPAR

Department of Chemistry, Washington University, Saint Louis, MO 63130

*Polyvalent recoiling atoms incorporate themselves into chemically stable product molecules via reaction sequences that generally contain multiple steps. The elucidation of the primary reactions of the polyvalent recoiling atoms requires the identification and study of the reactive intermediates that participate in these reaction sequences. Unusual product molecules as well as a wide variety of reactive radicals and ions are formed. There is a mutual reinforcement between recoil studies and chemical experiments that is illustrated by several detailed mechanistic studies of the chemistry of carbon and silicon atoms.*

Hot atom chemists are interested in understanding elementary bond-making and bond-breaking processes "over the whole range of energies for which such reactions are possible" (1). The recoil chemistry of polyvalent atoms has much to contribute to a multifaceted study of the fundamental factors that control chemical reactivity. The results of this work are becoming more and more visible. Not only has our understanding deepened but our ability to use that understanding to control the behavior of molecules and to make new classes of compounds has grown as well.

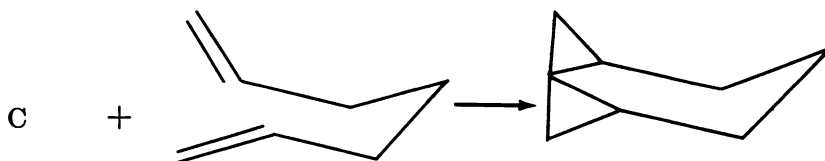
## ***Contrast Between Chemistry of Polyvalent Atoms and Reactions of Monovalent and Divalent Atoms***

Before we see what has been accomplished and what can be done through the study of polyvalent recoiling atoms, we should compare the field with the chemistry of monovalent and divalent atoms. It is by no means a historical accident that much of the progress made by hot atom

0065-2393/81/0197-0003\$07.25/0  
© 1981 American Chemical Society

chemists has been through the analysis of experimental data on the reactions of monovalent atoms—hydrogen and the halogens. These atoms can form chemically stable products in a single reactive collision. Table I compares the primary reactions of mono- and divalent atoms. Monovalent atoms can undergo abstraction and displacement reactions that produce in one step molecules that, after loss of excess vibrational and rotational energy, are chemically stable. Divalent atoms also have available single-step reactions like insertion and addition that produce, after collisional deexcitation, chemically stable products; but abstraction, and displacement reactions of divalent atoms produce valence-unsaturated intermediates.

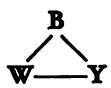
For atoms of higher valency the chances of saturating the covalence of a recoiling atom in a single reactive collision are slim. We recall the Wolfgang "Golden Rule" of hot atom chemistry, "Hot atom reactions requiring nuclear motions which are slow relative to the time of collision tend to be forbidden" (2). The interaction of a polyvalent recoiling atom with a reactive substrate in such a way as to saturate the valence of the recoil atom may require a considerable rearrangement of atomic position or an unlikely conformation of the substrate molecule. As a fanciful example, we might ask what fraction of gaseous 1,6-heptadiene molecules are in the proper conformation to form simultaneously four bonds to a recoiling carbon atom?



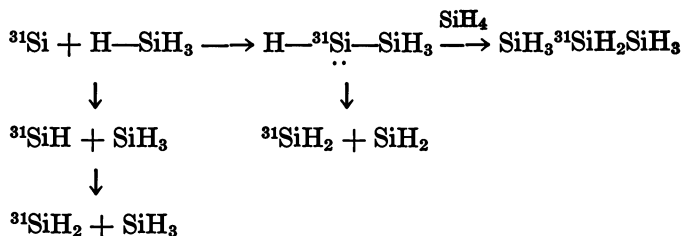
While such a reaction is in principle possible, it is expected to occur with very low efficiency. In the recoil chemistry of polyvalent atoms, chemically stable reaction products are likely to be formed in multistep reaction sequences rather than in single reactive collisions. This implies the formation of reactive intermediates, which is the feature that most clearly distinguishes the study of polyvalent atoms from the investigation of monovalent atoms.

**Formation of Reactive Intermediates: The Distinctive Feature of Polyvalent Atom Recoil Chemistry.** The possibility that reactions of recoiling silicon and germanium atoms would produce novel reactive intermediates originally attracted the author of this chapter to hot atom chemistry. Several such intermediates are shown in a reaction scheme for recoiling silicon atoms that has been under investigation in our laboratory for several years (3, 4).

**Table I. Schematic Representation of Some Primary Reactions of Monovalent (A) and Divalent (B) Recoiling Atoms\***

<i>Abstraction</i>	$A + X-Y-Z \rightarrow \mathbf{A-X} + \cdot Y-Z$
<i>Displacement</i>	$A + X-Y-Z \rightarrow \mathbf{A-Y-Z} + \cdot X$
<i>Displacement with bond cleavage</i>	$A + X-Y-Z \rightarrow \mathbf{A-Y\cdot} + X\cdot + Z\cdot$
<i>Addition</i>	$A + W=Y \rightarrow \mathbf{A-W-Y}$
<i>Insertion</i>	$B + X-Y-Z \rightarrow \mathbf{X-B-Y-Z}$
<i>Addition</i>	$B + W=Y \rightarrow$ <div style="text-align: center;">  </div>
<i>Abstraction</i>	$B + X-Y-Z \rightarrow \cdot \mathbf{B-X} + \cdot Y-Z$
<i>Displacement</i>	$B + X-Y-Z \rightarrow \cdot \mathbf{B-Y-Z} + X\cdot$
<i>Insertion with bond cleavage</i>	$B + X-Y-Z \rightarrow \mathbf{X-B-Y\cdot} + Z\cdot$

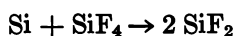
\* Stable products are shown in boldface (**§**).



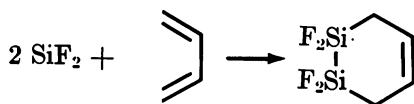
This reaction scheme is perhaps typical, both in its length and in its tentative nature, of those suggested for polyvalent atoms. It is being closely scrutinized, and parts of it are undergoing revision. However, it was the hope of making silylene  $\text{SiH}_2$  via recoil reactions that lured this author into hot atom chemistry.

The study of polyvalent recoiling atoms presents the opportunity of creating and studying a wide range of reactive radicals and ions at ambient temperatures in the presence of virtually any desired reaction partner. There are a number of examples of species such as methyne,  $\text{CH}$  (5); chloromethyne,  $\text{CCl}$  (6); silylsilylene,  $\text{SiH}_3\text{SiH}$ : (7); and difluorosilylene  $:\text{SiF}_2$  (8-11) whose gas-phase reaction products were obtained for the first time from recoil studies.

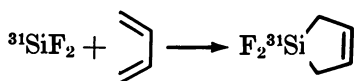
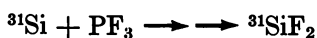
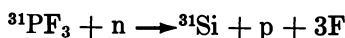
While  $\text{SiF}_2$  can be formed easily in a thermal retrodisproportionation (12, 13),



the products obtained from its chemical generation usually contain at least two  $\text{SiF}_2$  units, suggesting that dimerization was the initial process under these conditions (14).



The most successful means for studying monomeric  $\text{SiF}_2$  has been via hot atom reactions in which nucleogenic silicon atoms abstract two fluorine atoms from their  $\text{PF}_3$  precursor (9-11).



In the recoil system chemically stable products containing a single silylene unit predominate, since the low concentration of intermediates precludes dimerization. Thermally generated  $\text{SiF}_2$  is quite unreactive, with a 150-s half-life in the gas-phase (12), so nucleogenic  $\text{SiF}_2$  may also be reacting before it is thermally equilibrated.

**Product Studies and the Necessity of Unravelling Reaction Sequences.** One person's opportunity can be another's pitfall. To work out the reaction sequences that convert polyvalent recoiling atoms into the chemically stable products observable by standard radioanalytical techniques, we must be able to identify the short-lived intermediates that participate in these sequences. This is unquestionably the greatest challenge to present-day polyvalent recoil chemistry. The mechanistic study of polyvalent recoiling atoms has two necessary stages. First, the intermediates formed for a particular reaction system must be identified, and changes of their relative abundance along with changes in reaction conditions must be determined. Only then can the details about how a particular intermediate undergoes reaction be learned. In general, little is known about the behavior of these reactive intermediates, particularly at high energy, and a strong motive for carrying out these experiments is to increase our knowledge of the chemistry of these reactive intermediates.

Anyone who undertakes to design a polyvalent atom recoil experiment must keep clearly in mind that the observed reaction products will rep-

resent a convolution of the reactivities of the recoiling atoms themselves and of the reactive intermediates produced by the primary reactions of the recoiling atoms. The analysis of experimental results must then be a deconvolution if the reactions of each individual species are to be understood.

### *Investigation of Systematics of Polyvalent Atom Recoil Reactions*

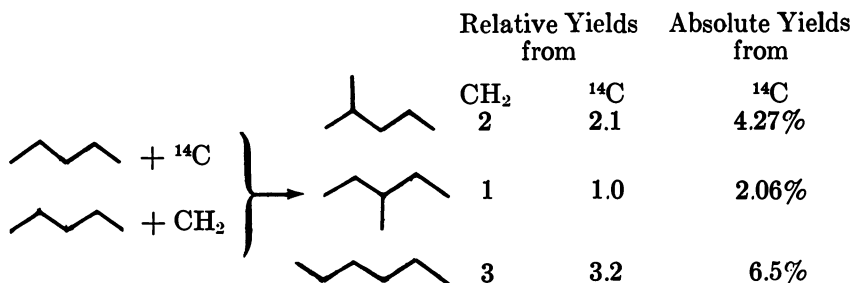
Let us begin to describe how the systematics of polyvalent atom recoil reactions are being investigated. We must remind ourselves that the small number of recoiling atoms created in a single experiment, typically  $10^6$  to  $10^{10}$ , makes it very difficult with present techniques to detect directly either the recoiling atoms or the reactive intermediates derived from them. The primary data in recoil chemistry have been, until now, the chemically stable end products into which the recoiling atoms incorporate themselves by their reactions. Thus, the end products of reaction sequences initiated by polyvalent recoiling atoms are the clues from which the whole sequence must be deduced.

The most important mechanistic clue for any chemical reaction is the structure of the reaction products, and a great strength of the recoil technique is that there is no more convenient or effective way to determine what products are formed from a polyvalent atom and a chosen reaction substrate than by examining its recoil chemistry. The harshness of the conditions required to liberate polyvalent atoms chemically severely limits the study of their reactions by other methods (*vide infra*).

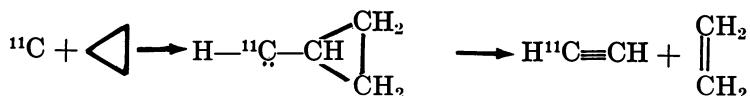
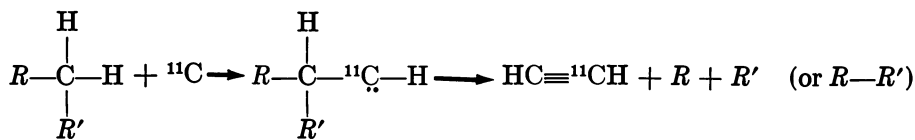
**Identification of Reactive Intermediates.** COMPARISON OF INTERMEDIATES IN RECOIL REACTIONS WITH CHEMICALLY GENERATED SPECIES. The reactive intermediates formed from recoiling polyvalent atoms must, for now, be identified by chemical means. Reaction substrates are chosen so that the structures of the products derived from them help us understand the nature of the intermediates. For this purpose it is useful to know the reactivities of the molecules used as reaction substrates toward short-lived intermediates of known structure. The most direct way in which a reactive intermediate in a recoil reaction can be identified is to generate the same intermediate by chemical means and to compare their behavior.

An example of the inferences that have been drawn is as follows. Methylene formation in the reactions of recoiling carbon atoms was deduced from comparison of product distributions from recoil experiments with those obtained from singlet state  $\text{CH}_2$  (16, 17). The hexanes produced from the reactions of recoiling  $^{14}\text{C}$  atoms with *n*-pentane were

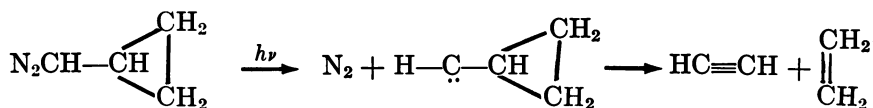
obtained in the relative yields expected from nearly indiscriminate insertion by  $^{14}\text{C}$  into C—H bonds.



Another example involves the source of acetylene as a major product from the reaction of recoiling carbon atoms and cyclopropane (18). MacKay and Wolfgang attributed the formation of acetylene from carbon-atom reactions with alkanes to an insertion into a C—H bond followed by fragmentation of the intermediate carbene (18). The high yield of labeled acetylene from cyclopropane was in accord with this mechanism, since the intermediate cyclopropylmethylene was believed to cleave into two stable molecules: ethylene in addition to acetylene.



This hypothesis received strong support when Shevlin and Wolf generated cyclopropylmethylene chemically and found that it does readily undergo fragmentation (19).



Recently Taylor, Ache, and Wolf have been able to define the spin states of the carbon atoms reacting to form acetylene by comparing the

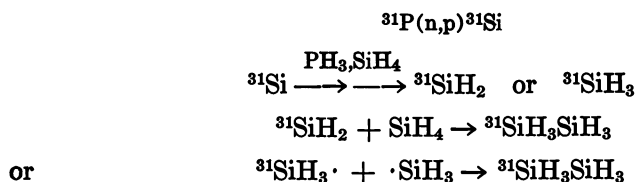
effects of different noble gas moderators on the acetylene yield from ethane (20). They concluded that high energy  $^3\text{P}$  and lower energy  $^1\text{D}$  atoms attack the C—H bonds of alkanes as shown.

These examples point to the symbiotic relationship between polyvalent atom recoil chemistry and the study of chemically generated reactive intermediates. Hot atom experiments identify products that suggest the intermediacy and delineate the reactivity of exotic species such as cyclopropylidene, methyne, and silylene. Thus, hot atom experiments have stimulated the search for other ways of generating these species, and in turn these chemical experiments can help interpret the hot atom experiments.

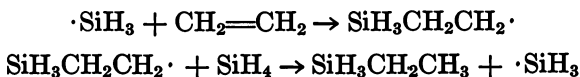
If a reactive intermediate in a polyvalent atom recoil reaction has been independently characterized, as has methylene or cyclopropylmethylene, above, then acceptable evidence for its intermediacy in a recoil system is the observation of a product spectrum characteristic of the given intermediate. Enough different substrates must be used, however, to ascertain that all the major reactions of the suspected intermediate are obtained from the recoil system.

In the case of species that have not been characterized in other kinds of experiments, conclusions about their presence or absence in recoil reactions may be considerably more tenuous.

Early in the study of silicon atom recoil chemistry, ethylene was used as a scavenger to differentiate between silyl radicals,  $\text{SiH}_3$ , and silylene,  $\text{SiH}_2$ , as the intermediate responsible for the formation of silane and disilane in phosphine-silane systems (21).



The failure of small quantities of ethylene to suppress completely the formation of disilane seemed to rule out the intermediacy of  ${}^{31}\text{SiH}_3$ , since silyl radicals were believed to add rapidly to ethylene and to form ethylsilane in a chain reaction (22).

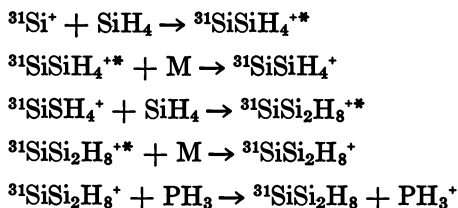


Since it was only a guess that the rate of addition of silyl radicals to ethylene was rapid, we decided to measure this rate for the first time, by a combination of flash photolysis and time-resolved ESR spectroscopy

(23). We found that silyl radicals  $\text{Me}_3\text{Si}\cdot$  and  $\cdot\text{SiH}_3$  do add rapidly to ethylene, thus confirming the efficiency of ethylene as a silyl radical scavenger in silane. Here hot atom studies had provided the stimulus for kinetic spectroscopy experiments whose results were useful in interpreting the recoil results.

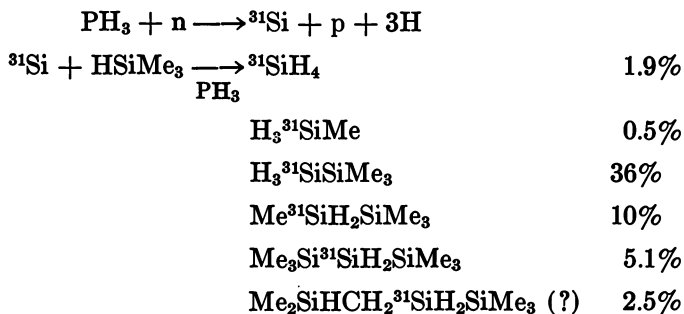
Another example that underlines the complementarity of hot atom reaction studies and other kinetic experiments involves the study of silicon ion reactions. Nearly ten years ago we began to wonder whether any of the products from the reactions of recoiling silicon atoms and silanes came from positively charged silicon ions. The low ionization potential of the silicon atom, 8.15 eV, prompted us to speculate whether some of the recoiling silicon atoms might reach the energy range of chemical reactions as positive ions. This in turn led us to study ion-molecule reactions of  $\text{Si}^+$  with  $\text{SiH}_4$  to see whether a sequence of reactions initiated by recoiling silicon ions would produce any of the end products found in the recoil reactions.

We found a number of interesting reactions (24) and were able to suggest the following mechanism as a possible source of labeled trisilane (25).



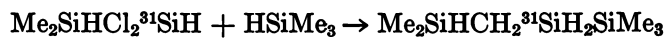
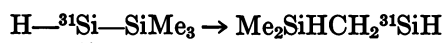
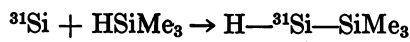
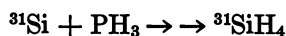
Experiments designed to demonstrate the intervention of ionic intermediates in the recoil system have proved, until recently, to be inconclusive.

However, we have found several products that are consistent with some participation by ion-molecule reactions in product formation. The reactions of recoiling silicon atoms in mixtures of phosphine and trimethylsilane produce some provocative minor products (26).





Three of these products can be explained by neutral reactions, and the silane is probably produced from phosphine.

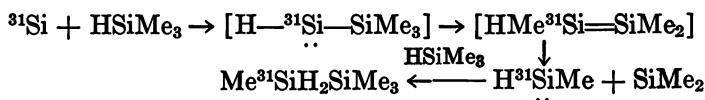


The rearrangement of  $\text{Me}_3\text{Si}^{31}\text{SiH}$  to  $\text{Me}_2\text{SiHCH}_2\overset{\cdot\cdot}{\text{Si}}\text{H}$  is a recently discovered silylene-to-silylene interconversion that is itself a multistep process (27, 28).

The product formed in second-highest yield, 1,1,1,2-tetramethyldisilane, as well as methylsilane require transfer of a methyl group for their formation. No neutral silicon species are known to abstract methyl groups, but Lampe has found that cations of various kinds do abstract methyl radicals and methide anions from methylsilanes (29–31).



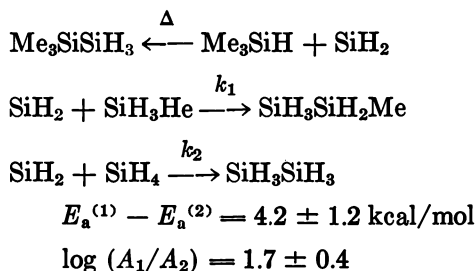
Thus the study of chemically generated silicon ions, stimulated by earlier recoil studies that raised the possibility of ionic intermediates, has provided mechanisms for their possible participation in recoil reactions. However, it is also possible that the apparent methyl group abstraction is actually the result of insertion followed by scrambling of methyl groups and hydrogens (32).



Often the intermediates in recoil reactions behave somewhat differently from species of the same structure generated chemically. This is not surprising since the species formed in recoil reactions are often quite different in energy or electronic state from thermally generated species.

Therefore, an important technique in the mechanistic study of polyvalent recoiling atoms is the use of inert moderators and high pressures to deactivate the high-energy species and thus facilitate comparison of intermediates in recoil systems with thermally generated species. The nature of the high-energy intermediates can often be deduced from the identification of lower-energy forms.

As an example, we have recently been comparing the reactivity of the intermediates derived from recoiling silicon atoms with the reactivity of thermally generated silylene  $\text{SiH}_2$  toward silane and methylsilane. This pair of substrates was chosen because Paquin and Ring have studied the temperature dependence of the relative rate of insertion of thermally generated silylene into the Si—H bonds of these molecules (33).



In the temperature range studied, 246–289°C, the relative reactivity of  $\text{MeSiH}_3$  and  $\text{SiH}_4$  varied from 0.97 to 1.3. When recoiling silicon atoms are allowed to react with a mixture of methylsilane and silane, labeled methyl-disilane and disilane are the major products and, as shown in Figure 1, the product ratio is a linear function of the substrate ratio. From the slope, a relative reactivity of  $1.34 \pm 0.02$  is deduced—very close to that for thermally generated  $\text{SiH}_2$  at 200°C but far too high for  $\text{SiH}_2$  at room temperatures if the long extrapolation with the activation parameters determined by Paquin and Ring is made. Rare gas moderators, polyatomic quencher molecules, and free radical scavengers reduce absolute yields but do not affect the relative reactivity in recoil experiments. Thus the intermediacy of  $^{31}\text{SiH}_2$  in recoil reactions has still not been proved by these relative rate determinations, but the data are consistent with a vibrationally or electronically excited silylene.

**CASES IN WHICH POSTULATED INTERMEDIATES IN RECOIL REACTIONS CANNOT BE CHEMICALLY GENERATED.** Turning to other approaches for the mechanistic study of recoiling polyvalent atoms, among the most interesting and difficult cases arise when observed products and postulated intermediates in the recoil systems cannot be generated by chemical means. Then the resourcefulness of the hot atom chemist is pressed to the utmost.

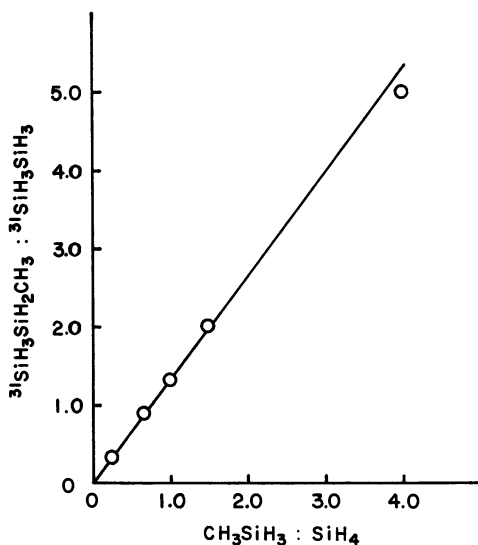
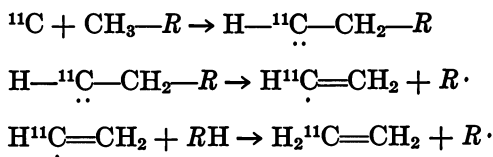


Figure 1. Ratio of product yields  $^{31}\text{SiH}_3\text{SiH}_2\text{CH}_3 : ^{31}\text{SiH}_3\text{SiH}_3$  vs. substrate ratio  $\text{CH}_3\text{SiH}_3 : \text{SiH}_4$  for reactions of recoiling  $^{31}\text{Si}$  atoms in mixtures of  $\text{PH}_3$  (500 Torr),  $\text{CH}_3\text{SiH}_3$  and  $\text{SiH}_4$  at constant total pressure (1000 Torr) (134)

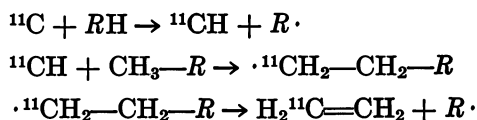
An example from the chemistry of carbon presents the vexing question, how is ethylene formed from reactions of recoiling carbon atoms and alkanes?

Two different mechanisms were proposed by Wolfgang (34, 35) and Wolf (5), invoking as key intermediates two species methyne,  $\text{CH}$  (5), and vinyl radicals,  $\cdot\text{CH}=\text{CH}_2$  (34, 35), neither of which can readily be formed under conditions such that reaction products can be identified.

#### Vinyl radical mechanism



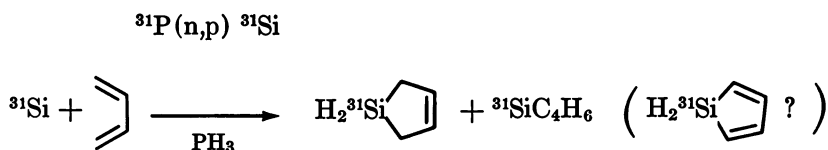
#### Methyne mechanism



Here there was very little information available from experiments with thermally generated species to assist in the choice between these two probable pathways. Wolf, Ache, and Taylor have carried out elegant double-labeling isotope-effect studies that weighted the evidence in favor of the methyne mechanism (36).

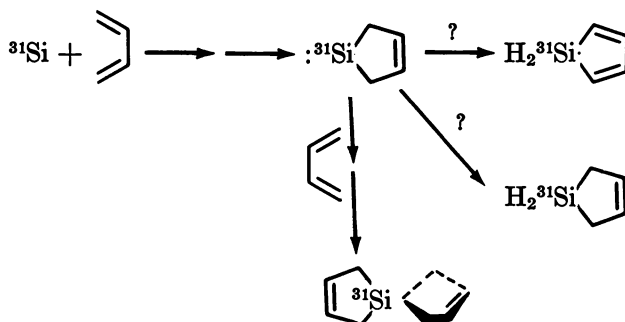
Recently these workers have also found evidence for formation of chloromethyne,  $^{11}\text{CCl}$ , in reactions of alkyl chlorides with recoiling carbon atoms (6). Chloromethyne, like the fluoromethyne earlier implicated as a reactive intermediate by Wolf (37) and Wolfgang (38), is a species whose reactivity has not been studied in conventional kinetic experiments.

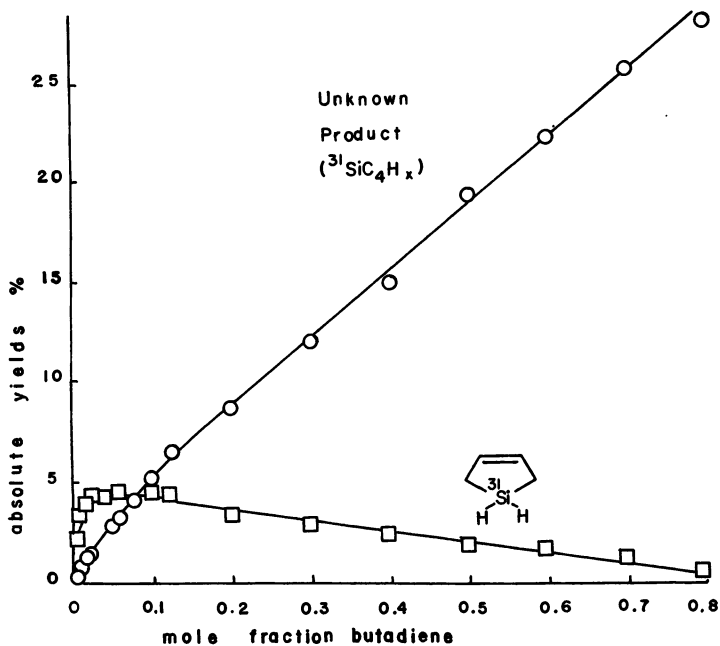
We were faced with a dilemma six years ago when the major product from reactions of recoiling silicon atoms with butadiene turned out to be one for which no authentic sample could be synthesized (4, 39).



Tang was the first to report the formation of  $^{31}\text{Si}$ -1-silacyclopent-3-ene, a product whose yield passes through a maximum of only 5%, as shown in Figure 2 (4, 39). An empirical formula,  $^{31}\text{SiC}_4\text{H}_6$ , was deduced for the major product, and the silacyclopentadiene structure was favored, but the authentic compound could not be synthesized (4). The experience of other workers with substituted silacyclopentadienes suggests that this molecule will dimerize quickly in macroscopic quantities (41), but for a carrier-free recoil product this process would be slow.

We have recently found evidence for the formation of five-membered rings in the interaction of recoiling silicon atoms with butadiene in a long-sought spirononadiene product (4), which can be compared with the authentic compound (42).

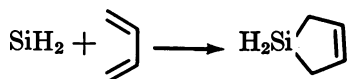
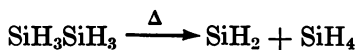




Journal of the American Chemical Society

Figure 2. Product yields from reactions of recoiling silicon atoms in phosphine-butadiene mixtures as function of mole fraction butadiene at constant total pressure (1000 Torr) (4)

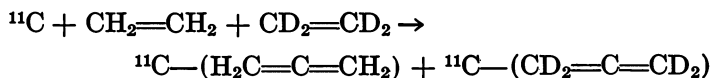
Tang has found direct evidence for formation of the silacyclopentadiene in its reduction to silacyclopentene (43). The cyclic silylene intermediate is also a possible source of the silacyclopentene, although the more likely route to this product is addition by silylene, which has been demonstrated to be an efficient process (4, 39).



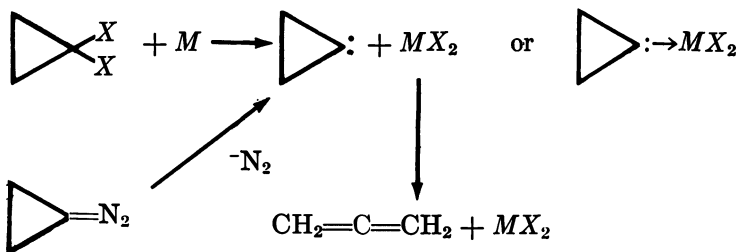
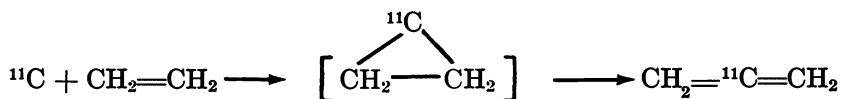
**Primary Reactions of Polyvalent Recoiling Atoms.** We have dwelled thus far on the identification of reactive intermediates in the reactions of polyvalent recoiling atoms. Only in the cases of carbon, silicon, germanium, nitrogen, and phosphorus have complete reaction

sequences been proposed for the conversion of the recoiling atoms into the observed reaction products. For these elements primary reactions of the recoiling atoms have been deduced by focusing on the mode of formation of the reactive intermediates.

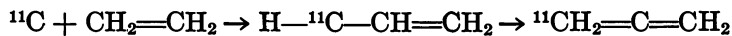
**FORMATION OF ALLENE FROM  $^{11}\text{C} + \text{CH}_2=\text{CH}_2$ .** Allene is formed in about 15% yield from the reactions of recoiling  $^{11}\text{C}$  atoms with ethylene (44). The intramolecular nature of the reaction was demonstrated by the finding of only fully deuterated and fully protiated allenes from  $\text{C}_2\text{H}_4$ - $\text{C}_2\text{D}_4$  mixtures.



Most of the labeled carbon was found in the center of the allene (45), and on this basis a cyclopropylidene intermediate has been suggested. Cyclopropylidene has been shown to undergo efficient rearrangement to allene (46-48).



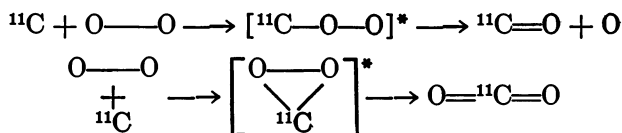
End-labeled allene has been attributed to C-H insertion:



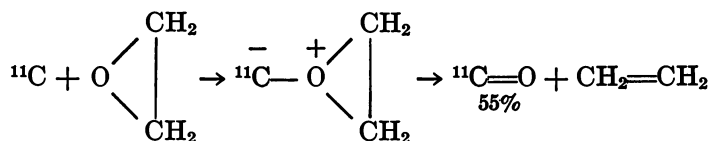
Recently Wolf and coworkers have shown that the fraction of center-labeling increases from 73% in the absence of additives to 100% in the presence of oxygen but decreases to 6% with 94% neon. This suggests that  $^1\text{D}$  carbon atoms attack exclusively the  $\pi$ -bond at higher energy than C-H insertion, which is possible for both  $^1\text{D}$  and  $^3\text{P}$  carbon atoms (49). In spectroscopic experiments,  $^1\text{D}$  carbon atoms have been shown to react very rapidly with ethylene (50).

Both a cyclopropylidene intermediate and the recently suggested high-energy direct  $\pi$ -insertion are compatible with a direct attack of a recoiling carbon atom on a double bond.

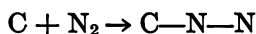
**CARBON MONOXIDE FORMATION FROM CARBON ATOMS.** In certain cases quite detailed pictures of primary reactions of recoiling polyvalent atoms have been developed. "End-on" attack of carbon atoms on oxygen molecules rather than attack normal to the oxygen-oxygen bond was deduced from the formation of carbon monoxide instead of carbon dioxide, even in condensed phases capable of stabilizing excited  $\text{CO}_2$  (51).



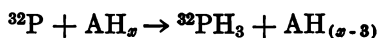
MacKay has explained the preference to end-on attack by a molecular orbital argument (52). The corollary that any exposed oxygen should be readily plucked off by a carbon atom has been amply demonstrated. The first reported deoxygenation by atomic carbon, in its reaction with ethylene oxide, is best described by direct attack on oxygen (53). Numerous deoxygenations of other oxygen-containing molecules by thermally generated carbon atoms have been reported (54-65).



End-on attack of carbon atoms on nitrogen molecules has been reported in spectroscopic experiments (66, 67).



**A POSTULATED SINGLE-STEP REACTION.** An unusual primary reaction of a polyvalent recoiling atom, simultaneous abstraction of three hydrogen atoms by phosphorus atoms, has been suggested by Tang (68). This is a reaction without a reactive intermediate:



The basis for this proposal was a thermochemical argument that stepwise abstraction would be endothermic for such substrates as  $\text{PH}_3$  and  $\text{SiH}_4$ , which give high yields of abstraction products. While such a

process would presumably require a very favorable geometry to occur rapidly, it should be pointed out that the lower velocity of a heavy atom at a given energy (compared with a light one) will increase the collision time and thus permit processes to occur that have not been observed with tritium and fluorine atoms, the most widely studied monovalent atoms.

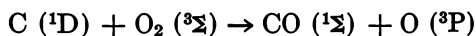
**DIATOMIC MOLECULES AS POSSIBLE DIAGNOSTIC REAGENTS AND THE USE OF CORRELATION DIAGRAMS.** Since the primary reactions of polyvalent atoms are expected to form reactive intermediates, the most general approach to characterizing these primary reactions is to pick substrates whose reactions are most likely to convey information about the electronic states of the reacting atom and the geometry of its attack on the substrate.

Diatomic molecules offer important advantages that have not been fully utilized for probing the primary reactions of recoiling polyvalent atoms. The primary products of the interaction of diatomic molecules with polyvalent atoms will, of course, be diatomic and triatomic reactive radicals whose gross structures and electronic states can, in favorable cases, be deduced from their subsequent reactions, as discussed earlier.

If the electronic states of the primary reaction products from a recoiling atom and a diatomic molecule can be determined, then adiabatic correlation diagrams could be used to deduce the electronic state of the reacting recoil atom, or the symmetry of attack, or both.

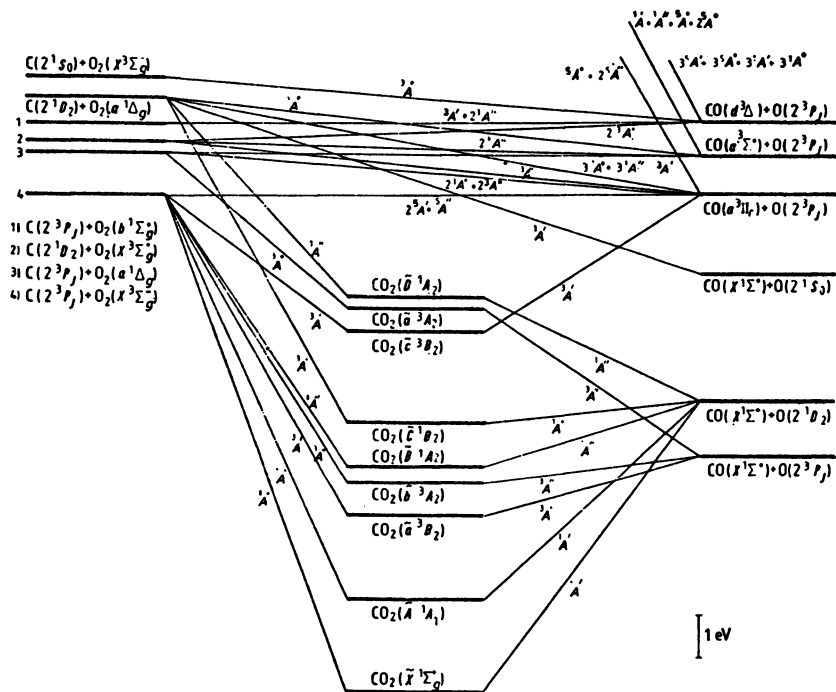
Donovan and Husain have pioneered the use of correlation diagrams connecting reactant atoms and molecules, collision complexes, and products (69,70). One can thus use the symmetry of the potential energy surfaces for reactive collisions to construct reasonable arguments predicting product structures from correlation diagrams. However, these predictions are rarely unambiguous even when the electronic state of the reacting atom is known.

An example of such a correlation diagram is given in Figure 3 for the previously discussed reaction of C + O<sub>2</sub>. Interestingly, it shows that the reaction of <sup>1</sup>D carbon atoms with ground-state oxygen molecules to give ground-state CO is symmetry-forbidden despite being exothermic by 116 kcal/mol, and spin-allowed!



Such correlation diagrams, like the Woodward-Hoffmann rules of organic chemistry, only indicate which reactions are symmetry allowed and are therefore unlikely to have large energies of activation if they are exothermic or thermo-neutral. These diagrams also indicate which reactions are symmetry forbidden and are likely to have either large energy barriers or small frequency factors because they cannot take place adiabatically.



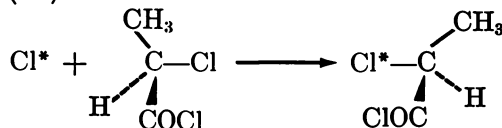


Faraday Society Discussions

Figure 3. Correlation diagram connecting the states of  $C + O_2$  and  $CO + O$  via those of  $CO_2$  (74)

THE ROLE OF THEORETICAL CALCULATIONS IN RECOIL CHEMISTRY.

Theory can and surely will play a more direct role in the understanding of polyvalent atom recoil chemistry. It is becoming feasible, at least for small reaction systems, to carry out ab initio quantum mechanical calculations of potential surfaces for reactions of interest to hot atom chemists and thus to obtain quantitative estimates of reaction probabilities (71). In any discussion of monovalent atom recoil chemistry the role of theoretical calculations in interpreting the results of experiments, and indeed in predicting them, is very important. Particularly for tritium atoms, the detailed insight provided by trajectory calculations into the dynamics of reactive collisions is remarkable, and has had a concrete result in stimulating experiments aimed at finding displacement reactions proceeding via Walden inversion. These have succeeded with recoiling chlorine atoms (72).

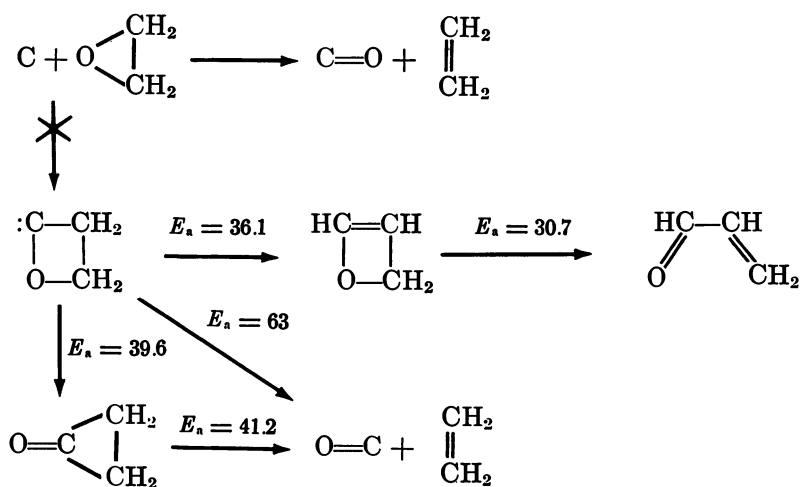


For polyvalent atoms, potential surfaces of sufficient accuracy for trajectory calculations are usually lacking.

For carbon atoms, however, the *ab initio* configuration interaction calculations of Blint and Newton on the reactions of  $^1\text{S}$ ,  $^1\text{D}$ , and  $^3\text{P}$  electronic states with molecular hydrogen have made an important contribution (73). A schematic representation of states and pathways is given in Figure 4. The calculations indicate that  $^1\text{S}$  carbon will not react with  $\text{H}_2$ , a result also obtained by Husain from a symmetry-derived correlation diagram (74). Therefore, the reactions of only the two lowest states of atomic carbon,  $^1\text{D}$  and  $^3\text{P}$ , were considered. The formation of methyne  $\text{CH}$  from the  $^1\text{D}$  state and insertion by  $^3\text{P}$  recoiling carbon atoms was indicated.

While *ab initio* calculations of reaction paths for polyvalent atoms are still scarce, the usefulness of semiempirical calculations has recently been demonstrated. Dewar employed his MINDO/2 molecular orbital method to examine the addition of  $^1\text{S}$  carbon atoms to ethylene and *trans*-2-butene (75). An unrealistically large activation energy was found for rearrangement of the intermediate cyclopropylidene to allene.

Shevlin examined the reaction of carbon atoms with ethylene oxide by the MINDO/3 formalism and found no energy barrier for direct removal of the oxygen atom (76). It was also concluded that if insertion of carbon into the  $\text{C}-\text{O}$  had occurred, other products would have been formed.



Shevlin has also examined theoretically the insertion of carbon atoms into the  $\text{C}-\text{H}$  bonds of propane (77). A preference of 6 to 1 for insertion into secondary vs. primary bonds for chemically generated

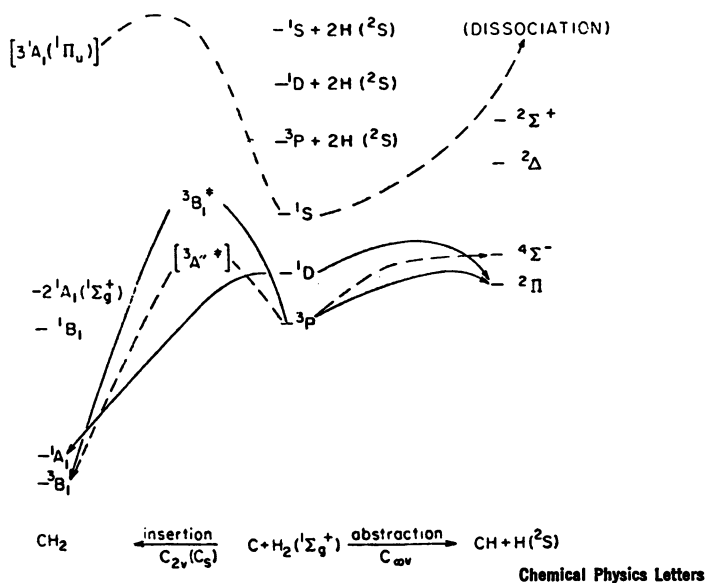


Figure 4. Schematic representation of calculated states and pathways for the  $C + H_2$  system (73)

carbon atoms was found. This was explained in terms of the transition state suggested by the calculations: initial hydrogen atom transfer to the attacking carbon atom.

### *Chemical Methods for the Generation of Free Atoms*

I have stressed the symbiosis between recoil reaction studies and the chemical generation of reactive species. The work already accomplished clearly demonstrates the considerable differences between the reactions of high-energy recoiling polyvalent atoms and their thermally generated counterparts. In the early days of recoil carbon chemistry it was believed that the high chemical potential of thermal-energy ground-state free carbon atoms would be the major determinant of reactivity, and the excess energy of the recoil species might not be important (2, 78). We know now from comparison of nucleogenic with thermal carbon, silicon, and germanium atoms that the reactivity of both the initial recoil species and the reactive intermediates formed from them are very different from that of their thermally generated counterparts. This means that there is much to learn from recoil studies about the effect of excess kinetic and electronic energy on the reactivity of polyvalent atoms. This does not, however, detract from the importance of the investigation of chemically

generated species—quite the opposite, for the differences in reactivity between nucleogenic and thermal species require accurate knowledge of both regimes.

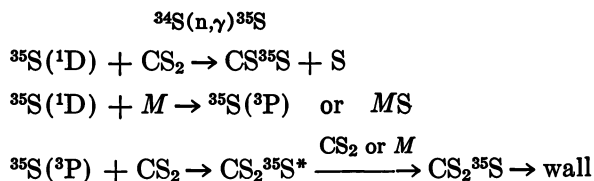
This brings us to some chemical methods for the generation of free atoms, and these have not been fully exploited in providing information useful for the interpretation of the reactions of polyvalent recoiling atoms.

**Time Resolved Kinetic Spectroscopy Following Generation by Flash Photolysis or Electric Discharge.** Kinetic studies of both ground states and excited states of polyvalent atoms have been published with increasing frequency in recent years. Flash photolysis, electric discharges, and pulse radiolysis have been used to liberate the atoms from polyatomic precursors, and the decay of discrete electronic states of the free atoms have been monitored by time-resolved atomic absorption spectroscopy (79). Very interesting kinetic data have been obtained for a number of polyvalent atoms, including carbon (50, 74, 81–84), silicon (85–90), germanium (91–94), nitrogen (95–98), phosphorus (99–104), and sulfur (105–106).

Many of these data have been obtained by Husain and his group in Cambridge, and some representative data for ground-state Group IV atoms are shown in Table II (86). The very rapid rates of reaction with NO and N<sub>2</sub>O validate the assumption that these molecules are excellent scavengers for thermalized ground state triplet Group IV atoms.

Unfortunately, the atomic absorption and fluorescence techniques used by Husain do not detect the molecular products of atomic reactions, since at the low concentrations of atoms used, the sensitivity does not suffice for the detection of diatomic and polyatomic molecules.

An interesting application of Husain's kinetic data to the interpretation of the results of a recoil experiment have been made by Kremer and Spicer (10). These workers studied the exchange reactions of sulfur atoms with carbon disulfide.



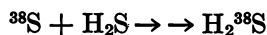
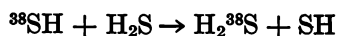
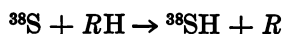
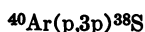
This mechanism was based on the observation that the yield of labeled CS<sub>2</sub> is reduced much more drastically by the presence of molecular hydrogen than by argon. Husain's kinetic measurements had revealed that the rate constant for removal of <sup>1</sup>D sulfur atoms is much larger for H<sub>2</sub> than for Ar (69). The nature of the interaction of recoiling sulfur atoms with H<sub>2</sub> could not be inferred from the hot-atom experiments

**Table II. Comparison of Second-Order Rate Constants for the Collisional Removal of Ground State Carbon, Silicon, and Germanium Atoms by Various Gases (86)<sup>a</sup>**

R	C( <sup>23</sup> P <sub>J</sub> )	Si( <sup>29</sup> P <sub>J</sub> )	Ge( <sup>73</sup> P <sub>0</sub> )
N <sub>2</sub>			2.5 ± 0.2 × 10 <sup>-13</sup> <sup>b</sup>
O <sub>2</sub>	2.6 ± 0.3 × 10 <sup>-11</sup> <sup>c</sup> 3.3 ± 1.5 × 10 <sup>-11</sup> <sup>f</sup> 3.3 × 10 <sup>-11</sup> <sup>e</sup> 2.5 × 10 <sup>-12</sup> <sup>h</sup>	2.7 ± 0.3 × 10 <sup>-10</sup> <sup>d</sup>	1.2 ± 0.1 × 10 <sup>-10</sup> <sup>b</sup>
Cl <sub>2</sub>		3.3 ± 0.3 × 10 <sup>-10</sup> <sup>a</sup>	
CO			3.6 ± 0.4 × 10 <sup>-13</sup> <sup>b</sup>
NO	4.8 ± 0.8 × 10 <sup>-11</sup> <sup>c</sup> 7.3 ± 2.2 × 10 <sup>-11</sup> <sup>f</sup> 1.1 × 10 <sup>-10</sup> <sup>e</sup>	1.1 ± 0.1 × 10 <sup>-10</sup> <sup>a</sup>	3.8 ± 0.6 × 10 <sup>-12</sup> <sup>b</sup>
CO <sub>2</sub>	< 10 <sup>-15</sup> <sup>e</sup> < 10 <sup>-14</sup> <sup>f</sup>	1.1 ± 0.1 × 10 <sup>-11</sup> <sup>a</sup>	6.0 ± 0.5 × 10 <sup>-12</sup> <sup>b</sup>
N <sub>2</sub> O	1.3 ± 0.3 × 10 <sup>-11</sup> <sup>c</sup> 2.5 ± 1.6 × 10 <sup>-11</sup> <sup>f</sup>	1.9 ± 0.2 × 10 <sup>-10</sup> <sup>d</sup>	5.8 ± 0.8 × 10 <sup>-12</sup> <sup>b</sup>
CH <sub>4</sub>	< 2 × 10 <sup>-15</sup> <sup>f</sup> < 5 × 10 <sup>-15</sup> <sup>g</sup> < 6 × 10 <sup>-15</sup> <sup>h</sup>	< 10 <sup>-14</sup> <sup>a</sup>	
CF <sub>4</sub>		2.4 ± 0.3 × 10 <sup>-12</sup> <sup>a</sup>	1.5 ± 0.1 × 10 <sup>-13</sup> <sup>b</sup>
C <sub>2</sub> H <sub>2</sub>	< 6.3 × 10 <sup>-17</sup> <sup>h</sup>	4.9 ± 0.3 × 10 <sup>-10</sup> <sup>a</sup>	2.7 ± 0.4 × 10 <sup>-10</sup> <sup>b</sup>
C <sub>2</sub> H <sub>4</sub>	< 6.3 × 10 <sup>-17</sup> <sup>h</sup>	2.2 ± 0.2 × 10 <sup>-10</sup> <sup>a</sup>	8.3 ± 0.4 × 10 <sup>-12</sup> <sup>b</sup>
SiCl <sub>4</sub>		7.2 ± 1.2 × 10 <sup>-11</sup> <sup>d</sup>	

<sup>a</sup> Data given as  $k_R/\text{cm}^3 \text{ molecule}^{-1} \text{ s}^{-1}$  at 300 K.<sup>b</sup> Ref. 92.<sup>c</sup> Ref. 84.<sup>d</sup> Ref. 85.<sup>e</sup> Ref. 91.<sup>f</sup> Ref. 82.<sup>g</sup> Ref. 81.<sup>h</sup> Ref. 80.

since no product was detected. Recently products have been obtained from the reactions of recoiling sulfur atoms in mixtures of alkanes and H<sub>2</sub>S (108).

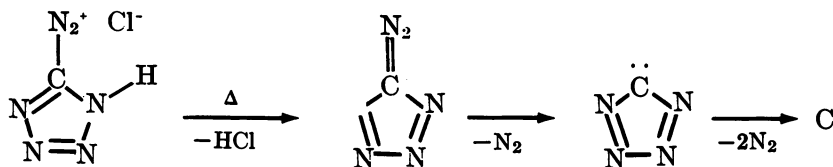


We can expect to see the relative reactivity of various substrates as determined in Husain's kinetic measurements applied to the detection of

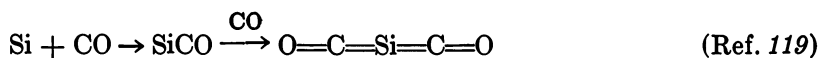
specific states of recoiling polyvalent atoms. The usefulness of the kinetic measurements would be greatly enhanced if one could determine the nature of the reaction products, distinguish between physical processes for the removal of atoms and chemical reactions, and characterize the reactions that occur.

It is likely that the enormous sensitivity of laser spectroscopy (109) will in the near future make possible the detection of reactive intermediates as well as the reactants and products of atomic reactions. It has been estimated that  $10^3$  molecules/cm<sup>3</sup> can be detected by laser absorption spectroscopy under realistic laboratory conditions for a moderately strong electronic transition in the visible region of the spectrum (110). If this sensitivity can be attained, then even the direct detection of recoil species appears to be possible.

**Creation of Metal Vapors by Bulk Element Evaporation.** Another chemical method for the generation of free atoms, the creation of atomic vapors by heating of the bulk element, has been used to generate Group IV atoms as well as a wide variety of metal atoms. The work on carbon using a carbon arc has recently been reviewed by Shevlin (111) together with his strictly chemical method for the generation of carbon atoms (112). Skell has also reviewed his work with the carbon arc (113).



Such limited experiments have been carried out with silicon and germanium vapor, created by electron beam sputtering and simple heating, that the results are given below.



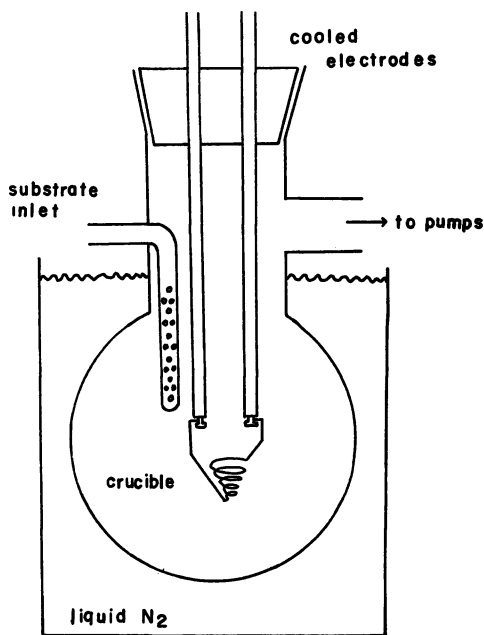
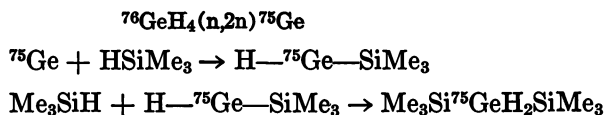


Figure 5. Diagram of Timms "fry-freeze" apparatus used for cocondensation of germanium vapor and trimethylsilane

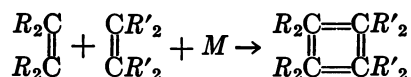
We see insertions into Si—H and O—H bonds and halogen abstraction, as well as two remarkable additions to N<sub>2</sub> and CO. Our germanium atom thermal study was carried out with a simple crucible of alumina deposited on a molybdenum spiral as shown in Figure 5, the by now classical "fry-freeze" technique of Timms (120). The advantage of simple cocondensation of atomic vapors with reactive substrates is that products can be easily isolated. The bis(trimethylsilyl)germane made by cocondensation of germanium vapor and trimethylsilane permitted the unambiguous identification of a recoil reaction product and lent credence to a mechanism consisting of consecutive insertions (121). The reaction of thermally generated germanium atoms with trimethylsilane provides a clear indication that gerylenes can insert into Si—H bonds.



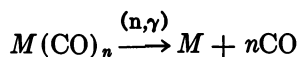
The disadvantage of metal evaporation-cocondensation is that the reaction conditions are not well defined. Reaction may occur in the gas-phase prior to condensation, on the disordered surface immediately upon

condensation, or in the melt after thawing of the frozen cocondensate. Nevertheless, useful information on the addition reactions of carbon atoms and the insertion reactions of silicon and germanium atoms have already complemented recoil studies, and the thermal experiments are being extended. Combinations of metal evaporation techniques with flow systems may provide clean sources of readily detectable quantities of thermal energy polyvalent atoms in the gas phase useful for both kinetic studies and the synthesis of products (122-124). A major advantage of metal evaporation over photochemical and plasma decomposition of molecular precursors is that less unwanted debris in the form of extraneous reactive species are produced when atoms are simply evaporated.

Many kinds of metals have been studied by evaporation-cocondensation (120, 124-126) but thus far, little recoil chemistry has been carried out. The mechanistic interest and commercial importance of olefin metathesis reactions (127) suggests



that many new recoil reaction systems including transition metals and olefins in the gas and liquid phases will be investigated. Only low recoil energies are required, and  $(n,\gamma)$  activation of metal carbonyls is a convenient precursor system.



The products of conventional metal evaporation-cocondensation experiments will provide products that will assist in the interpretation of the recoil experiments.

### ***Conclusion—A Positive View of Polyvalent Atom Recoil Chemistry***

In conclusion, the author would like to reiterate his belief that several factors argue for more rather than less intensive activity in the field of polyvalent atom recoil chemistry. These factors include the sharpening of our perceptions about the problems that face us and about what can be achieved, as well as the availability of new tools to facilitate our work.

One stimulus for future effort is the ability to produce a number of different molecules via recoil reactions—unusual stable molecules as well as reactive intermediates. There is growing interest in labeled molecules both for fundamental mechanistic studies and for biomedical purposes. The finding that polyvalent recoiling atoms undergo quite specific and novel reactions ensures considerable interest in the many atoms whose



recoil chemistry has not yet been investigated. The mutual reinforcement of recoil studies and chemical experiments will continue, as for many polyvalent atoms even their reactions at thermal energies are poorly understood or completely unexplored. This means that new methods for the chemical generation of the atoms and reactive intermediates will go hand in hand with new recoil experiments.

A detailed description of primary reactions of polyvalent recoiling atoms remains an appealing goal to those of us involved in their study. The larger holes in the outer electronic shells of polyvalent, vs. mono- and divalent atoms may well cause differences in the course of reactive collisions. The lower velocity of a heavy recoiling atom, whatever its valency, at a given kinetic energy increases the effective collision time over that for a light atom of the same energy. This lengthening of the time scale for heavy recoil atom collisions may also have a significant effect on the kinds of reactions that can be brought about by a recoiling atom, and this should be of particular importance for polyvalent atoms. For polyvalent recoiling atoms the larger vacancies in outer shells will lead to greater bonding in a collision complex and further extend its lifetime. This suggests that a polyvalent recoiling atom may tend to form loosely bound complexes in which multiple atom transfers and bond redistributions can occur. Such complexes have already been suggested for carbon (128).

A natural area of interest for chemists studying high-energy polyvalent atoms is cosmochemistry. With growing indications that high-energy reactions of carbon and silicon atoms are important processes in the formation of interstellar grains, it can be predicted with confidence that the recoil chemistry of polyvalent atoms will claim the attention of cosmochemists and laboratory astrophysicists (129-133).

Since the necessity for examining reaction sequences initiated by polyvalent recoiling atoms via their end products has been a severe experimental constraint, it may be worthwhile to repeat the prediction that high sensitivity laser absorption spectroscopy will in the near future permit direct detection of reactive intermediates in both chemical and recoil studies of atomic reactions. If this proves to be the case, then an exciting new era will have dawned in which recoil experiments may be able to answer many questions about the dynamics as well as the systematics of polyvalent atomic reactions.

### ***Acknowledgment***

Results obtained by my industrious and able coworkers have been the basis of this chapter: postdoctoral fellows Peter Markusch, Michael Sefcik, Maurizio Speranza, and Siu-Hong Mo; graduate students William Eckelman, Kwang Yul Choo, Robert Conlin, and Rong-juh Hwang;

undergraduates Alan Bock, Carl Levy, James Frost, Dewey Holten, Steven Lockhart, Adam Helfer, Bruce Cohen, and Roger Woods. The Department of Energy and its predecessor agencies have kindly provided financial support of this endeavor. This is technical report COO-1713-92.

### Literature Cited

1. Rowland, F. S. "Molecular Beams and Reaction Kinetics"; Schlier, C., Ed.; Academic: New York, 1970; p. 108.
2. Wolfgang, R. *Prog. React. Kinet.* 1965, 3, 97.
3. Gaspar, P. P.; Markusch, P.; Holten, III, J. D.; Frost, J. J. *J. Phys. Chem.* 1972, 76, 1352.
4. Hwang, R.-J.; Gaspar, P. P. *J. Am. Chem. Soc.* 1978, 100, 6626.
5. Stöcklin, G.; Wolf, A. P. "Chemical Effects of Nuclear Transformations," IAEA, Vienna, 1965; Vol. 1, p. 121.
6. Taylor, K. K.; Ache, H. J.; Wolf, A. P. *J. Phys. Chem.* 1978, 82, 2385.
7. Gaspar, P. P.; Markusch, P. *J. Chem. Soc. Chem. Commun.* 1970, 1331.
8. Tang, Y.-N.; Gennaro, G. P.; Su, Y. Y. *J. Am. Chem. Soc.* 1972, 94, 4355.
9. Zeck, O. F.; Su, Y. Y.; Tang, Y.-N. *J. Chem. Soc. Chem. Commun.* 1975, 156.
10. Zeck, O. F.; Su, Y. Y.; Tang, Y.-N. *J. Am. Chem. Soc.* 1976, 98, 3474.
11. Ferrieri, R. A.; Siefert, E. E.; Griffin, M. J.; Zeck, O. F.; Tang, Y.-N. *J. Chem. Soc. Chem. Commun.* 1977, 6.
12. Timms, P. L.; Ehlert, T. C.; Margrave, J. L. *Nature* 1965, 207, 189.
13. Timms, P. L.; Kent, R. A.; Ehlert, T. C.; Margrave, J. L. *J. Am. Chem. Soc.* 1965, 87, 2824.
14. Gaspar, P. P.; Herold, B. J. "Carbene Chemistry," 2nd ed.; Kirmse, W., Ed.; Academic: New York, 1971; p. 504.
15. Thompson, J. C.; Margrave, J. L. *Inorg. Chem.* 1972, 11, 931.
16. Gordon, B.; Steinberg, A.; Wolf, A. P. *Brookhaven Nat. Lab. Ann. Rep.* 1958, 523 (AS-12), 51.
17. Stöcklin, G.; Wolf, A. P. *J. Am. Chem. Soc.* 1963, 85, 229.
18. MacKay, C.; Wolfgang, R. *J. Am. Chem. Soc.* 1961, 83, 2399.
19. Shevlin, P. B.; Wolf, A. P. *J. Am. Chem. Soc.* 1966, 88, 4735.
20. Taylor, K. K.; Ache, H. J.; Wolf, A. P. *J. Am. Chem. Soc.* 1976, 98, 7176.
21. Gaspar, P. P.; Bock, S. A.; Eckelman, W. C. *J. Am. Chem. Soc.* 1968, 90, 6914.
22. White, D. G.; Rochow, E. G. *J. Am. Chem. Soc.* 1954, 76, 3897.
23. Choo, K. Y.; Gaspar, P. P. *J. Am. Chem. Soc.* 1974, 96, 1284.
24. Henis, J. M. S.; Stewart, G. W.; Tripodi, M. K.; Gaspar, P. P. *J. Chem. Phys.* 1972, 57, 389.
25. Stewart, G. W.; Henis, J. M. M.; Gaspar, P. P. *J. Chem. Phys.* 1973, 58, 890.
26. Holten, III, J. D.; Mo, S.-H.; Gaspar, P. P., unpublished data.
27. Wulff, W. D.; Goure, W. F.; Barton, T. J. *J. Am. Chem. Soc.* 1978, 100, 6236.
28. Chen, Y.-S.; Cohen, B. H.; Gaspar, P. P. *J. Organometal. Chem.*, in press.
29. Goodloe, G. W.; Austin, E. R.; Lampe, F. W. *J. Am. Chem. Soc.* 1979, 101, 3472.
30. Mayer, T. M.; Lampe, F. W. *J. Phys. Chem.* 1974, 78, 2422.
31. Goodloe, G. W.; Lampe, F. W. *J. Am. Chem. Soc.* 1979, 101, 6028.
32. Tang, Y.-N., personal communication.
33. Paquin, D. P.; Ring, M. A. *J. Am. Chem. Soc.* 1977, 99, 1793.
34. Mackay, C.; Pandow, M.; Polak, P.; Wolfgang, R. "Chemical Effects of Nuclear Transformations"; IAEA: Vienna, 1961; Vol. 2, p. 17.
35. Peterson, Jr., R. F.; Wolfgang, R. *Adv. High Temp. Chem.* 1971, 4, 43.

36. Taylor, K. K.; Ache, H. J.; Wolf, A. P. *J. Am. Chem. Soc.* **1975**, *97*, 5970.
37. Finn, R. D.; Ache, H. J.; Wolf, A. P. *J. Phys. Chem.* **1970**, *74*, 3194.
38. Blaxell, O.; Mackay, C.; Wolfgang, R. *J. Am. Chem. Soc.* **1970**, *92*, 50.
39. Gaspar, P. P.; Hwang, R.-J.; Eckelman, W. C. *J. Chem. Soc. Chem. Comm.* **1974**, 242.
40. Gennaro, G. P.; Su, Y.-Y.; Zeck, O. F.; Daniel, S. H.; Tang, Y.-N. *J. Chem. Soc. Chem. Comm.* **1973**, 637.
41. Barton, T. J.; Burns, G. T. *J. Organometal. Chem.* **1979**, *179*, C17.
42. Helfer, A. P.; Mo, S.-H.; Gaspar, P. P., unpublished data.
43. Siefert, E. E.; Loh, K.-L.; Tang, Y.-N. *J. Am. Chem. Soc.* **1980**, *102*, 2285.
44. Dubrin, J.; Mackay, C.; Wolfgang, R. *J. Am. Chem. Soc.* **1964**, *86*, 959.
45. Marshall, M.; Mackay, C.; Wolfgang, R. *J. Am. Chem. Soc.* **1964**, *86*, 4741.
46. Doering, W. v. E.; LaFlamme, P. M. *Tetrahedron* **1958**, *2*, 75.
47. Moore, W. R.; Ward, A. R. *J. Org. Chem.* **1960**, *25*, 2073.
48. Jones, W. M.; Grasley, M. H.; Brey, Jr., W. S. *J. Am. Chem. Soc.* **1963**, *85*, 2754.
49. Ferrieri, R. A.; Tang, Y.-N.; Wolf, A. P. "Abstract NUCL84," *178th Nat. Meet., ACS, Sept. 1979*.
50. Husain, D.; Kirsch, L. J. *Trans. Faraday Soc.* **1971**, *67*, 3166.
51. Dubrin, J.; Mackay, C.; Pandow, M.; Wolfgang, R. *J. Inorg. Nucl. Chem.* **1964**, *26*, 2113.
52. MacKay, C. "Carbenes;" Moss, R. A.; Jones, Jr., M., Eds.; John Wiley & Sons: New York, 1975; p. 1.
53. Mackay, C.; Wolfgang, R. *Radiochim. Acta* **1962**, *1*, 42.
54. Skell, P. S.; Plonka, J. H.; Engel, R. R. *J. Am. Chem. Soc.* **1967**, *89*, 1748.
55. Skell, P. S.; Harris, R. F. *J. Am. Chem. Soc.* **1969**, *91*, 4440.
56. Skell, P. S.; Plonka, J. H. *J. Am. Chem. Soc.* **1970**, *92*, 836.
57. Skell, P. S.; Plonka, J. H. *J. Am. Chem. Soc.* **1970**, *92*, 2160.
58. Plonka, J. H.; Skell, P. S. *J. Chem. Soc. Chem. Comm.* **1970**, 1108.
59. Skell, P. S.; Plonka, J. H.; Klabunde, K. J. *Chem. Comm.* **1970**, 1109.
60. Plonka, J. H.; Skell, P. S. *Tetrahedron Lett.* **1970**, 4557.
61. Skell, P. S.; Plonka, J. H. *Tetrahedron* **1972**, *28*, 3571.
62. Skell, P. S.; Klabunde, K. J.; Plonka, J. H.; Roberts, J. S.; Williams-Smith, D. L. *J. Am. Chem. Soc.* **1973**, *95*, 1547.
63. Kammula, S.; Shevlin, P. B. *J. Am. Chem. Soc.* **1974**, *94*, 7830.
64. Parker, R. H.; Shevlin, P. B. *Tetrahedron Lett.* **1975**, 2167.
65. Dyer, S. F.; Kammula, S.; Shevlin, P. B. *J. Am. Chem. Soc.* **1977**, *99*, 8104.
66. Milligan, D. E.; Jacox, M. E. *J. Chem. Phys.* **1966**, *44*, 2850.
67. Braun, W.; Bass, A. M.; Davis, D. D.; Simmons, J. D. *Proc. R. Soc. London, Ser. A* **1969**, *312*, 417.
68. Zeck, O. F.; Gennaro, G. P.; Tang, Y.-N. *J. Am. Chem. Soc.* **1975**, *97*, 4498.
69. Donovan, R. J.; Husain, D. *Chem. Rev.* **1970**, *70*, 489.
70. Husain, D. *Ber. Bunsenges. Phys. Chem.* **1977**, *81*, 168.
71. Gaspar, P. P.; Welch, M. J. "Chemical Effects of Nuclear Transformations in Inorganic Systems;" Harbottle, G.; Maddock, A. G., Eds.; North-Holland: Amsterdam, 1979; p. 75.
72. Wolf, A. P.; Schueler, P.; Pettijohn, R. P.; To, K.-C.; Rack, E. P. *J. Phys. Chem.* **1979**, *83*, 1237.
73. Blint, R. J.; Newton, M. D. *Chem. Phys. Lett.* **1975**, *32*, 178.
74. Husain, D.; Norris, P. E. *Faraday Discuss. Chem. Soc.* **1979**, *67*, 273.
75. Dewar, M. J. S.; Haselbach, E.; Shanshal, M. *J. Am. Chem. Soc.* **1970**, *92*, 3505.
76. Figuera, J. M.; Shevlin, P. B.; Worley, S. D. *J. Am. Chem. Soc.* **1976**, *98*, 3820.
77. Shevlin, P. B.; Kammula, S. *J. Am. Chem. Soc.* **1977**, *99*, 2627.

78. Mackay, C.; Wolfgang, R. *Science* 1965, 148, 899.
79. Meaburn, G. M.; Perner, D. *Nature* 1966, 212, 1042.
80. Martinotti, F. F.; Welch, M. J.; Wolf, A. P. *J. Chem. Soc. Chem. Comm.* 1968, 1, 15.
81. Braun, W.; Bass, A. M.; Davis, D. D.; Simmons, J. D. *Proc. R. Soc. London, Ser. A* 1969, 312, 417.
82. Husain, D.; Kirsch, L. J. *Trans. Faraday Soc.* 1971, 67, 2025.
83. *Ibid.*, 2886.
84. Husain, D.; Young, A. N. *J. Chem. Soc. Faraday Trans. 2* 1975, 71, 525.
85. Husain, D.; Norris, P. E. *J. Chem. Soc. Faraday Trans. 2* 1978, 74, 93.
86. *Ibid.*, 106.
87. *Ibid.*, 335.
88. *Ibid.*, 1483.
89. Husain, D.; Norris, P. E. *Chem. Phys. Lett.* 1977, 51, 206.
90. *Ibid.*, 1978, 53, 474.
91. Brown, A.; Husain, D. *Can. J. Chem.* 1976, 54, 4.
92. Chowdhury, M. A.; Husain, D. *J. Photochem.* 1977, 7, 41.
93. *Ibid.*, 1979, 10, 277.
94. Chowdhury, M. A.; Husain, D. *J. Chem. Soc. Faraday Trans. 2* 1977, 73, 1805.
95. Noxon, J. *J. Chem. Phys.* 1962, 36, 926.
96. Morse, F. A.; Kaufman, F. *J. Chem. Phys.* 1965, 42, 1785.
97. Black, G.; Slinger, T. G.; St. John, G. A.; Young, R. A. *J. Chem. Phys.* 1969, 51, 116.
98. Husain, D.; Mitra, S. K.; Young, A. N. *J. Chem. Soc. Faraday Trans. 2* 1974, 70, 1721.
99. Acuna, A. U.; Husain, D.; Wiesenfeld, J. R. *J. Chem. Phys.* 1973, 58, 494.
100. *Ibid.*, 5272.
101. Acuna, A. U.; Husain, D. *J. Chem. Soc. Faraday Trans. 2* 1973, 69, 585.
102. Husain, D.; Norris, P. E. *J. Chem. Soc. Faraday Trans. 2* 1977, 73, 415.
103. *Ibid.*, 1973, 69, 1107.
104. Husain, D.; Slater, N. K. H. *J. Chem. Soc. Faraday Trans. 2* 1978, 74, 1627.
105. Donovan, R. J.; Kirsch, L. J.; Husain, D. *Trans. Faraday Soc.* 1970, 66, 774.
106. Donovan, R. J.; Husain, D.; Fair, R. W.; Strausz, O. P.; Gunning, A. E. *Trans. Faraday Soc.* 1970, 66, 1635.
107. Kremer, L. N.; Spicer, L. D. *J. Am. Chem. Soc.* 1975, 97, 5021.
108. Lindner, L.; Brinkman, G. A.; Veenboer, J. T. *Radiochim. Acta* 1980, 27, 95.
109. Shimoda, K. *Appl. Phys.* 1973, 1, 77.
110. Smith, W. H., private communication.
111. Shevlin, P. B. In "Reactive Intermediates in Organic Chemistry"; Abramovitch, R., Ed.; Plenum: New York, in press.
112. Shevlin, P. B. *J. Am. Chem. Soc.* 1972, 94, 1379.
113. Skell, P. S.; Havel, J. J.; McGlinchey, M. J. *Acc. Chem. Res.* 1973, 6, 97.
114. Skell, P. S.; Owen, P. W. *J. Am. Chem. Soc.* 1967, 89, 3933.
115. Owen, P. W.; Skell, P. S. *Tetrahedron Lett.* 1972, 1807.
116. Skell, P. S.; Owen, P. W. *J. Am. Chem. Soc.* 1972, 94, 5434.
117. McGlinchey, M. J.; Tan, T.-S. *Inorg. Chem.* 1975, 14, 1209.
118. Conlin, R. T.; Lockhart, S. H.; Gaspar, P. P. *J. Chem. Soc. Chem. Comm.* 1975, 825.
119. Lembke, R. R.; Ferrante, R. F.; Weltner, Jr., W. *J. Am. Chem. Soc.* 1977, 99, 416.
120. Timms, P. L. *Adv. Inorg. Chem. Radiochem.* 1972, 14, 121.
121. Cohen, B. H.; Woods, R. P.; Gaspar, P. P., unpublished data.
122. West, J. B.; Bradford, Jr., R. S.; Eversole, J. D.; Jones, C. R. *Rev. Sci. Instrum.* 1975, 46, 164.

123. Linton, C.; Capelle, G. A. *J. Mol. Spectrosc.* **1977**, *66*, 62.
124. Fontijn, A.; Felder, W. "Reactive Intermediates in the Gas Phase"; Setser, D. W., Ed.; Academic: New York, 1979; p. 59.
125. *Angew. Chem. Int. Ed. Engl.* **1975**, *14*, 193-308.
126. Klabunde, K. J. *Acc. Chem. Res.* **1975**, *8*, 393.
127. Leconte, M.; Basset, J. M. *J. Am. Chem. Soc.* **1979**, *101*, 7296.
128. Welch, M. J.; Wolf, A. P. *J. Chem. Soc. (D)* **1968**, 117.
129. Watson, W. D. *Rev. Mod. Phys.* **1976**, *48*, 513.
130. Dalgarno, A.; Black, J. H. *Rep. Prog. Phys.* **1976**, *39*, 573.
131. Huntress, W. T. *Chem. Soc. Rev.* **1977**, *6*, 295.
132. Zuckerman, B. *Nature* **1977**, *268*, 491.
133. Sagan, C.; Khare, B. N. *Nature* **1979**, *277*, 102.
134. Mo, S. H.; Gaspar, P. P., unpublished data.

RECEIVED September 4, 1980.

# Chemical Mechanistic Studies Based on the Radioactive Decay of Multitritiated Molecules

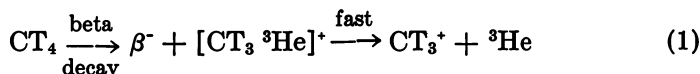
FULVIO CACACE

University of Rome, 00100 Rome, Italy

*Recent mechanistic applications of the decay technique, which uses the spontaneous  $\beta^-$  decay of multitritiated precursors to generate unsolvated cations in gaseous and condensed systems, are reviewed. The survey includes structural investigations, such as the demonstration of the existence of cyclic  $C_4H_7^+$  ions as stable species in the dilute gas state. Other applications concern the automerization of labeled phenylium ions from the decay of  $p-C_6H_4T_2$  in gaseous and liquid systems and the study of the reactivity of methyl cations from the decay of  $CT_4$  with a number of substrates, including n-type and  $\pi$ -type nucleophiles, for example carbon monoxide, arenes, and halobenzenes in the gaseous and liquid state.*

The radioactive decay of covalently bound T atoms contained in multitritiated molecules provides a unique source of labeled organic cations that has been extensively exploited in mechanistic studies carried out in a variety of systems, ranging from the dilute gas state to dense gases and to liquids (1-5).

The principles of the now well-established "decay technique" can be outlined as follows. Consider the radioactive decay of one of the atoms of a multitritiated molecule, e.g. methane- $T_4$ :



Following emission of the  $\beta^-$  particle, the T atom is suddenly converted into a  $^3\text{He}$  ion, imparting a positive charge to the whole primary decay fragment. Furthermore, no stable bond is formed between C and

0065-2393/81/0197-0033\$05.00/0  
© 1981 American Chemical Society

He (6), and the  $^3\text{He}$  atom is consequently lost by the primary decay fragment in a time comparable to the period of C— $^3\text{He}$  bond vibration. It should be noted that, due to the considerably higher IP of He with respect to those of all organic radicals,  $^3\text{He}$  is lost as a neutral atom, leaving the positive charge on the organic moiety. The overall result of the chain of events triggered by the decay is the formation of an organic cation, for example,  $\text{CT}_3^+$ , that can survive as such or undergo further dissociation.

The decay-induced fragmentation pattern of a number of representative organic molecules has been determined with appropriate mass spectrometric techniques (7), showing that, in most cases, the daughter organic cation escapes further dissociation, for example, the methyl cation from Equation 1 is obtained with a 82% yield, being formed in its ground electronic state with little or no vibrational excitation.

The theoretical analyses of the chemical consequences of the  $\beta^-$  decay of T fully concur (6, 7) in the conclusions.

It is worth mentioning that the cations from the decay are entirely free, in that they are not associated to any counterion, their positive charge being balanced by a far removed electron. Owing to the nuclear nature of the process, their formation is entirely insensitive to environmental factors, the process being equally effective in gaseous, liquid, or solid systems.

Finally, the decay ions are formed as unsolvated species (strictly, in the same solvation state as their neutral precursors) and in most cases their reactions occur well before an organized solvation sphere had time to assemble.

The above considerations justify the mechanistic interest attached to the decay technique as a unique tool for introducing organic cations, well defined from the structural and the energetic standpoint, into any system under investigation. In fact, owing to the presence of undecayed T atoms within the daughter ions, their reactions can be followed and the final products identified by sensitive and specific radiometric techniques, in particular radio chromatography.

In this way, ion-molecule reactions can be studied in a variety of environments, from very dilute gases to condensed systems, with the usual techniques of physical organic chemistry, including in the first place the actual isolation of the products, which provides the structural insight vital in mechanistic studies, yet generally precluded to the other major technique for the study of ion-molecule interactions, namely, mass spectrometry.

In the following paragraphs, after a brief account of recent experimental developments of the decay technique, a number of current applications to structural and mechanistic problems of organic ionic chemistry will be outlined.

**Recent Experimental Advances**

The preparation, purification, characterization, and even the storage of organic compounds containing more than one T atom in the same molecule has invariably represented a major experimental challenge in the application of the decay technique. The nature of the problem becomes immediately apparent if one takes into account the enormous specific activity of multitritiated substances in the pure state, for example, 120,000 Ci per mol for CT<sub>4</sub>.

Recently, the application of more advanced synthetic procedures and the availability of new analytical techniques, in particular tritium NMR spectroscopy, have allowed the preparation of a number of mechanistically useful multitritiated species.

Thus, cyclobutane-T<sub>x</sub> ( $x \leq 5$ ) has been obtained from the reaction of cyclobutene with excess T<sub>2</sub> over Pt black, that promotes extensive H/T exchange in addition to the saturation of the double bond (8).

The isotopic composition of the reaction product, purified by preparative GLC, was determined by high-resolution mass spectrometry and corresponded to 10.5 ± 1.0 mol% c-C<sub>4</sub>H<sub>7</sub>T, 12.8 mol% c-C<sub>4</sub>H<sub>6</sub>T<sub>2</sub>, 26.6 mol% c-C<sub>4</sub>H<sub>5</sub>T<sub>3</sub>, 28.9 mol% c-C<sub>4</sub>H<sub>4</sub>T<sub>4</sub>, 16.2 mol% c-C<sub>4</sub>H<sub>3</sub>T<sub>5</sub>, and <5 mol% of more heavily tritiated cyclobutanes.

Owing to the equivalence of all molecular positions in cyclobutane, the nonhomogeneous isotopic composition of the sample causes no problems in its mechanistic applications.

The situation is different for multitritiated propane, obtained from the H/T exchange of C<sub>3</sub>H<sub>8</sub> with excess T<sub>2</sub> over a Ni catalyst (9). The isotopic composition of a sample purified by preparative GLC was determined by mass spectrometry and corresponded to 16 mol% C<sub>3</sub>H<sub>8</sub>, 13 mol% C<sub>3</sub>H<sub>7</sub>T, 25 mol% C<sub>3</sub>H<sub>6</sub>T<sub>2</sub>, 29 mol% C<sub>3</sub>H<sub>5</sub>T<sub>3</sub>, 12 mol% C<sub>3</sub>H<sub>4</sub>T<sub>4</sub>, and about 5 mol% of more highly tritiated propanes. However, as the mechanistically significant information concerning the T distribution among the primary and the secondary positions could not be obtained by mass spectrometry, the sample was subjected to <sup>3</sup>H NMR spectrometry, which gave a 2.4 ± 0.3 mean ratio for the T atoms contained, respectively, in the methyl and methylene groups of propane. The recent preparation (10) of multicurie amounts of benzene 1,4-T<sub>2</sub> provides an excellent example of the degree of sophistication reached by the current synthetic procedures and the associated diagnostic techniques. Pure tritiated water, prepared from the oxidation of elemental tritium over copper oxide, was immediately allowed to react with the Grignard reagent.





The crude reaction product purified by preparative GLC was subjected to Fourier-transform tritium NMR spectrometry to evaluate the isotopic composition of the labeled benzene.

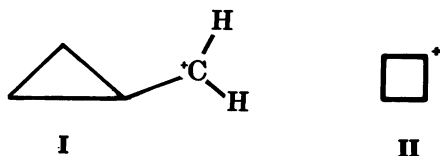
Calculations of the tritium NMR spectra of 1,2-, 1,3-, and 1,4-benzene-T<sub>2</sub>, as well as of C<sub>6</sub>H<sub>5</sub>T, had been previously carried out and were used to interpret the experimental data. The results showed that the radioactive sample was mainly (>95 mol%) composed of an almost equimolecular (44:56) mixture of C<sub>6</sub>H<sub>5</sub>T and 1,4-C<sub>6</sub>H<sub>4</sub>T<sub>2</sub>, free from appreciable amounts of isomeric products.

The high yield of C<sub>6</sub>H<sub>5</sub>T underlines the difficulty of eliminating minute traces of humidity from the reaction system, especially when tritiated water is not used in a large excess and highly hygroscopic reagents are involved.

Once a multilabeled compound containing more than two T atoms in the same molecule has been synthesized, it can be used for the preparation of other multitritiated molecules by simply allowing it to decay in the presence of a suitable nucleophile (11). Consider, for example, CT<sub>4</sub> stored in large excess of a gaseous hydrogen halide (HX), or of methanol, ammonia, or benzene. The CT<sub>3</sub><sup>+</sup> cation from Equation 1 will react with the gaseous nucleophile, yielding respectively CT<sub>3</sub>X, CT<sub>3</sub>OH, CT<sub>3</sub>NH<sub>2</sub>, or C<sub>6</sub>H<sub>5</sub>CT<sub>3</sub>. At first sight, the low rate of T decay (ca. 0.46% per month) makes its application to preparative purposes particularly unattractive. However, a closer examination reveals that, given the high CT<sub>4</sub> activity currently available, this admittedly lazy synthetic approach can provide quite respectable activities of multitritiated products, largely sufficient for most mechanistic applications, within quite reasonable periods of time. For instance, since the CT<sub>3</sub><sup>+</sup> decay ions contain approximately three times the decayed activity, storage of 1 Ci of CT<sub>4</sub> for 30 days will produce CT<sub>3</sub><sup>+</sup> cations containing the considerable activity of approximately 14 mCi. The method has been applied to the preparation of compounds such as CT<sub>3</sub>OH, CT<sub>3</sub>Br, and C<sub>2</sub>H<sub>2</sub>T<sub>3</sub>Br (11).

### *Structure of Gaseous Cations*

An example of the application of the decay technique to a structural problem is provided by the demonstration of the existence of cyclic C<sub>4</sub>H<sub>7</sub><sup>+</sup> isomers, namely, the cyclobutyl and the cyclopropylcarbiny cations, as stable species in the dilute gas state (12-15). Theoretical approaches led to somewhat conflicting conclusions, reliable STO-3G calculations showing that the cyclopropylcarbiny ion in the bisected configuration (I)

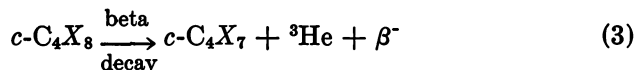


is the most stable species, to which other ones, including the cyclobutyl ion (II), collapse immediately, without activation energy. Mass spectrometry does not provide significant evidence on the specific problem. Indeed,  $C_4H_7^+$  ions had long been detected, but owing to the lack of structural discrimination their structure (cyclic or open), could be never substantiated by mass spectrometry.

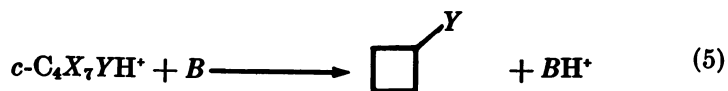
To apply the decay technique, the multitritiated cyclobutane, prepared as described in the previous section, was allowed to decay for several months in gaseous systems containing, as the major component, a suitable nucleophile, such as  $H_2O$  or  $NH_3$ , as illustrated in Table I.

Preliminary ICR studies (16) on the decay of monotritiated cyclobutane had shown that  $C_4H_7^+$  ions (of unknown structure) are formed in over 85% of the decays, and survive undissociated for at least  $10^{-5}$  s.

Consequently, isolation of cyclic tritiated products from the decay of multitritiated cyclobutane,  $c-C_4X_8$  ( $X = H, T$ ), in gaseous water and ammonia (Table I) can be reasonably traced only to the condensation of cyclic cations with the nucleophile  $HY$  ( $Y = OH$  or  $NH_2$ )

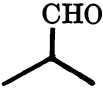

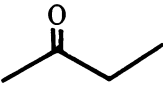


followed by proton transfer from the cyclic onium ion to a gaseous base, B, for example,



From the above considerations, it follows that the observed formation of cyclobutanol (cyclobutylamine) and cyclopropylcarbinol (cyclopropylcarbinylamine) requires that cyclobutyl and cyclopropylcarbinyl cations, or at least some cyclic precursor of these ions, such as a bicyclobutonium ion, must exist in the dilute gas state at least for the time necessary to encounter a molecule of nucleophile, with lifetimes in excess of  $10^{-9}$  s. Accordingly, cyclic  $C_4H_7^+$  ions must be regarded as fully legitimate ionic intermediates, characterized by significant minima on the  $C_4H_7^+$

**Table I. Relative Yields of the Products from the Gas-Phase**

System Composition (Torr)		Relative Yields <sup>b</sup> of Products (%)		
NH <sub>3</sub>	H <sub>2</sub> O			
400	—	n.d. <sup>a</sup>	n.d.	n.d.
2	19	33.3	36.6	0.9
—	25	6.8	26.5	19.3
—	6	44.4	23.6	15.4

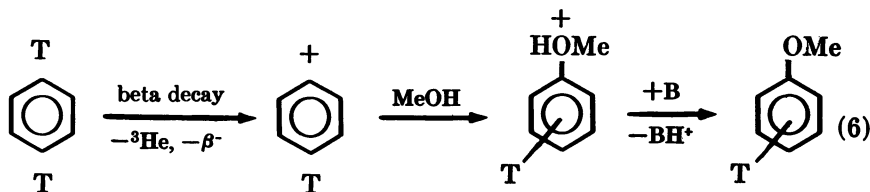
<sup>a</sup> Each 250-mL pyrex bulb contained ca. 10  $\mu$ Ci of *c*-C<sub>4</sub>X<sub>8</sub>.

<sup>b</sup> Ratio of the activity found in each product to the total activity of the products identified. The amines were purified to constant specific activity over a 4-m tricresyl phosphate column at 70°C, and a 4-m diisododecyl phthalate column at 80°C. The alcohols and the other oxygenated products were purified over a 10-m  $\beta,\beta'$ -oxydipropionitrile column at 80°C, and a 8-m diethyleneglycol adipate column at 100°C. Owing

potential surface. These conclusions agree with theoretical results as to the stability of the cyclopropylcarbinyl ion (I), but do not support the alleged lack of stability of other cyclic C<sub>4</sub>H<sub>7</sub> ions (15).

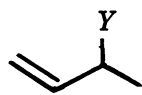
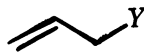
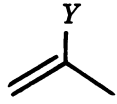

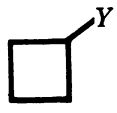

### Degenerate Rearrangement of Gaseous Ions

An interesting mechanistic application of the decay technique has been recently reported (17), concerning the automerization of gaseous phenylium ions. Benzene-1,4-T<sub>2</sub> was allowed to decay dissolved in liquid methanol, or in gaseous methanol, at 18 Torr, giving a high yield of tritiated anisole, as shown in Table II.



Measurement of the residual radioactivity of the product after gradual substitution of the ring H atoms with inactive groups, made it possible to determine the T distribution within the labeled anisole.

**Reactions of  $C_4X_7^+$  Decay Ions with Water and Ammonia<sup>o</sup>***Relative Yields<sup>b</sup> of Products (%)*

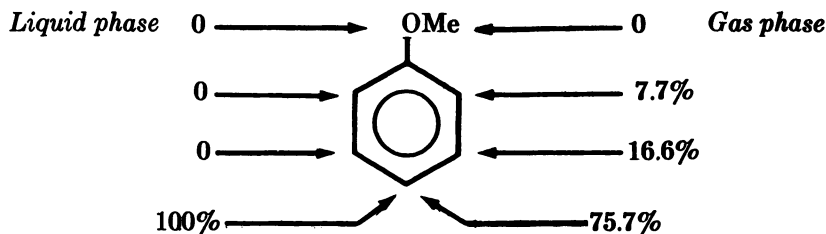
					
—	—	28.8 <sup>d</sup>	—	35.5 <sup>d</sup>	35.7 <sup>d</sup>
7.5 <sup>c</sup>	4.1 <sup>c</sup>	3.6 <sup>c</sup>	4.3 <sup>c</sup>	5.8 <sup>c</sup>	4.0 <sup>c</sup>
9.7 <sup>c</sup>	11.0 <sup>c</sup>	7.1 <sup>c</sup>	4.9 <sup>c</sup>	5.3 <sup>c</sup>	9.3 <sup>c</sup>
2.0 <sup>c</sup>	1.8 <sup>c</sup>	1.8 <sup>c</sup>	2.4 <sup>c</sup>	4.3 <sup>c</sup>	3.4 <sup>c</sup>

to the composition of the systems, and to the purification techniques used, the yields refer only to the T atoms contained in stable positions, without any contribution from the T content of  $-OH$  and  $-NH_2$  groups.

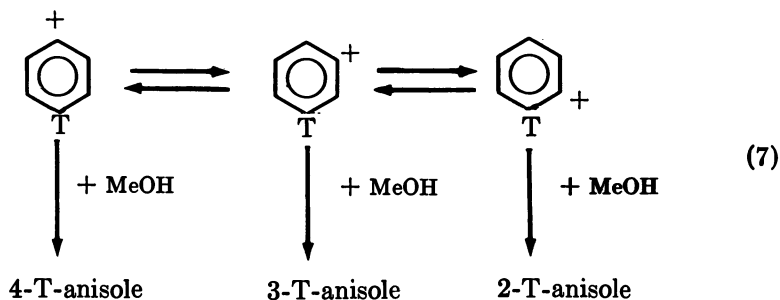
<sup>o</sup> Below detection limits, corresponding to a relative yield under 0.5%.

<sup>d</sup>  $Y = NH_2$ .

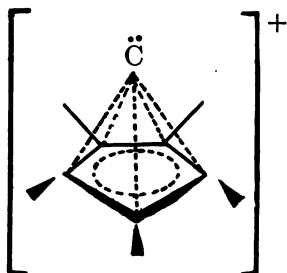
<sup>c</sup>  $Y = OH$ .



The label migration, observed only in the product from the gas-phase decay, provides the first experimental evidence for a degenerate rearrangement of the gaseous phenylium cation.



The complete retention of the original T position in the product from the liquid-phase reaction indicates that automerization is slow in comparison with the collision frequency in the condensed phase, in agreement with theoretical estimates (18) of the activation energy for Equation 7, ranging from 44 to 77 kcal mol<sup>-1</sup>. While no direct information is provided by the decay experiments as to the specific mechanism of automerization (H vs. CH-group migration), the results nevertheless exclude any significant intervention of the nonclassical carbene structure

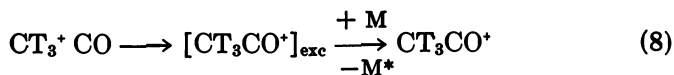


that would require an uniform distribution of T in all positions of the phenilium ion following its rearrangement.

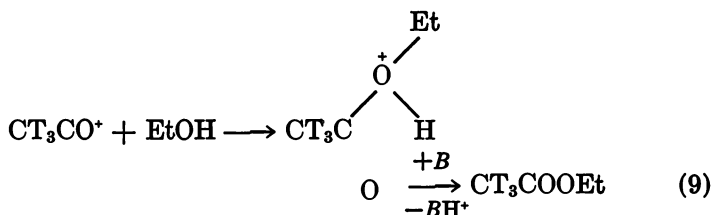
### *Gas-Phase Reactivity of Free Methyl Cations*

Equation 1, a convenient source of free, unsolvated methyl ions, has been exploited to study the gas-phase reactivity of this powerful electrophile, almost inaccessible to other techniques.

Reaction of CT<sub>3</sub><sup>+</sup> with carbon monoxide leads to formation of thermal acetylium ions (19) (Equation 8) whose attack to ethanol and benzene



yields the products listed in Table III. In contrast with the efficient acetylation of ethanol



**Table II. Radioactive Product Distribution from Phenylum-Ion Condensation with Methanol ( $T = 25^{\circ}\text{C}$ )<sup>a</sup>**

<i>System Composition</i> <sup>b</sup>	<i>Absolute Yields of Radioactive Products (%)</i>		
	<i>Anisole</i>	<i>Others</i> <sup>c</sup>	<i>Total</i> <sup>d</sup>
Liquid $\text{CH}_3\text{OH}$ saturated with $\text{O}_2$	64.7	26.8	91.5
Gaseous $\text{CH}_3\text{OH}$ (18 Torr) + $\text{O}_3$ (4 Torr)	44.9	23.9	68.8

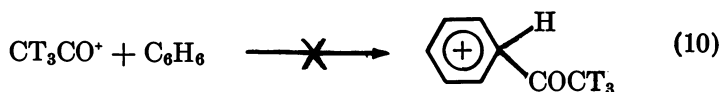
<sup>a</sup> Product analyses carried out by radio gas chromatography and liquid scintillation counting. Standard deviation of data ca. 10%.

<sup>b</sup> The liquid samples were stored in the absence of vapors, the gaseous ones in sealed vials.

<sup>c</sup> Aromatic condensation products.

<sup>d</sup> Low-boiling fragmentation products account for the residual activity.

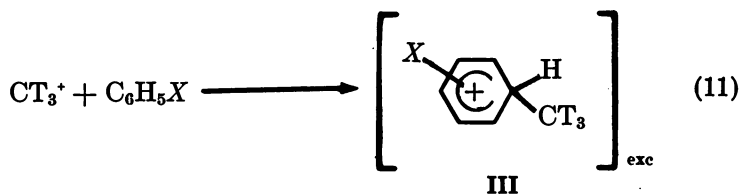
no tritiated acetophenone was obtained.



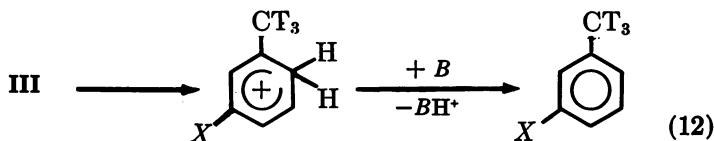
This result, confirmed by independent radiolytic and mass spectrometric evidence, is consistent with the endothermic nature of Equation 10, which in turn must be traced to the very mild electrophilic character of the acetylum ion.

Free methyl ions from Equation 1 react efficiently in the gas phase with halobenzenes, as shown in Tables IV and V, which summarize the nature, the yields, and the isomeric composition of the products from the  $\text{CT}_3^+$  attack to  $\text{C}_6\text{H}_5\text{X}$  ( $X = \text{F}, \text{Cl}, \text{Br}$ ), both neat and in competition with toluene (20).

The mechanistic picture is dominated by the high exothermicity ( $\Delta H^\circ = -85 \text{ kcal mol}^{-1}$ ) of the initial condensation step (Equation 11)

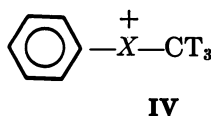


forming excited haloarenium ions, which can either undergo collisional stabilization or isomerization to a more stable structure, for example, Equation 12, before deprotonation to halotoluenes. An alternative reaction



pathway involves H scrambling between the sidechain and the ring, followed by loss of the methyl group, eventually yielding a tritiated halo-benzene.

Intervention of the  $\text{CT}_3^+$  attack to the *n*-donor substituent to give a methylphenyl halonium ion



has been demonstrated by kinetic evidence to increase in the order  $\text{Br} > \text{Cl} > \text{F}$ . The intermediate (IV) reacts as a selective methylating reagent for toluene, and its formation is suggested, among other things, by isolation of tritiated methyl halides.

A related research concerns the competition of the *n*-type and  $\sigma$ -type nucleophilic centers of  $\text{CH}_3\text{F}$  for gaseous  $\text{CT}_3^+$  ions (21).

When  $\text{CT}_4$  is allowed to decay for several months in gaseous  $\text{CH}_3\text{F}$  at 660 Torr, tritiated methyl fluoride is the only product detectable by radio GLC, with a 68% yield. Its formation has been traced to formation of a dimethylhalonium ion, following electrophilic attack to the *n*-center of the substrate (Equation 13) while the absence of labeled ethyl

**Table IV. Tritiated Products from the Gas-Phase Reactions of  $\text{CT}_3^+$**

Substrate Pressure* (Torr)		Relative Activity of Products <sup>b</sup> (%)		
		Methyl Halide	Benzene	Toluene
X = F	100	≤ 0.1	0.7	
	400	0.3	0.9	
X = Cl	30	3.2	2.8	0.8
	100	2.9	2.9	0.3
X = Br	30	3.3	2.2	11.8
	90	3.3	3.1	10.1

\*The system contained, besides the substrate, 2 Torr  $\text{O}_2$  and 0.2 Torr  $\text{CH}_4$  with tracer concentrations of  $\text{CT}_4$  in a 300-mL vessel.

<sup>b</sup>See the text for the absolute yields. The reported values are referred to the total recovered activity = 100 and represent the average of at least three independent

**Table III. Products Yield in the Gas-Phase Reactions of Decay-Formed  $CT_3CO^+$  Ions**

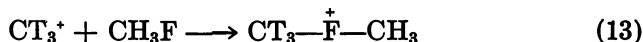
<i>System Composition (Torr)</i>	<i>Products Activity<sup>a, b</sup> (%)</i>
Co, 720	EtOAc, 90.6
EtOH, 9.8	MeOAc, 5.2
Methane, 0.19	EtOH, 2.4
	Unknowns, 2.0
CO, 720	Acetophenone, n.d. <sup>c</sup>
Benzene, 3.0	Benzene, 80.4
Methane, 0.19	Toluene, 8.2
	MeOAc, 5.6
	Unknowns, 5.8

<sup>a</sup> Standard deviation of data, ca. 10%.

<sup>b</sup> The total activity recovered in the products accounts for 35% of the theoretical yield in the case of EtOH and for 15% in the case of  $C_6H_6$ .

<sup>c</sup> This yield is not significant owing to labile hydrogen atoms exchange with GC columns.

<sup>d</sup> n.d. = not detectable.



fluoride among the products has been taken as an indication that the gaseous methyl cation fails to react with the methyl group of methyl fluoride, in contrast with the results obtained in superacid solutions.

### *Reactions of Decay Cations in the Liquid Phase*

**Comparison of Gas-Phase and Liquid-Phase Reactions.** As previously mentioned, the decay cations are formed by a process entirely

### **Decay Ions with the Halobenzenes ( $C_6H_5X$ , $X = F, Cl, Br$ )**

<i>Relative Activity of Products<sup>b</sup> (%)</i>		<i>Isomeric Composition of the Halotoluenes</i>		
<i>Halo- benzene</i>	<i>Halo- toluenes</i>	<i>Ortho</i>	<i>Meta</i>	<i>Para</i>
49.9	49.3	33.6	57.1	9.3
47.3	48.8 <sup>c</sup>	41.2	47.4	11.4
58.4	34.8	26.8	61.9	11.3
56.4	37.4	29.2	58.2	12.6
61.3	21.4	21.9	66.5	11.6
58.6	24.9	24.6	64.6	10.8

analyses. Standard deviation of data ca. 10%.

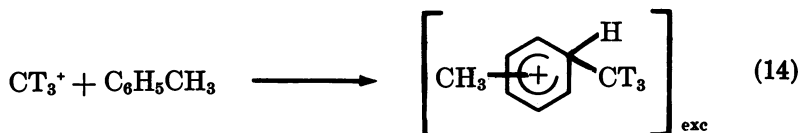
<sup>c</sup> The activity balance is provided by two unknown peaks (2.7%), whose retention times on both GC columns used are greater, yet very close, to that of *p*-fluorotoluene.



insensitive to the environment, in the site formerly occupied by their neutral precursor, and in a time (roughly  $10^{-14}$  s) that is very short on the chemical reactivity scale.

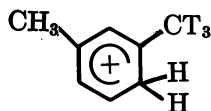
The cation that the nuclear transition brings into being is absolutely free and, when formed in a gaseous system, is unsolvated. Even when the decay occurs in a liquid, highly reactive decay cations, such as methyl or phenylium ions, are as unsolvated as is conceivable for charged species in condensed media. In fact, owing to the very high collision frequency with the molecules of the liquid substrate and to the ability of these ions to react at a rate approaching collision frequency even with relatively weak nucleophiles, the reactive event is likely to occur in a much shorter time than necessary for the formation of an organized solvation sphere, which requires, among other things, rotational relaxation of dipolar molecules in the field of the ion. From the above, it follows that the decay technique provides a unique tool for studying the reactions of genuinely free and unsolvated ions in condensed, as well as in gaseous, systems and, perhaps more significantly, for evaluating the effects of different environments on the reactivity of the same species, a feat unattainable with other techniques. Consider, for a comparison, the enormous differences in the structure, energetics, solvation state, and ion-pairing that exist between nominally identical species, for example, alkyl cations, generated respectively by electron impact in a mass spectrometer and by a solvolytic reaction in a liquid. These considerations have spurred extension of the technique to the liquid phase and especially comparative studies on the behavior of the same ions in liquid and gaseous systems.

An example is provided by the reaction of  $\text{CT}_3^+$  decay ions with gaseous and liquid arenes (22, 23), whose results are summarized in Tables VI and VII. The highly exothermic condensation step, for example, Equation 14,  $\Delta H^\circ = -89 \text{ kcal mol}^{-1}$ , yields excited arenium ions, whose



fate depends on the competition between collisional stabilization and fragmentation, or isomerization.

In the liquid phase, when the ions are formed from the decay of  $\text{CT}_4$  dissolved in the pure arene, collisional stabilization is very effective owing to the large collision frequency, as shown by the relatively low yields of fragmentation products. Isomerization to the thermodynamically most stable arenium ion



V

cannot be excluded, and the isomeric composition of the xylenes formed is probably affected to some degree by its occurrence.

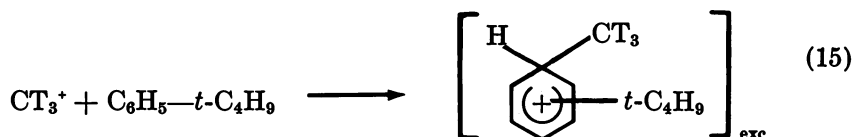
Nevertheless, the liquid-phase methylation displays the typical features of the aromatic substitution by an extremely reactive, unselective electrophile such as  $\text{CT}_3^+$ , which, however, appears capable of discriminating between the aromatic substrates ( $k_T/k_B \sim 2$ ), and gives a predominantly ortho/para orientation, characterized by a para:½ meta ratio of 2.5 in the formation of the xylenes.

The situation is entirely different in the gas phase, especially at low pressures, where collisional deactivation cannot prevent extensive fragmentation and isomerization of the primary, excited intermediates. This is clearly demonstrated by an apparent  $k_T/k_B$  ratio below unity, by the predominant meta orientation, attributable to isomerization of the primary arenium ions into (V) and by the large yields of tritiated products (such as  $\text{C}_6\text{H}_5\text{T}$  from benzene and  $\text{C}_6\text{H}_5\text{CT}_3$  from toluene) whose formation requires extensive isotopic scrambling, group migration, and fragmentation.

The effects of collisional stabilization are clearly shown by the pressure dependence of the products pattern, a tenfold decrease of the  $\text{C}_7\text{H}_8$  pressure (from 350 to 36 Torr) raising, for instance, the extent of meta substitution from 56% to 68%.

The profound alterations of the mechanistic picture revealed by comparison of liquid-phase and gas-phase results, and by the pressure effect, are a serious caveat against straightforward generalization of gas-phase data, for example, those from mass spectrometric studies of ion-molecule reactions, obtained under conditions that cannot ensure effective stabilization and quenching of excited primary intermediates.

The results of a comparative study of the gas-phase and liquid-phase alkylation of *t*-butylbenzene with decay  $\text{CT}_3^+$  ions fully support the above conclusions (24). The excited arenium ions from the exothermic alkylation step, Equation 15, are effectively stabilized in the liquid phase,



**Table V. Substrate Reactivity and Isomeric Composition of Halobenzenes**

System Composition (Torr)	Isomeric Composition of Products (%)				
	PhX	PhCH <sub>3</sub>	Xylenes		
			Ortho	Meta	Para
X = F	20	200	25.4	58.4	16.2
	200	200	25.3	57.8	16.9
	200	20	23.4	60.9	15.7
X = Cl	10	100	24.0	61.0	15.0
	100	100	28.8	54.3	16.9
	100	10	35.3	47.6	17.1
X = Br	10	100	25.0	75.0	
	90	90	28.1	71.9	
	90	10	29.6	70.4	

<sup>a</sup> Calculated assuming a first-order kinetics in the aromatics.

**Table VI. Tritiated Products from the**

System Composition <sup>a</sup> (Torr)			Relative Yields of Products <sup>b</sup> (%)			
C <sub>6</sub> H <sub>6</sub>	C <sub>7</sub> H <sub>8</sub>	O <sub>2</sub>	Benzene	Toluene	Ethyl- benzene	Xylenes
—	36	1.2	—	55.7	—	44.3
—	350	2.4	2.2	39.6	0.7	57.5
36	36	2.4	19.1	53.7	0.2	26.9
120	12	2.4	33.2	61.5	0.2	5.1
3.6	36	2.4	4.8	42.9	0.4	51.9

<sup>a</sup> All systems contained ca. 0.2 Torr of CH<sub>4</sub> and a tracer concentration of CT<sub>4</sub>.

<sup>b</sup> Ratio of the activity of each product to the combined activity of all products identified. For the absolute yields, see the text. Each value is the average of several determinations, with a standard deviation of ca. 5%.

**Table VII. Tritiated Products from the**

System Composition (mol %)		Relative Yields of Products <sup>a</sup> (%)				
C <sub>6</sub> H <sub>6</sub>	C <sub>7</sub> H <sub>8</sub>	Ben- zene	Tolu- ene	Ethyl- benzene	Un- known <sup>b</sup>	Xyl- enes
—	100	—	13.9	4.2	2.7	79.3
—	100	—	13.8	4.5	2.7	79.0
50	50	8.0	36.0	1.5	1.5	53.0
10	90	2.0	18.4	2.8	2.1	74.7
90	10	14.1	69.6	0.3	0.6	15.9

<sup>a</sup> Reproducibility of the data is illustrated by comparison of the first two lines.

<sup>b</sup> The elution volume of this product is close, if slightly lower, than that of ethylbenzene.

**Products from the Competitive Gas-Phase Methylation of  
with Toluene***Isomeric Composition of Products  
(%)*

<i>Halotoluenes</i>			$\frac{k_{PHX}^*}{k_{PnCH_3}}$
<i>Ortho</i>	<i>Meta</i>	<i>Para</i>	
35.3	51.4	13.3	0.76
42.4	46.6	11.5	0.80
39.9	48.7	11.4	0.89
30.8	56.9	12.3	0.59
30.4	57.2	12.4	0.51
30.8	56.9	12.3	0.41
27.6	52.2	21.2	0.54
26.6	57.8	15.6	0.41
27.2	60.1	12.7	0.23

**Attack of  $CT_3^+$  Decay Ions to Gaseous Arenes***Composition of Xylenes (%)*

<i>Ortho</i>	<i>Meta</i>	<i>Para</i>	<i>Apparent* <math>k_T/k_B</math></i>
19.5	68.5	12.0	—
26.1	56.4	17.5	—
22.0	64.0	14.0	0.80
21.9	63.8	14.3	0.89
21.8	64.4	13.8	0.80

\* Apparent values, not corrected (see text).

**Attack of  $CT_3^+$  Decay Ions to Liquid Arenes***Xylenes Composition (%)*

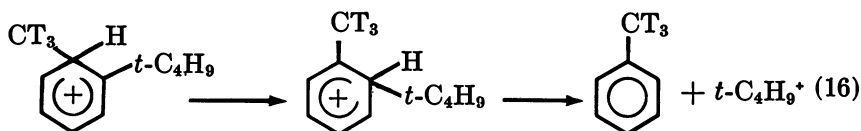
<i>Ortho</i>	<i>Meta</i>	<i>Para</i>	$\frac{k_T^*}{k_B}$
40.4	27.1	32.5	—
39.9	26.9	33.2	—
39.1	27.0	33.9	2.19
39.9	26.8	33.3	2.35
38.4	27.0	34.6	2.39

\* Apparent values, uncorrected (see text).

**American Chemical  
Society Library  
1155 16th St., N.W.  
Washington, D.C. 20036**

and, following deprotonation, give *t*-butyltoluenes as the major reaction product (59% yield). Despite the recognized migratory ability of the *t*-butyl group in the excited arenium ion, the isomeric composition of *t*-butyltoluenes still reflects the selectivity of the attack, with a para:½ meta ratio of 2:1. Incidentally, the extent of substitution ortho to the bulky *t*-butyl group (25%), when compared with the correspondent value in the methylation of toluene (40%), provides an estimate of the steric requirements of the free, unsolvated methyl cation. Methylation of gaseous *t*-butylbenzene (100 Torr) leads to an entirely different product pattern, giving high yields of species arising from extensive isotopic scrambling, isomerization, and fragmentation, including toluene (14%), *t*-butylbenzene (74%), *t*-amylbenzene (7%), at the expense of *t*-butyltoluenes (3.4%).

Comparison of these results with those from the methylation of toluene under similar conditions shows that more effective fragmentation channels are available to the excited arenium ions from *t*-butylbenzene. In particular, the loss of the very stable *t*-butyl ion, albeit endothermic by some 18 kcal mol<sup>-1</sup>, is largely allowed by the excitation energy (some 85 kcal mol<sup>-1</sup>) available to the arenium ion, and is strongly supported by the high yield of toluene, Equation 16.



**Table VIII. Tritiated Products from the Reaction of CT<sub>3</sub><sup>+</sup> Cl, Br) Mixtures in**

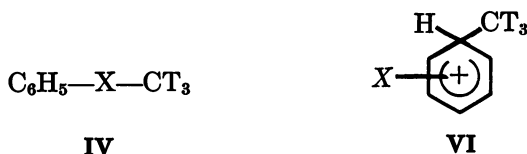
	System Composition <sup>a</sup> (mol %)		Relative Yields of Products <sup>b</sup> (activity %)		
	Halo-benzene	Toluene	Methyl Halide	Benzene	Toluene
X = F	9	91	≤ 0.2	0.4	14.8
	50	50	0.5	0.5	8.4
	91	9	1.1	0.8	2.2
X = Cl	9	91	1.3	0.7	14.9
	50	50	2.3	1.3	13.4
	91	9	5.4	1.8	9.7
X = Br	9	91	5.7	0.9	16.8
	50	50	13.5	2.0	16.2
	91	9	22.1	3.0	12.4

<sup>a</sup> The systems contained 2.7 mmol methane dissolved in 2.0 mL of the liquid substrates.

This finding closely recalls the parallel behavior observed by Munson and Field (25) in the chemical ionization mass spectrometry of aromatic hydrocarbons containing the *t*-butyl substituent.

Recently, a most interesting investigation has been reported (26), concerning the liquid-phase methylation of halobenzenes by decay  $\text{CT}_3^+$  ions, and its results, summarized in Table VIII, can be usefully compared with those of the gas-phase methylation previously discussed.

Competition between the two nucleophilic centers of the substrate, namely the  $\pi$ -system of the ring and the *n*-electrons of the halogen substituent, yields respectively the methylphenyl halonium ions (IV) and the methylhaloarenum ions (VI), excited by the considerable exothermicity of the condensation, of the order of  $80 \text{ kcal mol}^{-1}$ .



Following collisional stabilization and deprotonation, (VI) gives tritiated halotoluenes that represent the major reaction products, and whose yields depend on the nature of the halogen  $\text{X}$ , increasing in the order  $\text{F} > \text{Cl} > \text{Br}$ . The yields of the tritiated methyl halides,  $\text{CT}_3\text{X}$ , increase in the opposite order, following the trend  $\text{F} \ll \text{Cl} < \text{Br}$ . The  $\text{CT}_3^+$  selectivity toward the *n*-centers has been rationalized on the grounds

#### Decay Ions with Toluene/Halobenzene ( $\text{C}_6\text{H}_5\text{X}$ , $\text{X} = \text{F}$ , the Liquid Phase

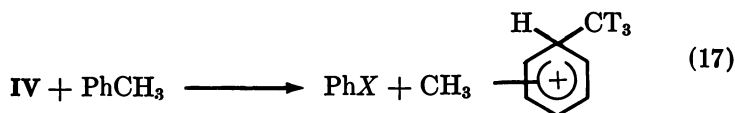
<i>Relative Yields of Products<sup>b</sup> (activity %)</i>				
<i>Halo- benzene</i>	<i>Unidentified Products</i>	<i>Ethyl- benzene</i>	<i>Xylenes</i>	<i>Halo- toluenes</i>
1.3	2.3	5.8	71.7	3.5
6.4	5.3	1.1	57.3	20.5
12.6		6.3	19.1	57.2
0.8	1.6	4.9	71.3	5.0
5.0	1.0	2.8	53.6	21.2
10.3			19.6	53.1
0.8		5.1	66.4	4.4
4.2		1.8	46.2	16.1
5.0			15.5	42.7

<sup>b</sup> See Table I (for an explanation of the meaning of figures).

of the HSAB principle, in that the reactivity toward the methyl cation, the softest of the charged carbon acids, increases with the softness of the halogen-atom bases, following the order  $F \ll Cl < Br$ .

The effective collisional stabilization typical of the liquid environments allows the isomeric composition of the products to reflect, at least to some extent, the original selectivity of the electrophilic attack to the ring, with a predominant ortho-para orientation and a para:½ meta ratio in excess of 3.

Formation of (IV), which reacts as an effective methylating reagent,



for example, does not allow the establishment of an accurate reactivity scale of the aromatic ring of halobenzenes toward  $CT_3^+$ . However, the approximate ratios deduced from this study, that is,  $PhF:PhCl:PhBr = 1.5:1.3:1$ , are comparable, if somewhat lower, than those measured for strong alkylating reagents of incipient cationic nature in aprotic apolar solvents (27), for example, the  $C_2H_5Br-CaBr_3$  complex in  $C_2H_4Cl_2$ , giving the ratios  $PhF:PhCl:PhBr = 2.1:1.6:1$ .

The comparison shows that the positional and the substrate selectivity of the free, unsolvated  $CT_3^+$  ions are most closely approached by those conventional reagents that combine a (necessarily incipient) cationic polarization with a state of limited solvation.

### Acknowledgments

This work has been financially supported by the Italian National Research Council (CNR).

### Literature Cited

1. Cacace, F. *Adv. Phys. Org. Chem.* **1970**, *8*, 79.
2. Cacace, F. In "Hot Atom Chemistry Status Report"; International Atomic Energy Agency: Vienna, 1975; p. 229.
3. Cacace, F. In "Interactions Between Ions and Molecules"; Ausloos, P., Ed.; Plenum: New York, 1975; p. 527.
4. Akulov, G. P. *Usp. Khim.* **1976**, *45*, 1970.
5. Cacace, F. In "Kinetics of Ion-Molecule Reactions"; Ausloos, P., Ed.; Plenum: New York, 1979; p. 199.
6. Ikuta, S.; Iwata, S.; Imamura, M. *J. Chem. Phys.* **1977**, *66*, 4671.
7. Wexler, S. In "Actions Chimiques and Biochimiques des Radiations"; Haïssinsky, M., Ed.; Masson: Paris, 1965; Vol. 8.
8. Cacace, F.; Speranza, M. *J. Am. Chem. Soc.* **1979**, *101*, 1587.
9. Cipollini, R.; Schüller, M. *J. Labelled Compd.* **1978**, *15*, 703.

10. Angelini, G.; Segre, A. L.; Altman, L.; Speranza, M. *J. Org. Chem.* **1980**, *45*, 3291.
11. Cacace, F.; Ciranni, G.; Schüller, M. *J. Am. Chem. Soc.* **1975**, *97*, 4747.
12. Cacace, F.; Speranza, M. *J. Am. Chem. Soc.* **1979**, *101*, 1587.
13. Hehre, W. J.; Hiberty, P. C. *J. Am. Chem. Soc.* **1974**, *96*, 302.
14. *Ibid.*, **1972**, *94*, 5917.
15. Levi, B. A.; Blurok, E. S.; Hehre, W. J. *J. Am. Chem. Soc.* **1979**, *101*, 5537.
16. Pobo, L. G.; Wexler, S.; Caronna, S. *Radiochim. Acta* **1973**, *19*, 5.
17. Speranza, M. *Tetrahedron Lett.* **1980**, *21*, 1983.
18. Dill, J. D.; Schleyer, P. v. R.; Binkley, J. S.; Seeger, R.; Pople, J. A.; Haselbach, E. *J. Am. Chem. Soc.* **1976**, *98*, 5428.
19. Giacomello, P.; Speranza, M. *J. Am. Chem. Soc.* **1977**, *99*, 7918.
20. Giacomello, P. *Radiochim. Acta* **1979**, *26*, 185.
21. Colosimo, M.; Bucci, R. *J. Phys. Chem.* **1978**, *82*, 2061.
22. Cacace, F.; Giacomello, P. *J. Am. Chem. Soc.* **1977**, *99*, 5477.
23. Cacace, F.; Giacomello, P. *J. Chem. Soc., Perkin Trans. 2* **1978**, 652.
24. Giacomello, P. *Radiochim. Acta* **1977**, *24*, 111.
25. Munson, M. S. B.; Field, F. H. *J. Am. Chem. Soc.* **1967**, *89*, 1047.
26. Giacomello, P. *J. Am. Chem. Soc.* **1979**, *101*, 4276.
27. Brown, H. C.; Neyens, A. J. *J. Am. Chem. Soc.* **1962**, *84*, 1955.

RECEIVED September 4, 1980.



# Unusual Compounds Synthesized via Nuclear Recoil Methods

YI-NOO TANG

Department of Chemistry, Texas A & M University, College Station TX 77843

*Various unusual intermediates and compounds have been formed via the nuclear recoil methods. The unusual intermediates thus formed include: free atoms with very high translational energies such as  $^3\text{H}$ ,  $^{11}\text{C}$ ,  $^{32}\text{P}$ ,  $^{31}\text{Si}$ , and  $^{75}\text{Ge}$ ; mono-, di-, and polyvalent free radicals such as monofluorocarbene (CTF and  $\text{CH}^{18}\text{F}$ ), silylenes ( $^{31}\text{SiF}_2$  and  $^{31}\text{SiHF}$ ), and methyne ( $^{11}\text{CH}$ ); and highly excited molecules such as  $\text{CH}_2\text{TCHF}_2^*$ , which is capable of undergoing a direct consecutive decomposition without intermediate energy-accumulation collisions. The unusual compounds formed via the nuclear recoil methods include: multitritiated molecules such as  $\text{CT}_4$  and  $\text{CT}_3\text{OH}$  formed by the technique of tritium decay-labeling; the alkyl-substituted fluorocyclopropanes through recoil tritium reactions; 1,2,3-pentatriene through recoil  $^{11}\text{C}$  reactions; methylenimine through recoil  $^{14}\text{C}$  reactions; and 1-silacyclopenta-2,4-diene, 1,1,1,2-tetramethyldisilane and 1-fluorosilacyclopent-3-ene through recoil  $^{31}\text{Si}$  reactions.*

The study of the chemical effects subsequent to nuclear transformations provide basic information about the reactions of the generated entities (1, 2, 3). The recoil species formed during nuclear transformations are initially ions, but in the majority of the systems with bath molecules of ionization potentials lower than that of the recoil species, the ions are likely to be neutralized prior to chemical interactions, giving stable products (4). As a result, the primary purposes of the nuclear recoil experiments are usually the study of reaction mechanisms and kinetics of the energetic atoms being formed (5-12).

0065-2393/81/0197-0053\$05.00/0  
© 1981 American Chemical Society

However, over the years a number of unusual compounds have also been synthesized via such nuclear recoil methods. Because of the enormous amount of kinetic energy possessed by the hot atoms, various kinds of high energy reaction channels become possible. For example, the highly excited molecular species formed during hot atom interactions may decompose or isomerize to generate certain unusual reaction intermediates, and some of the intermediates may react further to give unusual compounds as products. It is the purpose of this article to give a brief account of the various unusual intermediates and compounds produced via the nuclear recoil methods.

The term "unusual compounds" is defined here as species that either cannot be formed or have not been formed using conventional synthetic methods. It also applies to species that were first synthesized via the nuclear recoil methods, even if they were subsequently prepared by other means.

### *Unusual Intermediates via Nuclear Recoil Methods*

The intermediates formed in nuclear recoil systems can be in the form of free atoms, mono-, di-, and polyvalent free radicals, and excited molecules. Of course, in certain systems ionic species also can be involved as intermediates for the formation of final products. The various nonionic intermediates will be discussed below.

**Atoms.** Strictly speaking, all the atoms formed via the nuclear recoil methods are unusual species because they all possess kinetic energies far in excess of those that could be formed by conventional chemical means (5-12). On the qualitative side, such hot atoms will open various reaction channels that are not possible for their lower energy counterparts. On the quantitative side, the cross sections of various reactions for the hot atoms are normally very different from those for the thermal atoms. An additional unique feature of the atoms formed via nuclear recoil techniques is that they invariably include radioactive isotopes and, therefore, they are capable of functioning as tracers for their subsequent interactions.

The most commonly used nonmetallic atoms that are formed during nuclear recoil studies are listed below according to their valences in stable compounds.

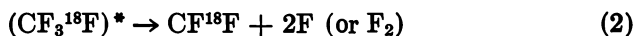
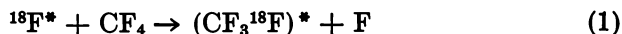
1. Monovalent:  $^3\text{H}(\text{T})$ ,  $^{18}\text{F}$ ,  $^{38}\text{Cl}$ ,  $^{39}\text{Cl}$ ,  $^{77}\text{Br}$ ,  $^{80\text{m}}\text{Br}$ ,  $^{82}\text{Br}$ ,  $^{82\text{m}}\text{Br}$ ,  
 $^{123}\text{I}$ ,  $^{125}\text{I}$ ,  $^{131}\text{I}$ ,  $^{133}\text{I}$ ,  $^{135}\text{I}$
2. Divalent:  $^{15}\text{O}$ ,  $^{35}\text{S}$ ,  $^{38}\text{S}$
3. Trivalent:  $^{13}\text{N}$ ,  $^{32}\text{P}$
4. Tetravalent:  $^{11}\text{C}$ ,  $^{14}\text{C}$ ,  $^{31}\text{Si}$ ,  $^{75}\text{Ge}$

Among these atoms, the reactions of recoil  $^3\text{H}$  and  $^{11}\text{C}$  have been very extensively studied and constitute the major wealth of hot atom chemistry (5–12). Our understanding of Si and Ge atom reactions is due mainly to nuclear recoil studies as well (13–22). The chemistry of all the other types of atoms (except  $^{32}\text{P}$ ) has also been studied to various degrees by using other means for their generation (23–25). However, the truly unusual recoil atom is  $^{32}\text{P}$ . There are essentially no other studies on the chemistry of phosphorus atoms, and all our present knowledge about phosphorus atom reactions has to be attributed to the recoil  $^{32}\text{P}$  studies (26–30). Of course, as mentioned earlier, all the hot atoms formed via the nuclear recoil method have the distinction of being highly energetic, and, therefore, in one sense they are all unusual atoms.

**Methyne.** Although the reactions of substituted methyne such as  $\text{EtOCO}\dot{\text{C}}$  have been extensively studied (31–33), the chemistry of unsubstituted methyne,  $(\text{CH})$ , is essentially unknown. The first clues for its possible chemical interactions can be found in recoil  $^{11}\text{C}$  reactions. For example, during the reactions of recoil  $^{11}\text{C}$  atoms with ethylene in the presence of  $\text{H}_2$ , the observation of  $^{11}\text{C}$ -labeled 1-pentene can be attributed to the successive interaction of  $^{11}\text{CH}$  with two molecules of  $\text{C}_2\text{H}_4$  followed by H-abstraction (34).

**Carbenes and Silylenes.** Carbenes such as CTF and CTCI were formed in recoil tritium systems (35–39), while carbenes such as  $\text{CH}^{18}\text{F}$ ,  $\text{CH}^{38}\text{Cl}$ , and  $\text{CF}^{18}\text{F}$  were formed in recoil halogen atom studies (40–44). Among them the truly unusual ones are the monofluorocarbenes, CTF and  $\text{CH}^{18}\text{F}$ , because their chemical interactions were first studied by these nuclear recoil methods (36, 37, 40, 41, 45). The details of such studies will be described in a later section.

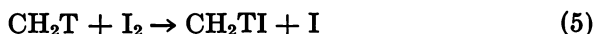
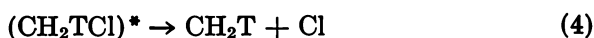
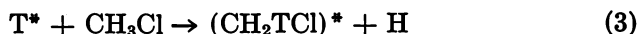
The formation of carbenes via the nuclear recoil method is illustrated below for  $\text{CF}^{18}\text{F}$  (40).



Silylenes such as  $^{31}\text{SiH}_2$ ,  $^{31}\text{SiF}_2$ , and  $^{31}\text{SiHF}$  were formed in recoil  $^{31}\text{Si}$  systems (13–21). Monomeric  $^{31}\text{SiF}_2$  is uniquely formed in these systems and react in the monomeric form (15, 18, 20) in contrast to the situation in which they are prepared by the high-temperature disproportionation method (46, 47). In the latter case, dimerization of  $\text{SiF}_2$  always predominates. The formation of  $^{31}\text{SiHF}$  via the nuclear recoil method is also observed. The details of these studies will be described later.

**Radicals.** After the hot atom substitution reactions, the resultant excited molecules may decompose via bond cleavages that give rise to

various free radicals. A typical example occurs after hot T-for-H substitution in  $\text{CH}_3\text{Cl}$ . The resultant excited  $\text{CH}_2\text{TCl}$  molecules may decompose via C—Cl cleavage to give  $\text{CH}_2\text{T}$  radicals, which could be scavenged by  $\text{I}_2$  to give  $\text{CH}_2\text{TI}$  as a final product (48).



However, essentially all the radicals generated by the nuclear recoil methods could also be formed through other chemical means. Nevertheless, some of the radicals thus formed are still regarded as unusual because of the high excitation energy they may possess. A typical example is found in the recoil  $^{38}\text{Cl}$  atom reactions with *trans*- or *cis*-dichloroethylene (49). The addition of  $^{38}\text{Cl}$  to the  $\pi$ -bond of these two compounds will give rise to excited trichloroethyl radicals that decompose back to *trans*- or *cis*- $^{38}\text{Cl}$ -labeled dichloroethylene. The branching ratio of the two isomeric products is much closer to unity compared with the equilibrium branching ratio measured for thermal Cl atom reactions. It also has been demonstrated that such branching ratios are functions of the excitation energy of the decomposing radicals (49).

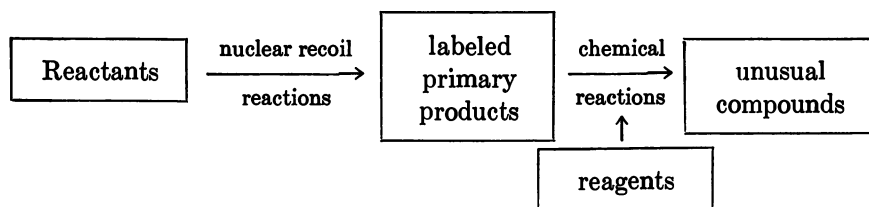
**Excited Molecules.** Because of the high initial kinetic energy of the recoil atoms, the excited molecules that result after hot substitution reactions are often orders of magnitude higher in excitation energy than their counterparts formed in thermal systems. As a result, new reaction channels for unimolecular processes may take place in addition to the threshold reactions observed in thermal systems. A unique demonstration of such unusual behavior is the establishment of consecutive decomposition for excited tritium-labeled  $\text{CH}_3\text{CHF}_2$  molecules after T-for-H substitution (50). The resultant  $\text{CH}_2\text{TCHF}_2$  molecules, for example, may undergo secondary decomposition to  $\text{CHT}=\text{CHF}$  and then tertiary decomposition to give  $\text{CT}\equiv\text{CH}$  as the final product. What is unique about such consecutive decomposition is that all the excitation energy is introduced at once into the molecule during the initial substitutional encounter. On the other hand, in the conventional thermal systems collisions are normally required between the two stages of decomposition to reaccumulate enough excitation energy for the tertiary decomposition steps.

### *Unusual Compounds via Nuclear Recoil Methods*

There are two types of unusual compounds that can be formed via nuclear recoil methods. The standard type includes the truly novel

molecules that have not been prepared in ordinary chemical systems. This type can be divided again into two more categories: the ones that are directly formed in nuclear recoil systems and the ones that are obtained afterward from synthetic steps. In the former case, the unusual compound is derived from chemical reactions occurring in situ and exists in its final form upon the completion of the irradiation process. This is the type of unusual compounds that will be emphasized in the latter sections of this article.

The other type of unusual compound is formed after certain synthetic steps. As shown in the illustration below, some labeled primary products are first derived from nuclear recoil systems and are then used as the starting reagents of certain synthetic steps to obtain the unusual compounds. This general method has been widely used in the synthesis of nuclear pharmaceuticals. Because of their inclusion in other chapters of this volume, the unusual compounds prepared after certain synthetic steps will not be discussed in this chapter.



In addition to the standard type of unusual compounds mentioned above, any radioactively labeled products that are formed in nuclear recoil systems and that cannot be prepared by conventional means may also be regarded as unusual. However, the species thus formed are always singly labeled. The chance of double labeling is negligible because in a typical recoil system only about  $10^{10}$  radioactive atoms are formed in an environment consisting of about  $10^{20}$  reactant molecules.

Recoil labeling with monovalent hot atoms is not extensively used for the preparation of radioactively labeled compounds mainly because it is believed that only low specific activities are attainable. However, this is only true for the products formed via the  $X^*$ -for- $X$  type of substitution process. In such cases the limited number of recoil atoms formed from nuclear transmutation in comparison with the large number of parent molecules present in the system will definitely give yields of low specific activities for the labeled parent compounds. Labeled compounds with a very high specific activity, or even carrier-free, can actually be obtained from other types of nuclear recoil interactions. For monovalent recoil atoms, the  $X^*$ -for- $Y$  substitution will give products with extremely high specific activity if the unlabeled counterparts are not generated by radiation damage of the parent molecules. On the

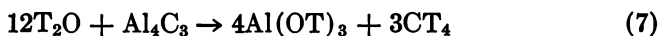
other hand, the radioactively labeled products formed by multivalent recoil atoms are all likely to be carrier-free. These products are normally formed via abstraction and/or insertion reactions of the recoil atoms. Their unlabeled counterparts are not likely to be formed through radiation damage in the recoil systems. Of course, if a different element is used as the precursor of the recoil atoms in the nuclear transmutation, the products obtained have to be carrier-free if impurities are absent.

Very recently, multiple tritium-labeled compounds have been synthesized by Cacace and coworkers via nuclear decay processes (51–54). The details of their studies will be described in the next section.

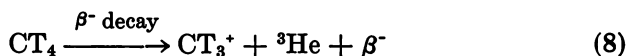
From this point on, a collection of several cases in which unusual compounds were synthesized via the nuclear recoil methods will be presented. They are arranged according to the valences of the recoil atoms involved.

### *Decay Synthesis of Multitritiated Compounds*

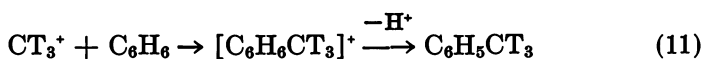
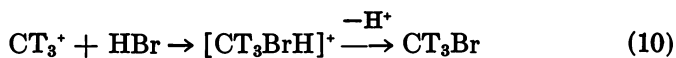
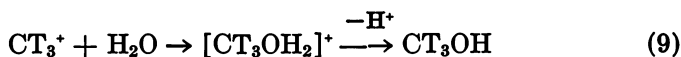
Cacace and coworkers have synthesized multitritiated compounds by using the radioactive decay of tritium in  $CT_4$  to obtain the reactive  $CT_3^+$  cations (51). Large amounts of  $CT_4$  were first prepared via the following reactions:



During the spontaneous  $\beta^-$  decay of  $CT_4$ , fully tritiated methyl cations were generated.



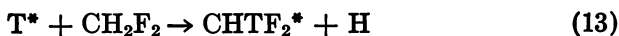
In the presence of various organic compounds labeled molecules containing the  $CT_3$  group were obtained (52–54). Typical examples are as shown below:



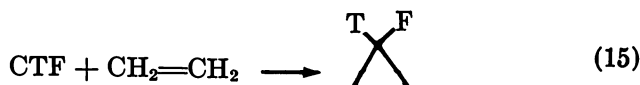
### *Formation of CTF and Synthesis of Substituted Fluorocyclopropanes*

Monofluorocarbene, a reaction intermediate whose chemistry was first studied by using the nuclear recoil methods as a means of formation,

can be produced in recoil tritium systems via the following sequence of reactions (36, 37):



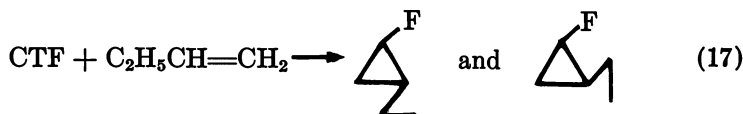
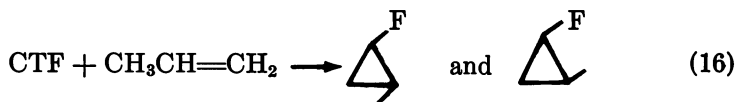
The direct proof for its formation is that it can be captured by ethylene to give fluorocyclopropane-*t* (36, 37).

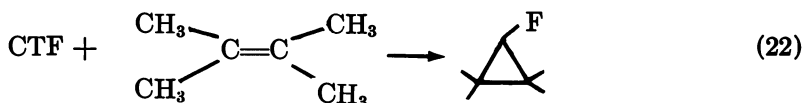
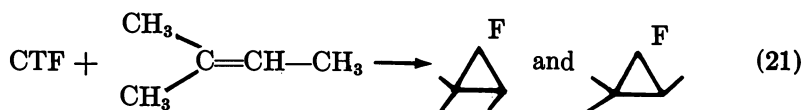
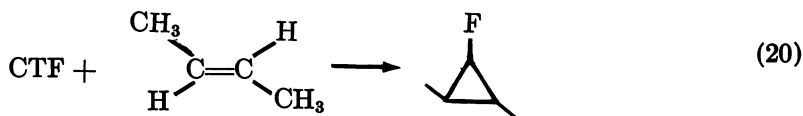
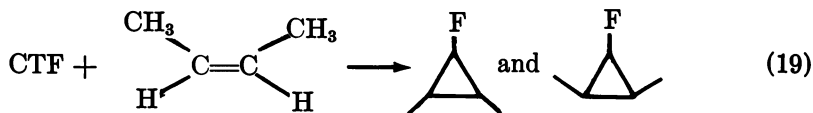


Various studies have been carried out for the monofluorocarbene thus formed (37). The important information obtained is summarized as follows:

1. The addition of CTF to the double bonds of either *cis*- or *trans*-2-butene is essentially stereospecific and is not affected by small amounts of molecular oxygen or large excesses of inert gases. This means that the reacting CTF is in its singlet electronic ground state.
2. Competition experiments between  $\text{C}_2\text{H}_4$  and alkyl-substituted ethylenes for the capture of CTF show that the relative efficiencies increase by a factor of six in going from ethylene to tetramethylethylene. The temperature dependence of these relative rates indicates that the variation is almost entirely the result of differences in activation energy for monofluorocarbene addition to alkenes.
3. The insertion of CTF into C—H bonds is very inefficient. In a related study involving  $\text{CH}^{18}\text{F}$ , it has been established that monofluorocarbene inserts very efficiently into hydrogen halides,  $\text{HX}$ , to give  $\text{CH}_2^{18}\text{FX}$  molecules (41).

Eleven alkyl-substituted fluorocyclopropanes were synthesized through the reactions of CTF with alkenes (37). All of them were novel compounds. The reactions involved for their formation are as follows:





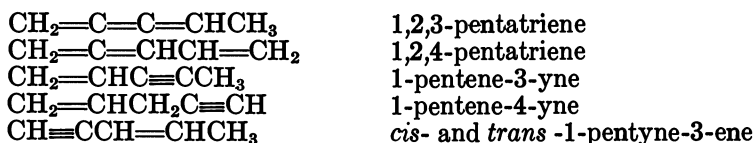
Whenever syn- and anti-isomers are possible, they are always formed in equal yields. On the practical side, these alkyl-substituted fluorocyclopropanes have been synthesized, trapped, and used for the purposes of finding out their retention times in various GC columns (55).

#### ***Formation of 1,2,3-Pentatriene from Recoil $^{11}\text{C}$ Atom Reactions with 1,3-Butadiene***

Unusual compounds can be formed more readily in multivalent recoil atom systems than in monovalent recoil atom systems. In the latter case, unusual compounds are rarely formed during the primary abstraction and substitution processes. The only likely way for their formation to occur is through the reactions of reactive intermediates formed via secondary decomposition processes. Typical examples are the formation of CTF and fluorocyclopropanes described previously. On the other hand, multivalent recoil atoms and the reactive intermediates resulting from their abstraction or insertion reactions can frequently react to give unusual products that would not be easily formed by other means. Therefore, it is not surprising that various unusual compounds are detected in recoil carbon and recoil silicon systems.



Recoil carbon-11 atoms formed via the  $^{12}\text{C}(n,2n)^{11}\text{C}$  nuclear transformation reacted with 1,3-butadiene to give a number of  $^{11}\text{C}$ -labeled products including  $\text{C}_5$  compounds such as 1,2,4-pentatriene and cyclopentadiene (56). A major unknown compound, which had a GC retention time similar to that of the other  $\text{C}_5$  products, was also observed (56, 57). The yields of this unknown compound increased with Ne-moderation but decreased with the addition of Xe or  $\text{O}_2$ , similar to the trends observed for cyclopentadiene formed in the same system (57). Catalytic hydrogenation and degradation of this unknown compound yielded straight-chain  $\text{C}_1$ - $\text{C}_4$  alkanes and alkenes plus  $\text{C}_5$  products such as 1-pentene, *cis*- and *trans*-2-pentenes, and *cis*- and *trans*-1,3-pentadienes. These hydrogenation results confirmed that the unknown compound is likely to be a highly unsaturated straight-chain  $\text{C}_5$  species with more unsaturation than the pentadienes. The only possibilities to satisfy such requirements are listed below.



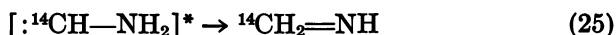
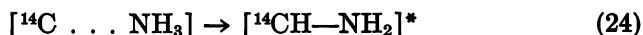
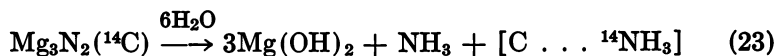
Since the unknown compound was definitely not 1,2,4-pentatriene, and its retention times on GC columns were also different from those of the three acetylenic compounds on the above list, the only possible candidate for its identity was 1,2,3-pentatriene (56, 57).

There is no information in the literature concerning the existence or formation of 1,2,3-pentatriene. Since the amount of this unusual compound formed in the present recoil  $^{11}\text{C}$  systems is extremely limited, conventional methods for the confirmation of its identity are mostly inapplicable. However, some additional information has been obtained during a pyrolysis experiment. This compound, after individual trapping and separation from other products, was observed to undergo a thermal conversion to  $\text{CH}\equiv\text{CCH}=\text{CHCH}_3$ , 1-pentyne-3-ene. This is consistent with the expectation that allenic types of compounds will isomerize to acetylenic types of compounds upon pyrolysis, which lends further support to the conclusion that the unusual compound, 1,2,3-pentatriene, has been synthesized in this recoil  $^{11}\text{C}$  system (57).

#### ***Formation of Methylenimine After $^{14}\text{N}(n,p)^{14}\text{C}$ Transmutation in Magnesium Nitride***

Finn, Ache, and Wolf have obtained a novel compound, methylenimine, when recoil  $^{14}\text{C}$  atoms were formed in magnesium nitride (58). In this system the major reaction products observed upon dissolution of

the recoil products in water were  $^{14}\text{CH}_4$ ,  $^{14}\text{CN}^-$ , and  $^{14}\text{CN}^{2-}$ . Thermal annealing of the neutron-irradiated magnesium nitride resulted in a sharp drop of the  $^{14}\text{CN}^-$  and  $^{14}\text{CN}^{2-}$  yields, and an unknown product was observed in high quantities. This unknown was identified as methylenimine, since it could be converted into formaldehyde by a method characteristic of such types of molecules. The mechanism for the formation of methylenimine has been proposed as follows:



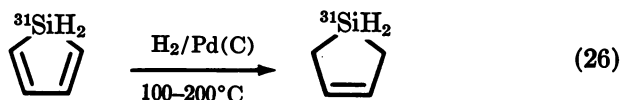
Upon dissolution, the attack of the solvent on the  $\text{Mg}_3\text{N}_2$  matrix trapped  $^{14}\text{C}$  atoms will give rise to  $\text{NH}_3$  with the  $^{14}\text{C}$  atom still loosely attached to it. Such a loosely attached complex will then undergo hydrogen migration to produce methylenimine as the final product (58).

#### ***Formation of 1-Silacyclopenta-2,4-diene through Recoil $^{31}\text{Si}$ Atom Reactions with 1,3-Butadiene***

The synthesis of silacyclopentadienes has been a long-term challenge to chemists during the past two decades (59-61). Although there has been some success in the synthesis of substituted silacyclopentadienes, the preparation of a compound with all the ring-carbons unsubstituted still cannot be achieved by ordinary chemical means (62, 63). During the reactions of recoil  $^{31}\text{Si}$  atoms formed via the  $^{31}\text{P}(n,p)^{31}\text{Si}$  nuclear transmutation with 1,3-butadiene, a major unknown product that was initially identified by Gaspar and coworkers as 1-silacyclopenta-2,4-diene was observed. The identification was based on the following reasons (16, 19): The product contains C, H, and Si but no phosphorus, because the same compound was obtained when  $^{30}\text{Si}$ , instead of  $^{31}\text{P}$ , was used as the  $^{31}\text{Si}$  source. The chromatographic behavior of this product suggests that it contains four carbon atoms. Its yield increases monotonically with 1,3-butadiene mole fraction. It was obtained in nearly identical ( $20\% \pm 3\%$ ) yields from 1:1  $\text{PH}_3$ -butadiene and 1:1  $\text{PF}_3$ -butadiene mixtures. This supposition was very recently confirmed through catalytic hydrogenation processes (22).

The unknown compound was first individually trapped and then was injected together with  $\text{H}_2$  through a catalyst tube containing Pd supported on active carbon. The fact that silacyclopenta-3-ene was

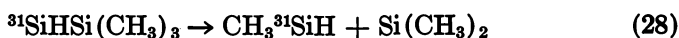
observed repeatedly as a hydrogenation product provides the strongest chemical evidence that the trapped compound is indeed 1-silacyclopenta-2,4-diene.



Subsequent studies have shown that this unusual compound is very sensitive to  $\gamma$ -ray irradiation, and it is also thermally unstable at a temperature higher than  $100^\circ\text{C}$  (22).

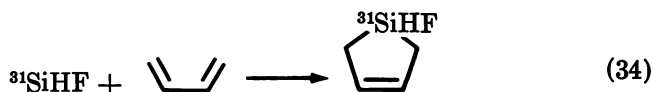
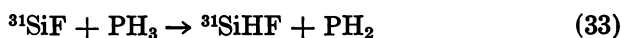
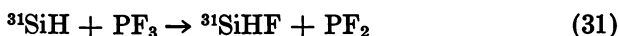
#### *Formation of Other Unusual Silicon-Containing Compounds from Recoil ${}^{31}\text{Si}$ Atom Reactions*

Recently Gaspar and coworkers prepared 1,1,1,2-tetramethyldisilane,  $\text{CH}_3{}^{31}\text{SiH}_2\text{Si}(\text{CH}_3)_3$ , from the reactions of recoil  ${}^{31}\text{Si}$  atoms with trimethylsilane (64). This novel compound was first synthesized with such nuclear recoil techniques. Two possible mechanisms could be proposed for its formation. The first is through a  $\text{CH}_3$  group abstraction by  ${}^{31}\text{Si}^+$  ions followed by ion-molecule interactions. Another possibility involves the insertion of  ${}^{31}\text{Si}$  atoms into the Si-H bond of trimethylsilane followed by unimolecular decomposition of the intermediate into two silylenes,  $\text{CH}_3{}^{31}\text{SiH}$  and  $\text{Si}(\text{CH}_3)_2$ . The insertion of  $\text{CH}_3{}^{31}\text{SiH}$  into the Si-H bond of another trimethylsilane molecule will result in the formation of this unusual compound:



Very recently, 1-fluorosilacyclopenta-3-ene, a novel compound, was also prepared via recoil  ${}^{31}\text{Si}$  atom reactions (65). It has been established that when  ${}^{31}\text{Si}$  atoms were formed with  $\text{PH}_3$  as its precursor, H-abstraction will give rise to  ${}^{31}\text{SiH}_2$  as an intermediate, which subsequently adds to 1,3-butadiene to give [ ${}^{31}\text{Si}$ ]-silacyclopenta-3-ene (17). On the other hand, when  $\text{PF}_3$  was used as a  ${}^{31}\text{Si}$  precursor, F-abstraction will give rise to  ${}^{31}\text{SiF}_2$  as an intermediate, which eventually forms [ ${}^{31}\text{Si}$ ]-1,1-difluorosilacyclopenta-3-ene (18). Therefore, when  ${}^{31}\text{Si}$  was formed in a mixture of  $\text{PH}_3$  and  $\text{PF}_3$ , a stepwise abstraction mechanism will give rise to  ${}^{31}\text{SiHF}$

as an intermediate, which will subsequently react with 1,3-butadiene to give [ $^{31}\text{Si}$ ]-1-fluorosilacyclopenta-3-ene. The recoil  $^{31}\text{Si}$  experiments with such a mixture have been carried out, and a new product with a GC retention time in the same range as the other silacyclopentene molecules was actually obtained. From the quantitative variation of the yields of this compound with the mole fractions of its two precursors,  $\text{PH}_3$  and  $\text{PF}_3$ , there is strong support that this new product is actually [ $^{31}\text{Si}$ ]-1-fluorosilacyclopenta-3-ene. Its quantitative yields also support the conclusion that the H- and F-abstraction processes were carried out in a stepwise manner instead of simultaneous abstraction of two entities during a single collisional encounter. The reactions involved for the formation of this unusual compound are shown below (65):



### Acknowledgments

This work is kindly supported by the U.S. Department of Energy under contract DE-ASO5-76ER03898. The valuable information provided by Drs. H. J. Ache, F. Cacace, P. P. Gaspar, G. Stocklin, and M. J. Welch is sincerely appreciated.

### Literature Cited

1. "Chemical Effects of Nuclear Transformations"; International Atomic Energy Agency: 1961; Vols. 1-2.
2. *Ibid.*, 1965; Vols. 1-2.
3. Stocklin, G. "Chemie Heisser Atome"; Verlag Chemie: Weinheim, 1969.
4. Masacy, H. S. W.; Burhop, E. H. S. "Electronic and Ionic Impact Phenomena"; Oxford Univ. Press: London, 1952.
5. Tang, Y.-N. "Isotopes in Organic Chemistry"; Buncl, E.; Lee, C. C., Eds.; Elsevier: New York, 1978; p. 85.
6. Urch, D. S. *MTP Int. Rev. Sci.; Inorg. Chem. Ser. 1* 1972, 8, 149.
7. Urch, D. S. *MTP Int. Rev. Sci.; Inorg. Chem. Ser. 2* 1975, 8, 49.
8. MacKay, C. "Carbenes"; Moss, R. A.; Jones, M., Jr., Eds.; John Wiley & Sons: New York, 1975; Vol. 2.
9. Rowland, F. S. "Molecular Beam and Reaction Kinetics"; Schlier, C., Ed.; Academic: New York, 1970.

10. Rowland, F. S. *MTP Int. Rev. Sci.: Phys. Chem. Ser. 1* 1972, 9, 109.
11. Wolfgang, R. *Ann. Rev. Phys. Chem.* 1965, 16, 15.
12. Wolf, A. P. *Adv. Phys. Org. Chem.* 1964, 2, 202.
13. Gaspar, P. P.; Bock, S. A.; Eckelman, W. C. *J. Am. Chem. Soc.* 1968, 90, 6914.
14. Gaspar, P. P.; Markusch, P.; Holton, J. D.; Frost, J. J. *J. Phys. Chem.* 1972, 76, 1352.
15. Tang, Y.-N.; Gennaro, G. P.; Su, Y. Y. *J. Am. Chem. Soc.* 1972, 94, 4355.
16. Gaspar, P. P.; Hwang, R.-J.; Eckelman, W. C. *J. Chem. Soc. Chem. Comm.* 1974, 242.
17. Zeck, O. F.; Su, Y. Y.; Gennaro, G. P.; Tang, Y.-N. *J. Am. Chem. Soc.* 1974, 96, 5967.
18. *Ibid.*, 1976, 98, 3474.
19. Hwang, R.-J.; Gaspar, P. P. *J. Am. Chem. Soc.* 1978, 100, 6626.
20. Siefert, E. E.; Ferrieri, R. A.; Zeck, O. F.; Tang, Y.-N. *Inorg. Chem.* 1978, 17, 2802.
21. Gaspar, P. P. "Reactive Intermediates"; Jones, M., Jr.; Moss, R. A., Eds.; John Wiley & Sons: New York, 1978.
22. Siefert, E. E.; Loh, K.-L.; Ferrieri, R. A.; Tang, Y.-N. *J. Am. Chem. Soc.* 1980, 102, 2285.
23. Acuna, A. U.; Husain, D. *J. Chem. Soc. Faraday Trans. 2* 1972, 585.
24. Acuna, A. U.; Husain, D.; Wiesenfeld, J. R. *J. Chem. Phys.* 1973, 58, 5272.
25. *Ibid.*, 494.
26. Stewart, G. W.; Hower, C. O. *J. Inorg. Nucl. Chem.* 1972, 34, 39.
27. Gennaro, G. P.; Tang, Y.-N. *J. Inorg. Nucl. Chem.* 1973, 35, 3087.
28. *Ibid.*, 1974, 36, 259.
29. Zeck, O. F.; Gennaro, G. P.; Tang, Y.-N. *J. Am. Chem. Soc.* 1975, 97, 4498.
30. Zeck, O. F.; Ferrieri, R. A.; Copp, C. A.; Gennaro, G. P.; Tang, Y.-N. *J. Inorg. Nucl. Chem.* 1979, 41, 785.
31. DoMinh, T.; Gunning, H. E.; Strausz, O. P. *J. Am. Chem. Soc.* 1967, 89, 6785.
32. Strausz, O. P.; DoMinh, T.; Font, J. *J. Am. Chem. Soc.* 1968, 90, 1930.
33. Strausz, O. P.; Kennepohl, G. J. A.; Garneau, F. X.; DoMinh, T.; Kim, B.; Valenty, S.; Skell, P. S. *J. Am. Chem. Soc.* 1974, 96, 5723.
34. Nicholas, J.; MacKay, C.; Wolfgang, R. *J. Am. Chem. Soc.* 1966, 88, 1065.
35. Tang, Y.-N.; Rowland, F. S. *J. Am. Chem. Soc.* 1965, 87, 1625.
36. *Ibid.*, 1966, 88, 626.
37. *Ibid.*, 1967, 89, 6420.
38. *Ibid.*, 1968, 90, 574.
39. Daniel, S. H.; Wong, N. B.; Tang, Y.-N. *J. Phys. Chem.* 1970, 74, 3148.
40. Tang, Y.-N.; Smail, T.; Rowland, F. S. *J. Am. Chem. Soc.* 1969, 91, 2130.
41. Smail, T.; Rowland, F. S. *J. Phys. Chem.* 1970, 74, 1866.
42. Smail, T.; Miller, G. E.; Rowland, F. S. *J. Phys. Chem.* 1970, 74, 3464.
43. Tang, Y.-N.; Smith, W. S.; Williams, J. L.; Lowery, K.; Rowland, F. S. *J. Phys. Chem.* 1971, 75, 440.
44. "Fluorine-Containing Free Radicals," *ACS Symp. Ser.* 1978, 66.
45. Hsu, D. S.; Umstead, M. E.; Lin, M. C. In "Fluorine-Containing Free Radicals," *ACS Symp. Ser.* 1978, 66, 128.
46. Thompson, J. C.; Margrave, J. L. *Science* 1967, 155, 669.
47. Timms, P. L. "Preparative Inorganic Reactions"; Jolly, W. L., Ed.; Interscience: New York, 1968; Vol. 4, p. 59.
48. Tang, Y.-N.; Lee, E. K. C.; Rowland, F. S. *J. Am. Chem. Soc.* 1964, 86, 1280.
49. Smith, W. S.; Daniel, S. H.; Tang, Y.-N. *J. Phys. Chem.* 1972, 76, 2711.
50. Smith, W. S.; Tang, Y.-N. *J. Phys. Chem.* 1974, 78, 2186.

51. Cacace, F.; Schyller, M. *J. Labelled Compd.* 1975, 11, 313.
52. Cacace, F.; Ciranni, G.; Schuller, M. *J. Am. Chem. Soc.* 1975, 97, 4747.
53. Cacace, F.; Giacomello, P. *J. Am. Chem. Soc.* 1977, 99, 5477.
54. Cacace, F.; Giacomello, P. *J. Chem. Soc., Perkin Trans. 2* 1978, 652.
55. Min, B. K.; Daniel, S. H.; Tang, Y.-N. *J. Radioanal. Lett.* 1973, 14, 29.
56. Baltuskonis, D. A., M.S. Thesis, Texas A & M Univ., 1975.
57. Ferrieri, R. A.; Baltuskonis, D. A.; Wolf, A. P.; Tang, Y.-N., unpublished data.
58. Finn, R. D.; Ache, H. J.; Wolf, A. P. *J. Phys. Chem.* 1969, 73, 3928.
59. Benkeser, R. A.; Grossman, R. F.; Stanton, G. M. *J. Am. Chem. Soc.* 1961, 83, 3716.
60. *Ibid.*, 5029.
61. Benkeser, R. A.; Stanton, G. M. *J. Am. Chem. Soc.* 1963, 85, 834.
62. Barton, T. J.; Wulff, W. D.; Arnold, E. V.; Clardy, J. *J. Am. Chem. Soc.* 1979, 101, 2733.
63. Barton, T. J.; Wulff, W. D. *J. Am. Chem. Soc.* 1979, 101, 2735.
64. Gaspar, P. P., presented at the 178th Ann. Meet., *Am. Chem. Soc., Washington, D.C., Sept. 1979.*
65. Siefert, E. E.; Loh, K.-L.; Tang, Y.-N., unpublished data.

RECEIVED September 4, 1980.

# Charge Distribution in $^{13}\text{N}$ Ions Produced by the $^{12}\text{C}(\text{d},\text{n})^{13}\text{N}$ Reaction

C. A. JONES and W. S. KOSKI

The Johns Hopkins University, Department of Chemistry,  
Charles and 34th Streets, Baltimore, MD 21218

*The short half-life of  $^{13}\text{N}$  requires that processing and synthesis steps be as least time-consuming as possible. A knowledge of the history of the  $^{13}\text{N}$  from the time of its creation until its ultimate fate can frequently be of help in shortening the preparation time. In this study we have examined the charge distribution of  $^{13}\text{N}$  produced by deuteron bombardment of carbon foils. The energy range covered was 8–14 MeV. The  $^{13}\text{N}$  ions produced were collimated, magnetically analyzed, and collected on a catcher foil that was scanned for activity with a Geiger counter. The peak of the charge distribution was +3 to +4. Such energetic, highly charged ions rapidly lose their charge as they slow down by collision, and do not undergo interesting chemical reactions until they reach epithermal energies and a charge of +1 or 0. Some of the ion–molecule reactions that take place as  $^{13}\text{N}$  recoils through various gaseous materials and the identity of the ultimate products are discussed.*

**I**n designing chemical syntheses incorporating nuclear recoils, one would like to know as much as possible about the creation and fate of those recoils. To this end we have measured the ionic charge state distribution of  $^{13}\text{N}$  recoiling from the  $^{12}\text{C}(\text{d},\text{n})^{13}\text{N}$  reaction. The energetic intermediates formed following this nuclear reaction depend on the state of the recoil. These intermediates in turn determine the ensuing kinetics and radiolysis in the synthetic medium.

A fast atomic ion traveling through matter picks up and loses electrons as dictated by its velocity-dependent, charge-changing cross sections in that material. A beam of such ions displays a distribution of

0065-2393/81/0197-0067\$05.00/0  
© 1981 American Chemical Society

charges that attains equilibrium after passing through a number of atomic layers, on the order of 100 (1), that number depending on the ions' initial charge state and velocity. After attainment of equilibrium, all memory of the initial charge state is lost. Using heavy-ion accelerators, a number of workers have determined equilibrium charge state distributions for  $^{14}\text{N}$  in various materials as a function of velocity (2, 3, 4, 5). Charge state distributions of nuclear recoils have received relatively little attention, few studies having been reported to date (6, 7, 8, 9), two of those dealing with recoils from simple elastic scattering (8, 9) and none dealing with nitrogen. It is then still pertinent to ask if the charge state distribution of recoils immediately after the nuclear reaction, the "instantaneous" distribution, is appreciably different from the equilibrium distribution. The present study attempts to shed some light on that question.

As recoils pass through matter, they lose kinetic energy through electronic excitation and ionization. Only when they have slowed to about 1 keV or less do they begin to form stable molecular bonds. At this point, the most probable charge state is, in general, either +1 or 0. Accordingly, we have included a brief discussion of the chemical fate of  $^{13}\text{N}$  recoils by considering literature data on reactions of N and  $\text{N}^+$ .

### Experimental

These experiments were carried out at the Tandem Van de Graaff facility at Edgewood Arsenal, Aberdeen Proving Grounds, Maryland. The accelerator provided up to  $5\ \mu\text{A}$  of deuteron beam current at the target after final beam shaping and collimation. The targets were self-supporting carbon foils mounted over 9-mm apertures. Their thicknesses were determined to within 10% by optical transmittance at  $5460\ \text{\AA}$  (10). As shown in Figure 1, the deuteron beam passed straight ahead to a Faraday cup. The  $^{13}\text{N}$  recoils were accepted at  $22.5^\circ$  to the deuteron beam, so the target was turned to this same angle to minimize the recoils' path through the target. The recoils were collimated and

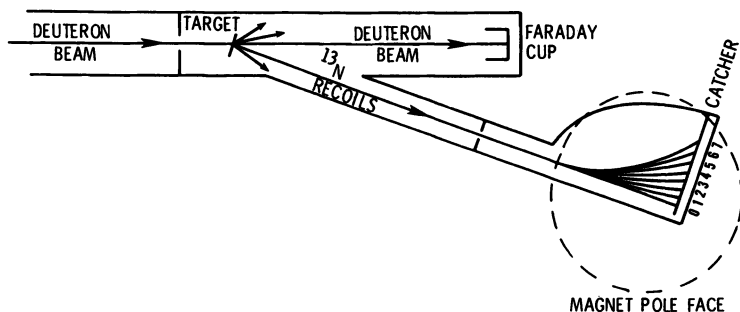


Figure 1. Experimental arrangement used to observe the  $^{13}\text{N}$  recoil charge state distribution



Table I. Reaction Parameters for  $^{12}\text{C}(\text{d},\text{n})^{13}\text{N}$ 

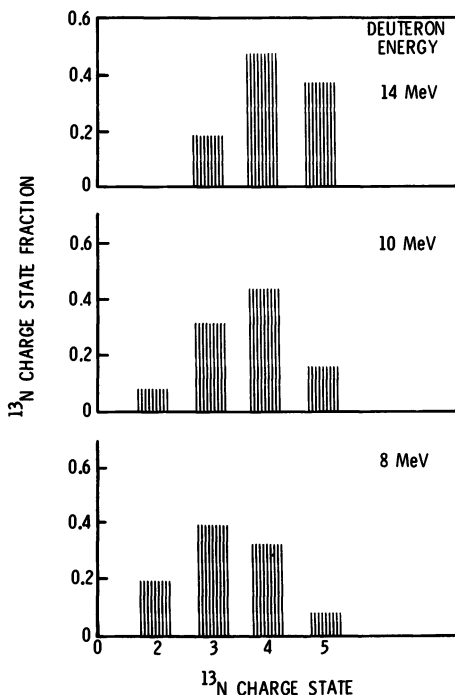
Deuteron Energy (MeV)	$^{13}\text{N}$ Recoil Energy at $58^\circ$ c.m. (MeV)	Differential (12, 13, 14) Cross Section at $58^\circ$ c.m. (mb/ster)	Total (15) Cross Section (mb)
8.0	2.31	5	110
10.0	2.90	4	90
14.0	4.08	1	60

then passed into a dispersing magnetic field provided by an electromagnet and maintained at 3.3 kG as measured with a Hall effect gaussmeter. The recoils came to rest on a tantalum catcher strip, successive charge state peaks being separated by about 15 mm. After a 30-min irradiation, the catcher was immediately removed and scanned with a properly shielded Geiger tube mounted on a carriage that could be advanced in precise steps along the catcher strip to measure the  $^{13}\text{N}$  charge state spectrum. Maximum count rates at charge state peaks were about 400 cpm. Based on the 9.96-min half-life of  $^{13}\text{N}$ , these count rates were extrapolated back to a common time, zero, to normalize the spectra.

Because all excited nuclear states of  $^{13}\text{N}$  are unstable to proton emission, only the ground state is detected in our experiments. This simplifies the kinematics associated with the charge state spectra, since for a given deuteron energy, only one  $^{13}\text{N}$  energy results in the center-of-mass reference frame, this energy dictated by the 281 keV endothermicity of the  $^{12}\text{C}(\text{d},\text{n})^{13}\text{N}$  reaction and momentum and energy conservation. However, the  $^{13}\text{N}$  center-of-mass angle and thus its lab energy are double-valued functions of lab angle. For the deuteron energy range used here and  $22.5^\circ$   $^{13}\text{N}$  lab angle, we observe  $^{13}\text{N}$  corresponding to center-of-mass angles of  $58^\circ$  and  $168^\circ$ . The  $168^\circ$  group is unimportant here, because it is of very low energy (less than 250 keV) and is slowed to such an extent by the target (11) that it is removed from our detection zone by the magnetic field and thus does not interfere with spectral resolution of the  $58^\circ$  group. The lab energies and differential cross sections for the  $58^\circ$  group and total reaction cross sections are listed in Table I for deuteron energies used in this work.

### Results and Discussion

Examples of experimental results are shown in Figure 2 for deuteron energies of 8, 10, and 14 MeV. The fraction of  $^{13}\text{N}$  recoils of a given charge state, that is, the probability of a recoil having that charge state, is plotted as a function of charge state. All charge states, 0–7, were sought, but charges 1, 6, and 7 were not detected, and, if present, constituted fractions of less than 0.05 each. Small amounts of neutrals detected are attributed to the slow group of recoils ( $168^\circ$  center-of-mass angle). The shapes of these distributions resemble those reported for equilibrium distributions, because these particular runs used relatively thick carbon targets,  $30 \mu\text{g}/\text{cm}^2$  or  $1250 \text{ \AA}$ ; whereas approximately  $5 \mu\text{g}/\text{cm}^2$  is more than sufficient for charge equilibration at these energies (1, 16).



*Figure 2. Examples of  $^{13}\text{N}$  recoil charge state distributions from  $30\text{-}\mu\text{g}/\text{cm}^2$  targets. Charge state fractions (probabilities) are plotted vs. charge state for the three deuteron energies used in this work.*

Our results at 10 MeV deuteron energy are plotted in Figure 3 as a function of target thickness. On the right are included the literature (16) equilibrium charge state fractions. Because of low-count rates, there is considerable statistical scatter; however, agreement with the equilibrium values is good, except for the thinnest target,  $16\ \mu\text{g}/\text{cm}^2$ , where the increased fraction of  $\text{N}^{+5}$  may reflect an "instantaneous" average charge higher than the equilibrium value. These and other data are tabulated in Table II, where agreement with the equilibrium values is good at all deuteron energies for the thicker targets but not the thinnest target at 10 MeV.

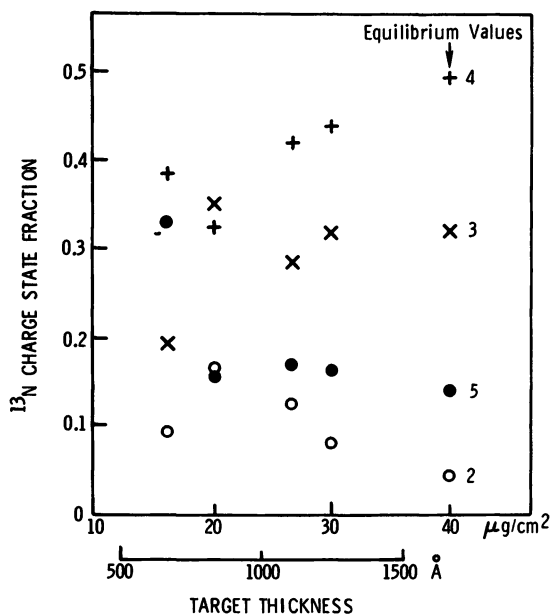
The average recoil charge calculated from the charge state fractions reported in Table II are plotted as a function of  $^{13}\text{N}$  recoil velocity in Figure 4. The solid line represents the equilibrium values (16). The values for  $30\text{-}\mu\text{g}/\text{cm}^2$  targets agree well with the equilibrium values. The only significant deviation from equilibrium is again in the data for the thinnest target.

Wolke and co-workers have observed nearly instantaneous nonequilibrium charge state distributions of  $^{12}\text{C}$  (8) and  $^{11}\text{B}$  (9) elastically scat-

**Table II.** <sup>13</sup>N Charge State Distributions

Deuteron Energy (MeV)	<sup>13</sup> N Charge State	Charge State Fraction for 30- $\mu\text{g}/\text{cm}^2$ Target	Equilibrium (16) Charge State Distribution	Charge State Fraction for 16- $\mu\text{g}/\text{cm}^2$ Target
8	2	0.190	0.115	
	3	0.397	0.432	
	4	0.330	0.383	
	5	0.083	0.069	
10	2	0.083	0.045	0.094
	3	0.317	0.322	0.193
	4	0.439	0.494	0.385
	5	0.162	0.140	0.328
14	3	0.176	0.151	
	4	0.462	0.523	
	5	0.362	0.326	

tered by deuterons by using extremely thin targets of carbon and boron, respectively. The average instantaneous charge was higher by 0.09 for <sup>12</sup>C recoiling at 4.4 MeV and by 0.31 for <sup>11</sup>B recoiling at 7 MeV. The difference in average charge was thought to be due to loss of electrons



**Figure 3.** <sup>13</sup>N recoil charge state fractions vs. carbon target thickness for 10-MeV deuteron energy. The equilibrium values (16) are shown on the right for charge states: (○) +2, (×) +3, (+) +4, and (●) +5.

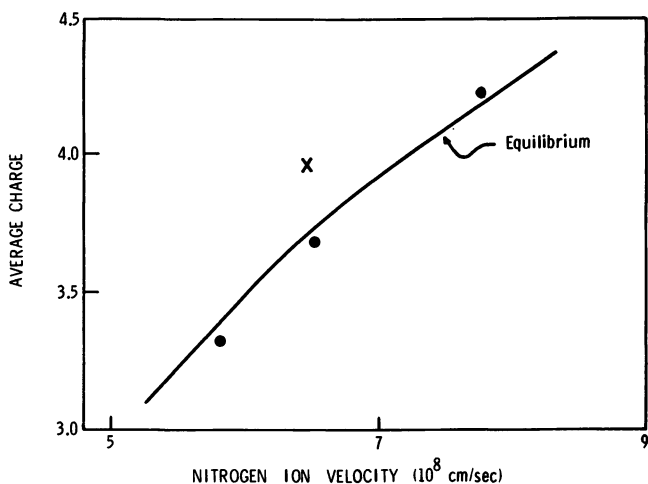


Figure 4. Average  $^{13}\text{N}$  recoil charge vs. recoil velocity for (●)  $30\text{-}\mu\text{g}/\text{cm}^2$  targets and (×)  $16\text{-}\mu\text{g}/\text{cm}^2$  targets. The solid line represents the equilibrium value (16) for  $^{14}\text{N}$  in carbon.

accompanying the sudden energetic recoil of the nucleus and passage of the fast deuteron through the electron cloud of the recoil. Those effects will also be present in our study but with an additional charge of  $+1$  due to the abrupt increase in atomic number resulting from pickup of a proton by  $^{12}\text{C}$ . We might then expect the average instantaneous charge on  $^{13}\text{N}$  to be about 5, that is, 1–1.5 units higher than the average equilibrium charge.

In our experiments, recoils originate over the entire thickness of the target, so that nonequilibrated instantaneous recoils originating near the exit side of the target are included in those we detect, regardless of the target thickness. The target thicknesses used in Wolfe's work (8), charge-changing cross sections (17,18), and other considerations (1) lead to the conclusion that charge equilibration requires approximately  $4\text{ }\mu\text{g}/\text{cm}^2$  of carbon for nitrogen ions in the velocity range pertinent to this study. Thus, the last  $4\text{ }\mu\text{g}/\text{cm}^2$  of our targets supply recoils not equilibrated upon exiting the target and not in sufficient quantities to be detected in our system, judging from count rates observed per  $\mu\text{g}/\text{cm}^2$  of target thickness. If the instantaneous charge of the recoils were  $+6$  or  $+7$ , peaks for those charge states should have been observed. Their absence implies that the average instantaneous charge of  $^{13}\text{N}$  recoils in these experiments is no greater than  $+5$ , in agreement with the conclusion reached above based on Wolfe's work with elastic scattering.

As a recoil travels through matter, it initiates a multitude of chemical reactions by ionization and charge transfer, which also slow the recoil to thermal energies. This process is very fast, on the order of  $10^{-12}$  s in

**Table III. Reactions of N<sup>+</sup>**

		<i>References</i>
H <sub>2</sub>	NH <sup>+</sup> + H, H <sub>2</sub> <sup>+</sup> + N	21, 22
N <sub>2</sub>	N <sub>2</sub> <sup>+</sup> + N	23
O <sub>2</sub>	NO <sup>+</sup> + O, O <sub>2</sub> <sup>+</sup> + N, O <sup>+</sup> + NO	21, 24
NO	NO <sup>+</sup> + N, N <sub>2</sub> <sup>+</sup> + O	21
CO	CO <sup>+</sup> + N, O <sup>+</sup> + C + N	21
CO <sub>2</sub>	CO <sub>2</sub> <sup>+</sup> + N, CO <sup>+</sup> + NO	21
H <sub>2</sub> O	H <sub>2</sub> O <sup>+</sup> + N, NO <sup>+</sup> + H <sub>2</sub>	21
NH <sub>3</sub>	NH <sub>3</sub> <sup>+</sup> + N, NH <sub>2</sub> <sup>+</sup> + NH, N <sub>2</sub> H <sup>+</sup> + H	21
CH <sub>4</sub>	CH <sub>4</sub> <sup>+</sup> + N, CH <sup>+</sup> + NH, CHN <sup>+</sup> + H, HCN <sup>+</sup> + H + H	21
CCl <sub>4</sub>	CCl <sub>3</sub> <sup>+</sup> , CCl <sub>2</sub> <sup>+</sup> , CCl <sup>+</sup> , Cl <sup>+</sup> , NCCl <sup>+</sup> , NCl <sup>+</sup> , CN <sup>+</sup> , NCCl <sub>2</sub> <sup>+</sup>	25

solids and 10<sup>-9</sup> s in gases at atmospheric pressure based on published stopping power data (19, 20). At the higher energies and charge states, relative collision energies are too great to permit formation of chemical bonds between recoils and atoms of the stopping medium. As the recoil slows, its charge decreases (*see* Figure 4) until the average charge becomes +1 at about 200 keV (2, 4). Below about 1 keV kinetic energy, the recoil may begin to undergo atom transfer reactions, forming stable chemical bonds. Thus the primary species involved in labeling reactions and N<sup>+1</sup> and N<sup>0</sup>.

We have reviewed the literature to gather a collection of reactions that N<sup>+1</sup> and N<sup>0</sup> undergo, and these are listed in Tables III and IV, respectively. These lists are by no means exhaustive but are intended

**Table IV. Reactions of N Atoms**

		<i>References</i>
NO	N <sub>2</sub> + O	32
O <sub>2</sub>	NO + O	33
N <sub>2</sub> '	N'N + N'	30
SO	NO + S	27
X <sub>2</sub>	NX + X (X = Cl, Br, I)	34
HX	NH + X (X = Br, I)	35
NO <sub>2</sub>	N <sub>2</sub> O + O, 2NO, N <sub>2</sub> + 2O, N <sub>2</sub> + O <sub>2</sub>	36
O <sub>3</sub>	NO + O <sub>2</sub>	37
N <sub>2</sub> O	N <sub>2</sub> + NO	38
SO <sub>3</sub>	SO <sub>2</sub> + NO	27
PH <sub>3</sub>	NH + PH <sub>2</sub>	39
Alkanes	HCN, NH <sub>3</sub> , (CN) <sub>2</sub> , CH <sub>3</sub> CN, hydrocarbons	27
Alkenes	HCN, CH <sub>3</sub> CN, (CN) <sub>2</sub> , NH <sub>3</sub> , hydrocarbons	27
Alkynes	(CN) <sub>2</sub> , HCN, NH <sub>3</sub> , NC <sub>3</sub> H, hydrocarbons	27
CHCl <sub>3</sub> , CH <sub>2</sub> Cl <sub>2</sub> ,		
CH <sub>3</sub> Cl	HCl, HCN	40
CCl <sub>4</sub>	ClCN, Cl <sub>2</sub>	40
CH <sub>3</sub> OH,		
C <sub>2</sub> H <sub>5</sub> OH	HCN, H <sub>2</sub> O	

Table V. Products of  $^{13}\text{N}$  Recoiling in Various Media

		References
NO	$^{13}\text{NN}$ , $^{13}\text{NO}$	42
CO	$^{13}\text{NN}$ , $^{13}\text{NNO}$	30
CO <sub>2</sub>	$^{13}\text{NN}$ , $^{13}\text{NNO}$	30, 43
H <sub>2</sub> O (l)	$^{13}\text{NH}_4^+$ , $^{13}\text{NO}_3^-$ , $^{13}\text{NH}_2\text{OH}$ , $^{13}\text{NO}_2^-$ , $^{13}\text{NO}$ , $^{13}\text{NN}$	44, 45
NaNO <sub>3</sub> (s)	$^{13}\text{NO}_3^-$ , $^{13}\text{NO}_2^-$	45
NaNO <sub>3</sub> (aq)	$^{13}\text{NH}_4^+$ , $^{13}\text{NO}_3^-$ , $^{13}\text{NO}_2^-$	45
NH <sub>4</sub> F (s)	$^{13}\text{NH}_4^+$ , $^{13}\text{NH}_2\text{NH}_2$	45
NH <sub>4</sub> (aq)	$^{13}\text{NH}_4^+$ , $^{13}\text{NO}_3^-$ , $^{13}\text{NO}_2^-$ , $^{13}\text{NH}_2\text{NH}_2$	45
NH <sub>4</sub> NO <sub>3</sub> (s)	$^{13}\text{NO}_3^-$ , $^{13}\text{NH}_4^+$ , $^{13}\text{NO}_2^-$ , $^{13}\text{NNO}$	46
(NH <sub>4</sub> ) <sub>2</sub> SO <sub>4</sub> (s)	$^{13}\text{NH}_2\text{OH}$ , $^{13}\text{NH}_2\text{NH}_2$ , $^{13}\text{NH}_4^+$ , $^{13}\text{NO}_3^-$	47
CH <sub>4</sub>	HC $^{13}\text{N}$ , $^{13}\text{NH}_3$ , CH <sub>3</sub> $^{13}\text{NH}_2$ , C <sub>2</sub> H <sub>5</sub> $^{13}\text{NH}_2$ , CH <sub>3</sub> C $^{13}\text{N}$ , $^{13}\text{NN}$	48, 49
CH <sub>3</sub> OH	HC $^{13}\text{N}$ , CH <sub>3</sub> C $^{13}\text{N}$ , $^{13}\text{NN}$	49, 50
CH <sub>3</sub> Cl	HC $^{13}\text{N}$ , $^{13}\text{NN}$ , $^{13}\text{NO}_2$	50, 51
CCl <sub>4</sub>	CIC $^{13}\text{N}$	50, 51

to illustrate the general characteristics of these reactions and to provide starting points for understanding product distributions in specific media.

Each reactant in Table III, including N<sub>2</sub>, undergoes charge transfer as well as atom transfer reactions with N<sup>+</sup>. The formation of H<sub>2</sub><sup>+</sup> from H<sub>2</sub> and CCl<sub>2</sub><sup>+</sup>, CCl<sup>+</sup>, and Cl<sup>+</sup> from CCl<sub>4</sub> are endothermic for ground state N<sup>+</sup> (<sup>3</sup>P). These channels as well as many of the exothermic ones probably involve excited N<sup>+</sup>, specifically N<sup>+</sup> (<sup>1</sup>D) with 1.9-eV excitation energy and 300-s lifetime and N<sup>+</sup> (<sup>1</sup>S) with 4.1-eV excitation energy and 0.9-s lifetime. Many of the products, e.g., NH<sup>+</sup> from H<sub>2</sub> (22), are probably excited as well.

Extensive reviews of N atom reactions do exist (26, 27, 28, 29). Much of the data in Table IV was obtained using "active" nitrogen and may involve electronically excited N atoms as is the case of the reaction with N<sub>2</sub>O where only excited N (<sup>2</sup>D) is reactive, not ground state N (<sup>4</sup>S). Atom transfer with N<sub>2</sub> proceeds only with excited N (<sup>2</sup>D) (excitation energy 2.38 eV, lifetime 26 h) or with N (<sup>2</sup>P) (excitation energy 3.57 eV, lifetime 12 s), or with hot N (<sup>4</sup>S), but not thermalized N (<sup>4</sup>S). N atoms are apparently unreactive toward H<sub>2</sub>, NH<sub>3</sub>, SO<sub>2</sub> (27), CO<sub>2</sub> (30), and COCl<sub>2</sub> (31), reactions reported with these molecules having been due to contaminant gases adsorbed on vessel walls or excited molecular nitrogen. Products are listed in the general order of decreasing abundance for the reactions with alkanes, alkenes, and alkynes.

Reactions such as those in Tables III and IV ultimately lead to  $^{13}\text{N}$ -labeled products such as those listed in Table V for  $^{13}\text{N}$  recoils reacting with various media. Products are again listed in order of decreasing abundance. Again, the list is not intended to be comprehensive.  $^{13}\text{N}$  was

produced by the reaction  $^{12}\text{C}(\text{d},\text{n})^{13}\text{N}$  in the studies on NO, CO,  $\text{CO}_2$ ,  $\text{CH}_4$ ,  $\text{CH}_3\text{OH}$ ,  $\text{CH}_3\text{Cl}$ , and  $\text{CCl}_4$ .  $^{13}\text{N}$  from  $^{14}\text{N}(\text{n},2\text{n})^{13}\text{N}$  was used in the studies on  $\text{NaNO}_3$ ,  $\text{NH}_4\text{F}$ ,  $(\text{NH}_4)_2\text{SO}_4$ , and  $\text{NH}_4\text{NO}_3$ .  $^{13}\text{N}$  from  $^{16}\text{O}(\text{p},\alpha)^{13}\text{N}$  as well as  $^{16}\text{N}$  from  $^{16}\text{O}(\text{n},\text{p})^{16}\text{N}$  were used in studies on  $\text{H}_2\text{O}$ . As for the primary reactions, impurities are also expected to be extremely important here, as is made clear by detection of  $^{13}\text{N}^{14}\text{N}$  and  $^{13}\text{N}^{14}\text{NO}$  after recoil reactions in CO and  $\text{CO}_2$ . To understand fully the entries in Table V, we must first gather more detailed information concerning reactant and product quantum states and velocity-dependent cross sections for the primary reactions and all radiolytic side reactions, particularly through the use of beam experiments. It may then become possible to design precise clean syntheses of radio-labeled products from first principles.

### *Acknowledgments*

We are indebted to Walter R. Van Antwerp for assistance with the experimental work and for arrangement of accelerator time. The work was carried out under the auspices of the U.S. Department of Energy.

### *Literature Cited*

1. Lutz, H. O.; Datz, S.; Moak, C. D.; Noggle, T. S. *Radiat. Eff.* **1970**, *33A*, 309.
2. Wittkower, A. B.; Betz, H. D. *At. Data* **1973**, *5*, 113.
3. Davidson, J.; Bickel, W. S. *Nucl. Instrum. Methods* **1973**, *110*, 253.
4. Wickholm, D.; Bickel, W. S. *J. Opt. Soc. Am.* **1976**, *66*, 502.
5. Clark, R. B.; Grant, I. S.; King, R.; Eastham, D. A.; Joy, T. *Nucl. Instrum. Methods* **1976**, *133*, 17.
6. Steiger, N. H. *Chem. Eff. Nucl. Transform., Proc. Symp., IAEA, Vienna* **1964**, *1*, 35.
7. Wolke, R. L. *Phys. Rev.* **1968**, *171*, 301.
8. Wolke, R. L.; Sorbo, R. A.; Volkar, M. A.; Gangadharan, S.; Mason, E. V., Jr. *Phys. Rev. Lett.* **1971**, *27*, 1449.
9. Mason, E. V., Jr.; Wolke, R. L.; Debiak, T. W.; Yesso, J. D. *Phys. Rev.* **1974**, *A9*, 1569.
10. Stoner, J. O., Jr. *J. Appl. Phys.* **1969**, *40*, 707.
11. Northcliffe, L. C. *Ann. Rev. Nucl. Sci.* **1963**, *13*, 67.
12. Gangadharan, S.; Wolke, R. L. *Phys. Rev.* **1970**, *CI*, 1333.
13. Mutchler, G. S.; Rendic, D.; Velleley, D. E.; Sweeney, W. E., Jr.; Phillips, G. C. *Nucl. Phys.* **1971**, *A172*, 469.
14. Davis, J. R.; Din, G. U. *Nucl. Phys.* **1972**, *A179*, 101.
15. Wilkinson, D. H. *Phys. Rev.* **1955**, *100*, 32.
16. Girardeau, R.; Knystautas, E. J.; Beauchemin, G.; Neveu, B.; Drouin, R. *J. Phys.* **1971**, *B4*, 1743.
17. Nikolaev, V. S. *Sov. Phys. Usp.* **1965**, *8*, 269.
18. Volodyagin, Y. S.; Dimitriev, I. S.; Nikolaev, V. S.; Tashaev, Y. A.; Teplova, Y. A. *J. Phys.* **1973**, *B6*, L171.
19. Fastrup, B.; Hvelplund, P.; Sautter, C. A. *K. Dan. Vidensk. Selsk., Mat.-Fys. Medd.* **1966**, *35*, 10.
20. Lindhard, J.; Scharff, M.; Schiott, H. E. *K. Dan. Vidensk. Selsk., Mat.-Fys. Medd.* **1963**, *33*, 14.

21. Tichy, M.; Rakshit, A. B.; Lister, D. G.; Twiddy, N. D.; Adams, N. G.; Smith, D. *Int. J. Mass Spectrom. Ion Phys.* 1979, 29, 231.
22. Gislason, E. A.; Mahan, B. H.; Tsao, C. W.; Werner, A. S. *J. Chem. Phys.* 1971, 54, 3897.
23. Maier, W. B., II; Murad, E. *J. Chem. Phys.* 1971, 55, 2307.
24. Tully, J. C.; Herman, Z.; Wolfgang, R. *J. Chem. Phys.* 1971, 54, 1730.
25. Weiner, E. R.; Hertel, G. R.; Koski, W. S. *J. Am. Chem. Soc.* 1964, 86, 788.
26. Wright, A. N.; Winkler, C. A. "Active Nitrogen"; Academic: New York, 1967.
27. Brown, R.; Winkler, C. A. *Angew. Chem. Int. Ed. Engl.* 1970, 9, 181.
28. Westley, F. *Natl. Bur. Stand.* 1971, NBS-OSRDB-71-2.
29. Westley, F. *Natl. Bur. Stand., Spec. Publ.* 1973, 371.
30. Stewart, G. W.; Dymerski, P. P.; Hower, C. O. *J. Chem. Phys.* 1974, 61, 483.
31. Baker, R. R.; Winkler, C. A. *Can. J. Chem.* 1971, 49, 3846.
32. Evans, H. G. V.; Winkler, C. A. *Can. J. Chem.* 1956, 34, 1217.
33. Vlastaras, T.; Winkler, C. A. *Can. J. Chem.* 1967, 45, 2837.
34. Phillips, L. F. *Can. J. Chem.* 1968, 46, 1429.
35. Milton, E. R. V.; Dunford, H. B. *J. Chem. Phys.* 1961, 34, 51.
36. Phillips, L. F.; Schiff, H. I. *J. Chem. Phys.* 1965, 42, 3171.
37. *Ibid.*, 1962, 36, 1509.
38. Black, G.; Slinger, T. G.; St. John, G. A.; Young, R. A. *J. Chem. Phys.* 1969, 51, 116.
39. Wiles, D. M.; Winkler, C. A. *Can. J. Chem.* 1958, 36, 1223.
40. Sobering, S. E.; Winkler, C. A. *Can. J. Chem.* 1958, 36, 1223.
41. Gartaganis, P. A. *Can. J. Chem.* 1965, 43, 935.
42. Dubrin, J.; MacKay, C.; Wolfgang, R. *J. Chem. Phys.* 1966, 44, 2208.
43. Welch, M. J. *Chem. Commun.* 1968, 1968, 1354.
44. Schleiffer, J. J.; Adloff, J. P. *Radiochim. Acta* 1964, 3, 145.
45. Aten, A. H. W., Jr.; Kapteyn, J. C. *Radiochem. Radioanal. Lett.* 1978, 32, 83.
46. Smith, R. D.; Aten, A. H. W., Jr. *J. Inorg. Nucl. Chem.* 1955, 1, 296.
47. Aten, A. H. W., Jr.; Michielsen, J. C. F. *J. Inorg. Nucl. Chem.* 1978, 40, 1700.
48. Tilbury, R. S.; Dahl, J. R.; Monahan, W. G.; Laughlin, J. S. *Radiochem. Radioanal. Lett.* 1971, 8, 317.
49. Perkins, W. C.; Koski, W. S. *J. Phys. Chem.* 1962, 66, 474.
50. Koski, W. S.; Schmied, H.; Perkins, W. C. In "Chemical Effects of Nuclear Transformations"; IAEA: Vienna, 1961; p. 217.
51. Schmied, H.; Koski, W. S. *J. Am. Chem. Soc.* 1960, 82, 4766.

RECEIVED September 4, 1980.



# Chemical Reactions of Nuclear Recoil $^{18}\text{F}$ Atoms with Gas-Phase Halocarbons

JOHN W. ROOT

Department of Chemistry and Crocker Nuclear Laboratory,  
University of California, Davis, CA 95616

RONALD G. MANNING

Department of Nuclear Medicine, National Institutes of Health,  
Bethesda, MD 20205

*The principal goals of  $^{18}\text{F}$  hot atom chemistry research involve the identification and study of energetic reaction pathways and the elucidation of the properties of the labeled products formed from such reactions. The salient features of this research carried out with halocarbon reagents during the past 10 years are summarized within the context of these two major areas of emphasis.*

The gas-phase reactions of translationally excited nuclear recoil  $^{18}\text{F}$  atoms have been extensively studied in recent years (1-51). A new and rapidly growing extension of this research involves the measurement of kinetic rate parameters for atomic  $^{18}\text{F}$  reactions under equilibrium, or "thermal," conditions. Because this topic has been considered elsewhere in this volume and in other recent reviews (47, 52, 53, 54), these additional references have not been listed here.

The principal goals of  $^{18}\text{F}$  hot atom chemistry research involve the identification and study of energetic reaction pathways and the elucidation of the properties of the labeled products formed from such reactions. Although a variety of organic and inorganic reagents have been investigated, most of the available results have been obtained with halocarbons. During the past 10 years extensive gas-phase measurements have been carried out at this laboratory with fluorinated alkanes (8, 14, 15, 16, 18, 25, 26, 28, 31, 34, 35, 40, 45, 47, 50, 55, 56). The salient features of this research are summarized in this chapter within the context of the two areas of emphasis noted above.

0065-2393/81/0197-0079\$11.00/0  
© 1981 American Chemical Society

## Experimental

General discussions concerning the production methods and the charge state upon reaction for recoiling  $^{18}\text{F}$  atoms have been presented elsewhere (1, 2, 14, 47, 54, 57, 58, 59). Due to its relative freedom from radiation damage complications, the  $^{19}\text{F}(n,2n)^{18}\text{F}$  nuclear reaction has been preferred at this laboratory for the production of recoil  $^{18}\text{F}$  atoms (54). Detailed descriptions of our other experimental procedures have been presented previously (14, 15, 29, 31, 34, 54, 55, 60).

The most useful type of data that can be obtained in these experiments consists of the absolute fractions of the initially produced  $^{18}\text{F}$  atoms corresponding to the various labeled products. Our preferred method for determining the absolute product yields has involved a combination of conventional radiochemical separations, which serve to establish the combined yields of organic and inorganic species, together with radio gas chromatographic assay of the individual organic products (54, 55).

The labeled products from recoil experiments are formed in amounts that are immeasurably small based on conventional mass sensitive detectors. Ordinary physical methods thus cannot aid the sometimes difficult task of product identification (61, 62). Our method for confirming product identities involves matching the chromatographic retention volumes with those for authentic standards using two different columns. The likelihood that accidental overlapping of product peaks will escape detection can be greatly reduced in this fashion, provided that the two assays exhibit pronounced chromatographic selectivity differences.

A typical comparison of this type has been shown in Table I. The cited peak retention data show that our (NPGS + DBPH) and (C9CROT + C7ACRY) columns exhibit different selectivities toward polar and nonpolar halocarbons. The measured product yields are in quantitative agreement within the allowed radioactive statistical measurement uncertainties. Products having  $\geq 0.2\%$  yields are easily detected, and expected species other than those reported are routinely monitored.

To improve the statistical precision, replicate samples are processed for each set of conditions. Our error analysis methods have been described previously (28, 54). The cited measurement uncertainties represent single standard deviations at the 68% confidence level. In the case of yield branching ratios these uncertainties follow directly from statistical random error analysis. Speculative estimates of the contributions from possible systematic mechanistic errors have not been included.

## Results

The recoil  $^{18}\text{F}$  reaction mechanisms reported from this laboratory have been determined using a combination of scavenger- and pressure-variation measurements (15, 18). Absolute yields are obtained at various pressures for samples scavenged with 15 mol %  $\text{O}_2$  or with 5 mol %  $\text{H}_2\text{S}$  or  $\text{Cl}_2$  (34, 45, 47-50).

Gas imperfection must be taken into account over the large range of pressures used in these experiments. The empirical equation of state  $PV = ZnRT$  rearranges to give  $(P/Z) = (\rho RT/M)$  in which  $Z$ ,  $\rho$ ,  $R$ ,

**Table I. Product Yields for  $\text{CH}_3\text{CF}_3$  Samples Obtained Using Different Gas Chromatography Columns\***

(P/Z) (atm)	3.0	2.9		
T (K) <sup>b</sup>	303	303		
Scavenger (mol %)	$\text{O}_2$ (15.0)	$\text{O}_2$ (15.0)		
Column Configuration <sup>c</sup>	NPGS + DBPH	C9CROT + C7ACRY		
Product	Elution Time (s)	Absolute Yield (%)	Elution Time (s)	Absolute Yield (%)
$\text{CF}_3^{18}\text{F}$	1400	0.82	1030	0.79
$\text{CF}_2=\text{CF}^{18}\text{F}$	1620	0.16	1200	0.20
$\text{CH}_2=\text{CF}^{18}\text{F}$	2740	0.93	1410	0.89
$\text{CF}_3\text{CH}_2^{18}\text{F}$	2260	1.65	3140	1.54
$\text{CHF}_2^{18}\text{F}$	3200	0.41	1580	0.22
$\text{CH}_3^{18}\text{F}$	3530	1.05	1720	1.18
$\text{CH}_3\text{CF}_2^{18}\text{F}$	} 3900	1.36	1910	1.18
$\text{CF}_2=\text{CH}^{18}\text{F}$			2200	0.28
$\text{CH}_2\text{F}^{18}\text{F}$	5380	< 0.1	2500	0.09

\* Cited data represent individual samples (Ref. 28).

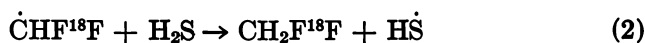
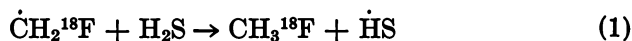
<sup>b</sup> Ambient irradiation temperature.

<sup>c</sup> The columns contained neopentyl glycol sebacate (NPGS) and di-*n*-butyl phthalate (DBPH) or the crotonic acid ester of  $\text{H}(\text{CF}_2)_8\text{CH}_2\text{OH}$  (C9CROT) and the acrylic acid ester of  $\text{H}(\text{CF}_2)_8\text{CH}_2\text{OH}$  (C7ACRY) (Refs. 15, 18, 28, 45, 55).

and  $M$  denote the gas compressibility factor, the mass density, the molar gas constant and the molecular weight. The effective pressure ( $P/Z$ ), which corresponds to the molecular density expressed in units of atm, is determined directly in our sample preparation procedure.

Table II lists representative yield data for  $\text{H}_2\text{S}$ - and  $\text{O}_2$ -scavenged  $\text{CH}_3\text{CHF}_2$ . Within the limiting statistical accuracy, at fixed ( $P/Z$ ) most of the yields are the same with either scavenger. Aliphatic free radicals react rapidly with both  $\text{O}_2$  and  $\text{H}_2\text{S}$ . Therefore, observations of yield insensitivity to the presence of these scavengers preclude the mechanistic involvement of labeled alkyl radicals.

From Table II the  $\text{CH}_3^{18}\text{F}$  and  $\text{CH}_2\text{F}^{18}\text{F}$  yields increase in samples containing  $\text{H}_2\text{S}$ , indicating the importance of radical precursors (Equations 1 and 2). Our separation procedure removes the products from



$\text{O}_2$  scavenging of labeled alkyl radicals from the volatile organic yield fraction (Equation 3). With the aid of a  $\text{K}_2\text{CO}_3 \cdot 1.5\text{H}_2\text{O}$  chemical



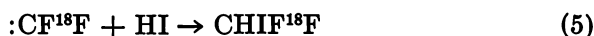
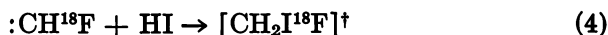
Table II. Single Sample Yield Data for Scavenged  $\text{CH}_3\text{CHF}_2$  (28)

(P/Z) (atm)	2.7	2.4	93.8	92.8
T (K) <sup>a</sup>	303	303	458	405
Scavenger (mol %)	$\text{H}_2\text{S}$ (5.6)	$\text{O}_2$ (14.5)	$\text{H}_2\text{S}$ (5.1)	$\text{O}_2$ (14.9)
Product	Absolute Yield (%)			
$\text{CF}_2=\text{CF}^{18}\text{F}$	0.19	0.02	< 0.05	< 0.05
$\text{CH}_2=\text{CF}^{18}\text{F}$	0.56	0.74	0.46	0.48
$\text{CH}_3\text{CHF}^{18}\text{F}$	1.14	1.06	1.63	1.84
$\text{CHF}_2^{18}\text{F}$	0.54	0.48	0.85	0.53
$\text{CH}_3^{18}\text{F}$	4.12	1.39	4.39	1.50
cis- $\text{CHF}=\text{CH}^{18}\text{F}$	0.39	0.32	0.19	0.20
$\text{CH}_3\text{CF}_2^{18}\text{F}$	0.58	0.64	1.05	1.01
$\text{CH}_2=\text{CH}^{18}\text{F}$	0.72	0.71	0.79	0.65
$\text{CH}_2\text{F}^{18}\text{F}$	0.63	< 0.05	0.81	0.17
trans- $\text{CHF}=\text{CH}^{18}\text{F}$	0.20	0.28	0.15	0.23
$\text{CHF}_2\text{CH}_2^{18}\text{F}$	1.67	1.71	2.37	2.37
Unknown	0.15	< 0.10	< 0.10	< 0.10

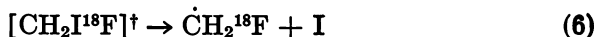
<sup>a</sup> Ambient irradiation temperature.

stripper, the combined yields from all such reactions are recovered in the volatile inorganic fraction (14, 54). The nonvolatile inorganic yield, which may include part or all of any  $\text{H}^{18}\text{F}$ ,  $\text{Cl}^{18}\text{F}$ ,  $\text{NO}^{18}\text{F}$ , and  $\text{COF}^{18}\text{F}$  products, is recovered from the interior surface of the irradiation vessel following transfer of the volatile sample contents (52, 54, 55).

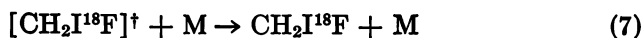
Our  $\text{CH}_3\text{CHF}_2$  and  $\text{CH}_3\text{CF}_3$  experiments have not provided for direct monitoring of the labeled diradicals  $:\text{CH}^{18}\text{F}$ ,  $:\text{CF}^{18}\text{F}$ , and  $:\dot{\text{C}}^{18}\text{F}$ . The two carbenes have been trapped using HI (Reactions 4 and 5) (6). Here



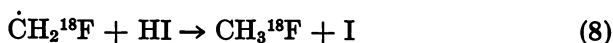
the superscript dagger ( $\dagger$ ) denotes sufficient nascent product excitation to induce unimolecular decomposition Reaction 6. At (P/Z) values



below several atm, dissociation Reaction 6 competes with collisional deactivation process 7. Any  $\dot{\text{C}}\text{H}_2^{18}\text{F}$  radicals formed from Reaction 6



undergo hydrogen abstraction from HI.

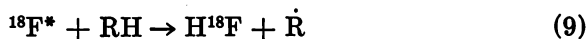


For the reasons listed below the HI-scavenging method has not been used in our experiments: (i) the presence in the samples of macroscopic concentrations of HI interferes with our recovery procedure for nonvolatile inorganic activity; (ii) scavenging reactions such as that shown in Reaction 8 present multiple pathways for  $\text{CH}_3^{18}\text{F}$  and  $\text{CH}_2^{18}\text{F}$  formation and thus increase the complexity of the mechanism; and (iii) our chromatographic separations are not suitable for determining  $\text{CH}_2^{18}\text{F}$  and  $\text{CHIF}^{18}\text{F}$  products.

The use of  $\text{Cl}_2$  scavenger in experiments with  $\text{CF}_4$  and  $\text{C}_2\text{F}_6$  allows direct monitoring of labeled alkyl radicals,  $:\text{CF}^{18}\text{F}$  and  $:\text{C}^{18}\text{F}$  (47, 48, 55). However, kinetic control of the reactions of  $:\text{CH}^{18}\text{F}$  and  $:\text{CF}^{18}\text{F}$  was not achieved in our previous  $\text{H}_2\text{S}$ -scavenged fluoroethane experiments. Table II shows that  $\text{CF}_2=\text{CF}^{18}\text{F}$  product is formed at low ( $P/Z$ ) in  $\text{H}_2\text{S}$ -scavenged  $\text{CF}_4$ ,  $\text{C}_2\text{F}_6$ ,  $\text{CH}_3\text{CF}_3$ , and  $\text{CH}_3\text{CHF}_2$ , suggesting that  $:\text{CF}^{18}\text{F}$  is present and that it is rather unreactive toward  $\text{H}_2\text{S}$ . The reactivity of excited  $:\text{CF}^{18}\text{F}$  toward  $\text{O}_2$  has been considered elsewhere (17, 54, 55).

Returning to Table II, at 2.5 atm two unidentified products, which exhibited poorly reproducible yields totaling approximately 0.2%, were observed. We suspect that these trace yields reflect unknown and poorly controlled scavenging mechanisms for labeled carbenes and carbynes. However, the yields of  $:\text{CH}^{18}\text{F}$  and  $:\text{CF}^{18}\text{F}$  diminish rapidly with increasing ( $P/Z$ ), and the lack of complete knowledge concerning the low-pressure mechanisms is not serious (34, 35).

Table II also illustrates the need for varying the irradiation temperature during measurements at elevated ( $P/Z$ ) to ensure that homogeneous gas-phase conditions are maintained. Recoil  $^{18}\text{F}$  experiments with  $\text{CH}_3\text{F}$  over wide ranges of ( $P/Z$ ) and temperature have been reported (11). In agreement with these results our organic product yields are insensitive to moderate temperature changes (34, 35). However, the yields from nonthermal hot hydrogen abstraction (Reaction 9) (24, 29, 40) or from



competing thermal  $^{18}\text{F}$  reactions (52, 54) exhibit marked temperature sensitivity. Here the asterisk (\*) denotes excess  $^{18}\text{F}$  translational excitation.

Tables III and IV summarize the  $\text{C}_1$  and  $\text{C}_2$  product yields obtained for  $\text{CH}_3\text{CHF}_2$ . Each result represents the average from 4–6 replicate measurements. Table III shows that the  $\text{C}_1$  product distributions are different in  $\text{H}_2\text{S}$ - and  $\text{O}_2$ -scavenged samples. Reproducible results were not obtained for  $\text{CH}_2^{18}\text{F}$  under  $\text{O}_2$ -scavenged conditions. However, this yield was only detected at low ( $P/Z$ ), and it never exceeded 0.2%. At

Table III. C<sub>1</sub> Product Distributions for  
Absolute Yield (%)

(P/Z) (atm)	CH <sub>3</sub> <sup>18</sup> F(H <sub>2</sub> S)	CH <sub>3</sub> <sup>18</sup> F(O <sub>2</sub> )
0.35	3.99 ± 0.34	1.17 ± 0.12
1.0	4.33 ± 0.25	1.23 ± 0.10
3.0	4.34 ± 0.26	1.18 ± 0.07
5.0	5.00 ± 0.24	1.30 ± 0.06
7.0	4.57 ± 0.21	1.41 ± 0.06
8.0	4.66 ± 0.20	1.46 ± 0.06
10	4.90 ± 0.20	1.54 ± 0.06
45	4.65 ± 0.25	1.55 ± 0.10
95	4.29 ± 0.24	1.47 ± 0.09
190	3.65 ± 0.28	1.54 ± 0.13

Table IV. C<sub>2</sub> Product Distributions  
Absolute Yield (%)

(P/Z) (atm)	CH <sub>3</sub> CHF <sup>18</sup> F	CH <sub>2</sub> =CH <sup>18</sup> F	CH <sub>3</sub> CF <sub>2</sub> <sup>18</sup> F
0.35	0.78 ± 0.10	0.98 ± 0.11	0.55 ± 0.06
1.0	0.98 ± 0.08	0.82 ± 0.09	0.59 ± 0.05
3.0	1.21 ± 0.07	0.88 ± 0.08	0.62 ± 0.05
5.0	1.32 ± 0.06	0.72 ± 0.07	0.73 ± 0.04
7.0	1.39 ± 0.06	0.78 ± 0.07	0.80 ± 0.04
8.0	1.44 ± 0.06	0.78 ± 0.07	0.85 ± 0.04
10	1.51 ± 0.07	0.76 ± 0.07	0.91 ± 0.05
45	1.62 ± 0.15	0.74 ± 0.09	0.98 ± 0.09
95	1.70 ± 0.12	0.72 ± 0.09	1.05 ± 0.08
190	2.01 ± 0.17	0.68 ± 0.08	1.34 ± 0.12

Table V. C<sub>1</sub> Product Distributions

(P/Z) (atm)	Absolute Yield (%)			
	CF <sub>3</sub> <sup>18</sup> F(H <sub>2</sub> S)	CF <sub>3</sub> <sup>18</sup> F(O <sub>2</sub> )	CHF <sub>2</sub> <sup>18</sup> F(H <sub>2</sub> S)	CHF <sub>2</sub> <sup>18</sup> F(O <sub>2</sub> )
0.30	0.65 ± 0.08	0.87 ± 0.07	1.04 ± 0.16	0.16 ± 0.08
1.5	0.83 ± 0.07	0.80 ± 0.07	1.29 ± 0.14	0.43 ± 0.12
3.0	0.75 ± 0.08	0.85 ± 0.05	1.35 ± 0.16	0.37 ± 0.14
5.0	0.87 ± 0.05	0.90 ± 0.05	1.21 ± 0.14	0.22 ± 0.11
8.0	0.96 ± 0.05	1.12 ± 0.06	1.22 ± 0.14	0.05 ± 0.10
10	1.05 ± 0.04	1.04 ± 0.07	1.21 ± 0.13	0.00 ± 0.10
40	0.98 ± 0.06	1.14 ± 0.09	1.07 ± 0.14	0.00 ± 0.10
70	1.01 ± 0.07	1.08 ± 0.12	0.99 ± 0.15	0.00 ± 0.10
100	1.04 ± 0.06	1.04 ± 0.09	0.90 ± 0.15	0.00 ± 0.10
170	1.08 ± 0.07	1.06 ± 0.08	0.82 ± 0.11	0.00 ± 0.10

**$\text{H}_2\text{S}$ - and  $\text{O}_2$ -Scavenged  $\text{CH}_3\text{CHF}_2$  (28, 45)***Absolute Yield (%)*

$\text{CHF}_2^{18}\text{F}(\text{H}_2\text{S})$	$\text{CHF}_2^{18}\text{F}(\text{O}_2)$	$\text{CH}_2\text{F}^{18}\text{F}(\text{H}_2\text{S})$
0.42 ± 0.10	0.31 ± 0.10	0.52 ± 0.11
0.80 ± 0.07	0.35 ± 0.09	0.57 ± 0.10
0.72 ± 0.08	0.37 ± 0.09	0.59 ± 0.10
0.65 ± 0.08	0.40 ± 0.10	0.85 ± 0.10
0.71 ± 0.07	0.42 ± 0.09	0.81 ± 0.10
0.69 ± 0.08	0.41 ± 0.08	0.79 ± 0.10
0.73 ± 0.06	0.41 ± 0.08	0.81 ± 0.11
0.73 ± 0.10	0.44 ± 0.11	0.69 ± 0.12
0.85 ± 0.12	0.50 ± 0.10	0.73 ± 0.12
0.82 ± 0.14	0.50 ± 0.12	0.68 ± 0.12

**for  $\text{CH}_3\text{CHF}_2$  (28, 45)***Absolute Yield (%)*

$\text{CH}_2=\text{CF}^{18}\text{F}$	$\text{CHF}_2\text{CH}_2^{18}\text{F}$	(cis + trans)- $\text{CHF}=\text{CH}^{18}\text{F}$
0.89 ± 0.17	1.39 ± 0.15	0.58 ± 0.08
0.65 ± 0.11	1.34 ± 0.11	0.41 ± 0.08
0.62 ± 0.08	1.60 ± 0.08	0.38 ± 0.07
0.61 ± 0.07	1.75 ± 0.07	0.38 ± 0.07
0.57 ± 0.07	1.86 ± 0.08	0.36 ± 0.07
0.56 ± 0.07	1.97 ± 0.08	0.35 ± 0.06
0.57 ± 0.09	2.09 ± 0.10	0.35 ± 0.05
0.54 ± 0.10	2.32 ± 0.20	0.35 ± 0.07
0.46 ± 0.09	2.53 ± 0.17	0.35 ± 0.07
0.41 ± 0.15	3.08 ± 0.12	0.36 ± 0.11

**for  $\text{H}_2\text{S}$ - and  $\text{O}_2$ -Scavenged  $\text{CH}_3\text{CF}_3$  (28)***Absolute Yield (%)*

$\text{CH}_2\text{F}^{18}\text{F}(\text{H}_2\text{S})$	$\text{CH}_2\text{F}^{18}\text{F}(\text{O}_2)$	$\text{CH}_3^{18}\text{F}(\text{H}_2\text{S})$	$\text{CH}_3^{18}\text{F}(\text{O}_2)$
0.28 ± 0.09	0.08 ± 0.08	4.29 ± 0.39	1.04 ± 0.11
0.31 ± 0.09	0.07 ± 0.12	4.14 ± 0.25	1.01 ± 0.08
0.20 ± 0.10	0.08 ± 0.11	4.02 ± 0.29	1.06 ± 0.07
0.20 ± 0.10	0.09 ± 0.09	4.34 ± 0.25	1.22 ± 0.07
0.24 ± 0.10	0.10 ± 0.11	4.58 ± 0.25	1.33 ± 0.08
0.37 ± 0.09	0.08 ± 0.13	4.75 ± 0.22	1.34 ± 0.08
0.20 ± 0.10	0.00 ± 0.10	4.56 ± 0.27	1.33 ± 0.08
0.31 ± 0.11	0.00 ± 0.10	4.36 ± 0.33	1.33 ± 0.12
0.21 ± 0.10	0.00 ± 0.10	4.08 ± 0.28	1.35 ± 0.10
0.19 ± 0.09	0.00 ± 0.10	3.29 ± 0.23	1.32 ± 0.10

Table VI. C<sub>2</sub> Product

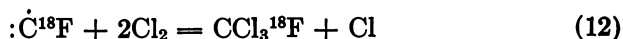
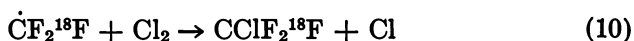
(P/Z) (atm)	Absolute Yield (%)	
	CH <sub>3</sub> CF <sub>2</sub> <sup>18</sup> F	CH <sub>2</sub> =CF <sup>18</sup> F
0.3	0.80 ± 0.10	1.29 ± 0.15
1.5	0.90 ± 0.06	0.98 ± 0.10
3	1.15 ± 0.07	1.02 ± 0.11
5	1.34 ± 0.06	0.97 ± 0.11
8	1.47 ± 0.06	0.94 ± 0.10
10	1.56 ± 0.07	0.93 ± 0.09
40	1.83 ± 0.11	0.87 ± 0.11
70	2.01 ± 0.15	0.75 ± 0.11
100	2.20 ± 0.10	0.75 ± 0.11
170	2.43 ± 0.12	0.72 ± 0.09

\* H<sub>2</sub>S-scavenged samples only.

constant (P/Z) the C<sub>2</sub> product distributions were the same for H<sub>2</sub>S- and O<sub>2</sub>-scavenged CH<sub>3</sub>CHF<sub>2</sub>.

Tables V and VI present yield results for CH<sub>3</sub>CF<sub>3</sub> analogous to those given in Tables III and IV for CH<sub>3</sub>CHF<sub>2</sub>. The labeled fluoromethanes again vary with the type of scavenging system. Except for the approximately 0.3% yield of CH<sub>3</sub>CHF<sup>18</sup>F, which was only detected in the presence of H<sub>2</sub>S, the C<sub>2</sub> product distributions at fixed (P/Z) were the same for both scavengers.

Results obtained for Cl<sub>2</sub>-scavenged CF<sub>4</sub> and C<sub>2</sub>F<sub>6</sub> have been given in Tables VII and VIII. The efficacy of this scavenger for providing quantitative recovery of all types of labeled radicals in these systems has been clearly demonstrated (Reactions 10, 11, and 12) (47-50, 55).



Chlorine atom transfers of the type depicted in Reaction 10 are well known for aliphatic radicals. From crude (O<sub>2</sub>/Cl<sub>2</sub>) mixed scavenger experiments with CF<sub>4</sub>, the phenomenological rate coefficient ratio ( $k_{10}^{273}/k_{13}^{273}$ ) exhibits an upper-bound value of 0.10 (49).



Unpublished laser-induced multiphoton dissociation experiments support a direct concerted bimolecular insertion mechanism for gas-phase

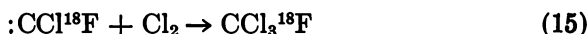
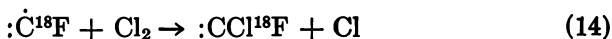


**Distributions for CH<sub>3</sub>CF<sub>3</sub> (28)**

<i>Absolute Yield (%)</i>		
<i>CF<sub>3</sub>CH<sub>2</sub><sup>18</sup>F</i>	<i>CF<sub>2</sub>=CH<sup>18</sup>F</i>	<i>CH<sub>3</sub>CHF<sup>18</sup>F<sup>a</sup></i>
1.35 ± 0.15	0.35 ± 0.11	0.17 ± 0.08
1.47 ± 0.08	0.28 ± 0.12	0.21 ± 0.11
1.64 ± 0.09	0.27 ± 0.11	0.23 ± 0.11
1.76 ± 0.07	0.26 ± 0.13	0.26 ± 0.10
1.95 ± 0.08	0.27 ± 0.12	0.28 ± 0.10
2.03 ± 0.09	0.26 ± 0.12	0.24 ± 0.10
2.34 ± 0.13	0.24 ± 0.12	0.28 ± 0.12
2.53 ± 0.17	0.21 ± 0.11	0.33 ± 0.09
2.84 ± 0.12	0.21 ± 0.11	0.30 ± 0.10
3.53 ± 0.15	0.20 ± 0.11	0.28 ± 0.10

Reaction 11 (63). Our (O<sub>2</sub>/Cl<sub>2</sub>) mixed scavenger studies support a similar interpretation. In experiments with Cl<sub>2</sub>-scavenged CF<sub>4</sub> the CCl<sub>2</sub>F<sup>18</sup>F yield is not diminished in the presence of O<sub>2</sub>. Therefore, a two-step sequential mechanism for Reaction 11 initiated by Cl-atom transfer can probably be discounted.

The gas-phase stoichiometric Reaction 12 necessarily involves a sequential mechanism. Because CCl<sub>3</sub><sup>18</sup>F is formed in the above noted (O<sub>2</sub>/Cl<sub>2</sub>) mixed scavenger experiments, a two-step sequence initiated by Cl-atom transfer and forming a singlet carbene product is probably important (Reactions 14 and 15). Further research is needed on these



elementary reactions, however.

**Table VII. Yield Results for Cl<sub>2</sub>-Scavenged CF<sub>4</sub><sup>a</sup>**

<i>(P/Z) (atm)</i>	1.3	132
<i>T (K)<sup>b</sup></i>	273	273
<i>Product</i>	<i>Yield (%)<sup>c</sup></i>	<i>Yield (%)<sup>d</sup></i>
CF <sub>3</sub> <sup>18</sup> F	2.08 ± 0.06	4.8 ± 0.5
CClF <sub>2</sub> <sup>18</sup> F	2.40 ± 0.08	3.7 ± 0.4
CCl <sub>2</sub> F <sup>18</sup> F	2.21 ± 0.09	3.0 ± 0.3
CCl <sub>3</sub> <sup>18</sup> F	0.73 ± 0.12	0.8 ± 0.1
Total	7.41 ± 0.19	12.3 ± 1.5

<sup>a</sup> Samples contain 5.0 mol % Cl<sub>2</sub> scavenger. Cited yields include statistical corrections for the unimolecular loss of <sup>18</sup>F atoms.

<sup>b</sup> Ambient irradiation temperature.

<sup>c</sup> Reference 49.

<sup>d</sup> References 50 and 56.

Table VIII. Yield Results for Cl<sub>2</sub>-Scavenged C<sub>2</sub>F<sub>6</sub><sup>a</sup>

(P/Z)	(atm)	1.3	13.2
T	(K) <sup>b</sup>	273	273 <sup>c</sup>
Product	Yield (%)	Yield (%)	Yield (%)
CF <sub>3</sub> <sup>18</sup> F	1.3 ± 0.2	1.8 ± 0.1	
C <sub>2</sub> F <sub>5</sub> <sup>18</sup> F	1.8 ± 0.1	2.8 ± 0.1	
C <sub>2</sub> ClF <sub>4</sub> <sup>18</sup> F	0.4 ± 0.1	0.5 ± 0.1	
CClF <sub>2</sub> <sup>18</sup> F	4.2 ± 0.2	3.6 ± 0.1	
CCl <sub>2</sub> F <sup>18</sup> F	3.7 ± 0.1	3.0 ± 0.1	
CCl <sub>3</sub> <sup>18</sup> F	0.6 ± 0.1	0.4 ± 0.1	

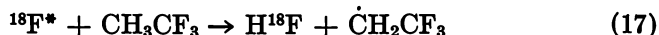
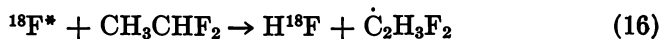
<sup>a</sup> Samples contain 5.0 mol % Cl<sub>2</sub> scavenger (References 55 and 56).

<sup>b</sup> Ambient irradiation temperature.

<sup>c</sup> Preliminary data.

### Discussion—Determination of Reaction Mechanisms

**Nonthermal Hydrogen Abstraction Reactions.** Energetic F-to-HF reactions predominate in experiments with hydrogen-containing substances (Reactions 16 and 17) (14, 15, 29, 31, 34, 35, 40, 45). At gas-phase



(P/Z) values below 200 atm other observed hot reactions involve direct replacements of singly bound atoms or alkyl radicals by atomic <sup>18</sup>F. These F-for-X atomic substitution and F-for- $\dot{\text{R}}$  alkyl replacement processes typically form excited organic products. Small yields of H<sup>18</sup>F, which follow from secondary decomposition reactions of such species, can be estimated from the respective reaction mechanisms.

The organic vs. inorganic product distributions measured for H<sub>2</sub>S-scavenged CH<sub>3</sub>CHF<sub>2</sub> and CH<sub>3</sub>CF<sub>3</sub> have been listed in Tables IX and X. The nonvolatile inorganic yields are believed to consist solely of H<sup>18</sup>F. The measured H<sup>18</sup>F results have been corrected as described above for the contributions from organic product decomposition. Because non-thermal F-to-HF Reactions 16 and 17 exhibit no (P/Z) dependence (14, 29, 34), constant values should be obtained for the corrected yields shown in the fifth column of both tables. However, both sets of results exhibit small systematic increases below 10 atm, reflecting the above-noted mechanistic uncertainties at low pressures. Primary yield values for Reactions 16 and 17 have thus been calculated from the high-pressure data.

**CH<sub>3</sub>CHF<sub>2</sub> Reaction Mechanism.** A complete mechanism for the gas-phase CH<sub>3</sub>CHF<sub>2</sub> system has been formulated from the data presented

**Table IX. Organic vs. Inorganic Product Distributions in  $\text{CH}_3\text{CHF}_2^a$**

(P/Z) (atm)	Absolute Yield (%) <sup>b</sup>			
	Volatile Organic	Volatile Inorganic	Nonvolatile Inorganic	Corrected Nonvolatile Inorganic <sup>c</sup>
0.35	10.1 ± 1.0	2.5 ± 1.0	87.4 ± 1.0	84.6 ± 1.0
1.0	10.5 ± 0.7	2.9 ± 0.7	86.6 ± 0.7	84.2 ± 0.7
3.0	10.9 ± 0.8	2.8 ± 0.8	86.3 ± 0.8	84.1 ± 0.8
5.0	11.4 ± 0.8	2.8 ± 0.8	85.8 ± 0.8	84.0 ± 0.8
7.0	11.9 ± 0.9	2.9 ± 0.9	85.3 ± 0.9	83.6 ± 0.9
8.0	12.1 ± 0.9	2.9 ± 0.9	85.0 ± 0.9	83.8 ± 0.9
10	12.6 ± 1.0	2.9 ± 1.0	85.5 ± 1.0	83.3 ± 1.0
45	12.6 ± 0.6	2.8 ± 0.6	84.5 ± 0.6	83.4 ± 0.6
95	12.7 ± 0.7	2.9 ± 0.7	84.4 ± 0.7	83.3 ± 0.7
190	12.8 ± 0.7	3.1 ± 0.7	84.2 ± 0.7	83.1 ± 0.7
Average value				83.8 ± 0.3
Primary nonthermal F-to-HF yield <sup>d</sup>				83.4 ± 0.2

<sup>a</sup> Samples contain 5.0 mol %  $\text{H}_2\text{S}$  scavenger (28, 45).

<sup>b</sup> Precision-based standard errors of estimate.

<sup>c</sup> Corrected for contributions from decomposing organic product species.

<sup>d</sup> Includes results for (P/Z) > 7 atm.

**Table X. Organic vs. Inorganic Product Distributions in  $\text{CH}_3\text{CF}_3^a$**

(P/Z) (atm)	Absolute Yield (%) <sup>b</sup>			
	Volatile Organic	Volatile Inorganic	Nonvolatile Inorganic	Corrected Nonvolatile Inorganic <sup>c</sup>
0.30	10.3 ± 1.0	2.5 ± 1.0	87.2 ± 1.0	85.5 ± 1.0
1.5	10.4 ± 0.5	2.5 ± 0.5	87.1 ± 0.5	85.5 ± 0.5
3.0	10.7 ± 0.6	2.5 ± 0.6	86.8 ± 0.6	85.2 ± 0.6
5.0	11.1 ± 0.7	2.6 ± 0.7	86.4 ± 0.7	85.2 ± 0.7
8.0	12.0 ± 0.9	2.3 ± 0.9	85.7 ± 0.9	85.0 ± 0.9
10	12.4 ± 1.0	2.3 ± 1.0	85.3 ± 1.0	84.8 ± 1.0
40	12.5 ± 0.3	2.8 ± 0.3	84.8 ± 0.3	84.4 ± 0.3
70	12.5 ± 0.3	2.7 ± 0.3	84.8 ± 0.3	84.4 ± 0.3
100	12.5 ± 0.3	2.7 ± 0.3	84.8 ± 0.3	84.4 ± 0.3
170	12.5 ± 0.3	2.7 ± 0.3	84.8 ± 0.3	84.4 ± 0.3
Average value				84.9 ± 0.2
Primary nonthermal F-to-HF yield <sup>d</sup>				84.4 ± 0.1

<sup>a</sup> Samples contain 5.0 mol %  $\text{H}_2\text{S}$  scavenger (28, 34).

<sup>b</sup> See footnote b in Table IX.

<sup>c</sup> See footnote c in Table IX.

<sup>d</sup> Includes results from (P/Z) > 10 atm.

Table XI. Primary Reactions and Yields for  $\text{CH}_3\text{CHF}_2$  and  $\text{CH}_3\text{CF}_3$ <sup>a</sup>

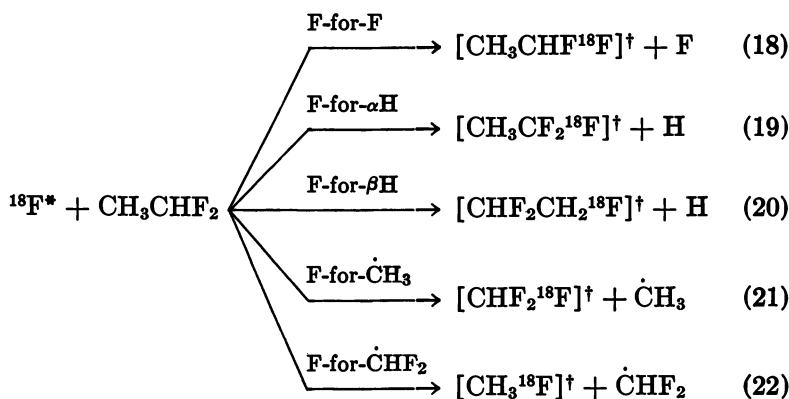
Primary Reaction	Primary Absolute Yields <sup>b</sup> (%)	
	$\text{CH}_3\text{CHF}_2$	$\text{CH}_3\text{CF}_3$
F-to-HF	83.40 ± 0.20	84.40 ± 0.10
F-for-F	3.86 ± 0.11	4.21 ± 0.10
F-for- $\alpha\text{H}$	2.08 ± 0.12	—
F-for- $\beta\text{H}$	5.84 ± 0.17	5.75 ± 0.14
F-for- $\dot{\text{C}}\text{F}_3$	—	1.33 ± 0.04
F-for- $\dot{\text{C}}\text{F}_2\text{H}$	1.51 ± 0.05	—
F-for- $\dot{\text{C}}\text{H}_3$	0.45 ± 0.06	1.04 ± 0.03
F-for-2F	< 0.2	0.26 ± 0.03
F-for-2H	< 0.2	< 0.2
F-for-H,F (HF)	< 0.2	—
Volatile inorganic (?)	2.90 ± 0.50	2.50 ± 0.50
Unassigned	< 0.7	< 0.6

<sup>a</sup> Samples contain 5.0 mol %  $\text{H}_2\text{S}$  scavenger (28, 45).

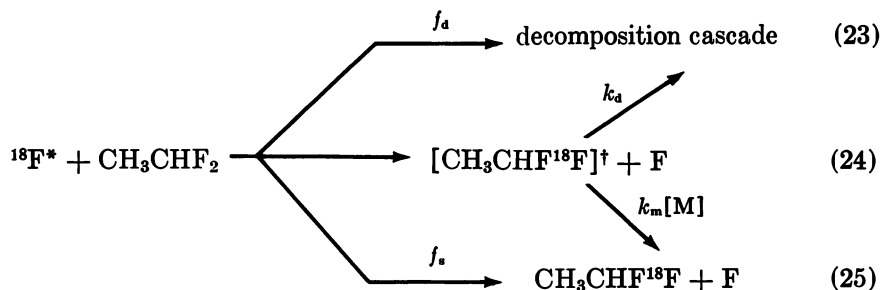
<sup>b</sup> The uncertainties in the assigned primary yields reflect precision-based random errors. Estimates of the magnitudes of systematic mechanistic errors have not been included (cf. text).

in Tables III, IV, and IX (45). The proposed primary reactions and yields have been summarized in Table XI. The five energetic reactions that are important in addition to F-to-HF abstraction include F-for-F, F-for- $\alpha\text{H}$ , and F-for- $\beta\text{H}$  atomic substitution together with F-for- $\dot{\text{C}}\text{H}_3$  and F-for- $\dot{\text{C}}\text{HF}_2$  alkyl replacement, Equations 18–22, respectively. The dagger (†) notation indicates that the energy disposal for these primary reactions leads to sufficient product excitation to induce decomposition.

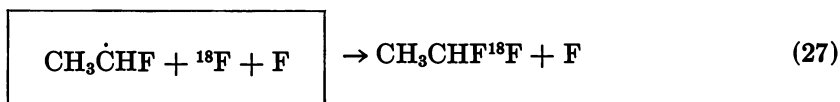
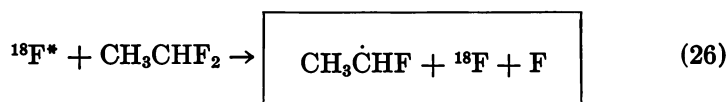
The products from substitution Reactions 18–20 dissociate via competitive  $\alpha,\beta$  HF-elimination and carbon-carbon scission processes. These “superexcited” species possess excitation energies extending well above 10 eV (8, 11, 16, 47).



**F-for-F Substitution in  $\text{CH}_3\text{CHF}_2$ .** To illustrate our procedure, this primary process receives detailed discussion below. Following the notation introduced by Spicer and coworkers (64, 65), the mechanism can be schematically represented as follows:



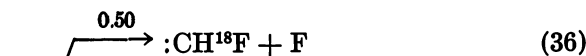
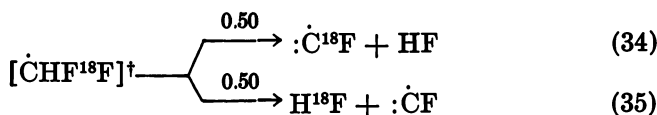
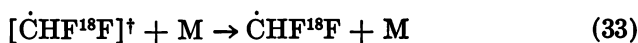
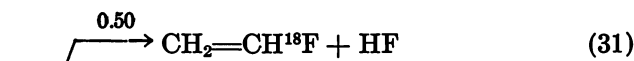
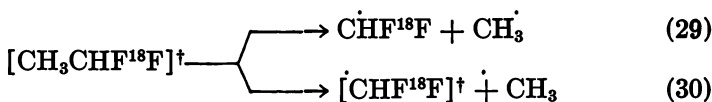
Through studies of the variation with ( $P/Z$ ) of the yields of  $\text{CH}_3\text{CHF}^{18}\text{F}$  and its decomposition products, the fractions of the nascent  $[\text{CH}_3\text{CHF}^{18}\text{F}]^\dagger$  that undergo competitive collisional deactivation and unimolecular decomposition have been determined. A portion of the primary substitution product,  $f_s$ , is formed with insufficient excitation energy to induce decomposition (16, 25). Another fraction,  $f_a$ , contains so much energy that it cannot be stabilized below the approximately 200-atm ( $P/Z$ ) threshold for the energetic caged recombination sequence shown in Reactions 26 and 27 (26, 31, 35). Here the boxed notation indi-



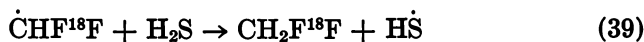
cates reaction via Franck-Rabinowitsch primary caged recombination (31, 66, 67).

The upper ( $P/Z$ ) limit at which the kinetic behavior of  $^{18}\text{F}$ -labeled superexcited molecules can be investigated is determined by the occurrence of caging reactions of this type. As a very approximate rule of thumb, the caging density threshold often occurs at roughly twice the mass density corresponding to the gas-liquid critical transition. The only technique of which we are aware that would allow experimental differentiation between caging and ordinary bimolecular hot reactions at elevated ( $P/Z$ ) would involve the application of strong external magnetic fields during the irradiations (47, 68, 69).

**The  $\text{CH}_3\text{CHF}^{18}\text{F}$  Unimolecular Decomposition Mechanism.** The large range of excitation energies for the nascent  $[\text{CH}_3\text{CHF}^{18}\text{F}]^\dagger$  from Reaction 24 leads to a complex decomposition mechanism in which secondary and tertiary unimolecular processes compete with collisional deactivation. As shown in Reactions 28–38, this cascading sequence continues until the excess energy is insufficient to induce further decomposition (70).



Through reactions with  $\text{H}_2\text{S}$  or  $\text{O}_2$ , thermalized  $\dot{\text{C}}\text{HF}^{18}\text{F}$  radicals from process 33 are converted either to  $\text{CH}_2\text{F}^{18}\text{F}$  or to volatile inorganic activity (Reactions 39 and 40). All the  $\text{CH}_2\text{F}^{18}\text{F}$  yields shown in Table



III have been assigned to the F-for-F process via the sequence shown in Equations 29, 30, 33, and 39.

Trial complementary yield mass balance Equation 41, follows from

$$Y^\circ(\text{CH}_3\text{CHF}^{18}\text{F}) = Y(\text{CH}_3\text{CHF}^{18}\text{F}) + 2.0Y(\text{CH}_2=\text{CH}^{18}\text{F}) + Y(\dot{\text{C}}\text{HF}^{18}\text{F})^\dagger \quad (41)$$

the above mechanism. Here  $Y^0(\text{CH}_3\text{CHF}^{18}\text{F})$  and  $Y(i)$  denote the primary F-for-F yield and the measured value for the  $i$ th decomposition product. The  $Y(\text{CH}_2=\text{CH}^{18}\text{F})$  yields from Table IV are multiplied by 2.0 to account for  $\text{H}^{18}\text{F}$ -loss, Reaction 32. This simple statistical correction procedure is possible because the ( $\text{H}^{19}\text{F}/\text{H}^{18}\text{F}$ ) kinetic isotope effect is negligibly small for a  $\alpha,\beta$  HF-elimination decomposition reaction (8, 15, 34, 45, 47).

Because  $Y(\dot{\text{C}}\text{HF}^{18}\text{F})^\dagger$  is not directly measured, Equation 41 cannot be used to test the proposed mechanism. Equation 42 involves the

$$Y^0(\text{CH}_3\text{CHF}^{18}\text{F}) \stackrel{?}{=} Y(\text{CH}_3\text{CHF}^{18}\text{F}) + 2.0Y(\text{CH}_2=\text{CH}^{18}\text{F}) + Y(\text{CH}_2\text{F}^{18}\text{F}) \quad (42)$$

additional assumption that all the  $\dot{\text{C}}\text{HF}^{18}\text{F}$  radicals from Reactions 29 and 30 have been detected as  $\text{CH}_2\text{F}^{18}\text{F}$ . To establish  $Y^0(\text{CH}_3\text{CHF}^{18}\text{F})$ , Equation 42 is tested for ( $P/Z$ ) independence over the widest possible measurement interval (cf. Table XII and Figure 1). The trial "mechanism yields" tabulated in the second column of Table XII exhibit the required constancy throughout the range  $7 \leq (P/Z) \leq 190$  atm. The  $Y^0(\text{CH}_3\text{CHF}^{18}\text{F})$  value obtained from these results is  $3.86\% \pm 0.11\%$ , and the fractional stabilization of excited  $[\text{CH}_3\text{CHF}^{18}\text{F}]^\dagger$  from Reaction 24 is  $0.41 \pm 0.06$  at 190 atm.

The calculated  $Y^0(\text{CH}_3\text{CHF}^{18}\text{F})$  increases shown in Table XII for liquid-phase  $\text{CH}_3\text{CHF}_2$  reflect contributions from the caging sequence shown in Reactions 26 and 27.

Tertiary decomposition Reactions 34–38 complicate the mechanism testing procedure at low pressures. The local maximum in the  $Y(\text{CH}_2\text{F}^{18}\text{F})$  data shown in Table III and Figure 1 indicates the onset of  $[\dot{\text{C}}\text{HF}^{18}\text{F}]^\dagger$  decomposition below 7 atm. Equation 42 thus fails in this region. However, the success of Equation 42 throughout the 30-fold range of increased ( $P/Z$ ) above 7 atm is sufficient to establish  $Y^0(\text{CH}_3\text{CHF}^{18}\text{F})$ . The mechanistic uncertainties at low ( $P/Z$ ) are not serious, and the yields of missing decomposition products can be estimated from  $Y^0(\text{CH}_3\text{CHF}^{18}\text{F})$  and Equation 42.

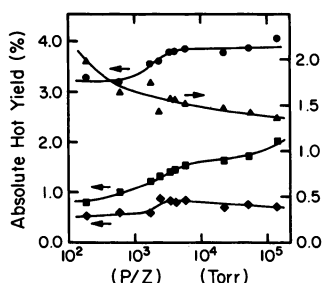


Figure 1. Absolute yield data for the F-for-F reaction channel in  $\text{CH}_3\text{CHF}_2$ : (●)  $Y^0(\text{CH}_3\text{CHF}^{18}\text{F})$ , Equation 42; (■)  $Y(\text{CH}_3\text{CHF}^{18}\text{F})$ ; (▲)  $2.0 Y(\text{CH}_2=\text{CH}^{18}\text{F})$ ; (◆)  $Y(\text{CH}_2\text{F}^{18}\text{F})$  (45)

Table XII. Determination of Primary Yields

(P/Z) (atm)	Trial Mechanism Yield (%) <sup>b</sup>	
	Y°(CH <sub>3</sub> CHF <sup>18</sup> F)	Y°(CH <sub>3</sub> CF <sub>2</sub> <sup>18</sup> F)
0.35	3.27 ± 0.27	2.00 ± 0.28
1.0	3.19 ± 0.22	2.02 ± 0.21
3.0	3.55 ± 0.20	1.90 ± 0.16
5.0	3.60 ± 0.18	1.89 ± 0.15
7.0	3.77 ± 0.18	1.95 ± 0.14
8.0	3.79 ± 0.18	1.97 ± 0.14
10	3.85 ± 0.19	2.08 ± 0.16
45	3.78 ± 0.27	1.97 ± 0.20
95	3.86 ± 0.24	2.09 ± 0.19
190	4.04 ± 0.26	2.27 ± 0.30
Liquid (303 K)	4.87 ± 0.27	2.82 ± 0.38
Liquid (195 K)	6.12 ± 0.41	3.59 ± 0.38
Primary yield (%) <sup>b, c</sup>	3.86 ± 0.11	2.08 ± 0.12

<sup>a</sup> Gas-phase data taken from References 28 and 45. Liquid-phase data taken from References 28 and 27.

An estimated 0.7% maximum labeled carbene yield from Reactions 34–38 follows from the lowest (P/Z) data given in Table XII. The combined yield of unmonitored products apparently diminishes below the measurement sensitivity at 5–8 atm.

**Other Primary Reactions in CH<sub>3</sub>CHF<sub>2</sub>.** Although the mechanisms for the other primary processes have not been presented in detail (45), the mass balance tests shown in Tables IX and XII have clearly been successful. The derived primary yields have been listed in Table XI.

From Table XII all the energetic substitution channels in CH<sub>3</sub>CHF<sub>2</sub> exhibit apparent yield enhancements in the 303 K and 195 K liquid phases. However, caging reactions do not contribute to the alkyl replacement yields in either condensed CH<sub>3</sub>CHF<sub>2</sub> or CH<sub>3</sub>CF<sub>3</sub> at temperatures as low as 195 K (26, 28, 31, 35).

Below 7 atm unmonitored tertiary decompositions accompany the primary F-for-βH substitution Reaction 20. This is not the case, however, for the F-for-αH primary Reaction 19.

The average fractional decomposition at low (P/Z) for the nascent alkyl replacement products in CH<sub>3</sub>CHF<sub>2</sub> exhibits the value 0.24 ± 0.03. The corresponding result for the substitution products is 0.79 ± 0.02. Similarly, the alkyl replacement species undergo complete collisional stabilization below 10 atm, whereas the average fractional stabilization of the activated substitution products at 190 atm is only 0.45 ± 0.10. The excitation levels accompanying primary substitution Reactions 18–20 apparently are much larger than those for alkyl replacement Reactions 21 and 22.

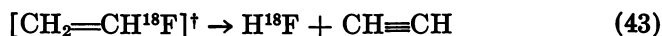


in CH<sub>3</sub>CHF<sub>2</sub> Through Mass-Balance Testing<sup>a</sup>

Trial Mechanism Yield (%) <sup>b</sup>		
Y <sup>o</sup> (CHF <sub>2</sub> CH <sub>2</sub> <sup>18</sup> F)	Y <sup>o</sup> (CH <sub>3</sub> <sup>18</sup> F)	Y <sup>o</sup> (CHF <sub>2</sub> <sup>18</sup> F)
5.08 ± 0.45	1.17 ± 0.12	0.31 ± 0.10
5.05 ± 0.32	1.23 ± 0.10	0.35 ± 0.09
5.34 ± 0.30	1.18 ± 0.07	0.37 ± 0.09
5.45 ± 0.28	1.30 ± 0.06	0.40 ± 0.10
5.56 ± 0.25	1.41 ± 0.06	0.42 ± 0.09
5.70 ± 0.24	1.46 ± 0.06	0.41 ± 0.08
5.98 ± 0.25	1.54 ± 0.06	0.41 ± 0.08
5.94 ± 0.35	1.55 ± 0.10	0.44 ± 0.11
5.87 ± 0.33	1.47 ± 0.09	0.50 ± 0.10
5.72 ± 0.37	1.54 ± 0.13	0.50 ± 0.12
6.48 ± 0.34	1.51 ± 0.08	1.05 ± 0.30
7.67 ± 0.45	1.51 ± 0.08	1.00 ± 0.30
5.84 ± 0.17	1.51 ± 0.05	0.45 ± 0.06

<sup>b</sup> Precision-based standard errors of estimate.<sup>a</sup> Includes Y<sup>o</sup>(i) values for 7 ≤ (P/Z) ≤ 190 atm.

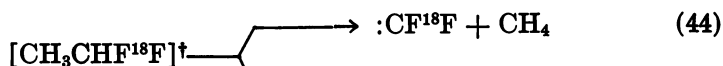
**Neglected Reaction Pathways.** From Table IV and Figure 1 the Y(CH<sub>2</sub>=CH<sup>18</sup>F) values from Reaction 31 exhibit a monotonic (P/Z) dependence, showing that tertiary decomposition process, Reaction 43,



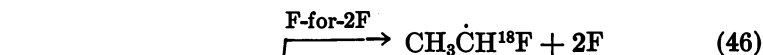
is unimportant. The respective unimolecular reaction threshold energy requirements for formation of CH≡CH, :C<sup>18</sup>F, :CH<sup>18</sup>F, and :CF<sup>18</sup>F via the reactions shown in Equations 43, 34, 36, and 38 are 5.81, 6.51, 8.59, and 7.03 eV (45). On energetics grounds it is surprising that carbene-forming tertiary decomposition reactions occur, whereas double HF-elimination does not. The more energetic [CH<sub>3</sub>CHF<sup>18</sup>F]<sup>†</sup> products from Reaction 24 decompose mainly via carbon-carbon scission Reaction 30.

Tertiary double HF-eliminations analogous to Reaction 31 followed by Reaction 43 have been noted in shock-tube experiments (71, 72) and also following hot <sup>3</sup>H-for-H atomic substitution in CH<sub>3</sub>CHF<sub>2</sub> (73). The recoil <sup>3</sup>H study yielded monotonically decreasing Y(CH≡C<sup>3</sup>H) values with increasing (P/Z). Due to the loss of <sup>18</sup>F label, the decomposition process, Reaction 43, cannot be directly detected in our system.

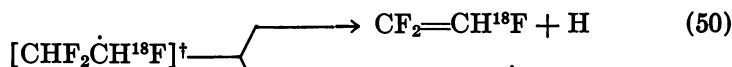
Other neglected reactions include unusual decomposition modes such as α,α-F<sub>2</sub>, β,β-H<sub>2</sub>, and α,β-H<sub>2</sub> molecular eliminations together with asymmetric carbon-carbon scissions of the types observed in radiation chemistry and vacuum ultraviolet photochemistry with alkanes.



In an early study with  $\text{CF}_4$ , F-for-2F double substitution was proposed to be important (1, 2). Energetic F-for-2F, F-for-2H, F-for-H,F, and F-for-HF reactions are feasible in  $\text{CH}_3\text{CHF}_2$ .



The primary F-for-2H process shown in Reaction 47 produces  $\text{CHF}_2\dot{\text{C}}\text{H}^{18}\text{F}$  radicals. If excited, these species should decompose preferentially via H-loss or carbon-carbon scission Reactions 50 and 51.



Based on thermochemical data tabulated elsewhere (45), the minimum threshold energy requirements for Reactions 50 and 51 are estimated as approximately 1.7 and 3.1 eV. Stabilized  $\text{CHF}_2\dot{\text{C}}\text{H}^{18}\text{F}$  radicals from Reaction 47 would be scavenged by  $\text{H}_2\text{S}$ . The species  $\text{CHF}_2\text{CH}_2^{18}\text{F}$  is



also formed via stabilization following F-for- $\beta$ H Reaction 20. Because identical  $Y(\text{CHF}_2\text{CH}_2^{18}\text{F})$  values are measured at fixed ( $P/Z$ ) for  $\text{H}_2\text{S}$ - and  $\text{O}_2$ -scavenged  $\text{CH}_3\text{CHF}_2$ , the upper-bound yield from the sequence shown in Reactions 47 and 52 corresponds to the approximately 0.2% measurement sensitivity. Similarly, the H-loss product  $\text{CF}_2=\text{CH}^{18}\text{F}$  from Reaction 50 has never been detected. On these grounds an upper-bound primary yield of 0.2% has been assigned to the primary F-for-2H substitution process.

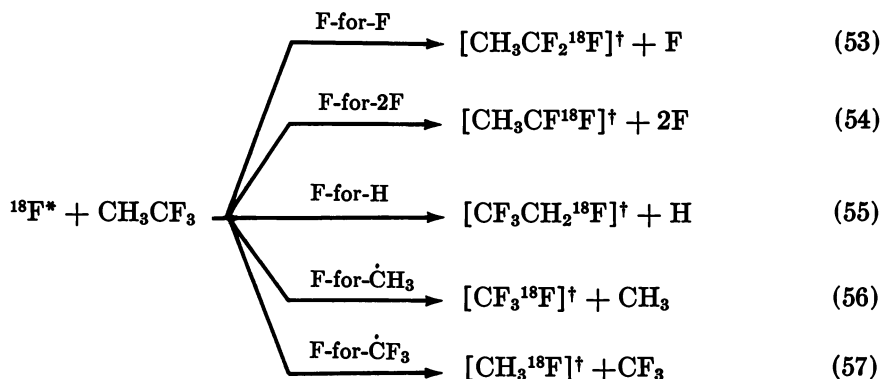
Based on similar arguments, 0.2% upper-bound primary yields have also been assigned to the processes shown in Reaction 46, 48, and 49.

**Mechanistic Uncertainties and Errors.** Mass-balance mechanism yield consistency tests are definitive only to the extent that complementary changes in the product yield distributions have been monitored. To illustrate the nature of this limitation, we recall that stable and activated nascent products are formed from F-for-F Reaction 18 via respective Reactions 24 and 25. Because the yield from Reaction 25 is not subject to decomposition, no (*P/Z*) interdependence is possible between these contributions to  $Y(\text{CH}_3\text{CHF}^{18}\text{F})$ . Chemical intuition thus provides the only basis for assigning the species from Reactions 24 and 25 to the same primary reaction channel (25, 34, 45).

In a similar vein, Equation 42 assigns the entire  $\text{CH}_2=\text{CH}^{18}\text{F}$  yield to  $[\text{CH}_3\text{CHF}^{18}]^\dagger$  decomposition Reaction 31. However, since  $Y(\text{CH}_2=\text{CH}^{18}\text{F})$  has not vanished at 190 atm, the residual approximately 0.7% could conceivably be due to other primary reactions such as F-for-2F double substitution. The residual decomposition product yields at 190 atm have also been assigned based on chemical intuition. Although our preferred mechanisms are consistent with the data, other interpretations are possible (34, 45). Due to the occurrence of caging reactions at large (*P/Z*), no experimental solution for this uniqueness problem is presently available.

The chemical identities of the volatile inorganic yields listed in Table XI are not known with certainty. Although energetic F-to- $\text{F}_2$  abstraction may be involved (14), further research is needed on this problem.

**$\text{CH}_3\text{CF}_3$  Reaction Mechanism.** The  $\text{CH}_3\text{CF}_3$  measurements span the range  $0.3 \leq (P/Z) \leq 170$  atm, and the detailed mechanism analysis has been presented elsewhere (8, 14, 15, 34). In addition to the F-to-HF process shown in Reaction 17, five energetic primary reactions are important in the gas phase (Reactions 53–57). The respective primary yields have been included in Table XI.

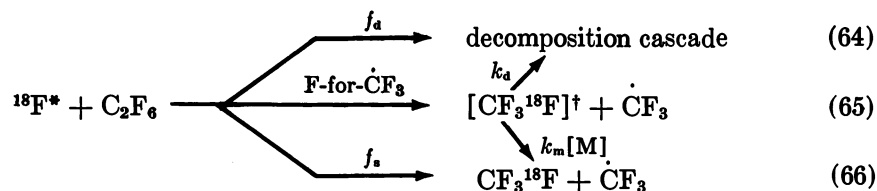
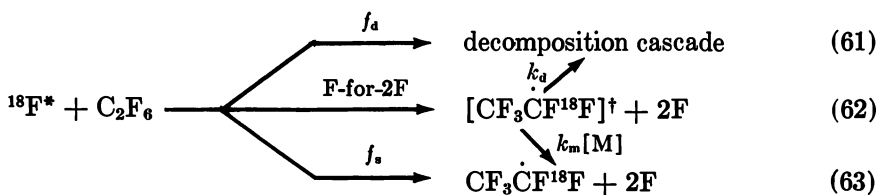
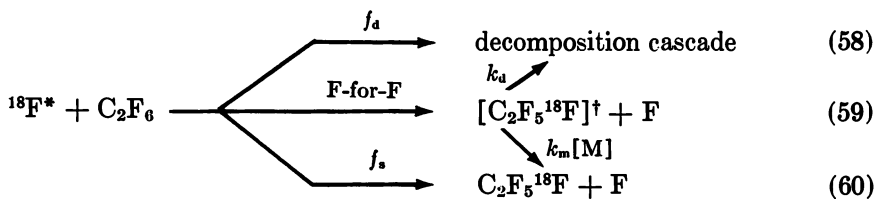


Corresponding primary reactions occurring with  $\text{CH}_3\text{CHF}_2$  and  $\text{CH}_3\text{CF}_3$  exhibit similar characteristics. From Table XI the respective primary yields are remarkably close. The total organic primary yields are  $13.7\% \pm 0.5\%$  for  $\text{CH}_3\text{CHF}_2$  vs.  $13.1\% \pm 0.3\%$  for  $\text{CH}_3\text{CF}_3$ . In  $\text{CH}_3\text{CHF}_2$  the per-bond primary yield ratios for F-for-H vs. F-for-F substitution are  $1.08 \pm 0.07$  at the same carbon atom and  $1.01 \pm 0.04$  at neighboring carbons. For  $\text{CH}_3\text{CF}_3$  this ratio exhibits the value  $1.37 \pm 0.04$ . Energetic substitution is favored relative to alkyl replacement by respective ratios of  $2.00 \pm 0.05$  and  $1.40 \pm 0.04$  in  $\text{CH}_3\text{CHF}_2$  and  $\text{CH}_3\text{CF}_3$ .

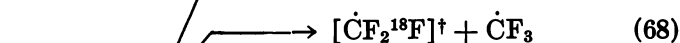
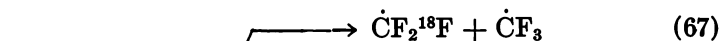
For  $\text{CH}_3\text{CF}_3$  only  $0.27 \pm 0.04$  average fractions of the nascent alkyl replacement products are capable of decomposing, and these unimolecular processes are subject to complete collisional stabilization above approximately 12 atm. The corresponding average fractional decomposition and stabilization ( $P/Z$ ) values for  $\text{CH}_3\text{CHF}_2$  are  $0.24 \pm 0.03$  and approximately 10 atm.

The nascent substitution products in  $\text{CH}_3\text{CF}_3$  undergo  $0.80 \pm 0.02$  fractional decomposition at low ( $P/Z$ ). The activated species from Reactions 53 and 55 are only  $0.50 \pm 0.04$  stabilized at 170 atm. The corresponding results for  $\text{CH}_3\text{CHF}_2$  are  $0.79 \pm 0.02$ ,  $0.45 \pm 0.10$ , and 190 atm.

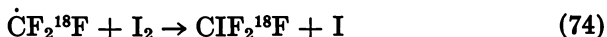
**$\text{C}_2\text{F}_6$  Reaction Mechanism.** The results shown in Table VIII suggest that three primary hot reactions (Reactions 58–66) may be important for



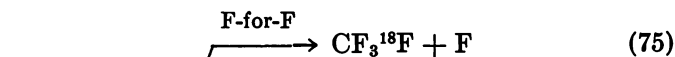
gas-phase  $\text{C}_2\text{F}_6$  (54, 55, 56). The available data are not sufficiently complete to allow primary yield assignments. Based upon the  $\text{Cl}_2$ -scavenging technique, we hope to monitor all the secondary and tertiary decompositions and to be able to choose between the F-for-F sequence shown in Equations 59, 69–73 and the F-for-2F sequence shown in Equations 62, 72–73 as the source for  $\text{C}_2\text{ClF}_4^{18}\text{F}$  product.



**$\text{CF}_4$  Reaction Mechanism.** The original gas-phase studies with  $\text{CF}_4$  demonstrated the formation of  $\text{CF}_3^{18}\text{F}$  and  $\dot{\text{C}}\text{F}_2^{18}\text{F}$  radicals, which were detected via the  $\text{I}_2$ -scavenging process shown in Reaction 74. These

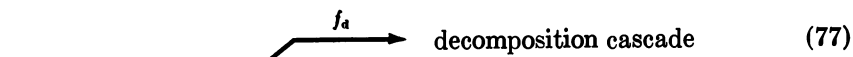


yields were insensitive to changes in ( $P/Z$ ) over the range 0.25–1.8 atm, suggesting the following conclusions (1, 2, 3): (i) unimolecular coupling between the  $\text{CF}_3^{18}\text{F}$  and  $\text{CIF}_2^{18}\text{F}$  products does not occur; (ii) both primary F-for-F and F-for-2F reactions are important; and (iii) these nonthermal processes exclusively yield stable products.

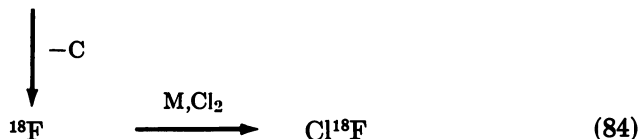
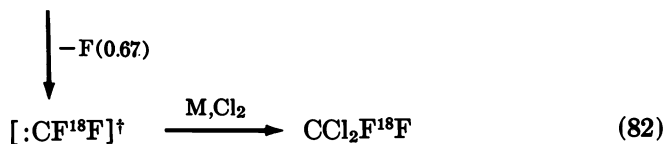
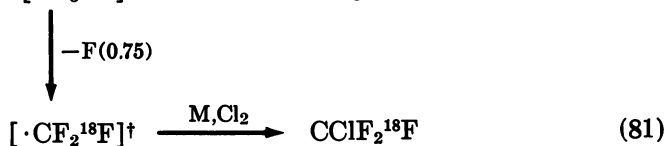


However, our recent research has shown that effective pressures above 1.8 atm are required to produce detectable yield changes in this system. From  $\text{Cl}_2$ -scavenged experiments over the range  $0.7 \leq (P/Z) \leq 132$  atm unimolecular coupling has been clearly demonstrated between the  $\text{CF}_3^{18}\text{F}$ ,  $\text{CClF}_2^{18}\text{F}$ ,  $\text{CCl}_2\text{F}^{18}\text{F}$ , and  $\text{CCl}_3^{18}\text{F}$  products (48, 49, 50, 56).

Therefore, the  $\text{CF}_4$  mechanism must include hot F-for-F substitution leading to highly energized nascent products.



The decomposition cascade represented by Equation 77 consists of a sequence of serially coupled reactions in which the unstable intermediates possessing sufficient excitation energy undergo further decomposition. Alternatively, the  $\text{Cl}_2$ -scavenging processes shown in Reactions 10–12



form stable products. The  $^{18}\text{F}$  label can be lost at any step in the cascade. It is invariably lost in Reaction 84, which thus cannot be directly monitored.

The ( $^{19}\text{F}/^{18}\text{F}$ ) kinetic isotope effect is negligibly small for F-loss unimolecular dissociations. The yield data presented in Table VII include statistical corrections for  $^{18}\text{F}$ -losses analogous to Reactions 81–83.

The CF<sub>4</sub> system presents a serious mechanistic uniqueness limitation. Gas-phase experiments are probably incapable of proving that the energetic F-for-2F process shown in Reaction 76 does not occur. By the arguments given above, such a demonstration would require the complete collisional stabilization of the nascent product from Reaction 78. The cascading sequence shown in Reactions 81–84 would then be quenched, and the full primary yield from Reactions 77–79 would be measured as CF<sub>3</sub><sup>18</sup>F.

The calculated RRKM unimolecular rate constants for molecules containing four or five atoms increase rapidly with increasing excitation energy above decomposition threshold. As a result, the unimolecular behavior of such species is difficult to investigate except at low levels of excitation. This topic has been discussed previously in the context of recoil <sup>3</sup>H-for-H activated CH<sub>3</sub><sup>3</sup>H (74). The ratio [Y(CH<sub>3</sub><sup>3</sup>H)/Y( $\dot{\text{C}}\text{H}_2^3\text{H}$ )] increases by only about 11% over the pressure range 1–30 atm, illustrating the difficulty of obtaining complete unimolecular falloff data for this system.

The formation of :CF from CF<sub>4</sub> is endoergic by 15 eV or more depending upon the assumed mechanism. For the F-for-F sequence shown in Reactions 77–84 the observation of CCl<sub>3</sub><sup>18</sup>F product from Equation 83 thus implies that the excitation energy probability density distribution from Reaction 78 extends to at least 15 eV (47, 48). Very substantial (*P/Z*) would be required to achieve complete collisional stabilization of these superexcited CF<sub>3</sub><sup>18</sup>F molecules.

Although liquid-phase experiments have not yet been attempted for Cl<sub>2</sub>-scavenged CF<sub>4</sub>, caging complications analogous to the sequence shown in Reactions 26 and 27 will likely occur at enhanced (*P/Z*). Evidence for caging reactions has been obtained in condensed-phase studies with CH<sub>3</sub>F (11, 31). Further CF<sub>4</sub> experiments at effective pressures above the present 132-atm cutoff therefore appear to have doubtful value.

The product distribution changes shown in Table VII can only be understood in the context of the unimolecular mechanism shown in Equations 77–84. However, because the nascent CF<sub>3</sub><sup>18</sup>F from Reaction 78 has been incompletely stabilized at 132 atm, this evidence is not sufficient to disprove the occurrence of the F-for-2F primary process (Reaction 76).

Our CH<sub>3</sub>CF<sub>3</sub> experiments demonstrate small yields from F-for-2F primary Reaction 54 (cf. Table XI). As noted above, the Y(C<sub>2</sub>ClF<sub>4</sub><sup>18</sup>F) results listed in Table VIII may reflect the C<sub>2</sub>F<sub>6</sub> F-for-2F sequence shown in Reactions 61–63. The reaction depicted in Reaction 76 thus cannot be discounted on grounds of precedent. From the mechanistic standpoint we have apparently reached an impasse. Unless magnetic field experiments prove to be capable of distinguishing the contributions

from caging reactions, the  $\text{CF}_4$  experiments at enhanced ( $P/Z$ ) needed to clarify this situation probably cannot yield definitive results.

Despite these uncertainties, several conclusions follow from the available  $\text{CF}_4$  studies. Mass-balance Equation 85 corresponds to the assumed mechanism shown in Reactions 77–84. Here  $Y^m(\text{CF}_3^{18}\text{F})$  denotes the

$$Y^m(\text{CF}_3^{18}\text{F}) = Y(\text{CF}_3^{18}\text{F}) + 1.33 Y(\text{CClF}_2^{18}\text{F}) + 2.0 Y(\text{CCl}_2\text{F}^{18}\text{F}) + 4.0 Y(\text{CCl}_3^{18}\text{F}) \quad (85)$$

$$Y^m(\text{CF}_3^{18}\text{F}) \leq Y^o(\text{CF}_3^{18}\text{F}) \quad (86)$$

mechanism yield estimated from data for decomposition Reactions 81–83; the weighting coefficients correct for statistical losses of  $^{18}\text{F}$  label, and inequality Equation 86 reflects the possible importance of  $:\dot{\text{C}}^{18}$  dissociation Reaction 84.

Respective  $Y^m(\text{CF}_3^{18}\text{F})$  values of  $7.4\% \pm 0.2\%$  and  $12.3\% \pm 1.5\%$  follow from Reaction 85 together with the  $Y(i)$  results given in Table VII. Within the present measurement uncertainty  $Y^m(\text{CF}_3^{18}\text{F})$  exhibits direct proportionality to ( $P/Z$ ) throughout the interval  $3.9 \leq (P/Z) \leq 132$  atm (47, 50, 56). It follows that  $12.3\% \pm 1.5\%$  represents a lower bound value for  $Y^o(\text{CF}_3^{18}\text{F})$ , and that 40% or more of the nascent primary  $\text{CF}_3^{18}\text{F}$  species from Reaction 78 undergo complete dissociation at 1.3 atm. Most of the nascent  $\text{CF}_3^{18}\text{F}$  decomposes to some extent at low ( $P/Z$ ), so that fewer than 35% of the primary F-for-F reactions were detected in the original study by Wolfgang and coworkers (1, 2, 3). Although these estimates are intended to be conservative, they may eventually require revision based on the availability of additional data measured at enhanced ( $P/Z$ ).

### *Discussion—Properties of $^{18}\text{F}$ -Labeled Superexcited Molecules*

**Thermochemical Excitation Energy Distribution for F-for-F Activated  $\text{CF}_3^{18}\text{F}$ .** When a recoil-activated species contains sufficient energy to make multiple or sequential unimolecular reaction pathways accessible, a rough mapping of its excitation energy distribution can be achieved based on measured yield data together with the corresponding decomposition threshold energies. The basis for this technique is shown in Figure 2 (16, 25), and a convenient example is provided by the reaction of nuclear recoil  $^{18}\text{F}$  atoms with gas-phase  $\text{CF}_4$ . The method for this system can be illustrated without great entanglement in mechanistic detail based on the assumed reaction sequence shown in Equations 77–84.

To take advantage of the simplicity of this mechanism, two types of recoil experiments are used. Studies at low ( $P/Z$ ) provide a lower-bound result for the  $\text{CF}_3^{18}\text{F}$  excitation energy distribution. High-pressure experi-



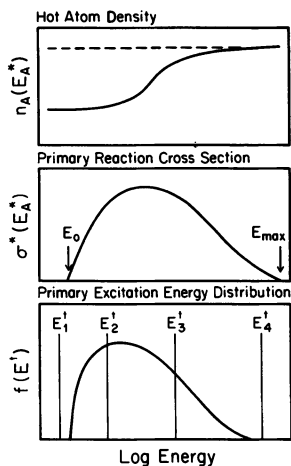


Figure 2. Important kinetic parameters for an hypothetical high-energy reaction. Although this has not been shown, the product excitation ( $E^+$ ) and center-of-mass reaction ( $E_A^*$ ) energy scales are different (47).

ments then allow this distribution to be revised based on an indirect estimate of the extent of  $:\text{C}^{18}\text{F}$  dissociation (Reaction 84).

Below 3.9 atm (see above) collisional deactivations of the excited intermediates in cascade sequence Equations 81–84, are effectively suppressed, so that the decomposition product yields mirror the unperturbed  $\text{CF}_3^{18}\text{F}$  excitation energy distribution (16, 25, 31, 34, 45, 47). Each nascent  $\text{CF}_3^{18}\text{F}$  molecule then progresses through the decomposition cascade to an extent limited only by its internal energy.

The fractional product yields and decomposition threshold energies corresponding to the mechanism shown in Reactions 77–84 have been shown in Table XIII. On simple thermochemical grounds the detection of  $\text{CCl}_3^{18}\text{F}$  product shows that the nascent  $\text{CF}_3^{18}\text{F}$  excitation energy distribution extends to at least 15 eV.

Table XIII. Scaled Product Distributions and Decomposition Threshold Energies for the  $\text{CF}_4$  Mechanism Shown in Equations 77–84<sup>a</sup>

<i>Assumed</i> $Y^o(\text{CF}_3^{18}\text{F})$ (%)	$7.41 \pm 0.19$	$12.30 \pm 1.20$	<i>Thermochemical</i> Energy Range (eV) <sup>b</sup>
<i>Product</i>	<i>Fractional Yield</i>		
$\text{CF}_3^{18}\text{F}$	$0.280 \pm 0.011$	$0.17 \pm 0.02$	1.7– 5.7
$\text{CClF}_2^{18}\text{F}$	$0.324 \pm 0.014$	$0.20 \pm 0.02$	5.7– 9.5
$\text{CCl}_2\text{F}^{18}\text{F}$	$0.298 \pm 0.015$	$0.18 \pm 0.02$	9.5–14.8
$\text{CCl}_3^{18}\text{F}$	$0.098 \pm 0.017$	$0.06 \pm 0.01$	14.8–20.4
Total	(1.000)	$0.61 \pm 0.06$	1.7–20.4

<sup>a</sup>  $Y(i)$  data from Table VII.

<sup>b</sup> The 1.7-eV  $\text{CF}_3^{18}\text{F}$  excitation threshold follows from extrapolation of low-pressure data for hot  $^3\text{H}$ -for-H and F-for-F substitution reactions. The other excitation energies represent lower-bound estimates obtained from standard heats of formation. Cf. References 25 and 45.

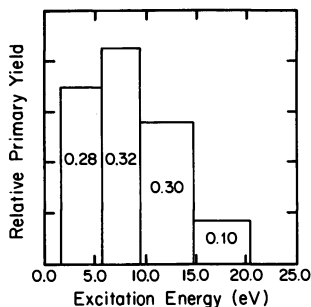


Figure 3. Approximate lower-bound thermochemical excitation energy distribution for F-for-F activated  $\text{CF}_3^{18}\text{F}$  (49)

The occurrence of F-for-2F reactions would not affect the conclusion that large excitation levels are involved in these reactions. However, there are two possibly serious sources of systematic error in the tabulated excitation energies. Translational energy disposal has been ignored in the above treatment of unimolecular F-atom elimination, so that the thermochemical excitation energy estimates are conservative (75). Concerted molecular elimination of  $\text{F}_2$  from the excited  $\text{CF}_3^{18}\text{F}$  also has been neglected. On energetics grounds  $\text{F}_2$ -elimination is slightly favored relative to the sequential elimination of two fluorine atoms. However, this effect is probably insufficient to compensate for the severe entropy requirement of the concerted process.

In Figure 3 the fractional product yields measured at 1.3 atm and corrected for statistical losses of  $^{18}\text{F}$  have been plotted against the decomposition threshold energies obtained from standard enthalpies of formation. This lower-bound model for the  $\text{CF}_3^{18}\text{F}$  primary excitation energy distribution extends to 20 eV even without inclusion of corrections for  $:\text{C}^{18}\text{F}$  dissociation or for the translational energy carried away by the dissociated F atoms.

The deposition of such a large amount of internal energy during F-for-F primary process Reaction 78 requires that the bound vicinal fluorine atoms must participate in the reaction. On energetics grounds  $\text{CF}_3^{18}\text{F}$  containing approximately 5 eV of internal excitation could be formed in a 3-center direct process. To permit the nascent  $\text{CF}_3^{18}\text{F}$  to survive even briefly, however, another C—F bond must be involved in the substitution event for each additional 5 eV of product excitation.

The nomographic distribution shown in Figure 3 is subject to several refinements (47–50). Based on standard RRKM calculations (75), the decomposition threshold energies listed in Table XIII have been corrected for unimolecular translational energy disposal (76,77). As shown in Figure 4, the corrected values exhibit small increases. The cumulative effect of these refinements raises the upper-bound energy cutoff for the cascade step shown in Reaction 83 from 20.4 to 23.5 eV. Rather clearly, the neglect of unimolecular translational energy disposal does not constitute a serious source of systematic error.

The occurrence of  $:\dot{\text{C}}^{18}\text{F}$  dissociation Reaction 84 leads to more significant corrections to the  $\text{CF}_3^{18}\text{F}$  excitation distributions shown in Figures 3 and 4. The respective low ( $P/Z$ ) limiting decomposition yields should be scaled by  $Y^\circ(\text{CF}_3^{18}\text{F})$  to determine their contributions to the primary excitation distribution. When this is done using the  $12.3\% \pm 1.5\%$  lower-bound  $Y^\circ(\text{CF}_3^{18}\text{F})$  value (cf. Table XIII), the cascade channels shown in Reactions 80–83 are shown to reflect no more than  $61\% \pm 6\%$  of the primary yield. The fractional yields shown in the figures are too large, and additional high-energy segments that are approximately equal in area to the other segments combined should be included in both nomograms. The upper cutoff energies for the missing segments cannot be determined from  $\text{CF}_4$  experiments of the present type.

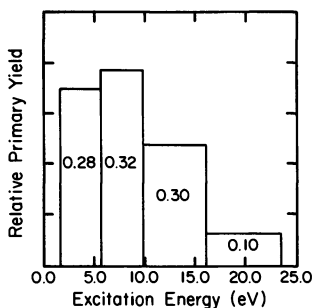


Figure 4. Lower-bound thermochemical excitation energy distribution for F-for-F activated  $\text{CF}_3^{18}\text{F}$  corrected for unimolecular translational energy disposal (49, 77)

Due to the importance of  $:\dot{\text{C}}^{18}\text{F}$  dissociation, Figures 3 and 4 provide conservative representations of the  $\text{CF}_3^{18}\text{F}$  excitation distribution from primary Reaction 78, which extends well above 23.5 eV.

A final refinement, which is not described here in detail due to space limitations, involves the derivation of an approximate continuous representation of the  $\text{CF}_3^{18}\text{F}$  excitation energy distribution from the data listed in Table XIII (47, 48, 49). This is possible based on accurate fractional decomposition yields as input data due to the serial nature of the cascade sequence shown in Reactions 81–84. The continuous distribution corresponding to Figure 3 is shown in Figure 5.

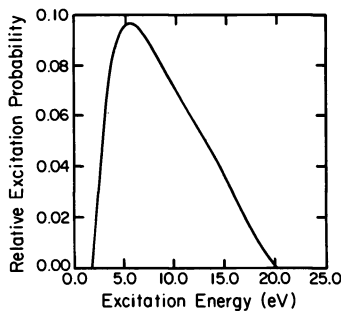


Figure 5. Continuous lower-bound thermochemical excitation energy distribution for F-for-F activated  $\text{CF}_3^{18}\text{F}$  (49, 77)

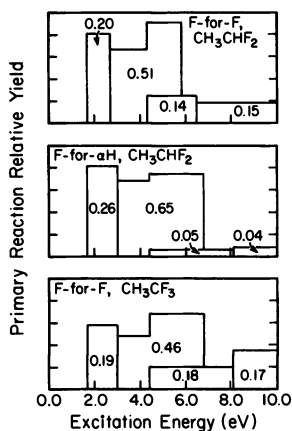


Figure 6. Approximate lower-bound thermochemical excitation energy distributions for the F-for- $\alpha$ H atomic substitution channels in  $\text{CH}_3\text{CHF}_2$  and  $\text{CH}_3\text{CF}_3$  (28, 77)

**Thermochemical Excitation Energy Distributions for Primary Reactions in  $\text{CH}_3\text{CHF}_2$  and  $\text{CH}_3\text{CF}_3$ .** The results from thermochemical analyses of the stabilization and decomposition products formed following hot  $^{18}\text{F}$  substitution reactions with  $\text{CH}_3\text{CHF}_2$  and  $\text{CH}_3\text{CF}_3$  have been shown in Figures 6 and 7. These crude nomographic distributions, which have arbitrarily been terminated at 10 eV, are similar for each primary process type. However, the thermochemical energy scales for F-for-F reactions in  $\text{CF}_4$  and fluorinated ethanes have been based on quite different energy disposal assumptions. For serial decomposition cascades all the excitation energy can be accounted for up to the limit corresponding to complete dissociation. Since this is not the case for branched decomposition mechanisms, Figures 6 and 7 have been based on the unrealistic assumption that the products from each monitored process contain no residual excitation.

When F-for-F activated  $\text{CH}_3\text{CF}_2^{18}\text{F}$  decomposes by carbon-carbon scission into  $\dot{\text{C}}\text{F}_2^{18}\text{F}$  and  $\dot{\text{C}}\text{H}_3$  radicals, for example, it would be more reasonable to postulate that the unmonitored  $\text{CH}_3$  fragment carries away about half of any excess internal energy. The energy scales shown on Figures 6 and 7 would then increase by roughly twofold, bringing the F-for-F scales for  $\text{CF}_3^{18}\text{F}$  and the fluorinated ethanes into improved

Table XIV. (P/Z)-Dependence of Substitution

Reactant (P/Z) (atm)	$\text{CH}_3\text{CHF}_2$ 0.35	$\text{CH}_3\text{CHF}_2$ 10
	Branching Ratio (C—C Scission):(HF-elimination)	
Primary Reaction		
F-for-F	$0.56 \pm 0.13$	$0.54 \pm 0.09$
F-for- $\alpha$ H	$0.14 \pm 0.10$	$0.38 \pm 0.11$
F-for- $\beta$ H	$4.10 \pm 0.80$	$6.30 \pm 1.00$

quantitative agreement. The qualitative consistency between the F-for-F excitation distributions shown in Figures 3 through 6 thus suggests that the present CF<sub>4</sub> mechanism (Reactions 77–84) is probably not grossly in error.

Figure 6 shows the uncorrected thermochemical excitation distributions corresponding to energetic substitution reactions at the fluorinated "alpha" carbon atom positions in CH<sub>3</sub>CHF<sub>2</sub> and CH<sub>3</sub>CF<sub>3</sub>. From the left the respective fractional yield segments include the undecomposed primary species and the decomposition products from  $\alpha,\beta$  HF-eliminations, from secondary carbon-carbon scissions to alkyl radicals, and from tertiary radical dissociations. Following these alpha substitution processes product decomposition occurs principally via  $\alpha,\beta$  HF-elimination.

Figure 7 shows that the nascent products from F-for-H substitutions at the "beta" positions in CH<sub>3</sub>CHF<sub>2</sub> and CH<sub>3</sub>CF<sub>3</sub> primarily decompose via carbon-carbon scission, giving these thermochemical excitation distributions a bimodal appearance. From Table XIV the low-pressure decomposition branching ratio trends illustrated in Figures 6 and 7 continue throughout the gas-phase (*P/Z*) range.

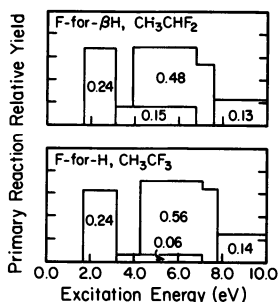
As discussed elsewhere in this volume (78), unimolecular dynamical effects of this type have been rationalized by Bunker in terms of the angular momentum characteristics of energetic substitution reactions (19).

The thermochemical excitation energy distributions derived for the primary alkyl replacement reactions in CH<sub>3</sub>CHF<sub>2</sub> and CH<sub>3</sub>CF<sub>3</sub> are shown in Figures 8 and 9. As argued above based on mechanistic evidence, these energy distributions extend to much lower maximum values than those shown in Figures 3 through 7. Only the first secondary decomposition step occurs to a significant extent for the nascent products from Reactions 21, 22, 56, and 57. The unimolecular mechanisms are simple, so that the energy scaling uncertainties in these cases reflect our lack of detailed knowledge concerning the decomposition reactions and the accompanying energy disposals. The latter problem is easily solved for simple bond dissociations or HF-eliminations in excited halomethanes (75, 76). The RRKM corrections to the conservative energy scales shown in Figures 8 and 9 are expected to be smaller than 20%.

#### Product Decomposition Branching Ratios (28)

CH <sub>3</sub> CHF <sub>2</sub> 190	CH <sub>3</sub> CF <sub>3</sub> 0.30	CH <sub>3</sub> CF <sub>3</sub> 10	CH <sub>3</sub> CF <sub>3</sub> 170
<i>Branching Ratio</i> (C—C Scission):(HF-elimination)			
0.50 ± 0.11	0.77 ± 0.19	0.86 ± 0.13	0.76 ± 0.14
0.52 ± 0.32	—	—	—
3.90 ± 1.30	11.50 ± 3.80	13.10 ± 6.10	9.80 ± 5.50

Figure 7. Approximate lower-bound thermochemical excitation energy distributions for the F-for- $\beta$ H atomic substitution channels in  $\text{CH}_3\text{CHF}_2$  and  $\text{CH}_3\text{CF}_3$  (28, 77)



Let us consider the dynamical significance of the present results for  $\text{CF}_3^{18}\text{F}$  produced from the  $\text{CH}_3\text{CF}_3$  F-for- $\dot{\text{C}}\text{H}_3$  primary process (Reaction 56). Based on the intrinsic unimolecular properties of 5-atom molecules, collisional deactivation of excited hot atom activated methanes should require large ( $P/Z$ ). This behavior has been demonstrated for  $\text{CH}_3^3\text{H}$ ,  $\text{CH}_3^{18}\text{F}$ ,  $\text{CH}_2\text{F}^{18}\text{F}$ , and  $\text{CF}_3^{18}\text{F}$  activated via energetic substitution reactions (11, 47–50, 74). The results shown in Table V thus indicate that the nascent  $\text{CF}_3^{18}\text{F}$  from Reaction 56 contains little internal excitation in excess of the decomposition threshold value.

This striking contrast in decomposition behavior between the products from recoil  $^{18}\text{F}$  substitution and alkyl replacement reactions is intriguing, but its dynamical basis remains uncertain. “Cold” alkyl replacement products could conceivably result from either of the following extreme mechanisms: (i) 3-center direct reactions in which product internal excitation is confined to the newly formed bond; or (ii) dynamically more complex processes that are Golden Rule forbidden (57, 79, 80) at large collision energies. The further study of this question represents a fertile area for future research.

Striking similarities exist between the product decomposition phenomena and the derived thermochemical excitation distributions for particular classes of hot  $^3\text{H}$  or  $^{18}\text{F}$  reactions occurring in closely related reactants (16, 25). Although further measurements would be useful, this evidence suggests that hot reactions related in this fashion may occur upon topologically similar potential energy hypersurfaces (77, 81, 82).

**Significance of Thermochemical Excitation Energy Distributions.** Two fundamentally different approaches have been used for the elucidation of primary product excitation distributions for hot atom activated species. Many workers have utilized the RRKM unimolecular rate theory to invert pressure falloff data measured for the products from energetic  $^3\text{H}$ -for-H (19, 64, 65, 74, 83, 84, 85) or F-for-X (19, 27) substitution reactions. More complete citations to the early literature are given elsewhere (57, 58, 59, 77, 80). This inversion procedure is computationally straightforward. However, it involves several a priori untested and

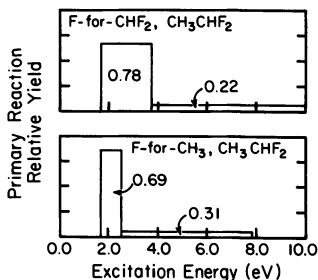


Figure 8. Approximate thermochemical excitation energy distributions for the F-for-R alkyl replacement channels in  $\text{CH}_3\text{CHF}_2$  (28, 77)

possibly drastic assumptions: (i) the decomposing molecules are assumed to exhibit random lifetime behavior (86, 87, 88); (ii) detailed structures and frequency assignments are chosen for both the activated and the decomposing molecules (89, 90); and (iii) the quantum state densities for these species are calculated using standard harmonic statistical expressions (91, 92, 93).

The availability of accurate phenomenologically derived excitation energy distributions would facilitate the testing and calibration of the RRKM theory for recoil chemistry applications. Accordingly, the approach preferred at this laboratory for investigating these distributions has eschewed any critical dependence on RRKM calculations (16, 25, 35, 47). The above described RRKM translational energy disposal corrections for activated halomethanes are both small in magnitude and insensitive to reasonable changes in the underlying statistical models (63). As shown in Figures 3 and 4, the neglect of these corrections leads to more conservative, less realistic descriptions of the excitation distributions.

The search for a phenomenological alternative to RRKM inversion distribution mapping does not represent a novel idea. The first step in the RRKM modeling procedure for a chemically activated species involves the a priori characterization of its initial excitation energy distribution (70, 89, 90). For species produced from exoergic reactions this information is normally obtained from thermochemical data. A correspondingly simple direct method has not yet emerged for hot atom activation processes, because the associated dynamics are incompletely understood.

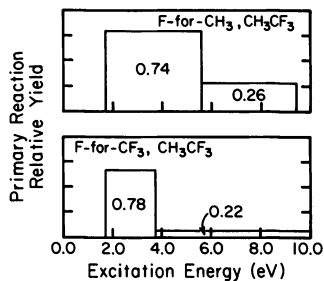


Figure 9. Approximate thermochemical excitation energy distributions for the F-for-R alkyl replacement channels in  $\text{CH}_3\text{CF}_3$  (28, 77)

Potentially severe uniqueness limitations that accompany the RRKM inversion procedure stem from the paucity of our present knowledge concerning the energy-dependent cross sections for hot substitution reactions and the associated energy disposal mechanisms (19, 25). Further complications result from the difficulty of assigning unique RRKM models for describing energy-rich polyatomic molecules in general (90), and hot atom activated species in particular (19).

Unimolecular rotational effects may strongly influence the decomposition behavior of hot atom activated molecules (19, 78). From Figure 7 the thermochemical excitation distributions accompanying F-for- $\beta$ H shown in Reactions 20 and 55 are very similar. However, the respective (C—C scission):(HF-elimination) decomposition branching ratios at low ( $P/Z$ ) are  $4.1 \pm 0.8$  and  $11.5 \pm 3.8$ , suggesting that unimolecular rotational effects are less pronounced for  $\text{CH}_3\text{CHF}_2$  reactant. This behavior is considered to be well established experimentally, but its significance remains uncertain due to the above noted deficiencies in our background knowledge.

We concur with Bunker (19) that recoil  $^{18}\text{F}$  activated fluoroethanes may obey the RRKM theory and that their unimolecular behavior cannot be accurately described using thermochemical excitation distributions together with RRKM models calibrated via conventional pyrolysis or chemical activation experiments. This uniqueness limitation has been illustrated in a later section through the use of nonsensical RRKM calculations to reproduce our ( $P/Z$ ) falloff data for the F-for-F primary process shown in Reaction 53.

Direct RRKM inversion has been applied to the original ( $P/Z$ ) falloff data reported from this laboratory (15, 16) for F-for-F activated  $\text{CH}_3\text{CF}_2^{18}\text{F}$  (27). In addition to any uniqueness limitations that may accompany this procedure, the calculated results are uncertain because the underlying falloff data were subsequently revised based on measurements carried out over an extended range of ( $P/Z$ ) (34).

On a more positive note, our recently derived detailed thermochemical  $\text{CF}_3^{18}\text{F}$  excitation distribution from Reaction 78 (47, 48, 49) exhibits excellent qualitative consistency with RRKM inversion results obtained for  $^3\text{H}$ -for-H activated cyclo- $\text{C}_4\text{H}_7^3\text{H}$  (66), suggesting that the general form of the derived excitation distributions may be characteristic of many hot atom systems. Significant quantitative discrepancies, however, have been noted between the RRKM and thermochemical (25) excitation distribution threshold energies for  $^3\text{H}$ -for-H activated molecules, suggesting the need for further research. It would be particularly useful to have both methods applied to the same recoil activated molecule.

**Phenomenological Approach to Energy Transfer from F-for-X Activated Molecules.** The study of collisional energy transfer from



internally excited polyatomic molecules represents an important goal of unimolecular kinetics research (89). Radiotracer experiments of this type involving activation via <sup>3</sup>H-for-H substitution (94) and conventional exoergic chemical reactions (70) have been considered elsewhere in this volume. Because of the large product excitation levels accompanying F-for-X substitution processes, <sup>18</sup>F-labeled superexcited molecules hold particular interest for this type of investigation.

This method can conveniently be illustrated for the CH<sub>3</sub>CHF<sub>2</sub> F-for-F substitution sequence (Reactions 23–25). The rate of disappearance of the activated CH<sub>3</sub>CHF<sup>18</sup>F molecules is given by Equation 87 (28, 31,

$$-\frac{d[R^\dagger]_t}{dt} = k_m[M][R^\dagger]_t + k_d[R^\dagger]_t \quad (87)$$

95, 96). Here the bracketed quantities denote the concentrations of activated (R<sup>†</sup>) and bath gas (M) species; and *k<sub>d</sub>* and *k<sub>m</sub>*, the nonequilibrium rate coefficients for decomposition and collisional stabilization, respectively. The suitability of conventional kinetic rate equations for describing hot atom experiments has been considered elsewhere (32, 37, 39, 54, 60). Equation 87 can be integrated and solved for the instantaneous R<sup>†</sup> concentration, [R<sup>†</sup>]<sub>*t*</sub>. In Equation 88 [M] is effectively

$$[R^\dagger]_t = [R^\dagger]_0 \exp \{-[k_m[M] + k_d]t\} \quad (88)$$

constant and [R<sup>†</sup>]<sub>0</sub> denotes the initial concentration of activated molecules. Integration of Equation 87 together with the assumption of mass balance leads to expressions for the fractional stabilization (*S*) and decomposition (*D*) yields following decay of all the activated molecules.

$$S = \frac{k_m[M]}{k_d + k_m[M]} \quad (89)$$

$$D = \frac{k_d}{k_d + k_m[M]} \quad (90)$$

These kinetic equations can be tested using the data shown in Tables III through VI provided that only the (*P/Z*)-dependent processes are considered. For the sequence of Reactions 23–25 the low (*P/Z*)-limiting CH<sub>3</sub>CHF<sup>18</sup>F yield, *Y*<sub>0</sub>(CH<sub>3</sub>CHF<sup>18</sup>F), must be subtracted from the measured stabilization values to take the (*P-Z*)-independent process (Reaction 25) into account (25, 31, 65, 84, 85, 94–98). From the equation of

$$\left(\frac{D}{S}\right) = \frac{Y^\circ(R^\dagger) - Y_0(R^\dagger)}{Y(R^\dagger) - Y_0(R^\dagger)} - 1 \quad (91)$$

state for imperfect one-component gases  $[M]$  can be expressed in terms of the effective pressure,  $(P/Z)$ . In Equation 92  $[M]$  has the units mole-

$$[M] = \left(\frac{P}{Z}\right) \left(\frac{L_o}{RT}\right) \quad (92)$$

cules  $\text{cm}^{-3}$ ,  $L_o$  denotes Avogadro's number, and the other quantities have been previously defined. Combining Equations 89, 90, and 92 leads to the following result for the  $(D/S)$  ratio:

$$\left(\frac{D}{S}\right) = \left(\frac{k_d}{k_m}\right) \left(\frac{Z}{P}\right) \left(\frac{RT}{L_o}\right) \quad (93)$$

The ratios calculated from Equation 91 are thus predicted to exhibit inverse proportionality to  $(P/Z)$ .

The above treatment is entirely analogous to that used in conventional chemical activation experiments (70). As illustrated in Figures 10 through 12 for F-for-F and F-for-H reactions with  $\text{CH}_3\text{CF}_3$ , Equation 93 is tested using plots of  $(D/S)$  ratios vs.  $(Z/P)$  (28, 31, 95, 96). Observations of linearity for such plots indicate  $(P/Z)$ -invariance for the  $(k_d/k_m)$  relative rate coefficients. For activated species possessing narrow initial excitation distributions this type of behavior is often observed at large  $(P/Z)$  with efficient colliders (70, 92, 93). In the "strong collision" limit single deactivating collisions prevent decomposition, and the apparent unimolecular rate coefficient  $(k_d^\infty)$  becomes constant.

From Figures 10 and 11 apparent  $(P/Z)$ -limiting falloff behavior is exhibited by the nascent products from energetic F-for-X reactions with  $\text{CH}_3\text{CF}_3$  over the range  $3 \leq (P/Z) \leq 10$  atm (Equation 94). The  $(D/S)$

$$\left(\frac{D}{S}\right) = \left(\frac{k_d^\infty}{k_m}\right) \left(\frac{Z}{P}\right) \left(\frac{RT}{L_o}\right) \quad (94)$$

ratios at 1.5 atm, however, reflect significant  $k_d$  increases above these constant  $k_d^\infty$  values. This effect has been further illustrated in Figure 12 in which the scales for F-for-H activated  $\text{CF}_3\text{CH}_2^{18}\text{F}$  have been adjusted to allow the inclusion of data obtained at 0.30 atm. These increases in  $(k_d/k_m)$  at low  $(P/Z)$  provide direct evidence for cascading multistep collisional deactivation of the nascent products from energetic F-for-X reactions (70, 89, 92, 93).

Our method of fitting the falloff data using Equation 94 has involved a linear regression statistical optimization procedure similar to that employed by Spicer and coworkers (64). The kinetic parameters obtained for  $\text{CH}_3\text{CHF}_2$  and  $\text{CH}_3\text{CF}_3$  at low  $(P/Z)$  have been summarized in Table XV. The average  $(k_d^\infty/k_m)$  values for the  $\alpha$  and  $\beta$  substitution

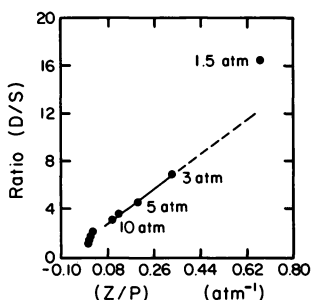


Figure 10. Cascading (P/Z) falloff plot for F-for-F activated  $\text{CH}_3\text{-CF}_2^{18}\text{F}$ : (●) experimental data; (—) Equation 94 and Table XV; (---) extrapolated Equation 94 (28, 95)

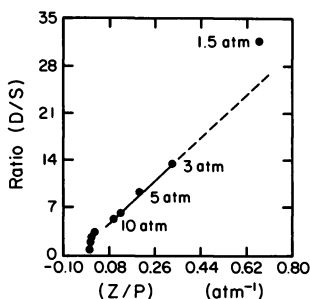


Figure 11. Cascading (P/Z) falloff plot for F-for-H activated  $\text{CF}_3\text{-CH}_2^{18}\text{F}$ : symbols as in Figure 10 (28, 95)

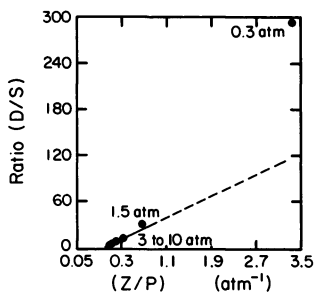


Figure 12. Expanded scale cascading (P/Z) falloff plot for F-for-H activated  $\text{CF}_3\text{CH}_2^{18}\text{F}$ : symbols as in Figure 10 (28, 95)

Table XV. Low (P/Z) Falloff Kinetic Analyses for F-for-X Activated  $\text{CH}_3\text{CHF}_2$  and  $\text{CH}_3\text{CF}_3$ <sup>a</sup>

Primary Reaction	Reactant Species	$(k_a^\infty/k_m)^b$	$Y_o(R^\dagger)$ (%)	$Y(R^\dagger)$ (%) <sup>c</sup>
F-for-F	$\text{CH}_3\text{CF}_3$	$1560 \pm 250$	$0.70 \pm 0.05$	$0.80 \pm 0.09$
F-for-F	$\text{CH}_3\text{CHF}_2$	$1240 \pm 200$	$0.89 \pm 0.07$	$0.78 \pm 0.08$
F-for- $\alpha\text{H}$	$\text{CH}_3\text{CHF}_2$	$1500 \pm 250$	$0.44 \pm 0.08$	$0.55 \pm 0.10$
F-for-H	$\text{CH}_3\text{CF}_3$	$830 \pm 140$	$1.34 \pm 0.10$	$1.35 \pm 0.10$
F-for- $\beta\text{H}$	$\text{CH}_3\text{CHF}_2$	$950 \pm 150$	$1.23 \pm 0.08$	$1.39 \pm 0.12$

<sup>a</sup> Equation 94 parameters valid over the range  $3 \leq (P/Z) \leq 10$  atm (28, 95, 96).

<sup>b</sup>  $(k_a^\infty/k_m)$  given in units of molecules  $\text{cm}^{-3}$ .

<sup>c</sup>  $Y(R^\dagger)$  values measured at ca. 0.3 atm.

**Table XVI. High ( $P/Z$ ) Falloff Kinetic Analyses for F-for-X Activated  $\text{CH}_3\text{CHF}_2$  and  $\text{CH}_3\text{CF}_3$ <sup>a</sup>**

Primary Reaction	Reactant Species	$(k_a^\infty/k_m)^b$	$Y_o(R^\dagger)$ (%)	$Y(R^\dagger)$ (%) <sup>c</sup>
F-for-F	$\text{CH}_3\text{CF}_3$	$121 \pm 20$	$1.53 \pm 0.05$	$1.56 \pm 0.07$
F-for-F	$\text{CH}_3\text{CHF}_2$	$43 \pm 10$	$1.50 \pm 0.12$	$1.51 \pm 0.06$
F-for- $\alpha\text{H}$	$\text{CH}_3\text{CHF}_2$	$136 \pm 26$	$0.74 \pm 0.12$	$0.91 \pm 0.08$
F-for-H	$\text{CH}_3\text{CF}_3$	$132 \pm 27$	$1.85 \pm 0.15$	$2.03 \pm 0.07$
F-for- $\beta\text{H}$	$\text{CH}_3\text{CHF}_2$	$68 \pm 12$	$2.03 \pm 0.10$	$2.09 \pm 0.08$

<sup>a</sup> Equation 94 parameters valid over the range  $10 < (P/Z) \leq 190$  atm (28, 95, 96).

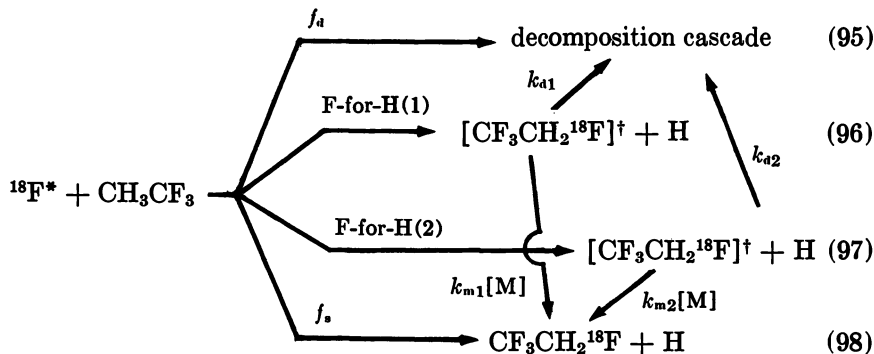
<sup>b</sup>  $(k_a^\infty/k_m)$  given in units of molecules  $\text{cm}^{-3}$ .

<sup>c</sup>  $Y(R^\dagger)$  values measured at 10 atm.

channels in these substances are  $1430 \pm 140$  and  $890 \pm 100$  molecules  $\text{cm}^{-3}$ . Below 10 atm the nascent products from F-for-H reactions are relatively more easily stabilized through collisions with  $\text{CH}_3\text{CHF}_2$  and  $\text{CH}_3\text{CF}_3$ .

Above 10 atm the experimental ( $D/S$ ) ratios deviate from the values predicted using Equation 94 and Table XV. We were surprised to note that the high ( $P/Z$ ) falloff data could be represented using the second set of kinetic parameters listed in Table XVI. As shown in Figures 13 and 14, this bimodal kinetic falloff analysis has yielded quantitative agreement between the experimental and calculated  $Y(R^\dagger)$  results throughout the range  $0.3 \leq (P/Z) \leq 190$  atm.

The significance of the bimodal falloff analyses for these superexcited molecule systems is not yet understood. The  $Y(R^\dagger)$  data for all five of the F-for-X substitution channels in  $\text{CH}_3\text{CHF}_2$  and  $\text{CH}_3\text{CF}_3$  exhibit the segmented appearance shown in Figures 13 and 14. The corresponding F-for-H excitation distributions also indicate bimodality, suggesting that we may think in terms of two primary F-for-X processes whose products exhibit experimentally distinguishable ( $P/Z$ ) falloff behavior (31). This is illustrated in the sequence of Reactions 95–99 for the F-for-H process



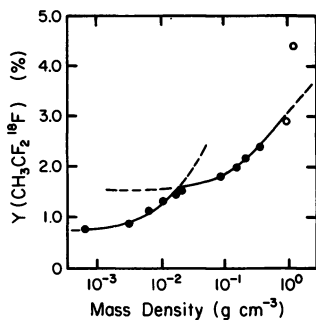


Figure 13. Kinetic falloff analysis of  $Y(\text{CH}_3\text{CF}_2^{18}\text{F})$  results for F-for-F activated  $\text{CH}_3\text{CF}_2^{18}\text{F}$ : (●) gas-phase  $Y(\text{CH}_3\text{CF}_2^{18}\text{F})$ ; (○) liquid-phase  $Y(\text{CH}_3\text{CF}_2^{18}\text{F})$ ; left-side curve, Equation 94 and Table XV; right-side curve, Equation 94 and Table XVI; (---) extended calculated results (28, 95, 96)

in  $\text{CH}_3\text{CF}_3$  (cf. Figures 11, 12, and 14). Figures 3 through 6 do not show evidence for excitation distribution bimodality for F-for-F reactions, however, although the qualitative features of the F-for-F and F-for-H unimolecular falloff analyses in these substances are the same.

At present we are unable to offer a more detailed explanation for this interesting behavior. We hope that future experiments with the mechanistically simpler  $\text{C}_2\text{F}_6$  reaction system will prove to be enlightening in this regard.

In summary, both the conventional cascading (70) and the  $k_a^\infty$  measurement (94) techniques appear to hold promise for future unimolecular energy transfer experiments involving  $^{18}\text{F}$ -labeled superexcited molecules in a variety of host gases.

**Theoretical Energy Transfer Calculations.** In this final section computer modeling is used to simulate the cascading falloff data shown in Figure 10 for F-for-F activated  $\text{CH}_3\text{CF}_2^{18}\text{F}$  (95). These calculations illustrate the difficulty of obtaining unique theoretical descriptions of the energy transfer behavior of hot atom activated molecules. The computational procedure, which is illustrated in Figure 15, has been described elsewhere in this volume for species activated using conventional exergic reactions (70).

The following input data are required: (i) a quantitative description of the initial excitation energy distribution function  $[f(E^\dagger)]$ ; (ii) a set

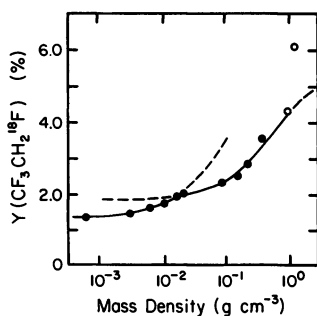


Figure 14. Kinetic falloff analysis of  $Y(\text{CF}_3\text{CH}_2^{18}\text{F})$  results for F-for-H activated  $\text{CF}_3\text{CH}_2^{18}\text{F}$ : (●) gas-phase  $Y(\text{CF}_3\text{CH}_2^{18}\text{F})$ ; (○) liquid-phase  $Y(\text{CF}_3\text{CH}_2^{18}\text{F})$ ; other notes as in Figure 13.

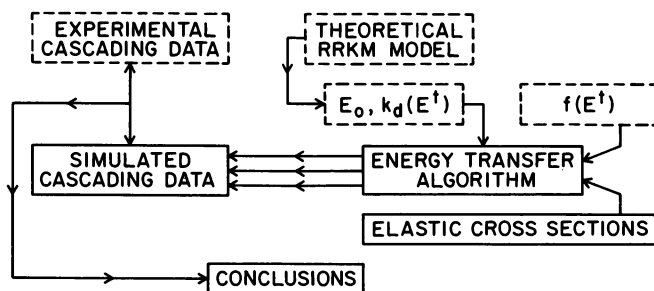
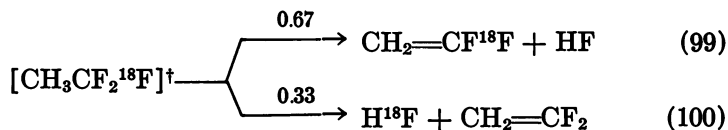


Figure 15. Flow chart for hot atom cascading falloff simulation; dashed boxes represent input data (95)

of numerical monoenergetic unimolecular rate coefficients [ $k_d(E^\dagger)$ ] (not necessarily RRKM) that encompasses the full  $E^\dagger$  range populated by  $f(E^\dagger)$ ; (iii) elastic collision cross sections for the colliding species; and (iv) a mathematical model for the energy transfer probability density distribution [ $P(\Delta E^\dagger)$ ].

We have utilized the stepladder transition probability model, which assumes that only constant energy increments [ $\langle \Delta E^\dagger \rangle$ ] are transferred during the deactivating collisions. The nascent  $\text{CH}_3\text{CF}_2^{18}\text{F}$  species have been assumed to be in translational equilibrium with the host reservoir and to decompose only by HF-elimination Reactions 99 and 100. These



processes have been described using a coplanar 4-center critical configuration model (89, 99) together with standard thermochemical (70, 100) and elastic cross section (101) data. The unimolecular rate constants have been obtained using the universal RRKM program of Hase and Bunker (102).

In this study  $f(E^\dagger)$  has been represented using flat, structureless distributions of the form given by Equation 101. The previously derived

$$f(E_0^\dagger, E^\dagger) = \text{Constant} \quad (101)$$

1.7-eV thermochemical  $E_0^\dagger$  threshold energy result for F-for-F reactions has been utilized as the starting point for trial-and-error flat  $f(E^\dagger)$  distributions extending to a common antithreshold value of 11.0 eV.

The calculated results corresponding to the various  $E_0^\dagger$  and  $\langle \Delta E^\dagger \rangle$  parameters consist of pairs of ( $k_d/k_d^\infty$ ) vs. ( $D/S$ ) ratios. The standard

procedure used in unimolecular energy transfer studies involves inter-comparisons between experimental and simulated ( $P/Z$ ) falloff results as a basis for choosing preferred transition probability models and  $\langle\Delta E^\ddagger\rangle$  values (70, 92, 99, 100, 101). Two such comparisons for F-for-F activated  $\text{CH}_3\text{CF}_2^{18}\text{F}$  have been shown in Figures 16 and 17.

The linear plotting schemes shown in these figures exaggerate the rather poor quality of the simulations obtained at large ( $P/Z$ ) values where the ( $D/S$ ) ratios become very small. The measured ( $D/S$ ) vs. ( $Z/P$ ) results exhibit pronounced curvature below 10 atm, corresponding to the falloff segment shown at the left side of Figure 13. Figures 16 and 17 emphasize comparisons between experiment and calculations within this falloff region.

From Figure 16 for 0.17 eV  $\langle\Delta E^\ddagger\rangle$  and 4.0 eV  $E_0^\ddagger$  the simulation is seriously inconsistent with the results measured at low ( $P/Z$ ). However, Figure 17 shows that good agreement can be obtained for this model simply by increasing  $E_0^\ddagger$  to 5.0 eV. The calculations are much less sensitive to changes in the 11.0 eV  $f(E^\ddagger)$  antithreshold value. This is physically reasonable since the more highly activated  $\text{CH}_3\text{CF}_2^{18}\text{F}$  species invariably decompose at low ( $P/Z$ ).

Several other stepladder simulations yielded reasonable consistency with the measured data. Parametric increases in  $\langle\Delta E^\ddagger\rangle$  shift the calculated results to progressively reduced ( $D/S$ ) ratios with increasing ( $P/Z$ ). This effect can be compensated by increasing  $E_0^\ddagger$ , though not without introducing curvature changes in the falloff plots.

From Figures 3 through 6 Equation 101 provides a grossly inaccurate model for  $f(E^\ddagger)$  for F-for-F activated molecules. We suspect that  $f(E^\ddagger)$  for  $\text{CH}_3\text{CF}_2^{18}\text{F}$  from Reaction 53 is populated from approximately 1.7 eV to considerably above 15 eV with an energy dependence crudely similar to that shown in Figure 5. In contrast with the predictions from conventional RRKM models for these processes (16, 19), Table XIV indicates that the nascent products from Reaction 53 decompose with roughly comparable rates via both HF-elimination and carbon-carbon scission processes. However, the C—C scission channels have been entirely neglected in the present model calculations.

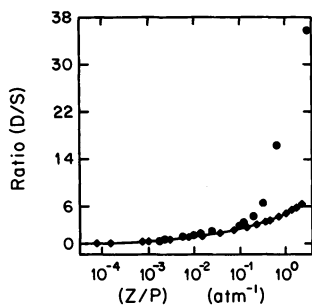


Figure 16. Stepladder simulation of ( $P/Z$ ) falloff data for F-for-F activated  $\text{CH}_3\text{CF}_2^{18}\text{F}$  (95). Input parameters:  $\langle\Delta E^\ddagger\rangle$ , 0.17 eV;  $E_0^\ddagger$ , 4.0 eV;  $f(E^\ddagger)$  given by Equation 101 to 11.0 eV. Key to plot points: (●) experimental data; (◆) calculated results.

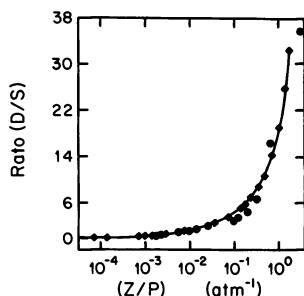


Figure 17. Stepladder simulation of  $(P/Z)$  falloff data for F-for-F activated  $\text{CH}_3\text{CF}_3^{18}\text{F}$  (95). Input parameters:  $E_0^\dagger$ , 5.0 eV; others and symbols as in Figure 16.

Several conclusions follow from the results presented here and in previous sections: (i) the nascent products from F-for-X reactions possess broad, peaked excitation energy distributions; (ii) the unimolecular falloff comparisons shown in Figures 16 and 17 are based on nonsensical theoretical assumptions; (iii) both multiple and demonstrably invalid theoretical models apparently can be rationalized with  $(P/Z)$  falloff data for F-for-X activated species; (iv) Figure 17 supports the utility, but not the validity, of the underlying theoretical model; and (v) falloff data comparisons of this type for recoil  $^{18}\text{F}$  activated systems in which  $f(E^\dagger)$  is not known a priori suffer from severe uniqueness limitations.

Radiotracer techniques have recently been used to obtain extended range  $(P/Z)$  falloff data for  $^{14}\text{CH}_3\text{CF}_3$  produced with a narrow  $f(E^\dagger)$  distribution and an average initial  $E^\dagger$  value of  $4.46 \pm 0.04$  eV (70). Even though an approximately 20-fold increase in the range of accessible  $(D/S)$  ratios was achieved in this investigation, unique modeling of the unimolecular energy transfer processes with  $\text{C}_2\text{F}_6$  and  $\text{C}_2\text{H}_6$  colliders was not possible based on the available statistical cascading models. Cascading simulations for systems possessing narrow  $f(E^\dagger)$  distributions should exhibit enhanced sensitivity to the underlying theoretical models. Because broad  $f(E^\dagger)$  distributions probably represent a general characteristic of hot substitution activation processes, the above proposed uniqueness limitations for F-for-X activated species may well also apply to other hot atom systems.

### Summary

The authors have attempted to provide an overview of knowledge gained during the past 10 years concerning the gas-phase reactions of recoiling  $^{18}\text{F}$  atoms with organic substances and the properties of  $^{18}\text{F}$ -labeled superexcited molecules produced from such reactions. Although the in-depth studies with halocarbons reported here have yielded much new information, many unsolved problems remain to be investigated (47).



In maintaining the narrow focus of this chapter, several important topics have been omitted. The caged recombination reactions that occur in condensed phase recoil  $^{18}\text{F}$  experiments exhibit unusual dynamical characteristics (11, 26, 28, 31, 35, 96). The energetic F-to-HF process shown in Equation 9 has been particularly important from a theoretical standpoint (22, 24, 29, 30, 32, 34–37, 39, 40, 43, 44, 49, 52). The moderated nuclear recoil technique has provided accurate kinetic parameters for thermal  $^{18}\text{F}$  reactions (24, 42, 46, 52–55, 60) that have facilitated the recent development of a realistic potential extended collision theory for activationless bimolecular reactions (42, 103).

Despite the omission of these topics, we hope that we have succeeded in indicating the types of materials science information that can be obtained from carefully designed experiments with recoiling  $^{18}\text{F}$  atoms. We have also attempted to suggest some directions for future research and to convey our strong sense of enthusiasm for the field of high-energy chemical kinetics.

### *Acknowledgments*

The research described here would not have been possible without the encouragement and continuous financial support provided by the U.S. Department of Energy under Contract No. AS03-76SF00034, Agreement No. AT03-76ER70158, and its predecessors. This critically important assistance is gratefully acknowledged.

Many coworkers have contributed to this work. For assistance with the experiments and calculations we would like to thank Professor E. R. Grant, Mr. R. Gurvis, Mr. M. B. Knickelbein, Dr. K. D. Knierim, Dr. C. A. Mathis, Mr. R. Okamoto, Dr. R. R. Pettijohn, and the Cyclotron Operations staff at the Crocker Nuclear Laboratory. Computer algorithms were generously provided by Professors D. L. Bunker, B. S. Rabinovitch, and D. W. Setser. We have enjoyed stimulating discussions with Professors D. L. Bunker (deceased), P. P. Gaspar, E. R. Grant, J. Keizer, K. A. Krohn, and L. D. Spicer.

### *Literature Cited*

1. Colebourne, N.; Wolfgang, R. *J. Chem. Phys.* **1963**, *38*, 2782.
2. Colebourne, N.; Todd, J. F. J.; Wolfgang, R. "Chemical Effects of Nuclear Transformations"; I.A.E.A.: Vienna, 1965; Vol. 1, p. 149.
3. Todd, J. F. J.; Colebourne, N.; Wolfgang, R. *J. Phys. Chem.* **1967**, *71*, 2875.
4. Tang, Y. N.; Rowland, F. S. *J. Phys. Chem.* **1967**, *71*, 4576.
5. Spicer, L.; Todd, J. F. J.; Wolfgang, R. *J. Am. Chem. Soc.* **1968**, *90*, 2425.
6. Tang, Y. N.; Smail, T.; Rowland, F. S. *J. Am. Chem. Soc.* **1969**, *91*, 2130.

7. McKnight, C. F.; Root, J. W. *J. Phys. Chem.* 1969, 73, 4430.
8. McKnight, C. F.; Parks, N. J.; Root, J. W. *J. Phys. Chem.* 1970, 74, 217.
9. Smail, T.; Rowland, F. S. *J. Phys. Chem.* 1970, 74, 1866.
10. Smail, T.; Miller, G. E.; Rowland, F. S. *J. Phys. Chem.* 1970, 74, 3464.
11. Richardson, A. E.; Wolfgang, R. *J. Am. Chem. Soc.* 1970, 92, 3480.
12. Palino, G. F.; Rowland, F. S. *Radiochim. Acta* 1971, 15, 57.
13. Smail, T.; Iyer, R. S.; Rowland, F. S. *J. Phys. Chem.* 1971, 75, 1324.
14. Parks, N. J.; Krohn, K. A.; Root, J. W. *J. Chem. Phys.* 1971, 55, 2690.
15. Krohn, K. A.; Parks, N. J.; Root, J. W. *J. Chem. Phys.* 1971, 55, 5771.
16. *Ibid.*, 5785.
17. Pauwels, E. K. J., Ph.D. Dissertation, Univ. of Amsterdam, 1971.
18. Krohn, Kenneth A., Ph.D. Dissertation, Univ. of California, Davis, 1971; University Microfilms No. 72-3587.
19. Bunker, D. L. *J. Chem. Phys.* 1972, 57, 332.
20. Williams, R. L.; Rowland, F. S. *J. Am. Chem. Soc.* 1972, 94, 1047.
21. Williams, R. L.; Rowland, F. S. *J. Phys. Chem.* 1972, 76, 3509.
22. Muckerman, J. T. *J. Chem. Phys.* 1972, 57, 3388.
23. Al-Dhahir, A. J. *Indian Chem. Soc.* 1974, 51, 465.
24. Grant, E. R., Ph.D. Dissertation, Univ. of California, Davis, 1974; University Microfilms No. 75-15434.
25. Manning, R. G.; Krohn, K. A.; Root, J. W. *Chem. Phys. Lett.* 1975, 35, 544.
26. Manning, R. G.; Root, J. W. *J. Phys. Chem.* 1975, 79, 1478.
27. Smith, Jr., W. S.; Rodgers, A. S.; Tang, Y. N. *J. Chem. Phys.* 1975, 62, 3310.
28. Manning, Ronald G., Ph.D. Dissertation, Univ. of California, Davis, 1975; University Microfilms No. 76-1795.
29. Grant, E. R.; Root, J. W. *J. Chem. Phys.* 1976, 64, 417.
30. Feng, D. F.; Grant, E. R.; Root, J. W. *J. Chem. Phys.* 1976, 64, 3450.
31. Manning, R. G.; Root, J. W. *J. Chem. Phys.* 1976, 64, 4926.
32. Knierim, K. D.; Root, J. W. *Radiochim. Acta* 1977, 24, 103.
33. Van der Linde, K. D.; Spoelotra-van Balen, S.; Kaspersen, F. M.; Louwrier, P. W. F.; Lindner, L. *Radiochim. Acta* 1977, 24, 167.
34. Manning, R. G.; Mo, S. H.; Root, J. W. *J. Chem. Phys.* 1977, 67, 636.
35. Manning, R. G.; Root, J. W. *J. Phys. Chem.* 1977, 81, 2576.
36. Koura, K. *J. Chem. Phys.* 1977, 66, 4078.
37. Grant, E. R.; Feng, D. F.; Keizer, J.; Knierim, K. D.; Root, J. W. In "Fluorine-Containing Free Radicals: Kinetics and Dynamics of Reactions," *ACS Symp. Ser.* 1978, 66, 314.
38. Palmer, A. J. *Int. J. Appl. Radiat. Isot.* 1978, 29, 545.
39. Grant, E. R.; Knierim, K. D.; Root, J. W. *Chem. Phys. Lett.* 1978, 53, 588.
40. Mo, S.-H., Ph.D. Dissertation, Univ. of California, Davis, 1978; University Microfilms No. TSZ-79-5201.
41. Brinkman, G. A.; Visser, J. *Int. J. Appl. Radiat. Isot.* 1979, 30, 517.
42. Mathis, C. A., Ph.D. Dissertation, Univ. of California, Davis, 1979.
43. Shizgal, B. *J. Chem. Phys.* 1980, 72, 3156.
44. Koura, K. *J. Chem. Phys.* 1980, 72, 1756.
45. Manning, R. G.; Root, J. W. *J. Chem. Phys.* 1980, 72, 6323.
46. Mathis, C. A.; Knierim, K. D.; Root, J. W. *Chem. Phys. Lett.* 1980, 72, 368.
47. Gaspar, P. P.; Root, J. W. *Radiochim. Acta* 1981, 28, 191.
48. Knierim, K. D.; Knickelbein, M.; Mathis, C. A.; Root, J. W., unpublished data.
49. Knierim, K. D., Ph.D. Dissertation, Univ. of California, Davis, 1980.
50. Gurvis, R., M.S. Thesis, Univ. of California, Davis, 1980.
51. Lindner, L., private communication.

52. Root, J. W.; Mathis, C. A.; Gurvis, R.; Knierim, K. D.; Mo, S. H., Chap. 10 in this book.
53. Rowland, F. S.; Rust, F.; Frank, J. P. In "Fluorine-Containing Free Radicals: Kinetics and Dynamics of Reactions," *ACS Symp. Ser.* 1978, 66, 26.
54. Mo, S. H.; Grant, E. R.; Little, F. E.; Manning, R. G.; Mathis, C. A.; Werre, G. S.; Root, J. W. In "Fluorine-Containing Free Radicals: Kinetics and Dynamics of Reactions," *ACS Symp. Ser.* 1978, 66, 59.
55. Mathis, C. A.; Gurvis, R.; Knickelbein, M.; Knierim, K. D.; Mo, S. H.; Root, J. W. *Int. J. Chem. Kinet.*, in press.
56. Knickelbein, M.; Root, J. W., unpublished data.
57. Wolfgang, R. *Prog. React. Kinet.* 1965, 3, 97.
58. Rowland, F. S. *Proc. Int. Sch. Phys. "Enrico Fermi"* 1970, 44, 108, 127.
59. Rowland, F. S. *Int. Rev. Sci. Phys. Chem., Ser. One* 1972, 9, 109.
60. Grant, E. R.; Root, J. W. *J. Chem. Phys.* 1975, 63, 2970.
61. Tang, Y. N., Chap. 3 in this book.
62. Caspar, P. P., Chap. 1 in this book.
63. Grant, E. R., private communication.
64. Nogar, N. S.; Dewey, J. K.; Spicer, L. D. *Chem. Phys. Lett.* 1975, 34, 98.
65. Ferro, L. J.; Spicer, L. D. *J. Chem. Phys.* 1978, 69, 4335.
66. Noyes, R. M. *Prog. React. Kinet.* 1961, 1, 129.
67. Bunker, D. L.; Jacobson, B. S. *J. Am. Chem. Soc.* 1972, 94, 1843.
68. Atkins, P. W.; Lambert, T. P. *Annu. Rep. Chem. Soc. (London)* 1975, A, 67.
69. Atkins, P. *Chem. Br.* 1975, A, 214.
70. Mathis, C. A.; Root, J. W. Chap. 8 in this book.
71. Simmie, J. M.; Quiring, W. J.; Tschuikow-Roux, E. *J. Phys. Chem.* 1970, 74, 992.
72. Tschuikow-Roux, E.; Quiring, W. J.; Simmie, J. M. *J. Phys. Chem.* 1970, 74, 2449.
73. Smith, W. S.; Tang, Y. N. *J. Phys. Chem.* 1974, 78, 2186.
74. Tang, Y. N.; Rowland, F. S. *J. Phys. Chem.* 1968, 72, 707.
75. Sudbo, A. S.; Schulz, P. A.; Grant, E. R.; Shen, Y. R.; Lee, Y. T. *J. Chem. Phys.* 1979, 70, 912.
76. Grant, E. R.; Root, J. W., unpublished data.
77. Root, J. W. Lecture No. NUCL 42 presented at 177th Nat. Meet. Am. Chem. Soc. Joint ACS/CSJ Chem. Congr., Honolulu, HI, Apr., 1979.
78. Grant, E. R.; Santamaria, J. Chap. 7 in this book.
79. Wolfgang, R. *Annu. Rev. Phys. Chem.* 1965, 16, 15.
80. Raff, L. M.; Thompson, D. L.; Sims, L. B.; Porter, R. N. *J. Chem. Phys.* 1972, 56, 5998.
81. Bogan, D.; Setser, D. W. In "Fluorine-Containing Free Radicals: Kinetics and Dynamics of Reactions," *ACS Symp. Ser.* 1978, 66, 237.
82. Polanyi, J. C.; Schreiber, J. C. *Faraday Discuss. Chem. Soc.* 1977, 62, 267.
83. Chou, C. C.; Hase, W. L. *J. Phys. Chem.* 1974, 78, 2309.
84. Nogar, N. S.; Callahan, M. B.; Spicer, L. D. *Radiochim. Acta* 1976, 23, 92.
85. Callahan, M. B.; Spicer, L. D. *J. Phys. Chem.* 1979, 83, 1013.
86. Bunker, D. L. *Sci. Am.* 1964, 211, 100.
87. Bunker, D. L.; Hase, W. L. *J. Chem. Phys.* 1973, 59, 4621.
88. Bunker, D. L. *Acc. Chem. Res.* 1974, 7, 195.
89. Setser, D. W. *Int. Rev. Sci. Phys. Chem., Ser. One* 1972, 9, 1.
90. Neely, B. D.; Carmichael, H. *J. Phys. Chem.* 1973, 77, 307.
91. Bunker, D. L. "Theory of Elementary Gas Reaction Rates"; Pergamon: Oxford, 1966.

92. Robinson, P. J.; Holbrook, K. A. "Unimolecular Reactions"; Wiley-Interscience: New York, 1972.
93. Forst, Wendell "Theory of Unimolecular Reactions"; Academic: New York, 1973.
94. Spicer, L. D., Chap. 6 in this book.
95. Root, J. W.; Manning, R. G.; Pettijohn, R. R. Lecture No. PHYS 002 presented at *170th Nat. Meet. Am. Chem. Soc., Chicago, Aug. 1975*.
96. Root, J. W. "U.S. Atomic Energy Commission Technical Report No. UCD-34P158-74-1," University of California, Davis, 1975.
97. Nogar, N. S.; Spicer, L. D. *J. Phys. Chem.* **1976**, *80*, 1736.
98. Nogar, N. S.; Spicer, L. D. *J. Chem. Phys.* **1977**, *66*, 3624.
99. Chang, H. W.; Craig, N. L.; Setser, D. W. *J. Phys. Chem.* **1972**, *76*, 954.
100. Marcoux, P. J.; Setser, D. W. *J. Phys. Chem.* **1978**, *82*, 97.
101. Pettijohn, R. R.; Mutch, G. W.; Root, J. W. *J. Phys. Chem.* **1975**, *79*, 1747, 2077.
102. "General Program for Unimolecular Rate Constants," available through the Quantum Chemistry Program Exchange, Indiana University Chemistry Department, Program No. 234, R.R.K.M.
103. Root, J. W., Lecture No. NUCL 067 presented at *178th Nat. Meet. Am. Chem. Soc., Washington, D.C., Sept., 1979*.

RECEIVED September 4, 1980.

# Recoil Generated Radiotracers in Studies of Molecular Dynamics

LEONARD D. SPICER

Department of Chemistry, University of Utah, Salt Lake City, UT 84112

*This chapter summarizes many of the contributions that the recoil technique of generating excited radiotracer atoms in the presence of a thermal environment is making to the field of chemical dynamics. Specific topics discussed critically include characterization of the generation and behavior of excited molecules including fragmentation kinetics and energy transfer, measurement of thermal and hot kinetic parameters, and studies of reaction mechanisms and stereochemistry as a function of reaction energy. Distinctive features that provide unique approaches to dynamical problems are evaluated in detail and the complementarity with more conventional techniques is addressed. Prospects for future applications are also presented.*

The recoil technique of generating excited radiotracer atoms in a thermal environment offers a unique approach to exploring many problems of modern chemical dynamics. From its inception the study of chemistry with recoil radiotracers has expanded rapidly to its current state of providing fundamental information about molecular interactions. Several areas where applications have been demonstrated include excited molecule production and characterization, hot atom and molecular kinetics, thermal bimolecular kinetics of fast reactions, and reaction stereochemistry and mechanisms. In addition, recent results have provided evidence that gas-phase thermal ion chemistry can be studied using this technique. In each case the recoil radiotracer approach has developed into a powerful tool that provides information complementary to and often unavailable via classical kinetic techniques.

Several characteristics specific to recoil radiotracer methods provide significant advantages for dynamical studies. The most obvious is the large range of energies available, which, unlike the usual domain in

0065-2393/81/0197-0123\$05.75/0  
©, 1981 American Chemical Society

thermal kinetics, can include even the highest energies at which reaction cross sections are significant. Indeed, because translational recoil energy often is derived from nuclear sources, excess energy well above the range of normal chemical events must be degraded or moderated before results of chemical interest can be obtained. Nevertheless the two extremes of high-energy neutral atom or molecule processes and low-energy ion interactions that are often inaccessible with standard kinetic procedures are available in recoil studies.

The second principal advantage comes from the nature of radiotracer studies in general. Because the radiation emitted from radioisotopes as they decay can be detected with high sensitivity, ultratrace analysis is easily accomplished. This means that chemical phenomena involving labeled species can be studied essentially at infinite dilution. Thus, particularly in the gas phase, the chemical environment can often be preserved in its initial state during the entire course of the dynamical study and it will depend only on the certainty with which the initial state is known in carefully executed experiments. Finally, the recoil technique provides *in situ* generation of excited reactants in all phases. The uniformity of the distribution of reactant species is a function only of the homogeneity of the chemical sample and the stimulating radiation source, and in general because so few recoil events are initiated, no two nascent radiotracer containing reactants or intermediates interact with one another.

All kinetic techniques have limiting constraints that determine their applicability to specific dynamical problems. Like most nonbeam methods, recoil studies are limited in principle by the fact that the experiment involves a statistical accumulation of collision data rather than a probe of single collision characteristics. Thus direct measurement of cross section data and studies of discrete state-to-state phenomena are not available. Nevertheless, cleverly designed experiments can provide good insight into both of these areas as will be discussed below particularly for regions of phase space normally inaccessible to more refined kinetic techniques.

The other principal constraint derives from the requirement of a radiation source for recoil stimulation. In the case of nuclear recoil this means that a high-energy accelerator or nuclear reactor must be available, often on site if the isotopes generated are short-lived. It should be pointed out, however, that while the cost factor to install such a major facility is prohibitive, the charges for the required routine use at centers where this nuclear equipment already exists can be comparable with other conventional instrumental techniques in physical chemistry.

The effects of radiation on the chemical system being studied must also be considered in experimental design. Undesirable consequences

may result in either radiation damage causing molecular fragmentation or production of unwanted isotopes in the case of nuclear excitation. In general, the former problem can be controlled adequately using molecular scavengers so that radiation chemistry does not macroscopically perturb the system. The interference from concurrently produced isotopic species is most frequently eliminated or minimized either by avoiding source molecules with nucleogenic precursors or by discriminant isotope detection in the analysis of results.

In this review a summary of some of the recent progress in applying recoil radiotracers to three areas of dynamics will be outlined. No attempt has been made to be encyclopedic but rather selected examples have been chosen, often from the author's own work. The areas into which this review is divided are: excited molecule dynamics; kinetic parameter characterization; and reaction mechanisms and stereochemistry.

### *Excited Molecule Dynamics*

It has been well documented that hot atom replacement reactions deposit large amounts of internal energy in primary products (1, 2, 3). In cases where a heavy translationally excited reactant atom carries sizable momentum into a hot reaction, the products may also be generated with large excess kinetic energy. As a consequence of this excitation, the nascent molecules can undergo secondary processes that eventually lead to stable species. The most thoroughly studied secondary process is unimolecular decomposition resulting from excess vibrational and rotational energy. Prospects for studying collisional dissociation and translationally hot, neutral polyatomic reactions are on the horizon and will be commented on at the end of this section.

A systematic study of excited molecule dynamics begins by characterizing the energy deposition and partitioning during hot reactions. The degradation of the energy deposited via collisional transfer or unimolecular reaction provides a second avenue of investigation that is of fundamental importance. Data in several hot reaction systems that undergo unimolecular decomposition have been reported and used to obtain estimates for the average energy deposited. One of the most thoroughly studied systems is excited cyclobutane produced in the hot T-for-H replacement reaction (4, 5, 6).

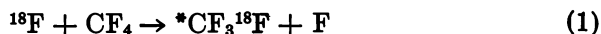
A discussion of recent published results on the cyclobutane reaction illustrates the kind of excited molecule dynamical information available from recoil techniques. The primary assumption in the approach reported is that the RRKM (Rice-Ramsperger-Kassel-Marcus) method for describing statistical energy redistribution and calculating decomposition rate constants is valid. Thus, deviations from expected RRKM behavior

are considered to be symptomatic of nonstatistical intramolecular energy redistribution resulting from either intrinsic molecular properties or intermolecular encounters rather than errors in the RRKM method. The expected behavior of excited molecules is most often compared with experimentally measured yield results to characterize the molecular activation and deactivation processes.

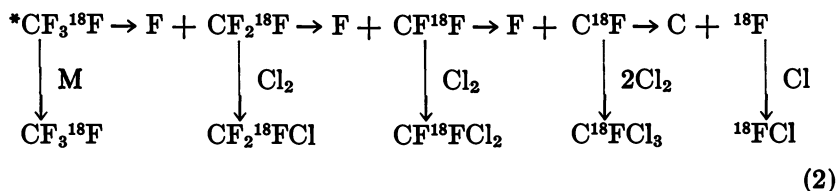
The initial detailed demonstration for this approach was pioneered by Bunker and his co-workers (7,8). The technique was applied to excited cyclobutane (9), and based on the results, methods have been developed to further explore the energetics of excited molecule formation (5) and the degradation of that energy by collisional transfer (6,10). Fortunately, results from independent ion beam studies of T-for-H replacement reactions with selective hydrocarbons are available (11-14), and these data have been used to approximate the required cross sections as a function of energy for hydrogen replacement reactions (15,16). The excitation functions developed in this way are consistent with the general features of trajectory calculations in simple hot reaction systems involving hydrogen atom replacement (17,18,19). With these excitation functions and the hot atom reaction data for cyclobutane in various bath gases, the first refined estimate for a secondary excitation function of a reaction product was published (5) based on the general RRKM approach (9). Thus, the partitioning of total available energy into internal modes of cyclobutane during hot hydrogen replacement reaction was determined over the entire translational energy range for the replacement reaction cross section.

Based on that work (5) it was possible to verify both that the average internal energy deposited in cyclobutane was about 100 kcal/mol and that the molecule exhibited statistical behavior in redistributing energy intramolecularly at least to the highest limits explored of 180 kcal/mol (20). It should also be noted that about 10% of the total energy generated in cyclobutane by recoil reaction appears as rotation. Such partitioning, of course, depends markedly on the mass of the hot atom that initiates reaction as well as the cross-section function, and a much higher rotational contribution can be expected in some recoil chemical activation processes.

Another more direct approach has recently been used to define the excitation function for a reaction product from a recoil reaction (21). Instead of using an RRKM method for a single competitive unimolecular process, the sequential decomposition of excited  $\text{CF}_4$  was studied. The fragments formed were scavenged with  $\text{Cl}_2$  to give direct yield data for each path as indicated below:



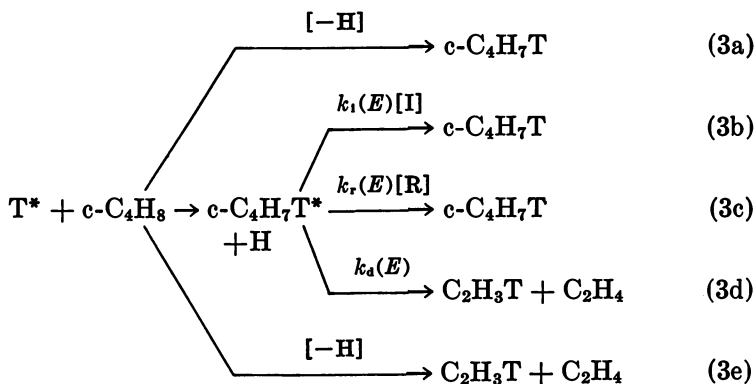




Here M is any component of the reaction mixture that stabilizes vibrationally excited products on one or more collisions. Thermodynamic energy limits for each process were established. Thus, the integral of the  $CF_4$  excitation function could be estimated and used to obtain the initial internal energy distribution of the  $CF_3^{18}F$  formed in Equation 1. The qualitative features of both results (5, 21) are the same, and, as expected, the total energy deposited by hot fluorine atoms (22) is somewhat greater than by hot tritium in these replacement reactions.

Due to the extreme levels of internal energy available, chemically activated molecules produced by kinetic techniques can be used, in principle, to study inter- and intramolecular energy transfer in a region of energy space beyond that normally probed with standard methods. In this capacity, such kinetic chemical activation offers the distinct advantage of being free of the thermochemical constraints on the energy produced that accompany processes dependent on addition or insertion reactions. The controlling factors inherent in reactive stimulation via translational energy are momentum transfer and the efficiency with which a product molecule can distribute energy among its internal degrees of freedom.

Recoil, kinetic chemical activation, as illustrated above, is characterized by dynamical features that dictate a rather broad distribution of energies. In fact, the manifold of energies produced in a typical experiment can be roughly divided into three main regions: (i) molecules with internal energy below that required for unimolecular reaction, that is, the decomposition threshold; (ii) molecules that have enough energy to decompose in the absence of collisions but that can be competitively stabilized by collisional energy transfer in the range of pressures convenient for recoil studies; and (iii) molecules with extreme internal energy, which decompose on a time scale that is fast compared with collision times even at the highest pressures explored in the experiment. This latter case may include processes that are direct in nature since all reaction channels that give the same product but are independent of pressure are classified together. A representation for the chemical activation of cyclobutane and its use in studies of energy transfer is shown in Equation 3.



Here I represents a reactively inert diluent, R is reactant cyclobutane,  $k_i$  and  $k_r$  are bimolecular rate constants for energy transfer, and  $k_d$  is the rate constant for unimolecular decomposition. This particular system exhibits a relatively straightforward chemistry giving ethylene as the only decomposition product of excited cyclobutane.

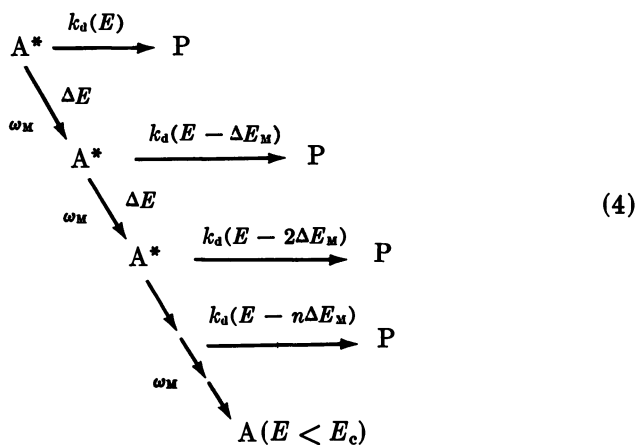
The energy transfer information that can be obtained from recoil activation processes like those in Equation 3 depends on the level of sophistication used to represent the system quantitatively. The simplest approach provides relative average rate constants  $k_i$  for various diluents, I, and is based on an algebraic analysis in which the energy-dependent rate constants  $k_i(E)$ ,  $k_r(E)$  and  $k_d(E)$  are replaced with average values over the competitive stabilization-decomposition energy range. Using the pressure dependence at fixed composition and the concentration dependence at fixed pressure for two component systems, ratios for  $k_i/k_r$  and, hence, the relative energy transfer efficiencies have been obtained for several monatomic, diatomic, and polyatomic colliders (10, 23, 24).

In this approach, processes represented in Equations 3a and 3e were identified by curve fitting a three-parameter equation to the pressure dependence over the range from a few Torr to 2 atm in several systems independently. The composition dependence for the competitive yields in Equations 3b, 3c, and 3d at a fixed pressure of 800 Torr were then determined experimentally by subtracting the noncompetitive contributions from the raw data. Extrapolation of the refined data to pure reactant and infinite dilution with bath gas provides intercepts whose ratio gives the desired relative rate constants. Correction for reduced mass and molecular size then provides relative energy transfer efficiencies on an equal collision basis.

An assumption of the method is that the average internal excitation energies for the pure and diluted recoil systems are approximately the same. One-dimensional recoil trajectory calculations in the energy coordinate for translational cooling of hot hydrogen atoms have focused on this

issue and verify that only minor changes in the average energy for reaction are evident for highly moderated or diluted cases compared with pure reactant if the reactive process has a threshold significantly above the thermal collision energy region (25). This condition is satisfied for the hydrogen replacement reaction in cyclobutane used in the above test case, and thus it is likely that the internal energy distribution for product molecules is also reasonably constant for the systems studied.

A more carefully constructed approach to energy transfer explicitly accounts for the energy distribution of the chemically activated product (5, 6, 26, 27). The initial distribution of energies upon production as well as the transient distributions formed by collisional relaxation of internal energy are used to calculate rate constants for unimolecular reaction. The formalism of Bunker (7, 8, 9) based on general RRKM theory is convenient for recoil chemical activation, since it explicitly accounts for both rotational and vibrational excitation in the product. In the cyclobutane model system reported, a stepladder approach to deactivation was incorporated, with the step size being a parameter determined by the best fit to the data (6). The overall processes considered are illustrated in Equation 4.



In Equation 4,  $\Delta E_M$  is the average internal energy transferred from excited species  $A^*$  upon collision with M, which may be either nonreactive bath gas or reactant molecules, and  $k_d(E')$  is the RRKM rate constant for unimolecular decomposition calculated at each energy  $E'$ . Eventually after successive energy degrading collisions without unimolecular decomposition the excited molecule may be stabilized to an energy level below the critical decomposition threshold  $E_c$ .

The ratios of total yields of stabilization to decomposition products are determined in this approach over a pressure range from several Torr

to 2 atm, and a best-fit curve is used to determine  $\Delta E$  for the bath gas used. Since the low-pressure data are the most sensitive to the specific selection for the average quanta of energy transferred on collision, they must be obtained with good precision. It should be noted that the procedure specifically treats the full range of the excited-molecule energy distribution and thus only one experimental variable is required, that is, in the case cited, the pressure at fixed composition. Those molecules created with energies below  $E_c$  are placed directly in the stabilized category, whereas cases with noncompetitively high energies have decomposition rate constants much faster than the average time interval between collisions even at 2 atm and thus react. Rate constants calculated for levels of excitation in excess of 7 eV probably represent lower limits, depending on the efficiency for intramolecular relaxation. Errors associated with this approximation, however, are thought to be minor, because the contributions to the initial energy distribution from this energy range are relatively small and the results do not show any systematic deviation from that expected for statistical RRKM behavior. For cyclobutane as the energy transfer agent, precision in the average quanta of energy transferred has been reported as high as  $\pm 1.0$  kcal/mol per collision (6).

Results of the treatment confirm that strong colliders like parent cyclobutane can transfer on the order of 10 kcal/mol per collision and that even monatomic weak colliders can transfer up to 3 or 4 kcal/mol on collision if they have sufficient mass. A combined tabulation of results to date on absolute quanta of internal energy transferred from excited cyclobutane to various bath gases is given in Table I (6, 10).

Further developments in the use of kinetic chemical activation for energy transfer studies will undoubtedly be based on more detailed attention to the energy dependence of the transition probabilities and more accurately defined initial product excitation functions. Each extension will require that the unimolecular decomposition rate constant be calculated or measured as a function of energy. In cases where adequate

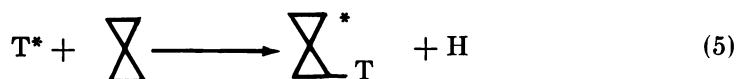
**Table I. Average Step Sizes for Collisional Energy Transfer from Vibrationally Excited Cyclobutane Generated by Recoil Kinetic Chemical Activation**

<i>Bath Gas</i>	$\Delta E$ (kcal/Collision)
c-C <sub>4</sub> H <sub>8</sub>	10.0 $\pm$ 2.0
CF <sub>4</sub>	10.0 $\pm$ 2.0
CO <sub>2</sub>	5.0 $\pm$ 1.0
N <sub>2</sub>	2.5 $\pm$ 1.0
Xe	4.0 $\pm$ 1.0
Kr	3.0 $\pm$ 1.0
Ar	2.5 $\pm$ 1.0
Ne	2.4 $\pm$ 1.0
He	0.5 $\pm$ 0.5

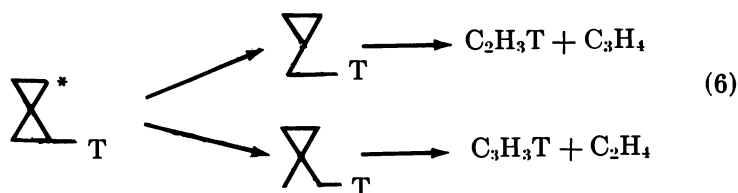
spectroscopic data is available and where statistical energy randomization prevails, the RRKM method for calculation of the rate constant is sufficiently good to provide reliable energy transfer results.

Another area in which chemical activation by recoil kinetic techniques has provided a useful tool is in the search for and study of nonstatistical intramolecular energy transfer in excited molecules. Since very high levels of internal excitation are generated in localized reaction sites, one might expect this method of activation to provide a good test for the efficiency of energy randomization in a wide variety of molecules. In fact, the type of recoil hot reactant atom used will determine both the time scale during which the energy is deposited and the degree to which the reaction site is isolated during the activation process. This provides a rather broad range of conditions from the fast localized hydrogen replacement reactions to the slow, disruptive halogen atom reactions that may deposit 10–15 eV of energy. One good example on the use of recoil activation to explore nonstatistical behavior in molecules is the study of spiro-pentane decomposition following recoil tritium replacement reaction (28). The particular symmetry of this molecule and the unimolecular behavior that provides a distinction between the resultant tritium-labeled ring and the unlabeled ring are notable.

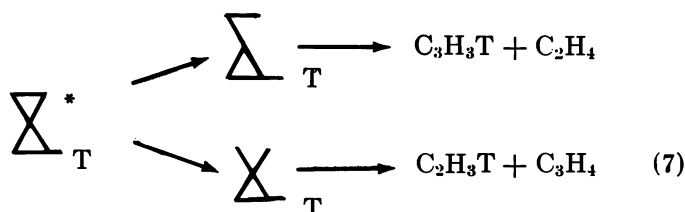
The overall reaction scheme for hydrogen replacement by hot tritium atoms in spiro-pentane is illustrated in Equations 5, 6, and 7.



Scission of adjacent ring:



Scission of opposite ring:



All replacement sites are equivalent in Equation 5, but once replacement has occurred, the ring adjacent to the reaction site, which is labeled with tritium, can be distinguished from the other ring, which is unlabeled. Unimolecular decomposition of the adjacent ring does not require extensive energy migration from the reaction site, whereas decomposition of the ring opposite the site of labeling does. Both rings decompose via the same mechanisms as illustrated in Equations 6 and 7, but the labeled products distinguish which ring contributes to each process. Thus, ratios of labeled products corrected for isotope effects in the decomposition can be used as an indication of energy randomization between the two distinct ring systems.

The results reported give a direct measurement of the extent of energy randomization as a function of pressure. In these experiments the average energy content of the excited spiropentane that decomposes is greater at higher pressures because stabilizing collisions effectively compete with slower, lower-energy processes. Thus, pressure variation tends to sample the energy distribution inherent in recoil activation. At pressures in excess of 1000 Torr a noticeable deviation from random redistribution of the energy deposited was observed, although quantitative assignment of the time scale for intramolecular energy redistribution was not possible for this recoil system (28). This result confirms the conclusion reached for conventional chemical activate in alternate bicyclopropane molecules (29–31) that, indeed, highly specialized configurations can inhibit efficient communication of vibrational energy among adjacent bonds in a molecule, although even in these cases the deviations from randomization are relatively small.

Finally, the prospects for studies of translationally excited polyatomic molecules should be mentioned. In this case, a region of energy-state selection of reactants that is not accessible to conventional techniques can be studied. The preparation of translationally excited neutral molecules with energies well in excess of those found for controlled thermal experiments results from momentum conservation in hot atom reactions. Particularly useful are heavy hot atoms that exhibit significant high-energy cross sections for replacement or abstraction reactions. Recoil halogen atoms such as  $^{34}\text{Cl}$ ,  $^{38}\text{Cl}$ ,  $^{39}\text{Cl}$ , and  $^{18}\text{F}$  appear to be best suited for such studies and, in addition, are easily generated via nuclear processes.

Two important areas of collision dynamics can be addressed via recoil methods and should receive increased attention in the future. The first is collisional dissociation of translationally hot molecules. Indirect evidence for the importance of this process has been obtained in hot atom reaction studies of the recoil Cl atom reaction with  $\text{CH}_4$  and  $\text{H}_2$ . A consistent kinetic theory interpretation for the production of the replacement reaction product,  $\text{CH}_3\text{Cl}$ , in the first case indicated that a

collisional decomposition process accounts for the depletion of observable product, and, as expected, the efficiency for dissociation was dependent on the molecular properties of the bath gas (32). In the recoil chlorine atom reaction with molecular hydrogen, the initial momentum carried into the process is expected to have an even more pronounced effect on the levels of excitation of the HCl product, in all likelihood leading to translational energies of up to 10 or 20 eV. While no detailed study of the secondary decomposition of this product has been reported to date, the results of a study of hydrogen isotope effects indicate that collisional dissociation of excited product undoubtedly contributes to the overall reaction process (33, 34).

The second area projected for future studies involves hot molecule reactions. The recoil technique provides a unique approach to generating translationally excited neutral molecules. Other methods are limited in range to thermal velocities either of the reactant directly or of a seeded beam. In general, the highest energies achievable are 5–6 eV for very specific nozzle beam systems. This is still modest compared with the full energy range expected for typical reaction cross sections and is limited to vibrationally and rotationally cold reactants characteristic of expansion methods. To date, the only report on the direct use of a translationally excited recoil reaction product as a secondary reactant involves hydrogen halide addition to ethylene (35). In this case a recoil chlorine atom was first allowed to react with hydrogen or hydrogen chloride to produce hot HCl. It is expected that in addition to translational excitation the hydrogen chloride generated in this way is formed with excess rotational and vibrational energy that may contribute to its reactivity. The hot HCl was formed in a bath of ethylene that served as a second reactant, and the addition reaction producing ethyl chloride was reported. A direct four-center addition was postulated to occur due to the extra energy carried into the reaction by the HCl (35). Four-center addition of this type is not observed thermally, presumably due to the high activation barrier although it does represent the microscopic reverse of 1,2-elimination from excited alkyl halides observed in unimolecular reaction studies. More work on the study of such thermally forbidden reactions should be carried out in the future using recoil reactions as unique sources of exceptionally hot diatomic and polyatomic neutral molecules.

### ***Kinetic Parameter Characterization***

Recoil reactions present a highly specialized approach to certain kinetic problems that are of both fundamental and practical interest. The broad distribution of energies available provides access to both high energy and to thermal kinetic parameters. The ultratrace nature of the

technique also permits studies of very reactive species involved in fast kinetic processes. Insofar as recoil studies bridge the area between conventional kinetics and exotic chemical processes, a broad overview of much of the unexplored domain of physically reasonable but unusual laboratory environments can also be obtained. Of particular importance are processes associated with uncontrolled chemical phenomena such as detonations and explosions and with advance energy technologies including fusion and solar furnaces.

To date, the types of kinetic processes characterized via recoil techniques have largely been reactive bimolecular events involving a hot or thermal atomic species as one reactant. As mentioned earlier in this chapter, secondary processes involving polyatomics can be investigated in certain cases, but the fact that the nuclear recoil and photochemical recoil methods almost always generate excited atomic species makes atom reactions most easily studied. With the range of energies available in recoil studies, the entire cross section for most reactions can be explored, but the experimental data are most often obtained in the form of integral properties of the cross section. In principle, if the initial reaction energy can be varied, as with photochemical recoil but not generally with nuclear recoil, the integral data can be deconvoluted to yield estimates for primary cross-section function for specific reactions, and indeed this may provide the only route to these properties at higher energies than those available with beam techniques.

Two types of experiments designed to explore the cross section for specific chemical reactions can be cited. Both involve photochemical recoil processes in which atomic emission line sources of light in the ultraviolet and vacuum ultraviolet region are used to photodissociate a diatomic hydrogen halide molecule. The methods consist of varying the incident light energy in excess of that needed to induce photodissociation. As a result, the fragments recoil from one another with the excess energy manifest as translation or electronic excitation to low-lying levels of the resultant atoms. The total range of translational energies available is limited both by the available light sources and by the characteristics of the absorbing molecule. In general, therefore, the applications have been limited to the reaction threshold region.

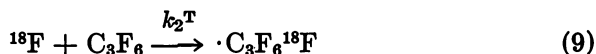
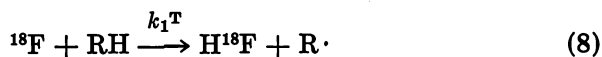
The first successful application of cross-section mapping was reported over a decade ago for the hydrogen abstraction reaction from butane (36-38). Since that time little further work of this type has been reported, undoubtedly due to the imprecision of the deconvolution technique required and the difficulty of identifying appropriate low-energy reactions that are chemically clean. Much more successful has been the determination of apparent translational energy thresholds for reactions. This has been particularly true for high-energy processes like direct substitu-



tion reactions that are not observed thermally. Since this type of experiment requires only extrapolation to the minimum recoil energy at which a particular product is observed, the result is obtained directly with accuracy and precision equal to that with which the initial recoil energies are known. A recent example of this type of application is the report of the thresholds for tritium for hydrogen and tritium for fluorine substitution reactions in fluoroform (39).

The second major area in which recoil techniques have provided a valuable new kinetic tool is the measurement of rate constants for thermal abstraction reactions by fluorine atoms (40, 41). Basically, the experimental method involves the generation of atomic reactant species via a nuclear recoil process in the presence of a second molecular reactant and an excess of nonreactive moderator gas. At sufficiently high dilution with moderator, the nascent recoil atom has ample opportunity to lose excess energy via collision before a reactive encounter can occur. Thus, it reaches the thermal energy regime where it may react with any species having an excitation function with a thermal or near-thermal threshold. It is important to note that this technique, which depends on nonreactive collisional moderation of the hot species excess energy before reaction, appears to be relatively ineffective at lowering the average energy for truly hot reactions (25). In this case the increase in the number of lower-energy encounters is compensated for by the decrease in reactant concentration, which limits reaction. In addition, as the reactant atom approaches thermal energies, scavenging reactions compete effectively in a practical, well-controlled experiment.

The successful use of this technique for thermal reactions is based on the measurement of the product yields for competitive processes under identical conditions over the same time interval (40, 41). Equations 8 and 9 illustrate the type of reactions reported for recoil fluorine.



Kinetic analysis of the thermal contribution to the yield of abstraction product gives a linear relationship between the inverse of the abstraction yield and the inverse of the relative concentration of reactant RH with a slope equal to  $k_2^{\text{T}}/k_1^{\text{T}}$ .

Rate constants for a large number of hydrogen abstraction reactions by fluorine atoms determined in this way compare favorably with those reported earlier (40, 41). In these cases, 90–99.95%  $\text{C}_2\text{F}_6$  diluent gas was used to moderate the kinetic energy of the recoil fluorine, and a

scaled ratio for  $k_2/k_1$  based on a previously determined rate constant for fluorine addition to perfluoropropene was used. The success of this method for studying thermal fluorine abstraction reactions and the enormous advantage inherent in the use of radiochemistry as the prime analytical tool has prompted further investigation into the generality of recoil techniques in determining thermal rate constants (42). Because the experiment is carried out at the ultratrace reactant level and the time scale is determined only by the rate for the competitive thermal process used, it is particularly well suited for the study of fast atomic reactions in difficult chemical systems.

Modeling of the recoil process provides a detailed rationale for the success of this important new approach to thermal kinetics. Initial work was designed to explore both the conditions under which best results might be obtained and the limitations anticipated as applications are broadened (42). Calculated results based on earlier methods for determining recoil reaction yields (25) and parameterized forms for cross-section functions (15, 16) were used for this analysis. The cross sections used, while not precisely valid for real chemical systems, were approximated representations for hydrogen atom abstraction and addition reac-

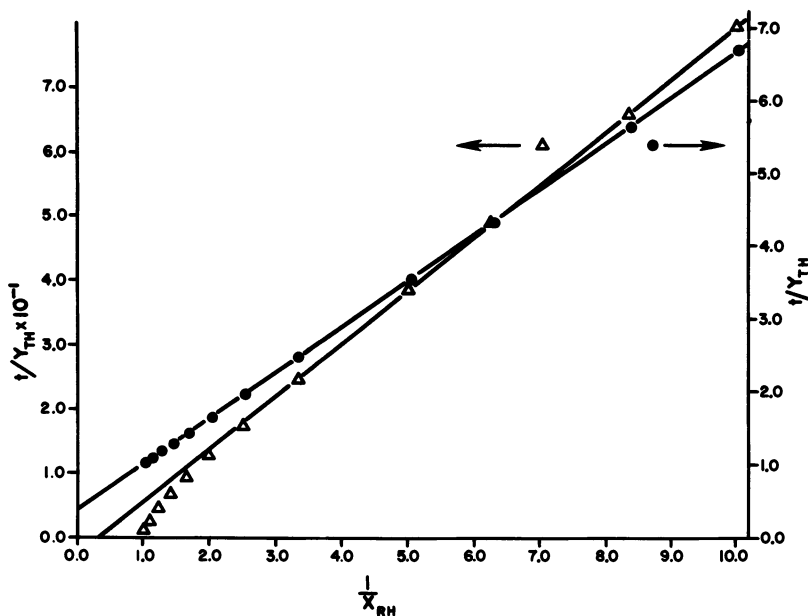


Figure 1. Calculated kinetic behavior of the yield for abstraction product HT from ( $\Delta$ )  $c\text{-C}_6\text{H}_{12}$  (Case I) and ( $\bullet$ )  $\text{CH}_3\text{SH}$  (Case III) as a function of reactant concentration at 95% moderation with Ne.  $\text{C}_2\text{H}_4$  was used as the competing thermal reactant. The kinetic model is reported in References 40, 41.

**Table II. Calculated Results for Thermal Rate Constant Ratios Determined by the Moderated Nuclear Recoil Method in Model Systems**

Case <sup>a</sup>	$k_2/k_1^b$ (Recoil)	$k_2/k_1^c$ (Cross Section)
I	8.2	18.6
II	1.8	2.1
III	0.63	0.64

<sup>a</sup> All model systems were based on  $k_2 = 5.24 \times 10^8$  L/mol · s, an approximate rate for hydrogen addition to ethylene at 25°C. Cases I, II, and III approximately represent *c*-C<sub>6</sub>H<sub>12</sub>, H<sub>2</sub>S, and CH<sub>3</sub>SH reactants.

<sup>b</sup> Determined from the slope of the linear part of the kinetic plot for simulated recoil data.

<sup>c</sup> Calculated from the respective cross sections and the Boltzmann distribution at 25°C.

tions with hydrocarbons. Of particular importance is the fact that the same cross sections used to calculate recoil yields were used to calculate thermal rate constants from the integral of the overlap with the Boltzmann distribution. Thus, the results are internally consistent and as such provide an adequate representation of characteristic features.

Three specific cases were investigated initially in an attempt to understand the conditions under which the higher-energy contributions to cross sections for thermal reactions were negligible. The very nature of recoil experiments guarantees that the reactant atom samples the entire energy range. The conditions tested were cases in which the ratio  $k_2/k_1$  was greater than, nearly equal to, and less than unity. In this calculation the addition reaction of hydrogen atoms with ethylene was used as the standard for  $k_2$ , and the other reactants studied had thermal abstraction rate constants similar to *c*-C<sub>6</sub>H<sub>12</sub>, H<sub>2</sub>S, and CH<sub>3</sub>SH, respectively. All recoil simulations were maintained at 95% dilution with Ne, so that the sum of the abstraction and addition reactant concentrations was equal to 5%.

The characteristics of these curves are shown in Figure 1. The immediate observation from the results of these calculations is that there is significant deviation from linearity in the kinetic relationship between the inverse abstraction yield and the inverse of the relative concentration of reactant for cases in which  $k_2/k_1 \geq 1$ . The curvature is most apparent at high relative concentration of the reactant in Equation 8. In each case an approximately linear region exists for concentrations of RH less than 2%, but the slope provides a reasonable value for the rate constant ratio only when  $k_2/k_1 < 1$ , that is, for very fast abstraction reactions compared with addition. For this combination of reactants the entire concentration curve was also nearly linear. Results from these calculations are shown in Table II.

It is evident from these results that the best data are obtained for cases in which the standard competitive reaction, here addition, is slower than the reaction of interest. To gain insight into why this is observed, the absolute yields from the recoil reactions were studied in each case. Differentiation was made between the yields of truly thermal reactions and yields from processes occurring in the recoil cascade before the average thermal Boltzmann energy was reached. Results at 1% reactant concentration for Cases I and II showed 51% and 13% contributions respectively from hot processes to the overall abstraction yield. By comparison Case III gave only a 6% contribution. Undoubtedly this result reflects the small yields of truly thermal abstraction product in systems where there is an unfavorable competition with the addition reaction. In these studies the thermal contributions to the total yield for abstraction were 1.2%, 10%, and 26%, respectively, for Cases I, II, and III, with the largest part of the remaining yield appearing as the addition product. Since the kinetic approach outlined for the moderated nuclear recoil method is critically dependent on the yield of the product from the thermal reaction of interest, it appears that the truly thermal contribution to this yield must be sizable enough to compensate for any added small hot component if accurate constants are to be obtained.

The results derived from these calculations confirm the importance of this technique for use in thermal kinetics, while at the same time further clarifying its range of applicability. The following general conclusions are summarized as a basis for further experimental and theoretical investigation into the generality of the method.

1. The moderated nuclear recoil procedure for measuring thermal rate constants gives best results when the standard reaction against which the unknown is measured has a rate constant smaller than the unknown, that is,  $k_2/k_1 < 1$ . This minimizes the importance of any hot contribution to the total yield from the unknown reaction.
2. Linearity in the yield plots at high relative mole fraction unknown appears to be a much better indicator of the validity for a specific system than linearity in other regions.

These constraints should not be interpreted as limiting the potential applicability of this important new method. In practice, these results suggest that an appropriate standard thermal reaction is most important in generating accurate thermal rate constants.

Kinetic descriptions of high energy recoil reactions have also been developed. While the results obtained are not directly relevant to conventional thermal kinetics, they do provide considerable insight into high-energy collision dynamics. The recoil process itself consists of an irreversible dispersion of energy via elastic and inelastic collisions, and

as a result the parameters obtainable often represent integral values over a rather broad energy range. The clear advantage of the technique for dynamical studies is that it can frequently be used to explore the full range of energies over which reactive cross sections exist. Thus, more information about reactive collisions can be obtained than is available from thermal methods that are confined to the energy threshold region for reactions. Unfortunately, the recoil process is rather exotic in that it is specific to the atom or fragment generated. This means that descriptive hot kinetic parameters are portable only for the class of reactions involving the same recoil reactant atom.

Rather than review the development of hot atom kinetic theory here, the reader is directed to several recent approaches and the references therein (43–48). While there continues to be debate over the initial relaxation of the hot atom velocity distribution and the conditions under which a Maxwell–Boltzmann-like temperature profile for reaction can be established, the general dynamical features of at least one very important high energy reaction,  $F^* + H_2 \rightarrow HF + H$ , have been described consistent with experimental results.

### *Reaction Mechanisms and Stereochemistry*

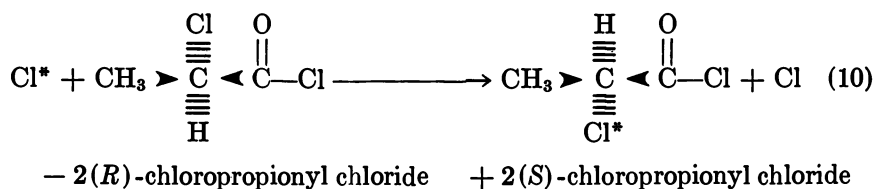
The use of recoil-generated radiotracers in studies of reaction mechanisms and stereochemistry has been extensive both for inorganic and organic systems. Much of the effort has involved energetic atoms and reactive intermediates in all phases of matter. The contributions from this technique are well recognized for carbon and silicon systems as well as for several inorganic crystalline materials. Instead of reviewing that work here, two emerging areas of investigation will be emphasized: stereochemical studies, particularly in halocarbon systems; and isolated carbonium ion reactions.

Important contributions to each of these areas are possible due to specific features of the nuclear recoil technique. Truly isolated molecules are formed and can be studied efficiently because they are labeled with radioactive nuclides. In addition, extra energy available from recoil can be degraded or used effectively for chemical purposes, thus contributing a dynamic species in a stationary relative environment.

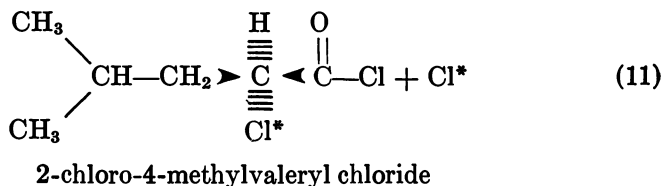
Early interest in stereochemistry of recoil reactions focused on developing a model for hot processes. The conventional view was that such reactions were direct in nature in the gas phase, occurring on a time scale that promoted retention of configuration. In condensed phases the picture was complicated by the expectation that the local environment caged fragments generated in the recoil process, and thus the stereochemical outcome of the reaction was either random or dependent on specific features of the nearest neighbors.

More recent efforts have been directed toward carefully designed tests of structural and environmental influences on the stereochemical course of hot reactions and also toward isolated thermal atom reactions. Much of the work in this area has involved recoil halogen atom reactions, particularly chlorine, because they are characterized by simple addition and replacement processes that occur with sizable momentum transfer on a relatively slow time scale, even at higher energies.

The most careful study to date of the stereochemistry of high-energy substitution reactions involving a heavy recoil atom characterized the chlorine-for-chlorine replacement reactions in 2-chloropropionyl chloride and 2-chloro-4-methylvaleryl chloride (49). Definitive evidence for a predominance of inversion of the chiral center in the 2(*S*) and 2(*R*)-chloropropionyl chlorides during reaction in the gas phase was obtained as illustrated in Equation 10.



This represents the first case in which a direct hot atom reaction has been unambiguously observed to give inversion of configuration. The consequences of steric inhibition were tested with the hindered 2-chloro-4-methylvaleryl chloride (Equation 11). Results indicated net gas-phase



retention, suggesting that the reactant geometry plays a major role in directing the stereochemistry even for highly disruptive hot chlorine atom reactions. Condensed phase studies of the same reactions show racemization probably via radical-radical recombination within the nearest neighbor cage.

The influence of solvent molecules on the stereochemical course of hot substitution reactions in the condensed phase has also been studied in some detail. Of particular interest is whether there is a significant directing effect on the course of these cagelike reactions due to structural features or electronic interactions between solvent molecules and reaction intermediates. A careful study of the chlorine substitution reaction in

diastereomeric 2,4-dichloropentane and 2,3-dichlorobutane carried out in thirty solvents has been reported (50). Results indicated the major factor that correlates with the stereochemical course of reaction is the dielectric property of the solvent. Thus, the retention to inversion ratio for these reactions appears to be determined primarily by the intermolecular forces between reactant and the solvent cage. The molecular size of the solvent was also identified as having a minor influence in this study. The specific role of the solvent is undoubtedly complex in that several concurrent processes may be involved for any one system. The issue of direct excited product formation vs. radical-radical recombination continues to be of interest in stereochemical studies (51). Participation of the solvent in competing reactions has also been suggested (52). Finally the possibility that unusual mixing or aggregation of reactant in solvent plays a significant role, particularly for cases where large polarity differences exist, must be considered (53, 54). For cases of this type the composition of the nearest neighbor cage may not specifically be related to the bulk concentration of the condensed phase, and, thus, product formation may be critically dependent on microscopic properties of a localized domain.

The stereochemistry of certain thermal reactions involving atom addition processes and resultant radical intermediates can also be studied conveniently by recoil techniques. In this type of experiment the recoil atom used to initiate the process must be thermalized before reaction, by diluting the system with a large concentration of nonreactive bath molecules. Two recently reported results on geometric isomerization serve as examples of the type of processes that can be studied (55, 56). Both involve recoil chlorine atom reactions with unsaturated substrates.

The first example reports the addition-elimination reaction of thermal chlorine atoms with 2,3-dichlorohexafluoro-2-butene (55). The overall process formally produces a substitution reaction at chlorine, although the energetics indicate that an intermediate formed by chlorine addition is involved. Results show the products converge to a trans/cis ratio of 1.3 starting with either of the two pure isomers as reactants. This suggests that a radical adduct is formed with free rotation prior to the chlorine elimination step that reestablishes the olefin. The study of such vinylic substitution reactions has received recent attention, particularly for cases of ionic nucleophilic attack at the site of unsaturation (57). In these systems, substituent-directing effects via hyperconjugation are postulated to determine the course of geometrical isomerism following addition, based on molecular orbital considerations.

For ion systems, retention is the predominant mode for reaction. This is to be compared with the few reports of atom attack in neutral systems like that reported here where barriers for rotation are expected to be lower and convergence is more common. The fluorinated olefin

considered in the above example has been studied via conventional physical organic methods for anionic addition, with the result that a tendency toward isomerization was observed under specific conditions (58). This result has been attributed to the availability of a good leaving group for displacement and supports the observation made previously for atom attack. It is interesting to note that, in the recoil studies, as the translational energy of the hot chlorine atom is increased above the normal thermal region, the stereospecificity of the replacement process increases (55). While there are no similar cases studied via more conventional techniques with which to make comparisons, it is most likely that a new reaction path involving direct replacement rather than a radical intermediate becomes effective at higher energies and is responsible for the change in stereochemistry of the overall process. The point to be made here, however, is that the recoil technique provides a route to study such thermal stereochemistry for isolated neutral reactions without the side effects of macroscopic changes in the chemical system.

A second very interesting stereochemical result has been reported for an unsaturated halohydrocarbon (56). The thermal reaction of chlorine atoms with propyne is reported to be a highly efficient process that gives predominantly the 1-chloropropenyl radical. When this radical is stabilized by abstraction of hydrogen from HI, the *cis* isomer of the 1-chloropropene is formed with very high selectivity. Although this particular result is not yet fully understood, it does once again show that the recoil technique provides a clean route to interesting stereochemistry of importance in mechanistic physical organic chemical research.

The final area to be discussed here involves the study of thermal ion reactions by recoil methods. This represents one of the newest applications reported and potentially one of the most exciting. Studies to date are unique in that they incorporate a combination of radiochemical detection that allows investigation of submicroscopic ion concentrations and recoil energetics that often ensures escape from solvation. Thus, isolated ions can be studied in the liquid phase without the complications of ion pairing or solvation, and truly thermal processes involving gas phase ions that are difficult at best to observe in chemical accelerators due to space change limits can be investigated.

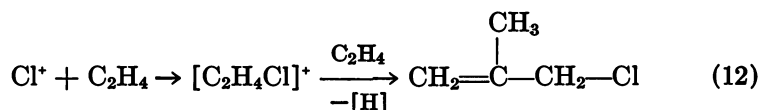
Recent work indicates that free carbonium ions can be generated via  $\beta$  decay of tritiated alkanes (59, 60, 61). The time scale for  $\beta$ -particle emission and the recoil range of the energetic electron ensures that the ion produced is isolated with respect to reorientation of its surroundings and any resultant solvation. Furthermore, the fact that carbocations often react with a rate approaching the collision frequency even in the liquid phase determines that the unsolvated ions indeed survive to react unaf-



ected by geometric or energetic constraints from an oriented solvent cage. The ability to separate real ion reactivities from solvent effects is unique to this method and gives new information on important ion processes in solution. To date, aromatic substitution in the liquid phase of methyl cations in benzene and toluene (59, 60) and the production and reaction of gas-phase four-carbon cyclic ions (61) have been reported. This new method of studying ions shows good promise for further exploration of common organic solution chemistry.

Equally important is the prospect just now being realized that ions can be trapped directly from atomic nuclear recoil sources under appropriate chemical circumstances (62, 63, 64). In general, the high energies associated with nuclear recoil promote initial ionization of the atom generated, but through a series of energy-degrading and charge-transfer collisions with the medium the hot atom eventually reaches the energy range of chemical reactivity as a neutral atom. Only in cases where the initial recoil energy is insufficient to ensure charge transfer before reaction have ionic contributions to recoil reactions been previously reported (65, 66). The most thoroughly studied hot process of this type involves recoil iodine atoms and ions produced via thermal neutron reactions. The chemistry of these iodine systems is exceedingly complex, in part due to the fact that a variety of electronic ground and excited states of both neutrals and ions are involved in the reactions observed.

More tractable chemical systems result with trapped recoil chlorine (62, 63) and fluorine ions (64). The high recoil energies, particularly for fluorine, ensure neutralization on successive cooling collisions unless the medium inhibits it. This interference is expected to occur only when the components of the reaction medium exhibit exceptionally high ionization potentials. In the case of recoil chlorine this apparently is manifest in systems having large concentrations of SF<sub>6</sub> (62). This result is suggested by experiments in which recoil chlorine atoms were generated in the presence of 2% ethylene reactant, iodine at its ambient temperature vapor pressure, and varying mole fractions of SF<sub>6</sub> and CF<sub>3</sub>Cl. At high freon concentrations the normal low-energy chlorine atom reactions were observed (67). At equimolar mixtures of diluents small yields of a new branched, unsaturated, four-carbon ethylene coupling product is observed. This product, 2-methyl 3-chloropropene, grows significantly until it represents a major yield in pure SF<sub>6</sub>. The following ionic mechanism is postulated:



In Equation 12 the ionic intermediate is unspecified as to structure since it is not possible to distinguish in this experiment between a cyclic or open adduct. This chemistry, however, is thought to be identical to conventional thermal ion chemistry and raises the prospect that thermal carbonium ion intermediates can be generated and studied in this way at high dilution and very low energy in the gas phase. This exciting result provides a welcome new method complementary to ion cyclotron resonance and ion beam techniques.

The potential of recoil systems for studies of conventional organic ion chemistry has just been touched upon. New information of considerable interest but unavailable in other ways apparently can be obtained via this technique. This prospect provides a significant challenge for future work as the use of recoil methods expands even further and provides new solutions to traditional problems in chemistry.

### *Acknowledgment*

Major contributions to the work reported from the author's laboratory by Drs. N. Nogar and D. Stevens, and Messrs. L. Ferro and J. Chang are acknowledged. This work was supported by the U.S. Department of Energy under Grant #DE-ACO2-76ER02190.

### *Literature Cited*

1. Parks, N. J.; Krohn, K. A.; Root, J. W. *J. Chem. Phys.* **1971**, *55*, 2690.
2. *Ibid.*, 5771, 5785.
3. Rowland, F. S. *Phys. Chem., Ser. One* **1972**, *9*, 109.
4. Lee, E. K. C.; Rowland, F. S. *J. Am. Chem. Soc.* **1963**, *85*, 897.
5. Ferro, L. J.; Spicer, L. D. *J. Chem. Phys.* **1978**, *69*, 4335.
6. Callahan, M. B.; Spicer, L. D. *J. Phys. Chem.* **1979**, *83*, 1013.
7. Bunker, D. L. *J. Chem. Phys.* **1972**, *57*, 332.
8. The computer program developed for R.R.K.M. treatment of recoil hot reaction products is available from QCPE, Indiana University, Program No. 234.
9. Chou, C. C.; Hase, W. L. *J. Phys. Chem.* **1974**, *78*, 2309.
10. Nogar, N.; Spicer, L. D. *J. Chem. Phys.* **1977**, *66*, 3624.
11. Menzinger, M.; Wolfgang, R. *J. Chem. Phys.* **1969**, *50*, 2991.
12. Menzinger, M.; LeRoy, R. L.; Yench, A. J. *J. Phys. Chem.* **1972**, *76*, 2937.
13. Beatty, J. W.; Wexler, S. *J. Phys. Chem.* **1971**, *75*, 2417.
14. Wexler, S. *J. Phys. Chem.* **1972**, *76*, 2939.
15. LeRoy, R. L. *J. Phys. Chem.* **1969**, *73*, 4338.
16. LeRoy, R. L.; Yench, A. J.; Menzinger, M.; Wolfgang, R. *J. Chem. Phys.* **1973**, *58*, 1741.
17. Karplus, M.; Porter, R. N.; Sharma, R. D. *J. Chem. Phys.* **1966**, *45*, 3871.
18. Valencich, T.; Bunker, D. L. *Chem. Phys. Lett.* **1973**, *20*, 50.
19. Valencich, T.; Bunker, D. L. *J. Chem. Phys.* **1974**, *61*, 21.
20. Callahan, M. B.; Spicer, L. D., unpublished data.
21. Knierim, K. D.; Mathis, C. A.; Gurvis, R.; Root, J. W., unpublished data.
22. Manning, R. G.; Root, J. W., Chap. 5 in this book.
23. Nogar, N. S.; Spicer, L. D. *J. Phys. Chem.* **1976**, *80*, 1736.
24. Nogar, N. S.; Dewey, J. K.; Spicer, L. D. *Chem. Phys. Lett.* **1975**, *34*, 98.

25. Spicer, L. D. *J. Chem. Soc., Faraday II* 1978, 74, 527.
26. Robinson, P. J.; Holbrook, K. A. "Unimolecular Reactions"; Wiley-Interscience: New York, 1972.
27. Forst, W. "Theory of Unimolecular Reactions"; Academic: New York, 1973.
28. Tang, Y.-N.; Su, Y. Y. *J. Chem. Phys.* 1972, 57, 4048.
29. Rynbrandt, J. D.; Rabinovitch, B. S. *J. Phys. Chem.* 1970, 74, 4175.
30. *Ibid.*, 1971, 75, 2164.
31. Rynbrandt, J. D.; Rabinovitch, B. S. *J. Chem. Phys.* 1971, 54, 2275.
32. Spicer, L. D.; Wolfgang, R. *J. Chem. Phys.* 1969, 50, 3466.
33. Stevens, D. J.; Spicer, L. D. *J. Phys. Chem.* 1978, 82, 627.
34. Stevens, D. J.; Spicer, L. D. *J. Chem. Phys.* 1976, 64, 4798.
35. Clancy, J.; Urch, D. S., presented at 10th Internat. Hot Atom Chem. Symp., Loughborough, England, 1979.
36. Gann, R. G.; Dubrin, J. *J. Chem. Phys.* 1969, 50, 535.
37. Gann, R. G.; Ollison, W. M.; Dubrin, J. *J. Am. Chem. Soc.* 1970, 92, 450.
38. Gann, R. G.; Ollison, W. M.; Dubrin, J. *J. Chem. Phys.* 1971, 54, 2304.
39. Min, B. K.; Yeh, C.-T.; Tang, Y.-N. *J. Phys. Chem.* 1978, 82, 971.
40. Mo, S.-H.; Grant, E. R.; Little, F. E.; Manning, R. G.; Mathis, G. S.; Werre, G. S.; Root, J. W. In "Fluorine-Containing Free Radicals: Kinetics and Dynamics of Reactions," ACS Symp. Ser. 1978, 66, 59.
41. Root, J. W.; Mathis, C. A.; Gurvis, R.; Knierim, K. D.; Mo, S.-H., Chap. 10 in this book.
42. Chang, J.; Spicer, L. D., presented at the 179th Natl. Meet. Am. Chem. Soc., Houston, TX Mar. 1980.
43. Adams, J. T.; Porter, R. N. *J. Chem. Phys.* 1973, 59, 4105.
44. *Ibid.*, 60, 3354.
45. Keizer, J. *J. Chem. Phys.* 1972, 56, 5958.
46. *Ibid.*, 1973, 58, 4524.
47. Shizgal, B. *J. Chem. Phys.* 1980, 72, 3143, 3156.
48. Grant, E. R.; Feng, D.-F.; Keizer, J.; Knierim, K. D.; Root, J. W. In "Fluorine-Containing Free Radicals: Kinetics and Dynamics of Reactions," ACS Symp. Ser. 1978, 66, 314.
49. Wolf, A. P.; Schueler, P.; Pettijohn, R. P.; To, K.-C.; Rack, E. P. *J. Phys. Chem.* 1979, 83, 1237.
50. Wu, J.; Ache, H. J. *J. Am. Chem. Soc.* 1977, 99, 6021.
51. Wu, J.; Boothe, T. E.; Ache, H. J. *J. Chem. Phys.* 1978, 68, 5285.
52. Berei, K.; Ache, H. J. *J. Phys. Chem.* 1980, 84, 687.
53. Berei, K.; Vasaros, L.; Ache, H. J. *J. Phys. Chem.* 1980, 84, 1063.
54. Arsenaull, L. J.; Blotcky, A. J.; Medna, V. A.; Rack, E. P. *J. Phys. Chem.* 1979, 83, 893.
55. Stevens, D. J.; Spicer, L. D. *J. Am. Chem. Soc.* 1978, 100, 3295.
56. Lee, F. S. C.; Rowland, F. S. *J. Phys. Chem.* 1980, 84, 1876.
57. Apeloig, Y.; Rappoport, Z. *J. Am. Chem. Soc.* 1979, 101, 5096.
58. Park, J. D.; Cook, E. W. *Tetrahedron Lett.* 1965, 4853.
59. Cacace, F.; Giacomello, P. *J. Am. Chem. Soc.* 1977, 99, 5477.
60. Cacace, F.; Speranza, M. *J. Am. Chem. Soc.* 1979, 101, 1587.
61. Cacace, F., Chap. 2 of this book.
62. Ferro, L. J.; Spicer, L. D., presented at the 178th Natl. Meet., Am. Chem. Soc., Washington, D.C., Sept., 1979.
63. Ferro, L. J.; Spicer, L. D., unpublished data.
64. Root, J. W., private communication.
65. Garmestani, S. K.; Firouzbakht, M. L.; Rack, E. P. *J. Phys. Chem.* 1979, 83, 2827.
66. Garmestani, S. K.; Rack, E. P. *J. Phys. Chem.* 1979, 83, 2316.
67. Stevens, D. J.; Spicer, L. D. *J. Phys. Chem.* 1977, 81, 1217.

RECEIVED September 26, 1980.

# Dynamical Effects of High Rotational Excitation in Unimolecular Decomposition Activated by Hot Atom Substitution

EDWARD R. GRANT

Department of Chemistry, Baker Laboratory, Cornell University,  
Ithaca, NY 14853

JESUS SANTAMARIA

Departamento de Química Física, Facultad de Químicas,  
Cindad Universitaria, Madrid-3, Spain

*Studies of unimolecular decomposition rates in classical trajectory simulations of highly excited C<sub>2</sub>H<sub>6</sub>, using several different initial condition sampling biases, have shown that in this system high rotational excitation accelerates the flow of energy into and out of C—H stretching modes. C—C scission reaction rates with initial energization biased toward skeletal modes behaved, on rotational excitation, in reasonable accord with statistical expectation. However, strong deviation from expected behavior was seen for the C—C reaction channel, with initial condition scrambling patterns biased in favor of C—H modes, and for C—H reaction with all sampling patterns. In these cases the extent of rate enhancement with rotational excitation was significantly greater than that predicted by simple statistical theory.*

Hot atom radio labeling processes often leave primary products with large amounts of internal excitation. As a consequence, secondary unimolecular fragmentations can play an important, if not dominant, role in the chemical systematics of nuclear recoil activated compounds. This particular aspect of hot atom chemistry has been used to advantage by a number of workers who have applied nuclear recoil chemical activation to probe the kinetics and dynamics of unimolecular rate processes (1-15).

American Chemical  
Society Library  
0065-9594/82/0017\$05.00/0  
© 1981 American Chemical Society  
1155 16th St., N.W.  
Washington, D.C. 20036

Statistical models for unimolecular decomposition (16) have figured prominently in these applications. For example, theoretically predicted energy dependencies of branching ratios have often been compared with experimental yields to estimate excitation distributions (3, 4, 5, 12-15). Significantly, one of the first experimental indications of the importance of dynamical influences in unimolecular decomposition was provided by a nuclear recoil experiment (3). In more recent work, hot atom activation combined with statistical rate theory and cascade models for collisional deactivation have been used to investigate energy transfer for highly excited polyatomics (17).

Due to the work of Bunker (18), it is now generally recognized in such applications that a special property of hot atom activated molecules should be considered in formulating theoretical models for their subsequent decomposition. This property is related to the state of rotational excitation for reactively energized molecules. In this work we examine the detailed nature of rotational effects for hot atom activated systems both from a conventional, energetics point of view and from the dynamical perspective of classical trajectory simulations. We show the physical basis for the perturbation of a predicted yield distribution by rotational relaxation in the conventional sense, using RRKM theory. We then show how the predicted behavior can be significantly modified by the dynamical effect of angular momentum on intramolecular energy transfer.

### *Energetic Basis for Rotational Effects in Hot Atom Activated Systems*

The very high average velocity of substituting hot atoms taken over a distribution of reactive impact parameters yields a broad distribution of orbital angular momenta. Following substitution, especially that involving the displacement of a lightweight leaving group or atom, such an incident orbital angular momentum distribution transforms into a high average rotational energy for activated molecules. If formed with sufficient internal energy and not rapidly stabilized by collisional energy transfer, these molecules will proceed to undergo unimolecular decomposition. Such processes will, in general, be accompanied by overall moment of inertia changes. Depending on the nature of the fragmentation pathway, these changes, proceeding from reactant toward critical configuration (transition state), may either be small, as in the case of hydrogen atom loss, or large, as might accompany a hydrocarbon skeletal C—C scission. In all cases angular momentum will be conserved. For constant angular momentum, as a moment of inertia increases, the rotational energy associated with that moment decreases. Total energy is, of course, conserved, and the rotational energy lost appears as an increase

in the internal energy of the reactant; it adds to the energy available to drive the reaction. Thus, for unimolecular decomposition accompanied by appropriate structural changes, rotational excitation accelerates the reaction.

It is clear that just as moment of inertia changes are different for different reaction channels, this rotational acceleration effect will differ for competing reaction pathways depending on the particular geometries involved. This difference can significantly affect branching ratios for a given initial internal energy. Within the limits of statistical rate theory the extent of such effects can be approximately predicted by assuming reasonable models for critical configuration geometries (19).

For example, consider the following model for ethane decomposition. We assume that at high energy the competing dissociation channels are C—H and C—C scission, the thresholds of which are 93.4 and 70.0 kcal mol<sup>-1</sup>, respectively. We adopt the critical configuration models of Reference 20, so that the relevant moment of inertia changes proceeding through the transition state are from 6.46, 25.50, 25.50 amu-Å<sup>2</sup> to 11.64, 28.14, 33.31 amu-Å<sup>2</sup> for the C—H channel and to 6.46, 65.42, 65.42 amu-Å<sup>2</sup> for the C—C channel. If we carry out RRKM calculations using the above model with an excitation energy of 210 kcal mol<sup>-1</sup> and a cold (300 K) overall rotational energy distribution, we compute a branching ratio (C—C/C—H) of 0.34, with the detailed rate constants given in Table I. If, on the other hand, we reapportion 17.9 kcal of the above 210 kcal internal energy to external rotation, giving a total rotational excitation corresponding to a temperature of 6000 K [corresponding roughly to the distribution that would be created by an average hot atom-molecule collision energy of 13 eV, with an impact parameter of 1.8 Å and a fractional energy deposition in the activated molecule of 0.64 (18)], the branching ratio we calculate from RRKM theory becomes 0.78, based on the rate constants additionally listed in Table I.

**Table I. Unimolecular Rate Constants Predicted by RRKM Theory for C—H and C—C Reaction Channels in Rotationally Cold (300 K) and Rotationally Hot (6000 K) Model Ethane Molecules<sup>a</sup>**

<i>C—H Channel</i>	<i>k</i> (s <sup>-1</sup> )
300 K	7.3 × 10 <sup>12</sup>
6000 K	5.0 × 10 <sup>12</sup>
<i>C—C Channel</i>	
300 K	2.5 × 10 <sup>12</sup>
6000 K	3.9 × 10 <sup>12</sup>

<sup>a</sup> Total energy 210 kcal mol<sup>-1</sup>.

The source of the effect shown in this sample calculation is strictly energetic. Its basis is illustrated graphically in Figures 1 and 2. In Figure 1 we show the potential energy function, total energy, and rotational energy for the rotationally cold model ethane molecule as a function of the progress of reaction coordinates for dissociation via C—H and C—C scission. For both reactions there is a relatively small contraction of rotational energy and a corresponding increase in available internal energy as reactant proceeds to products. Figure 2 shows a similar diagram for the case discussed above in which the same total energy is apportioned to place a relatively large amount in rotation and correspondingly less in vibration.

The source of the branching ratio difference and, in the case of the C—C channel, of the net acceleration is clear from these figures. The substantial reduction in  $E_r$  for rotationally hot molecules as they proceed to their critical configurations makes a significant contribution to the vibrational energy available to drive their reaction. Within the statistical assumption the decomposition rate constant for an ensemble of molecules with specified energy is given by Equation 1 (16).

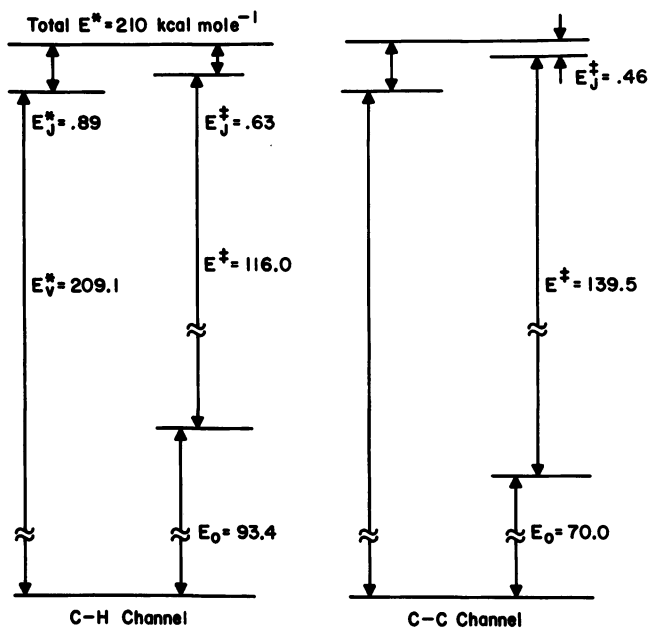


Figure 1. Energetics diagram for decomposition of rotationally cold  $C_2H_6$  ( $T_R = 300\text{ K}$ )

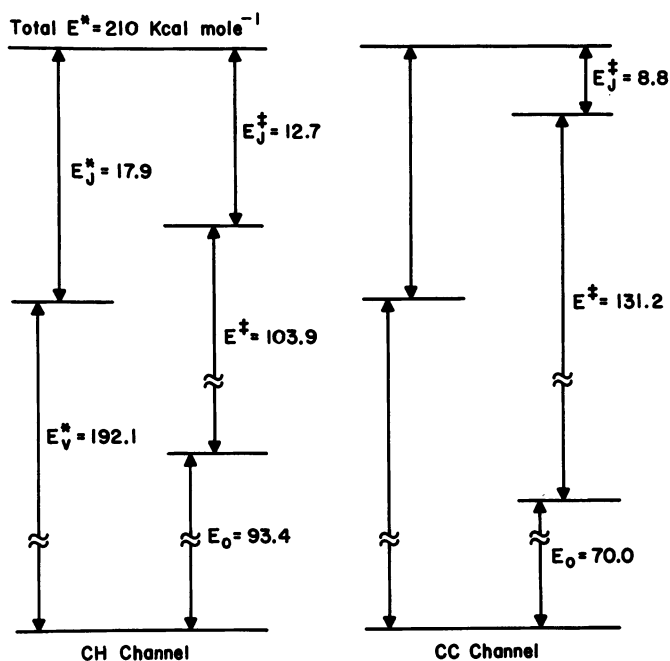


Figure 2. Energetics diagram for decomposition of rotationally hot  $C_2H_6$  ( $T_R = 6000$  K)

$$k_a(E^*) = \frac{L^\ddagger \sum_{E^\ddagger} P(E^\ddagger)}{hN(E_v^*)} \quad (1)$$

In the case of the C—H channel the added energy increases the magnitude of the summation over states in the critical configuration, partially offsetting the fact that in this example the reaction takes place at lower internal energy. For the C—C channel, the rotational energy increment is large enough to make the reaction with less initial vibrational energy actually proceed faster than the reaction in which nearly all the  $210 \text{ kcal mol}^{-1}$  is placed initially in vibration. Physically we can interpret these result by viewing rotation as a mechanism for effectively increasing the state density in a molecular system as its progress of reaction coordinate is extended toward the critical configuration.

In our computational procedure for investigating the dynamics of unimolecular reactions by the method of classical trajectories, we can use our initialization routines to select hot rotational energy distributions



for reactant molecules. As a test of our previous comparisons between trajectory and statistical RRKM theory calculations, we sought to extend our study to include the effects of rotational excitation, the purely energetic effects of which could readily be predicted as outlined above. Beyond this, we were especially interested to see if the high rotational excitation characteristic of hot atom activation produced any additional effect on the dynamics of decomposition. Our findings show the energetic effect expected, which confirms our statistical model. They also contain a rather dramatic additional indication that high rotational excitation enhances restricted intramolecular energy transfer. The following section presents the results of our calculations preceded by a brief review of the decomposition dynamics observed for rotationally cold molecules.

### *Dynamic Effects of Rotational Excitation on Unimolecular Decomposition*

The classical trajectory program used to carry out our studies of rotational effects was identical to that described in Reference 20. Its potential surface of Morse and attenuated angular harmonic oscillators permitted decomposition via C—H and C—C scission (Equations 2 and 3). The surface was fully characterized so that it was possible to compare



trajectory results to precisely drawn RRKM calculations.

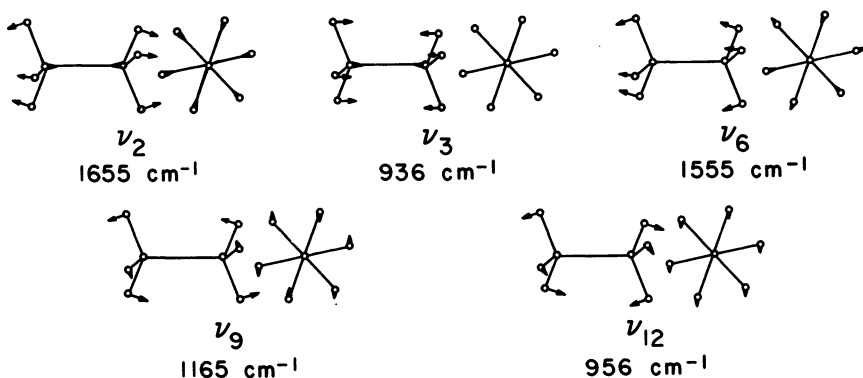


Figure 3. Normal modes energized to create sampling bias labeled C—CI

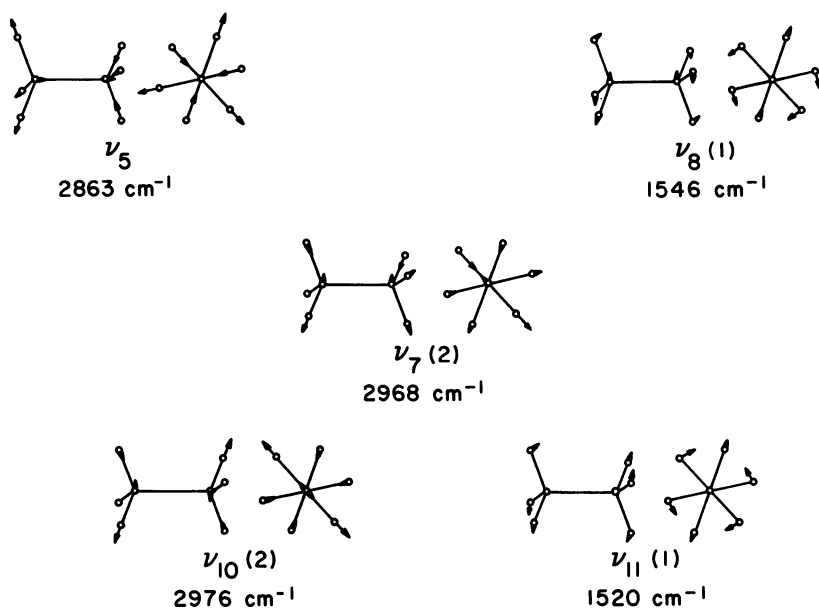


Figure 4. Normal modes energized to create sampling bias labeled C—HI

Results of the earliest study of this system (20) showed that randomly sampled trajectories reacted through both channels at rates that were slower than expected, with a greater deviation for the C—H channel. Excitation biased in favor of C—H modes further retarded both C—C and C—H reaction channels. These observations led to the conclusion that our classical model molecule was intrinsically non-RRKM. Intramolecular energy randomization was restricted on the time scale of dissociation. C—H bonds were the worst offenders.

In a subsequent study (21) energy was localized on one end of the molecule, all in either symmetric or antisymmetric stretch. Antisymmetric stretch excitation was found to produce reaction of nearly all molecules by C—H scission within a couple of vibrational periods. The same amount of energy placed in symmetric stretch resulted in an induction period of several vibrational periods in which no reaction occurred at all, followed by an enhanced C—H reactivity and, after a bit longer induction, a retarded C—C contribution. This work confirmed earlier suggestions of restricted intramolecular energy transfer by direct observation.

Several broadly localized sampling patterns, two from the first study and two new ones, were chosen to examine the dynamical effects of rotational excitation. Modes sampled to create the patterns C—CI and C—HI are illustrated respectively in Figures 3 and 4. The sampling

Table II. Summary of Trajectory and RRKM

Sampling Bias:	$k(s^{-1})$	
	<i>CC Mode</i>	<i>CC Mode II</i>
<i>C—H Channel</i>		
300 K	$8.5 \times 10^{11}$	$4.3 \times 10^{11}$
6000 K	$7.8 \times 10^{11}$	$6.1 \times 10^{11}$
<i>C—C Channel</i>		
300 K	$1.5 \times 10^{12}$	$1.1 \times 10^{12}$
6000 K	$1.9 \times 10^{12}$	$3.9 \times 10^{12}$

pattern labeled C—HII is simply the complement of C—CI. The same logic applies to C—CII.

To facilitate comparison with existing 210 kcal mol<sup>-1</sup> rotationally cold data for these patterns, rotationally hot trajectories were run with the same total energy. To achieve this, angular momentum was sampled from a thermal distribution at 6000 K, and the remaining available energy was apportioned to vibration by scaling.

Following initialization, each trajectory was integrated for 0.4 ps or until a reaction occurred. Reactive events were counted and rate constants computed in the normal way (20).

Results for both 300 K and 6000 K rotational temperatures are given, together with the RRKM predictions presented earlier, in Table II. Sample sizes for these computations range from 522 for C—CII sampling at 6000 K to 646 for C—HII sampling at 300 K. Estimated two-thirds error bounds in all cases are no greater than  $\pm 20$  percent. Examination of this table shows that for the C—H channel, rotational excitation is, in all cases, more effective than predicted in promoting reaction. By statistical calculation, molecules with a total energy of 210 kcal mol<sup>-1</sup> should decompose more slowly via C—H scission when an average 18 kcal mol<sup>-1</sup> of this energy is placed in rotation. Instead, decomposition of trajectory molecules through this channel is, in every case but one, accelerated.

When we turn to the C—C channel, where enhancement is predicted, we find that, for C—C sampling, enhancements in accord with expectations are obtained. However, for C—H biased sampling, where the C—C channel is severely retarded at low rotation, we find that rotational excitation produces significantly greater enhancements.

The effects observed here form a systematic pattern when considered in the light of earlier results. We have evidence that the C—H vibrational degrees of freedom for our classical model of C<sub>2</sub>H<sub>6</sub> transfer energy on a time scale that is slow compared with reaction at the energies studied. This produces retarded reaction rates for C—H scission with all but the

**Theory Unimolecular Decomposition Rate Constants**

$k(s^{-1})$		
<i>RRKM</i>	<i>CH Mode</i>	<i>CH Mode II</i>
$7.3 \times 10^{12}$	$2.2 \times 10^{11}$	$3.3 \times 10^{11}$
$5.0 \times 10^{12}$	$2.6 \times 10^{11}$	$4.0 \times 10^{11}$
$2.5 \times 10^{12}$	$9.4 \times 10^{10}$	$2.5 \times 10^{11}$
$3.9 \times 10^{12}$	$3.9 \times 10^{11}$	$5.2 \times 10^{11}$

most localized initial excitation pattern and makes C—H biased excitation less effective in producing reaction.

In this study we see rotational excitation (taken away from vibrational) accelerating C—H reaction when it should be retarding it. Furthermore, and perhaps more significantly, we see substantial enhancement of C—C reactivity for a highly unfavorable C—H sampling pattern. This enhancement can be explained if we conclude that rotational excitation accelerates intramolecular energy transfer into and out of the C—H modes in our model ethane. Enhanced energy transfer into and among C—H modes increases C—H reactivity for all sampling patterns. Enhanced energy transfer out of these modes increases the C—C scission rate for C—H biased excitation.

These results tend to validate our earlier conclusions (20, 21) about the importance of dynamical effects in the unimolecular decomposition of highly excited molecules. In that sense we feel that they must stand as a qualification of unimolecular rate models for such species. Interestingly, this work shows that this qualification is lessened under the more realistic condition of high rotational excitation.

**Literature Cited**

1. McKnight, C. F.; Parks, N. J.; Root, J. W. *J. Phys. Chem.* **1970**, *74*, 217.
2. McKnight, C. F.; Root, J. W. *J. Phys. Chem.* **1969**, *73*, 4430.
3. Krohn, K. A.; Parks, N. J.; Root, J. W. *J. Chem. Phys.* **1971**, *55*, 2690, 5771, 5785.
4. Manning, R. G.; Mo, S.-H.; Root, J. W. *J. Chem. Phys.* **1977**, *67*, 636.
5. Manning, R. G.; Krohn, K. A.; Root, J. W. *Chem. Phys. Lett.* **1975**, *35*, 544.
6. Wolfgang, R. *J. Phys. Chem.* **1970**, *74*, 4601.
7. Wolfgang, R. *Acc. Chem. Res.* **1969**, *2*, 248.
8. Wolfgang, R. *Prog. React. Kinet.* **1965**, *3*, 99.
9. Lee, E. K. C.; Rowland, F. S. *J. Am. Chem. Soc.* **1965**, *85*, 897.
10. Rust, F.; Frank, J. P.; Rowland, F. S. In "Fluorine Containing Free Radicals," *ACS Symp. Ser.* **1978**, *66*, 26.
11. Chou, C. C.; Hase, W. L. *J. Phys. Chem.* **1974**, *78*, 2309.
12. Nogar, N. S.; Spicer, L. D. *J. Chem. Phys.* **1977**, *66*, 3524.

13. Nogar, N. S.; Spicer, L. D. *J. Phys. Chem.* **1976**, *80*, 1736.
14. Nogar, N. S.; Dewey, J. K.; Spicer, L. D. *Chem. Phys. Lett.* **1975**, *34*, 98.
15. Smith, W. S.; Rodgers, A. S.; Tang, Y. N. *J. Chem. Phys.* **1975**, *62*, 3310.
16. Robinson, P. J.; Holbrook, K. A. "Unimolecular Reactions"; John Wiley & Sons: New York, 1972.
17. Callahan, M. B.; Spicer, L. D. *J. Phys. Chem.* **1979**, *83*, 1013.
18. Bunker, D. L. *J. Chem. Phys.* **1972**, *57*, 332.
19. Bunker, D. L.; Pattengill, M. *J. Chem. Phys.* **1968**, *48*, 772.
20. Grant, E. R.; Bunker, D. L. *J. Chem. Phys.* **1978**, *68*, 628.
21. Santamaria, J.; Bunker, D. L.; Grant, E. R. *Chem. Phys. Lett.* **1978**, *56*, 170.

RECEIVED September 4, 1980.

# Radiotracer Studies of Unimolecular Energy Transfer

CHESTER A. MATHIS and JOHN W. ROOT

Department of Chemistry, University of California, Davis, CA 95616

*Vibrationally excited  $^{14}\text{CH}_3\text{CF}_3$ , containing  $102.8 \pm 1.0$  kcal mol $^{-1}$  of excess energy has been produced via the photochemically initiated cross combination of  $^{14}\dot{\text{C}}\text{H}_3$  and  $\dot{\text{C}}\text{F}_3$  radicals in the gas phase. The samples contained dilute concentrations of  $^{14}\text{CH}_3\text{CO}^{14}\text{CH}_3$  and  $\text{CF}_3\text{COCF}_3$  photolysis precursors together with  $\text{C}_2\text{H}_6$  or  $\text{C}_2\text{F}_6$  host gases. The pressure dependences of the ( $^{14}\text{CH}_3=\text{CF}_2$ : $^{14}\text{CH}_3\text{CF}_3$ ) decomposition-stabilization product ratios were measured for these host substances throughout the range  $0.5 \leq (\text{D/S}) \leq 1000$  and then compared with the stepladder, Gaussian, and exponential theoretical transition probability models. None of the model calculations accounted for the qualitative characteristics of the extended range data, so that mathematically unique energy transfer models and  $\langle \Delta E \rangle$  values could not be assigned.*

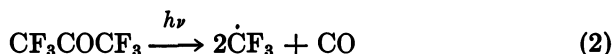
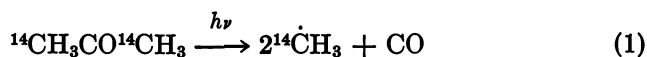
Vibrationally excited molecules and radicals influence the kinetics of numerous reaction systems, and the determination of collisional energy transfer probabilities for such species is of primary concern in chemical dynamics. The unimolecular behavior of highly internally excited species has provided insight into vibrational energy transfer mechanisms (1-4).

One method of producing vibrationally excited molecules involves "chemical activation" via exoergic reactions. The energy released upon chemical bond formation produces energized molecules or unstable radicals that can undergo either unimolecular decomposition or collisional deactivation to stable products. Some advantages of the chemical activation method, which has been extensively used during the past 20 years, include the following: the experiments are relatively simple; the

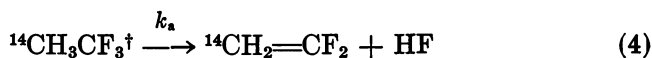
0065-2393/81/0197-0157\$05.50/0  
© 1981 American Chemical Society

measurements are performed under isothermal conditions; the activated species have known energy distributions via known thermochemistry; the excitation energy probability density distribution function  $[f(E)]$  of the activated species often is rather narrow; and the molecular host environment, or "bath gas," can be controlled and widely varied.

Pettijohn, Mutch, and Root demonstrated that radiotracer techniques can be adapted for chemical activation studies (5). The cophotolysis of gas-phase  $^{14}\text{CH}_3\text{CO}^{14}\text{CH}_3$  and  $\text{CF}_3\text{COCF}_3$  mixtures provides a convenient source of  $^{14}\dot{\text{C}}\text{H}_3$  and  $\dot{\text{C}}\text{F}_3$  radicals that can undergo cross combination to produce chemically activated  $^{14}\text{CH}_3\text{CF}_3^\ddagger$  (Equations 1, 2, and 3). Here



the superscript dagger ( $\ddagger$ ) denotes an excess average internal energy content of  $102.8 \pm 1.0 \text{ kcal mol}^{-1}$ . The nascent  $^{14}\text{CH}_3\text{CF}_3^\ddagger$  molecules can either decompose via HF-elimination or transfer energy upon collision with bath gas molecules (Equations 4 and 5). The nonequilibrium



apparent unimolecular rate coefficient ( $k_a$ ) is defined by Equation 6, and the bimolecular collision frequency ( $\omega$ ) for the activated molecule is defined by Equation 7. Here  $P$  denotes the pressure in Torr and  $Z$  the

$$k_a = (D/S)\omega \quad (6)$$

$$\omega = ZP \quad (7)$$

collision number in units of  $\text{s}^{-1} \text{ Torr}^{-1}$ . The fractional yield of  $^{14}\text{CH}_2=\text{CF}_2$  is denoted as  $D$  (decomposition product), and that of  $^{14}\text{CH}_3\text{CF}_3$  as  $S$  (stabilization product).

In the high-pressure falloff region ( $D/S$ ) vs. ( $1/P$ ) plots are predicted by Equations 6 and 7 to be linear with slopes corresponding to ( $k_a/Z$ ) for each different bath gas. Some typical experimental results for the  $^{14}\text{CH}_3\text{CF}_3$  system have been shown in Figure 1. The failure of

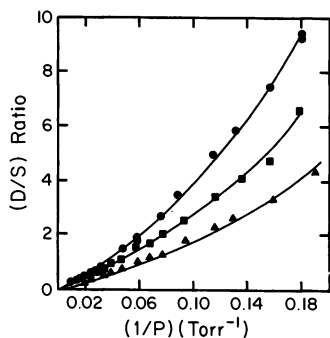


Figure 1. Comparison of  $^{14}\text{CH}_3\text{CF}_3$  (D/S) ratios vs. reciprocal pressure for  $\text{CH}_3\text{CF}_3$ ,  $\text{CF}_3\text{CFH}_2$  and  $\text{CF}_2\text{HCF}_2\text{H}$  bath gases; note the deviations from unit deactivation behavior at low pressures; key to symbols: (●)  $\text{CH}_3\text{CF}_3$ , (■)  $\text{CF}_3\text{CFH}_2$ , (▲)  $\text{CF}_2\text{HCF}_2\text{H}$

the predicted linear relationships in the low-pressure region represents a common characteristic of chemically activated systems. The nature of this "cascading" phenomenon is now considered.

In the high-pressure falloff region the internal energy content of a nascent excited molecule from Reaction 3 has been assumed in Equation 6 to fall below the unimolecular decomposition threshold energy ( $E_0$ ) in a single "strong" collision (Equation 5) with a bath gas molecule. The resulting constancy of  $k_a$  then leads to the predicted inverse proportional relationship between  $P$  and  $(D/S)$ . Such unit deactivation may be observed with large efficient colliders, but many experimental systems exhibit cascading at reduced pressures.

In a single "weak" collision the nascent activated molecule transfers some increment of energy ( $\Delta E$ ) to its collision partner. By definition, the magnitude of  $\Delta E$  is too small to allow the excitation energy to fall below  $E_0$ , so that the activated species remains capable of decomposing. The competition between decomposition and energy transfer continues throughout a cascading collision sequence until the internal energy content of the  $^{14}\text{CH}_3\text{CF}_3$  falls below  $E_0$ .

A representation of the cascading process is shown in Figure 2 for the hypothetical stepladder situation in which only constant  $\Delta E$  increments are allowed. More complex transition probability models utilize statistical descriptions of the energy transfer probability density [ $P(\Delta E)$ ]. For such cases individual collisions probe a range of  $\Delta E$  values, but the average energy transfer increment ( $\langle \Delta E \rangle$ ) remains constant.

As shown in Figure 3, the excitation energy specific, "delta function" or "monoenergetic," unimolecular rate constants ( $k_E$ ) are strongly energy dependent. The magnitude of  $k_E$  diminishes rapidly as the excess internal energy of the  $^{14}\text{CH}_3\text{CF}_3$  approaches  $E_0$ . The initial probability density distribution [ $f(E)$ ] for the nascent  $^{14}\text{CH}_3\text{CF}_3$  molecules from Equation 3 follows from thermochemistry (see above).



From Figure 3,  $f(E)$  for  $^{14}\text{CH}_3\text{CF}_3$  extends from  $99.7 \text{ kcal mol}^{-1}$  to roughly  $112 \text{ kcal mol}^{-1}$ , and the average initial excitation energy is  $102.8 \pm 1.0 \text{ kcal mol}^{-1}$ . Because of the strong energy dependence of  $k_B$ , different pressure ranges probe different portions of  $f(E)$ . For example, the more energetic nascent  $^{14}\text{CH}_3\text{CF}_3$  species are effectively isolated in the high-pressure limit.

As shown in Figure 1, the extent of deviation from unit deactivation behavior varies with the nature of the bath gas. Efficient colliders actually may approach the strong collision limit. The chemical activation method attempts to extract information concerning the vibrational energy transfer processes for excited molecules in different bath gases based on the observed deviations from unit deactivation behavior. The pressure dependence of the measured  $(D/S)$  ratios is compared with computer simulated cascading falloff results corresponding to specific energy transfer transition probability models. Good agreement between experimental and calculated results then serves to identify the preferred cascading model and  $\langle \Delta E \rangle$  value.

Marcoux and Setser investigated chemically activated  $\text{CH}_3\text{CF}_3^\dagger$  and reported preferred energy transfer models and  $\langle \Delta E \rangle$  values for several bath gases (4). The typical experimental range employed in these non-

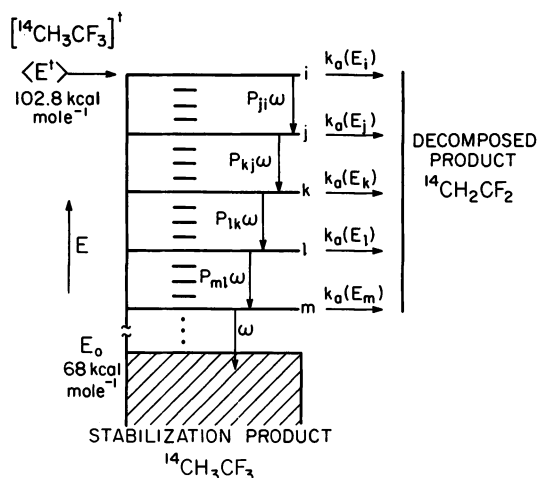


Figure 2. Diagram of the cascade deactivation process; note the competition between collisional stabilization ( $P_{ji}\omega$ ) and unimolecular reaction [ $k_o(E_i)$ ] at each cascade step. The activated  $^{14}\text{CH}_3\text{CF}_3^\dagger$  is formed via the reaction shown in Equation 3 with  $102.8 \pm 1.0 \text{ kcal mol}^{-1}$  average internal energy. Decomposition ceases when the excitation energy falls below the  $68 \text{ kcal mol}^{-1}$  threshold energy requirement for HF-elimination (Reaction 4).

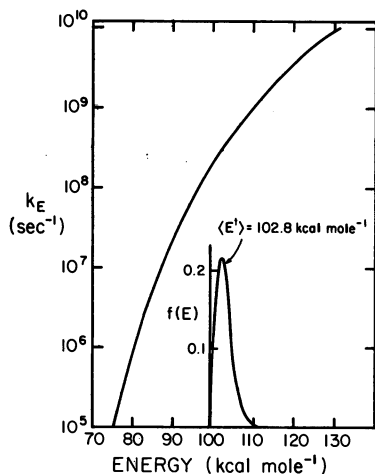


Figure 3. Calculated RRKM rate constant ( $k_E$ ) and distribution function [ $f(E)$ ] results for  $^{14}\text{CH}_3\text{CF}_3$ ; note the strong energy dependence for  $k_E$ .

radiotracer studies was  $0.1 < (D/S) < 50$ , and the derived  $\langle \Delta E \rangle$  values were reported as accurate to  $\pm 1.0 \text{ kcal mol}^{-1}$ .

With the aid of the sensitivity increase obtained with carbon-14 radiotracer, we have been able to extend the measurement range for  $^{14}\text{CH}_3\text{CF}_3$  to  $0.5 \leq (D/S) \leq 1000$ . Our purpose has been to provide an enhanced sensitivity experimental test of the available chemical activation cascade modeling procedures for  $^{14}\text{CH}_3\text{CF}_3$  in  $\text{C}_2\text{H}_6$  and  $\text{C}_2\text{F}_6$  bath gases.

### Experimental

Our methods of sample preparation, photolysis, and analysis have been described elsewhere (5, 6), so that only a brief summary follows below.

**Sample Preparation.** Pierce Chemical Co.  $\text{CF}_3\text{COCF}_3$  (HFA, 99.0%), Phillips research grade  $\text{C}_2\text{H}_6$  (99.99%), and Matheson Gas Products  $\text{C}_2\text{F}_6$  (99.6%) were purified by bulb-to-bulb distillation and multiple freeze-pump-thaw cycles at 77 K immediately prior to each series of measurements. The  $^{14}\text{CH}_3\text{CO}^{14}\text{CH}_3$  was obtained from Amersham with a specific radioactivity of  $25.0 \pm 0.1 \text{ mCi mmol}^{-1}$ , corresponding to  $20.0 \pm 0.1 \text{ mol } \%$  of acetone-1,3- $^{14}\text{C}$  diluted with unlabeled carrier acetone. The chemical and radioisotopic purities of the acetone were greater than 99.9%.

The photolysis vessels consisted of 100–12,000  $\text{cm}^3$  Kimax KG-33 spherical flasks provided with Kontes high-vacuum Teflon plug O-ring stopcocks. Samples were filled using standard high-vacuum techniques on a grease-free apparatus. Pressure measurements were performed with a Barocell model 1174 capacitance manometer provided with a model 570D-1000T-1B2-H5 temperature-stabilized 0–1000 Torr probe. The calibrated Barocell manometer had an absolute accuracy of  $\pm 0.012 \text{ Torr}$ .

During the filling procedure the bath gas was metered into the evacuated photolysis flask and condensed at 77 K. The precursor ketone mixture consisting of 90 mol % HFA and 10 mol % labeled acetone was then introduced, and the condensed mixture was thoroughly outgassed. The photolysis samples

contained approximately 0.5 mol % of the ketone mixture. Freshly prepared samples were allowed to stand in the dark for 12 h to ensure completeness of mixing.

**Photolysis.** The ultraviolet light source consisted of 24 Westinghouse type FS20T12 20-W sunlamps housed in a cylindrical drum provided with 12-in. circular openings at both ends. To achieve nearly steady-state irradiation conditions, the lamps were divided into three groups with alternate positioning within the housing. Each group was powered by a different branch of the three-phase power supply. The overlap of the three 120° out-of-phase sinusoidal ac signals produced an effectively dc source with only 7% of residual ac ripple. The emission spectrum extended from 280–350 nm with a maximum intensity at 310 nm.

The KG-33 glass photolysis vessels effectively filter the spectrum below 290 nm, eliminating photosensitization complications caused by mercury vapor introduced from the Toepler pump. During irradiation the samples were maintained at  $304 \pm 1$  K by means of air circulation provided by a blower mounted at the base of the lamp housing. Individual samples were photolyzed for 12–24 h with photochemical conversions never exceeding 2%.

**Sample Analysis.** For analysis via radio gas chromatography the irradiated sample mixture was quantitatively transferred into a greaseless injection loop by means of a 1-L mercury Toepler pump. The chromatography column consisted of 150 ft of 0.25-in. o.d. stainless steel beverage tubing packed with 30 wt % of the crotonic acid ester of  $\text{H}(\text{CF}_2)_8\text{CH}_2\text{OH}$  coated upon 30/40 ASTM mesh Chromosorb PA solid support. The column was operated at 273 K with a helium carrier gas flow rate of  $25 \text{ cm}^3 \text{ min}^{-1}$  (NTP).

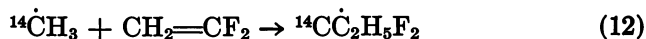
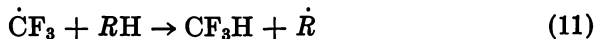
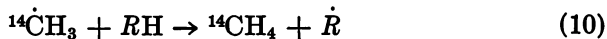
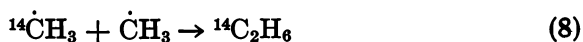
The radioactivity detector consisted of an internal flow proportional counter. The counting chamber was fabricated from a 1 in. o.d.  $\times$  16 in. long section of hardened copper pipe having a nominal volume of about  $200 \text{ cm}^3$ . A length of 2-mil nominal diameter tungsten wire was suspended along the central lengthwise axis of the chamber between two Amphenol high-voltage connectors with tension maintained by means of small stainless steel springs (5, 6).

The high-voltage power supply, amplifier–discriminator, and scalers were homebuilt (5, 7). During the operation of the detector, propane counting gas was mixed with the helium carrier gas in a 4:1 ratio, and the total combined helium and propane flow rate was maintained at  $125 \text{ cm}^3 \text{ min}^{-1}$  (NTP). With 2 in. of lead shielding, the typical counter background level was 100–200 cpm.

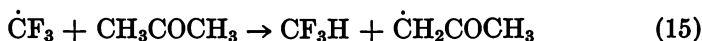
Each radioactive product peak was corrected for detector background, and the activity ratio ( $^{14}\text{CH}_2\text{CF}_2/^{14}\text{CH}_3\text{CF}_3$ ) error was calculated using standard radioactive decay statistics. The cited errors represent single standard deviations (68% confidence level). The reproducibility of replicate measurements was generally 97% or better.

## Results

**Experimental Complications.** The  $^{14}\dot{\text{C}}\text{H}_3$  and  $\dot{\text{C}}\text{F}_3$  radicals produced via gas-phase photolysis processes 1 and 2 can undergo reactions other than the desired cross combination. Thus, other secondary products may be formed in addition to  $^{14}\text{CH}_3\text{CF}_3$  and  $^{14}\text{CH}_2\text{CF}_2$  (5).



Optimal yields of  $^{14}\text{CH}_3\text{CF}_3^\dagger$  were obtained when a 9:1 HFA to  $^{14}\text{C}$ -acetone ratio was used (5, 6). Reactions of the type shown in Equations 8 and 9 deplete the  $^{14}\text{CH}_3\text{CF}_3^\dagger$  yield but do not cause other kinetic complications. The processes shown in Equations 10 and 11 can lead to depletion of the  $^{14}\text{CH}_2\text{CF}_2$  and  $^{14}\text{CH}_3\text{CF}_3$  products. More likely abstraction reactions involving rate constants  $10^2$ – $10^3$  larger and activation energies 3–5 kcal mol $^{-1}$  smaller than the respective values corresponding to abstraction from  $^{14}\text{CH}_2\text{CF}_2$  and  $^{14}\text{CH}_3\text{CF}_3$  are given by Equations 14 and 15.



In these experiments the ( $\text{CH}_3\text{COCH}_3/^{14}\text{CH}_3\text{CO}^{14}\text{CH}_3$ ) concentration ratio has been maintained at 4:1, so that most abstraction reactions of the type shown in Equations 14 and 15 occur with the unlabeled carrier acetone. The  $^{14}\text{CH}_2\text{CF}_2$  and  $^{14}\text{CH}_3\text{CF}_3$  products can be protected from depletion by the reactions shown in Equations 10 and 11 if their concentrations during the irradiations are kept much smaller than that of acetone. In the absence of a protective RH additive, this condition thus serves to limit the permissible photochemical conversion.

Because the reactions shown in Equations 12 and 13 can lead to the loss of the decomposition product  $^{14}\text{CH}_2\text{CF}_2$ , they represent more serious complications than Equations 10 and 11. The presence in the samples of 6 mol % of  $\text{C}_2\text{H}_6$  additive suppresses the depletion processes shown in Equations 12 and 13 (5, 6). This protective scavenging action results from the large hydrogen abstraction rate constant of  $\dot{\text{C}}\text{F}_3$  radicals toward  $\text{C}_2\text{H}_6$  together with the large ( $\text{C}_2\text{H}_6/^{14}\text{CH}_2\text{CF}_2$ ) concentration ratio, which has been maintained in excess of 600:1 in this study.

The calculation of the average energy content of the excited nascent  $^{14}\text{CH}_3\text{CF}_3$  molecules from Reaction 3 assumes that the reacting  $^{14}\dot{\text{C}}\text{H}_3$  and  $\text{CF}_3$  radicals are in thermal equilibrium. This important condition is easily achieved with radiotracers, since the bath gas to photolysis precursor concentration ratio exceeds 200:1. The large relative concentration of bath gas to photolysis precursor species virtually eliminates  $^{14}\text{CH}_3\text{CF}_3^\dagger$  energy transferring collisions to HFA and acetone, representing an important advantage of the radiotracer method.

Because the photolysis vessel wall provides an additional source of  $^{14}\text{CH}_3\text{CF}_3^\dagger$  deactivating collisions, the possible importance of wall effects increases at low pressures. This spurious heterogeneous deactivation mechanism can be suppressed by increasing the flask size. To ensure that heterogeneous deactivation has not influenced our low-pressure falloff results, a series of measurements has been carried out at 0.51 Torr with  $\text{C}_2\text{F}_6$  bath gas in flasks ranging in volume from 500–12,000  $\text{cm}^3$ . The results shown in Table I indicate that the ( $D/S$ ) ratio increases with increasing vessel size, establishing the importance of heterogeneous deactivation for small vessels and showing that the wall is a stronger collider than  $\text{C}_2\text{F}_6$ . At 0.51 Torr the contribution from wall effects becomes undetectable for 5000- $\text{cm}^3$  vessels under the present  $\pm 2\%$  measurement sensitivity conditions. Similar tests were performed throughout the range of conditions used in this work, and the contributions from heterogeneous deactivation were routinely maintained below the measurement sensitivity.

**Calculated Results.** Because the standard computational procedure for simulating the energy transfer cascade has been thoroughly described elsewhere (3, 4, 8, 9, 10), only a brief outline follows.

The steady-state concentration of  $^{14}\text{CH}_3\text{CF}_3$  molecules corresponding to the  $i$ th energy interval ( $[^{14}\text{CH}_3\text{CF}_3]_i$ ) can be calculated via the steady-state stochastic master equation (Equations 16 and 17). Here

$$d[^{14}\text{CH}_3\text{CF}_3]_i/dt = 0 \quad (16)$$

$$= Rf(E_i) - k_E[^{14}\text{CH}_3\text{CF}_3]_i - k_M[M][^{14}\text{CH}_3\text{CF}_3]_i \sum_j P_{ji} \quad (17)$$

$Rf(E_i)$  denotes the rate of formation of  $^{14}\text{CH}_3\text{CF}_3$  molecules containing sufficient internal energy to populate the  $i$ th level;  $k_E$ , the energy-dependent Rice–Ramsperger–Kassel–Marcus (RRKM) rate constant;  $k_M[M]$ , the bimolecular collision rate per activated molecule; and  $P_{ji}$ , the collisional probability that a molecule in the  $i$ th level transfers energy to a bath gas molecule and enters the  $j$ th level. Marcoux and Setser have shown that energy releasing “down” transitions predominate in this system and that “up” transitions account for negligible net energy transfer (4).

**Table I. The Effect of the Photolysis Vessel Size on the (D/S) Ratio for C<sub>2</sub>F<sub>6</sub> Bath Gas at 0.5 Torr**

Vessel Size (L)	Pressure (Torr) <sup>a</sup>	(D/S) Ratio <sup>b</sup>
0.50	0.513	204.2 ± 3.8
<b>1.0</b>	0.513	274.1 ± 6.2
2.0	0.515	301.6 ± 9.6
<b>5.0</b>	0.517	308.7 ± 7.4
12.0	0.512	309.7 ± 6.9

<sup>a</sup> Accurate to ± 0.012 Torr; consistent to ± 0.001 Torr.

<sup>b</sup> Relative errors are based on radioactivity statistics and represent single standard deviations at the 68% confidence level.

The  $R_f$  and  $k_B$  values for <sup>14</sup>CH<sub>3</sub>CF<sub>3</sub><sup>†</sup> comprise input data for the various transition probability cascading models, which then yield the corresponding  $k_a$  and (S/D) ratio values. These calculations have been performed with the aid of a computer algorithm generously provided by Professor B. S. Rabinovitch (11). The unimolecular rate constants were computed using the Universal RRKM program of Hase and Bunker (12), together with reverse dissociation and four-center 1334 HF-elimination critical configuration models (3,6). A plot of  $k_B$  vs.  $E$  has been shown in Figure 3 along with the calculated initial density distribution function [f(E)]. The start of the excitation distribution ( $E_{min}$ ) was set at 99.7 kcal mol<sup>-1</sup>, the decomposition threshold ( $E_o$ ) at 68 kcal mol<sup>-1</sup>, and the average energy content of the nascent <sup>14</sup>CH<sub>3</sub>CF<sub>3</sub><sup>†</sup> [ $\langle E^\dagger \rangle$ ] at 102.8 ± 1.0 kcal mol<sup>-1</sup>. The step-size increments between energy levels were maintained at 1.0 kcal mol<sup>-1</sup>. All these values agree with the input data used for activated CH<sub>3</sub>CF<sub>3</sub><sup>†</sup> by Marcoux and Setser (4).

Three transition probability models have been investigated in this study. The Gaussian (GS) probability density function for down transitions is given by Equation 18. Here  $C$  denotes the normalization constant;

$$P_{ji} = C \exp[-(\Delta E - \langle \Delta E \rangle)^2 / 2\sigma^2] \quad (18)$$

$\Delta E$ , the energy difference between energy levels  $E_i$  and  $E_j$ ;  $\langle \Delta E \rangle$ , the average  $\Delta E$  value; and  $\sigma$ , the half-width at half maximum of the probability density distribution. The Gaussian distribution half-width has been maintained at 1.0 kcal mol<sup>-1</sup> in these calculations. For this model the largest energy transfer probability occurs at  $\langle \Delta E \rangle$ , and the probability falls off with a Gaussian dependence to either side of this value.

The stepladder (SL) model is simply a collapsed Gaussian, or delta function, distribution centered at the constant energy transfer increment value  $\langle \Delta E \rangle$  (Equations 19 and 20). Thus, in the spirit of quantized

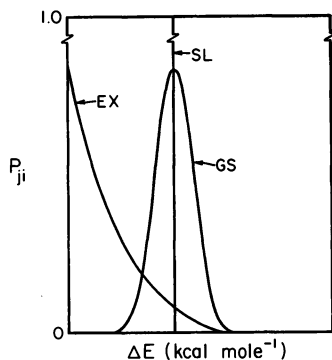


Figure 4. Qualitative intercomparison of the exponential (EX), stepladder (SL), and Gaussian (GS) transition probability models

$$P_{ji} = 1.0 \quad \text{if } (E_i - E_j = \langle \Delta E \rangle) \quad (19)$$

$$P_{ji} = 0 \quad \text{if } (E_i - E_j \neq \langle \Delta E \rangle) \quad (20)$$

energy transfer increments, only discrete energy step sizes are allowed.

Small energy step sizes are favored for the exponential (EX) distribution model (Equation 21). The three transition probability models

$$P_{ji} = C \exp(-\Delta E / \langle \Delta E \rangle) \quad (21)$$

have been illustrated in a qualitative fashion in Figure 4.

Since the  $C_2F_6$  bath gas contained a constant 6 mol % of  $C_2H_6$  protective additive, the computational model for this system involved a two-component simulation that accounted for the deactivating collisions taking place with  $C_2H_6$ . No attempt was made to explore the predicted cascading behavior of  $C_2H_6/C_2F_6$  mixtures as a function of composition.

**The High-Pressure Rate Constant.** The apparent chemical activation rate coefficient ( $k_a$ ) for a given system decreases with increasing pressure, eventually achieving a minimum value at high pressure. The limiting high-pressure chemical activation rate constant ( $k_a^\infty$ ) provides a useful basis for comparing experimental and calculated cascading results.

Experimental rate coefficients have been measured here in units of pressure (Torr) (Equation 22). The calculated rate coefficients, however,

$$k_a = (D/S)P \quad (22)$$

are obtained in absolute units of  $s^{-1}$ . To permit intercomparisons between the measured and calculated results, suitable unit conversions must be performed. The experimental results have been converted to  $s^{-1}$  units with the aid of Equations 23–27.

$$k_M = S_{\text{CH}_3\text{CF}_3-\text{M}}^2 \left[ \frac{8\pi kT}{\mu} \right]^{1/2} \quad (23)$$

$$S_{\text{CH}_3\text{CF}_3-\text{M}} = \sigma_{\text{CH}_3\text{CF}_3-\text{M}}^{\circ} \Omega^{(2,2)*}(T^*)^{1/2} \quad (24)$$

$$T^* = (kT / \epsilon_{\text{CH}_3\text{CF}_3-\text{M}}) \quad (25)$$

$$\sigma_{\text{CH}_3\text{CF}_3-\text{M}}^{\circ} = (\sigma_{\text{CH}_3\text{CF}_3}^{\circ} + \sigma_{\text{M}}^{\circ}) / 2 \quad (26)$$

$$\epsilon_{\text{CH}_3\text{CF}_3-\text{M}} = [\epsilon_{\text{CH}_3\text{CF}_3} \cdot \epsilon_{\text{M}}]^{1/2} \quad (27)$$

Following standard practice the realistic potential elastic collision diameters ( $S_{\text{CH}_3\text{CF}_3-\text{M}}$ ) have been estimated using Lennard-Jones collision diameters ( $\sigma_{\text{CH}_3\text{CF}_3-\text{M}}^{\circ}$ ) and the  $\Omega^{(2,2)*}(T^*)$  Lennard-Jones universal reduced collision integral for gas-phase viscosity (13). The  $\Omega^{(2,2)*}(T^*)$  values were obtained using Equation 27 to estimate the effective attractive potential constant for these mixed interactions. The computed  $S_{\text{CH}_3\text{CF}_3-\text{M}}$  values for  $\text{C}_2\text{F}_6$  and  $\text{C}_2\text{H}_6$  bath gases at 304 K were 7.1 Å and 5.6 Å, respectively.

The experimental high-pressure rate constants [ $k_a^{\infty}(\text{exptl})$ ] have been intercompared with the corresponding calculated values [ $k_a^{\infty}(\langle \Delta E \rangle)$ ] in Tables II and III. The [ $k_a^{\infty}(\text{exptl})$ ] results were obtained

**Table II. Summary of Calculated and Experimental High-Pressure Rate Constants for  $\text{C}_2\text{F}_6$  Bath Gas**

<i>Model</i>	$\langle \Delta E \rangle$ ( $\text{kcal mol}^{-1}$ )	$k_a^{\infty}(\langle \Delta E \rangle)$ ( $10^8 \text{ s}^{-1}$ )	$k_a^{\infty}(\text{exptl})$ ( $10^8 \text{ s}^{-1}$ )
SL	2	12	4.1 ± 0.1
SL	3	8.0	
SL	4	6.4	
SL	6	4.9	
SL	8	4.3	
SL*	10	4.0	
GS	2	8.2	4.1 ± 0.1
GS	3	4.9	
GS*	4	3.9	
GS	5	3.5	
GS	6	3.3	
EX	2	16	
EX	3	12	
EX	4	9.2	
EX	8	6.2	
EX	10	5.6	
EX	12	5.2	

\* Best-fit models (cf. text).



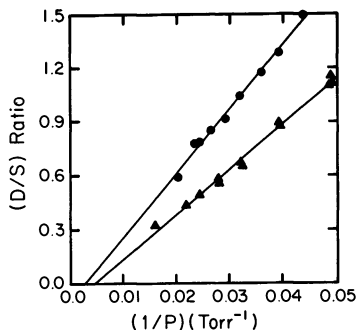
**Table III. Summary of Calculated and Experimental High-Pressure Rate Constants for C<sub>2</sub>H<sub>6</sub> Bath Gas**

<i>Model</i>	$\langle \Delta E \rangle$ (kcal mol <sup>-1</sup> )	$k_a^\infty (\langle \Delta E \rangle)$ (10 <sup>8</sup> s <sup>-1</sup> )	$k_a^\infty$ (exptl) (10 <sup>8</sup> s <sup>-1</sup> )
SL*	2	12	10.0 ± 0.4
SL*	3	8.0	
SL	4	6.4	
SL	6	4.9	
SL	8	4.3	
SL	10	4.0	
GS*	2	8.2	10.0 ± 0.4
GS	3	4.9	
GS	4	3.9	
GS	5	3.5	
GS	6	3.3	
EX	2	16	
EX	3	12	
EX*	4	9.2	
EX	8	6.2	
EX	10	5.6	

\* Best-fit models (cf. text).

from the slopes of (D/S) vs. (1/P) plots (cf. Figure 5) and converted as described above to units of s<sup>-1</sup>. The  $k_a^\infty$  slope value for C<sub>2</sub>F<sub>6</sub> was corrected for the 6-mol % C<sub>2</sub>H<sub>6</sub> scavenging additive.

The  $k_a^\infty$ (exptl) values for C<sub>2</sub>F<sub>6</sub> and C<sub>2</sub>H<sub>6</sub> bath gases were (4.08 ± 0.14) × 10<sup>8</sup> and (1.02 ± 0.04) × 10<sup>9</sup> s<sup>-1</sup>. Here the cited uncertainties reflect only the random noise error components arising from data scatter. The  $k_a^\infty$  test for C<sub>2</sub>F<sub>6</sub> matches both the 10-kcal mol<sup>-1</sup> stepladder and the 4-kcal mol<sup>-1</sup> Gaussian models. The exponential model indicates a  $\langle \Delta E \rangle$  in excess of 12 kcal mol<sup>-1</sup>. The C<sub>2</sub>H<sub>6</sub> data fit 3-kcal mol<sup>-1</sup> stepladder, 2-kcal mol<sup>-1</sup> Gaussian, and 4-kcal mol<sup>-1</sup> exponential distribution models.



**Figure 5. Linear regression analysis plots used to determine the high-pressure unimolecular rate constants ( $k_a^\infty$ ). The slope of a linear (D/S) vs. (1/P) plot in the high-pressure region corresponds to  $k_a^\infty$ . Key to symbols: (●) C<sub>2</sub>H<sub>6</sub>, (▲) C<sub>2</sub>F<sub>6</sub> bath gas.**

The average numbers of cascade deactivation steps for the 10-kcal mol<sup>-1</sup> stepladder and 4-kcal mol<sup>-1</sup> Gaussian models are approximately 3.5 and 9, respectively. The matching of the experimental  $k_a^\infty$  value for C<sub>2</sub>F<sub>6</sub> for these highly different cascading models thus is surprising. Rather clearly, good agreement between  $k_a^\infty$  (exptl) and  $k_a^\infty$  ( $\langle \Delta E \rangle$ ) does not serve to identify a mathematically unique transition probability model or  $\langle \Delta E \rangle$  value. The  $k_a^\infty$  test is useful for investigating a particular  $\langle \Delta E \rangle$  value for a given model. However, it does not permit selection of the best model or  $\langle \Delta E \rangle$  value.

The usefulness of absolute  $k_a^\infty$  matching is severely limited by the validity of the assigned S<sub>CH<sub>3</sub>CF<sub>3</sub>-M</sub> values used for unit conversion. No reliable procedure is presently available for the independent specification of these values. It is also not clear that the  $\Omega^{(2,2)*}(T^*)$  Lennard-Jones gas-phase viscosity collision integral provides the proper realistic potential correction for the bimolecular collision rate. Further research is needed on this problem.

**Comparison of Pressure Falloff Curves.** The assignment of energy transfer models and  $\langle \Delta E \rangle$  values has often been based upon comparisons between the curvatures of experimental vs. calculated ( $k_a/k_a^\infty$ ) vs. ( $S/D$ ) plots. This type of comparison obviates the requirement for accurately known  $k_a^\infty$  values in s<sup>-1</sup> units, because the  $k_a$  values are scaled by dividing by  $k_a^\infty$ .

However, using the ( $k_a/k_a^\infty$ ) plotting scheme our experimental and calculated results did not yield quantitative consistency with any of the transition probability models throughout the full pressure range included in the measurements. To obtain the optimized matching results reported below, it has been necessary to scale the experimental ( $k_a/k_a^\infty$ ) results using empirically determined constant multiplicative factors. For the present plotting scheme these values were 1.16 and 1.19 for C<sub>2</sub>F<sub>6</sub> and C<sub>2</sub>H<sub>6</sub>, respectively. Scaling factors of similar magnitude are generally required for this mode of data analysis (3, 4).

The calculated log ( $k_a/k_a^\infty$ ) vs. log ( $S/D$ ) falloff curves for the three transition probability models have been intercompared in Figure 6. Subtle differences in curvature exist for these various hypothetical cascading models over the range  $0.001 < (S/D) < 0.4$ . However, from Figure 6 the slopes of all the calculated falloff plots increase monotonically with decreasing ( $S/D$ ), and thus also with diminishing pressure.

Our attempts to fit the measured falloff data for C<sub>2</sub>F<sub>6</sub> and C<sub>2</sub>H<sub>6</sub> bath gases using log ( $k_a/k_a^\infty$ ) vs. log ( $S/D$ ) plots for the various cascading models are shown in Figures 7 through 12. Figures 9 and 10 show that particular energy transfer models can be rationalized with the measured falloff data over narrow ranges of pressure. However, none of the

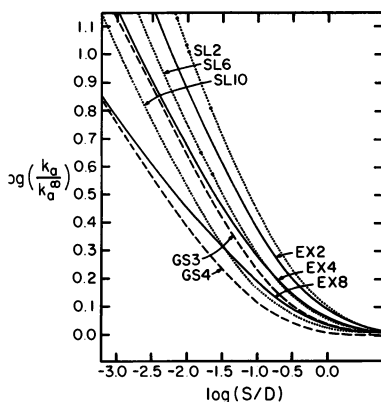


Figure 6. Plots of  $\log(k_a/k_a^\infty)$  vs.  $\log(S/D)$  for several theoretical models. The  $\langle \Delta E \rangle$  values in kcal mol<sup>-1</sup> have been indicated for each model.

presently tested models appears to be capable of representing all of our data for either bath gas.

Much of the difficulty with these comparisons results from apparent points of inflection in the experimental  $\log(k_a/k_a^\infty)$  vs.  $\log(S/D)$  plots that occur within the approximate range  $0.01 < (S/D) < 0.03$ . Further work is needed to permit more precise characterizations of the locations of these inflection points. The present authors are not aware of the existence of any previous high-precision falloff results measured within the above noted range for a chemically activated system. The sensitive region in which the discrepancies between measured and simulated

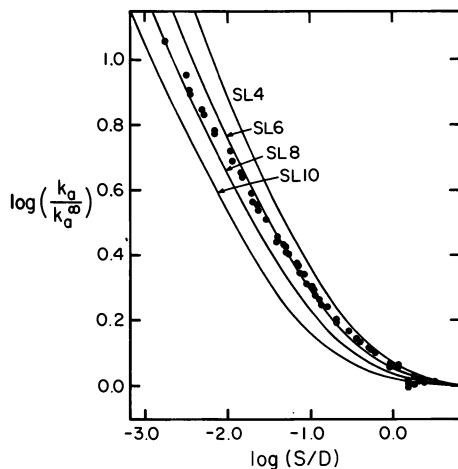


Figure 7. Stepladder model  $\log(k_a/k_a^\infty)$  vs.  $\log(S/D)$  cascading plots for  $C_2F_6$  bath gas. Calculated curves have been shown for several  $\langle \Delta E \rangle$  values. The data points represent experimentally measured values.

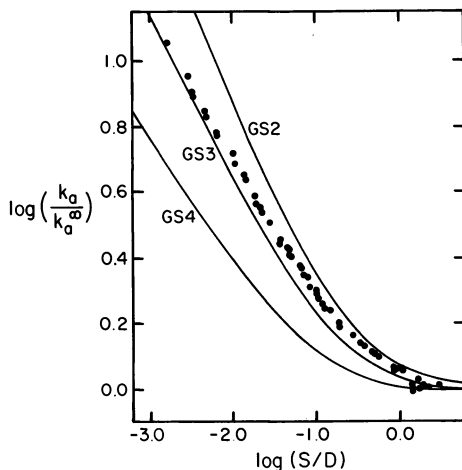


Figure 8. Gaussian model  $\log(k_a/k_a^\infty)$  vs.  $\log(S/D)$  cascading plots for  $C_2F_6$  bath gas

cascading results become serious appears to lie just outside the range of most of the available data.

The physical basis for the apparent inflection points in the  $\log(k_a/k_a^\infty)$  vs.  $\log(S/D)$  plots is presently uncertain. As noted above, we do not feel that this behavior can be ascribed to heterogeneous deactivation. One possible explanation could be based on an energy dependence for

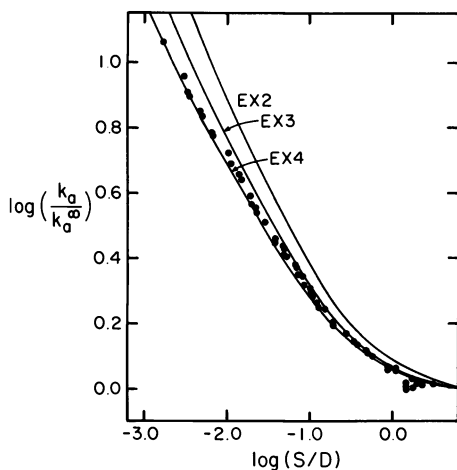


Figure 9. Exponential model  $\log(k_a/k_a^\infty)$  vs.  $\log(S/D)$  cascading plots for  $C_2F_6$  bath gas

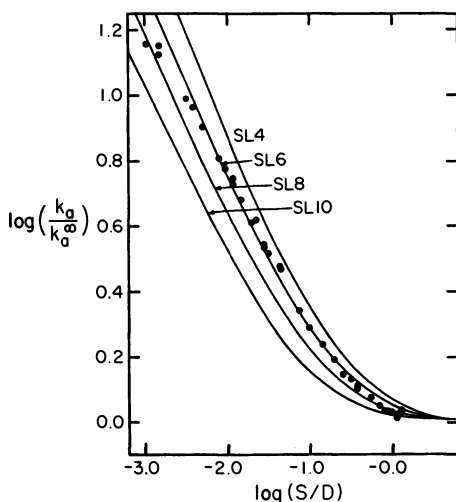


Figure 10. Stepladder model  $\log(k_a/k_a^\infty)$  vs.  $\log(S/D)$  cascading plots for  $C_2H_6$  bath gas

$\langle \Delta E \rangle$ . Larger  $\langle \Delta E \rangle$  values at higher energy levels for  $^{14}CH_3CF_3^\dagger$  could perhaps lead to an inflection point at small  $(S/D)$  values. Additional modeling calculations of more complex character are required to demonstrate this effect.

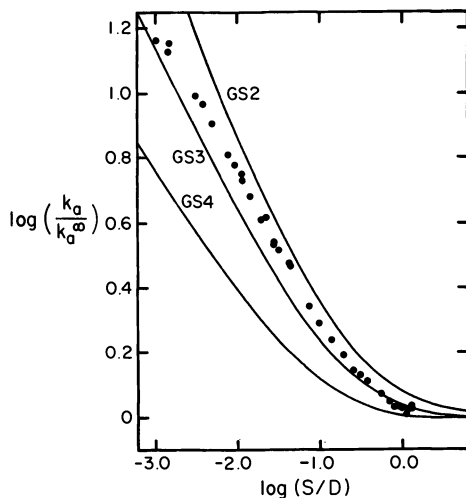


Figure 11. Gaussian model  $\log(k_a/k_a^\infty)$  vs.  $\log(S/D)$  cascading plots for  $C_2H_6$  bath gas

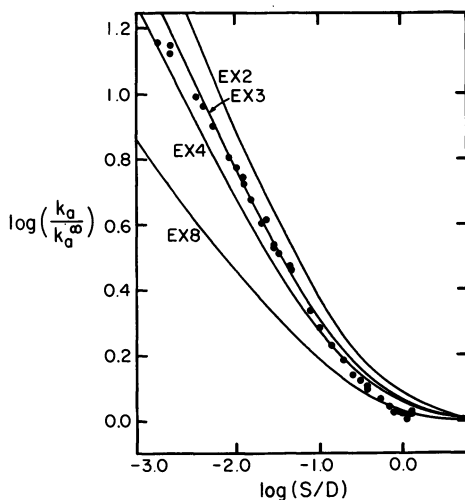


Figure 12. Exponential model  $\log(k_a/k_a^\infty)$  vs.  $\log(S/D)$  cascading plots for  $C_2H_6$  bath gas

An alternative plotting method for determining preferred energy transfer models and  $\langle \Delta E \rangle$  values involves unscaled rate constant vs.  $(S/D)$  ratio comparisons. Several calculated  $\log(k_a)$  vs.  $\log(S/D)$  plots for the three transition probability models have been shown in Figure 13. The exponential model gives larger calculated  $k_a$  values at a particular  $(S/D)$  ratio and displays less curvature than the stepladder or Gaussian models. Curvature differences between the models are apparently more evident using this plotting method.

Although the  $\log(k_a)$  vs.  $\log(S/D)$  testing scheme presupposes the existence of good agreement between measured and calculated  $k_a^\infty$  values,

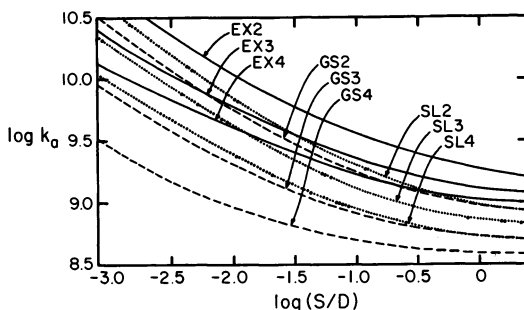


Figure 13. Plots of  $\log(k_a)$  vs.  $\log(S/D)$  for several theoretical models. The  $\langle \Delta E \rangle$  values in  $\text{kcal mol}^{-1}$  have been indicated for each model.

the experimental  $k_a$  results may still be scaled to obtain optimal curvature matching. Based on this technique the constant scaling factors determined for  $C_2F_6$  and  $C_2H_6$  were 1.29 and 1.26. These empirical factors are required to compensate for uncertainties in either the calculated  $k_B$ ,  $S_{CH_3CF_3-M}$ , or  $\epsilon_{CH_3CF_3-M}$  values (4). The scaled experimental data have been compared with the various energy transfer models in Figures 14 through 19. These results again demonstrate that the present cascading models are incapable of representing the full falloff data set for either bath gas.

### Discussion

The present results exhibit pronounced scatter in the high-pressure range ( $S/D$ )  $> 1$ , seriously limiting the accuracy of our  $k_a^\infty$  (exptl) values. This type of scatter has been a consistent feature of our studies with chemically activated  $^{14}CH_3CF_3$ . Collisional quenching of the electronically excited HFA photolysis precursor, which severely reduces the quantum yield for  $\dot{C}F_3$  radical production, is responsible for this nuisance problem (5, 14). Quenching of HFA at high pressures decreases the radioactive yield of  $^{14}CH_3CF_3$  from Reaction 3, leading to poor statistical accuracy for the measured  $^{14}CH_2CF_2$  and  $^{14}CH_3CF_3$  product yields.

Preliminary results recently obtained using a mixture of  $^{14}CH_3CO-^{14}CH_3$  and trifluoromethylazomethane ( $CF_3N_2CH_3$ ) as photolysis precursor largely circumvented the quenching problem. Precursor  $CF_3N_2CH_3$  is less subject to quenching than HFA (15). Based on this improved photolysis system, it is hoped that the accessible pressure falloff range can be extended in future experiments to  $0.001 < (S/D) < 10$ . Work along these lines is currently in progress.

**Significance of  $\log(k_a/k_a^\infty)$  vs.  $\log(S/D)$  Plots.** As shown in Figures 7 through 9, the best overall fit to the scaled  $C_2F_6$  falloff data was obtained for the 4-kcal mol $^{-1}$  exponential transition probability distribution model. Although the mid-range results deviate systematically from the model calculation, the 4-kcal mol $^{-1}$  curve more or less tracks the experimental data throughout the range  $0.0015 < (S/D) < 1$ . The stepladder and Gaussian models are consistent with the data over limited ( $S/D$ ) ranges, but no single model curve matches all of the measured falloff results. Interestingly, either the 6-kcal mol $^{-1}$  stepladder or the 3–4-kcal mol $^{-1}$  exponential model exhibits rather good consistency with the  $0.05 < (S/D) < 1$  truncated  $C_2F_6$  data set. This portion of our  $C_2F_6$  data corresponds to the conditions used for this species by Marcoux and Setser, whose preferred interpretation involved the 6-kcal mol $^{-1}$  stepladder model (4).

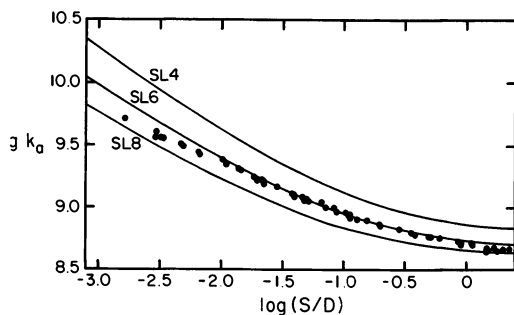


Figure 14. Stepladder model  $\log(k_a)$  vs.  $\log(S/D)$  cascading plot for  $C_2F_6$  bath gas

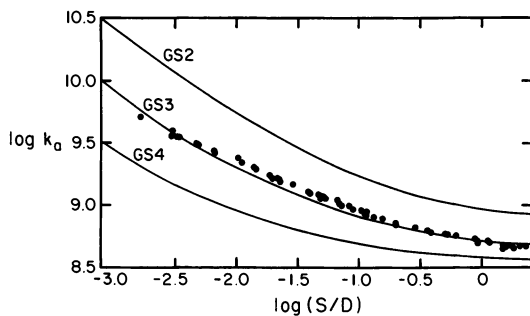


Figure 15. Gaussian model  $\log(k_a)$  vs.  $\log(S/D)$  cascading plot for  $C_2F_6$  bath gas

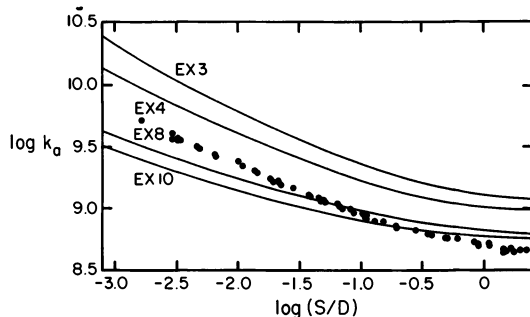


Figure 16. Exponential model  $\log(k_a)$  vs.  $\log(S/D)$  cascading plot for  $C_2F_6$  bath gas



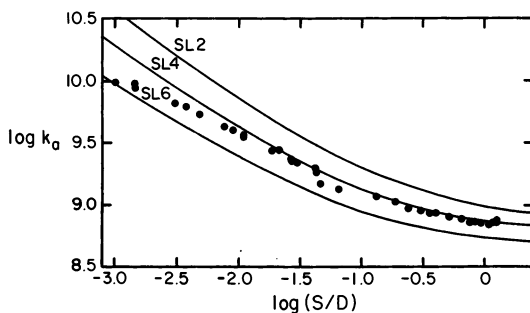


Figure 17. Stepladder model  $\log(k_a)$  vs.  $\log(S/D)$  cascading plot for  $C_2H_6$  bath gas

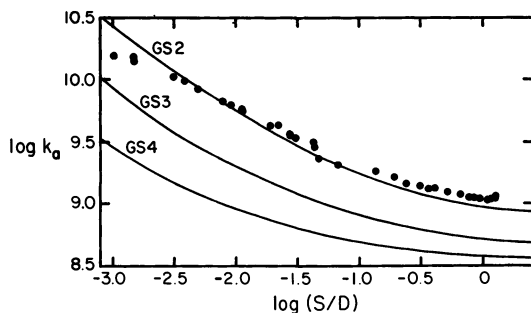


Figure 18. Gaussian model  $\log(k_a)$  vs.  $\log(S/D)$  cascading plot for  $C_2H_6$  bath gas

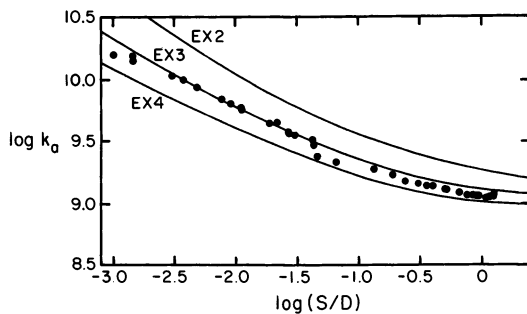


Figure 19. Exponential model  $\log(k_a)$  vs.  $\log(S/D)$  cascading plot for  $C_2H_6$  bath gas

Figures 10 through 12 show that none of the tested models successfully fits the  $C_2H_6$  data over the complete ( $S/D$ ) ratio range for any single  $\langle \Delta E \rangle$  value. The 6-kcal mol<sup>-1</sup> stepladder model exhibits good consistency with the  $0.006 < (S/D) < 0.4$  mid-range falloff results. The 2- and 3-kcal mol<sup>-1</sup> Gaussian distribution models bracket the measured results over the complete ( $S/D$ ) ratio range. The exponential distribution model provides the poorest fit to the  $C_2H_6$  data.

**Significance of log ( $k_a$ ) vs. log ( $S/D$ ) Plots.** From Figures 14–16, on a curvature matching basis either the 4-kcal mol<sup>-1</sup> exponential or the 3-kcal mol<sup>-1</sup> Gaussian model demonstrates reasonable consistency with the measured results. To obtain good matching for this exponential model, however, the data require scaling by a factor of 2.5. This uncertainty illustrates the importance of accurate knowledge of absolute  $k_a^\infty$  values for the log ( $k_a$ ) vs. log ( $S/D$ ) testing method.

Figures 17 through 19 show that the 2-kcal mol<sup>-1</sup> Gaussian and the 3-kcal mol<sup>-1</sup> exponential models both provide a limited degree of consistency with the  $C_2H_6$  falloff data. Neither model, however, represents the full  $C_2H_6$  data set.

### Summary

A summary of the best fits to our measured falloff results based on curvature matching has been presented in Table IV. We prefer the log ( $k_a/k_a^\infty$ ) vs. log ( $S/D$ ) mode of analysis due to its diminished dependence on the collision cross section input data and an absolute match to  $k_a^\infty(\langle \Delta E \rangle)$  (3, 4). The present simple cascading models cannot account for the points of inflection that are apparently characteristic of both of our extended falloff plots. Even if this effect is ignored, the present comparisons do not allow the choice of mathematically unique model types or  $\langle \Delta E \rangle$  values.

Our original goal of identifying preferred cascading models and  $\langle \Delta E \rangle$  values for  $C_2F_6$  and  $C_2H_6$  colliders has not been realized. However, these measurements have clearly demonstrated the feasibility of obtaining accurate low-pressure cascading falloff data based on the radio-

**Table IV. Summary of Best Fits Based on Curvature Matching**

<i>Bath Gas</i>	<i>Preferred Model and <math>\langle \Delta E \rangle</math> Value*</i>	
	<i>log(<math>k_a/k_a^\infty</math>) vs. log (<math>S/D</math>)</i>	<i>log(<math>k_a</math>) vs. log (<math>S/D</math>)</i>
$C_2F_6$	EX4	GS3, EX4
$C_2H_6$	GS3	GS2, GS3, EX3

\*  $\langle \Delta E \rangle$  values in kcal mol<sup>-1</sup>.

tracer technique as well as the importance of such information with respect to the detailed quantitative understanding of the cascading deactivation process. We feel that the radiotracer method should be utilized for obtaining accurate extended range pressure falloff data for other bath gases and other activated species. A substantial improvement in the experimentally accessible dynamic range should be possible for photolysis systems less subject to quenching. On the theoretical side, the origin of the above described points of inflection in the cascading falloff curves appears to be worth exploring.

### *Acknowledgments*

Financial support for this research has been provided by the U.S. Department of Energy under Contract No. AS03-76SF00034, Agreement No. AT03-76ER70158. The authors also thank Dr. Siu-Hong Mo and Dr. Richard Pettijohn for assisting with the early experiments and Mr. Robert Okamoto for synthesizing and purifying the the trifluoromethylazomethane.

### *Literature Cited*

1. Kohlmaier, G. H.; Rabinovitch, B. S. *J. Chem. Phys.* **1963**, *38*, 1692, 1709.
2. Tardy, D. C.; Rabinovitch, B. S. *J. Chem. Phys.* **1968**, *48*, 5194.
3. Chang, H. W.; Craig, N. L.; Setser, D. W. *J. Phys. Chem.* **1972**, *76*, 954.
4. Marcoux, P. J.; Setser, D. W. *J. Phys. Chem.* **1978**, *82*, 97.
5. Pettijohn, R. R.; Mutch, G. W.; Root, J. W. *J. Phys. Chem.* **1975**, *79*, 1747, 2077.
6. Mutch, George W., Ph.D. Dissertation, University of California, Davis, 1973; University Microfilms No. 74-8530.
7. Lucas, Larry L., Ph.D. Dissertation, University of California, Davis, 1973; University Microfilms No. 74-8523.
8. Robinson, P. J.; Holbrook, K. A. "Unimolecular Reactions"; John Wiley & Sons: New York, 1972.
9. Georgakakos, J. H.; Rabinovitch, B. S. *J. Chem. Phys.* **1972**, *56*, 5921.
10. Duewer, W. H.; Coxon, J. A.; Setser, D. W. *J. Chem. Phys.* **1972**, *56*, 4355.
11. Setser, D. W. *Phys. Chem., Ser. One* **1972**, *9*, 1ff.
12. General Program for Unimolecular Rate Constants Available Through the Quantum Chemistry Program Exchange, Indiana University, Chemistry Department, Program No. 234, R.R.K.M.
13. Hirschfelder, Joseph O.; Curtis, Charles F.; Bird, R. Byron "Molecular Theory of Gases and Liquids"; John Wiley & Sons: New York, 1964.
14. Whytock, D. A.; Kutschke, K. O. *Proc. R. Soc. Ser. A* **1968**, *306*, 503.
15. Craig, N. L.; Setser, D. W. *Int. J. Chem. Kinet.* **1974**, *6*, 517.

RECEIVED September 4, 1980.

# Crossed Beam Studies of Chemical Kinetics Using Radiotracer Techniques

GEORGE H. KWEI

University of California, Los Alamos National Laboratory,  
Los Alamos, NM 87545

*Radiotracer techniques have been used in crossed beam studies of the chemical kinetics of reactions in which: (i) product detection and/or discrimination in the presence of large backgrounds would be difficult using conventional techniques; (ii) detection of the labeled products provides improved kinematics; and (iii) the labeling itself provides the opportunity for studying isotope effects or new reactions involving radioisotopes. At the present, three pairs of systems have been studied. Studies of the  $K, Cs + TBr \rightarrow KBr, CsBr + T$ , and the  $H, D + T_2 \rightarrow HT, DT + T$  reactions using  $T$  atom collection and detection exemplify all three of the above features. On the other hand, the study of the  $Cl, Br + HAt \rightarrow HCl, HBr + At$  reactions provides information on two new reactions and illustrates the technique for short-lived isotopes. These studies clearly demonstrate the utility of radiotracer detection techniques in crossed beam studies. A discussion of the possible application of these techniques to the study of other chemical reactions and to photofragmentation processes concludes this review.*

In the early 1950s, when Taylor and Datz (1) were planning their pioneering crossed molecular beam reactive scattering experiments, they planned to use neutron activation analysis to measure the angular distribution of condensed product KBr molecules formed in Reaction 1



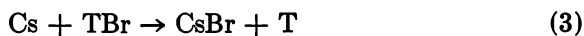
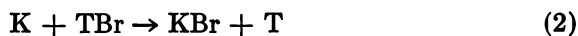
in the event that differential surface ionization for  $K + KBr$  and  $K$  on hot W and Pt filaments, respectively, failed. Preparatory experiments on

0065-2393/81/0197-0179\$07.00/0  
© 1981 American Chemical Society

the detection of trace quantities of bromine using neutron activation by Chastagner and Taylor (2, 3, 4) had already begun to show some promise, but the technique was never used in a scattering experiment. The discovery of the great sensitivity and selectivity of surface ionization for detection of alkali halides in the presence of alkali atoms (5, 6) was responsible for this and for the subsequent explosive growth in crossed beam kinetics that is now a part of history (7).

The complete dominance of surface ionization detection was somewhat unfortunate, since radiotracer techniques are extremely sensitive and, when coupled with a selectively adsorbing surface to distinguish products from reactants, are well suited for product detection in crossed beam experiments. Differing physical and chemical properties of reactants and products may be exploited so that only a product, which may either be radioactively labeled or later neutron activated, is adsorbed on a detector surface. For many atoms and free radicals, specific getter-surfaces are already known. To date, only three crossed beam studies using radioisotope detection have been reported. These studies illustrate the advantages of this technique in the study of reactions in which: product detection and/or discrimination in the presence of large backgrounds would be difficult using conventional techniques; detection of the labeled products improved kinematics; and the labeling itself provides the opportunity for studying isotope effects or new reactions involving radioisotopes.

Appropriately, the first chemical reactions studied using molecular beam techniques with radioisotope detection was an isotopic variant of Reaction 1, namely, Reaction 2, and the latter's Cs analogue (Reaction



3) (8). Surface ionization studies of Reaction 1 necessarily involved the detection of the much heavier product, KBr, which was constrained by the conservation of momentum to scatter close to the center of mass (c.m.). In this case, the small recoil velocity of the product KBr from the c.m. is masked by the spread of the c.m. velocity vectors arising from the distribution of parent beam velocities. Thus, it becomes difficult to extract any information about the motion of the KBr relative to the c.m., which would provide the desired description of the mechanism and energetics of the reaction (9). High velocity resolution experiments have since been done by Bernstein and coworkers (10, 11), but the studies of Reactions 2 and 3 by Martin and Kinsey (8) were the first to provide some information on the dynamics of these reactions from a measurement of product distributions. In these experiments tritium labeling allowed radioisotope

detection of the product T atoms, which are selectively adsorbed on MoO<sub>3</sub> detector surfaces. The detection of the lighter product provided greatly improved kinematics: the T atom recoil velocity is much larger than the velocity of the c.m., and the single-valued laboratory  $\longleftrightarrow$  c.m. transformation, to a good approximation, merely involves a rotation of coordinates. The measured laboratory angular distributions showed that Reactions 2 and 3 proceed via a direct rebound mechanism like their K + CH<sub>3</sub>I predecessor (12, 13, 14), in which the product T atoms scatter forward [and the complementary KBr (or CsBr) molecules backward] in the c.m. system with respect to the initial reactant K (or Cs) atom velocity. (We follow the usual convention of calling the scattering "forward" if the molecular product velocity is parallel to the initial reactant atom velocity in the c.m. system, and "backward" for the opposite situation. With this convention, the transferred particle continues to move in the same direction for backward scattering and changes direction for forward scattering; the "stripping" and "rebound" mechanisms then correspond to direct processes in which the newly formed molecule scatters forward and backward, respectively.) Fits to the data also suggested that the final recoil energy  $E'$  is less than the initial relative translational energy  $E$ . On the other hand, the subsequent surface ionization studies of Reaction 1 showed that the product KBr c.m. angular distributions are broadly backwards peaked for K + HBr and nearly isotropic for K + DBr; the recoil distributions also differ in that they are quite broad and extend to the maximum value allowed energetically (10, 11). Unfortunately the trends with the isotropic substitutions HBr  $\rightarrow$  DBr  $\rightarrow$  TBr predicted by these two experiments are not consistent, and the situation still remains unresolved.

The tritium labeling and detection technique developed by Martin and Kinsey (8) proved to be especially well suited to the study of the hydrogen-exchange reaction. The selectivity and cumulative feature of T-atom collection provides signal-to-noise ratios that are a considerable improvement over mass spectral studies, and the mass changes introduced by the labeling again provide much more favorable kinematics (15, 16). Thus the laboratory angular distributions for Reactions 4 and 5 do not



display the kinematic "edge" singularities present in the laboratory data for Reaction 6 (17), making comparison with theory difficult. The



angular distributions obtained in the tritium experiments showed that the hydrogen-exchange reaction proceeded via a direct rebound mechanism in qualitative agreement with the mass spectral results for Reaction 6. However, the dependence of the actual shapes of the angular distributions on collision energy range showed that the c.m. distributions must broaden or shift forward substantially with increasing collision energy and, when approximate theoretical distributions are properly averaged over collision energy, theory and experiment agree reasonably well (16, 18). The dominant effect of isotopic substitution is a change in kinematics, which results in different collision energy distributions. Use of theoretical H + H<sub>2</sub> distributions gives slightly better agreement for Reaction 5 than for Reaction 4; this could result either from an isotope effect or from an incorrect energy dependence of the theoretical c.m. cross sections. Product yields for Reactions 4 and 5 indicate a large isotope effect. However, reaction cross section ratios obtained from classical trajectory calculations on several different potential energy surfaces (19) do not show such a strong dependence on isotopic substitution.

The techniques of radioisotope detection of selectively adsorbed atoms have been extended to the detection of short-lived isotopes by Grover and coworkers (20–24) who measured angular distributions of <sup>217</sup>At formed in the Reactions 7 and 8 by counting the At atoms selectively



adsorbed on freshly deposited Te surfaces. From measured laboratory angular distributions, the authors were able to obtain crude c.m. angular and recoil velocity distributions that were in general agreement with the



results for Reaction 9 obtained from infrared chemiluminescence experiments (25), crossed beam mass spectrometric experiments (26), and classical trajectory calculations (27). In addition, an accurate on-line calibration of sticking coefficients has allowed a relatively precise determination of the reaction cross section at several different collision energies.

The experimental techniques used and the results obtained for all three systems will be discussed in greater detail in the following sections. The final section concludes the review with a brief discussion of future prospects for the use of radioisotope detection in the study of collision and photofragmentation dynamics.

**Experiments Using Long-Lived Radioisotopes**

**Studies of the Reactions of K and Cs Atoms with TBr Molecules.** Since the observed product KBr is so much heavier than its H-atom partner, it is restricted kinematically to a very slight recoil from the c.m. and resolution of the motion of KBr in the c.m. system becomes extremely difficult. However, since the KBr distribution closely follows the distribution of centroids and since the latter depends on the energy dependence of the reaction cross section, it has been shown that the data obtained by Taylor and Datz (1) is consistent with a reaction threshold of approximately 2.5 to 3.5 kcal/mol (28). The localization of the product recoil vectors in the laboratory also made it easier to determine the yield by integrating the product signals: this gave an estimate of 0.1 for the fraction of gas kinetic collisions that lead to reaction (1). There is no kinematic restriction for the nonreactive scattering of K atoms from HBr, and further information about the entrance channel for reaction has been obtained by studying the decrease of small-impact-parameter wide-angle nonreactive scattering events that results from reactive collisions (29, 30, 31). Using a two-body optical model, it has been possible to deduce information about interaction potentials, probability for reaction as functions of collision energy and impact parameter, and total reaction cross sections. For  $K + HBr$ , these experiments predict a much lower threshold energy ( $\sim 0.15$  kcal/mol) and a somewhat larger cross section ( $\sim 31 \text{ \AA}^2$  at a mean collision energy of 2 kcal/mol). The complementary information on the product channel angular and recoil velocity distributions has been much more difficult to obtain (9). Martin and Kinsey (8) reversed the unfavorable mass ratio and turned it to their advantage using tritium labeling and detection in studies of Reactions 2 and 3. In the remainder of this section, we will describe the techniques and results obtained from these experiments.

**COMPARISON OF REACTION KINEMATICS.** Figure 1 shows the average velocity vector diagrams for collisions between K atoms at 675 K and HBr (or TBr) at 300 K. The vectors  $V_K$  and  $V_{HBr}$  (or  $V_{TBr}$ ) are drawn for reactants emerging from the scattering center without colliding, so that the final position of the c.m. velocity vector,  $V_{c.m.}$ , which is conserved throughout the collision, can be drawn more easily. Energy conservation then requires that the products emerge within a sphere of radius  $V_{KBr}$  (or  $V_T$ ) drawn about the tip of  $V_{c.m.}$ . The average relative kinetic energy of the reactants is approximately 1.4 kcal/mol at these beam temperatures. The difference,  $Q = E' - E$ , between the final and initial relative kinetic energies can be at most 4.8 kcal/mol for  $K + HBr$ ; where 4.2 kcal/mol comes from  $\Delta D_0^\circ$ , the zero-point energy difference between products and reactants, and 0.6 kcal/mol comes from the average internal energy of



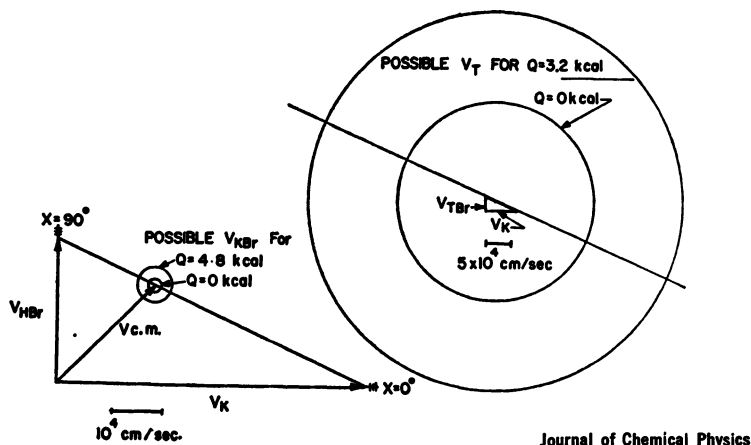


Figure 1. Velocity vector diagrams for Reactions 1 and 2 illustrating the striking improvement in kinematics for detection of product T atoms in Reaction 2 as compared with detection of product KBr molecules in Reaction 1 (8).

The left-hand figure shows the diagram for  $K(673 \text{ K}) + HBr(298 \text{ K})$  here the product KBr is restricted by the low exoergicity ( $Q_{max} = 4.8$  kcal/mol) and unfavorable mass ratio to lie within a small sphere about the tip of the c.m. velocity vector. The right-hand figure shows the corresponding figure (at 1/10th scale) for  $K + TBr$ ; here the allowed T-atom recoil velocity is much larger and the transformation between laboratory and c.m. angles is well defined.

HBr at 300 K. For  $K + TBr$ ,  $\Delta D_0^\circ = 2.6$  kcal/mol, so the maximum value of  $Q$  is lowered to 3.2 kcal/mol. The value of the recoil velocity  $V'_{KBr}$  (or  $V'_T$ ) will be determined by the value of  $E'$  and by the product mass ratio; for example for KBr formed in Reaction 1,

$$|V'_{KBr}| = [2E'm_H/m_{KBr}/(m_H + m_{KBr})]^{1/2}$$

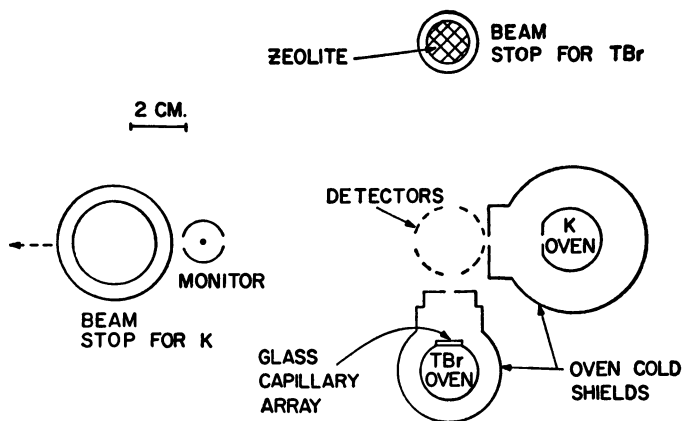
and the small mass ratio  $m_H/m_{KBr}$  will restrict all KBr product to scatter within the  $Q = 4.8$  kcal/mol circle shown in the lower left-hand side of Figure 1. Thus, the entire c.m. angular distribution will appear within a very small angular region in the laboratory, and the motion of the products with respect to the c.m. will be obscured by the distribution of centroids introduced by averaging over reactant velocities. For  $Q = 0$ , the situation becomes even worse. As can be seen in the upper right-hand diagram in Figure 1 (drawn at 1/10 the scale of the  $K + HBr$  diagram), the change to the larger mass ratio  $M_{KBr}/m_T$  reverses the situation and  $V'_T$  is much larger than  $V_{c.m.}$ , even for  $Q = 0$  kcal/mol. The transformation between laboratory and c.m. intensities is now well defined and, to a good approxi-

mation, the laboratory and c.m. systems differ merely by a rotation of coordinates. Under these conditions, velocity averaging of the centroid distribution will not obscure this transformation.

**EXPERIMENTAL DETAILS.** As shown in Figure 2, K (or Cs) atoms at 675 K (or 575 K, respectively) and TBr molecules at 300 K effuse from ovens equipped with multichannel slits and are further collimated by slits mounted on cold shields surrounding the ovens. Ribbon-shaped beams, 1 cm tall and approximately  $5^\circ$  wide, intersect at the scattering center at  $90^\circ$ ; atoms and molecules that escape a hard collision are trapped on beam stops to prevent them from reentering the interaction region. Angular distributions of reactively scattered T atoms are obtained by surrounding the scattering center with small aluminum plates uniformly coated with  $\text{MoO}_3$ ; these surfaces had previously been shown to be efficient "getter" surfaces for atomic hydrogen and, in these experiments, were found to have a low sticking coefficient for TBr molecules, the only other radioactive species present. After exposure (approximately 15 min), the detector plates are removed from the vacuum system via a vacuum lock and counted for the weak tritium  $\beta$ -activity in a windowless proportional counter well shielded from background.

The TBr was prepared by combining excess  $\text{Br}_2$  vapor with carrier-free  $\text{T}_2$  gas (obtained from New England Nuclear) and quantitatively converting the  $\text{T}_2$  to TBr on a red-hot Pt filament in a baked glass system. After removal of the excess  $\text{Br}_2$ , the TBr was frozen into a gold-plated stainless steel container and then transferred to the beam source.

The detectors were made from pure (Series 1100) aluminum plates with a coated area of  $3 \times 20$  mm. They were arranged cylindrically with their long dimension vertical about the line of intersection of the two vertical ribbon beams. The detectors were equally spaced (except for beam entrances and exits) and mounted on two aluminum support rings that formed the edges of a



Journal of Chemical Physics

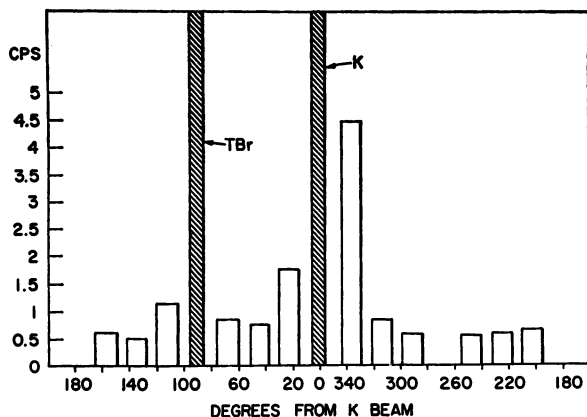
*Figure 2. Geometry of ovens and detectors (8). Twelve  $\text{MoO}_3$ -coated detector plates surround the scattering center on a 2.5-cm diameter circle. The alkali beam stop and the monitor detector are shown displaced to the right of their actual positions by 27 and 20 cm, respectively.*

cylindrical cage 25 mm in diameter and 40 mm tall. No part of this structure could be struck by either of the direct beams. With this geometry, each detector plate subtends  $14^\circ$  of in-plane angle.

The  $\text{MoO}_3$  coatings were applied by subliming  $\text{MoO}_2$  from a hot Mo filament in about 4 Torr of  $\text{O}_2$  and then oxidizing the  $\text{MoO}_2$  to  $\text{MoO}_3$  by heating the detector plates to 825 K in air. Extremely careful baking of the detectors was found to be necessary to obtain stable films, and the rate of heating and the final baking temperature both had to be precisely controlled (32).

The samples were counted in Matheson P-10 (10%  $\text{CH}_4$  in Ar) counting gas flowing through a modified Amperex 400PC windowless proportional counter. The counter was modified by replacing the anode with a 0.025-mm diameter W wire. Operating at a plateau of 1850 V, pulses of 10–14 mV across the 10 M $\Omega$  input load were counted in a pulse height analyzer. An overall counting efficiency for tritium adsorbed on  $\text{MoO}_3$  films of approximately 25% was estimated by dissolving some of the films in water, converting the water to hydrogen gas, and counting the gas in a batch-type proportional counter with known efficiency.

**RESULTS AND DISCUSSION.** Representative data for the  $\text{K} + \text{TBr}$  reaction are shown in Figure 3. The data are presented as bar graphs in which the heights are in measured counts per second (less a cosmic ray background of  $\sim 0.7$  cps and an isotropic system background of 0.2–0.6 cps due to residual TBr pressure in the system), and the angular widths and positions correspond to the angular widths and positions of the detectors. Reasonable counting errors are  $\pm 0.05$  cps. Since the observed peak in the T-atom distribution appears in the vicinity of elastically scattered K atoms, an experiment was performed to rule out the possible reaction of TBr molecules with adsorbed K atoms to produce false signals. In this experiment, four of the twelve detector plates were exposed to a K-atom beam to produce various amounts of discoloration

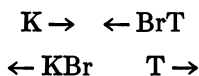


Journal of Chemical Physics

Figure 3. Tritium atom distribution for  $\text{K} + \text{TBr}$  (8). Beam exits are indicated by cross hatches.

after which all twelve were exposed to a transient of TBr; no correlation between counting rate and exposure to the K-atom beam was observed.

From Figure 1 it is clear that the reactive T-atom peak observed in Figure 3 corresponds to forward scattering of the T atoms (and, by momentum conservation, backward scattering of the companion KBr molecules) with respect to the initial K-atom velocity vector. Schematically, the collision proceeds in the following manner:



and the transferred Br atom continues to move in the same direction after the collision. This observed behavior is the same as had been previously observed for the analogous  $\text{K} + \text{CH}_3\text{I}$  reaction, which has now become a prototype example of the rebound mechanism. The wide spacing of points in the measured laboratory angular distribution makes it difficult to extract c.m. distributions in scattering angle and recoil velocity. However, fits to the laboratory data using various trial c.m. T-atom distributions separable in scattering angle and recoil velocity have shown that only narrow forward-peaked angular distributions with a full width at half maximum (FWHM) of less than  $30^\circ$  and a recoil velocity distribution with a mean recoil energy less than 0 kcal/mol are consistent with the data for both Reactions 2 and 3.

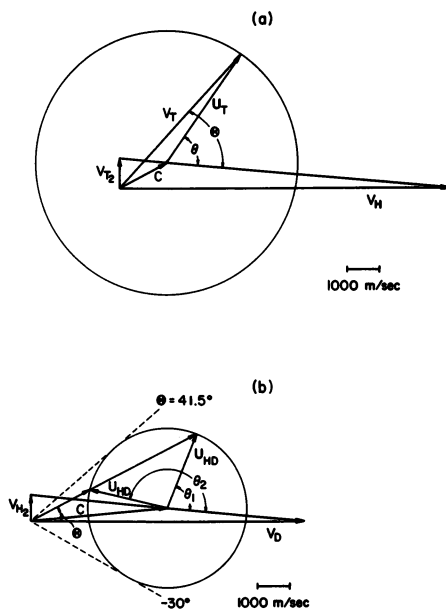
Shortly after these results were published, Bernstein and coworkers (10, 11) completed a crossed beam study of the reaction of K atoms with HBr and DBr, with velocity selection of the incident K-atom beam and velocity analysis of the KBr product. Analysis of the data showed that the product KBr c.m. angular distributions are broadly backward-peaked for  $\text{K} + \text{HBr}$  and nearly isotropic for  $\text{K} + \text{DBr}$  and that the recoil velocity distributions are broad and extend to the maximum value allowed energetically. These results differ considerably from the results for  $\text{K} + \text{TBr}$  since (i) when taken together, the angular distributions imply that the KBr product shifts nonmonotonically from broadly backward-peaked to nearly isotropic to sharply backward-peaked with the isotopic substitutions  $\text{HBr} \rightarrow \text{DBr} \rightarrow \text{TBr}$ ; and (ii) the mean recoil energy is much lower (and therefore the product excitation much higher) for  $\text{K} + \text{TBr}$ . These differences are still unresolved at this writing.

**Studies of the Hydrogen-Exchange Reaction: The Reaction of H and D Atoms with  $\text{T}_2$  Molecules.** The hydrogen exchange reaction serves as a prototype for bimolecular gas-phase exchange reactions and occupies a position of fundamental importance in the development of chemical kinetics (18, 33). Much attention has been lavished on this system both in the calculation of potential energy surfaces and in theo-

retical treatments of the evolution of the reaction on these surfaces. Classical studies of various isotopic combinations of this reaction in bulk gaseous mixtures and in flow systems now provide accurate rate constants for several reactions over a wide temperature range. However, the agreement of the experimental Arrhenius plots with latest rate calculations has not been entirely satisfactory and many questions remain unanswered. More detailed experimental information to provide us with a deeper insight into this reaction is therefore necessary.

A crossed-beam study of Reaction 6 using mass-spectrometric detection (17) showed that (i) the product HD scatters predominantly in the backward direction with respect to the incident D atoms, in general agreement with theoretical predictions of a rebound mechanism; (ii) the reaction cross section is in rough agreement with previous estimates; and (iii) the lock-in phase angle that maximizes the product signal gives a mean recoil velocity consistent with the condition that  $Q = 0$ . Unfortunately, although the kinematics are considerably better than for  $K + HBr$ , the laboratory  $\longleftrightarrow$  c.m. transformation is still double-valued. Since the recoil velocity distribution is narrow, the laboratory angular distribution is dominated by two "edge" peaks produced by singularities in the transformation. An accurate determination of the c.m. angular distribution would then require detailed knowledge of the apparatus resolution and the recoil velocity distribution, neither of which are very well known. This is demonstrated by the reasonably good agreement obtained in comparisons of crossed-beam (17) and trajectory (34) data in the laboratory when the latter is in fact approximately  $25^\circ$  broader (FWHM) in the c.m. system (35) (a more appropriate comparison of widths should include nearly twice the FWHM of the c.m. distribution, since contributions from both positive and negative c.m. angles are transformed to give the laboratory distribution).

Crossed beam mass-spectrometric studies of the hydrogen-exchange reaction are unfortunately very difficult. Some problems, like the high threshold and small reaction cross section, are inherent; but others, such as high backgrounds, beam impurities with interfering masses, difficulty in cryogenic trapping of hydrogen, and small ionization cross sections, are all problems associated with mass-spectrometric detection. These problems, together with the kinematic restrictions, can be avoided by using the tritium atom detection scheme developed by Martin and Kinsey (8). The low noise level provided by the selectivity for adsorption and detection, the elimination of small detector apertures [which also necessitate viewing factor corrections that plagued an earlier attempt to study Reaction 6 (36)], and the cumulative feature of T-atom collection and counting more than compensate for the low sensitivity inherent in tritium counting. As in the earlier  $K + TBr$  studies, the mass changes resulting



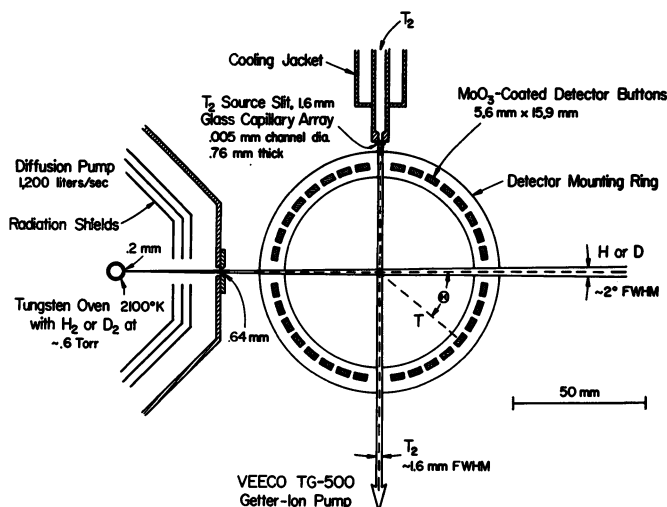
Journal of Chemical Physics

**Figure 4.** Velocity vector diagrams for Reaction 4 [panel (a)] and Reaction 6 [panel (b)] that illustrate the differences in the kinematics for the two systems (16).

These are drawn so that the laboratory molecular velocities,  $V_{T_2}$  and  $V_{H_2}$ , correspond to the most probable velocity at the experimental source temperature and the atomic velocities,  $V_H$  and  $V_D$ , correspond to the velocities necessary to give a relative velocity corresponding to the classical trajectory threshold energy. In panel (a), for product T-atom c.m. velocities,  $U_T$ , corresponding to  $Q = 0$  (the circle indicates the  $U_T$  loci), there is a one-to-one transformation between c.m. and laboratory scattering angles  $\theta$  and  $\Theta$ , respectively. For Reaction 5 [panel (b)], the velocity of the center of mass, C, is greater than the product HD recoil velocity (designated by the circle), and the transformation becomes double valued. For example, scattering at c.m. angles  $\theta_1$  and  $\theta_2$  both contribute to the signal at the laboratory angle  $\Theta$ . At the "edges" of the circle representing the  $U_{HD}$  loci (where  $\Theta \simeq 41.5^\circ$  and  $-28.5^\circ$ ), these branches coalesce to produce sharp singularities in the laboratory angular distribution.

from detection of the lighter atomic product again provide improved kinematics and result in a single valued laboratory  $\longleftrightarrow$  c.m. transformation and a more efficient laboratory  $\longleftrightarrow$  c.m. conversion of the collision energy.

**COMPARISON OF REACTION KINEMATICS.** Figure 4 compares the most probable threshold velocity vector diagrams for Reactions 4 and 6. For both diagrams, the velocity vector for the molecular beam is drawn to correspond to the most probable velocity at the temperature of the beam source used in the experiments (300 K for  $T_2$  and 77 K for  $H_2$ ). The atomic beam velocity is then drawn so that the relative collision



Journal of Chemical Physics

Figure 5. Schematic of the crossed molecular beam apparatus (16).

Molecular beams of H (or D) and  $T_2$ , formed by effusion, intersect at the scattering center at  $90^\circ$ . Reactively scattered T atoms are collected on  $MoO_3$ -coated detector buttons that are equally spaced at  $10^\circ$  intervals on a 5.6-cm diameter circle. Gas inlet lines, vacuum lock, chamber walls, and other vacuum hardware are not shown.

energy to the classical trajectory (19) collision threshold for reaction (0.32 eV for Reaction 4 and 0.26 eV for Reaction 6). The circles represent the loci of the tips of the recoil velocity vectors for  $Q = 0$ .

As shown in Figure 4a, the reaction  $H + T_2$  with product tritium atom detection represents a case where the magnitude of the velocity of the center of mass  $|C|$  is less than the magnitude of the recoil velocity  $|U_T|$ . In this case, there is a one-to-one correspondence between the signal at a given laboratory angle  $\Theta$  and the signal at the corresponding c.m. angle  $\theta$ . For  $D + H_2$  with product HD molecule detection (Figure 4b),  $|C| > (U_{HD})$  and all scattering is restricted to the angular range  $\Theta = -28.5^\circ$  to  $41.5^\circ$  in the laboratory. The transformation is double-valued within this angular range and the Jacobian for the transformation displays singularities near the "edges" of this range. These singularities arise from the  $\cos(\mathbf{V}_{HD}, \mathbf{U}_{HD})$  term in the denominator of the Jacobian for the transformation between c.m. and laboratory intensities over surface elements corresponding to a fixed value of  $|U_{HD}|$ . If a distribution of  $|U_{HD}|$  is allowed, the appropriate transformation involves volume elements and the cosine term does not appear. Therefore, the sharpness of the singularity will depend sensitively on apparatus resolution, which tends to integrate over the singularity, and on the width of the recoil velocity distribution, which weakens the effect of the cosine term.

Measurement of product velocity distributions was not feasible in the  $D + H_2$  study; however, even in experiments where the recoil velocity distribution is accurately measured, it is difficult to extract a c.m. cross section due to the difficulty of estimating a resolution that depends on beam shapes, detector geometry, and electron density gradients in the ionizer.

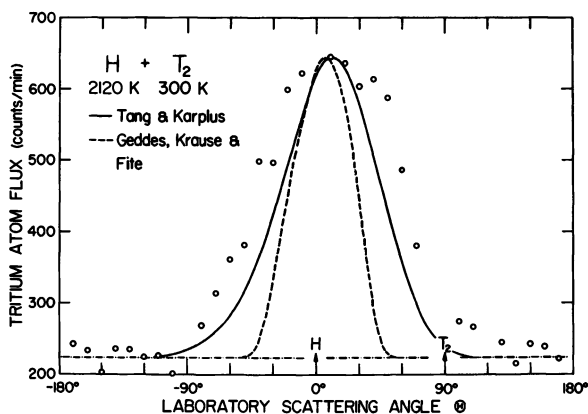
**EXPERIMENTAL DETAILS.** The salient features of the experimental apparatus, which is very similar to the apparatus used by Martin and Kinsey, are shown in Figure 5. An H-atom beam, formed by thermal dissociation of  $H_2$  at 2120 K or 2600 K and approximately 0.5 Torr in a differentially pumped source chamber, intersects at  $90^\circ$  a  $T_2$  (4% in  $H_2$ ) beam effusing from a glass capillary source at 300 K and a total pressure of approximately 0.05 Torr. Thirty-two  $MoO_3$ -coated detector "buttons" equally spaced (except for beam entrances and exits) at  $10^\circ$  intervals in the plane of the crossed beams collect the reactively scattered T atoms. A 4-in. diameter (nominal) diffusion pump maintains a vacuum within the range of 5–10  $\mu$ Torr in the H-atom source chamber, while a trapped and valved getter-ion pump facing the  $T_2$  beam source serves as a beam trap and maintains a vacuum of 1  $\mu$ Torr in the collision chamber. Five-minute runs alternate with five-minute "rest" periods during which the beam sources are turned off, the chamber walls surrounding the atomic beam source are allowed to cool down, and a fresh getter surface is sometimes sublimed onto the interior of the valved-off getter-ion pump. Upon completion of the experiment (approximately 2.5 h total elapsed time), the buttons are removed from the collision chamber through a vacuum lock; the  $MoO_3$  coatings are then scraped into counting vials and suspended in a gel with a phosphor. Each sample is then counted in an automated liquid scintillation counter.

With the exception of the use of liquid scintillation counting, the detection scheme used was identical to that of Martin and Kinsey. In the initial stages of these studies, an attempt was made to count the radioactivity on each detector button using a gas-flow windowless proportional counter. However, difficulty was experienced with erratic count rates and high backgrounds. Liquid scintillation counting also gave a counting efficiency of  $53.5 \pm 5\%$ , which is substantially higher than that obtainable with surface counting.

Since the cross section for reaction is much smaller than the reaction cross section for  $K + TBr$ , even small spurious signals could contribute to give an erroneous result. A number of experiments were carried out to verify the absence of such signals: these established that (i) the sticking coefficient for  $T_2$  molecules striking the  $MoO_3$  surfaces is small enough that it will not interfere with the reactive signal; (ii) the thermal dissociation of background  $T_2$  on the hot atomic beam source surface does not contribute to the signal; and (iii) the reaction of H or D atoms with  $T_2$  molecules on the detector surfaces is unimportant. These sources of error would all be expected to produce signals that are symmetric in the laboratory about one of the parent beams. Since the observed distributions of reactively scattered T atoms are distinctly asymmetric, it is clear that none of the above problems can be serious, even without the results of these independent confirmatory experiments.

**RESULTS AND DISCUSSION.** The experimental data for the reactions  $H + T_2$  (Reaction 4) and  $D + T_2$  (Reaction 5) are shown in Figures 6 and 7, respectively; data for Reaction 4 with the H-atom beam source





Journal of Chemical Physics

**Figure 6.** Complete in-plane laboratory angular distribution of reactively scattered T atoms formed in the reaction of H atoms (at 2120 K) with  $T_2$  molecules (at 300 K) (16).

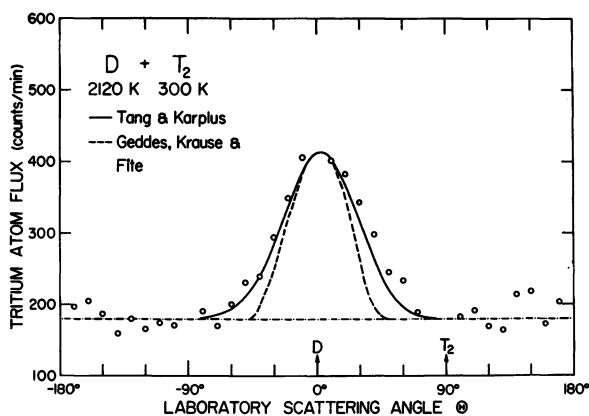
The solid curve is obtained by transforming the linear distorted-wave Born approximation predictions for  $H + H_2$  (37) to the laboratory system and then averaging the results over the appropriate recoil energy distribution. The dashed curve is obtained from an energy-independent c.m. angular distribution fit to the experimental data for  $D + H_2$  (17) and transformed to the laboratory and energy averaged. Energy-dependent reaction cross sections for  $H + T_2$  obtained from classical trajectory calculations on the Porter-Karplus potential energy surface (19) were used for weighing both energy averages.

at the higher temperature of 2600 K is not shown. As can be seen by referring to the velocity vector diagram in Figure 4a, the observed peaks at small laboratory angles for both Reactions 4 and 5 consist of T atoms that are scattered forward in the c.m. system, along the initial atomic beam velocity; by conservation of momentum, the product HT and DT molecules are scattered backwards. These angular distributions imply that these reactions proceed via a direct rebound mechanism in the collision energy range studied. This finding is consistent with the earlier crossed beam mass-spectrometric study of Reaction 6 (17) and with theoretical predictions and expectations (18).

The laboratory angular distributions ranging from approximately  $70^\circ$  FWHM for Reaction 5 to approximately  $110^\circ$  FWHM for Reaction 4 (at the higher H-atom source temperature of 2600 K, the distribution broadens to  $\sim 125^\circ$  FWHM). Since the laboratory  $\longleftrightarrow$  c.m. transformation is closely approximated by a rotation of coordinates and both  $\theta$  and  $-\theta$  c.m. scattering angles contribute to the laboratory distribution, the averaged c.m. angular distributions will have roughly half the widths of the laboratory distributions. A more quantitative description of the shape of the averaged c.m. cross section can be obtained in the customary way (when molecular beam data without velocity analysis is not available):

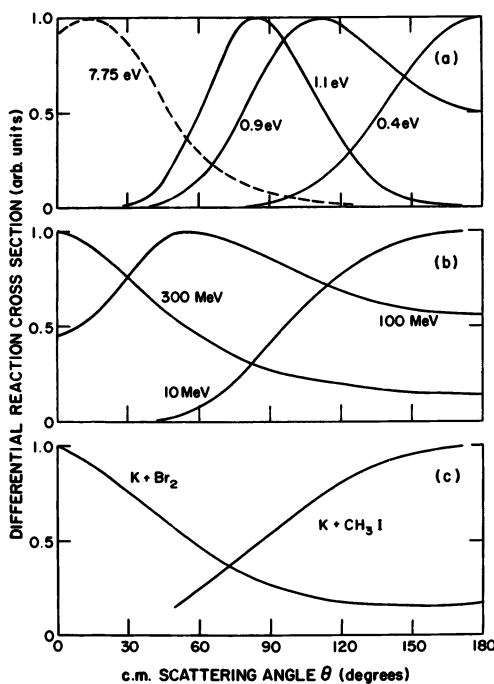
a separable c.m. cross section in scattering angle  $\theta$ , recoil velocity  $|U'|$ , and initial relative velocity  $|V|$  is assumed, and the two latter terms are chosen or varied to fit a c.m. angular distribution to the laboratory data. This was done earlier for illustrative purposes (15), when a c.m. angular distribution with a FWHM of approximately  $86^\circ$  provided a good fit to the laboratory data for Reaction 4 at the lower H-atom source temperature at 2120 K. However, at the same time it was pointed out that the separability assumption breaks down severely for this reaction since the recoil velocity and scattering angle are strongly coupled for this reaction, as both theory and these experiments have shown. Therefore, a c.m. angular distribution obtained in this manner has little meaning, and it is more appropriate to compare assumed c.m. distributions with the experimental data in the laboratory system.

As shown in Figure 8a, both classical and quantum mechanical scattering calculations show a strong backward-to-forward shift in the c.m. angular distribution of the molecular product as the collision energy increases (e.g., as the reaction mechanism changes from rebound to stripping). Since these calculations also predict that  $Q = 0$  (at least at lower collision energies), the recoil velocity and scattering angle become strongly coupled. This is also evident from the experimental data for Reactions 4 and 5. Since the more favorable kinematic conversion of laboratory translational energy and the higher beam source temperature also used in a study of Reaction 4, the systems Reaction 5 (2120 K)  $\rightarrow$  Reaction 4 (2120 K)  $\rightarrow$  Reaction 4 (2600 K) sample increasingly higher



Journal of Chemical Physics

**Figure 7.** Complete in-plane laboratory angular distribution of reactively scattered T atoms formed in the reaction of D atoms (at 2120 K) with  $T_2$  molecules (at 300 K) (16). Energy-dependent total reaction cross sections for  $D + T_2$  used for weighting in the energy averaging are from (19). Other notation as in Figure 6.



Journal of Chemical Physics

Figure 8. Comparison of c.m. angular distributions for various direct interaction processes illustrating the backward-to-forward shift with increasing collision energy (16).

(a) Angular distributions (—) from linear DWBA calculations for  $H + H_2$  from (37) and (---) from classical trajectory calculations for  $T + H_2$  from (35). (b) Calculated angular distributions of protons produced in a (d,p) reaction on a  $Z = 92$  nucleus (40). (c) Angular distributions of product alkali halide molecules formed in the reactions  $K + Br_2$  (41) and  $K + CH_3I$  (13) at thermal energies. Not all data from (37), (35), and (40) are shown.

effective collision energies. The observed increase in the widths of the laboratory angular distributions then implies that the c.m. angular distributions either broaden rapidly or shift in the forward direction as the collision energy increases.

This broadening or shift is illustrated in comparisons of experimental angular distributions with the transformed and averaged c.m. cross section extracted by Geddes et al. (17) despite the unfavorable transformation kinematics. The c.m. angular distribution was obtained by assuming independence of recoil energy and equality of the initial and final collision energies; the latter assumption is, of course, well supported by their measurements of the phase shift of the scattered products and by theoretical calculations. Their c.m. distribution is then transformed to the laboratory with  $Q = 0$  and collision energy averaged with the appropriate

classical trajectory cross sections (19) to give laboratory angular distributions corresponding to the isotopic masses and beam source temperatures corresponding to Figures 6 and 7. The results are shown as dashed curves in these figures. The agreement between the transformed distributions, which correspond to the lowest mean collision energy, and the data for Reactions 4 and 5, which correspond to higher mean collision energies, is poor and worsens as higher effective collision energy ranges are explored. This suggests that a collision energy dependent c.m. angular distribution is necessary and reemphasizes the difficulty of obtaining c.m. angular distributions when separability cannot be invoked.

Theoretical predictions of this forward-to-backward shift are illustrated in Figure 8a. This panel displays results from both a quantum mechanical distorted-wave Born approximation (DWBA) calculation (37, 38, 39) and a classical trajectory calculation (35) (at  $\sim 0.4$  eV, the classical results nearly coincide with the DWBA results). The DWBA c.m. angular distributions give much better agreement with the experiment when transformed and collision energy averaged (solid curves in Figures 6 and 7). This backward-to-forward shift with collision energy is in fact a familiar feature of direct interaction mechanisms, and examples can be found both in nuclear reactions (40) and in the alkali reactions studied in earlier crossed-beam experiments (12, 13, 14, 41). For deuteron stripping (d,p) reactions in a coulomb field, the scattering is predominantly backward when the incident energy is small compared with the coulomb barrier but shifts to the forward direction at higher incident energies (see Figure 8b) or for lighter nuclei (40). Similarly, in the reaction of K with  $\text{CH}_3\text{I}$  at thermal energies, the strong product repulsive interactions lead to backward scattering of the product KI and rebound behavior (12, 13, 14); while for the reaction of K with  $\text{Br}_2$  at similar energies (41), a larger range of impact parameters leads to reaction and the product interaction is much weaker, which both contribute to produce a forward-peaked KBr distribution characteristic of a stripping mechanism (Figure 8c).

No recoil velocity data are available from these experiments. In all data analysis,  $E = E'$  was used for want of a better assumption. Both the data of Geddes et al. (17) and theoretical calculations support this assumption. The quality of fit to the data shown in Figures 6 and 7 for both branches of the DWBA c.m. cross sections provides some additional support.

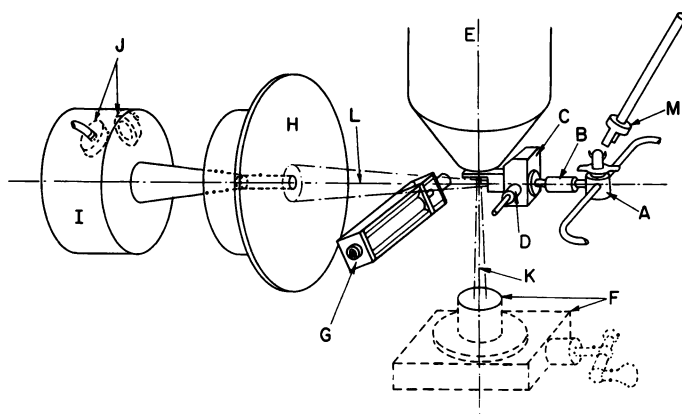
Ideally, one wishes that experimental results could help distinguish between various scattering calculations or between differing potential energy surfaces. Clearly, the distributions shown in Figures 6 and 7 indicate that there is a backward-to-forward shift in the angular distribution as the collision energy is increased. The shift predicted by the

DWBA calculations is not sufficiently rapid; however, it is not clear if this shortcoming results from the approximate nature of the calculation, from inaccuracies in the semiempirical potential energy surface used, or from the use of angular distributions calculated for the  $H + H_2$  reaction for the isotopic Reaction 4 and 5. Accurate scattering calculations (18) have been carried out for the  $H + H_2$  system on the semiempirical Porter-Karplus (PK) surface (42) (although these cover too small a collision energy range for use in comparison with the beam data); calculations extending the collision energy range and using isotopic masses corresponding to Reactions 4 and 5 on both the PK surface and the recently available accurate ab initio surface (SLTH) (43, 44) should be carried out. On the experimental side, an effort should be made to study these experiments with greater collision energy resolution. With current nozzle technology and with the development of arc-heated nozzles (45), this should be possible. Since the PK and SLTH surfaces differ more in their prediction of cross-section values near threshold than in the prediction of reaction dynamics (46), accurate experimental estimates of reaction cross sections in this region should be especially useful.

### *Experiments Using Short-Lived Radioisotopes*

At the time that the work of Martin and Kinsey (8) appeared, Grover and coworkers were beginning to develop techniques for crossed-beam studies of chemical reactions using short-lived radioisotopes. Both beam source (20, 21) and detector surfaces (22) had to be developed. With short-lived species (nuclides with half-lives in the range  $10^{-5}$ – $10^{-1}$  s), the beam particles have to be generated on-line, either as a daughter of a longer-lived species or, more generally, using a nuclear accelerator source, and the necessary chemistry has to be done within the source. Formation of a beam of the desired radioisotopic and chemical purity then becomes a major challenge. Grover et al. (20, 21) found that beams of HAt made with 0.032 s  $^{217}\text{At}$  could be formed by prompt emanation from parent 10-day  $^{225}\text{Ac}$  embedded in a lanthanum stearate matrix. Organic compounds of At are formed as well but are removed from the beam with a Pt "scrubber." This scrubber can also be heated to produce an At atomic beam by thermal dissociation of the HAt molecules. Many different metallic surfaces were tested for differential sticking coefficients for At and HAt. Of these, Te surfaces were found to be the most suitable, with sticking coefficients of 0.7–0.9 for At and not greater than  $10^{-4}$  for HAt. These two developments made it possible for Grover et al. (24) to study Reactions 7 and 8. This work is described in the following sections.

**Experimental Details.** A view of the essential parts of the crossed-beam apparatus using short-lived radioisotope labeling and detection is shown in Figure 9 (23). An HAt beam is produced in the beam source (A) from the



Review of Scientific Instruments

**Figure 9.** View of the essential parts of the crossed beam apparatus using short-lived radioactive labeling and detection (23): A, radioactive beam source; B, scrubber-furnace; C, LN<sub>2</sub>-cooled collimator; D, shut-off plug; E, nozzle beam furnace and cryopump; F, gate valve; G, hodoscope; H, LN<sub>2</sub>-cooled beam trap; I, calibrated beam monitor; J, silicon surface barrier detectors; K, halogen crossed beam; L, radioactive beam; M, rotary feed-through used to close the source stopcock.

decay of 10-day <sup>225</sup>Ac embedded in a lanthanum stearate matrix, is stripped of organic astatide impurities (or heated to thermally dissociate the HAt molecules to At atoms) in a Pt scrubber-furnace (B), and finally is collimated by a liquid nitrogen cooled beam collimator. The HAt beam is crossed at the scattering center by a beam of Cl (or Br) atoms that are formed by thermal dissociation in resistance-heated mullite beam source located inside the liquid nitrogen cooled cryopump (E). Reactively scattered At atoms are collected on a thin film of Te on the surface of a rotating drum and the  $\alpha$ -activity is detected successively by three surface barrier detectors. Single channel analyzers windowed at 7.06 MeV count the signal pulses as the drum rotates the collected atoms into the view of the detectors. The Te-coated drum is sufficiently long to accommodate five sets of surface barrier detectors so that signals at one in-plane and five out-of-plane laboratory angles can be collected simultaneously at a given in-plane angle. The mean distance of the detectors from the scattering center is 9.8 cm, and the in-plane detector aperture is 2.54 cm high by 2.0 cm wide (giving an approximate angular resolution of 15° by 12°). Part of the HAt parent beam is trapped on a liquid nitrogen cooled surface (H), but the central portion enters a calibrated beam monitor (I and J) through a small tunnel. Undeflected Cl (or Br) atoms (K) continue traveling through a gate valve (F), captured in a cold trap, and are subsequently analyzed to obtain a measure of the Cl or Br beam intensity.

**Results and Discussion.** Experimental distributions of reactively scattered At atoms taken at various out-of-plane laboratory angles  $\Phi$  as a function of in-plane angle  $\Theta$  are shown in Figure 10 for Reaction 7 at a collision energy of 6.5 kcal/mol (24). The data for Reaction 8 at the same collision energy is similar, but the signals are substantially lower

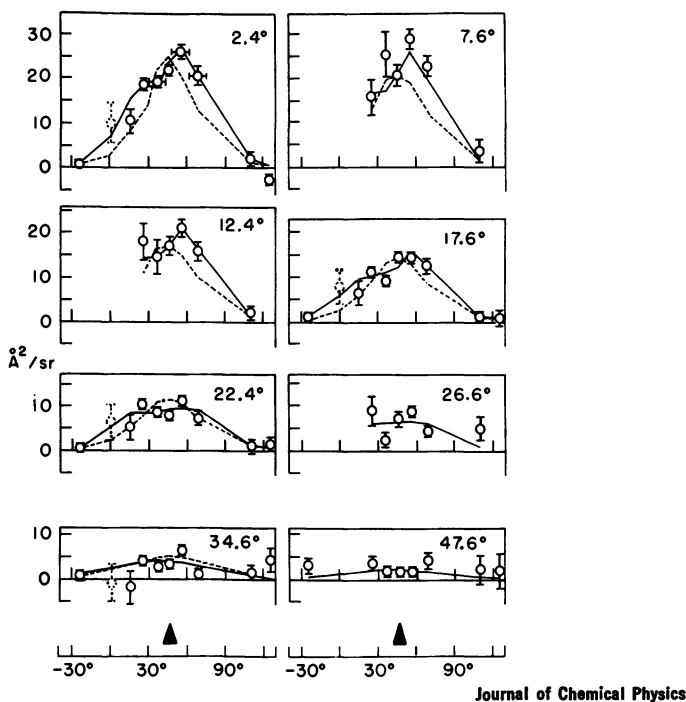


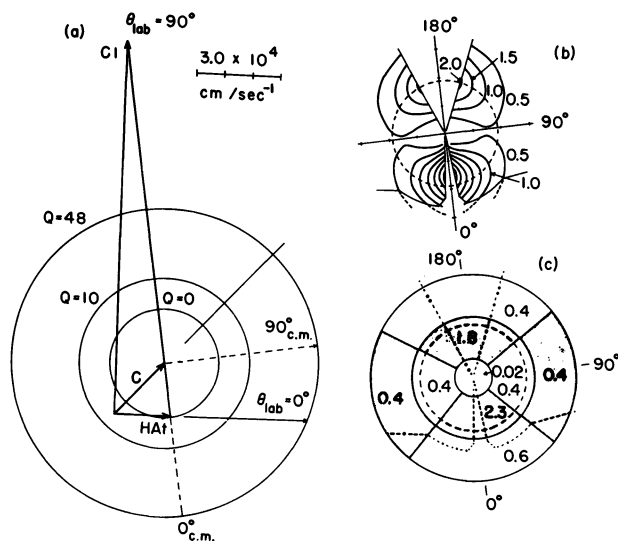
Figure 10. Experimental data for Reaction 7 (24).

*In-plane laboratory scattering angles  $\theta$  are plotted on the abscissas while the out-of-plane laboratory scattering angle  $\Phi$  is shown in the upper right-hand corner of each panel. The position of the c.m. vector is given by  $\Phi = 0$  and  $\theta$  corresponding to the location of the solid triangles. Data points are shown with vertical error bars giving the standard deviation of counting statistics and some horizontal error bars indicating the angular acceptance of the detectors. The data points at  $\theta = 0$  may be subject to unidentified systematic errors and are shown dashed. The solid curves represent fits to the laboratory data using the histogram c.m. distribution from Figure 11c. The dashed curves are from an unacceptable histogram solution constrained to have an isotropic angular dependence.*

and the angular distributions are narrower in both in-plane and out-of-plane dimensions. Both distributions peak near the c.m. and are nearly symmetric about the direction of the c.m. vector. This means that for both reactions, products are scattered in the forward and backward directions with nearly equal intensity. The relatively narrow width of the angular distributions suggest that the product recoil velocities are low, especially for Reaction 8, and the measured out-of-plane distributions play an important role in fitting the average recoil velocity.

More detailed information is obtained from fits of assumed c.m. cross sections to the laboratory data. Figure 11 shows a velocity vector diagram for Reaction 7 together with two of the best-fit cross sections

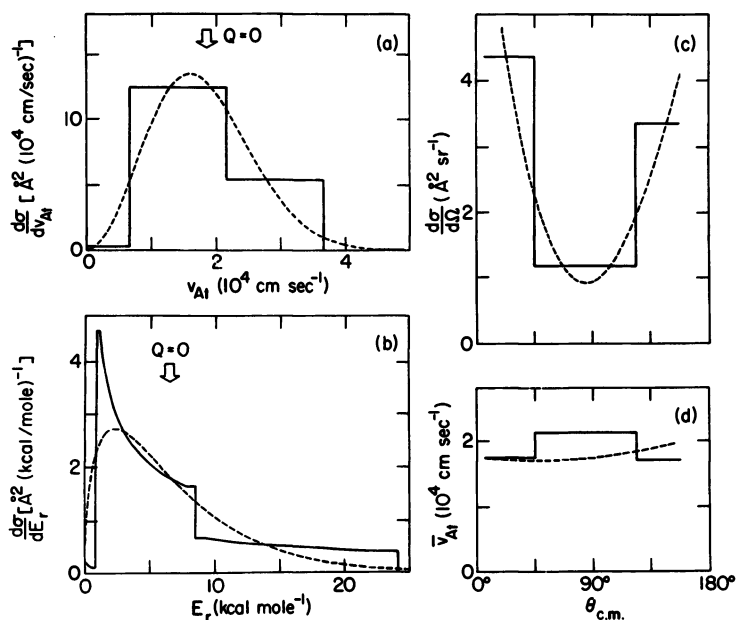
obtained; the latter are drawn to the same scale and with the same orientation as the vector diagram so that they can be superposed on the diagram merely by a translation. The two fits shown in Figures 11b and 11c have very different functional forms, one being analytic and the other histogrammatic. However, with the exception of a somewhat larger cross section for sideways emission of higher velocity products in the histogram solution, the two fits are in general agreement. Both show that the product At distribution is peaked in the forward ( $\theta = 0^\circ$ ) and backward ( $\theta = 180^\circ$ ) directions in the c.m. system, with perhaps a slightly higher peak forward. The average final energy in product translation is  $7.2 \pm 0.6$  kcal/mol (of an estimated total available energy of  $\sim 55$  kcal/mol), and there is only weak or no coupling of scattering angle and recoil velocity within the experimental uncertainty. The calculated laboratory cross sections obtained by transforming and averaging the histogram fit in Figure 11c are shown as the solid curves in Figure 10 and show the quality of the fit. Results of a poor fit in which the  $\theta$ -dependence of the cross section was suppressed are also shown (dashed curves).



Journal of Chemical Physics

**Figure 11.** (a) Velocity vector diagram for Reaction 7. The  $Q = 48$  kcal/mol spherical surface is the locus of product At atoms for which the entire reaction exoergicity goes into translation, while the  $Q = 0$  surface is one for which none of the exoergicity appears as translation. (b) Center-of-mass velocity-angle contour diagram used to fit the laboratory data. Lines show loci of constant cross section in units of  $A^2 \cdot (10^4 \text{sr} \cdot \text{cm/s})^{-1}$ . The dashed circle gives the locus for  $Q = 0$ . (c) Alternate histogram c.m. velocity-angle contour diagram used to fit the laboratory data. Notation is the same as in (b). Both (b) and (c) are drawn to the same scale as (a), and their  $0$ - $180^\circ$  axes are aligned with the same axis as in (a) (24).





Journal of Chemical Physics

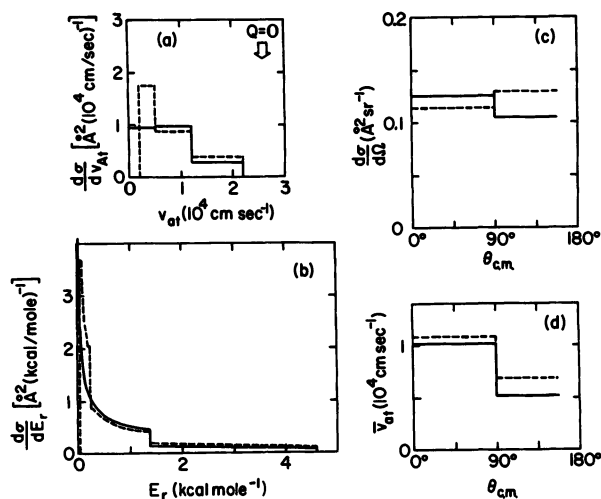
**Figure 12.** Partially integrated c.m. distributions for Reaction 7 corresponding to the c.m. distributions in (---) Figure 11b and (—) 11c (24). (a) Velocity distributions integrated over scattering angle. (b) Recoil energy distributions, integrated over scattering angle. (c) Angular distributions, integrated over product velocities. (d) Mean product velocity as a function of scattering angle.

Partially integrated c.m. distributions corresponding to the fits given by Figures 11b and 11c are shown in Figure 12 and again reveal the similarity of the two solutions. Both fits show that (i) the cross section peaks at low recoil velocities with an average value  $\leq 2 \times 10^4$  cm/s; (ii) the corresponding recoil energy distribution peaks at a low value but has an average value that lies close to  $Q = 0$ ; (iii) the angular distribution is peaked in the forward and backward directions; and (iv) the coupling between scattering angle and recoil velocity is weak. Corresponding distributions for the reaction of Br atoms with HAt molecules are shown in Figure 13. Both fits are of the histogram type and both provide good agreement with the laboratory data. These distributions resemble the ones for Reaction 7 but the average recoil velocity is much lower and only  $1.0 \pm 0.2$  kcal/mol of a total available energy of approximately 40 kcal/mol appears in product translation. The low recoil velocity again restricts the products kinematically (as in the studies of Reactions 1 and 6), and c.m. fits to the laboratory distributions are not as well determined. Since the angular resolution is only  $90^\circ$ , the measurements provide only the

degree of anisotropy in the forward-backward scattering; the observed near isotropy is similar to that observed for Reaction 7. The coupling between recoil angle and velocity appears to be somewhat stronger than that for Reaction 7.

For Reaction 8, c.m. cross sections have also been determined over a range of collision energies (47). The latter was varied by changing the Br atom velocity; this was done by changing the temperature of the nozzle and by mixing the bromine with He and CO<sub>2</sub> to change the average molecular weight of the expanding gas mixture. At all collision energies studied (from 4.2 to 11.7 kcal/mol), the product At atoms are formed with low recoil velocity and appear within the  $Q = 0$  locus and are scattered both forward and backward in substantial proportions (only at the highest collision energy studied did forward scattering seem to predominate).

Integration of the c.m. cross sections over c.m. angles [equivalently, the laboratory data (as in Figure 10) could have been integrated over laboratory angles] gave reaction cross sections of  $26 \pm 4$  and  $1.5 \pm 0.3 \text{ \AA}^2$  for Reactions 7 and 8, respectively, both at mean collision energies of 6.5 kcal/mol. For Eq. (8), the energy dependence of the reaction cross section is shown in Figure 14 (47). The cross section is roughly level from 4 to 8 kcal/mol, but then rises appreciably at 12 kcal/mol. A simple straight line can be drawn through four of the five points within the indi-



Journal of Chemical Physics

Figure 13. Histogram c.m. distributions, both of which fit the laboratory data for Reaction 8 (24). Notation as in Figure 12.

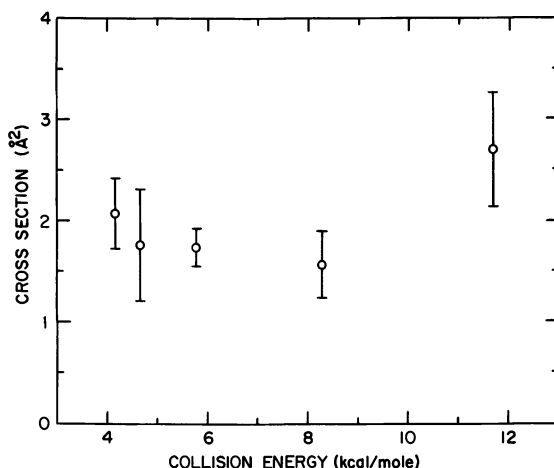


Figure 14. The dependence of the total reaction cross section on collision energy for Reaction 8 (47)

cated uncertainties without seriously missing the remaining point. However, the internal consistency of the data demands that the rise with energy be real. Moore and coworkers (48, 49) have measured thermal rate constants for the analogous reactions of Cl and Br with HI. At 295 K, they obtain 33.5 and 2.9 Å<sup>2</sup> for the Cl and Br reactions, respectively. The values of the cross sections for these reactions at room temperature are thus closely comparable to the corresponding cross sections for the HAT reactions at a 6.5 kcal/mol collision energy. However, this agreement may be deceptive since the dependence of the cross section on temperature obtained from the photochemical work shows a decrease with temperature at higher temperatures in apparent disagreement with the beam results for Reaction 8.

The results for Reactions 7 and 8 indicate that the collision time is sufficiently long to provide c.m. angular distributions with forward-backward symmetry but not sufficiently long to provide equipartitioning of the chemical energy between internal and external modes. These dynamical features are in partial agreement with results from previous infrared chemiluminescence (25), crossed molecular beam (26), and classical trajectory (27) studies of the analogous reaction of Cl atoms with HI and DI molecules. The chemiluminescence studies provide detailed rate constants into specific product vibrational and rotational states: these show that a substantial fraction of the available energy is channeled into product internal excitation. Despite different product quantum state distributions for the two isotopic reactions, the fraction of energy channeled into translation (0.71) and rotation (0.13) are in close agreement. As a corollary, there appears to be an inverse correlation

between vibrational and rotational excitation with the remaining energy, which represents only a small fraction (0.16) of the energy available, appearing as relative translation. Molecular beam studies of the angular distribution of product DCI molecules at collision energies of 400 K and 5 kcal/mol displays sharp forward scattering (unfortunately, the backward peak was not accessible within the angular scanning range of the detector). The classical trajectory studies on a "repulsive" surface similar to ones for  $\text{H} + \text{Cl}_2$ ,  $\text{K} + \text{HBr}$ , and  $\text{K} + \text{CH}_3\text{I}$  seem to provide a reasonable description of the observed dynamics. Predicted distributions of product vibrational and rotational energy closely resemble the chemiluminescence results. Although repulsive surfaces generally lead to higher product translational excitation (as in  $\text{H} + \text{Cl}_2$  and  $\text{K} + \text{CH}_3\text{I}$ ), the mass combinations, which allow rapid motion of the H-atom between the slowly moving halogen atoms, results in a H—I separation as the Cl approaches (thus the trajectory "cuts the corner" on the potential surface) and to a "mixed" release of the repulsive energy, which produces greater product internal excitation. These results on energy partitioning agree well with the conclusions from beam studies of Reactions 7 and 8. The calculated angular distributions are nearly isotropic at thermal collision energies but begin to peak forward at a collision energy of 6 kcal/mol. The collisions seem to be describable in terms of an approximate two-body model perturbed weakly by the H-atom motion: a correlation of impact parameter with scattering angle closely resembles specular reflection of hard spheres and is reminiscent of optical model treatments of the reactive scattering of  $\text{H} + \text{H}_2$  and other direct interaction processes (35, 50). The trajectory predictions of a direct process (at least as far as the heavy-atom motion is concerned) seems to be at variance with the conclusions from beam studies of Reaction 7 where a forward-backward peaked c.m. angular distribution was found to be necessary to fit the laboratory data and would therefore imply the formation of a complex. Grover has recently constructed an "attractive" potential surface for Reaction 8 in which all three atoms are temporarily trapped as the H-atom motion absorbs the excess energy (51); this surface also provides many of the observed dynamic properties. However, further work in both theory and experiment will probably be necessary before this situation is resolved.

### **Conclusion**

These three examples have demonstrated the great utility of radioisotope detection in crossed molecular beam experiments. The systems chosen for study have all been systems whose study with conventional techniques would be difficult, and specific radioisotope collection and counting techniques were necessarily developed. The techniques devel-

oped are extremely sensitive and compete favorably with other detection techniques. Consequently, it would not only be worthwhile to extend the previous studies but to apply these techniques to other systems and processes.

Certainly, radioisotope techniques have proved to be important to the study of the hydrogen-exchange reaction. Further study of this fundamental reaction should be carried out, and the results will lead to a more complete understanding of the dynamics of this reaction. With this in mind, it should be possible (i) to increase the collision energy range and the energy resolution by using nozzle and arc-heated nozzle atomic hydrogen beam sources; (ii) to obtain accurate total reaction cross sections as a function of collision energy by measuring the sticking coefficients for T atoms on MoO<sub>3</sub> surfaces and by measuring the atomic beam flux; and (iii) to extend the study to include reactions of H and D atoms with HT and DT molecules. All these experiments can be done with existing techniques.

Since both H atoms and small organic radicals are known to be selectively adsorbed on MoO<sub>3</sub> surfaces, a large variety of chemical processes such as reactive collision (e.g.,  $H + TCl \rightarrow HCl + T$  and  $Cl + {}^{14}CH_4 \rightarrow HCl + {}^{14}CH_3$ ), collisional dissociation (e.g.,  $Cd^* + T_2 \rightarrow Cd + T + T$ ), and photofragmentation (e.g.,  $TI + h\nu \rightarrow T + I$ ) can be studied. In all cases, the lower mass of the detected fragment will provide excellent kinematics.

The study of reactions involving short-lived isotopes offers the opportunity to study a large number of new reactions (20) and, perhaps more significantly, offers the possibility of measuring recoil velocity distributions using time-of-flight techniques. Extension to other radioisotopes will require beam source and detector development. The beam source design will again include on-line chemical preparation and may include the incorporation of a nuclear accelerator; the inconvenience of the latter will be offset by a substantially greater beam intensity. Although the out-of-plane data was helpful in estimating the mean recoil velocity, time-of-flight measurements of the recoil velocity distribution are necessary for a more accurate determination of energy disposal and for carrying out a quantitative transformation of the laboratory data to the c.m. system (52). The detection of short-lived isotopes should allow the time-of-flight velocity analysis of products formed from pulsed beams.

No further attempts have been made to use neutron activation analysis following the work of Chastagner and Taylor (2, 3, 4). Neutron activation allows the use of stable isotopes in the beam experiments and may be useful in some applications. Some aspects of the experiments would be greatly simplified, and difficulties encountered with apparatus contamination by long-lived isotopes or with the formation of beams of short-lived species are avoided.

For all these studies, the feasibility will ultimately depend on the discovery of a suitable getter surface. In some cases, such surfaces may already be known from earlier work. Deposition targets with optical or radioisotope detection were commonly used in the early atomic beam deflection and resonance experiments (53), and some of the surfaces used may also be useful in reactive scattering experiments. For example, surfaces of PbO, which changes color from pale yellow to brown (PbO<sub>2</sub>) when exposed to oxygen atoms, may find use as detectors in reactions producing oxygen atoms as products. Some precautions are necessary in choosing a surface and it is generally important to ensure that the sticking coefficient for the other radioactive species present is sufficiently low; that the surface characteristics do not change with the presence of reactant and product chemical species; and that surface reactions are absent. Since the labeled reactants and products will often have very different physical and chemical properties, specific surfaces that meet these requirements should be available for most systems of interest. The systems studied so far only constitute a beginning. Hopefully, the necessary surfaces will be found when future workers in the field study other systems and other dynamical processes using radioisotope detection.

### **Acknowledgments**

The author is grateful to J. R. Grover, J. L. Kinsey, and L. R. Martin for helpful discussions and for their permission to use the figures shown. This article was prepared under the auspices of the U.S. Department of Energy.

### **Literature Cited**

1. Taylor, E. H.; Datz, S. *J. Chem. Phys.* 1955, 23, 1711.
2. Chastagner, P. J. P.; Taylor, E. H., Oak Ridge National Laboratory Report ORNL-336, May, 1949.
3. Chastagner, P. J. P.; Taylor, E. H., Oak Ridge National Laboratory Report ORNL-607, Mar., 1950.
4. Chastagner, P. J. P.; Taylor, E. H., Oak Ridge National Laboratory Report ORNL-795, Oct., 1950.
5. Datz, S.; Taylor, E. H. *J. Chem. Phys.* 1956, 25, 389.
6. *Ibid.*, 395.
7. Herm, R. R. In "The Alkali Halide Vapors"; Davidovits, P.; McFadden, D. L., Eds.; Academic: New York, 1979; p. 189.
8. Martin, L. R.; Kinsey, J. L. *J. Chem. Phys.* 1967, 46, 4834.
9. Grosser, A. E.; Blythe, A. R.; Bernstein, R. B. *J. Chem. Phys.* 1965, 42, 1268.
10. Riley, C.; Gillen, K. T.; Bernstein, R. B. *J. Chem. Phys.* 1967, 47, 3672.
11. Gillen, K. T.; Riley, C.; Bernstein, R. B. *J. Chem. Phys.* 1969, 50, 4019.
12. Herschbach, D. R.; Kwei, G. H.; Norris, J. A. *J. Chem. Phys.* 1961, 34, 1842.
13. Kwei, G. H.; Norris, J. A.; Herschbach, D. R. *J. Chem. Phys.* 1970, 52, 1317.

14. Bernstein, R. B.; Rulis, A. M. *Faraday Discuss. Chem. Soc.* 1973, 55, 293.
15. Kwei, G. H.; Lo, V. W. S.; Entemann, E. A. *J. Chem. Phys.* 1973, 59, 3421.
16. Kwei, G. H.; Lo, V. W. S. *J. Chem. Phys.* 1980, 72, 6265.
17. Geddes, J.; Krause, H. F.; Fite, W. L. *J. Chem. Phys.* 1972, 56, 3298.  
Erratum: *Ibid.*, 1973, 59, 566.
18. Truhlar, D. G.; Wyatt, R. E. *Ann. Rev. Phys. Chem.* 1976, 27, 1.
19. Kwei, G. H.; Thompson, D. L., unpublished data.
20. Grover, J. R.; Kiely, F. M.; Lebowitz, E.; Baker, E. *Rev. Sci. Instrum.* 1971, 42, 293.
21. Grover, J. R.; Lilenfeld, H. V. *Rev. Sci. Instrum.* 1972, 43, 690.
22. Grover, J. R.; Lilenfeld, H. V. *Nucl. Instrum. Methods* 1972, 105, 189.
23. Grover, J. R.; Iden, C. R.; Lilenfeld, H. V.; Kiely, F. M.; Lebowitz, E. *Rev. Sci. Instrum.* 1976, 47, 1098.
24. Grover, J. R.; Iden, C. R.; Lilenfeld, H. V. *J. Chem. Phys.* 1976, 64, 4657.
25. Maylotte, D. H.; Polanyi, J. C.; Woodall, K. B. *J. Chem. Phys.* 1972, 57, 1547.
26. McDonald, J. D.; Herschbach, D. R., unpublished data quoted in Ref. 27.
27. Parr, C. A.; Polanyi, J. C.; Wong, W. H. *J. Chem. Phys.* 1973, 58, 5.
28. Datz, S.; Herschbach, D. R.; Taylor, E. H. *J. Chem. Phys.* 1961, 35, 1549.
29. Beck, D. *J. Chem. Phys.* 1962, 37, 2884.
30. Beck, D.; Greene, E. F.; Ross, J. *J. Chem. Phys.* 1962, 37, 2895.
31. Greene, E. F.; Moursund, A. L.; Ross, J. *Adv. Chem. Phys.* 1966, 10, 135.
32. Martin, L. R., Ph.D. Thesis, MIT, 1966.
33. Johnston, H. S. "Gas Phase Reaction Rate Theory"; Ronald: New York, 1966; pp. 158-206.
34. Brumer, P.; Karplus, M. *J. Chem. Phys.* 1971, 54, 4955.
35. Karplus, M. In "Molecular Beams and Reaction Kinetics"; Schlier, C., Ed.; Academic: New York, 1970; p. 372.
36. Datz, S.; Taylor, E. H. *J. Chem. Phys.* 1963, 39, 1896.
37. Karplus, M.; Tang, K. T. *Discuss. Faraday Soc.* 1967, 44, 56.
38. Tang, K. T.; Karplus, M. *Phys. Rev.* 1971, A4, 1844.
39. Choi, B. H.; Tang, K. T. *J. Chem. Phys.* 1976, 65, 5161.
40. Biedenharn, L. C.; Boyer, K.; Goldstein, M. *Phys. Rev.* 1956, 104, 383.
41. Birely, J. H.; Herm, R. R.; Wilson, K. R.; Herschbach, D. R. *J. Chem. Phys.* 1967, 47, 993.
42. Porter, R. N.; Karplus, M. *J. Chem. Phys.* 1964, 40, 1105.
43. Siegbahn, P.; Liu, B. *J. Chem. Phys.* 1978, 68, 2457.
44. Truhlar, D. G.; Horowitz, C. J. *J. Chem. Phys.* 1978, 68, 2466.
45. Way, K. R.; Yang, S. C.; Stwalley, W. C. *Rev. Sci. Instrum.* 1976, 47, 1049.
46. Mayne, H. R.; Toennies, J. P. *J. Chem. Phys.* 1979, 70, 5314.
47. Grover, J. R., unpublished data.
48. Bergmann, K.; Moore, C. B. *J. Chem. Phys.* 1975, 63, 643.
49. Mei, C. C.; Moore, C. B. *J. Chem. Phys.* 1977, 67, 3936.
50. Kwei, G. H.; Herschbach, D. R. *J. Phys. Chem.* 1979, 83, 1550.
51. Grover, J. R. *Bull. Am. Phys. Soc.* 1980, 25, 289.
52. Herschbach, D. R. *Faraday Discuss. Chem. Soc.* 1973, 55, 233.
53. Ramsey, N. F. "Molecular Beams"; Oxford Univ. Press: London, 1956; pp. 374-394.

RECEIVED September 4, 1980.

# Limitations of the Moderated Nuclear Recoil Technique for Investigating Thermal Hydrogen Abstraction Reactions by Atomic Fluorine

JOHN W. ROOT<sup>1</sup>, CHESTER A. MATHIS, RAFAEL GURVIS,  
KATHLEEN D. KNIERIM, and SIU-HONG MO

Department of Chemistry and Crocker Nuclear Laboratory,  
University of California, Davis, CA 95616

*A sensitive technique has been developed for characterizing the nonthermal  $H^{18}F$  yields formed from the dilute concentrations of hydrogen donors present in moderated nuclear recoil (MNR)  $^{18}F$  experiments. The relative nonthermal mean collisional reactivities of cyclopentane and of  $C_1$ - $C_6$  alkanes present in excess  $C_2F_6$  have been measured using this method. The nonthermal reactivities per carbon-hydrogen bond in these substances exhibit  $\pm 10\%$  maximum variations about the constant average value that is characteristic of unbranched  $C_2$ - $C_6$  alkanes. The MNR method can be utilized for the investigation at enhanced sensitivity of thermal hydrogen abstraction reactions by atomic  $^{18}F$ . Quantitative relative-to-absolute scaling relationships have been used for the estimation of absolute rate constants for many such reactions. The advantages, limitations, and physical basis of the MNR technique are considered.*

The nuclear recoil method can be used to produce many radioactive free hot atoms and unstable polyatomic radicals (1, 2, 3). With atomic  $^{18}F$  quantitative kinetics measurements have been carried out under both equilibrium (1-6) and nonequilibrium (3, 7-12) conditions.

The species recoiling from the  $^{19}F(n,2n)^{18}F$  nuclear reaction possess  $10^5$ - $10^8$  eV of translational energy that must be removed before equilibrium, or "thermal,"  $^{18}F$  kinetics studies can be initiated. The rapid

<sup>1</sup> Author to whom correspondence should be addressed.

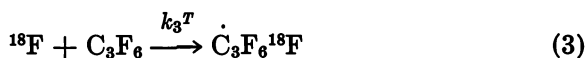
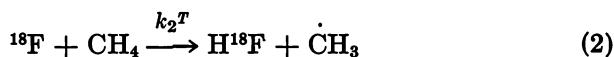


dissipation of this excess energy should be effected by including an unreactive "moderator" (M) in the samples. In well-designed moderated nuclear recoil (MNR) experiments hot atom deenergization takes place prior to the onset of thermal reaction (4).

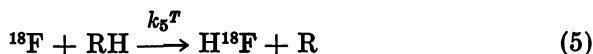
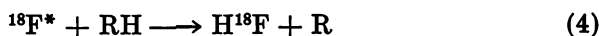


Here the asterisk denotes translational excitation, and Equation 1 represents a cascading sequence of momentum transferring collisions.

The available  $^{18}\text{F}$  MNR parameters exhibit about  $\pm 20\%$  consistency with conventional kinetic data (1). Although the sensitivity of the MNR technique is often greater than this, the accuracy of the measured results depends on the degree with which equilibrium conditions have been established. Direct testing of the MNR equilibrium hypothesis at enhanced sensitivity has not been accomplished because of the lack of refined conventional data (1, 4, 13, 14, 15). An indirect test at  $\pm 1\%$  sensitivity has used the  $\text{C}_2\text{F}_6$  moderator concentration dependence of phenomenological MNR ( $k_3^{273}/k_2^{273}$ ) relative rate coefficients (4, 6).



This investigation represents an attempt to assess the importance of nonthermal F-to-HF reactions in MNR experiments with reactive hydrogen donors. Reaction 4 and its thermal counterpart, Reaction 5, are



typically both important under nuclear recoil conditions (6, 7, 9, 10, 11, 16). However, no general technique is available for partitioning the measured  $\text{H}^{18}\text{F}$  yields into thermal and nonthermal components (1, 7, 10). The present measurements have thus been carried out to provide an empirical method for estimating the nonthermal  $\text{H}^{18}\text{F}$  yield corrections in MNR experiments with  $\text{C}_1\text{-C}_6$  alkanes.

### Experimental

Most of our techniques have been described previously (1, 4-9, 16, 17). Thus only pertinent additional details are presented below.

Measurements have been performed at effective pressures, ( $P/Z$ ), throughout the range 1.0-100 kTorr. To account for gas imperfection the experi-

mentally determined quantity ( $P/Z$ ) has been used (1, 4, 11). The empirical equation of state  $PV = ZnRT$  rearranges to give  $P/Z = \rho RT/M$  in which  $Z$ ,  $\rho$ ,  $R$ , and  $M$  denote the gas compressibility factor, the mass density, the molar gas constant, and the molecular weight. The quantity ( $P/Z$ ) thus corresponds to the sample density expressed in units of pressure.

Irradiation vessels suitable for use at 20 kTorr have been described elsewhere (5). Thick-walled KG-33 capillaries with dimensions 9.0 mm o.d.  $\times$  3.5 mm i.d.  $\times$  110 mm l can be used over the range 20–100 kTorr. Capillaries with dimensions 9.0 mm o.d.  $\times$  2.7 mm i.d.  $\times$  115 mm l have been used at this laboratory up to 500 kTorr. Because these procedures are dangerous, reliable safety precautions should be routinely observed (5).

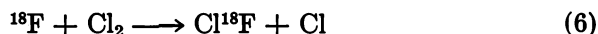
All materials had minimum purities of 98 mol % and, except as detailed below, were used without further purification. Although  $O_2$  is not an important competitor for  $^{18}F$  atoms, it interferes with the recovery of labeled aliphatic radicals (1, 16). The  $O_2$  concentration in the samples must therefore be reduced to the sub-ppm level. Freeze-pump-thaw cycles were used for degassing 77 K condensable materials. Methane was purified from  $O_2$  using Cs gettering (17, 18). Since  $CF_4$  reacts with Cs, the approximately 0.001 mol fraction  $O_2$  contaminant in commercial Freon-14 was removed using Ridox R-30 scavenger (Fisher Scientific Co.) (19).

Reagent sources and purities included the following: (i) Pierce Chemical Co.  $C_3F_8$  ( $\geq 99.0\%$ ); (ii) Matheson Gas Products Purified  $H_2$  ( $\geq 99.95\%$ ), R. G.  $Cl_2$  ( $\geq 99.96\%$ ), C. P.  $CH_4$  ( $\geq 99.97\%$ ), C. P.  $H_2S$  ( $\geq 99.5\%$ ), Freon 14  $CF_4$  ( $\geq 99.7\%$ ), Freon 116  $C_2F_6$  ( $\geq 99.6\%$ ), and Genetron 23  $CHF_3$  ( $\geq 98.0\%$ ); (iii) Phillips Specialty Gas Products R. G.  $C_2H_6$  ( $\geq 99.99\%$ ), R. G.  $C_3H_8$  ( $\geq 99.98\%$ ), R. G.  $n-C_4H_{10}$  ( $\geq 99.95\%$ ), R. G.  $n-C_5H_{12}$  ( $\geq 99.98\%$ ), R. G. neo- $C_5H_{12}$  ( $\geq 99.99\%$ ), and R. G.  $n-C_6H_{14}$  ( $\geq 99.98\%$ ); (iv) Chemical Samples Co. cyclo- $C_5H_{10}$  ( $\geq 99.9\%$ ); and (v) Merck, Sharpe, and Dohme of Canada  $CD_4$ ,  $C_3D_8$ ,  $n-C_4D_{10}$ ,  $n-C_5D_{12}$ , and cyclo- $C_5D_{10}$  (isotopic purity  $\geq 99.0$  atom % D).

Other sample handling and data analysis methods have been fully described (1, 5, 6). Unless noted otherwise, the cited measurement uncertainties represent standard errors of estimate at the 68% confidence level.

## Results

**Reactivity of  $Cl_2$  Toward Hot  $^{18}F$  Atoms.** A  $Cl_2$ -scavenging technique has been used to determine the thermalized atom fractions,  $t$ , in recoil  $^{18}F$  experiments with  $SF_6$  and  $C_2F_6$  (1, 6, 15).



If Reaction 6 is selective for thermal  $^{18}F$  atoms, then intercomparisons between  $Cl_2$ - and RH-scavenged samples can be used to estimate the nonthermal  $H^{18}F$  yield corrections in MNR experiments.

As shown in Tables I and II, the thermal specificity of  $Cl_2$  has been tested using  $Cl_2/H_2/CF_4$  and  $Cl_2/RH/C_2F_6$  MNR experiments. From Table I the organic yield data exhibit a significant increase in statistical reliability for this type of data comparison at enhanced sensitivity. The

Table I. Determination of the

Moderator (Pressure: Number of Samples)*	Additive Concentrations <sup>b</sup> [mol(collision) fractions] × 10 <sup>2</sup>	
	[Cl <sub>2</sub> ]	[H <sub>2</sub> ]
CF <sub>4</sub> (1.00:5)	1.00(0.94)	0.00(0.00)
CF <sub>4</sub> (1.00:14)	2.00(1.88)	0.00(0.00)
CF <sub>4</sub> (1.00:26)	5.00(4.70)	0.00(0.00)
CF <sub>4</sub> (1.00:9)	10.00(9.43)	0.00(0.00)
CF <sub>4</sub> (1.00:5)	2.00(2.26)	49.00(38.56)
CF <sub>4</sub> (1.00:27)	5.00(5.64)	47.50(37.22)
C <sub>2</sub> F <sub>6</sub> (1.00:4)	5.00(4.02)	0.00(0.00)
CF <sub>4</sub> (10.0:2)	5.00(4.70)	0.00(0.00)
C <sub>2</sub> F <sub>6</sub> (10.0:4)	0.500(0.398)	0.00(0.00)
C <sub>2</sub> F <sub>6</sub> (10.0:4)	5.00(4.02)	0.00(0.00)
CF <sub>4</sub> (20.0:4)	5.00(4.70)	0.00(0.00)
C <sub>2</sub> F <sub>6</sub> (20.0:4)	0.500(0.398)	0.00(0.00)
CF <sub>4</sub> (30.0:4)	5.00(4.70)	0.00(0.00)
CF <sub>4</sub> (40.0:5)	5.00(4.70)	0.00(0.00)
CF <sub>4</sub> (55.0:4)	5.00(4.70)	0.00(0.00)
CF <sub>4</sub> (100.0:5)	5.00(4.70)	0.00(0.00)

\* All samples at 273 K. Cited pressures represent (*P/Z*) values in kTorr.

<sup>b</sup> Energetic collision fractions estimated using elastic cross sections obtained from gas-liquid critical data (4, 9, 22, 23). The mixed elastic cross sections for <sup>18</sup>F atom vs. R<sub>i</sub> collisions were as follows: H<sub>2</sub>, 25.9; Cl<sub>2</sub>, 37.3; CF<sub>4</sub>, 39.8; and C<sub>2</sub>F<sub>6</sub>, 46.9 Å<sup>2</sup>.

inorganic activity partitioning procedure based on adsorption of H<sup>18</sup>F upon the glass sample vessel walls is not consistently reproducible at large (*P/Z*) (8, 9).

The nonthermal reactivities of H<sub>2</sub> and Cl<sub>2</sub> can be assessed from competitive gas-phase recoil <sup>18</sup>F experiments with CF<sub>4</sub>. If either substance exhibits significant nonthermal reactivity, then its addition to CF<sub>4</sub> would be accompanied by a characteristic composition-dependent decrease in the organic product yield (9). From Table I the organic yields exhibit no dependence on Cl<sub>2</sub> concentration. The 5.41% ± 0.12% average from nine independent measurements with CF<sub>4</sub> at 0.100 Cl<sub>2</sub> mol fraction is equivalent to the 54-sample average of 5.24% ± 0.07%. In the presence of 0.475 mol fraction of H<sub>2</sub>, however, the organic yield in CF<sub>4</sub> decreases from 5.24% ± 0.07% to 4.01% ± 0.05%, and the product distribution also changes (3, 12, 19).

On both theoretical (19-22) and experimental (7, 9, 10, 23-26) grounds, under conditions involving uniform total hot reactivity the yields from competing nonthermal processes should exhibit rough proportionality to the reactant collision fractions. The yield depressions for individual organic products in recoil <sup>18</sup>F experiments with H<sub>2</sub>S/CH<sub>3</sub>CF<sub>3</sub> and H<sub>2</sub>S/CH<sub>3</sub>CHF<sub>2</sub> mixtures were directly proportional to the competitor

Reactivity of Cl<sub>2</sub> Toward Hot <sup>18</sup>F Atoms

## Absolute Yields\* (%)

<i>Nonvolatile Inorganic</i>	<i>Total Inorganic</i>	<i>Total Organic</i>
94.3 ± 0.4	94.9 ± 0.3	5.1 ± 0.3
94.1 ± 0.2	94.7 ± 0.17	5.3 ± 0.17
94.5 ± 0.11	94.8 ± 0.08	5.2 ± 0.08
93.9 ± 0.2	94.6 ± 0.1	5.4 ± 0.12
95.7 ± 0.3	96.1 ± 0.2	3.9 ± 0.2
95.6 ± 0.07	96.0 ± 0.05	4.0 ± 0.05
88.2 ± 0.2	89.5 ± 0.07	10.5 ± 0.07
94.1 ± 0.2	94.1 ± 0.2	5.9 ± 0.2
85.3 ± 0.3	87.2 ± 0.3	12.8 ± 0.3
85.3 ± 0.1	86.7 ± 0.2	13.3 ± 0.2
80.6 ± 8.2	93.5 ± 0.2	6.5 ± 0.2
84.5 ± 0.2	85.6 ± 0.1	14.4 ± 0.1
81.2 ± 6.4	92.4 ± 0.3	7.6 ± 0.3
84.6 ± 3.0	91.9 ± 0.3	8.1 ± 0.3
60.6 ± 7.4	91.1 ± 0.1	8.9 ± 0.1
73.8 ± 6.7	88.1 ± 0.4	11.9 ± 0.4

\* Precision based standard errors of estimate.

collision fractions estimated using elastic cross sections (4, 22, 23) derived from gas-liquid critical data (9).

$$f_{AR_i} = \frac{X_{R_i} \sigma_{AR_i}^o}{\sum_i X_{R_i} \sigma_{AR_i}^o} \quad (7)$$

In Equation 7  $f_{AR_i}$ ,  $X_{R_i}$ , and  $\sigma_{AR_i}^o$  denote the fraction of hot atom (A) collisions with the *i*th mixture component ( $R_i$ ), the mole fraction of  $R_i$ , and the hard sphere cross section for A vs.  $R_i$  elastic collisions.

The collision fraction law fails in competitive experiments in which the reactive collision energy probability density distribution is strongly dependent on sample composition. Such behavior arises when the excitation functions for nonthermal reactions exhibit dissimilar collision energy dependences (7, 9, 10, 19-26). Despite this caveat, the simple collision fraction rule exhibits good utility for many types of competitive systems (9, 23).

From Table I and Equation 7 an H<sub>2</sub> collision fraction of 0.0943 should decrease the absolute organic yield in CF<sub>4</sub> by approximately 0.31% ± 0.03%. This contrasts with the observed apparent 0.18% ± 0.13% increase noted for 0.0943 Cl<sub>2</sub> collision fraction. This approximate

**Table II. Nonthermal Reactivities for Cl<sub>2</sub> and Various Hydrogen Donors in Approximately 99.5 Mol % C<sub>2</sub>F<sub>6</sub>**

<i>Reactant (Pressure: Number of Samples)<sup>a</sup></i>	<i>Reactant Concentration<sup>b</sup> [mol (collision) fraction] × 10<sup>2</sup></i>	<i>Nonvolatile Inorganic Yield<sup>c</sup> (%)</i>
Cl <sub>2</sub> (1.00:4)	5.00 (4.02)	88.22 ± 0.08
Cl <sub>2</sub> (10.00:4)	0.500 (0.398)	85.30 ± 0.32
Cl <sub>2</sub> (10.00:4)	5.00 (4.02)	85.33 ± 0.14
Cl <sub>2</sub> (20.00:4)	0.500 (0.398)	84.51 ± 0.22
H <sub>2</sub> (10.00:3)	0.500 (0.277)	85.62 ± 0.06
CHF <sub>3</sub> (10.00:3)	0.500 (0.428)	85.74 ± 0.45
CH <sub>4</sub> (10.00:4)	0.500 (0.364)	86.97 ± 0.07
CD <sub>4</sub> (10.00:2)	0.500 (0.362)	86.31 ± 0.10
H <sub>2</sub> S (10.00:1)	0.500 (0.365)	89.43 ± 0.13
C <sub>2</sub> H <sub>6</sub> (10.00:6)	0.500 (0.430)	88.11 ± 0.05
C <sub>3</sub> H <sub>8</sub> (10.00:2)	0.500 (0.493)	89.07 ± 0.11
C <sub>3</sub> D <sub>8</sub> (10.00:2)	0.500 (0.490)	88.62 ± 0.21
<i>n</i> -C <sub>4</sub> H <sub>10</sub> (10.00:2)	0.500 (0.549)	89.94 ± 0.14
<i>n</i> -C <sub>4</sub> H <sub>10</sub> (10.00:4)	0.0500 (0.0549)	88.48 ± 0.24
<i>n</i> -C <sub>4</sub> H <sub>10</sub> (10.00:2)	0.0050 (0.0055)	87.90 ± 0.14
<i>n</i> -C <sub>4</sub> D <sub>10</sub> (10.00:2)	0.500 (0.547)	90.04 ± 0.15
cyclo-C <sub>5</sub> H <sub>10</sub> (10.00:3)	0.20 (0.22)	90.54 ± 0.11
cyclo-C <sub>5</sub> D <sub>10</sub> (10.00:2)	0.10 (0.11)	90.62 ± 0.13
neo-C <sub>5</sub> H <sub>12</sub> (10.00:2)	0.20 (0.24)	90.32 ± 0.13
<i>n</i> -C <sub>5</sub> H <sub>12</sub> (10.00:3)	0.20 (0.24)	91.05 ± 0.09
<i>n</i> -C <sub>5</sub> D <sub>12</sub> (10.00:2)	0.10 (0.12)	90.68 ± 0.13
<i>n</i> -C <sub>6</sub> H <sub>14</sub> (10.00:3)	0.10 (0.13)	91.55 ± 0.10

<sup>a</sup> All samples at 273 K. Cited pressures represent (*P/Z*) values in kTorr.

<sup>b</sup> Energetic collision fractions estimated using elastic cross sections obtained from gas-liquid critical data (4, 9, 22, 23). The mixed elastic cross sections for <sup>18</sup>F atom vs. R<sub>i</sub> collisions are as follows: H<sub>2</sub>, 25.9; CD<sub>4</sub>, 33.9; CH<sub>4</sub>, 34.1; H<sub>2</sub>S, 34.2; Cl<sub>2</sub>, 37.3; CHF<sub>3</sub>, 40.1; C<sub>2</sub>H<sub>6</sub>, 40.3; C<sub>3</sub>D<sub>8</sub>, 46.0; C<sub>3</sub>H<sub>8</sub>, 46.2; C<sub>2</sub>F<sub>6</sub>, 46.9; *n*-C<sub>4</sub>D<sub>10</sub>, 51.3; *n*-C<sub>4</sub>H<sub>10</sub>, 51.5; cyclo-C<sub>5</sub>D<sub>10</sub>, 51.5; cyclo-C<sub>5</sub>H<sub>10</sub>, 51.8; neo-C<sub>5</sub>H<sub>12</sub>, 56.1; *n*-C<sub>5</sub>D<sub>12</sub>, 56.6; *n*-C<sub>5</sub>H<sub>12</sub>, 57.0; and *n*-C<sub>6</sub>H<sub>14</sub>, 62.0 Å<sup>2</sup>.

<sup>c</sup> The cited standard errors represent the larger of the values estimated from measurement precision or from radioactivity statistics.

comparison shows that the mean collisional nonthermal reactivity of Cl<sub>2</sub> is smaller than that of H<sub>2</sub> by at least 300% (95% confidence level). Thus, nonthermal <sup>18</sup>F reactions with Cl<sub>2</sub> contribute negligibly to the Cl<sup>18</sup>F yield at 0.050 Cl<sub>2</sub> mol fraction, and the present Cl<sub>2</sub>-scavenging technique is quite selective for thermalized <sup>18</sup>F atoms.

The quantitative reliability of the above conclusions could be improved with additional measurements at increased Cl<sub>2</sub> mol fractions. This refinement has not been attempted because the increased yields of <sup>32</sup>P impurity seriously interfere with the chromatographic product analysis measurements (5, 19).

**Discussion**

**Nonthermal Reactivities of C<sub>1</sub>–C<sub>6</sub> Hydrocarbons under MNR Conditions.** From the Cl<sub>2</sub>/CF<sub>4</sub> and Cl<sub>2</sub>/C<sub>2</sub>F<sub>6</sub> mixture results shown in Tables I and II, the apparent *t*-values exhibit independence of Cl<sub>2</sub> concentration and a decreasing dependence with increasing (*P/Z*). The average *t*-value for C<sub>2</sub>F<sub>6</sub> at 10.0 kTorr is 0.8532 ± 0.0017. In Table III the measured nonvolatile inorganic yields (*Y*<sub>4</sub>) have been compared for several hydrogen donors in mixtures (10.0 kTorr) containing C<sub>2</sub>F<sub>6</sub> moderator. Although the respective 0.856 ± 0.001 and 0.857 ± 0.005 results obtained for H<sub>2</sub> and CHF<sub>3</sub> at 0.0050 mol fraction agree with the C<sub>2</sub>F<sub>6</sub> *t*-value, the enhanced *Y*<sub>4</sub> yields noted for C<sub>1</sub>–C<sub>6</sub> hydrocarbons reflect contributions from nonthermal Reaction 4. For these latter species the nonthermal H<sup>18</sup>F yields can be estimated as the quantity (*Y*<sub>4</sub> – *t*).

Nonthermal yield intercomparisons at constant additive collision fraction are possible for the species CD<sub>4</sub> vs. CH<sub>4</sub> vs. H<sub>2</sub>S, CHF<sub>3</sub> vs. C<sub>2</sub>H<sub>6</sub>, C<sub>3</sub>D<sub>8</sub> vs. C<sub>3</sub>H<sub>8</sub>, *n*-C<sub>4</sub>D<sub>10</sub> vs. *n*-C<sub>4</sub>H<sub>10</sub>, cyclo-C<sub>5</sub>D<sub>10</sub> vs. cyclo-C<sub>5</sub>H<sub>10</sub>, and *n*-C<sub>5</sub>D<sub>12</sub> vs. *n*-C<sub>5</sub>H<sub>12</sub>. Because (*Y*<sub>4</sub> – *t*) does not exhibit constant values for all of these cases, the mean collisional nonthermal reactivity for Reaction 4 varies with the individual reagent characteristics.

**Table III. Variation of Nonthermal F-to-HF(DF) Yields with Calculated [*n*<sub>R1</sub>/σ<sup>o</sup><sub>AR1</sub>] Ratios**

Reactant (collision fraction) × 10 <sup>2</sup>	( <i>Y</i> <sub>4</sub> – <i>t</i> ) (%) <sup>a</sup>	σ <sup>o</sup> <sub>AR1</sub> (Å <sup>2</sup> ) <sup>b</sup>	[ <i>n</i> <sub>R1</sub> /σ <sup>o</sup> <sub>AR1</sub> ] (bonds Å <sup>-2</sup> )
H <sub>2</sub> (0.277)	0.3 ± 0.3	25.9	0.0772
CHF <sub>3</sub> (0.428)	0.4 ± 0.5	40.1	0.0249
CH <sub>4</sub> (0.364)	1.7 ± 0.3	34.1	0.117
CD <sub>4</sub> (0.362)	1.0 ± 0.3	33.9	0.118
H <sub>2</sub> S (0.365)	4.1 ± 0.3	34.2	0.0585
C <sub>2</sub> H <sub>6</sub> (0.430)	2.8 ± 0.3	40.3	0.149
C <sub>3</sub> H <sub>8</sub> (0.493)	3.8 ± 0.3	46.2	0.173
C <sub>3</sub> D <sub>8</sub> (0.490)	3.3 ± 0.4	46.0	0.174
<i>n</i> -C <sub>4</sub> H <sub>10</sub> (0.549)	4.6 ± 0.3	51.5	0.194
<i>n</i> -C <sub>4</sub> D <sub>10</sub> (0.547)	4.7 ± 0.3	51.3	0.195
cyclo-C <sub>5</sub> H <sub>10</sub> (0.22)	5.2 ± 0.3	51.8	0.193
cyclo-C <sub>5</sub> D <sub>10</sub> (0.11)	5.3 ± 0.3	51.5	0.194
neo-C <sub>5</sub> H <sub>12</sub> (0.24)	5.0 ± 0.3	56.1	0.214
<i>n</i> -C <sub>5</sub> H <sub>12</sub> (0.24)	5.8 ± 0.3	57.0	0.211
<i>n</i> -C <sub>5</sub> D <sub>12</sub> (0.12)	5.4 ± 0.3	56.6	0.212
<i>n</i> -C <sub>6</sub> H <sub>14</sub> (0.13)	6.2 ± 0.3	62.0	0.226

<sup>a</sup> Precision based standard errors of estimate.

<sup>b</sup> The σ<sup>o</sup><sub>AR1</sub> values have been taken from Reference 23. Cf. notes *b* of Tables I and II.

Figure 1. Nonthermal F-to-HF reaction yields for various hydrogen donors in 99.5–99.9 mol %  $C_3F_8$  moderator: (●) protiated; (▲) deuterated reagents; (—) linear regression Equation (8) for alkanes and perdeuteroalkanes

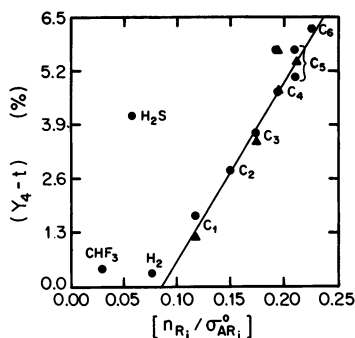


Figure 1 and Table III show that a simple proportional relationship exists between the  $(Y_4 - t)$  values and the  $(n_{R_i}/\sigma_{AR_i}^{\circ})$  ratios for alkanes. Here  $\sigma_{AR_i}^{\circ}$  is as defined above, and  $n_{R_i}$  denotes the number of protium or deuterium atoms per  $R_i$  molecule. In the absence of per-bond reactivity differences between the various  $R_i$ ,  $(n_{R_i}/\sigma_{AR_i}^{\circ})$  approximates the mean collisional reactivity for process (4). The solid line connecting the data points on Figure 1, which corresponds to linear regression Equation 8, corroborates this simple reactivity model for alkanes.

$$(Y_4 - t) = (43.6 \pm 1.9) \left( \frac{n_{R_i}}{\sigma_{AR_i}^{\circ}} \right) - (3.8 \pm 0.3) \quad (8)$$

Here the units for  $(Y_4 - t)$  and  $(n_{R_i}/\sigma_{AR_i}^{\circ})$  are percent absolute yield and carbon-hydrogen bonds  $\text{\AA}^{-2}$ .

Because of vapor pressure limitations, the  $C_5$ – $C_6$  hydrocarbon concentrations could not be maintained at 0.0050 mol fraction without decreasing  $(P/Z)$  below 10.0 kTorr. Further research is needed to establish the  $R_i$ -concentration dependences for these species. From Tables II and III  $(Y_4 - t)$  for  $n$ - $C_4H_{10}$  does not exhibit simple proportionality to the  $n$ - $C_4H_{10}$  collision fraction over the mol fraction range  $5 \times 10^{-3}$  to  $5 \times 10^{-5}$ . The total hot reactivity is varying in these latter experiments, so that a nonlinear dependence is not unreasonable (7, 9, 10). The results obtained at mol fractions smaller than approximately  $1 \times 10^{-3}$ , however, are suspect because of interference from  $H^{18}F$ -producing impurity reactions (5, 15).

**Significance of Nonthermal Reactivities.** Indistinguishable  $(Y_4 - t)$  results have been obtained for protiated and deuterated isotopic cyclopentanes and  $C_3$ – $C_5$  alkanes. These comparisons were carried out to suppress the importance of  $(n_{R_i}/\sigma_{AR_i}^{\circ})$  ratio variations, so that sensitive measurement reproducibility and zero-point energy reactivity correlation tests could be accomplished. From the statistical quality of correlation

Equation 8, the combined effects of random measurement errors and internal inconsistencies in the  $(n_{R_i}/\sigma^{\circ}_{AR_i})$  ratios contribute roughly 5% data scatter. Because these random noise sources are uncorrelated, the consistency of the alkane  $(n_{R_i}/\sigma^{\circ}_{AR_i})$  values with respect to the present application is 95% or better (68% confidence level). The utility of the alkane  $\sigma^{\circ}_{AR_i}$  values estimated from gas-liquid critical data is thus quite good.

Although these measurements are not sufficiently accurate to justify assigning relative nonthermal rate coefficients to the various  $R_i$ , several reactivity trends are clearly apparent. The  $(Y_4 - t)$  yields for  $\text{CHF}_3$ ,  $\text{H}_2$ ,  $\text{CD}_4$ , and  $\text{CH}_4$  increase in the same order as the thermal  $k_5^{300}$  values, and in the reverse order as the corresponding  $E_5$  Arrhenius activation energies. The activation energy is related in a complex fashion to the effective hot reaction barrier (7, 27, 28), and the rates of several nonthermal atom and radical transfer reactions vary with barrier height (3, 23, 24, 28-35). It is thus not surprising that Reaction 4 exhibits similar behavior.

The  $(Y_4 - t)$  values for protiated and deuterated  $\text{C}_3$ - $\text{C}_5$  hydrocarbons are identical (see above). As determined from gas kinetics experiments, the zero-point energy contribution to the dissociation energy difference between C-D and C-H bonds in hydrocarbons is  $2.8 \pm 0.2 \text{ kcal mol}^{-1}$  (23, 36, 37). This quantity also corresponds to the mean C-H bond dissociation energy difference between neo- $\text{C}_5\text{H}_{12}$  and  $n$ - $\text{C}_5\text{H}_{12}$ , measured using hydrogen abstraction reactions by thermal  $\dot{\text{C}}\text{D}_3$  radicals or by nuclear recoil  $^3\text{H}$  atoms (23, 24). Because the magnitudes of the various mean carbon-hydrogen bond dissociation energy differences are the same, it is surprising that Reaction 4 bond strength effects are evident for the species  $\text{CH}_4/\text{CD}_4$  and  $n$ - $\text{C}_5\text{H}_{12}/\text{neo-C}_5\text{H}_{12}$  but not for the isotopic  $\text{C}_3$ - $\text{C}_5$  hydrocarbons.

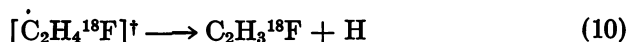
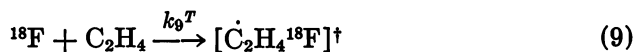
The activation energies for thermal Reaction 5 are negligibly small for cyclo- $\text{C}_5\text{H}_{10}$  and for  $\text{C}_2$ - $\text{C}_6$  alkanes with the exception of neo- $\text{C}_5\text{H}_{12}$  (15). For alkane reagents it therefore follows (i) That bond-strength effects occur for nonthermal Reaction 4 only when the corresponding thermal  $E_5$  values are nonzero, (ii) That  $E_5$  provides a qualitative indicator concerning the barrier for nonthermal Reaction 4, and (iii) That for a given aliphatic  $R_i$ , Reactions 4 and 5 probably involve similar microscopic reaction dynamics. From the  $\text{CH}_4/\text{CD}_4$  and  $n$ - $\text{C}_5\text{H}_{12}/\text{neo-C}_5\text{H}_{12}$   $(Y_4 - t)$  results shown in Table III, the magnitude of the carbon-hydrogen bond-strength dependence for "activated" ( $E_5 > 0$ ) nonthermal F-to-HF reactions with hydrocarbons is  $0.25\% \pm 0.04\%$  absolute-yield decrease per  $\text{kcal mol}^{-1}$  dissociation-energy increase.

The cyclopentane data points deviate significantly from the alkane reactivity correlation shown in Figure 1. In the absence of systematic



inconsistencies in the underlying ( $n_{R_i}/\sigma^{\circ}_{AR_i}$ ) ratios, these results suggest 10–15% relative increases in the mean collisional nonthermal reactivities for cycloalkanes. Although such behavior could reflect steric differences between alkanes and cycloalkanes, the magnitude of any systematic  $\sigma^{\circ}_{AR_i}$  inconsistencies between these hydrocarbon types is not known. Further research is needed to establish the more detailed characteristics of steric and bond strength effects for nonthermal F-to-HF reactions.

**Significance of Nonthermal Yields in MNR Experiments.** Figure 1 and Table III show that Reaction 4 contributes to the yield of  $H^{18}F$  under the conditions used in MNR thermal kinetics experiments. Qualitatively similar effects have been noted by Rowland et al., who detected  $0.3\% \pm 0.1\%$  absolute yields of  $CH_2^{18}F$  radicals in 283 K  $C_2H_4/SF_6$   $^{18}F$  MNR experiments at 0.95  $SF_6$  mol fraction (2).



Since Reaction 11 is endothermic by about 50 kcal mol<sup>-1</sup>, it cannot have been induced by thermal  $^{18}F$  atoms at 283 K. Similarly, Lee and Rowland reported trace yields from 10–50 kcal mol<sup>-1</sup> endothermic reactions for the  $C_2H_4/CFCl_3$  and  $C_3H_6/CFCl_3$   $^{38}Cl$  MNR systems, again demonstrating the impossibility of achieving complete suppression of nonthermal processes at finite reagent concentrations (38, 39, 40).

The enhanced velocities possessed by hot atoms dramatically shorten the time scales associated with nonthermal collisions. Approximate recoil  $^{18}F$  mean thermalization times,  $\langle\tau^{*e}\rangle$ , corresponding to simulated MNR conditions have been calculated (4) using the local equilibrium steady-state hot atom kinetic theory (21, 22, 41). The  $\langle\tau^{*e}\rangle$  values can be compared with the mean reactive lifetimes for thermal Reaction 5,  $\langle\tau_5^{R_i}\rangle$ , obtained from absolute  $k_5^T$  and MNR sample composition data. At readily accessible moderator concentrations, the  $\langle\tau_5^{R_i}\rangle$  were shown to be tenfold or more larger than the  $\langle\tau^{*e}\rangle$ , even for very reactive  $R_i$  species. A calculated [ $\langle\tau_5^{R_i}\rangle/\langle\tau^{*e}\rangle$ ] ratio of 160 was obtained for  $C_2H_6$  present at  $5.0 \times 10^{-4}$  mol fraction in  $C_2F_6$ , showing that hot atom moderation is effectively completed prior to the onset of Reaction 5 in this system.

Mean hard sphere elastic intercollision lifetimes,  $\langle\tau^e\rangle$ , have been calculated using cross sections derived from gas–liquid critical data, leading to a [ $\langle\tau_5^{R_i}\rangle/\langle\tau^e\rangle$ ] ratio of 3600 for the  $C_2H_6/C_2F_6$  experiment

described above. Since [ $\langle \tau_5^{R_1} \rangle / \langle \tau^e \rangle$ ] represents the mean relative thermal  $^{18}\text{F}$  collision rate for hard sphere elastic vs. reactive encounters, many elastic collisions occur prior to Reaction 5 in this system for those recoil atoms that have failed to undergo hot reaction. The mean reactive collision efficiencies for thermal Reaction 5 with alkanes are unusually large, so that the corresponding  $\langle \tau_5^{R_1} \rangle$  values are small (1, 15). The nonthermal  $\text{H}^{18}\text{F}$  yield corrections for reactive  $\text{R}_i$  species also tend to be large. The combination of these effects greatly increases the difficulty of MNR studies of Reaction 5 with reactive hydrogen donors.

Mean nonthermal reactive lifetimes are generally shorter than the corresponding  $\langle \tau^{*e} \rangle$  values (4, 15, 21, 22). Under conditions of extreme moderation, therefore, the mean lifetimes for thermal vs. nonthermal reactions become vastly different. In the absence of unusual complications involving ionic or electronically excited recoil atoms (3), several general conclusions then follow (i) Hot and thermal reaction modes are temporally and dynamically uncoupled, or effectively independent, in well-designed MNR experiments, (ii) The formation of small nonthermal yields has no direct bearing on the applicability of the MNR equilibrium hypothesis, (iii) Under conditions of extreme moderation, the only important consequence of nonthermal contamination involves the introduction of spurious yield contributions for which corrections may have to be included in the kinetic analysis, and (iv) The temporal uncoupling that underlies these conclusions is more easily achieved in experiments involving inefficient thermal reactions. Of course, moderator impurity effects become increasingly serious as the thermal reactivity diminishes (1, 5).

Although the scattering cross sections that underlie these  $\langle \tau^{*e} \rangle$  and  $\langle \tau^e \rangle$  values are subject to uncertainty, the above conclusions are believed to be valid for many atom transfer reactions. The replacement of hard sphere  $\langle \tau^e \rangle$  by mean elastic intercollision lifetimes corresponding to a realistic potential description of the intermolecular forces, for example, would reinforce the present arguments (4).

**Bimolecular Reaction Tests of the MNR Equilibrium Hypothesis.** Relative MNR Arrhenius parameters for the  $^{18}\text{F}$  vs.  $\text{H}_2(\text{D}_2)$  reactions (17) exhibited close agreement with equilibrium discharge flow reactor results (42). If carried out over broad temperature ranges, such comparisons can reveal deviations from Maxwellian behavior for MNR-produced species (7, 10, 27, 43). The recent demonstration of  $^{18}\text{F}$ -loss decomposition of  $\dot{\text{C}}_3\text{F}_6^{18}\text{F}$  radicals accompanying Reaction 2 at 1.0 kTorr, however, diminishes the accuracy of these MNR parameters (6). Although the cited experiments yielded quantitative agreement, the significance of this demonstration is uncertain. Additional MNR measurements should be carried out at elevated ( $P/Z$ ) to suppress the decomposition of  $\text{C}_3\text{F}_6^{18}\text{F}$  radicals.

Table IV. Comparison of H<sup>18</sup>F Product Analysis vs. Chemiluminescence Relative Rate Coefficients

Substance (RH)	( $k_s^{300}/k_f^{300}$ ) (This Work) <sup>a</sup>	( $k_s^{300}/k_f^{300}$ ) (Ref. (44))	( $k_s^{300}/k_f^{300}$ ) (Calculated)
CHF <sub>3</sub>	89 ± 10	330 ± 50	0.266 ± 0.050
CH <sub>2</sub> F <sub>2</sub>	2.05 ± 0.22	> 33	< 0.062
H <sub>2</sub>	0.721 ± 0.014	2.7 ± 0.4	0.267 ± 0.040
CH <sub>3</sub> F	0.55 ± 0.02 <sup>b</sup> 0.54 ± 0.02 <sup>c</sup>	2.1 ± 0.3	0.263 ± 0.041
CH <sub>4</sub>	0.316 ± 0.012	(1.00 ± 0.15)	0.316 ± 0.049
cyclo-C <sub>3</sub> H <sub>6</sub>	0.102 ± 0.009	0.42 ± 0.06	0.245 ± 0.043
C <sub>2</sub> H <sub>6</sub>	0.074 ± 0.010	0.39 ± 0.06	0.188 ± 0.039
neo-C <sub>5</sub> H <sub>12</sub>	0.063 ± 0.005	0.22 ± 0.03	0.283 ± 0.047
cyclo-C <sub>6</sub> H <sub>12</sub>	0.045 ± 0.007	0.23 ± 0.04	0.193 ± 0.040
Nonweighted Average ( $k_s^{300}/k_f^{300}$ )			0.253 ± 0.044
Weighted Average <sup>d</sup> ( $k_s^{300}/k_f^{300}$ )			0.247 ± 0.015
Calculated <sup>e</sup> $k_2^{300}$ (cm <sup>3</sup> mol <sup>-1</sup> s <sup>-1</sup> )			(4.4 ± 0.3) × 10 <sup>13</sup>
Literature <sup>f</sup> $k_2^{300}$ (cm <sup>3</sup> mol <sup>-1</sup> s <sup>-1</sup> )			4.8 × 10 <sup>13</sup>

<sup>a</sup> Our previous MNR Arrhenius parameters have been revised based on weighted linear regression analysis. The present temperature corrections have been based on the new results, which have been included in Appendix A.

<sup>b</sup> Temperature correction based upon the assumption that  $E_{\text{CHF}_3} = E_{\text{CH}_4}$ .

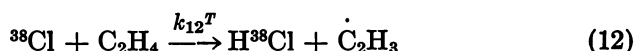
<sup>c</sup> 303 K.

<sup>d</sup> Reference 45.

<sup>e</sup> Based on weighted average ( $k_3^{300}/k_2^{300}$ ).

<sup>f</sup> Reference 13.

Recoil <sup>38</sup>Cl MNR experiments have been performed for the C<sub>2</sub>H<sub>4</sub>/CF<sub>2</sub>Cl<sub>2</sub> system at 300 K and 1.0 kTorr throughout the CF<sub>2</sub>Cl<sub>2</sub> mol fraction range 0.60–0.95 (43).



The CF<sub>2</sub>Cl<sub>2</sub> concentration-dependent absolute H<sup>38</sup>Cl yields,  $Y_{12}$ , were fitted using linear regression analysis. Below 0.90 CF<sub>2</sub>Cl<sub>2</sub> mol fraction  $Y_{12}$  exhibited a constant 1.0% increase per 0.10 mol fraction C<sub>2</sub>H<sub>4</sub> increase. In relative reactivity terms Reaction 12 became increasingly important with decreasing moderation. The equivalent kinetic description would involve a progressive reduction in the phenomenological ( $k_{13}^{300}/k_{12}^{300}$ ) relative rate coefficients below 0.90 CF<sub>2</sub>Cl<sub>2</sub> mol fraction.

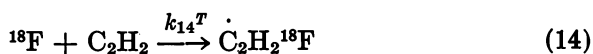
These results demonstrate the occurrence of nonthermal reactions at intermediate CF<sub>2</sub>Cl<sub>2</sub> concentrations. Since the total nonthermal yield becomes effectively constant, the establishment of equilibrium conditions for the remaining <sup>38</sup>Cl atoms at large CF<sub>2</sub>Cl<sub>2</sub> concentration would lead to

a constant  $Y_{12}$  value. With a precision of approximately  $\pm 8\%$ , the results obtained at 0.90 and 0.95  $\text{CF}_2\text{Cl}_2$  mol fractions exhibited such behavior. Although equilibrium conditions may have been established at  $\text{CF}_2\text{Cl}_2$  mol fractions above 0.90, the data obtained in this critical concentration region were not sufficiently detailed to warrant firm conclusions.

Analogous  $^{18}\text{F}$  measurements have been obtained for the  $\text{CH}_4/\text{C}_3\text{F}_6/\text{C}_2\text{F}_6$  MNR system (4, 6). With a sensitivity of approximately  $\pm 1\%$ , both the phenomenological ( $k_3^{273}/k_2^{273}$ ) values and the  $\text{H}^{18}\text{F}$  yields from Reaction 2 exhibited constancy throughout the  $\text{C}_2\text{F}_6$  mol fraction range 0.9500–0.9995. Within the available sensitivity, nonequilibrium effects were suppressed at  $\text{C}_2\text{F}_6$  mol fractions above 0.950.

Relative ( $k_2^{300}/k_5^{300}$ ) measurements based upon an HF chemiluminescence method (44) have been intercompared in Table IV with  $\text{H}^{18}\text{F}$  product analysis MNR results. A useful consistency test is provided by the ( $k_3^{300}/k_2^{300}$ ) ratios estimated from the two sets of data. With the exception of  $\text{CH}_2\text{F}_2$  reactant quantitative consistency was obtained with about 20% standard error of estimate.

An analogous comparison has been given in Table V between the  $\text{H}^{18}\text{F}$  product analysis and  $^{18}\text{F}$  atom loss MNR techniques (1, 2, 46, 47). Here the consistency test involves intercomparisons between ( $k_3^{283}/k_{14}^{283}$ ) ratios.



With approximately 20% standard error of estimate, quantitative agreement was obtained between these MNR techniques.

**Table V. Comparison of  $\text{H}^{18}\text{F}$  Product Analysis vs.  $^{18}\text{F}$  Loss Relative Rate Coefficients**

Substance (RH)	( $k_3^{283}/k_5^{283}$ ) (This work) <sup>a</sup>	( $k_{14}^{283}/k_5^{283}$ ) (Ref. (46, 47))	( $k_3^{283}/k_{14}^{283}$ ) (Calculated)
$\text{D}_2$	$1.75 \pm 0.03$	$12.5 \pm 3.1$	$0.140 \pm 0.035$
$\text{H}_2$	$0.766 \pm 0.013$	$7.1 \pm 1.0$	$0.108 \pm 0.015$
$\text{CD}_4$	$0.509 \pm 0.019$	$4.1 \pm 0.7$	$0.124 \pm 0.022$
$\text{CH}_4$	$0.246 \pm 0.010$	$2.4 \pm 0.2$	$0.102 \pm 0.010$
$\text{C}_2\text{H}_6$	$0.066 \pm 0.009$	$0.71 \pm 0.06$	$0.093 \pm 0.015$
Nonweighted Average ( $k_3^{283}/k_{14}^{283}$ )			$0.113 \pm 0.019$
Weighted Average <sup>b</sup> ( $k_3^{283}/k_{14}^{283}$ )			$0.105 \pm 0.007$
Calculated <sup>c</sup> $k_{14}^{283}$ ( $\text{cm}^3 \text{mol}^{-1} \text{s}^{-1}$ )			$(9.4 \pm 0.7) \times 10^{13}$
Literature <sup>d</sup> $k_{14}^{283}$ ( $\text{cm}^3 \text{mol}^{-1} \text{s}^{-1}$ )			$1.0 \times 10^{14}$

<sup>a</sup> For temperature corrections cf. note a of Table IV.

<sup>b</sup> Reference 45.

<sup>c</sup> Based on weighted average ( $k_3^{283}/k_{14}^{283}$ ).

<sup>d</sup> Reference 2.

**Table VI. Comparison of H<sup>18</sup>F Product Analysis ( $k_3^{300}/k_5^{300}$ ) Results with Absolute  $k_5^{300}$  Values for CHF<sub>3</sub>, H<sub>2</sub>, and CH<sub>4</sub>**

$$k_s^{300} = k_s^{300}(k_3^{300}/k_5^{300}) \text{ (cm}^3 \text{ mol}^{-1} \text{ s}^{-1}) \times 10^{-13}$$

Sub- stance (RH)	( $k_3^{300}/k_5^{300}$ ) (This work) <sup>a</sup>	(Ref. (48))	(Refs. (49, 50, 51))	(Refs. (52-62))
CHF <sub>3</sub>	89 ± 10	1.063	1.063	1.683, 0.797
H <sub>2</sub>	0.721 ± 0.014	1.082	0.800	2.740, <sup>b</sup> 1.298, 1.096, 1.082, 0.721, 0.721
CH <sub>4</sub>	0.316 ± 0.012	1.136	1.514	1.357
<i>Nonweighted Group Averages</i> <sup>c</sup>				
		1.094 ± 0.038	1.126 ± 0.361	1.094 ± 0.343
<i>Nonweighted Average <math>k_3^{300}</math> (cm<sup>3</sup> mol<sup>-1</sup> s<sup>-1</sup>)</i>			(1.10 ± 0.29) × 10 <sup>13</sup>	
<i>Weighted Average<sup>d</sup> <math>k_3^{300}</math> (cm<sup>3</sup> mol<sup>-1</sup> s<sup>-1</sup>)</i>			(1.09 ± 0.04) × 10 <sup>13</sup>	

<sup>a</sup> For temperature corrections cf. note *a* of Table IV.

<sup>b</sup> Reference 54 value for H<sub>2</sub> excluded from averages.

<sup>c</sup> Cited uncertainties represent standard deviations from the mean.

<sup>d</sup> Reference 4b.

Reliable absolute  $k_5^{300}$  values are available for CHF<sub>3</sub>, HCl, H<sub>2</sub>, and CH<sub>4</sub> (1, 13, 14), which have been summarized in Table VI together with the corresponding MNR results. As indicated by the constancy of  $k_3^{300}$  values obtained by combining the various data sets, the present temperature corrected results exhibit consistency with the absolute  $k_5^{300}$  measurements of Clyne, McKenney, and Walker (48), of Wagner and coworkers (49, 50, 51), and of various others (52-62). The standard deviations from the mean calculated  $k_3^{300}$  for these various groupings were 4%, 32%, and 31%. Here the enhanced consistency with the results of Clyne et al. suggests that their standard error assignments were probably conservative. Combining all these data leads to a calibrated absolute  $k_3^{300}$  result of (1.09 ± 0.12) × 10<sup>13</sup> cm<sup>3</sup> mol<sup>-1</sup> s<sup>-1</sup>, which can be compared with a 1.2 × 10<sup>13</sup> cm<sup>3</sup> mol<sup>-1</sup> s<sup>-1</sup> literature value (2) and which provides a useful basis for relative ( $k_3^{300}/k_5^{300}$ ) to absolute  $k_5^{300}$  rate coefficient scaling. The apparent  $k_3^{300}$  value at 1.0 kTorr has thus been established with an absolute accuracy (99.5% confidence level) of approximately ±20%.

The consistent success of the data comparisons shown in Tables IV-VI supports the utility of the <sup>18</sup>F MNR technique for obtaining approximately ±20% accurate thermal relative rate coefficients. Recently reported ( $k_3^{273}/k_2^{273}$ ) results, however, suggest that this reliability estimate may be conservative with respect to measurements carried out at enhanced moderator concentrations and within the ( $k_3^T/k_5^T$ ) range 0.10-10 (3, 4, 6).

Figure 1 shows that the nonthermal  $\text{H}^{18}\text{F}$  yields obtained from low reactivity hydrogen donors at large  $\text{C}_2\text{F}_6$  concentrations are negligibly important at ordinary MNR measurement sensitivity levels (1, 4, 5, 6). However, for reactive substances corrections based on calibration experiments of the type reported here must be included in the kinetic analysis (1).

**Unimolecular Reaction Tests of the MNR Equilibrium Hypothesis.** Atomic halogen olefinic addition reactions provide an alternative probe for nonthermal contamination (2, 6, 39, 43). The unimolecular rate constant for activated  $\dot{\text{C}}_2\text{H}_4^{38}\text{Cl}$  radicals produced via Reaction 13 has been investigated using the  $^{38}\text{Cl}$  vs.  $\text{C}_2\text{H}_4/\text{CF}_2\text{Cl}_2(\text{CF}_3\text{Cl})$  MNR systems. Although high-pressure limiting bimolecular  $k_{13}^T$  values were not obtained and the experimental sensitivity was not specified, Lee and Rowland reported that the apparent  $k_{13}^{288}$  exhibited constancy at  $\text{CF}_3\text{Cl}$  mol fractions above 0.90 (39).

In the absence of collisional energy transfer complications, the unimolecular technique can reveal changes in energy content for the radicals formed via Reactions 2, 8, or 13. At 300 K the high-pressure unimolecular rate constant for  $\dot{\text{C}}_2\text{H}_4^{38}\text{Cl}$  radicals formed from Reaction 13 increases by a factor of  $2.5 \pm 0.5$  accompanying a  $1.5 \pm 0.5$  kcal mol $^{-1}$  increase in the average excitation energy (40). Excess  $^{38}\text{Cl}$  translational energy would lead to this type of behavior.

The high-pressure unimolecular rate constant has not been measured for  $\dot{\text{C}}_2\text{H}_4^{38}\text{Cl}$  radicals produced from thermalized chlorine atoms. Further  $^{38}\text{Cl}$  experiments at increased  $\text{CF}_2\text{Cl}_2$  concentrations are needed to provide an indirect unimolecular test of the  $^{38}\text{Cl}$  MNR equilibrium hypothesis.

**The Epithermal Nonequilibrium Model.** The MNR thermalization tests may be conceptualized in terms of an epithermal steady-state hot atom collision energy probability density distribution (4, 20, 21, 22, 41, 43, 63, 64, 65). In epithermal terminology, high-pressure unimolecular rate constants for Reaction 13 can reveal "temperature" changes for the reacting  $^{38}\text{Cl}$  atoms. Based on the reported energy dependence for this system (40), experiments with  $\pm 20\%$  sensitivity could detect temperature variations of about  $100 \pm 35$  K.

Epithermal reasoning may also be applied to bimolecular tests for nonthermal contamination. For the  $^{18}\text{F}$  vs.  $\text{CH}_4/\text{C}_3\text{F}_6/\text{C}_2\text{F}_6$  system the phenomenological ( $k_3^{273}/k_2^{273}$ ) ratio decreased at  $\text{C}_2\text{F}_6$  mol fractions below 0.950 (4). Unimolecular complications were suppressed at 10.0 kTorr, and a constant ( $k_3^{273}/k_2^{273}$ ) value of  $0.326 \pm 0.004$  was obtained at  $\text{C}_2\text{F}_6$  mol fractions in the range 0.9500–0.9995. Apparent ( $k_3^{273}/k_2^{273}$ ) values of  $0.239 \pm 0.004$  and  $0.236 \pm 0.001$  corresponded to 0.700 (10.0 kTorr) and 0.000 (1.0 kTorr)  $\text{C}_2\text{F}_6$  mol fractions, clearly indicating nonthermal complications. Since these results exhibited consistency with

the thermal MNR kinetic analysis, deviations from equilibrium behavior cannot be detected in this fashion at a single  $C_2F_6$  concentration. In epithermal terms the  $(k_3^{237}/k_2^{273})$  value obtained at 0.700  $C_2F_6$  mol fraction indicates an approximately 100 K apparent temperature increase for the  $^{18}F$  atom pool.

These arguments suggest that bimolecular and unimolecular tests for nonthermal behavior exhibit roughly comparable sensitivity. Because of the neglect of time-dependent phenomena, however, epithermal modeling cannot reveal the microscopic nature of nonequilibrium effects in MNR experiments (4, 6, 21, 22, 41, 65).

**Absolute Thermal Rate Constants.** The absolute  $k_3^{300}$  result obtained above leads to many additional  $k_5^{300}$  values. In Table IV  $k_2^{300}$  has been calculated from the average  $(k_3^{300}/k_2^{300})$  ratio. An analogous determination of  $k_{14}^{283}$  appears in Table V based on the assumption that the  $E_5$  values for  $C_2D_6$  and neo- $C_5H_{12}$  are vanishingly small. Although reliable  $E_5$  results are not yet available for alkanes, the present temperature corrections have not been large enough in magnitude to constitute a serious source of systematic error.

Selected scaled  $k_5^{300}$  results have been presented in Table VII. A more extensive listing follows in Appendix B. Many thermal hydrogen abstraction and olefinic addition reactions have been tabulated that are too fast to be characterized using the available direct measurement methods. Based on comparisons with the scaled MNR data, the HF chemiluminescence (52), electron spin resonance (53, 66), and laser pulse decay (54, 67), absolute  $k_5^T$  techniques apparently involve large systematic errors.

### Summary

Several conclusions follow from the present results (i) The per-bond nonthermal F-to-HF reactivities for  $C_1$ - $C_6$  alkanes are roughly equivalent. Steric and/or bond strength effects in these substances may give rise to 10–15% reactivity differences, (ii) The deuterium kinetic isotope effects for the per-bond nonthermal F-to-HF (DF) reactivities are quite small for cyclopentane and  $C_2$ - $C_5$  alkanes, (iii) The nonthermal corrections to the MNR  $H^{18}F$  yields for low-reactivity hydrogen donors are negligibly small, and (iv) For reactive hydrocarbons the uniform per-bond reactivity model may be combined with the simple collision fraction mixture law and hard sphere elastic cross sections obtained from gas-liquid critical data to estimate the nonthermal  $H^{18}F$  yield corrections in MNR experiments. The simple mixture law should provide a good description of the trace nonthermal yields in experiments in which the total thermal competitor concentration is held constant.

**Table VII. Absolute Rate Constants for Selected Thermal Hydrogen Abstraction and Olefinic Addition Reactions by Atomic Fluorine<sup>a</sup>**

<i>Substance</i> ( <i>RH</i> )	<i>Competitor</i>	<i>Reference</i>	$k_3^{300}$ ( $\text{cm}^3 \text{mol}^{-1} \text{s}^{-1}$ ) $\times 10^{-13}$
CHF <sub>3</sub>	—	(13)	0.012 <sup>b</sup>
	—	(51)	0.012 ± 0.003
CH <sub>2</sub> F <sub>2</sub>	C <sub>3</sub> F <sub>6</sub>	(this work)	[0.0123 ± 0.0015]
	C <sub>3</sub> F <sub>6</sub>	(this work)	[0.54 ± 0.06] <sup>c</sup>
D <sub>2</sub>	C <sub>2</sub> H <sub>2</sub>	(46, 47)	0.76 ± 0.19 <sup>d</sup>
	C <sub>3</sub> F <sub>6</sub>	(this work)	[0.78 ± 0.03]
C <sub>3</sub> F <sub>6</sub>	H <sub>2</sub> , CH <sub>4</sub> , C <sub>2</sub> H <sub>2</sub>	(2)	1.2 <sup>e</sup>
	H <sub>2</sub> , CH <sub>4</sub> , CHF <sub>3</sub>	(this work)	[1.09 ± 0.04] <sup>f</sup>
	H <sub>2</sub> , CH <sub>4</sub> , CHF <sub>3</sub>	(this work)	[1.38 ± 0.21] <sup>g</sup>
H <sub>2</sub>	—	(13)	1.5 <sup>b</sup>
	—	(48)	1.5 ± 0.8
	C <sub>3</sub> F <sub>6</sub>	(this work)	[1.51 ± 0.06]
CH <sub>3</sub> F	CH <sub>4</sub>	(44)	2.1 ± 0.3
	C <sub>3</sub> F <sub>6</sub>	(this work)	2.0 ± 0.1
	weighted average <sup>h</sup>	(44, this work)	[2.0 ± 0.1]
CD <sub>4</sub>	C <sub>2</sub> H <sub>2</sub>	(46, 47)	2.2 ± 0.4 <sup>d</sup>
	C <sub>3</sub> F <sub>6</sub>	(this work)	[2.50 ± 0.12]
CH <sub>4</sub>	—	(13)	4.8 <sup>b</sup>
	—	(48)	3.6 ± 3.6
	C <sub>2</sub> H <sub>2</sub>	(46, 47)	3.9 ± 0.4 <sup>d</sup>
	C <sub>3</sub> F <sub>6</sub>	(this work)	4.7 ± 0.3
cyclo-C <sub>3</sub> H <sub>6</sub>	Table IV	(44, this work)	[4.4 ± 0.3]
	CH <sub>4</sub>	(44)	10.5 ± 1.6
	C <sub>3</sub> F <sub>6</sub>	(this work)	10.7 ± 1.0
C <sub>2</sub> H <sub>6</sub>	weighted average <sup>h</sup>	(44, this work)	[10.6 ± 0.8]
	C <sub>2</sub> H <sub>2</sub>	(46, 47)	13.3 ± 1.5 <sup>d</sup>
	CH <sub>4</sub>	(44)	11.2 ± 1.9
	C <sub>3</sub> F <sub>6</sub>	(this work)	14.7 ± 2.1
neo-C <sub>5</sub> H <sub>12</sub>	weighted average <sup>h</sup>	(44, this work)	[12.8 ± 1.4]
	CH <sub>4</sub>	(44)	20.0 ± 3.0
	C <sub>3</sub> F <sub>6</sub>	(this work)	17.3 ± 1.5
	weighted average <sup>h</sup>	(44, this work)	[17.8 ± 1.3]

<sup>a</sup> Recommended values enclosed in brackets.

<sup>b</sup> Recommended literature survey value.

<sup>c</sup> 303 K.

<sup>d</sup> 283 K.

<sup>e</sup> Apparent  $k_3^{283}$ .

<sup>f</sup> Apparent  $k_3^{300}$  at 1.00 kTorr.

<sup>g</sup> High-pressure limiting  $k_3^{300}$ .

<sup>h</sup> Reference 45.



In well-designed experiments the mean hot atom lifetime is much shorter than the mean thermal reactive lifetime. The MNR technique thus offers good utility for precise equilibrium kinetics studies with the radioactive atoms and unstable radicals produced using nuclear recoil methods. Small residual nonthermal reaction yields are invariably observed in recoil experiments, but these have no direct bearing on the validity of the MNR equilibrium hypothesis.

Both unimolecular and bimolecular rate coefficient measurements can be used for testing the MNR equilibrium hypothesis. The largest practicable moderator concentration should always be utilized in experiments designed to produce kinetic data. This is particularly important for systems involving efficient thermal reactions.

The above arguments strictly pertain only to the establishment of reagent translational equilibrium. In unfavorable situations nonequilibrium charge state, electronic state, or internal state effects may be more difficult to suppress than translational disequilibrium (3).

### *Acknowledgments*

Financial support has been provided by the U.C.D. Crocker Nuclear Laboratory and the U.S. Department of Energy under Contract No. AS03-76SF00034, Agreement No. AT03-76ER70158.

### *Literature Cited*

1. Mo, S. H.; Grant, E. R.; Little, F. E.; Manning, R. G.; Mathis, C. A.; Werre, G. S.; Root, J. W. *ACS Symp. Ser.* 1978, 66, 59.
2. Rowland, F. S.; Rust, R.; Frank, J. P. *ACS Symp. Ser.* 1978, 66, 26.
3. Gaspar, P. P.; Root, J. W. *Radiochim. Acta*, in press.
4. Mathis, C. A.; Knierim, K. D.; Root, J. W. *Chem. Phys. Lett.* 1980, 72, 368.
5. Mathis, C. A.; Gurvis, R.; Knickelbein, M.; Knierim, K. D.; Mo, S. H.; Root, J. W., *Int. J. Chem. Kinet.* 1981, 28, 191.
6. Mathis, C. A.; Root, J. W., unpublished data.
7. Grant, E. R.; Root, J. W. *J. Chem. Phys.* 1976, 64, 417.
8. Manning, R. G.; Root, J. W. *J. Chem. Phys.* 1976, 64, 4926.
9. Manning, R. G.; Root, J. W. *J. Phys. Chem.* 1977, 81, 2576.
10. Manning, R. G.; Mo, S. H.; Root, J. W. *J. Chem. Phys.* 1977, 67, 636.
11. Manning, R. G.; Root, J. W. *J. Chem. Phys.* 1980, 72, 6323.
12. Root, J. W.; Manning, R. G. Chapter 5 in this book.
13. Foon, R.; Kaufman, M. *Prog. React. Kinet.* 1975, 8, 81.
14. Jones, W. E.; Skolnik, E. G. *Chem. Rev.* 1976, 76, 563.
15. Mathis, C. A., Ph.D. Dissertation, Univ. of California, Davis, 1979.
16. Parks, N. J.; Krohn, K. A.; Root, J. W. *J. Chem. Phys.* 1971, 55, 2690.
17. Grant, E. R.; Root, J. W. *J. Chem. Phys.* 1975, 63, 2970.
18. Grant, E. R., Ph.D. Dissertation, Univ. of California, Davis, 1980.
19. Knierim, K. D., Ph.D. Dissertation, Univ. of California, Davis, 1980.
20. Wolfgang, R. *J. Chem. Phys.* 1963, 39, 2983.
21. Knierim, K. D.; Root, J. W. *Radiochim. Acta* 1977, 24, 103.
22. Grant, E. R.; Feng, D. F.; Keizer, J.; Knierim, K. D.; Root, J. W. *ACS Symp. Ser.* 1978, 66, 314.

23. Root, J. W., Ph.D. Dissertation, Univ. of Kansas, Lawrence, 1964.
24. Root, J. W.; Breckenridge, W.; Rowland, F. S. *J. Chem. Phys.* **1965**, *43*, 3694.
25. Root, J. W.; Rowland, F. S. *J. Chem. Phys.* **1967**, *46*, 4299.
26. Root, J. W.; Rowland, F. S. *J. Phys. Chem.* **1970**, *74*, 451.
27. Menzinger, M.; Wolfgang, R. *Angew. Chem. Int. Ed.* **1960**, 438.
28. Chapman, S.; Valencich, T.; Bunker, D. L. *J. Chem. Phys.* **1974**, *60*, 329.
29. Tachikawa, E.; Tang, Y. N.; Rowland, F. S. *J. Am. Chem. Soc.* **1968**, *90*, 3584.
30. Tachikawa, E.; Rowland, F. S. *J. Am. Chem. Soc.* **1968**, *90*, 4767.
31. Tominaga, T.; Rowland, F. S. *J. Phys. Chem.* **1968**, *72*, 1399.
32. Tachikawa, E.; Rowland, F. S. *J. Am. Chem. Soc.* **1969**, *91*, 559.
33. Root, J. W. *J. Phys. Chem.* **1969**, *73*, 3174.
34. Hosaka, A.; Rowland, F. S. *J. Phys. Chem.* **1973**, *77*, 705.
35. Williams, J. L.; Daniel, S. H.; Tang, Y. N. *J. Phys. Chem.* **1973**, *77*, 2464.
36. Roginsky, S. Z. "Theoretical Principles of Isotope Methods for Investigating Chemical Reactions;" (Enl. Transl. by Consultants Bur., Inc.; TIS Document AEC-tr-2873); Academy of Sciences: U.S.S.R.: Moscow, 1956.
37. Honig, R. E. In: *Symposium on the Use of Isotopes in Petroleum Chemistry*. Petroleum Chemistry Division, Amer. Chem. Soc.: Chicago, 1950, p. 37.
38. Lee, F. S. C.; Rowland, F. S. *J. Phys. Chem.* **1977**, *81*, 1222.
39. *Ibid.*, 1229.
40. *Ibid.*, 1235.
41. Keizer, J. *J. Chem. Phys.* **1973**, *58*, 4524.
42. Persky, A. *J. Chem. Phys.* **1973**, *59*, 3612, 5578.
43. Stevens, D. J.; Spicer, L. D. *J. Phys. Chem.* **1977**, *81*, 1217.
44. Smith, D. J.; Setser, D. W.; Kim, K. C.; Bogan, D. J. *J. Phys. Chem.* **1977**, *81*, 898.
45. Meyer, S. L. "Data Analysis for Scientists and Engineers;" John Wiley & Sons: New York, 1975.
46. Williams, R. L.; Rowland, F. S. *J. Phys. Chem.* **1971**, *75*, 2709.
47. *Ibid.*, **1973**, *77*, 301.
48. Clyne, M. A. A.; McKenney, D. J.; Walker, R. F. *Can. J. Chem.* **1973**, *51*, 3596.
49. Homann, V. K.; Solomon, W. C.; Warnatz, J.; Wagner, H. G.; Zetzsch, C. *Ber. Bunsenges. Phys. Chem.* **1970**, *74*, 585.
50. Wagner, H. G.; Warnatz, J.; Zetzsch, C. *An. Asoc. Quim. Argent.* **1971**, *59*, 169.
51. Wagner, H. G., private communication.
52. Pollock, T. L.; Jones, W. E. *Can. J. Chem.* **1973**, *51*, 2041.
53. Goldberg, I. B.; Schneider, G. R. *J. Chem. Phys.* **1976**, *65*, 147.
54. Komp, K. L.; Wanner, J. *Chem. Phys. Lett.* **1972**, *12*, 560.
55. Dodnov, A. F.; Lavrovskaya, G. K.; Morozov, I. I.; Talroze, V. L. *Dokl. Phys. Chem. (Engl. transl.)* **1971**, *198*, 440.
56. Igoshin, V. I.; Kulakov, L. V.; Nikitin, A. I. *Kratk. Soobshch. Fiz.* **1973**, *1*, 3; *Chem. Abstr.* **1973**, *79*, 149944.
57. Igoshin, V. I.; Kulakov, L. V.; Nikitin, A. I. *Krantovaya Elektron Moscow* **1973**, 50.
58. Igoshin, V. I.; Kulakov, L. V.; Nikitin, A. I. *Sov. J. Quant. Electron.* **1972**, *3*, 306.
59. Bozzelli, J., Thesis, Princeton Univ., Princeton, N.J., 1972.
60. Kapralova, G. A.; Margolina, A. L.; Chaikin, A. M. *Kinet. Katal.* **1970**, *11*, 669.
61. Kapralova, G. A.; Margolina, A. L.; Chaikin, A. M. *Dokl. Phys. Chem. (Engl. Transl.)* **1971**, *197*, 281.
62. *Ibid.*, **1971**, *198*, 452.

63. Stevens, D. J.; Spicer, L. D. *J. Am. Chem. Soc.* **1978**, *100*, 3295.
64. Feng, D. F.; Grant, E. R.; Root, J. W. *J. Chem. Phys.* **1976**, *64*, 3450.
65. Keizer, J. *J. Chem. Phys.* **1972**, *56*, 5958.
66. Rabideau, S. W.; Hecht, H. G.; Lewis, W. B. *J. Magn. Reson.* **1972**, *6*, 384.
67. Pearson, R. K.; Cowles, J. O.; Hermann, G. L.; Gregg, D. W.; Creighton, J. R. *IEEE J. Quantum Electron.* **1973**, *9*, 879.
68. Warnatz, J.; Wagner, H. G.; Zetzsch, C., Report T-0240/92410/01017 to the Fraunhofer Gesellschaft, 1972.
69. Wolfrum, J., Ph.D. Dissertation, Georg-August Univ., Göttingen, 1968.
70. Zetzsch, C., Ph.D. Dissertation, Georg-August Univ., Göttingen, 1971.
71. Jonathan, N.; Melliar-Smith, C. M.; Okuda, S.; Slater, D. H.; Timlin, D. *Mol. Phys.* **1971**, *22*, 561.
72. Warnatz, J., Ph.D. Dissertation, Georg-August Univ., Göttingen, 1968.

### Appendix A

This appendix includes a summary of the available MNR ( $k_3^T/k_5^T$ ) relative rate coefficients (Table VIII) and Arrhenius parameters (Table IX). In light of the recent demonstration (6) that  $\dot{C}_3F_6^{18}F$  unimolecular complications accompany thermal Reaction 3 at 1.0 kTorr, the quantitative significance of these Arrhenius parameters is uncertain. They are thus only provisionally endorsed pending the availability of new measurements carried out at increased ( $P/Z$ ). In the present study Table IX has provided the basis for small ( $k_3^T/k_5^T$ ) adjustments in the neighborhood of 300 K.

**Table VIII. Summary of ( $k_3^T/k_5^T$ ) Results Obtained from RH/C<sub>3</sub>F<sub>6</sub>/C<sub>2</sub>F<sub>6</sub> <sup>18</sup>F MNR Experiments at 1.00 kTorr<sup>a</sup>**

<i>Substance (RH)</i>	<i>T (K)</i>	<i>(k<sub>3</sub><sup>T</sup>/k<sub>5</sub><sup>T</sup>)</i>
CHF <sub>3</sub>	308	84 ± 10
CH <sub>2</sub> F <sub>2</sub>	303	2.05 ± 0.22
D <sub>2</sub>	273	1.90 ± 0.03
D <sub>2</sub>	303	1.44 ± 0.02
D <sub>2</sub>	345	0.847 ± 0.029
D <sub>2</sub>	405	0.659 ± 0.008
D <sub>2</sub>	475	0.441 ± 0.022
H <sub>2</sub>	273	0.826 ± 0.012
H <sub>2</sub>	303	0.703 ± 0.013
H <sub>2</sub>	353.5	0.404 ± 0.013
H <sub>2</sub>	405	0.338 ± 0.022
CH <sub>3</sub> F	303	0.547 ± 0.023
CD <sub>4</sub>	273	0.507 ± 0.024
CD <sub>4</sub>	303	0.445 ± 0.013
CD <sub>4</sub>	357.5	0.348 ± 0.010
CD <sub>4</sub>	429	0.177 ± 0.018
CH <sub>4</sub>	273	0.256 ± 0.006
CH <sub>4</sub> <sup>b</sup>	273	0.326 ± 0.004
CH <sub>4</sub> <sup>c</sup>	273	0.321 ± 0.007
CH <sub>4</sub> <sup>d</sup>	273	0.301 ± 0.007
CH <sub>4</sub> <sup>e</sup>	273	0.330 ± 0.005
CH <sub>4</sub> <sup>f</sup>	273	0.327 ± 0.006
CH <sub>4</sub>	303	0.312 ± 0.012
CH <sub>4</sub>	357.5	0.190 ± 0.002
CH <sub>4</sub>	429	0.217 ± 0.009
CH <sub>4</sub>	475	0.166 ± 0.026
C <sub>2</sub> D <sub>6</sub>	273	0.102 ± 0.013
C <sub>2</sub> D <sub>6</sub>	303	0.120 ± 0.007
C <sub>2</sub> D <sub>6</sub>	473	0.249 ± 0.025
cyclo-C <sub>3</sub> H <sub>6</sub>	303	0.102 ± 0.009
neo-C <sub>5</sub> D <sub>12</sub>	303	0.102 ± 0.009
C <sub>2</sub> H <sub>6</sub>	303	0.074 ± 0.010
neo-C <sub>5</sub> H <sub>12</sub>	273	0.060 ± 0.012
neo-C <sub>5</sub> H <sub>12</sub>	303	0.064 ± 0.007
neo-C <sub>5</sub> H <sub>12</sub>	473	0.103 ± 0.013
cyclo-C <sub>5</sub> H <sub>10</sub>	303	0.047 ± 0.005
cyclo-C <sub>6</sub> H <sub>12</sub>	303	0.045 ± 0.007

<sup>a</sup> 0.950 C<sub>2</sub>F<sub>6</sub> moderator mol fraction unless noted otherwise.<sup>b</sup> 10.0 kTorr (*P/Z*).<sup>c</sup> 20.0 kTorr (*P/Z*).<sup>d</sup> 0.900 C<sub>2</sub>F<sub>6</sub> mol fraction and 10.0 kTorr (*P/Z*).<sup>e</sup> 0.9950 C<sub>2</sub>F<sub>6</sub> mol fraction and 10.0 kTorr (*P/Z*).<sup>f</sup> 0.9995 C<sub>2</sub>F<sub>6</sub> mol fraction and 10.0 kTorr (*P/Z*).

**Table IX. Relative MNR Arrhenius Parameters Obtained at 273–475 K and 1.00 kTorr**

Substance (RH)	( $E_5 - E_s$ ) ( $\text{kJ mol}^{-1}$ )	$\text{Log}_e(A_s/A_5)$
D <sub>2</sub>	7610 ± 390	0.068 ± 0.010
H <sub>2</sub>	6450 ± 1150	0.049 ± 0.023
CHF <sub>3</sub> <sup>a</sup>	5140 ± 590	—
CD <sub>4</sub>	4940 ± 1460	0.062 ± 0.034
CH <sub>4</sub>	2490 ± 680	0.085 ± 0.023
neo-C <sub>5</sub> H <sub>12</sub>	−3160 ± 600	0.229 ± 0.025
C <sub>2</sub> D <sub>6</sub>	−4970 ± 600	0.872 ± 0.108

<sup>a</sup> Estimated based upon  $E_{\text{CHF}_3} = 9200 \pm 710$  (51) and the assumption, obtained by averaging the above C<sub>2</sub>D<sub>6</sub> and neo-C<sub>5</sub>H<sub>12</sub> results, that  $E_{\text{C}_2\text{F}_6} = 4070 \pm 920$  kJ mol<sup>−1</sup>.

### Appendix B

A comprehensive listing of absolute thermal rate coefficients for hydrogen abstraction and olefinic addition reactions by atomic fluorine has been given in Table X.

**Table X. Compendium of Absolute Rate Constants for Thermal Hydrogen Abstraction and Olefinic Addition Reactions by Atomic Fluorine<sup>a</sup>**

Substance (RH)	Competitor	Reference	$k_s^{300}$ ( $\text{cm}^3 \text{mol}^{-1} \text{s}^{-1}$ ) × 10 <sup>−13</sup>
CHF <sub>3</sub>	—	(13)	0.012 <sup>b</sup>
	—	(48)	0.012 ± 0.018
	—	(51)	0.012 ± 0.003
	CH <sub>4</sub>	(44)	0.013 ± 0.002
	C <sub>3</sub> F <sub>6</sub>	(this work)	[0.0123 ± 0.0015]
CHCl <sub>2</sub> F	—	(13, 68)	0.09
CHClF <sub>2</sub>	—	(52)	0.15
	—	(13, 68)	0.05
CHCl <sub>3</sub>	—	(48)	[0.32 ± 0.08]
C <sub>2</sub> H <sub>2</sub>	—	(14, 69)	[0.35 ± 0.10]
	C <sub>2</sub> H <sub>2</sub>	(46, 47, this work)	1.3 ± 0.6 <sup>c</sup>
CH <sub>3</sub> NO <sub>2</sub>	CH <sub>4</sub>	(44)	[0.40 ± 0.08]
H <sub>2</sub> O <sub>2</sub>	CH <sub>4</sub>	(44)	0.44 ± 0.09
CH <sub>3</sub> CF <sub>3</sub>	C <sub>2</sub> H <sub>2</sub>	(46, 47)	[0.49 ± 0.12] <sup>c</sup>
CH <sub>2</sub> F <sub>2</sub>	—	(52)	1.1
	CH <sub>4</sub>	(44)	0.13 ± 0.02
	C <sub>3</sub> F <sub>6</sub>	(this work)	[0.54 ± 0.06] <sup>d</sup>
CH <sub>2</sub> Cl <sub>2</sub>	—	(48)	[0.58 ± 0.14]
H <sub>2</sub> O	—	(70)	0.66

Table X. Continued

Substance (RH)	Competitor	Reference	$k_f^{300}$ ( $\text{cm}^3 \text{mol}^{-1} \text{s}^{-1}$ ) $\times 10^{-13}$
HCl	—	(13)	0.65 <sup>b</sup>
	—	(52)	0.73
	—	(13, 68)	0.65
	CH <sub>4</sub>	(44)	0.57 ± 0.10
	CH <sub>4</sub>	(71)	0.83 ± 0.11
	average		[0.68 ± 0.09]
D <sub>2</sub>	—	(56-58)	1.3
	C <sub>2</sub> H <sub>2</sub>	(46, 47)	0.76 ± 0.19 <sup>c</sup>
	C <sub>3</sub> F <sub>6</sub>	(this work)	0.56 ± 0.02 <sup>c</sup>
CH <sub>3</sub> CN	C <sub>3</sub> F <sub>6</sub>	(this work)	[0.78 ± 0.03]
	CH <sub>4</sub>	(44)	[0.83 ± 0.27]
	H <sub>2</sub> , CH <sub>4</sub> , C <sub>2</sub> H <sub>2</sub>	(2)	1.2 <sup>c,c</sup>
	H <sub>2</sub> , CH <sub>4</sub> , CHF <sub>3</sub>	(this work)	0.99 ± 0.05 <sup>c,c</sup>
C <sub>3</sub> F <sub>6</sub>	H <sub>2</sub> , CH <sub>4</sub> , CHF <sub>3</sub>	(this work)	[1.09 ± 0.04] <sup>c</sup>
	H <sub>2</sub> , CH <sub>4</sub> , CHF <sub>3</sub>	(this work)	[1.17 ± 0.18] <sup>c</sup>
	H <sub>2</sub> , CH <sub>4</sub> , CHF <sub>3</sub>	(this work)	[1.38 ± 0.21] <sup>c</sup>
	H <sub>2</sub> , CH <sub>4</sub> , CHF <sub>3</sub>	(this work)	[1.4 ± 0.4]
CH <sub>3</sub> Cl	—	(48)	2.6 ± 0.5
	CH <sub>4</sub>	(44)	1.5 <sup>b</sup>
H <sub>2</sub>	—	(13)	1.5 ± 0.8
	—	(48)	1.3 ± 0.2 <sup>c</sup>
	C <sub>2</sub> H <sub>2</sub>	(46, 47)	1.29 ± 0.05 <sup>c</sup>
	C <sub>3</sub> F <sub>6</sub>	(this work)	1.6 ± 0.3
	CH <sub>4</sub>	(44)	[1.51 ± 0.06]
	C <sub>3</sub> F <sub>6</sub>	(this work)	1.7 <sup>c</sup>
CFCl=CFCl <sup>c</sup>	C <sub>2</sub> H <sub>2</sub>	(2)	1.5 <sup>c</sup>
	C <sub>2</sub> H <sub>2</sub>	(2, this work)	5.3
	—	(52)	2.1 ± 0.3
CH <sub>3</sub> F	CH <sub>4</sub>	(44)	2.0 ± 0.1
	C <sub>3</sub> F <sub>6</sub>	(this work)	[2.0 ± 0.1]
	weighted average	(44, this work)	2.2 ± 0.4 <sup>c</sup>
CD <sub>4</sub>	C <sub>2</sub> H <sub>2</sub>	(46, 47)	1.94 ± 0.11 <sup>c</sup>
	C <sub>3</sub> F <sub>6</sub>	(this work)	[2.50 ± 0.12]
	C <sub>3</sub> F <sub>6</sub>	(this work)	[2.4 ± 0.4]
C <sub>2</sub> H <sub>4</sub>	CH <sub>4</sub>	(44)	4.0
	—	(72)	2.9 ± 0.4
HBr	CH <sub>4</sub>	(44)	3.7 ± 0.7
	CH <sub>4</sub>	(71)	[3.5 ± 0.6]
	average	(44, 71, 72)	3.4 ± 0.6 <sup>c</sup>
	C <sub>2</sub> H <sub>2</sub>	(46, 47)	3.1 ± 0.5
HI	CH <sub>4</sub>	(44)	5.3 ± 0.6
	CH <sub>4</sub>	(71)	[4.0 ± 0.4]
	weighted average	(44, 71)	[4.4 ± 0.7]
	CH <sub>4</sub>	(71)	4.8 <sup>b</sup>
C <sub>6</sub> H <sub>6</sub>	—	(13)	3.6 ± 3.6
	—	(48)	3.9 ± 0.4 <sup>c</sup>
	C <sub>2</sub> H <sub>2</sub>	(46, 47)	4.0 ± 0.2 <sup>c</sup>
	C <sub>3</sub> F <sub>6</sub>	(this work)	4.7 ± 0.3
	C <sub>3</sub> F <sub>6</sub>	(this work)	[4.4 ± 0.3]
	Table IV	(44, this work)	

Table X. Continued

Substance (RH)	Competitor	Reference	$k_f^{300}$ ( $\text{cm}^3 \text{mol}^{-1} \text{s}^{-1}$ ) $\times 10^{-13}$
$\text{CH}_3\text{COCH}_3$	$\text{CH}_4$	(44)	$[7.0 \pm 1.1]$
$\text{CH}_3\text{CHO}$	$\text{CH}_4$	(44)	$[7.0 \pm 1.1]$
$\text{C}_2\text{H}_4^*$	$\text{C}_2\text{H}_2$	(2)	$8.4^*$
	$\text{C}_2\text{H}_2$	(2, this work)	$[7.7 \pm 0.6]^*$
$\text{H}_2\text{S}$	$\text{C}_2\text{H}_2$	(46, 47)	$12.4 \pm 1.3^*$
	$\text{CH}_4$	(44)	$[8.8 \pm 1.5]$
$\text{C}_2\text{D}_6$	$\text{C}_3\text{F}_6$	(this work)	$[9.3 \pm 0.6]$
$\text{C}_2\text{H}_2^*$	$\text{CH}_4$	(2)	$10.2^*$
	Table V	(2, this work)	$[9.4 \pm 0.7]^*$
$\text{CHCl}=\text{CHCl}^*$	$\text{CH}_4$	(2)	$10.2^*$
	RH, RD, $\text{C}_3\text{F}_6$	(2, this work)	$[9.4 \pm 0.7]^*$
cyclo- $\text{C}_3\text{H}_6$	$\text{CH}_4$	(44)	$10.5 \pm 1.6$
	$\text{C}_3\text{F}_6$	(this work)	$10.7 \pm 1.0$
	weighted average	(44, this work)	$[10.6 \pm 0.8]$
neo- $\text{C}_5\text{D}_{12}$	$\text{C}_3\text{F}_6$	(this work)	$[10.9 \pm 1.0]^*$
$\text{CH}_3\text{OCH}_3$	$\text{CH}_4$	(44)	$[11.9 \pm 2.1]$
$\text{C}_2\text{H}_6$	$\text{C}_2\text{H}_2$	(46, 47)	$13.3 \pm 1.5^*$
	$\text{C}_3\text{F}_6$	(this work)	$14.9 \pm 2.1^*$
	$\text{CH}_4$	(44)	$11.2 \pm 1.9$
	$\text{C}_3\text{F}_6$	(this work)	$14.7 \pm 2.1$
	weighted average	(44, this work)	$[12.8 \pm 1.4]$
neo- $\text{C}_5\text{H}_{12}$	$\text{CH}_4$	(44)	$20.0 \pm 3.0$
	$\text{C}_3\text{F}_6$	(this work)	$17.3 \pm 1.5$
	weighted average	(44, this work)	$[17.8 \pm 1.3]$
cyclo- $\text{C}_6\text{H}_{12}$	$\text{CH}_4$	(44)	$19.1 \pm 3.6$
	$\text{C}_3\text{F}_6$	(this work)	$24.2 \pm 3.9$
	weighted average	(44, this work)	$[21.4 \pm 2.6]$
cyclo- $\text{C}_5\text{H}_{10}$	$\text{C}_3\text{F}_6$	(this work)	$[23.2 \pm 2.6]$
$\text{GeH}_4$	$\text{CH}_4$	(44)	$[25.6 \pm 4.9]$
$\text{SiH}_4$	$\text{CH}_4$	(44)	$[29.3 \pm 4.4]$

\* Recommended values enclosed in brackets.

† Recommended literature survey value.

\* 283 K.

\* 303 K.

\* Apparent olefinic addition rate constant.

† High-pressure limiting olefinic addition rate constant at 273 K.

\* High-pressure limiting olefinic addition rate constant at 300 K.

RECEIVED September 4, 1980.

# The Use of Isotopic Nitrogen as a Biochemical Tracer

KENNETH A. KROHN<sup>1</sup> and CHESTER A. MATHIS

Department of Radiology (Nuclear Medicine) and Crocker Nuclear Laboratory, University of California, Davis, CA 95616

*Nitrogen chemistry involving such diverse problems as food production, metabolism, and environmental control has been impeded by unavailability of good tracers. Stable isotopes have been useful but their value is limited by the requirement for large amounts of carrier and by variations in natural N-isotope abundance. The longest lived radioisotope of nitrogen, <sup>13</sup>N ( $t_{1/2} = 10$  min), is inconveniently short-lived for biological research, but it is uniquely valuable in experiments requiring high specific activity nitrogen to trace rapid kinetics and metabolic pathways. It offers 10<sup>8</sup>-fold increased detection sensitivity over stable isotope methods. Simple <sup>13</sup>N-metabolites such as ammonia, nitrite, and nitrate have been synthesized and their distribution kinetics and biochemical transformations have been measured in plants and animals. These experiments involve sampling the biological model's constituents and HPLC analysis to detect metabolic products of only 10<sup>-5</sup>%.*

Of those elements that comprise most of our living world—carbon, hydrogen, nitrogen, and oxygen—there are no  $\gamma$ -emitting radionuclides of convenient half-life for widespread distribution and large-scale application in the research laboratory. There are no  $\gamma$ -emitting isotopes of hydrogen at all, and the longest-lived  $\gamma$ -emitting nuclides of carbon, nitrogen, and oxygen have half-lives of 20, 10, and 2 min, respectively. These are all inconveniently short and require that the isotope be used at the accelerator site where it was produced. However, a short half-life can be an advantage. Such nuclides can be prepared at a very high specific activity, and they decay rapidly. These characteristics allow

<sup>1</sup> Current address: Department of Nuclear Medicine, RC-70, University of Washington Hospital, Seattle, WA 98195.

0065-2392/81/0197-0233\$05.00/0  
© 1981 American Chemical Society



experiments to be spiked with multiple consecutive batches of radioisotope, resulting in serial studies following perturbations of the chemical or biological system under investigation.

Stable isotopes of each of these elements have played important roles in elucidation of their chemistries. Specifically,  $^{14}\text{N}$  and  $^{15}\text{N}$  have been used as stable tracers for research on N-chemistry dealing with food and fiber production, metabolic pathways, and environmental control. Their value is ultimately limited because macroscopic amounts of carrier often exceed in situ concentrations (and therefore influence the biochemistry), and natural nitrogen isotope fractionation leads to variances in natural abundance. Nevertheless, stable tracers have been used effectively in many studies, including following N-cycle processes in soils (1) and unraveling metabolic pathways (2, 3).

### *History of $^{13}\text{N}$ Tracer Studies*

The first radioisotope of nitrogen to be identified was  $^{13}\text{N}$ , a positron emitter with a 10-min half-life. Subsequent investigations have confirmed this isotope as the longest-lived radioisotope of nitrogen. The original observation of the nuclear synthesis of  $^{13}\text{N}$  was reported in 1934 by Joliot and Curie (4). They irradiated boron nitride with  $\alpha$  particles and found that by heating the BN with caustic soda, gaseous ammonia could be produced. The activity was conveniently separated from the boron nitride by simple distillation. This represents not only the first synthesis of radioisotopic nitrogen but also the first synthesis of a labeled nitrogen compound,  $^{13}\text{NH}_3$ .

Nitrogen-13 was first used as a biological tracer by Martin Kamen and his colleagues at the Crocker Cyclotron, Berkeley, in 1940 (5). These investigators irradiated charcoal (carbon) with 8-MeV deuterons to make radioactive  $^{13}\text{NN}$  gas, which was contained in a desiccator and used to quantitate the assimilation of  $\text{N}_2$  by barley plants. Kamen et al. estimated that the plants assimilated  $10^{-4}$  to  $10^{-5}$  of the radioactive  $\text{N}_2$  and considered their experiments positive evidence for nitrogen fixation by nonleguminous plants. Their pioneering research is only marred by a wrong conclusion; barley plants do not fix nitrogen. Perhaps these researchers were led astray by traces of either  $^{13}\text{NH}_3$  or  $^{13}\text{NO}_3^-$  in their radiochemical product. Either of these radiochemicals would be assimilated by barley.

The next contribution to the  $^{13}\text{N}$  literature came from the laboratory of Joseph Varner, but it has been recorded only in a paper presented at the University of Pennsylvania in 1959 (6). Varner and Carangal bombarded thin graphite targets with deuterons at the Ohio State University cyclotron and prepared  $^{13}\text{N}$ -labeled  $\text{NO}_3^-$ ,  $\text{NO}_2^-$ ,  $\text{NH}_3$ , and  $\text{N}_2$ . These

compounds were intended for studies of inorganic nitrogen metabolism; however, there is no further report of their application in Varner's laboratory. Many of the  $^{13}\text{N}$  radiochemical methods used today originated with Varner's brief but benchmark studies.

In 1961 Nicholas and coworkers reported their use of  $^{13}\text{N}$  for studying nitrogen fixation by bacteria (7). They bombarded coarsely granulated charcoal with 15-MeV deuterons from the MRC cyclotron at Hammersmith Hospital, England. Radioactive  $\text{N}_2$  gas was continuously swept from the target by the carrier argon and with a 40- $\mu\text{A}$  deuteron beam the activity produced ranged from 30–60 mCi/L. Various microorganisms confined in 50-mL Erlenmeyer flasks were exposed to the  $^{13}\text{NN}$  during agitation in a water bath at 30°C. Aliquots of supernatant were removed periodically for measurement of  $^{13}\text{N}$  uptake. The effects of various experimental parameters were noted, and the authors commented on the possibility of determining the chemical composition of early fixation products. However, since that time the research interests of the Hammersmith cyclotron team have evolved toward a more medical emphasis, and these initially exciting observations have not been pursued.

Researchers at the University of Manitoba cyclotron introduced the  $^{14}\text{N}(\text{p,d})^{13}\text{N}$  nuclear reaction to produce  $^{13}\text{NN}$  for rapid screening of the N-fixation potential of microorganisms (8). Their target was melamine plastic powder (40% N), which was irradiated with 50-MeV protons to give a gaseous yield of 5 mCi/L of gas. The high proton irradiation energy was chosen as a result of physical design limitations inherent in their cyclotron. The experimental arrangement for preparing the nitrogen gas and exposing microorganisms was similar to that described above. They exposed a number of subarctic soil bacteria to  $^{13}\text{NN}$  and found that several had N-fixing potential. These researchers were enthusiastic about the potential of tracer nitrogen techniques for N-fixation research, particularly as a means of rapid screening of fixation potential. The fact that  $^{13}\text{N}$  has not achieved widespread use as a screening agent for N-fixation research is probably attributable to the advent of the acetylene reduction technique for equivalent measurements (9).

In the mid-1960s cyclotrons dedicated to biomedical research became available in several hospitals. These were used for preparing several  $^{13}\text{N}$ -labeled radiopharmaceuticals, principally  $^{13}\text{NN}$  and  $^{13}\text{NH}_3$ . While the short half-life limited general clinical utility of  $^{13}\text{N}$ -radiopharmaceuticals, nitrogen gas found some use for lung ventilation studies and ammonia has been used as a myocardial imaging agent (10, 11). The pioneering work in promoting  $^{13}\text{N}$  radiopharmaceuticals was done by Welch in the United States (12) and Clark in the United Kingdom (13).

Nitrogen-13 research was initiated at our laboratory in 1971 by Parks, Peek, and Goldstein (14). They produced  $^{13}\text{NO}_2$  gas by the  $^{16}\text{O}(\text{p},\alpha)^{13}\text{N}$

nuclear reaction in a high-pressure oxygen target. Cryogenically recovered  $^{18}\text{NO}_2$  was used in a study of the intrapulmonary and extrapulmonary distribution of inhaled  $\text{NO}_2$ , a major air pollutant (15). The intrapulmonary location and concentration of  $\text{NO}_2$  inhaled by monkeys was detected continuously by an Anger camera monitoring the  $^{18}\text{N}$  radiation. The  $^{18}\text{N}$  concentration of arterial blood was also measured by serial sampling and counting, and the blood concentrations were compared with those of the lung. Parks, Peek, and Goldstein found that during normal inspiration 50–60% of the  $^{18}\text{NO}_2$  was retained by the animal. The absorbed  $^{18}\text{NO}_2$  or its reaction products remained within the lungs for prolonged periods after exposure, but labeled pollutant was also carried to extrapulmonary sites via the bloodstream.

In 1973 we began an experimental measurement of denitrification kinetics using  $^{18}\text{NO}_3^-$  (16). Again the  $^{18}\text{O}(\text{p},\alpha)^{18}\text{N}$  reaction was used, but on a  $\text{H}_2\text{O}$  target. The radiochemical form of the  $^{18}\text{N}$  was nitrate with no measureable nitrite or ammonia. The nitrate produced in this manner was used as a tracer for direct quantitative measurements of denitrification rates in soils from flooded rice fields and in natural lake systems. Core samples were transferred with minimal agitation and under anaerobic conditions to the cyclotron laboratory, where  $^{18}\text{NO}_3^-$  was added (again anaerobically) and the rate of gaseous  $^{18}\text{N}$  evolution was monitored over short time intervals. The high specific activity of the  $^{18}\text{NO}_3^-$  allowed us to make these kinetic measurements without changing the nitrate concentration in situ, and the rate of denitrification could be measured over a period of 10–20 min. By contrast, state-of-the-art denitrification measurements using the stable tracer  $^{15}\text{NO}_3^-$ , involved several-fold enrichments of the sample nitrate content and resulted in significant overestimates of the actual denitrification rates (16).

Our same research group used tracer  $^{18}\text{N}$  to measure the rate of inorganic N-uptake by phytoplankton to evaluate the relative importance of nitrogen cycling mechanisms for phytoplankton productivity in aquatic ecosystems (17). We measured nitrate uptake rates of  $54.2 \pm 14.6$   $\mu\text{g-N/h}$  in an oligotrophic lake. The precision of these measurements as well as the wide range over which they have been effectively used demonstrate the advantages of short-lived radioisotopes for tracer biochemistry.

A research effort has also been initiated at the Michigan State University Plant Research Laboratory and Cyclotron Laboratory to make  $^{13}\text{NN}$  and to measure the kinetics and mechanisms of nitrogen transformations after fixation by blue-green algae (18–24). Their laboratory preferred the  $^{13}\text{C}(\text{p},\text{n})^{13}\text{N}$  reaction using 11-MeV protons on an isotopically enriched  $^{13}\text{C}$  target (25). The irradiated material was removed from the target, combusted in an automated Dumas apparatus, and the resulting

$^{13}\text{N}^{14}\text{N}$  gas compressed into a 1-mL vial. The technique produced a usable product of 20 mCi/ $\mu\text{A}$  of beam current. Tracer fixed by algal filaments was localized by a technique that permitted track autoradiography with short-lived isotopes (18). Electrophoretic and thin-layer chromatographic methods were also developed for rapid isolation and characterization of the first organic products of  $\text{N}_2$  fixation by blue-green algae (19).

Although the experimental demands of working with short-lived radiotracers are often severe, hot atom chemists have used them profitably for many years. In the historical portion of this chapter we have seen how pioneering research by Kamen, Varner, Wolk, and others has extended the methodology of short-lived radiotracers to biological research. In other chapters of this book several research groups will discuss their experience with  $^{13}\text{N}$ , with the recurring theme that the scientific rewards justify the additional demands inherent in these experiments, particularly when novel or uniquely precise results are achieved.

### *Experimental Methods in $^{13}\text{N}$ Radiobiochemistry*

**Nuclear Reactions for Producing  $^{13}\text{N}$ .** Nitrogen-13 can be produced in useful yields from nuclear reactions on either carbon, nitrogen, or oxygen. The reaction used by each laboratory will thus be dictated primarily by accelerator characteristics, convenience of target design, and the specific activity and radiochemical form of the  $^{13}\text{N}$  produced directly in the different targets.

The  $^{12}\text{C}(\text{d},\text{n})^{13}\text{N}$ ,  $^{13}\text{C}(\text{p},\text{n})^{13}\text{N}$ ,  $^{12}\text{C}(\text{p},\gamma)^{13}\text{N}$ ,  $^{14}\text{N}(\text{p},\text{pn})^{13}\text{N}$ , and  $^{16}\text{O}(\text{p},\alpha)^{13}\text{N}$  nuclear reactions have all been used to produce labeled compounds of nitrogen. The third and fourth of these reactions have serious disadvantages that have eliminated them from contention as important sources of radioisotopically and radiochemically pure tracer nitrogen. To evaluate the other reactions, Austin et al. calculated yields expected from bombardment of thick targets of pure isotopes (25). Both the  $^{13}\text{C}(\text{p},\text{n})^{13}\text{N}$  and the  $^{12}\text{C}(\text{d},\text{n})^{13}\text{N}$  nuclear reaction yields are large, and convenient solid targets of high-purity  $^{12}\text{C}$  and  $^{13}\text{C}$  are available. A bombarding energy  $\leq 14.5$  MeV is below the threshold for producing any radionuclides other than  $^{13}\text{N}$  with half-lives greater than 1 s. The (p,n) reaction on  $^{13}\text{C}$  produced more activity than the (d,n) reaction of  $^{12}\text{C}$  (25); however, both yield curie quantities of  $^{13}\text{N}$ , and thus the selection of a reaction is generally based on whether proton or deuteron beams are more conveniently available from a given accelerator. The (p, $\alpha$ ) reaction on oxygen-containing materials has been used successfully in many laboratories; however, the product is always contaminated with traces of  $^{18}\text{F}$ , and the initial radiochemical product spectrum may contain a variety

of oxides of nitrogen, demanding rigorous purification to yield the desired  $^{13}\text{N}$  radiochemical (16, 26, 27).

Cyclotrons have been the accelerator of choice for production of  $^{13}\text{N}$  because of their versatility. However, for short-lived isotopes that will not be stored, Van de Graaff accelerators have been used successfully in many laboratories to produce as much activity as is needed for many  $^{13}\text{N}$  radiobiochemical tracer experiments. A group from New Zealand has reported their experience with a 2-MeV Van de Graaff (28). They achieved a yield of only 200  $\mu\text{Ci}$  with a 1- $\mu\text{A}$  beam. The Australian AEC laboratory irradiated graphite with 2.5-MeV deuterons and produced  $^{13}\text{NN}$  at a continuous flow rate of 8 mCi/min, taking advantage of their 200- $\mu\text{A}$  beam current (29). The 5- $\mu\text{A}$  beam of 5.4-MeV deuterons at the University of Kentucky Van de Graaff has been used to irradiate  $\text{CH}_4$  gas at 1 atm pressure to give 21 mCi of  $^{13}\text{N}$  following a 25-min bombardment (30). All the above-mentioned laboratories have been restricted by their accelerators to low-energy reactions using carbon targets. Nickles and coworkers (31) at the University of Wisconsin have used their 11-MeV tandem Van de Graaff with a 1.5- $\mu\text{A}$  beam to irradiate water and initiate the  $^{16}\text{O}(p,\alpha)^{13}\text{N}$  nuclear transformation with a yield of about 12 mCi at saturation. Our experience has been that this level of radioactivity is adequate for most of the experiments described in this review.

**Radioanalytical Chemistry of  $^{13}\text{N}$ .** Nitrogen can combine to make simple molecules in oxidation states from  $-3$  to  $+7$ . Nucleogenic  $^{13}\text{N}$  reacting in a chemical target can potentially make multiple primary chemical products. It is thus essential that anyone synthesizing  $^{13}\text{N}$  compounds determine the radiochemical form of the newly formed radionuclide.

Varner was the first to describe many of the chemical tests available for measuring the radiochemical composition of  $^{13}\text{N}$  systems (6); however, much of his analytical methodology has been superseded by the rapid growth of high-performance chromatographic techniques during the last decade.

Perhaps the simplest application of analytical chemistry to separation of  $^{13}\text{N}$  products involved trapping of the gaseous end products of denitrification. Gersberg et al. (16) used molecular sieve at liquid nitrogen temperature to trap all the gaseous products following incubation of  $^{13}\text{NO}_3^-$  with denitrifying bacteria. Tiedje et al. (32, 33) reported similar experiments except they used differential trapping of  $^{12}\text{N}_2\text{O}$  and  $^{13}\text{NN}$  at different temperatures to arrive at a more complete picture of denitrification kinetics and mechanisms.

One of the most important applications of  $^{13}\text{N}$  involves identification of metabolic products. Most of the biological experiments that are contemplated with  $^{13}\text{N}$  involve incubating a simple  $^{13}\text{N}$ -labeled molecule

with a biological system, plant or animal, and allowing natural biochemical processes to proceed for some interval of time. The biology is then abruptly interrupted and the labeled metabolic products are identified. In this way one can unambiguously identify the transformation of the  $^{13}\text{N}$  label from a simple inorganic precursor to a complex organic product. By interrupting biology after different times of incubation and measuring the radiochemical composition of the labeled products, one is able to unravel both the kinetics and metabolic pathways of nitrogen biochemistry.

The first approach to rapid separation of complex mixtures of metabolic products of  $^{13}\text{N}$  was the high-voltage electrophoresis system pioneered by Wolk and colleagues at Michigan State University (19, 20). Their methodology involved preparation of a methanolic extract of blue-green algae, 50  $\mu\text{L}$  of which was spotted on a thin-layer plate of cellulose (0.1 mm thick  $\times$  5  $\times$  20 cm). The separation was improved if the lipid-soluble compounds in the methanolic extract were first displaced from the region of spotting by about 3 min of chromatography along the short axis of the plate using chloroform/methanol. The plate was then dried, sprayed with buffer, and electrophoresed at 3000 V. To identify all the metabolic products unambiguously, these researchers developed two buffering systems in which the mobility of the various organic metabolic products was different. The electrophoretic mobilities of nitrite and nitrate were nearly equal under the analytical conditions described above.

In view of the frequently expressed concern that the  $t_{1/2}$  of  $^{13}\text{N}$  is too short for interesting biochemistry, it is significant to note that the incubation time in these experiments was of the order of seconds to minutes. After longer times the spectrum of  $^{13}\text{N}$ -labeled products became so complex that thin-layer chromatography had to be done following electrophoresis. The extent of incorporation of  $^{13}\text{N}$  into metabolic products was sufficient to allow analytical chemistry of the products as late as 2 h after a cyclotron irradiation. In fact, the  $t_{1/2}$  of  $^{13}\text{N}$  was nearly ideally suited to these interesting and significant biochemical experiments.

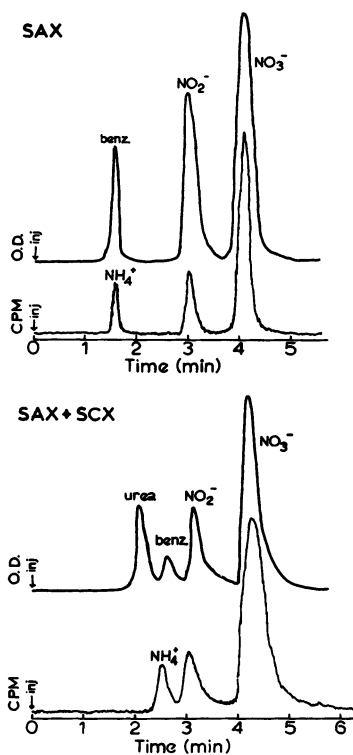
Comparing each of the oxidation states of nitrogen and some simple N-containing molecules with their associated ionization constants suggests the potential of ion-exchange chromatography for separating these molecules. With the advent of high-pressure solvent delivery systems for column chromatography and new packing materials of very uniform size, porosity, and coating thickness, we have techniques that are rapid, even compared with the  $t_{1/2}$  of  $^{13}\text{N}$ , and are conducive to quantitation by simply flowing the column effluent across the face of a scintillation detector and then applying simple corrections for radioactive decay and background. This technique can be accomplished over a very wide range in peak size.

Tilbury and coworkers (27) were the first systematically to develop high-performance ion-exchange chromatography to separate simple inorganic forms of nitrogen-13. Most of the systems used currently for separation of  $^{13}\text{N}$  compounds involve duplication with only minor variations of the system reported by Tilbury and demonstrated by the chromatograms of Figures 1 and 2. Thayer and Huffaker (34) have studied the effect of varying operating parameters on this chromatographic separation, and they concluded that when  $\text{NO}_3^-$  was the major component of a sample in nearly pure water, 0.05M phosphate buffer at pH 3.5 was the optimal mobile phase. Alternatively, assays involving biological extracts where protein was abundant required lower pH and ionic strength to separate the organic acids and proteins from nitrate and nitrite. They recommended 0.045M phosphate at pH 2.9 and use of a guard column to remove sample components that could otherwise irreversibly bind to the analytical column and reduce its useful lifetime.

**The Synthesis of  $^{13}\text{N}$ -Labeled Radiochemicals.** In this section we discuss the chemical targets and synthetic procedures applicable to preparing simple  $^{13}\text{N}$ -labeled compounds. More than one method will be given for many of the compounds, reflecting the fact that some groups

Figure 1. High-performance liquid chromatograms of  $^{13}\text{N}$ -labeled radiochemicals.

(A) Separation of anions with a Whatman 4.6-mm Partisil SAX column: instrument, Waters M-6000A pump and U6K injector; flow rate, 3.0 mL/min; eluent, 0.030M  $\text{NaH}_2\text{PO}_4$  and 0.004  $\text{H}_3\text{PO}_4$ ; detectors, lower chromatogram— $\text{NaI}(\text{Tl})$  radiation detector with an energy window set on the N-13 511-keV photopeak, upper chromatogram—Schoeffel 770 variable wavelength UV/Visible spectrophotometer set at 210 nm. The strong anion-exchange media gives baseline separation of  $\text{NO}_2^-$  and  $\text{NO}_3^-$  and elutes cations and neutral molecules [e.g.,  $\text{NH}_4^+$  and benzyl alcohol (benz)] at or near the column breakthrough. (B) separation of anions and cations with tandem Whatman 4.6-mm Partisil SAX and 3.2-mm SCX columns; conditions same as (A). This column combination separates anions, cations, and neutral species.



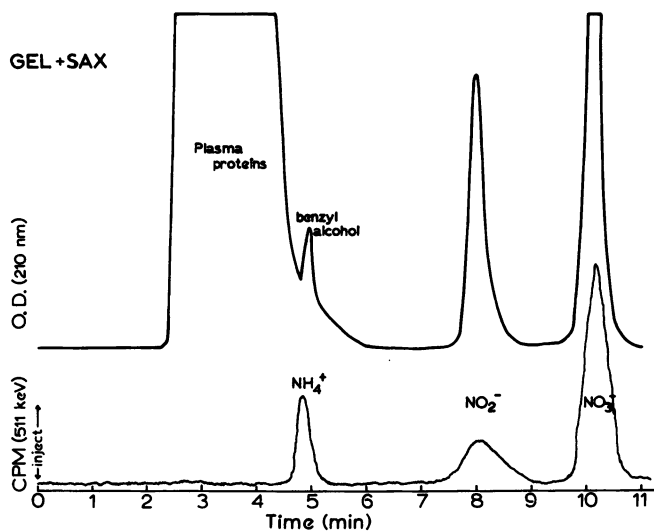


Figure 2. Separation of high-molecular-weight plasma components ( $\approx 50000$  amu) from low-molecular-weight species with a Waters I-125 gel permeation column in series with a Whatman 4.6-mm Partisil SAX column; conditions same as Figure 1(A) except eluent is  $0.015M$   $NaH_2PO_4$  and  $0.004M$   $H_3PO_4$ .

have developed their production methods around oxygen and/or water targets while others have preferred carbon targets. The choice between these two target systems was frequently dictated by engineering parameters specific for each accelerator. There are some fundamental differences in the chemical form of nucleogenic  $^{13}N$  produced in these two environments, which have led us to prefer proton-irradiated water targets for all our radiochemical syntheses.

**$^{13}N$ -NITRATE.** The product of nucleogenic  $^{13}N$  in water has been the subject of some controversy in the literature (16, 26, 27, 31). Welch's original work (35) reported radiochemical yields of  $>99.3\%$   $^{13}NO_3^-$  when water was irradiated with doses in excess of 1 eV per molecule, but at lower irradiation doses he identified some  $^{13}NH_3$ . While one cannot be certain that calculations of dose deposited in chemical targets are exactly comparable from one laboratory to another, we found nearly quantitative yields of  $^{13}NO_3^-$  at even lower absorbed radiation doses (16, 26). In contrast, Tilbury (27) and coworkers found high radiochemical yields of  $^{13}NH_3$  at relatively low radiation doses. Gatley and Nickles (31, 36) found that with a tandem Van de Graaff accelerator, the radiochemical yield was nearly all  $^{13}NO_3^-$ . There is no question about the differences in radiochemical composition measured by these different laboratories. The analytical chromatography is essentially identical in



each laboratory and is the system described above and illustrated by Figure 1. The different results are probably attributable to gases and other trace impurities in the water, to other chemical materials to which the aqueous target solution is exposed during and immediately after irradiation, including any metals in the target, and to whether the target solution is static or recirculating. At the present time we do not know the primary radiochemical product spectrum associated with a nitrogen atom recoiling through water, a problem that is discussed further in another chapter in this volume (37).

For many kinds of research  $^{13}\text{NO}_3^-$  prepared directly in water targets is of acceptable purity; however, it can be purified (38) by addition of  $\text{H}_2\text{O}_2$  to oxidize any residual nitrite to nitrate, followed by adjustment of the pH and rotary evaporation to distill any  $^{13}\text{NH}_3$ . The rotary evaporation process also increases the concentration of the  $^{13}\text{NO}_3^-$ . Any excess  $\text{H}_2\text{O}_2$  can be destroyed by reaction with a small amount of catalase.

Lindner et al. (39) developed a loop system for irradiation of water to produce  $^{13}\text{N}$ . Their system differed from the one described above in that the loop for recirculation contained a 40% shunt provided with a small mixed-bed ion-exchange column for on-line separation and collection of  $^{13}\text{NH}_4^+$ ,  $^{13}\text{NO}_2^-$ , and  $^{13}\text{NO}_3^-$  produced in the water. At the conclusion of an irradiation the target solution was circulated for a few minutes for complete collection of the products on the ion-exchange resin. About 85% of the radioactivity was displaced from the columns within 2 min by 50 mL of concentrated KI. The primary reaction product was 10–30%  $^{13}\text{NH}_3$  and 90–70% oxidized  $^{13}\text{N}$  under their irradiation conditions.

Chasko and Thayer (40) of our laboratory developed a system for rapid concentration and purification of  $^{13}\text{N}$ -labeled anions using high-performance anion-exchange media. Target solution containing  $^{13}\text{NO}_3^-$ ,  $^{13}\text{NO}_2^-$ , and  $^{13}\text{NH}_3$  was pumped directly onto a short column of Partisol SAX converted to the  $\text{Cl}^-$  form with dilute  $\text{NaCl}$ . A high-pressure pump was used to apply the target solution to the column at 6 mL/min. Further washing of the column with 10 mL of distilled and deionized water ensured removal of all  $^{13}\text{NH}_3$ . The pump was then switched to isotonic saline, and the anions were collected in fractions. This procedure took about 12 min and typically resulted in about 150 mCi of  $^{13}\text{NO}_3^-$  in 0.5 mL of isotonic saline.

The specific activity of  $^{13}\text{NO}_3^-$  synthesized and concentrated in this manner was measured by liquid chromatography using a radiation detector in tandem with a UV-absorbance monitor. The latter operated at 210 nm to measure the concentration of nitrate and nitrite in the product. The deionized and distilled water used in our targets contained 0.01 ppm  $\text{NO}_3^-$  but after irradiation it contained 0.12 ppm  $\text{NO}_3^-$ , which

resulted in a product specific activity of about 5000 Ci/mmol. The source of the carrier nitrogen may be nitrates on the surface of the apparatus or radiolytic fixation of gaseous nitrogen, which is always dissolved in water.

<sup>13</sup>N-NITRITE. The <sup>13</sup>NO<sub>3</sub><sup>-</sup> prepared in any of the water targets described above can be quantitatively reduced to <sup>13</sup>NO<sub>2</sub><sup>-</sup> using a copperized cadmium column developed by McElfresh et al. (41). A small column of cadmium filings cleaned with water and treated with copper sulfate could be stored for months under 0.15M NH<sub>4</sub>Cl. The column was washed with 300 mL of distilled water prior to addition of 50 mL of irradiated aqueous target solution containing <sup>13</sup>NO<sub>3</sub><sup>-</sup>. A peristaltic pump was used to move the target solution through the column at approximately 80 mL/min. McElfresh measured an average H<sub>2</sub>O<sub>2</sub> concentration of 0.5mM in the target water following a 20-min irradiation with 20-MeV protons at 20-μA beam current (41). The H<sub>2</sub>O<sub>2</sub> was completely removed by a single pass through the cadmium reduction column. The nearly quantitative conversion of nitrate to nitrite by cadmium reduction on a column makes it preferable to the batch procedure using copper dust (42).

The eluent from the cadmium column was concentrated by transferring it directly to a rotary evaporator preloaded with NaOH. The base raised the pH to ≥ 11 so that any <sup>13</sup>NH<sub>3</sub> from the target solution or from excessive reduction in the cadmium column was distilled from the <sup>13</sup>NO<sub>2</sub><sup>-</sup> preparation. Routinely <sup>13</sup>NO<sub>2</sub><sup>-</sup> of radiochemical purity ≥ 97% was obtained directly from elution of the cadmium column, and rotary evaporation resulted in a final solution of ≥ 99.2% <sup>13</sup>NO<sub>2</sub><sup>-</sup>. Purification and concentration has also been accomplished by the anion-exchange method of Chasko and Thayer (40) described above and typically resulted in 90 mCi of <sup>13</sup>NO<sub>2</sub><sup>-</sup> in 0.5 mL of isotonic saline, but the radiochemical purity was only 97%.

The entire synthesis from collection of irradiated target water to delivery of sterile <sup>13</sup>NO<sub>2</sub><sup>-</sup> solution for biological experimentation took less than 10 min and resulted in useful yields of about 120 mCi in a small volume. The specific activity of the concentrated <sup>13</sup>NO<sub>2</sub><sup>-</sup> measured by HPLC with serial radioactivity and UV-absorbance detectors ranged from 2500 to 5000 Ci/mmol without any special precautions to maximize it.

There have been no recent reports of the synthesis of <sup>13</sup>NO<sub>3</sub><sup>-</sup> or <sup>13</sup>NO<sub>2</sub><sup>-</sup> from proton or deuteron irradiation of carbon targets. Amorphous carbon targets require elaborate chemical conversions and/or collections to obtain <sup>13</sup>N in an oxidized form. Nuclear reactions on CO<sub>2</sub> give a small yield of gaseous oxidized products such as <sup>13</sup>NO<sub>2</sub>, <sup>13</sup>NO, and <sup>13</sup>N<sub>2</sub>O, but the radiochemical product spectrum is complex and most of the radioactivity is <sup>13</sup>NN arising from trace N<sub>2</sub> in the CO<sub>2</sub> (13).

**<sup>13</sup>N-AMMONIA.** The <sup>13</sup>NH<sub>3</sub> yields associated with the cadmium reduction column (41) suggest that this technique might be applicable to synthesis of <sup>13</sup>NH<sub>3</sub>; however, the experimental parameters have not yet been optimized to establish this as a practical synthetic method. Direct production of <sup>13</sup>NH<sub>3</sub> has been achieved in good yields with the <sup>12</sup>C(d,n)<sup>13</sup>N reaction on methane gas (43, 44), but the product invariably contained a small percentage of labeled methylamine and some HCN (44) as well as radiolytic NH<sub>3</sub> carrier. Similar products were found following irradiation of metal carbides (45).

Chemical reduction of labeled oxides of nitrogen formed in water targets provide a relatively simple synthesis for <sup>13</sup>NH<sub>3</sub>. The reduction reaction can be followed immediately by a micro-Keldahl distillation to purify and to concentrate the volatile <sup>13</sup>NH<sub>3</sub>. Two reductants have been described for rapid conversion of oxidized <sup>13</sup>N to <sup>13</sup>NH<sub>3</sub>. Our research program has used DeVarda's alloy (46); however, other laboratories have advocated the use of TiCl<sub>3</sub> converted in situ to Ti(OH)<sub>3</sub> (47). The chemistry and techniques of both of these reductions are described in the literature, but neither offers a clear-cut advantage. The DeVarda's alloy reaction is easy to set up with standard glassware, but we have had some difficulty achieving reliable yields due to the variable but always violent rate at which this reduction proceeds. Conversion yields of 65–80% are achievable, but further research is needed to optimize all the reaction parameters and to automate the system.

The titanous chloride reaction is more difficult to set up but is more reproducible and well behaved once established. Ido has developed a fully automated synthesis of <sup>13</sup>NH<sub>3</sub> via the titanous method (48). It consists of a reaction vessel, four syringe pumps as reagent injectors, and a controller for time, temperature, and valve sequencing. The controller has three settings, one to add the reagents and to establish the temperature, one to introduce the irradiated target water and TiCl<sub>3</sub> and to complete the distillation, and one to wash the vessel and to prepare for the next run. Optimum time, temperature, and reagent volumes have been determined, which result in a radiochemical yield of 87–91% and a radiochemical purity of 99.9% within 10 min after the end of bombardment (48). The specific activity of <sup>13</sup>NH<sub>3</sub> has not been measured.

**<sup>13</sup>N-NITROGEN.** Several groups have prepared <sup>13</sup>NN at relatively low specific activity by taking advantage of the high chemical reaction cross section for the reaction  $^{13}\text{N} + \text{N}_2 \rightarrow ^{13}\text{NN} + \text{N}$ . Welch (49) reported the production of <sup>13</sup>NN by deuteron bombardment of CO<sub>2</sub> in which the <sup>13</sup>N atoms were proposed to react with trace N<sub>2</sub> impurity. Clark and Buckingham (13) described a method for providing saline solutions of <sup>13</sup>NN in which target graphite was bombarded in the presence of CO<sub>2</sub> sweep gas. Various experimental parameters involved in production of <sup>13</sup>N-nitrogen were evaluated.

Biological studies requiring much higher specific activities of  $^{13}\text{NN}$  have led to new production schemes. Austin et al. (18, 25) used the  $^{13}\text{C}(\text{p,n})^{13}\text{N}$  reaction on isotopically enriched (97%) amorphous carbon targets that were carefully degassed to prepare high specific activity nitrogen. After irradiation, the powder in the target was mixed with  $\text{CuO}$  and  $\text{KNO}_3$  in an automated Dumas combustion apparatus and the resultant gas automatically transferred into a 2-mL vial. This procedure could be completed in high yield in 15 min, and the nitrogen prepared in this manner was useful for studies of N-fixation biochemical pathways described earlier in this review (18–24) and detailed by Meeks elsewhere in this volume (50).

$^{13}\text{N}$ -Nitrogen can also be prepared from water targets irradiated with protons. The  $^{13}\text{NO}_3^-$  from a water target has been used to prepare  $^{13}\text{NH}_3$ , which was steam-distilled from DeVarda's alloy and then oxidized by hypobromite ion to yield very high specific activity  $^{13}\text{NN}$  (51). When a high specific activity gaseous product was required, a small amount of carrier  $\text{NH}_4\text{Cl}$  was added prior to treatment with  $\text{OBr}^-$ . Excess  $\text{OBr}^-$  was removed by an ion retardation resin. Approximately 50 mCi of  $^{13}\text{NN}$  dissolved in a few milliliters of water was prepared within 20 min after bombardment. Gas radiochromatography verified that all radioactivity was present as molecular nitrogen. The techniques of Austin (25) and of Nickles (51) produced  $^{13}\text{N}$ -nitrogen of very high specific activity, although neither produced carrier-free nitrogen that would be doubly labeled  $^{13}\text{N}^{13}\text{N}$ . Carrier-free  $^{13}\text{N}^{13}\text{N}$  would not be useful for biological experimentation due to the uncertain consequences of decay of one  $^{13}\text{N}$  atom on the chemical form of the second  $^{13}\text{N}$  atom.

The most convenient method for production of  $^{13}\text{NN}$  was first reported by Suzuki and Iwata (52). They investigated recoil reactions of  $^{13}\text{N}$  in various aqueous solutions irradiated with protons and found that irradiation of 0.1M  $\text{NH}_4\text{OH}$  resulted in production of 100 mCi of  $^{13}\text{NN}$  with a radiochemical purity >99.9%. The specific activity of the  $^{13}\text{NN}$  obtained at end of bombardment was 80 mCi/mmol for 1  $\mu\text{A}$  of beam. We have irradiated 0.1M  $\text{NH}_4\text{OH}$  in the same recirculating aqueous target system described above and found a radiochemical yield of 75%  $^{13}\text{NN}$ , which was easily removed in the gas phase and trapped in a spirometer (46). Sixteen percent  $^{13}\text{NO}_3^-$ , 6%  $^{13}\text{NO}_2^-$ , and 3%  $^{13}\text{NH}_4^+$  remained in the aqueous target solution. We have not measured the specific activity of the  $^{13}\text{NN}$  produced; however, total radiation-induced decomposition of the  $\text{NH}_4\text{OH}$  would give a maximum of 3 mmol of carrier  $\text{N}_2$  and the specific activity would be approximately 200 mCi/mmol. By contrast, the specific activity of Austin's preparation was 20,000 mCi/mmol of  $\text{N}_2$  and the calculated specific activity of carrier-free  $^{13}\text{NN}$  would be  $4 \times 10^{10}$  mCi/mmol.

**<sup>13</sup>N-NITROUS OXIDE.** Nickles and Gatley (51) have described two similar methods for synthesis of <sup>13</sup>N<sub>2</sub>O by pyrolysis of NH<sub>4</sub>NO<sub>3</sub> in sulfuric acid. Both methods began with <sup>13</sup>NO<sub>3</sub><sup>-</sup> produced by proton bombardment of water, but in one the precursor was <sup>13</sup>NO<sub>3</sub><sup>-</sup> and in the other <sup>13</sup>NH<sub>4</sub><sup>+</sup> was synthesized first via DeVarda's alloy. When the tracer <sup>13</sup>NO<sub>3</sub><sup>-</sup> was used directly, it was reduced in volume to 1 mL by rotary evaporation, then 1 mmol of NH<sub>4</sub>NO<sub>3</sub> was added, followed by 25 mL of H<sub>2</sub>SO<sub>4</sub>. Nitrous oxide was evolved at 260°C in a pyrolysis apparatus swept by N<sub>2</sub>. When <sup>13</sup>NH<sub>3</sub> was used, it was mixed with 4 mmol of NH<sub>4</sub>NO<sub>3</sub> and the same cold H<sub>2</sub>SO<sub>4</sub>. A temperature was selected at which the rate of evolution of gas approximately balanced the rate of decay of the <sup>13</sup>N<sub>2</sub>O collected. When either of these synthetic routes were used, the <sup>13</sup>N<sub>2</sub>O was contaminated with 30% ± 10% <sup>13</sup>NN produced directly from a competing pyrolysis reaction, not by breakdown of <sup>13</sup>N<sub>2</sub>O. No <sup>13</sup>NO or <sup>13</sup>NO<sub>2</sub> was observed in radio-gas chromatograms of the product. When pyrolysis at 220°C was in the presence of a fivefold excess of (NH<sub>4</sub>)<sub>2</sub>SO<sub>4</sub>, the contamination by <sup>13</sup>NN was reduced to < 2%. Total processing time averaged 18 min after end of bombardment and resulted in delivery of 20% of the initial <sup>13</sup>N activity in 100 mL of carrier-added N<sub>2</sub>O. The <sup>13</sup>N<sub>2</sub>O produced in this manner has been used for measurement of cerebral blood flow at the University of Wisconsin (51).

**<sup>13</sup>N-NITROGEN DIOXIDE.** Parks et al. (14) bombarded a 15-atm high-purity O<sub>2</sub> target with 15-MeV protons at 10 μA and found that the <sup>13</sup>N atoms were incorporated into <sup>13</sup>NN (65%), <sup>13</sup>N<sub>2</sub>O (8%), and <sup>13</sup>NO<sub>2</sub> (28%). The target was a stainless steel cylinder heated to 475°C and filled with oxygen that was circulated by a stainless steel diaphragm pump with selectable flow rates. The effluent gases were separated by a trap at -45°C that retained NO<sub>2</sub> but not the more volatile N<sub>2</sub>, N<sub>2</sub>O, and NO components. Approximately 1 mCi of cryogenically recovered <sup>13</sup>NO<sub>2</sub> was produced per microamp under steady-state production conditions. The concentration of radiolytically produced NO<sub>2</sub> carrier was approximately 0.5 ppm in O<sub>2</sub>.

**<sup>13</sup>N-AMINO ACIDS.** In addition to its use in studies of ammonia metabolism, <sup>13</sup>NH<sub>3</sub> is useful as a synthetic precursor for preparation of labeled amino acids. Because amino acids are optically active and chemical syntheses invariably result in racemic mixtures, enzymatic reactions provide the best synthetic route to <sup>13</sup>N-labeled amino acids. Enzymatic pathways are characterized by speed, a high degree of chemical specificity under mild reaction conditions, and a product involving only the optical isomer of interest. It is not the purpose of this chapter to detail the many amino acid syntheses that have been described in the literature and recently reviewed exhaustively by Straatmann (53).

**OTHER ORGANIC MOLECULES.** Another interesting class of <sup>13</sup>N-labeled organic molecules can be formed from <sup>13</sup>NO<sub>2</sub><sup>-</sup> precursor. This work has

been pioneered by Digenis and his coworkers (54, 55) and is described in another chapter in this volume (56). They have synthesized several interesting N-nitroso and C-nitroso compounds with the goal of elucidating mechanisms of toxicity for these important families of compounds.

Direct recoil labeling of organic molecules with  $^{13}\text{N}$  atoms has been attempted without success. Studies of  $^{13}\text{N}$  reactions with liquid-phase acetic acid, acetaldehyde, and ethanol (35) as well as with larger biologic molecules like  $\alpha$ -chymotrypsin (57) led only to radiolysis and labeled fragmentation products. It is unlikely that this approach to  $^{13}\text{N}$  labeling will ever be successful for preparation of  $^{13}\text{N}$  radiochemicals due to the multivalency of nitrogen.

### Summary

The technical complexity of  $^{13}\text{N}$  research, that is, the requirement for a cooperative effort between accelerator physicists and engineers, radiochemists and experimental biologists, as well as access to sophisticated hardware, will inevitably limit the use of  $^{13}\text{N}$  for research. Nevertheless, the technology for making  $^{13}\text{N}$ , synthesizing simple  $^{13}\text{N}$  compounds, and separating and quantitating  $^{13}\text{N}$  metabolic products has all been developed. Many small accelerators capable of producing  $^{13}\text{N}$  are available throughout the United States and more are being built each year, primarily in hospital settings. This new technology is waiting to be applied imaginatively to a host of important problems in nitrogen biochemistry. It has the potential of answering important questions in disciplines ranging from medicine to soil science and from environmental toxicology to genetics.

### Acknowledgment

The authors extend their appreciation to the many colleagues who have contributed to the literature described in this review, especially to our colleagues at Davis including Drs. N. J. Parks, J. R. Thayer, Joe Chasko, Professors N. F. Peek and C. R. Goldman, and to John Jungerman, Director of Crocker Nuclear Laboratory, for his encouragement and support of biological research at the laboratory. Also appreciated were the suggestions of J. C. Meeks and M. G. Straatmann, who reviewed this manuscript. This research was supported in part by the California Air Resources Board (A7-190-30) and the National Science Foundation (DEB 77-01199).

### Literature Cited

1. Hauck, R. D. *J. Environ. Qual.* 1973, 2, 317.
2. Ratner, S. *Annu. Rev. Biochem.* 1977, 46, 101-126.

American Chemical  
Society Library  
1155 16th St., N.W.  
Washington, D.C. 20036

3. Duda, G. D.; Handler, P. *J. Biol. Chem.* 1958, 232, 303.
4. Joliot, F.; Curie, I. *Nature* 1934, 133, 201.
5. Ruben, S.; Hassid, W. Z.; Kamen, M. D. *Science* 1940, 91, 578.
6. Carangal, A. R.; Varner, J. E., presented at the *Am. Soc. Plant Physiol., Univ. Pennsylvania, Philadelphia, 1959.*
7. Nicholas, D. J. D.; Silvester, D. J.; Fowler, J. F. *Nature* 1961, 189, 634.
8. Campbell, N. E. R.; Dular, R.; Lees, H.; Standing, K. G. *Can. J. Microbiol.* 1967, 13, 587.
9. Burris, R. H. In "The Biology of Nitrogen Fixation"; Quispel, A., Ed.; Elsevier; New York; 1974; pp. 9-33.
10. Harper, P. V.; Lathrop, K. A.; Krizek, H.; Lembares, N.; Stark, V.; Hoffer, P. B. *J. Nucl. Med.* 1972, 13, 278.
11. Hoop, Jr., B.; Smith, T. W.; Burnham, C. A.; Correll, J. E.; Brownell, G. L.; Sanders, C. A. *J. Nucl. Med.* 1973, 14, 181.
12. Welch, M. J. *Chem. Commun.* 1968, 1354.
13. Clark, J. C.; Buckingham, P. D. "Short-lived Radioactive Gases for Clinical Use"; Butterworth: Boston, 1975; Chap. 6.
14. Parks, N. J.; Peek, N. F.; Goldstein, E. *Int. J. Appl. Radiat. Isot.* 1975, 26, 683.
15. Goldstein, E.; Peek, N. F.; Parks, N. J.; Hines, H. H.; Steffey, E. P.; Tarkington, B. *Am. Rev. Respir. Dis.* 1977, 115, 403.
16. Gersberg, R.; Krohn, K.; Peek, N.; Goldman, C. *Science* 1976, 192, 1229.
17. Gersberg, R. M.; Axler, R. P.; Krohn, K.; Peek, N.; Goldman, C. R. *Verh. Int. Ver. Limnol.* 1978, 20, 388.
18. Wolk, C. P.; Austin, S. M.; Bortins, J.; Galonsky, A. *J. Cell Biol.* 1974, 61, 440.
19. Thomas, J.; Wolk, C. P.; Shaffer, P. W.; Austin, S. M.; Galonsky, A. *Biochem. Biophys. Res. Commun.* 1975, 67, 501.
20. Wolk, C. P.; Thomas, J.; Shaffer, P. W.; Austin, S. M.; Galonsky, A. *J. Biol. Chem.* 1976, 251, 5027.
21. Thomas, J.; Meeks, J. C.; Wolk, C. P.; Shaffer, P. W.; Austin, S. M.; Chien, W.-S. *J. Bacteriol.* 1977, 129, 1545.
22. Meeks, J. C.; Wolk, C. P.; Thomas, J.; Lockau, W.; Shaffer, P. W.; Austin, S. M.; Chien, W.-S.; Galonsky, A. *J. Biol. Chem.* 1977, 252, 7894.
23. Meeks, J. C.; Wolk, C. P.; Schilling, N.; Shaffer, P. W. *Plant Physiol.* 1978, 61, 980.
24. Meeks, J. C.; Wolk, C. P.; Lockau, W.; Schilling, W.; Shaffer, P. W.; Chien, W.-S. *J. Bacteriol.* 1978, 134, 125.
25. Austin, S. M.; Galonsky, A.; Bortins, J.; Wolk, C. P. *Nucl. Instrum. Methods* 1975, 126, 373.
26. Krohn, K. A.; Parks, N. J. *J. Labelled Compd. Radiopharm.* 1979, 16, 87.
27. Tilbury, R. S.; Dahl, J. R. *Radiat. Res.* 1979, 79, 22.
28. McNaughton, G. S.; More, R. D. *Int. J. Appl. Radiat. Isot.* 1979, 30, 489.
29. Ritchie, A. I. M. *Nucl. Instrum. Methods* 1968, 64, 181.
30. Reed, M. F.; McEllistrem, M. T.; Pettit, W. A. *Phys. Med. Biol.* 1975, 20, 493.
31. Nickles, R. J.; Gatley, S. J.; Hichwa, R. D.; Simpkin, D. J.; Martin, J. L. *Int. J. Appl. Radiat. Isot.* 1978, 29, 225.
32. Smith, M. S.; Firestone, M. K.; Tiedje, J. M. *Soil Sci. Soc. Am. J.* 1978, 42, 611.
33. Tiedje, J. M.; Firestone, M. K.; Smith, M. S.; Betlach, M. R.; Firestone, R. B. In "Microbial Ecology"; Loutit, M. W.; Miles, J. A. R. Eds.; Springer-Verlag: Berlin, 1979.
34. Thayer, J. R.; Huffaker, R. C. *Anal. Biochem.* 1980, 102, 110.
35. Welch, M. J.; Straatmann, M. G. *Radiochim. Acta* 1973, 20, 124.
36. Witter, J. P.; Gatley, S. J.; Balish, E. *Science* 1979, 204, 411.
37. Tilbury, R. S., Chap. 13 in this book.

38. Skokut, T. A.; Wolk, C. P.; Thomas, J.; Meeks, J. C.; Shaffer, P. W.; Chien, W. S. *Plant Physiol.* 1978, 62, 299.
39. Lindner, L.; Helmer, J.; Brinkman, G. A. *Int. J. Appl. Radiat. Isot.* 1979, 30, 506.
40. Chasko, J. H.; Thayer, J. R. *Int. J. Appl. Radiat. Isot.*, in press.
41. McElfresh, M. W.; Meeks, J. C.; Parks, N. J. *J. Radioanal. Chem.* 1979, 53, 345.
42. Pettit, W. A.; Tilbury, R. S.; Digenis, G. A.; Mortara, R. H. *J. Labelled Compd. Radiopharm.* 1977, 13, 119.
43. Tilbury, R. S.; Dahl, J. R.; Monahan, W. G.; Laughlin, J. S. *Radiochem. Radioanal. Lett.* 1971, 8, 317.
44. Straatmann, M. G.; Welch, M. J. *Radiat. Res.* 1973, 56, 48.
45. Welch, M. J.; Lifton, J. F. *J. Am. Chem. Soc.* 1971, 93, 3385.
46. Parks, N. J.; Krohn, K. A. *Int. J. Appl. Radiat. Isot.* 1978, 29, 754.
47. Lathrop, K. A.; Harper, P. V.; Rich, B. H.; Dinwoodie, R.; Krizek, H.; Lembares, N.; Gloria, I. "Radiopharmaceuticals and Labelled Compounds"; I.A.E.A.: Vienna, 1973; Vol. 1, p. 471.
48. Ido, T.; Iwata, R. *J. Labelled Compd. Radiopharm.* 1981, 18, 244.
49. Welch, M. J. In "Prog. Nucl. Med."; University Park Press: Baltimore, Vol. 3, p. 37.
50. Meeks, J. C., Chap. 14 in this book.
51. Vaalburg, W.; Reiffers, S.; Paans, A.; Beerling, E.; Nickles, R. J.; Krizek, H.; Harper, P. V. *J. Nucl. Med.* 1977, 18, 638.
52. Suzuki, K.; Iwata, R. *Radiochem. Radioanal. Lett.* 1977, 28, 263.
53. Straatman, M. G. *Int. J. Appl. Radiat. Isot.* 1977, 28, 13.
54. Digenis, G. A.; Quinn, R. L.; Freed, B.; Tilbury, R. S.; Reiman, R. E.; Change, Y. C. *J. Labelled Compd. Radiopharm.* 1979, 16, 95.
55. McQuinn, R. L.; Cheng, Y. C.; Digenis, G. A. *Synth. Commun.* 1979, 25.
56. Digenis, G. A., Chap. 18 in this book.
57. Kasche, V. *Radiochem. Radioanal. Lett.* 1970, 3, 51.

RECEIVED September 4, 1980.



# The Feasibility of Producing $^{11}\text{C}$ , $^{13}\text{N}$ , $^{15}\text{O}$ , and $^{18}\text{F}$ with Heavy-Ion Beams

R. B. FIRESTONE—Nuclear Science Division, Lawrence Berkeley Laboratory, University of California, Berkeley, CA 94720

M. K. FIRESTONE—Department of Plant and Soil Biology, University of California, Berkeley, CA 94720

M. R. BETLACH and J. M. TIEDJE—Department of Crop and Soil Sciences and Microbiology and Public Health, Michigan State University, E. Lansing, MI 48824

*The feasibility of producing the short-lived tracers  $^{11}\text{C}$ ,  $^{13}\text{N}$ ,  $^{15}\text{O}$ , and  $^{18}\text{F}$  with heavy-ion beams was investigated. Production cross sections for 15-MeV  $p$ , 75-MeV  $^3\text{He}$ , and 300-MeV  $^{12}\text{C}$  beams incident on  $\text{H}_2\text{O}$  targets were calculated using the particle evaporation code ALICE (3). These calculations predicted substantial thick target yields of all four activities with the heavier beams. Experiments were performed with 15-MeV  $p$  and 75-MeV  $^3\text{He}$  beams to check the accuracy of the theoretical calculations. Absolute product yields were measured with NaI well counters, and chemical composition was determined by GC and HPLC.*

For several years we have been developing techniques for the production, purification, and utilization of the short-lived tracer  $^{13}\text{N}$  ( $t_{1/2} = 9.96$  min) in our studies of biological nitrogen transformations (1, 2). Sources of  $^{13}\text{N}$  were typically produced by the  $^{16}\text{O}(p,^4\text{He})^{13}\text{N}$  reaction using 15-MeV protons from the Michigan State University Cyclotron to bombard natural  $\text{H}_2\text{O}$  targets. This beam energy was chosen to optimize the production of  $^{13}\text{N}$  without significant contamination from  $^{11}\text{C}$  and  $^{15}\text{O}$ , which are produced at higher beam energies. Small amounts of  $^{18}\text{F}$  were produced from the  $^{18}\text{O}(p, n)^{18}\text{F}$  reaction; however, this did not interfere with our experiments. The sources varied in chemical purity containing typically about 85%  $^{13}\text{NO}_3^-$  with the remainder  $^{13}\text{NH}_4^+$ ,  $^{13}\text{NO}_2^-$ , and small amounts of labeled  $\text{N}_2\text{O}$  and  $\text{N}_2$  (<2%). Purified

0065-2393/81/0197-0251\$05.00/0  
© 1981 American Chemical Society

sources of all these species were routinely obtained by fast chemical techniques, gas chromatography (GC) and high-pressure liquid chromatography (HPLC).

With the closing of the low-energy accelerator at Michigan State University and the subsequent construction of a new heavy-ion facility there, it was desirable to investigate the feasibility of producing  $^{13}\text{N}$  with the less optimal heavy-ion beams. Although it was anticipated that the heavy-ion reactions would produce substantial quantities of  $^{11}\text{C}$ ,  $^{15}\text{O}$ , and  $^{18}\text{F}$ , we hoped that simple chemical techniques, which we had already developed, would be adequate to purify the sources. Thus, if sufficient quantities of  $^{13}\text{N}$  were produced by heavy-ion reactions, it would be possible to continue our tracer studies with these beams.

Two methods were chosen to investigate the usefulness of  $^{13}\text{N}$  production by heavy-ion beams. First we performed theoretical calculations of  $^{13}\text{N}$  yields with 15-MeV p, 75-MeV  $^3\text{He}$ , and 300-MeV  $^{12}\text{C}$  beams on water targets (typical MSU energies) using the particle evaporation code ALICE (3). Then we experimentally tested the accuracy of these calculations by producing  $^{13}\text{N}$  activity with a 75-MeV  $^3\text{He}$  beam from the Michigan State University Cyclotron. This beam should produce similar reactions and experimental conditions to those expected for heavier ions of the same energy-to-mass ratio. Sources produced by the  $^3\text{He}$  beam were analyzed by decay half-life, HPLC, and GC to determine absolute yields and chemical composition. Comparisons between this analysis of  $^3\text{He}$ -induced products, previous 15-MeV p experimental results, and the ALICE calculations were then made to determine both the usefulness of the calculations and the feasibility of producing experimentally useful short-lived isotopes with heavy-ion bombardments.

### *ALICE Calculations*

Cross sections for the production of  $^{11}\text{C}$ ,  $^{13}\text{N}$ ,  $^{15}\text{O}$ , and  $^{18}\text{F}$  were calculated for 15-MeV p, 75-MeV  $^3\text{He}$ , and 300-MeV  $^{12}\text{C}$  beams incident on natural  $\text{H}_2\text{O}$  targets using the particle evaporation code ALICE (3). This program was used to calculate the total  $p + n + \alpha$  evaporation cross sections for all partial waves, assuming the parabolic model (4) to determine the compound nucleus cross section and using the n, p, and  $\alpha$  binding energies of Wapstra (5). The thick target yields for the isotopes were then calculated by integration using the ALICE cross sections and the particle range tables in Lederer et al. (6). These yields, expressed in the units  $\text{mCi}/\mu\text{A}$  per 10-min bombardment and corrected for decay during irradiation, are shown in Table I. For  $^3\text{He}$  and  $^{12}\text{C}$  the calculations assume a particle beam current and not a charge current. In Figures 1–3 we have shown the calculated thick target yields of  $^{11}\text{C}$ ,  $^{13}\text{N}$ ,  $^{15}\text{O}$ , and  $^{18}\text{F}$  as a function of incident beam energy. Here the yields

**Table I. Calculated and Experimental Isotope Yields for Various Beams on  $\text{H}_2\text{O}$  Targets**

Iso- tope	$t_{1/2}$ (m)	$E_\beta$ (MeV)	Yield (mCi/ $\mu\text{A}$ per 10 min) <sup>a</sup>				
			15-MeV p		75-MeV $^3\text{He}$		300-MeV $^{12}\text{C}$
			Experi- ment	Theory <sup>b</sup>	Experi- ment	Theory <sup>b</sup>	Theory <sup>b</sup>
$^{13}\text{N}$	9.96	1.20	20	31	96	81	26
$^{11}\text{C}$	20.4	0.96	0	0	< 1 <sup>c</sup>	51	8.2
$^{15}\text{O}$	2.03	1.73	0	0	67	384	109
$^{18}\text{F}$	109.8	0.63	0.2	0.1	12	5.5	4.2

<sup>a</sup> Assuming beam stops in the target.

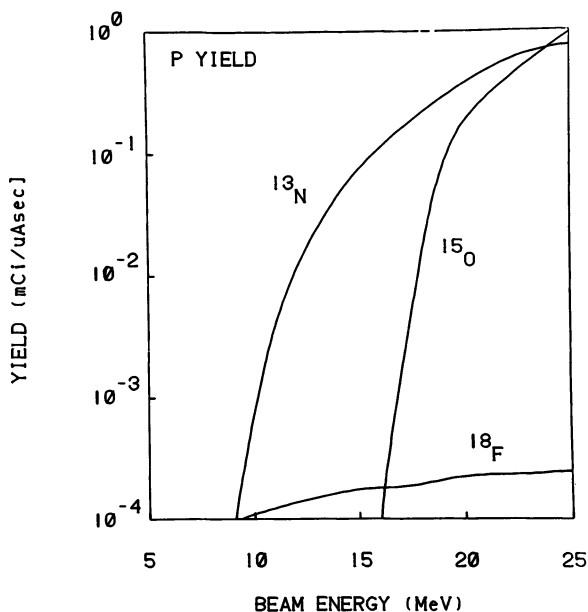
<sup>b</sup> Calculated using the ALICE compound nuclear particle evaporation code (3).

<sup>c</sup> None observed.

are expressed in the units mCi/ $\mu\text{A}$  per second. To calculate the yield for a given bombardment interval, one should use the relation

$$Y = Y^\circ \frac{t_{1/2}}{\ln 2} (1 - e^{-\lambda t})$$

where:  $t$  = bombardment interval,  $t_{1/2}$  = half-life,  $Y^\circ$  = yield from Figures 1-3, and  $X$  = yield per  $\mu\text{A}$  beam current for a bombardment interval  $t$ .



**Figure 1. Calculated isotope yields from proton bombardments with incident beam energy. No  $^{11}\text{C}$  is predicted.**

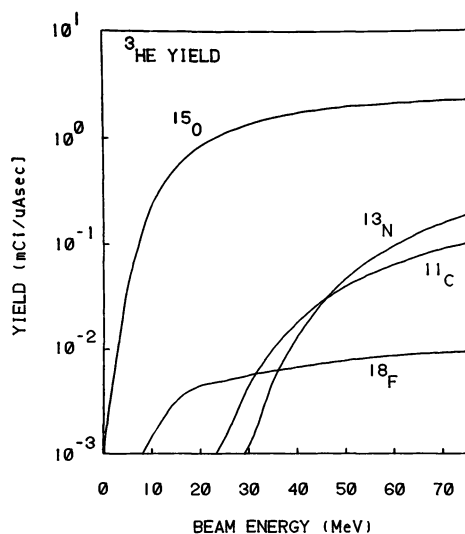


Figure 2. Calculated isotope yields from  $^3\text{He}$  bombardments with incident beam energy

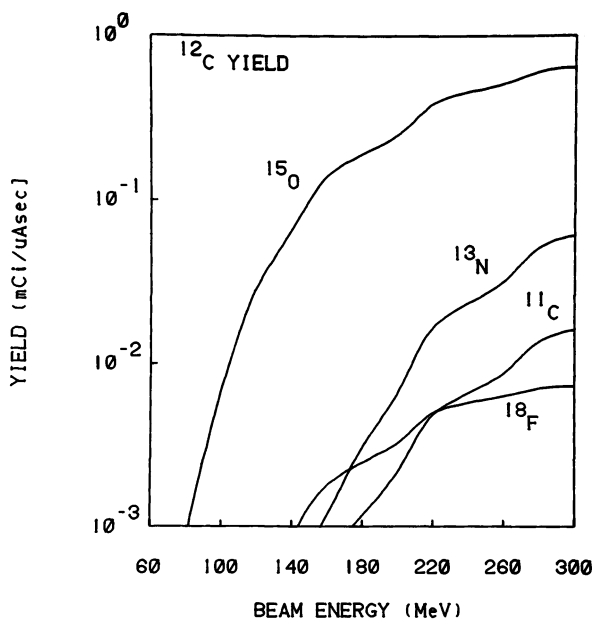


Figure 3. Calculated isotope yields from  $^{12}\text{C}$  bombardments with incident beam energy

### Experimental Results

The procedures for bombardment and analysis that we discuss below are described in greater detail in (1). After both the proton and  $^3\text{He}$  bombardments, samples were counted in calibrated NaI well detectors to establish absolute source intensity and time-decay characteristics. Sources were simultaneously analyzed by HPLC (with a NaI coincidence detector) and by GC (with a proportional counter detector) to determine their chemical composition. After chemical purification, the sources were again analyzed to determine purity. All absolute activities discussed below are normalized to a zero time at the end of the bombardment.

**15-MeV Proton Bombardment.** Sources produced by 15-MeV protons were shown by a two-component fit half-life analysis of the multiscaled well counter data to contain about 1%  $^{18}\text{F}$  (by activity) and no detectable  $^{11}\text{C}$  or  $^{15}\text{O}$ . The total absolute activity recovered after this bombardment is indicated in Table I and represents 84% of the calculated yield. This agreement is especially striking when we consider that the bombardment system was not gas tight and that some  $^{13}\text{N}$  gases were probably lost. A typical HPLC separation for a raw source of  $^{13}\text{N}$  is shown in Figure 4. The chemical composition varied with beam conditions, but we typically found 75–90%  $\text{NO}_3^-$ , 5–10%  $\text{NO}_2^-$ , and 0.5–25%  $\text{NH}_4^+$ . Various separation techniques, described in (1), were utilized to produce samples of > 99% purity in the desired chemical species as confirmed by HPLC or GC analysis. Activity from  $^{18}\text{F}$  did not elute from the Partisil 10-SAX strong anion exchange column used in HPLC and hence could be easily removed from the samples. Analysis showed that about 90% of the gas retained in the source water was  $\text{N}_2$ , the remainder being  $\text{N}_2\text{O}$ . An unknown amount of  $^{13}\text{N}$  gas was lost during bombardment and handling. No measurable increase in the activity of the air surrounding the bombardment system was observed, leading us to believe that the amount of radioactive gas produced by the proton beam on water was small. The amount of gaseous activity found in the water was small and could be effectively removed by evaporation to dryness or by sparging the sample with helium.

**75-MeV  $^3\text{He}$  Bombardment.** The sources produced with  $^3\text{He}$  were handled similarly to those from proton irradiations except that only a 2-min bombardment at 100 particle nA was performed. The yields were then nor-

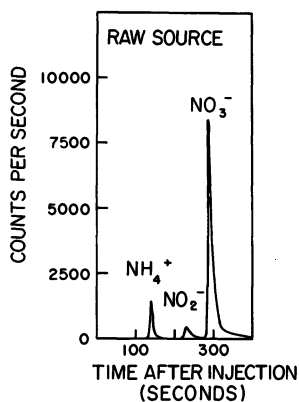
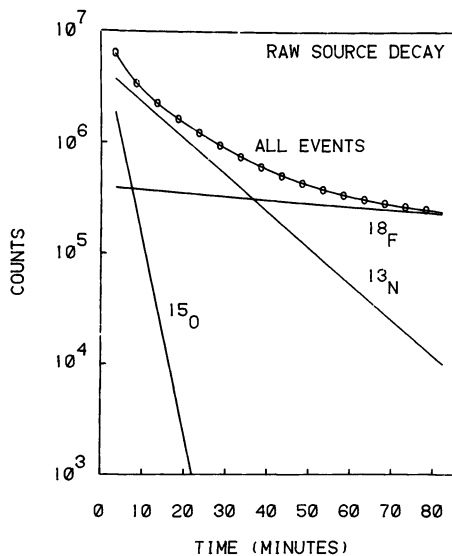


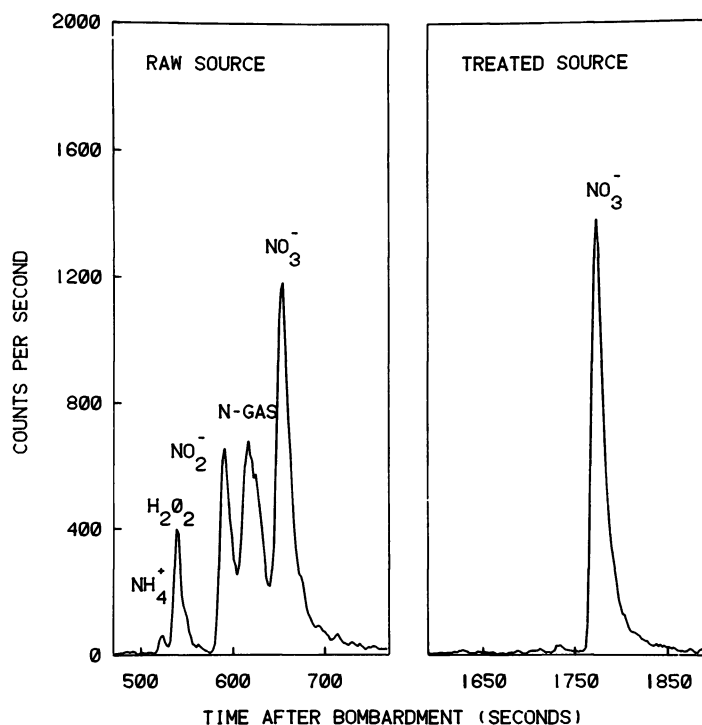
Figure 4. Typical HPLC determination of the chemical composition of a source produced by proton bombardment.  $^{18}\text{F}$ , while produced by the conditions of bombardment, does not elute from the HPLC column. The count rate is corrected for decay.

malized to  $\text{mCi}/\mu\text{A}$  per 10 min for comparison with the other data. The decay data from the NaI well counter for the raw source were analyzed by a four-component half-life fit to determine the relative amounts of activity present. The stripped decay curve is shown in Figure 5, and the resultant analysis is given in Table I. Again, the  $^{13}\text{N}$  and  $^{18}\text{F}$  production rates agreed qualitatively with the calculations, with larger amounts of activity being produced than were predicted. However, no  $^{11}\text{C}$  was observed and only 25% of the expected  $^{15}\text{O}$  was recovered. An HPLC analysis of the raw source is shown in Figure 6a. In addition to  $\text{NO}_3^-$ ,  $\text{NO}_2^-$ , and  $\text{NH}_4^+$  we observed two previously undetected peaks. The first new peak, occurring near the solvent front, is apparently  $^{15}\text{O}\text{-H}_2\text{O}_2$  (personal communication Joe Chasko), and the second peak elutes at the position expected for the  $^{13}\text{N}$  gases  $\text{N}_2\text{O}$ ,  $\text{N}_2$ , or  $\text{NO}$ . A further analysis of the HPLC spectrum peak areas, after correction for decay, indicates that the amount of  $^{15}\text{O}\text{-H}_2\text{O}_2$  produced represents 41% of the total activity observed by HPLC. This is the same quantity of  $^{15}\text{O}$  that was observed by half-life analysis (correcting for  $^{18}\text{F}$  that remained on the HPLC column). GC analysis of the raw source gases indicates the presence of one major and one minor component. The elution characteristics of these gases from a Poropak Q column correspond to an identification of the major component as  $^{13}\text{N}\text{-N}_2\text{O}$  and the minor component as  $^{13}\text{N}\text{-N}_2$  and/or  $^{13}\text{N}\text{-NO}$ .

The 0.7-mL raw source was acidified by the addition of 0.1 mL of 0.01 N HCl. The head space gas of the acidified source was sampled and analyzed by GC for the presence of  $^{11}\text{C}\text{-CO}_2$ ; none was detected. The sample was then evaporated to dryness with a flash evaporator and reconstituted to 1 mL with  $\text{H}_2\text{O}$ , after which 0.1 mL of 0.01N NaOH was added and the sample was again evaporated to dryness. Water was then added and the treated source was



**Figure 5.** Time decay curves of the raw source from  $^3\text{He}$  bombardment. The upper curve, representing the sum of the fitted, component decay curves (shown below), is compared with the observed decay data (O).



*Figure 6 a: Chemical composition of raw source, as determined by HPLC separation; the count rate corrected for decay to the end of bombardment; b: Chemical composition of purified source, as determined by HPLC separation; the count rate corrected for decay to the end of bombardment.*

counted in the NaI well detector. Half-life analysis of the multiscaled decay curve indicated only  $^{13}\text{N}$  and  $^{18}\text{F}$  activity (Figure 7), and the relative proportion of these two isotopes was nearly the same as in the original source. The HPLC analysis of the treated source is shown in Figure 6b. Only  $^{13}\text{N}\text{-NO}_3^-$  was observed in this sample, which is consistent with the removal of virtually all other activities. However, too much time elapsed before completion of the second analysis (about 30 min) to verify that all the  $^{15}\text{O}$  was removed by this treatment. After purification 50% of the  $^{13}\text{N}$  activity remained (all as  $^{13}\text{N}\text{-NO}_3^-$ ). This represents the fraction that existed as  $\text{NO}_3^-$  in the original source. Thus, apparently all  $\text{NH}_4^+$ ,  $\text{NO}_2^-$ , and N-gases were removed by the treatment.

### Discussion

We have demonstrated that useful sources of  $^{13}\text{N}$  can be generated by 75-MeV  $^3\text{He}$  beams. For both 15-MeV p and 75-MeV  $^3\text{He}$ , the ALICE calculations were successful in predicting  $^{13}\text{N}$  and  $^{18}\text{F}$  production rates.  $^{11}\text{C}$  and  $^{15}\text{O}$  yields appear to be significantly overestimated by ALICE.

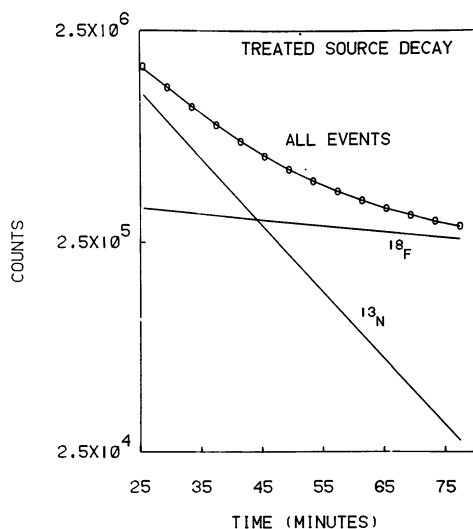


Figure 7. Time decay curve of purified source. The upper curve, representing the sum of the fitted, component decay curves (shown below), is compared with the observed decay data (O).

However, this result may reflect losses from the bombardment system that was not designed to be gas tight. One might expect  $^{11}\text{C}$  to be produced partly as  $\text{CO}_2$  and/or  $\text{CH}_4$ , both of which could be subject to loss from the thermally hot target.  $^{15}\text{O}$  may be produced primarily as  $\text{H}_2\text{O}_2$ ,  $\text{H}_2\text{O}$ , and  $\text{O}_2$ , so that much of the  $\text{O}_2$  and some of the  $\text{H}_2\text{O}$  may be lost. Conversely,  $^{13}\text{N}$  will be produced largely as the ionic forms  $\text{NO}_3^-$ ,  $\text{NO}_2^-$ , and  $\text{NH}_4^+$ , with only portions of the minor gaseous products  $\text{N}_2\text{O}$ ,  $\text{N}_2$ , and  $\text{NO}$  being lost. This is consistent with our experience from low-energy protons, where only small amounts of the gases were observed. Finally,  $^{18}\text{F}$  may be produced almost entirely as  $\text{F}^-$  and should not be lost from solution. This is consistent with the fact that no detectable loss of  $^{18}\text{F}$  occurs during evaporation to dryness.

These results lead us to believe that usable sources of  $^{13}\text{N}$ ,  $^{15}\text{O}$ , and  $^{18}\text{F}$  can be produced with heavy ions. Although  $^{11}\text{C}$  was not observed here, nuclear reaction theory strongly predicts substantial production of this species. Various fast chemical techniques such as separation by HPLC or GC can provide pure sources of the different  $^{13}\text{N}$ -labeled chemical species. Similarly, the use of gas-tight target systems, variation of target materials, and innovative separation techniques such as differential trapping should allow enhanced production of the other short-lived tracers. In addition, the yields of these activities can be qualitatively predicted by the computer code ALICE. In Table I we have shown our



calculations for a 300-MeV  $^{12}\text{C}$  beam. Although the yields are estimated to be somewhat lower for  $^{12}\text{C}$  than for  $^3\text{He}$ , substantial quantities of activity are expected (comparable with 15-MeV p). If our experience with  $^3\text{He}$  can be used as a guideline, these estimates may be somewhat conservative for  $^{13}\text{N}$  and  $^{18}\text{F}$  production. For ion beams heavier than  $^{12}\text{C}$ , the predicted yields will be further increased by reactions of the beam with H in the target. For example, the yield of  $^{13}\text{N}$  from the  $^{16}\text{O}(p, \alpha)^{13}\text{N}$  reaction at 400 MeV is predicted by ALICE to be 140 mCi/ $\mu\text{A}$  per 10-min bombardment.

### *Acknowledgments*

This work was supported by the NSF Grants DEB-77-19273 and PHY-78-01684. Partial support for one of the authors was provided by the Director, Office of Energy Research, Nuclear Sciences of the Basic Energy Sciences Program of the U.S. Department of Energy under Contract W-7405-ENG-48.

### *Literature Cited*

1. Tiedje, J. M.; Firestone, R. B.; Firestone, M. K.; Betlach, M. R.; Smith, M. S.; Caskey, W. H. *Soil Sci. Soc. Am. J.* 1979, 43, 700.
2. Firestone, M. K.; Smith, M. S.; Firestone, R. B.; Tiedje, J. M. *Soil Sci. Soc. Am. J.* 1979, 43, 1140.
3. Blann, M.; Placil, F. "ALICE: A Nuclear Evaporation Code," U.S. Atomic Energy Commission Report # COO-3494-10, 1973.
4. Thomas, T. D. *Phys. Rev.* 1959, 116, 703.
5. Wapstra, A. H.; Bos, K. *At. Nucl. Data Tables* 1977, 19, 215.
6. Lederer, C. M.; Shirley, V. S., Eds. "Table of Isotopes", 7th ed.; John Wiley & Sons: New York, 1978; p. A16.

RECEIVED September 4, 1980.

# The Chemical Form of $^{13}\text{N}$ Produced in Various Nuclear Reactions and Chemical Environments: A Review

ROY S. TILBURY<sup>1</sup>

Memorial Sloan-Kettering Cancer Center, 1275 York Avenue,  
New York, NY 10021

*The literature on the chemistry of recoil N-13 atoms is reviewed with emphasis on the chemical form of the N-13 atom in various nuclear reactions and target materials. The nuclear reactions considered are:  $^{12}\text{C}(d,n)^{13}\text{N}$ ,  $^{16}\text{O}(p,\alpha)^{13}\text{N}$   $^{14}(n,2n)^{13}\text{N}$ . The mechanisms of the reaction of the  $^{13}\text{N}$  recoils are discussed.*

The chemistry of excited nitrogen atoms or molecules has an extensive literature [see, for example, the book "Active Nitrogen" by Wright and Winkler (1) and the more recent review by Brown and Winkler (2)]. The hot atom or recoil chemistry of nitrogen-13, a radioactive isotope with half-life of 10.0 min, has been studied for many years as basic research into the mechanisms of reactions of excited nitrogen atoms. The more recent use of  $^{13}\text{N}$ -labeled compounds as tracers for studying biological and medical problems has given renewed interest and importance to these studies. In this chapter I shall review the various methods for producing of nitrogen-13 and the chemical forms of the  $^{13}\text{N}$ -labeled compounds formed in various target materials.

## *Deuterons on Carbon-Containing Compounds*

A common method of making N-13 is the (d,n) nuclear reaction on carbon-12. This reaction has a Q value of  $-0.28$  MeV and a coulomb barrier of 1.8 MeV, and so it will occur with deuterons of energy greater

<sup>1</sup> Current address: Nuclear Medical Section, M. D. Anderson Hospital, 6723 Bertner Avenue, Houston, TX 77030.

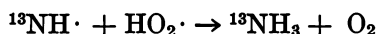
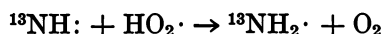
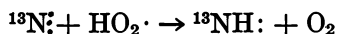
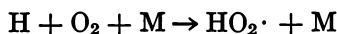
0065-2393/81/0197-0261\$05.00/0  
© 1981 American Chemical Society

than 1.8 MeV. The maximum cross section occurs at about 5 MeV, and yields of about 10 mCi/ $\mu$ A at saturation can be achieved with 8-MeV deuterons.

Schmied and Koski (3) studied the  $^{13}\text{N}$ -labeled products when various organic compounds were irradiated with 2-MeV deuterons. When methyl bromide, methyl chloride, or chloroform was irradiated,  $\text{HC}^{13}\text{N}$  was the main product. In  $\text{CHCl}_3$ ,  $\text{ClC}^{13}\text{N}$  was also observed. In  $\text{CCl}_4$ ,  $\text{ClC}^{13}\text{N}$  was the main product. Also,  $^{13}\text{NN}$  and  $^{13}\text{NO}$  were formed from traces of nitrogen and oxygen in the target chamber. No significant amounts of  $^{13}\text{NH}_3$  were detected, indicating that no abstraction of hydrogen occurred, which agrees with the earlier work on active nitrogen. Perkins and Koski (4) irradiated methane, methanol, and ethanol with 2-MeV deuterons and detected  $\text{HC}^{13}\text{N}$ ,  $\text{CH}_3\text{C}^{13}\text{N}$ , and  $\text{C}_2\text{H}_5\text{C}^{13}\text{N}$ . Again, no  $^{13}\text{NH}_3$  was detected. Dubrin et al. (5) also reported  $\text{HC}^{13}\text{N}$  as the major product of the deuteron irradiation of methane and ethylene, but they stress that these were volatile products only.

Welch (6) irradiated carbon dioxide with 7-MeV deuterons and found  $\text{N}^{13}\text{N}$  and  $^{13}\text{N} \cdot \text{NO}$  to be formed in approximately equal amounts over a range of dose from 0.008 to 0.2 eV/molecule and with nitrogen present in the range 0.2–10%. At higher doses the  $^{13}\text{N} \cdot \text{NO}$  content decreased due to its radiolytic decomposition. Welch and Lifton (7) irradiated several inorganic carbides with 7-MeV deuterons and measured the  $^{13}\text{N}$ -labeled products produced on acid dissolution.  $\text{Al}_4\text{C}_3$ , a methanide, gave 80%  $^{13}\text{NH}_3$  and 20%  $\text{CH}_3^{13}\text{NH}_2$  as the major products, while  $\text{CaC}_2$ , an acetylide, gave 20%  $^{13}\text{NH}_3$ , 40%  $\text{C}^{13}\text{N}^-$ , and 30%  $\text{CH}_3\text{C}^{13}\text{N}$  as the major products. These products and yields were correlated with the crystal structure of the metallic carbides.

Tilbury et al. (8) irradiated methane flowing through a glass tube with 7.8-MeV deuterons and bubbled the irradiated gas through water or isotonic saline solution. The solution was analyzed by radio-gas chromatography and was found to contain 95%  $^{13}\text{NH}_3$ , 2%  $\text{CH}_3^{13}\text{NH}_2$ , and 0.2%  $\text{C}_2\text{H}_5^{13}\text{NH}_2$ . Less than 3%  $\text{HC}^{13}\text{N}$  and no  $\text{CH}_3\text{C}^{13}\text{N}$  were detected. These results were strikingly different from those of Koski et al. (3, 4). Welch and Straatmann (9) suggested a mechanism involving water and oxygen impurities to account for the observations of Tilbury et al., with H atoms being formed radiolytically (M represents a third body):



Dewhurst (10) found significant amounts of ammonia when active nitrogen was reacted with silanes and hydrocarbons. He thought it unlikely that ammonia was formed by hydrogen abstraction reactions, since in the first step immine radicals are formed, which very likely disproportionate to hydrogen and nitrogen. He therefore postulated that ammonia was formed by combination of nitrogen and hydrogen atoms and that this may also be the mechanism of formation of  $^{13}\text{NH}_3$ .

Straatman and Welch (11), on irradiating methane with 7-MeV deuterons and bubbling the gas through dilute acid, found, by high-pressure liquid chromatography (HPLC) on an anion-exchange column, a large unidentified  $^{13}\text{N}$ -labeled component near the solvent front as well as  $^{13}\text{NH}_3$ . This unidentified peak disappeared on gas chromatography and was presumably decomposed to  $^{13}\text{NH}_3$ , giving the same product distribution as observed by Tilbury et al.

All the above methods of producing  $^{13}\text{NH}_3$  yielded significant quantities of nonradioactive ammonia that interfered with the enzymatic synthesis of amino acids, and for this reason most workers have subsequently used the proton irradiation of water to produce  $^{13}\text{NH}_3$  (see below).

Stewart et al. (12) studied the reactions of recoil  $^{13}\text{N}$  atoms in the gas phase with  $\text{CO}_2$ ,  $\text{N}_2$ ,  $\text{O}_2$ ,  $\text{N}_2\text{O}$ , and  $\text{NO}$ . Recoil nitrogen atoms were generated by the  $^{12}\text{C}(\text{d},\text{n})^{13}\text{N}$  reaction using  $\text{CO}_2$  as the target molecule and 1.7-MeV deuterons. The only products observed were  $^{13}\text{N} \cdot \text{N}$  and  $^{13}\text{N} \cdot \text{NO}$ . Other products sought but not detected were  $\text{NO}$ ,  $\text{NO}_2$ , and  $\text{CN}$  radicals. The  $^{13}\text{N} \cdot \text{NO}$  yield was independent of  $\text{CO}_2$  concentration but increased rapidly with the addition of oxygen. It was concluded that recoil  $^{13}\text{N}$  atoms do not react directly with  $\text{CO}_2$ .

### *Protons on Oxygen-Containing Compounds*

Probably the most common method for making  $^{13}\text{N}$  for labeled compound synthesis is now the  $(\text{p},\alpha)$  nuclear reaction on  $^{16}\text{O}$ , usually in the form of water. Several groups have used this reaction to produce  $^{13}\text{NH}_3$  (13–16). This reaction has a  $Q$  value of  $-5.2$  MeV, a threshold energy of 5.52 MeV, and a peak cross section of about 200 mb at 8 MeV. A yield of 25 mCi/ $\mu\text{A}$  at saturation can be achieved with 14.5-MeV protons (17).

Welch and Straatmann (9) studied the reaction of  $^{13}\text{N}$  recoil atoms produced in a variety of organic compounds and in water, and they reported 7%  $^{13}\text{NH}_3$ , 93%  $^{13}\text{NO}_3^-$  at dose rates less than 1 eV/molecule and 0.3%  $^{13}\text{NH}_3$ , 99.7%  $^{13}\text{NO}_3^-$  at dose rates greater than 1 eV/molecule. They did not observe any  $^{13}\text{NO}_2^-$  in the proton irradiation of water, but by irradiating diamond dust in water with deuterons, they observed 70%  $^{13}\text{NH}_3$ , 24%  $\text{NO}_3^-$ , and 4%  $\text{NO}_2^-$ . Gersberg and Krohn (18)

reported the production of 99% pure  $^{13}\text{NO}_3^-$  by irradiation of water with 14.5 MeV protons in a thin-walled quartz breaker. Suzuki and Iwata (19) have reported the production of 99.9% pure  $^{13}\text{N} \cdot \text{N}$  by proton irradiation of 0.1–0.003M ammonia solutions while passing helium gas through the solution.

Tilbury and Dahl (17) studied the  $^{13}\text{N}$  species produced by 14.5-MeV protons on water as a function of dose and in the presence of various additives. They found that for aerated or oxygenated water the yield of  $^{13}\text{NH}_4^+$  varied from 40% at low dose (0.01  $\mu\text{Ah}$ ) to 0.4% at high dose (25  $\mu\text{Ah}$  or 10.5 eV/molecule);  $^{13}\text{NO}_3^-$  varied from 50% at low dose to 95% at high dose; and  $^{13}\text{NO}_2^-$  varied from 10% at low dose to 5% at high dose and could be as high as 40% at intermediate doses. If the water was purged with nitrogen or helium to remove dissolved oxygen, or in the presence of ethanol, ascorbic acid, or formic acid, almost pure  $^{13}\text{NH}_3$  could be produced at doses up to 2  $\mu\text{Ah}$ . They postulated that  $^{13}\text{NH}_3$  was formed first by successive abstraction of H atoms by the recoiling  $^{13}\text{N}$  atom, followed by the oxidation of  $^{13}\text{NH}_3$  to  $^{13}\text{NO}_2^-$  and  $^{13}\text{NO}_3^-$  by oxidizing species in the water formed radiolytically. This was first suggested to the author by T. Nozaki during discussions at the First International Symposium on Radiopharmaceutical Chemistry in 1976.

Parks and Krohn (16) used a recirculating water target for the production of  $^{13}\text{NO}_3^-$  and used chemical methods subsequently to produce  $^{13}\text{NO}_2^-$  and  $^{13}\text{NH}_3$ . Lindner et al. (20) also used a recirculating water target and collected  $^{13}\text{NO}_3^-$ ,  $^{13}\text{NO}_2^-$ , and  $^{13}\text{NH}_4^+$  during bombardment by means of a mixed-bed ion-exchange column in a side loop. The column was subsequently eluted to yield 10–30%  $^{13}\text{NH}_4^+$  and 90–70%  $^{13}\text{NO}_3^- + ^{13}\text{NO}_2^-$ . About 0.5%  $^{13}\text{N}$  was formed as  $^{13}\text{N} \cdot \text{N}$ . Parks et al. (21) irradiated oxygen with 15-MeV protons and detected  $^{13}\text{N}_2$ ,  $^{13}\text{NNO}$ , and  $^{13}\text{NO}_2$  in the ratio 8:1:3.5.

### *Fast Neutrons on Nitrogen Compounds*

Aten and Kapteyn (22) irradiated solids and aqueous solutions of sodium nitrate and ammonium fluoride with fast neutrons (generated by 35-MeV deuterons on beryllium) and measured  $^{13}\text{N}$ -labeled nitrate, nitrite, ammonia, hydrazine, and gaseous activity. The  $^{13}\text{N}$  was formed by ( $n,2n$ ) reaction on  $^{14}\text{N}$ . In pure water, by interpolation, they found 14%  $^{13}\text{NO}_3^-$ , 60%  $^{13}\text{NO}_2^-$ , 9%  $^{13}\text{NH}_4^+$ , and 15% gaseous activity. No  $\text{H}_2\text{NNH}_2$ – $^{13}\text{N}$  was detected in the sodium nitrate solutions. Schleiffer and Adloff (23) irradiated water with 14-MeV neutrons and studied the chemical form of  $^{16}\text{N}$  ( $t_{1/2} = 7.35$  s) formed by ( $n,p$ ) reaction on  $^{16}\text{O}$ . They found 90% of the radioactivity was water-soluble and was identified as 30%  $\text{NH}_4^+$ , 16%  $\text{NH}_2\text{OH}$ , 25%  $\text{NO}_3^-$ , and 10%  $\text{NO}_2^-$ . The volatile radioactive products were 9% NO and 1%  $\text{N}_2$ .

### *Discussion*

The foregoing review of the experimental studies on the chemical form of  $^{13}\text{N}$  produced in various nuclear reactions and target materials presents rather confusing, often contradictory, results. There is little quantitative agreement among the different reports, but in general there is qualitative agreement. This is not too surprising considering the very small numbers of recoil nitrogen-13 atoms produced in a nuclear reaction, the very energetic and reactive nature of these atoms, and the fact that the presence of trace impurities can have a large effect on the nature and distribution of the products. The situation is perhaps similar to the early studies on the radiation chemistry of water. Indeed, it is not easy to differentiate between hot atom reactions on the one hand, in which abstraction of atoms or groups by  $^{13}\text{N}$  or insertion of  $^{13}\text{N}$  into other molecules may occur, and radiation chemistry reactions on the other hand, in which the energetic  $^{13}\text{N}$  atom dissociates or fragments molecules in its path and then reacts or combines with these fragments. One must bear in mind that normal bond energies of say, C—H in methane, H—O in water, and H—N in ammonia, are in the range 4.5–5.2 eV/molecule.

A full discussion of the mechanism of hot atom reactions is beyond the scope of this chapter. Wolfgang (24) has reviewed the hot atom chemistry of gas-phase systems and uses a theoretical approach analogous to that of nuclear reactions to describe hot atom reactions; with others he has developed a kinetic theory of hot reactions also known as Wolfgang's Adiabatic Theory. The theory is believed to be applicable to liquid and solid phases as well, with some differences due to cage and steric effects.

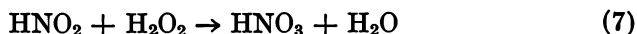
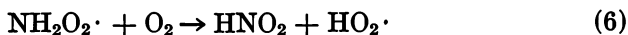
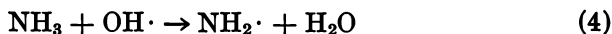
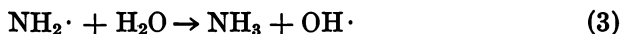
Let us now trace the history of the  $^{13}\text{N}$  atom from its birth in the  $^{16}\text{O}(p,\alpha)^{13}\text{N}$  nuclear reaction, as an example, to its final chemical form. It is born as a bare nucleus with an average recoil kinetic energy of 4.2 MeV (25). It will then lose energy by colliding with molecules in its environment and causing them to ionize, splitting off H atoms or other radicals until it is less than its seventh ionization potential of 667 eV (26). The bare nucleus will then start picking up electrons until it becomes a neutral atom with its full complement of seven electrons. It will then continue to lose energy due to collision, passing through the known spectroscopic energy levels of the nitrogen atom. These levels are shown in Table I together with the mean lifetime of the levels if known. When the hot atom has reached an energy of about 5 eV, it can start forming chemical bonds, and in water, we postulate that it picks up H atoms either directly or by abstraction from water molecules. In either case there will be an excess of OH radicals left, which can react with OH radical scavengers in the solution, such as hydrogen, ethanol, formic acid, or ascorbic acid, or can back-react with  $^{13}\text{NH}_3$  to form the  $^{13}\text{NH}_2$  radical.

**Table I. Energy Levels for Atomic Nitrogen (27)**

<i>Energy (eV)</i>	<i>Designation</i>	<i>Lifetime</i>
0.0	2p <sup>4</sup> S	stable
2.38	2p 2D	26 h
3.57	2p 2P	12 s
10.2	3s <sup>4</sup> p	—
10.6	3S 2P	—
10.8	Sp <sup>4</sup> 4P	—
14.48	1st ionization potential	

The <sup>13</sup>NH<sub>2</sub> radical is known to react with oxygen to produce the radical NH<sub>2</sub>O<sub>2</sub>, which can further react with oxygen to give HNO<sub>2</sub> and HO<sub>2</sub> (22). This explains the importance of oxygen in the reactions of <sup>13</sup>N recoils with water.

This mechanism can be summarized by the following formalistic equations:



Note that Reaction 4 is the reverse of Reaction 3. The H<sub>2</sub>O<sub>2</sub> in Reaction 7 comes from the radiolysis of water.

Molecular nitrogen is probably formed by the combination of two NH<sub>2</sub> radicals to give hydrazine, which subsequently decomposes to nitrogen and hydrogen. The formation of molecular nitrogen should be very small in water due to the low concentration of <sup>13</sup>NH<sub>2</sub> radicals, but in the presence of NH<sub>4</sub>OH radiolysis can generate NH<sub>2</sub> radicals, so the formation of <sup>13</sup>N · N increases.

It seems probable that Koski et al. and Dubrin et al. did not detect <sup>13</sup>NH<sub>3</sub> in that work because they only sampled the gas phase, and the <sup>13</sup>NH<sub>3</sub> probably adhered to the walls of the brass target chambers used.

### Literature Cited

1. Wright, A. N.; Winkler, C. A. "Active Nitrogen"; Academic: New York, 1968.

2. Brown, R.; Winkler, C. A. *Agew. Chem.* 1970, 9(3), 181–254.
3. Schmied, H.; Koski, W. S. *J. Am. Chem. Soc.* 1960, 82, 4766–4770.
4. Perkins, W. C.; Koski, W. S. *J. Phys. Chem.* 1962, 66, 474–477.
5. Dubrin, J.; MacKay, C.; Wolfgang, R. *J. Am. Chem. Soc.* 1965, 87, 2208–2209.
6. Welch, M. J. *Chem. Commun.* 1968, 1354–1355.
7. Welch, M. J.; Lifton, J. F. *J. Am. Chem. Soc.* 1971, 93, 3385–3388.
8. Tilbury, R. S.; Dahl, J. R.; Monahan, W. G.; Laughin, J. S. *Radiochem. Radioanal. Lett.* 1971, 8(6), 317–323.
9. Welch, M. J.; Straatmann, M. G. *Radiochemica. Acta* 1973, 20, 124–129.
10. Dewhurst, H. A. *J. Phys. Chem.* 1959, 63, 1976–1977.
11. Straatmann, M. G.; Welch, M. J. *Radiat. Res.* 1973, 56, 48–54.
12. Stewart, G. W.; Dymerski, P. P.; Hower, C. O. *J. Chem. Phys.* 1974, 61, 483–490.
13. Gelbard, A. S.; Hara, T.; Tilbury, R. S.; Laughlin, J. S. In “Radiopharmaceuticals and Labeled Compounds”; I.A.E.A.: Vienna, 1973; Vol. 1, pp. 239–247.
14. Lathrop, K. A.; Harper, P. V.; Rich, B. H.; Dinwoodie, R.; Krizek, H.; Lembares, N.; Gloria, I. In “Radiopharmaceuticals and Labeled Compounds”; I.A.E.A.: Vienna, 1973; Vol. 1, pp. 471–481.
15. Vaalburg, W.; Kamphuis, J. A. A.; Beerhing-van der Molen, H. D.; Rijis-kamp, A.; Woldring, M. G. *Int. J. Appl. Radiat. Isot.* 1975, 26, 316–318.
16. Parks, N. J.; Krohn, K. A. *Int. J. Appl. Radiat. Isot.* 1978, 29, 754–756.
17. Tilbury, R. S.; Dahl, J. R. *Radiat. Res.* 1979, 79, 22–33.
18. Gersberg, R.; Krohn, K. A. *Science* 1976, 192, 1229–1231.
19. Suzuki, K.; Iwata, R. *Radiochem. Radioanal. Lett.* 1977, 28, 263–268.
20. Lindner, L.; Helmer, J.; Brinkman, G. A. *Int. J. Appl. Radiat. Isot.* 1970, 30, 506–507.
21. Parks, N. J.; Peek, N. F.; Goldstein, E. *Int. J. Appl. Radiat. Isot.* 1975, 26, 683–687.
22. Aten, A. H. W.; Kapteyn, J. C. *Radiochem. Radioanal. Lett.* 1978, 32(1–2), 83–86.
23. Schleiffer, J. J.; Adloff, J. P. *Radiochim. Acta* 1964, 3, 145–151.
24. Wolfgang, R. *Prog. React. Kinet.* 1965, 3, 97–169.
25. Barne, J. W.; Burgess, W. H.; Miskel, J. A. In “Radioactivity Applied to Chemistry”; Wahl, A. C.; Bonner, D., Eds.; John Wiley & Sons: New York, 1951; p. 263.
26. Weast, R. C., Ed. “Handbook of Chemistry and Physics”; 56th ed.; CRC: Cleveland, 1975; p. E 68.
27. Hertzberg, G. “Atomic Spectra and Atomic Structure”; Dover: New York, 1944; p. 144–145.

RECEIVED September 4, 1980.



# Radiotracer Studies of Nitrogen Metabolism in Cyanobacteria

J. C. MEEKS

Department of Bacteriology, University of California, Davis, CA 95616

*<sup>15</sup>N has been used as a probe to examine the metabolic pathways and control of inorganic nitrogen assimilation in a number of cyanobacteria. Data derived from kinetic and inhibitor studies indicate that the primary pathway of <sup>15</sup>NH<sub>4</sub><sup>+</sup> assimilation, whether metabolically derived from [<sup>15</sup>N]N<sub>2</sub>, <sup>15</sup>NO<sub>3</sub><sup>-</sup>, or <sup>15</sup>NO<sub>2</sub><sup>-</sup>, or supplied exogenously, consists of the sequential activities of glutamine synthetase and glutamate synthase in all dinitrogen-fixing species examined. Aerobic reduction of dinitrogen to ammonium occurs in heterocysts of those species that differentiate these specialized cells. In heterocysts [<sup>15</sup>N]N<sub>2</sub>-derived <sup>15</sup>NH<sub>4</sub><sup>+</sup> is rapidly assimilated into glutamine. However, the newly synthesized glutamine must be translocated to adjacent vegetative cells for transamidation to form glutamate. A portion of the synthesized glutamate is then returned to heterocysts for continued amidation.*

Vegetative cells of certain filamentous cyanobacteria can differentiate to form thick-walled cells termed heterocysts and, in species of *Nostoc* and *Anabaena*, the heterocysts form at semiregular intervals along the filaments (Figure 1). Heterocysts have been shown to be the major (if not only) sites of dinitrogen fixation under aerobic growth conditions in these cyanobacteria (1, 2, 3). The regulation of heterocyst formation is of interest because understanding the mechanisms that control the differentiation of heterocysts would be a major step toward establishing manipulations that could convert these cyanobacteria into biological "ammonia factories" for agricultural use (4). Moreover, differentiation processes in the morphologically simple cyanobacteria provide a unique experimental system in which to study the detailed biochemical mechanisms that govern the formation of multicellular patterns (5).

0065-2393/81/0197-0269\$06.50/0  
© 1981 American Chemical Society

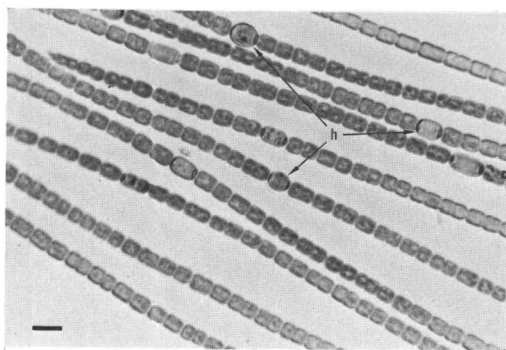


Figure 1. Photomicrograph of  $N_2$ -grown *Anabaena cylindrica*: h points to heterocyst; marker is  $4 \mu M$

Wolk and Quine (6) indicated that the semiregular spacing of heterocysts in the filaments occurs because heterocysts produce a diffusible substance(s) that inhibits nearby vegetative cells from differentiating into heterocysts. Since heterocysts are the major sites of aerobic dinitrogen fixation, it is possible that the inhibitory substance(s) produced by heterocysts is a nitrogenous compound. It is also well known that growth of heterocyst-forming cyanobacteria in the presence of ammonium and, in some cases, nitrate represses heterocyst formation (7, 8). These observations indicate that the differentiation of vegetative cells into heterocysts is under control of the external nitrogen concentration and may be analogous to nitrogen control in certain enteric eubacteria (9, 10). We have utilized the radioactive isotope of nitrogen,  $^{15}N$  ( $\beta^+$ ,  $t_{1/2} = 10$  min), to study nitrogen metabolism in intact filaments, to study interactions between vegetative cells and heterocysts and, in particular, to attempt to identify the regulatory compound(s).

In this chapter I shall review the results of studies, most of which were performed in collaboration with C. P. Wolk, J. Thomas, members of the staff of the Michigan State University cyclotron, and other colleagues, in which the initial products of assimilation of  $^{15}N$ -labeled dinitrogen, ammonium, nitrate, and nitrite by intact cyanobacteria (11-14) and by isolated heterocysts (1) were identified. Most of the experiments were performed using *Anabaena cylindrica*, which forms intercalary heterocysts. Other cyanobacteria used were: *A. variabilis* and *A. PCC 7120*, which also form intercalary heterocysts; *Cylindrospermum licheniforme*, which normally forms heterocysts only at terminal positions; *Plectonema boryanum*, which does not form heterocysts but grows with  $N_2$  as the sole nitrogen source under microaerobic conditions; *Gloeothece* sp., a unicellular species that does not form heterocysts but grows slowly with  $N_2$  as the sole nitrogen source under the aerobic conditions; and *Anacystis*

*nidulans* (syn. *Synechococcus* PCC 6301 [15]), a unicellular species that does not form heterocysts or grow with  $N_2$  as the sole nitrogen source aerobically or microaerobically.

### *Experimental*

**Preparation of Cyanobacteria for Labeling.** Details of the fermenter culture of cyanobacteria have been presented elsewhere (1, 11–14). In all cases a short time before exposure to  $^{13}N$  the cyanobacteria were harvested and concentrated to 27  $\mu g$  of chlorophyll *a* per mL by centrifugation and were incubated aerobically or microaerobically in the absence of  $N_2$  prior to use, depending on the experiment and species. In some experiments, L-methionine-DL-sulfoximine (MSX; Sigma Chemical Company, St. Louis, Missouri), O-diazoacetyl-L-serine (azaserine; Calbiochem, La Jolla, California), or aminoxy acetate (AOA; Sigma) were added singly or in combination to the cyanobacterial suspensions at the time of resuspension to a concentration of each of 1mM ( $[^{13}N]N_2$  experiments) or 2mM ( $^{13}NH_4^+$  or  $^{13}NO_3^-$  experiments; final concentration 1mM upon dilution with the aqueous label).

**Generation of, and Labeling with,  $^{13}N$ .**  $^{13}N$  was generated by one of two reactions. At the Michigan State University cyclotron,  $^{13}N$  was generated by the  $^{13}C(p,n)^{13}N$  nuclear reaction with beams of 11-MeV protons at a bombardment current of 1–4  $\mu A$  for 20–30 min (16, 17). The target was 18.6-mg amorphous carbon, 97 at. %  $^{13}C$  (Monsanto Research Corporation, Mound Laboratory, Miamisburg, Ohio). At the University of California, Davis, Crocker Nuclear Laboratory cyclotron,  $^{13}N$  was generated by the  $^{16}O(p,\alpha)^{13}N$  nuclear reaction with beams of 20-MeV protons at bombardment current of 20  $\mu A$  for 20 min. The target was glass-distilled water in a 60-mL recirculation target system (18).

$[^{13}N]N_2$  and  $^{13}NH_4^+$  were generated from the irradiated  $^{13}C$  target;  $^{13}NO_3^-$  was purified and  $^{13}NO_2^-$  generated from the irradiated  $H_2O$  target.  $[^{13}N]N_2$  was generated by subjecting the irradiated target, together with 0.18 mg  $KNO_3$ , to Dumas combustion in a Coleman Nitrogen Analyzer, Model 29 (Coleman Instruments Corporation, Maywood, Illinois) supplemented with an additional postheater. Carrier  $CO_2$  and oxides of nitrogen were removed with a liquid nitrogen trap, and a Toepler mercury pump was used to compress the  $[^{13}N]N_2$  into 1.0-mL evacuated vials (16, 17).

$^{13}NH_4^+$  was generated by acid digestion (approximately 250°C, 10 min) of the irradiated target with concentrated sulphuric acid saturated with potassium dichromate. The solution was made alkaline with saturated sodium borate and 40% (w/v) NaOH, and oxides of nitrogen were reduced with saturated silver sulfate.  $^{13}NH_3$  was then distilled under vacuum and collected in a liquid nitrogen trap (1, 13).

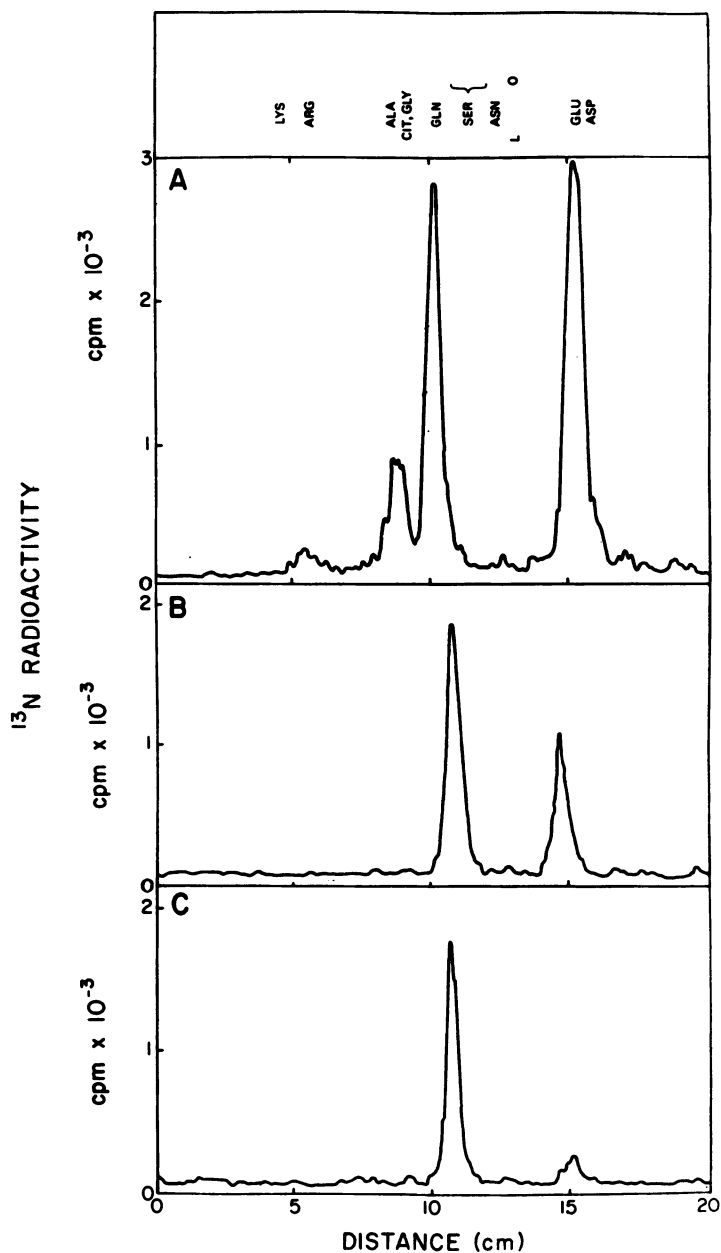
$^{13}NO_3^-$  was purified from contaminating  $^{13}NO_2^-$  and  $^{13}NH_4^+$  in a two-step procedure modified from (19).  $^{13}NO_2^-$  was first oxidized to  $^{13}NO_3^-$  by 1% (v/v, final concentration)  $H_2O_2$  with the solution pH adjusted to 2.0 with formic acid. The solution was evaporated to dryness, removing most of the hydrogen peroxide and formic acid. The residue, containing  $^{13}NO_3^-$  and  $^{13}NH_4^+$ , was resuspended with distilled water and the pH adjusted to 10.0. The sample was evaporated to a dryness a second time to remove contaminating  $^{13}NH_3$ . The final residue was resuspended with buffer to a final pH of 7.0–7.5, and 50  $\mu g$  of catalase was added to remove any residual  $H_2O_2$ .

$^{13}\text{NO}_2^-$  was synthesized from  $m^{13}\text{NO}_3^-$  by reduction in a cadmium-copper column and purified from  $^{13}\text{NH}_4^+$  by vacuum evaporation at pH 10.0 (20).

Fixation of  $[^{13}\text{N}]\text{N}_2$  by 250  $\mu\text{L}$  of concentrated cyanobacterial suspension took place in the light (ca. 400 ft-c from an incandescent lamp) at room temperature (ca. 23°C) under an atmosphere of  $\text{Ar}:\text{N}_2:\text{CO}_2$  (97:2:1, vol. ratio) in 1.0-mL Reactivials (Pierce Chemical Company, Rockford, Illinois) fitted with stopcocks. The suspensions were stirred with a small triangular stirring bar set in the cone of the vial. A short length of tubing led from the stopcock through a serum stopper to a centrifuge tube containing 1.0 mL of methanol. The reaction was initiated by addition of the cyanobacterial suspension and at prescribed times the stopcock was opened, the reaction stopped by injection of the suspension into the methanol, and the unfixed  $[^{13}\text{N}]\text{N}_2$  then removed by flushing with cylinder gas (11, 12, 14).

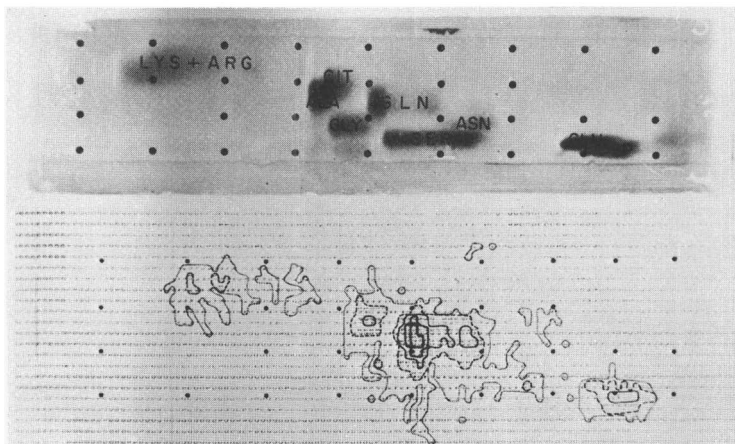
Assimilation of  $^{13}\text{NH}_4^+$ ,  $^{13}\text{NO}_3^-$ , and  $^{13}\text{NO}_2^-$  by the suspended cyanobacteria took place in the light, generally in 15-mL conical centrifuge tubes under air. Reactions were initiated by combining 50 or 250  $\mu\text{L}$  of  $^{13}\text{N}$  solution with 250  $\mu\text{L}$  of cyanobacterial suspension and were terminated by mixing the resulting suspension with 4 volumes of methanol. The methanolic suspensions in all cases were mixed for 1 min on a vortex micromixer to complete extraction and centrifuged at  $1000 \times g$  for 1 min. The supernatant solution was decanted and subjected to analysis.

The supernatant methanolic extract was treated in one of two ways (1, 12, 13): (i) The fluid was subjected sequentially to vacuum distillation at pH 10.0 to recover free ammonia and then to steam distillation in strong alkali to recover amide nitrogen-derived ammonia. Radioactivity in the distillates and in a portion of the original solution was determined by scintillation spectroscopy and was corrected for decay to a standard time. (ii) Alternatively, in preparation for electrophoresis, the fluid was dried under vacuum at 50°C, the residue dissolved in 200  $\mu\text{L}$  of 80% methanol and redried as before, and the final residue dissolved in 50  $\mu\text{L}$  of 80% methanol to which were added 5  $\mu\text{L}$  of a standard amino acid solution. The final methanolic solution was spotted on a  $2 \times 10$  mm area parallel to the short axis of  $5 \times 20$  cm glass plate bearing a 0.1-mm layer of cellulose (E. Merck and Company, Darmstadt, West Germany). The lipid-soluble substances in the dried spotted material were displaced by ascending chromatography in the short axis of the plate in chloroform/methanol (3:1, vol. ratio or—for extracts of isolated heterocysts—1.3:1, vol. ratio). The plate was then dried, sprayed with buffer, and subjected to electrophoresis at 3000 V for 1.5–12 min using a high-voltage electrophoresis apparatus (Model Q11 SAE 3202, Shandon Scientific Company, London, England; or custom-built). Buffers used were with 70mM sodium borate, pH 9.2 and, on occasion, 750mM formic acid, pH 2.0. After electrophoresis, the distribution of  $^{13}\text{N}$  on the thin-layer plates was determined with a radiochromatogram scanner (Model 7201, Packard Instruments Company, Downers Grove, Illinois). Radioactive amino acids were identified by comigration with stable and  $^{14}\text{C}$ -labeled amino acids during electrophoresis (1, 11, 12). The radioactivity in amino acids was quantitated by integration of peaks in radioscan, with corrections applied for decay to a standard time. An example of one-dimensional separation and radioelectrophoretogram scanning following fixation of  $[^{13}\text{N}]\text{N}_2$  for varying periods of time is shown in Figure 2. Aspartate and glutamate migrate very closely during electrophoresis at pH 9.2. Thus radioactivity from aspartate generally appeared first as a shoulder on, then as a composite with, glutamate as one major peak. In most instances, radioactivity in this region was calculated as a combined glutamate plus aspartate



Journal of Biological Chemistry

**Figure 2.** Scan of radioactivity from  $^{13}\text{N}$  in electrophoretograms of compounds extracted from *A. cylindrica* with 80% methanol after (A) 120, (B) 60, and (C) 20s of fixation of  $^{13}\text{N}_2$  (12): O, origin; L, lipids displaced by chromatography prior to electrophoresis. Distance is measured from the negative (left) end of the plate. The standard amino acids were visualized by spraying the thin-layer plate with acidic ninhydrin solution after radioelectrophoretogram scanning.



Journal of Biological Chemistry

**Figure 3.** Two-dimensional scan of radioactivity from  $^{13}\text{N}$  in two-dimensional electrophoretogram (positive end of the plate to the right) and chromatogram of  $^{13}\text{N}$ -labeled compounds extracted from *A. cylindrica* with 80% methanol after 900 s of assimilation of  $^{13}\text{NH}_4^+$  (13): (●) points labeled with radioactivity. Peak areas of radioactivity were localized by drawing isorads on the printout at (· · ·) 3, (---) 9, (—) 24, (—) 63, and (—) disintegrations per area element. The mean background during the 20-min scan was approximately 0.08 counts per area element.

peak. To determine the respective radioactive contribution of these two amino acids in this region, in certain experiments the plates were scanned and sprayed with ninhydrin solution, and then the ninhydrin positive areas ascribed to aspartate and to glutamate were excised, eluted with water, and  $^{13}\text{N}$  radioactivity in the eluents were determined by scintillation spectroscopy.

To obtain additional verification of the identity of the  $^{13}\text{N}$ -labeled amino acids, the methanolic extracts from certain  $^{13}\text{NH}_4^+$  experiments were subjected to two-dimensional separation and scanning. In these experiments the concentrated methanolic solution was spotted on a  $2 \times 5$  mm area parallel to the long axis of a  $5 \times 20$  cm thin-layer cellulose glass plate. Following initial chromatography (along the short axis of the plate) and electrophoresis, (at pH 9.2 for 9 mm), the thin-layer plate was dried and subjected to ascending chromatography in the short direction of the plate in phenol/water (3:1, v/v) equilibrated with 3% (v/v) aqueous  $\text{NH}_4\text{OH}$  for 17 min. The plate was scanned in two dimensions using the scanner described by Markam et al. (21). The rays arising from a given area element were added. After the scan was completed, the sums were printed in a corresponding two-dimensional array. The standard amino acids were visualized with ninhydrin and their positions in the two-dimensional scan determined by reference to points labeled with radioactivity. An example of this separation and scanning is shown in Figure 3.

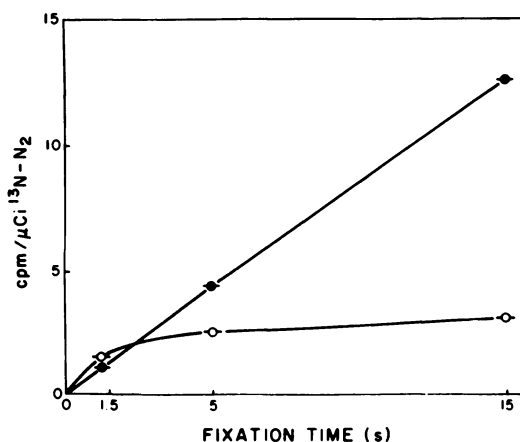
### Results and Discussion

**Pathways of Assimilation of  $^{13}\text{N}$  by Intact Cyanobacteria.** FIXATION OF  $[^{13}\text{N}]\text{N}_2$ . The first stable product of fixation of  $[^{13}\text{N}]\text{N}_2$  by

intact *Anabaena cylindrica* was  $^{13}\text{NH}_4^+$  (Figure 4). After 1.25 s of fixation approximately 61% of the total  $^{13}\text{N}$  recovered in methanolic extracts distilled as  $^{13}\text{NH}_3$ . The fraction of  $^{13}\text{NH}_4^+$  in extracts then declined until, after 15 s of fixation, it accounted for less than 20% of the total radioactivity. The radioactivity in the ammonium ion pool, once apparently saturated, remained low; the  $^{13}\text{N}$ -labeling of the amide nitrogen increased linearly for at least up to 15 s (Figure 4) and probably to 60 s (12).

Incubation for up to 120 s with  $[^{13}\text{N}]\text{N}_2$  resulted in incorporation of  $^{13}\text{N}$  into three to six organic constituents (depending on the species) by the five  $\text{N}_2$ -fixing cyanobacteria examined (12, 14). These radioactive constituents were tentatively identified as glutamine, glutamate, aspartate, citrulline, alanine, and arginine by their comigration with stable standard amino acids during electrophoresis at pH 9.2 (Figure 2). In *A. cylindrica* the identity of certain of these amino acids was also determined by coelectrophoresis at pH 2.0 and pH 9.2 with  $^{14}\text{C}$ -labeled amino acids and by two-dimensional coelectrophoresis and cochromatography followed in each dimension by radioscanning (12). Moreover, after 60 s of fixation by *A. cylindrica*, up to 87% of the  $^{13}\text{N}$  radioactivity that coelectrophoresed with stable glutamine distilled as amide nitrogen, and approximately 14% could be recovered as  $\alpha$ -amino nitrogen (12).

The initial organic products of fixation of  $[^{13}\text{N}]\text{N}_2$  were glutamine and glutamate in all species examined (Figure 5). After 15 s of fixation,



Journal of Biological Chemistry

**Figure 4.** Time course of incorporation of  $^{13}\text{N}$  into pools of  $\text{NH}_4^+$  and amide nitrogen (12). After fixation of  $[^{13}\text{N}]\text{N}_2$  for 1.25, 5, and 15 s, the suspensions of *A. cylindrica* were extracted and the methanolic extract subjected sequentially (○) to vacuum distillation at pH 10.0 to recover free  $^{13}\text{NH}_3$ , and then (●) to steam distillation in the presence of alkali to recover amide-derived  $^{13}\text{NH}_3$ . The ordinate represents cpm of  $^{13}\text{NH}_4^+$  or  $[^{13}\text{N}]$ amide nitrogen in the fixation vial, corrected to the time of the start of fixation, and normalized to equal amounts of  $[^{13}\text{N}]\text{N}_2$  (in  $\mu\text{Ci}$ ) in the vial.

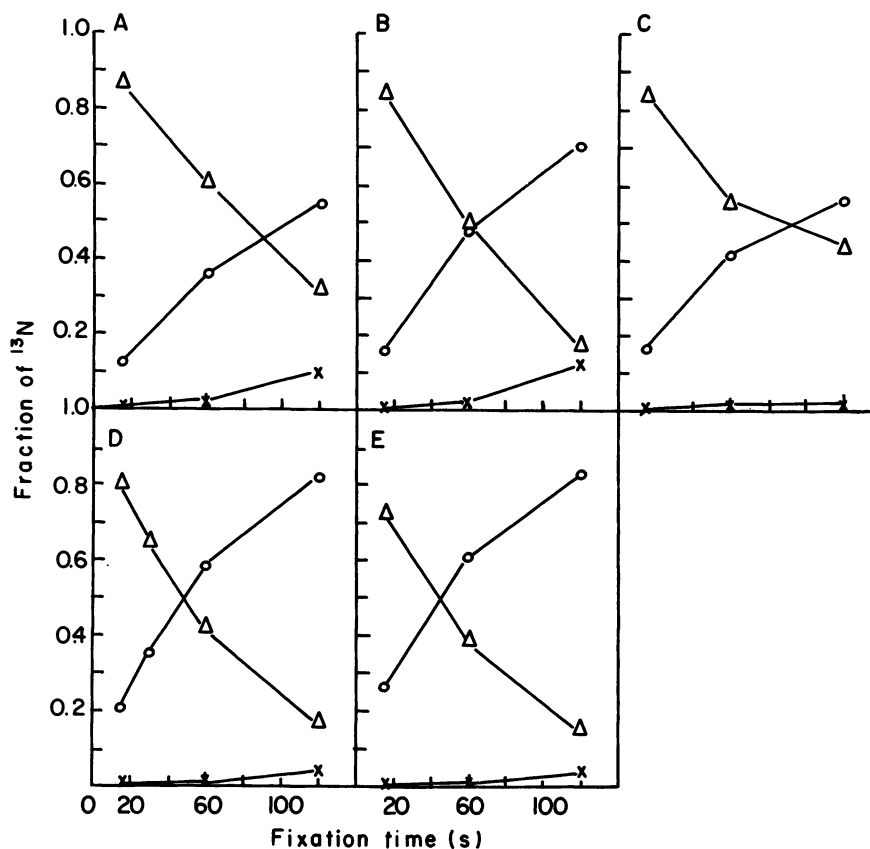


Figure 5. Time course of the distribution of  $^{13}\text{N}$  in amino acids extracted after fixation of  $[^{13}\text{N}]\text{N}_2$  for 15, 60, and 120 s by (A) *A. cylindrica*, (B) *A. variabilis*, (C) *C. licheniforme*, (D) *P. boryanum*, and (E) *Gleothecae sp.* (12, 14). The radioactivity of amino acids in methanolic extracts, subjected to electrophoresis, was quantitated by integration of peaks in radioscanes, with corrections applied for decay: ( $\Delta$ ) glutamine, ( $\circ$ ) glutamate plus aspartate, ( $\times$ ) citrulline (or, in the case of *C. licheniforme*, alanine).

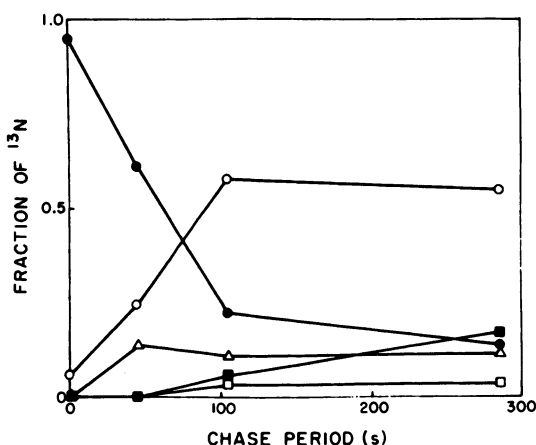
radioactivity associated with glutamine accounted for 77% (*Gleothecae sp.*) to 88% (*A. cylindrica*) of the total  $^{13}\text{N}$  recovered in organic products. The remainder of the  $^{13}\text{N}$  recovered after 15 s of fixation was associated with glutamate. The fraction of  $^{13}\text{N}$  in glutamine decreased and that in glutamate increased during longer incubation periods until, after 60–120 s of fixation, glutamate was more highly radioactive than glutamine in all five species. In *A. cylindrica*, after 120 s of fixation, radioactivity was additionally associated with aspartate, citrulline, and arginine (Figure 2). Neither aspartate nor arginine were detectably radioactive after 120 s of



fixation by the other four species. However,  $^{13}\text{N}$ -labeled citrulline was observed in *A. variabilis*, *Plectonema boryanum*, and *Gleothoece* sp. within 60–120 s of fixation. Radioactivity was detected in alanine but not citrulline after 60–120 s fixation by *Cylindrospermum licheniforme* (14). When  $^{14}\text{C}$ -labeled carbamyl phosphate was added to methanolic extracts and was recovered in thin-layer electrophoretograms, no  $^{13}\text{N}$  radioactivity was detected to be associated with this compound after 60 s of fixation of  $^{13}\text{N}$  by *A. cylindrica* (12).

When *A. cylindrica* was exposed to  $^{13}\text{N}$  for 15 s, the gas phase evacuated and then replaced with a mixture of  $\text{N}_2/\text{CO}_2$  (99:1, v/v), radioactivity associated with glutamine decreased while that associated with glutamate correspondingly increased as a fraction of the total  $^{13}\text{N}$  extracted with methanol (Figure 6). The change in the fraction of  $^{13}\text{N}$  in glutamine and glutamate was more rapid during the chase period than in typical time-course experiments (compare Figures 5 and 6).

The time-course and pulse-chase experiments indicate that glutamine is the initial organic product of assimilation of  $^{13}\text{N}$ -derived  $^{13}\text{NH}_4^+$ , presumably by direct amidation of glutamate. Then glutamate becomes labeled, presumably by a sequential amination of  $\alpha$ -ketoglutarate. To verify that the labeling of these amino acids occurs in a sequential



Journal of Biological Chemistry

**Figure 6.** Time course of the distribution of  $^{13}\text{N}$  in amino acids extracted from *A. cylindrica* when fixation of  $^{13}\text{N}$  for 15 s was followed by evacuation of the label and then continued fixation of  $\text{N}_2/\text{CO}_2$  (99:1, v/v) for 45, 105, and 285 s (12). The radioactivity of amino acids in methanolic extracts, subjected to electrophoresis, was quantitated by integration of peaks in radioscan, with corrections applied for decay: (●) glutamine, (○) glutamate (plus a small fraction of aspartate after 45 s of chase), (△) citrulline, (■) arginine; and (□) an unknown substance that migrated between arginine and alanine.

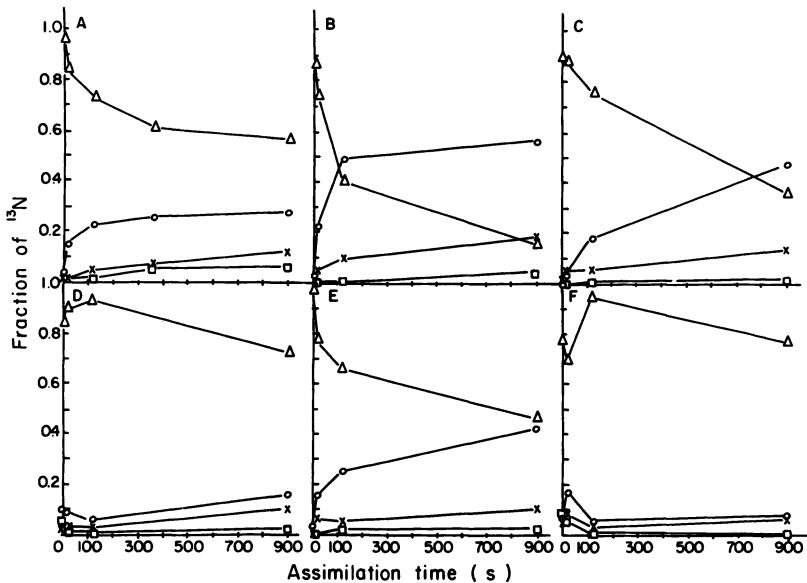
reaction, a number of experiments were performed using specific inhibitors of enzymes (12). When *A. cylindrica* was incubated with [ $^{13}\text{N}$ ]N $_2$  in the presence of methionine sulfoximine, an inhibitor of glutamine synthetase, little or no  $^{13}\text{N}$  was detected to be associated with glutamate, glutamine, or any other organic product, and the amount of  $^{13}\text{NH}_4^+$  distilled from methanolic extracts increased nearly 18-fold over that in extracts from cells incubated in the absence of the inhibitor (12). Fixation of [ $^{13}\text{N}$ ]N $_2$  in the presence of azaserine, an inhibitor of glutamine amide transfer reactions, resulted in extensive accumulation of  $^{13}\text{N}$  radioactivity in glutamine alone (12).

**ASSIMILATION OF  $^{13}\text{NH}_4^+$ .** Studies on the assimilation of exogenous  $^{13}\text{NH}_4^+$  by N $_2$ - and  $\text{NH}_4^+$ -grown cultures were initiated to determine whether the pathways of assimilation of exogenous ammonium differed from the pathway operative during N $_2$  fixation.

Metabolic products of assimilation of  $^{13}\text{NH}_4^+$  after 900 s of incubation included glutamine, glutamate, aspartate, citrulline, alanine, and arginine. These constituents were tentatively identified by their comigration with stable amino acids standards during electrophoresis at pH 9.2, sometimes followed by chromatography in an orthogonal direction and subsequent two-dimensional scanning (e.g., Figure 3).  $^{13}\text{N}$  in certain amino acids, such as aspartate and glutamate was also measured by elution of the ninhydrin reacting material on the thin-layer plate and by scintillation spectroscopy. Moreover, a major fraction of the  $^{13}\text{N}$  radioactivity associated with glutamine after incubation periods of 15 s or less could, in the case of each species, be distilled as amide nitrogen.

After 1 s of assimilation of  $^{13}\text{NH}_4^+$ , 77 (*Anacystis nidulans*) to 97% (*C. licheniforme* and *A. cylindrica*) of the  $^{13}\text{N}$  in organic compounds extracted with methanol was associated with glutamine (Figure 7). In *A. cylindrica*, approximately 88% of the  $^{13}\text{N}$  associated with glutamine after 3 s of assimilation distilled as amide nitrogen (13). The second major radioactive product of assimilation of  $^{13}\text{NH}_4^+$  was glutamate in all species examined. In all cases the fraction of label in glutamine decreased and that in glutamate increased with longer incubation periods. There were some species-dependent variations in the extent of the shift in the fractions of  $^{13}\text{N}$  in glutamine and glutamate, but only in the case of *A. variabilis* did the fraction of label in glutamate exceed that in glutamine within 120 s of incubation, as occurred during the fixation of  $^{13}[\text{N}]\text{N}_2$  (compare Figures 5 and 7).

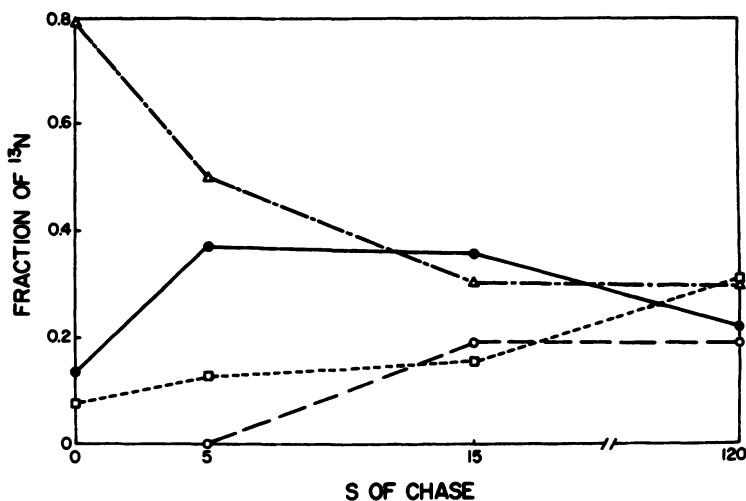
Aspartate was detectably radioactive in all the species as of 120 or 900 s of assimilation and, in *A. cylindrica*, was equal to the radioactivity in glutamate after 900 s of assimilation. Alanine was detectably radioactive within 1 s of assimilation by *A. variabilis*, *C. licheniforme*, and *A. nidulans* and within 15 s of assimilation by *Gleothecae* sp., but it was



**Figure 7.** Time course of the distribution of  $^{13}\text{N}$  in amino acids extracted after assimilation of  $^{13}\text{NH}_4^+$  for 1, 15, 120, and 900 s by (A) *A. cylindrica*, (B) *A. variabilis*, (C) *C. licheniforme*, (D) *P. boryanum*, (E) *Gleothecae sp.*, and (F) *A. nidulans* (12, 14). The radioactivity of amino acids in methanolic extracts, subjected to electrophoresis, was quantitated by integration of peaks in radioscan, with corrections applied for decay: ( $\Delta$ ) glutamine, ( $\circ$ ) glutamate plus aspartate, ( $\times$ ) citrulline plus alanine, ( $\square$ ) arginine plus other compounds. See text for species-dependent variations of  $^{13}\text{N}$  in glutamate plus aspartate and citrulline plus alanine.

detected only as a shoulder on the citrulline peak after 120 and 900 s in *P. boryanum* and was detected only in experiments with inhibitors and high exogenous  $\text{NH}_4^+$  concentrations in *A. cylindrica*. Radioactivity in citrulline was detected within 360 to 900 s of assimilation by *A. cylindrica*, *P. boryanum*, and *Gleothecae sp.*, but it was observed only as a shoulder on the alanine peak after 900 s of assimilation by *A. variabilis*, *C. licheniforme*, and *A. nidulans*. Low levels of radioactivity were observed associated with arginine after 900 s of assimilation. (i.e., <7–11% of the total in *A. variabilis* and *A. cylindrica*, and <3% of the total in the other species). The time course of appearance of  $^{13}\text{NH}_4^+$ -derived label in metabolic pools of *A. cylindrica* was essentially the same whether the cells were grown with  $\text{N}_2$  or  $\text{NH}_4^+$  as the nitrogen sources (13).

In *A. cylindrica* radioactivity derived from exogenous  $^{13}\text{NH}_4^+$  could be chased out of glutamine and into glutamate. When 3-s pulses of  $^{13}\text{NH}_4^+$  were chased with 5mM stable  $\text{NH}_4^+$  for varying periods of time, there was an initial rapid decrease in glutamine [ $^{13}\text{N}$ ]amide together with



Journal of Biological Chemistry

**Figure 8.** Time course of the distribution of  $^{13}\text{N}$  in amino acids extracted from *A. cylindrica* after assimilation of  $^{13}\text{NH}_4^+$  for 3 s followed by addition of 5mM  $\text{NH}_4\text{Cl}$  and subsequent incubation for 5, 15, and 120 s. The radioactivity in (●) glutamate plus aspartate, total glutamine (not shown), and (○) other constituents in methanolic extracts subjected to electrophoresis was determined by integration of peaks in radioscan, with corrections applied for decay. Time-corrected radioactivity of  $^{13}\text{N}$  in (Δ) amide and (□)  $\alpha$ -amino groups of glutamine was determined by elution of the glutamine region from the thin-layer plates and scintillation spectroscopy of the  $^{13}\text{N}$  in distillates of the eluent subjected to steam distillation in the presence of alkali. In this instance, nondistillable  $^{13}\text{N}$  in the glutamine eluent was taken to be  $\alpha$ -[ $^{13}\text{N}$ ]amino nitrogen.

a correspondingly immediate increase in [ $^{13}\text{N}$ ]glutamate (Figure 8). Following a lag of approximately 15 s,  $^{13}\text{N}$  then began to accumulate in the  $\alpha$ -amino nitrogen of glutamine. After 120 s of chasing, the  $\alpha$ -amino nitrogen of glutamine sometimes appeared to be as radioactive as the amide group and as glutamate. Aspartate, citrulline, and arginine were conspicuously radioactive within 360 s of chase (13).

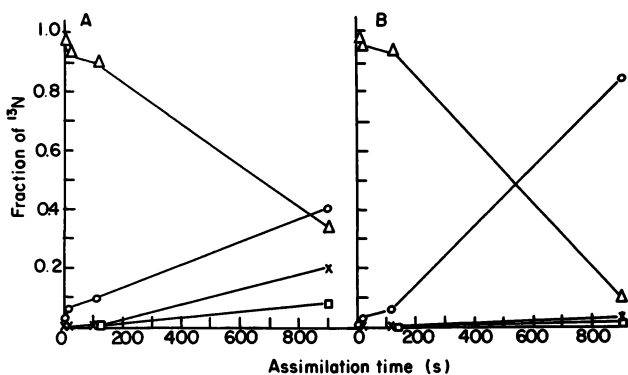
The effect of 1mM methionine sulfoximine on the incorporation of  $^{13}\text{NH}_4^+$  into organic metabolites after 900 s of incubation is shown in Table I. In these experiments, *A. cylindrica* and *A. nidulans* were grown under air with  $\text{NH}_4^+$  and  $\text{NO}_3^-$ , respectively, as the nitrogen source; the other species were grown with  $\text{N}_2$  as the sole nitrogen source. In the presence of methionine sulfoximine, incorporation of  $^{13}\text{N}$  into total organic products extractable with methanol was inhibited by 86–99.5% in the dinitrogen-fixing species. Although [ $^{13}\text{N}$ ]glutamate formation was inhibited by at least 84%, [ $^{13}\text{N}$ ]glutamine formation was, in the case of each dinitrogen-fixing species, more strongly inhibited. Formation of [ $^{13}\text{N}$ ]-

glutamine in the presence of methionine sulfoximine by *A. nidulans* was inhibited by 81%, but [ $^{13}\text{N}$ ]glutamate formation increased about sevenfold, so that net assimilation decreased only about 31%. Incorporation of  $^{13}\text{NH}_4^+$  into alanine by *C. licheniforme*, *A. cylindrica*, and *A. nidulans* was not decreased in the presence of methionine sulfoximine, but citrulline formation was strongly inhibited in all species.

When *A. cylindrica* was incubated for 120 s in the presence of  $^{13}\text{NH}_4^+$  and 1mM azaserine, incorporation of  $^{13}\text{N}$  into glutamate was inhibited over 98%, while formation of [ $^{13}\text{N}$ ]glutamine was reduced only 10% (13).  $^{13}\text{N}$  radioactivity was not detected in a separate aspartate, citrulline, or arginine peak, when *A. cylindrica* was incubated with  $^{13}\text{NH}_4^+$  in the presence of azaserine. Aminooxy acetate, a general inhibitor of amino transfer reactions, reduced incorporation of  $^{13}\text{N}$  into aspartate, citrulline, and arginine in *A. cylindrica* (13) and of alanine by *A. variabilis* (14) but did not reduce formation of [ $^{13}\text{N}$ ]alanine by *C. licheniforme* (14) or by *A. cylindrica* (13).

**ASSIMILATION OF  $^{13}\text{NO}_3^-$  AND  $^{13}\text{NO}_2^-$ .** Incubation of 10mM  $\text{NO}_3^-$ -grown *A. cylindrica* and *A. PCC 7120* for 900 s in the presence of either  $^{13}\text{NO}_3^-$  or  $^{13}\text{NO}_2^-$  resulted in incorporation of  $^{13}\text{N}$  into five organic products tentatively identified as glutamine, glutamate, aspartate, citrulline, and arginine on the basis of their comigration with stable amino acids during electrophoresis at pH 9.2.

The kinetic pattern of assimilation of  $^{13}\text{NO}_3^-$  into organic metabolites by *A. cylindrica* and *A. PCC 7120* was very similar to the pattern when  $^{13}\text{NH}_4^+$  was the nitrogen source (Figure 9). Glutamine was the most



**Figure 9.** Time course of the distribution of  $^{13}\text{N}$  in amino acids extracted from (A) *A. cylindrica* and (B) *A. PCC 7120* after assimilation of  $^{13}\text{NO}_3^-$  for 5, 15, 120, and 900 s. The radioactivity of amino acids in methanolic extracts subjected to electrophoresis was quantitated by integration of peaks in radioscan, with corrections applied for decay: ( $\Delta$ ) glutamine, ( $\circ$ ) glutamate plus aspartate, ( $\times$ ) citrulline, and ( $\square$ ) arginine plus other compounds.

**Table I. Principal Radioactive Constituents Observed After 900 s or  $\text{NO}_3^-$  as the Nitrogen Sources and Incubated in the**

<i>Cyanobacterium</i>	<sup>13</sup> N Found in Compound as Percent of the <sup>13</sup> N Added	
	Treatment	Total
<i>A. cylindrica</i> <sup>b</sup>	– MSX	13.56
	+ MSX	0.062 (99) <sup>c</sup>
<i>A. variabilis</i> <sup>b</sup>	– MSX	2.82
	+ MSX	0.35 (88) <sup>c</sup>
<i>C. licheniforme</i> <sup>b</sup>	– MSX	3.29
	+ MSX	0.47 (86) <sup>c</sup>
<i>P. boryanum</i> <sup>b</sup>	– MSX	5.35
	+ MSX	0.53 (90) <sup>c</sup>
<i>A. nidulans</i> <sup>b</sup>	– MSX	1.82
	+ MSX	1.22 (31) <sup>c</sup>

<sup>a</sup> Values are means of two or more experiments (except in the case of *A. cylindrica*, for which the results of a representative experiment are presented) and were determined by integration and time correction of peaks of radioactivity from <sup>13</sup>N after electrophoresis at pH 9.2, in comparison with <sup>13</sup>NH<sub>4</sub><sup>+</sup> radioactivity added as determined by scintillation spectroscopy. Nitrogen sources for growth of cyanobacteria were: *A. cylindrica*, NH<sub>4</sub><sup>+</sup>; *A. nidulans*, NO<sub>3</sub><sup>-</sup>; and all others, N<sub>2</sub>. Asp, aspartate; Glu, glutamate; Gln, glutamine; Cit, citrulline; Ala, alanine; Arg, arginine.

<sup>b</sup> Data from Ref. 13.

highly radioactive compound within 15 s of assimilation, accounting for approximately 97% of the total radioactivity. Glutamate was the next most highly labeled compound. Citrulline, arginine, and aspartate were detectably radioactive only after 900 s of assimilation, and aspartate constituted less than 25% of the glutamate plus aspartate region.

The distribution of <sup>13</sup>N in organic metabolites was essentially the same whether *A. cylindrica* cells were incubated with <sup>13</sup>NO<sub>3</sub><sup>-</sup> or <sup>13</sup>NO<sub>2</sub><sup>-</sup>,

**Table II. Principal Radioactive Constituents Observed After 900 s**

Nitrogen Source	<sup>13</sup> N Found in Compound as Percent of the <sup>13</sup> N Added <sup>a</sup>	
	Total	Asp + Glu <sup>b</sup>
<sup>13</sup> NO <sub>2</sub> <sup>-</sup>	17.34 ± 0.75	13.43 ± 0.6
<sup>13</sup> NO <sub>3</sub> <sup>-</sup>	8.85 ± 1.06	3.25 ± 1.2

<sup>a</sup> Values are means (± standard deviation of the mean) of four experiments and were determined by integration and time correction of peaks of radioactivity from <sup>13</sup>N in radioscan after electrophoresis at pH 9.2, in comparison with <sup>13</sup>NO<sub>2</sub><sup>-</sup> or <sup>13</sup>NO<sub>3</sub><sup>-</sup> radioactivity added as determined by scintillation spectroscopy. Asp, aspartate; Glu, glutamate; Gln, glutamine; Cit, citrulline; Ala, alanine; Arg, arginine.

**of Assimilation of  $^{13}\text{NH}_4^+$  by Cyanobacteria Grown with  $\text{N}_2$ ,  $\text{NH}_4^+$ , Absence and Presence of Methionine Sulfoximine (MSX)<sup>a</sup>** *$^{13}\text{N}$  Found in Compound as Percent of the  $^{13}\text{N}$  Added*

<i>Asp + Glu</i>	<i>Gln</i>	<i>Cit + Ala</i>	<i>Arg + Others</i>
5.87° 0.044' (99)°	5.29 0.00 (100)°	0.86 <sup>d</sup> 0.009' (99)°	1.54 0 (100)°
1.64° 0.25' (85)°	0.34 0.01 (97)°	0.56 <sup>d</sup> 0.09' (84)°	0.09 0 (100)°
1.27° 0.11' (91)°	1.70 0.09 (95)°	0.24 <sup>d</sup> 0.26' (0)°	0.08 0 (100)°
0.86° 0.14' (84)°	3.97 0.32 (92)°	0.52 <sup>d</sup> 0.07' (86)°	0.01 0 (100)°
0.10° 0.84° (0)°	1.67 0.32 (81)°	0.05° 0.06' (0)°	0.00 0.00

° *Asp + Glu* was calculated as one peak, but the peak was primarily *Glu* except in the case of *A. cylindrica*, where it was 50% *Asp* after 900 s of assimilation.

<sup>a</sup> Peak was primarily *Cit* with a trace of *Ala*.

' Numbers in parentheses refer to percent inhibition.

° No *Asp* observed.

° No *Cit* observed.

<sup>b</sup> Data from Ref. 14.

<sup>d</sup> Peak was primarily *Ala* with a trace of *Cit*.

although total label did appear to accumulate to a greater extent, especially in glutamate when  $^{13}\text{NO}_2^-$  was the nitrogen source (Table II).

**SUMMARY OF THE METABOLIC ROUTES OF ASSIMILATION OF  $^{13}\text{N}$ .** The finding that the first stable product of in vivo fixation of  $^{13}\text{N}$  by *Anabaena cylindrica* was  $^{13}\text{NH}_4^+$  was not unexpected, since  $\text{NH}_4^+$  is the first product of in vitro fixation of  $\text{N}_2$  by nitrogenase from heterotrophic bacteria (22). Moreover,  $^{13}\text{NH}_4^+$  accumulated from both  $^{13}\text{N}$  ( $^{13}\text{N}_2$ ) (12)

**Assimilation of  $^{13}\text{NO}_2^-$  and  $^{13}\text{NO}_3^-$  by  $\text{NO}_3^-$ -Grown *A. Cylindrica*** *$^{13}\text{N}$  Found in Compound as Percent of the  $^{13}\text{N}$  Added<sup>a</sup>*

<i>Gln</i>	<i>Cit + Ala</i> <sup>°</sup>	<i>Arg + Others</i>
1.79 ± 0.8	1.31 ± 0.6	0.81 ± 0.3
3.77 ± 0.65	1.31 ± 0.78	0.51 ± 0.28

<sup>b</sup> Peak primarily *Glu* with a shoulder of *Asp* in both cases.

° No *Ala* observed.

and  $^{13}\text{NO}_3^-$  (23) when assimilation of  $\text{NH}_4^+$  by *A. cylindrica* was inhibited with methionine sulfoximine.

The first major organic product of assimilation of  $^{13}\text{NH}_4^+$ , supplied exogenously or derived from  $[^{13}\text{N}]\text{N}_2$  or  $^{13}\text{NO}_3^-$ , by all cyanobacteria that we have examined is glutamine (Figures 2, 5, 7, and 9). The identity of this product as glutamine was supported by a variety of lines of evidence. The  $^{13}\text{N}$ -labeled product comigrated with stable and  $^{14}\text{C}$ -labeled glutamine during cochromatography and during coelectrophoresis at pH 2.0 and pH 9.2 (cf. Figures 2 and 3). After short incubation periods, the majority of the  $^{13}\text{N}$  in the glutamine region of the thin-layer plates could be distilled as amide nitrogen. The residual  $^{13}\text{N}$  in this region could be accounted for as  $\alpha$ -amino nitrogen (13). Finally, addition of 1mM methionine sulfoximine (an inhibitor of glutamine synthetase) reduced incorporation of  $^{13}\text{N}$  into the glutamine region as well as into total organic materials by 86% or more in all dinitrogen-fixing species examined (Table I). Thus, the quantitatively most important first step in the assimilation of ammonium, exogenously supplied or derived from dinitrogen or nitrate, appears to be catalyzed by glutamine synthetase in a wide range of cyanobacteria.

Glutamate is the second major product of assimilation of  $^{13}\text{NH}_4^+$ , exogenously supplied or derived from  $[^{13}\text{N}]\text{N}_2$  or  $^{13}\text{NO}_3^-$ . In the  $\text{N}_2$ -fixing species four observations indicate that glutamate is labeled primarily by glutamate synthase in series with, rather than by glutamic acid dehydrogenase in parallel with, glutamine synthetase. First, glutamate becomes labeled at the expense of glutamine amide nitrogen during pulse-chase experiments with  $[^{13}\text{N}]\text{N}_2$  and  $^{13}\text{NH}_4^+$  (Figures 6 and 8). Second, methionine sulfoximine greatly reduces incorporation of  $^{13}\text{N}$  into glutamate (Table I). Third, azaserine, an inhibitor of amide transfer from glutamine, greatly inhibits the formation of glutamate from  $[^{13}\text{N}]\text{N}_2$  or  $^{13}\text{NH}_4^+$  in *A. cylindrica* (12, 13). These results would not be expected if the major fraction of glutamate were formed by the action of glutamic acid dehydrogenase. Fourth, in the case of  $^{13}\text{NH}_4^+$  assimilation by *A. cylindrica*, increasing the concentration of exogenous stable  $\text{NH}_4^+$  to 2mM, a value approaching the  $K_m$  ( $[\text{NH}_4^+] = 12.5\text{mM}$ ; Reference 24) of glutamic acid dehydrogenase and greater than the  $K_m$  ( $[\text{NH}_4^+] = 1\text{mM}$ ; Reference 25) of glutamine synthetase, had little effect on the relative rates of appearance of  $^{13}\text{N}$  in glutamate and glutamine (13).

The presence of glutamine synthetase and glutamate synthase was also confirmed by in vitro assays of  $\text{N}_2$  and  $\text{NH}_4^+$ -grown cultures of *A. cylindrica* (13). The specific activity of glutamate synthase was similar in  $\text{NH}_4^+$ - and  $\text{N}_2$ -grown cultures ( $8.6 \pm 1.5$  and  $8.0 \pm 7.7$  nmol/[mg protein  $\cdot$  min] [mean  $\pm$  standard deviation of the mean], respectively). The mean specific activity of glutamine synthetase from  $\text{NH}_4^+$ -grown cultures ( $18.6 \pm 1.9$  nmol/[mg protein  $\cdot$  min]) was half that of  $\text{N}_2$ -grown



cultures ( $37.5 \pm 3.6$  nmol/[mg protein  $\cdot$  min]). This limited reduction in the activity of glutamine synthetase of  $\text{NH}_4^+$ -grown cultures of *A. cylindrica* compared to  $\text{N}_2$ -grown cultures has also been observed in another strain of *A. cylindrica* (25).

Nevertheless, a minor fraction—varying with the species—of the assimilation of  $^{13}\text{NH}_4^+$  may also be attributable to the action of glutamic acid dehydrogenase and alanine dehydrogenase. Incorporation of  $^{13}\text{N}$  from  $^{13}\text{NH}_4^+$  into glutamate by the  $\text{N}_2$ -fixing species was consistently less inhibited by 1mM methionine sulfoximine than was incorporation of  $^{13}\text{N}$  into glutamine (Table I). Similarly, residual synthesis of [ $^{13}\text{N}$ ]glutamate was observed when *A. cylindrica* was incubated with  $^{13}\text{NH}_4^+$  in the presence of azaserine (13). The observation that in the nondinitrogen-fixing species, *A. nidulans*, glutamate became much more radioactive in the presence of methionine sulfoximine that in its absence indicates that, in this organism, glutamate may be formed principally by glutamic acid dehydrogenase and that the low level of [ $^{13}\text{N}$ ]glutamate in the absence of methionine sulfoximine was due to its catabolism by glutamine synthetase.

Alanine appears to be formed primarily by alanine dehydrogenase in *A. cylindrica*, *C. licheniforme*, *P. boryanum*, and *A. nidulans*, because the inhibition of formation of glutamate and glutamine by methionine sulfoximine is not accompanied by a comparable inhibition in the formation of alanine (Table I). Moreover, alanine formation by these species was not reduced in the presence of aminoxy acetate, an inhibitor of amino transfer reactions (13,14). However, in *A. variabilis* alanine appears to be formed by a transamination reaction, because synthesis of [ $^{13}\text{N}$ ]alanine from  $^{13}\text{NH}_4^+$  was strongly inhibited in the presence of methionine sulfoximine and aminoxy acetate (14).

Two observations indicate that aspartate is formed primarily by a transamination reaction, probably from glutamate, rather than by a direct amination with  $^{13}\text{NH}_4^+$  in *A. cylindrica*. First,  $^{13}\text{N}$ -label in aspartate was reduced more than 90% by the presence of aminoxy acetate, while labeling of glutamate and glutamine was not reduced (13). Second, [ $^{13}\text{N}$ ]aspartate was not detected when glutamate formation was inhibited either directly, by azaserine, or indirectly, when glutamine synthesis was inhibited by methionine sulfoximine (13). Moreover, activity of a glutamate-aspartate aminotransferase reaction has been detected in vitro in two strains of *A. cylindrica* (1,26).

The sequential labeling of first citrulline and then arginine are consistent with the idea that citrulline is a substrate for the synthesis of arginine. In cyanobacteria, citrulline appears to be formed by the condensation of carbamyl phosphate with ornithine (27). The inhibition of formation of citrulline (and arginine) by methionine sulfoximine, azaserine, and aminoxy acetate could be due to the reduced formations of ornithine from glutamate and carbamyl phosphate from glutamine. In

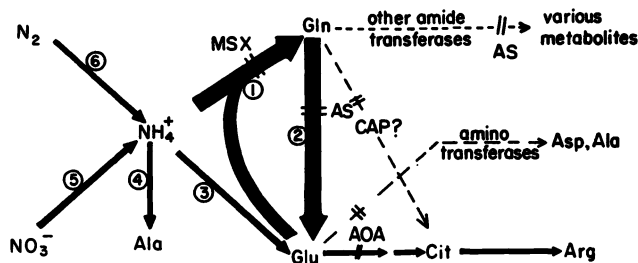


Figure 10. Diagram of the major and minor routes of the initial metabolism of ammonium, supplied exogenously or derived from  $N_2$  or  $NO_3^-$ , in cyanobacteria, based on experiments with  $^{13}N$  (13).

The heavy lines represent the major pathway of the initial assimilation of ammonium. Minor and secondary pathways for the metabolism of ammonium are presented by light lines, uncertain pathways by long-dashed lines, and presumed amide transfer reactions by a short-dashed line. Some of the enzymes involved are: 1, glutamine synthetase; 2, glutamate synthase; 3, glutamic acid dehydrogenase; 4, alanine dehydrogenase; 5, nitrate and nitrite reductases; and 6, nitrogenase. The sites of presumed inhibition by methionine sulfoximine (MSX), azaserine (AS), and aminooxy acetate (AOA) are indicated by the double parallel lines. Gln, glutamine; Glu, glutamate; Asp, aspartate; Ala, alanine; Cit, citrulline; Arg, arginine; CAP, carbamyl phosphate.

experiments with both  $[^{13}N]N_2$  and  $^{13}NH_4^+$  as substrates and in the presence of various metabolic inhibitors, we were unable to detect the presence of  $[^{13}N]$ carbamyl phosphate, although  $^{14}C$ -labeled carbamyl phosphate survived processing of the methanolic extracts (12, 13).

The pathways of initial metabolism of ammonium, supplied exogenously, or derived from  $N_2$  or  $NO_3^-$ , by cyanobacteria as determined by experiments with  $^{13}N$  are summarized in Figure 10.

**The Cellular Sites of Fixation of  $N_2$  and of Metabolism of  $N_2$ -Derived  $NH_4^+$ . FIXATION OF  $[^{13}N]N_2$  AND ASSIMILATION OF  $^{13}NH_4^+$  BY ISOLATED HETEROCYSTS.** To study nitrogen metabolism in heterocysts, a procedure was devised to isolate these cells from adjoining vegetative cells (1). Heterocysts were first detached from vegetative cells by mild cavitation of filaments that had been preincubated in the presence of 650mM mannitol, 26mM  $Na_2EDTA$ , 5mM TES buffer, pH 7.6, and either 6.5mM  $Na_2S_2O_4$  (sodium dithionite) or 5mM sodium ascorbate. The preincubation conditions appeared to render the vegetative cells more susceptible than usual to sonic disruption without affecting the heterocysts. The detached heterocysts were then purified by differential centrifugation under anaerobic conditions (1). Heterocysts isolated in this manner and incubated in the presence of an ATP generating system and dithionite as reductant retained up to as high as 34% of the acetylene reducing (nitrogenase) activity of whole filaments, with a specific activity of 1.5  $\mu\text{mol}/\text{mg}$  heterocyst chlorophyll/min (1).

The isolated heterocysts also reduced [ $^{15}\text{N}$ ]N<sub>2</sub> to radioactive products that could be steam-distilled in the presence of alkali from the methanolic extracts, with a fixation rate of up to 23% of the rate (per unit heterocysts/min) of intact filaments (Table III; Reference 1). When the suspension of isolated heterocysts was additionally supplemented with 1mM glutamate, incubated for 120 s with [ $^{15}\text{N}$ ]N<sub>2</sub> and the methanolic extracts subjected to sequential vacuum distillation at pH 10.0 and steam distillation in the presence of alkali, 66% of the fixed  $^{15}\text{N}$  distilled as amide nitrogen and the remainder distilled as free ammonia (Table IV). The higher fraction of free  $^{15}\text{NH}_4^+$  in these experiments compared to [ $^{15}\text{N}$ ]N<sub>2</sub> reduction by intact filaments (12) is probably due to leakage of low-molecular-weight metabolites such as  $\text{NH}_4^+$  from the isolated heterocysts. We assume that these preparations of heterocysts were not completely intact due to their dependence on exogenous ATP for nitrogenase activity (1): more recent preparations of isolated heterocysts require only light for maximal nitrogenase activity (2). Formation of both [ $^{15}\text{N}$ ]amide nitrogen and  $^{15}\text{NH}_4^+$  from [ $^{15}\text{N}$ ]N<sub>2</sub> was inhibited about 99% by the presence of 10% (v/v) acetylene (Table IV; acetylene, an alternate substrate for nitrogenase, inhibits nitrogen reduction). Isolated heterocysts were also allowed to fix [ $^{15}\text{N}$ ]N<sub>2</sub> for up to 900 s in the presence of supplements including 1mM stable glutamate. When the methanolic extract of a suspension following such an incubation was subjected to electrophoresis, only one  $^{15}\text{N}$ -labeled compound was detected. This compound comigrated with  $^{14}\text{C}$ -labeled glutamine during electrophoresis at pH 9.2 (1).

**Table III. Comparison of Rates of Fixation of [ $^{15}\text{N}$ ]N<sub>2</sub> by Intact Filaments and Isolated Heterocysts of *A. cylindrica* (1)**

Culture Fraction	Fixation Time (s)	Cpm $^{15}\text{N}$ Distilled/ $\mu\text{Ci}$ [ $^{15}\text{N}$ ]N <sub>2</sub> Added <sup>a</sup>	Total Heterocysts/Vial	Cpm $^{15}\text{N}/\mu\text{Ci}$ [ $^{15}\text{N}$ ]N <sub>2</sub> per min/ $10^6$ Heterocysts
Filaments	15	2.20	$1.09 \times 10^6$	8.07 (100) <sup>b</sup>
Heterocysts <sup>c</sup>	120	8.56	$2.27 \times 10^6$	1.88 (23) <sup>b</sup>

<sup>a</sup> After fixation of [ $^{15}\text{N}$ ]N<sub>2</sub> for the specified times, the suspensions were extracted with 80% methanol and the extract subjected to sequential vacuum and steam distillation to recover free and amide-derived  $^{15}\text{NH}_3$ . Cpm of  $^{15}\text{N}$  in distillate was determined by scintillation spectroscopy, corrected (as was the  $\mu\text{Ci}$  added) to the time of the start of fixation and normalized to equal microcuries of [ $^{15}\text{N}$ ]N<sub>2</sub> in the 1.0-mL reaction vial.

<sup>b</sup> Numbers in parentheses are percentages.

<sup>c</sup> The reaction mixture for heterocysts contained in 0.25 mL, 4mM ATP, 4mM MgCl, 40mM phosphocreatine, 0.05 mg creatine phosphokinase, 10mM Na<sub>2</sub>S<sub>2</sub>O<sub>4</sub>, 24mM TES pH 7.2 under an atmosphere of 97% argon, 2% N<sub>2</sub>, and 1% CO<sub>2</sub>. Filaments were incubated in growth medium under the same atmosphere.

**Table IV. Distribution of  $^{13}\text{N}$  Radioactivity in Products Distilling as Free Ammonia and Amide Nitrogen After Fixation of  $[^{13}\text{N}]\text{N}_2$  for 120 s by Heterocysts Isolated from *A. cylindrica* (1)**

Vial Contents <sup>a</sup>	Cpm $^{13}\text{N}/\mu\text{Ci } [^{13}\text{N}]\text{N}_2$ Added <sup>b</sup>	
	$^{13}\text{NH}_3$	$[^{13}\text{N}]\text{Amide}$
+ Heterocysts	15.93 ± 0.29	31.74 ± 0.23
+ Heterocysts + 0.1 atm of $\text{C}_2\text{H}_2$	0.18 ± 0.02	0.28 ± 0.03
- Heterocysts	-0.04 ± 0.04	0.04 ± 0.13

<sup>a</sup>The reaction mixture was the same as in Table III, footnote c, with the addition of 1mM glutamate and, as indicated,  $2.55 \times 10^6$  total or no heterocysts.

<sup>b</sup>After fixation of  $[^{13}\text{N}]\text{N}_2$ , the suspensions were extracted with 80% methanol and the extract subjected first to vacuum distillation at pH 10.0 to recover free  $^{13}\text{NH}_3$  and then to the steam distillation in the presence of alkali to recover amide-derived  $^{13}\text{NH}_3$ . Cpm  $^{13}\text{N}/\mu\text{Ci } [^{13}\text{N}]\text{N}_2$  added represents  $^{13}\text{N}$  associated with free or amide-derived  $^{13}\text{NH}_3$  determined by scintillation spectroscopy, corrected to the time of the start of fixation and normalized to equal microcuries of  $[^{13}\text{N}]\text{N}_2$  in the vial. Data expressed as mean ± standard deviation of the mean.

Journal of Bacteriology

The results of these  $[^{13}\text{N}]\text{N}_2$  labeling experiments thus show that isolated heterocysts are capable of reducing  $\text{N}_2$  to  $\text{NH}_4^+$  and that the  $\text{NH}_4^+$  was assimilated into glutamine. That is, activity of glutamine synthetase is coupled to nitrogenase in these cells. It is possible that a fraction of the  $[^{13}\text{N}]\text{glutamine}$  was catabolized in heterocysts, but due to the relatively low amount of total  $^{13}\text{N}$  assimilated we were unable to detect the products. We have consistently observed in cyanobacteria that approximately  $10^3$ -fold higher levels of incorporation of  $^{13}\text{N}$  can be attained with  $^{13}\text{NH}_4^+$  than with  $[^{13}\text{N}]\text{N}_2$  as substrate. Therefore, to study metabolism of  $\text{NH}_4^+$  and glutamine further, we incubated isolated heterocysts with  $^{13}\text{NH}_4^+$  and other substrates of amidation and amide transfer reactions.

The formation of  $[^{13}\text{N}]\text{glutamine}$  from  $^{13}\text{NH}_4^+$  by isolated heterocysts was greatly stimulated by the addition of stable glutamate and inhibited by the presence of methionine sulfoximine (Table V). When the glutamine region of the thin-layer plate was eluted and the eluent steam-distilled in the presence of alkali, all the radioactivity, within experimental error, could be accounted for as amide nitrogen. These results verify the presence and activity of glutamine synthetase in heterocysts previously indicated from  $[^{13}\text{N}]\text{N}_2$  experiments. However, a ratio of  $[^{13}\text{N}]\text{-glutamate}$  to  $[^{13}\text{N}]\text{glutamine}$  of at most 0.02 was detected under the conditions given in Table V and a variety of other conditions. The  $[^{13}\text{N}]\text{glutamate}$  formed could be accounted for by the low level of vegetative-cell contamination in the isolated heterocyst preparation. Moreover, no other products of amide transfer reactions involving glutamine could be detected when isolated heterocysts were incubated together with  $^{13}\text{NH}_4^+$  or  $[^{13}\text{N}]\text{amide-labeled}$  glutamine and appropriate substrates and cofactors (28).

**CELLULAR LOCALIZATION OF THE ACTIVITY OF GLUTAMINE SYNTHETASE AND GLUTAMATE SYNTHASE.** The results of the  $^{13}\text{N}$  experiments with isolated heterocysts imply that the  $^{13}\text{N}$  glutamate observed when intact filaments were incubated with  $^{13}\text{N}$   $\text{N}_2$  may have been formed in adjacent vegetative cells. We therefore attempted to localize the site of activity of glutamate synthase by the technique of differential disruption of vegetative cells and heterocysts, followed by in vitro enzyme assays of supernatant and pellet fractions (1). This technique relies on the fact that the thick-walled heterocysts are more resistant to cavitation than are vegetative cells. An enzyme associated only with vegetative cells or only with heterocysts will be solubilized as rapidly as the respective cells are broken. An enzyme associated with both cell types will display biphasic kinetics of solubilization.

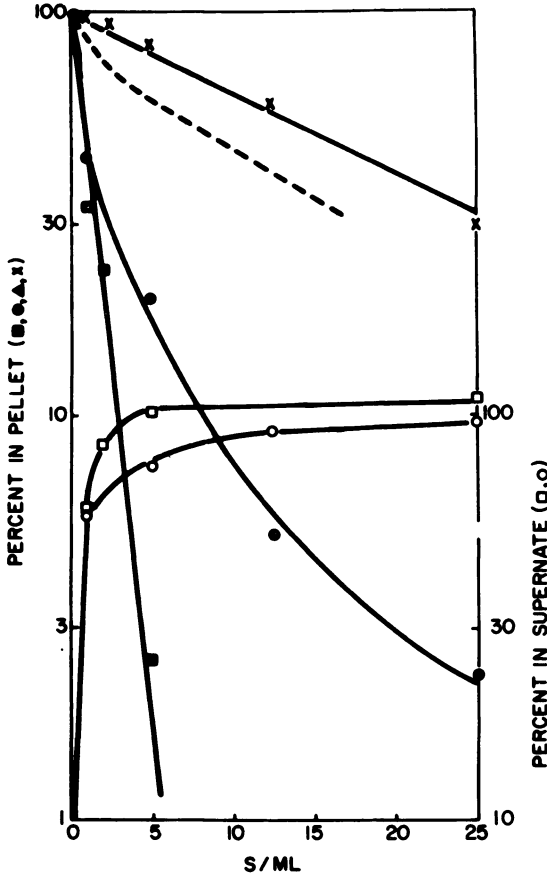
The time course of destruction of heterocysts and solubilization of the activities of glutamine synthetase and glutamate synthase are shown in Figure 11. Total activities of glutamine synthetase and glutamate synthase were determined on supernatant fluid of suspensions cavitated for 60 s/mL and centrifuged for 5 min at  $5,000 \times g$ . These activities were 25.4 and 5.2 nmol per mg protein per min, respectively, as assayed by a  $^{14}\text{C}$ -labeled substrate/product reaction described in (1). Enzymatic activities associated with pellet fractions were measured by resuspending the pellets, cavitating for an additional 60 s/mL, centrifuging as before, and assaying the supernatant fluid. Also given in Figure 11 is the time course of solubilization of the activity of glucose-6-phosphate dehydrogenase. Glutamate synthase activity was solubilized as rapidly as vegetative cells were broken. Within 5 s/mL of sonication essentially 100% of the glutamate synthase activity was found in the supernatant fraction,

**Table V. Assimilation of  $^{13}\text{NH}_4^+$  by Isolated Heterocysts of *A. Cylindrica*, Incubated for 600 s in the Presence and Absence of Glutamate and Methionine Sulfoximine (MSX) (1)**

<i>Vial Contents</i>	<i>Dpm <math>^{13}\text{N}</math> Glutamine/ dpm <math>^{13}\text{NH}_4^+</math> Added, %<sup>a</sup></i>
Basic mixture <sup>b</sup>	0.032
Basic mixture + 1mM glutamate	1.21
Basic mixture + 1mM glutamate + 1mM MSX	0.023

<sup>a</sup>  $^{13}\text{N}$  radioactivity in glutamine was determined by integration and time correction of peaks in radioscan of methanolic extracts after electrophoresis at pH 9.2 and was normalized to dpm of  $^{13}\text{NH}_4^+$  added at the start of incubation, as determined by scintillation spectroscopy, corrected to the same time.

<sup>b</sup> Reaction vials contained in a total volume of 0.4 mL,  $2.27 \times 10^6$  heterocysts isolated in the presence of sodium ascorbate, 5mM ATP, 8mM  $\text{MgCl}_2$ , 13mM TES pH 7.2, 5mM sodium ascorbate, 50 $\mu\text{M}$  dichlorophenol indophenol as reductant, and 5mM  $\alpha$ -keto-glutarate.



Journal of Bacteriology

Figure 11. Time course of the destruction of heterocysts and solubilization of the activities of glutamine synthetase and glutamate synthase during sonic cavitation of  $N_2$ -grown *A. cylindrica* (1): (X) the number of heterocysts apparently intact as percentage of the initial number of heterocysts; activities of (●) glutamine synthetase and (■) glutamate synthase associated with 5-min,  $5000 \times g$  pellets (left-hand ordinate) and activities of (○) glutamine synthetase and (□) glutamate synthase associated with supernatant fractions (right-hand ordinate), all as percentage of total activity, after cavitation for varying periods of time. The time course of the solubilization of (---) glucose-6-phosphate dehydrogenase is also shown for comparison to an enzyme largely associated with heterocysts (29).

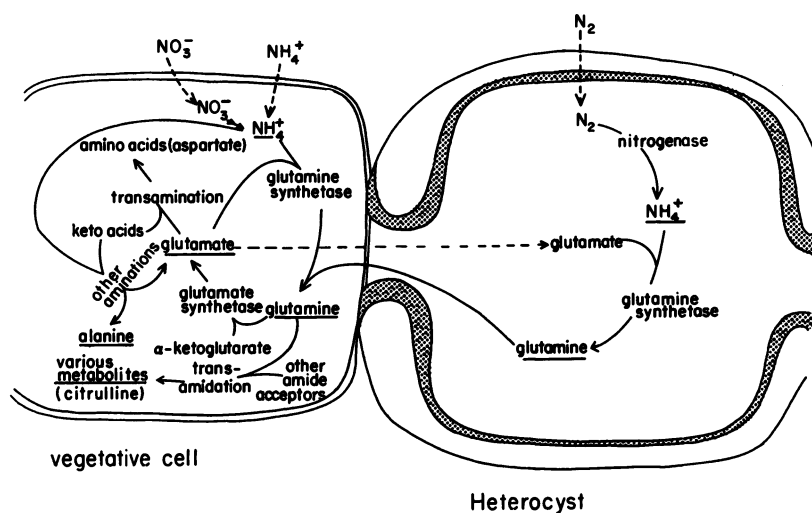
whereas less than 20% of the heterocysts had been broken. Glutamine synthetase activity displayed intermediate solubilization kinetics; after 12.5 and 25 s/mL of sonication a significant portion of the glutamine synthetase activity remained associated with the pellet (heterocyst)

fraction. However, by extrapolation, only about 8% of the initial glutamine synthetase activity was associated with heterocysts (about 6% of the total cells), in contrast to glucose-6-phosphate dehydrogenase, of which 70–80% of that activity is associated with heterocysts (29). That glutamine synthetase activity is only minimally enriched in heterocysts is consistent with the findings of others (25).

These results reinforce the idea that under  $N_2$ -fixing conditions, glutamate is formed from glutamine primarily, and perhaps only, in vegetative cells.

**SUMMARY OF THE CELLULAR SITES OF METABOLISM OF NITROGEN, EXOGENOUSLY SUPPLIED AS AMMONIUM OR DERIVED FROM  $N_2$  OR  $NO_3^-$ .** The sites of assimilation of inorganic nitrogen and of metabolism of the initial organic products of assimilation are depicted in Figure 12. This schematic is based primarily on experiments using *Anabaena cylindrica*, but we suggest that it is also applicable to the other heterocyst-forming cyanobacteria we have studied.

$NH_4^+$  derived from  $N_2$  through the activity of nitrogenase in heterocysts is rapidly incorporated into glutamine through the activity of glutamine synthetase in heterocysts as well. Although we were able to recover only up to 34% of the nitrogenase activity of intact filaments in these isolated heterocysts (1), recent experiments have indicated that essentially all the nitrogenase activity is localized in heterocysts under aerobic growth conditions (2). Thus, the major, and perhaps only, site



**Figure 12.** Schematic of the sites of the initial metabolism of ammonium, exogenously supplied or derived from  $N_2$  or  $NO_3^-$ , in heterocyst-forming cyanobacteria

for the initial incorporation of  $N_2$ -derived  $NH_4^+$  into cellular material is in heterocysts catalyzed by glutamine synthetase. The newly formed glutamine moves into adjacent vegetative cells where glutamate is synthesized by the action of glutamate synthase. Since, in *A. cylindrica*, it requires about 90 s before glutamate becomes as radioactive as glutamine (Figures 2 and 5), the time required for translocation of glutamine from heterocysts to vegetative cells must on the order of 90 s or less (12, 13). Rapid translocation of  $^{13}N$  out of heterocysts and into vegetative cells was also observed in the first published study of  $[^{13}N]N_2$  assimilation in cyanobacteria, which involved autoradiographic localization of  $^{13}N$  within filaments (17). A portion of the glutamate moves back to the heterocysts, where  $NH_4^+$  formation occurs and reacts to form additional glutamine. Because we were unable to detect products of other amide transfer reactions in isolated heterocysts, it would appear that a fraction of the glutamine translocated into vegetative cells is used as substrate for these reactions (e.g., formation of citrulline). Transaminations from glutamate to form other amino acids would also appear to occur in vegetative cells (e.g., formation of aspartate). We have not, however, ruled out the possibility that other reactions of nitrogen metabolism, in addition to the nitrogenase–glutamine synthetase pathway, take place in heterocysts.

When exogenous  $NH_4^+$  or  $NO_3^-$  are the nitrogen sources, incorporation of  $NH_4^+$  into glutamine can occur in all cells. Because glutamate synthase activity is also present in vegetative cells,  $^{13}N$  appears in glutamate much more rapidly as a fraction of the total  $^{13}N$  extracted when  $^{13}NH_4^+$  or  $^{13}NO_3^-$  are supplied than when  $[^{13}N]N_2$  is supplied (12, 13, 14). However, the newly synthesized  $[^{13}N]$ glutamate is also utilized by all vegetative cells to produce more glutamine, resulting in rapid labeling of the  $\alpha$ -amino, in addition to the amide group, of the glutamine pool. This dual labeling has the effect of maintaining a high level of radioactivity in the glutamine pool compared to the glutamate pool, so that glutamine is always more highly labeled than glutamate after 120 s of assimilation (Figures 7 and 9). When  $[^{13}N]N_2$  is the nitrogen source, glutamate is consistently more highly radioactive than glutamine after 120 s of assimilation (Figure 5). These differences in kinetics can be explained, in part, by the spatial separation of glutamine synthetase and glutamate synthase activity under  $N_2$ -fixing conditions and the time required to translocate  $[^{13}N]$ glutamate back into heterocysts compared to the time required to synthesize glutamine from  $[^{13}N]$ glutamate within the same cell.

Depending on the species, a minor fraction of exogenous  $NH_4^+$  is directly incorporated into glutamate and alanine by the activity of their respective dehydrogenases in vegetative cells.



### Conclusions

**Possible Implications for Control of Heterocyst Formation.** When cyanobacteria are grown under conditions that repress heterocyst differentiation (i.e., in the presence of  $\text{NH}_4^+$ ), the exogenous ammonium is rapidly assimilated into glutamine (13). However, when glutamine formation is inhibited by the presence of methionine sulfoximine, heterocyst differentiation continues in the presence of ammonium (30). Conversely, differentiation can be repressed when glutamine is added to cultures in the presence or absence of methionine sulfoximine (31, 32). Mature heterocysts, actively fixing  $\text{N}_2$ , inhibit nearby cells in the same filament from differentiating into heterocysts, and the inhibition is mediated by a diffusible substance produced by heterocysts (6, 33). The only nitrogenous compound that has heretofore been shown to be produced by, and exported from, heterocysts is glutamine (1). Proheterocysts (vegetative cells in the process of differentiating into heterocysts) inhibit the continued differentiation of adjacent proheterocysts (33, 34). Although proheterocysts are incapable of fixing  $\text{N}_2$  (35), they appear to contain a number of proteolytic enzymes that could release glutamine, precursors of glutamine (glutamate and ammonium), or other amino acids (36, cf. also 37). It is possible that the inhibitor formed from exogenous ammonium that moves from cell to cell (heterocyst and proheterocysts to vegetative cells and proheterocysts) is glutamine. If so, the glutamine itself, or a metabolic derivative of glutamine, is the intracellular signal molecule that controls the differentiation of vegetative cells into heterocysts.

### Acknowledgments

Research performed at the Michigan State University was supported by the U.S. Department of Energy under contract EY-76-C-02-1338. Research performed at the University of California, Davis, was supported in part by the California Agricultural Experiment Station under project number CAD\*-3620-H and by grant PCM 79-04136 from the U.S. National Science Foundation. I thank C. Peter Wolk for his comments during preparation of this chapter.

### Literature Cited

1. Thomas, J.; Meeks, J. C.; Wolk, C. P.; Shaffer, P. W.; Austin, S. M.; Chien, W.-S. *J. Bacteriol.* 1977, 129, 1545.
2. Peterson, R. B.; Wolk, C. P. *Proc. Natl. Acad. Sci. USA* 1978, 75, 6271.
3. Fleming, H.; Haselkorn, R. *Proc. Natl. Acad. Sci. USA* 1973, 70, 2727.
4. Meeks, J. C.; Wolk, C. P.; Thomas, J.; Austin, S. M.; Galonsky, A. In "Isotopes in Biological Dinitrogen Fixation"; Internatl. Atomic Energy Agency: Vienna, Austria, 1978; p. 170.

5. Wolk, C. P. In "Spores VI"; Am. Soc. Microbiol.: Wash. D. C., 1975; p. 85.
6. Wolk, C. P.; Quine, M. P. *Dev. Biol.* 1975, 46, 370.
7. Fogg, G. E. *Ann. Bot. (London)* 1949, 13, 241.
8. Tyagi, V. V. S. *Biol. Rev.* 1975, 50, 247.
9. Magasanik, B. *Prog. Nucleic Acid Res. Mol. Biol.* 1976, 17, 99.
10. Kustu, S.; Burton, D.; Garcia, E.; McCarter, L.; McFarland, N. *Proc. Natl. Acad. Sci. USA.* 1979, 76, 4576.
11. Thomas, J.; Wolk, C. P.; Shaffer, P. W.; Austin, S. M.; Galonsky, A. *Biochem. Biophys. Res. Comm.* 1975, 67, 501.
12. Wolk, C. P.; Thomas, J.; Shaffer, P. W.; Austin, S. M.; Galonsky, A. *J. Biol. Chem.* 1976, 251, 5027.
13. Meeks, J. C.; Wolk, C. P.; Thomas, J.; Lockau, W.; Shaffer, P. W.; Austin, S. M.; Chien, W.-S.; Galonsky, A. *J. Biol. Chem.* 1977, 252, 7894.
14. Meeks, J. C.; Wolk, C. P.; Lockau, W.; Schilling, N.; Shaffer, P. W.; Chien, W.-S. *J. Bacteriol.* 1978, 134, 125.
15. Rippka, R.; Deruelles, J.; Waterbury, J. B.; Herdman, M.; Stanier, R. Y. *J. Gen. Microbiol.* 1978, 134, 125.
16. Austin, S. M.; Galonsky, A.; Bortins, J.; Wolk, C. P. *Nucl. Instrum. Methods* 1975, 126, 373.
17. Wolk, C. P.; Austin, S. M.; Bortins, J.; Galonsky, A. *J. Cell Biol.* 1974, 61, 440.
18. Parks, N. J.; Krohn, K. *Int. J. Appl. Radiat. Isotopes* 1978, 29, 754.
19. Skokut, T. A.; Wolk, C. P.; Thomas, J.; Meeks, J. C.; Shaffer, P. W.; Chien, W.-S. *Plant Physiol.* 1978, 62, 299.
20. McElfresh, M. W.; Meeks, J. C.; Parks, N. J. *J. Radioanal. Chem.* 1979, 53, 345.
21. Markam, R. G.; Austin, S. M.; Styra, M. *Nucl. Instrum. Methods* 1979, 160, 49.
22. Dalton, H.; Mortenson, L. E. *Bacteriol. Rev.* 1972, 36, 231.
23. Meeks, J. C., unpublished data.
24. Haystead, A.; Dharmawardene, M. W. N.; Stewart, W. D. P. *Plant Sci. Lett.* 1973, 1, 439.
25. Dharmawardene, M. W. N.; Haystead, A.; Stewart, W. D. P. *Arch. Mikrobiol.* 1973, 90, 281.
26. Rowell, P.; Enticott, S.; Stewart, W. D. P. *New Phytol.* 1977, 79, 41.
27. Wolk, C. P. *Bacteriol. Rev.* 1973, 37, 32.
28. Wolk, C. P.; Meeks, J. C., unpublished data.
29. Winkenbach, F.; Wolk, C. P. *Plant Physiol.* 1973, 52, 480.
30. Stewart, W. D. P.; Rowell, P. *Biochem. Biophys. Res. Commun.* 1975, 65, 846.
31. Ownby, J. *Planta.* 1977, 136, 277.
32. Chapman, J. S.; Meeks, J. C., unpublished data.
33. Wolk, C. P. *Proc. Natl. Acad. Sci. USA.* 1967, 57, 1246.
34. Wilcox, M.; Mitchison, G. J.; Smith, R. J. In "Microbiology—1975"; Schlessinger, D., Ed.; Amer. Soc. Microbiol.: Wash., D. C. 1975; p. 453.
35. Kulasooriya, S. A.; Lang, N. J.; Fay, P. *Proc. R. Soc. London, Ser. B* 1972, 181, 199.
36. Wood, N. B.; R. Haselkorn, R. In "Limited Proteolysis in Microorganisms"; Cohen, G. N.; Holzer, H., Eds.; U.S. Dept. Health, Education, and Welfare, Bethesda, MD, 1979; publ. no. (NIH) 79-1591, p. 159.
37. Haselkorn, R. *Ann. Rev. Plant Physiol.* 1978, 29, 319.

RECEIVED September 4, 1980.

## Use of $^{13}\text{N}$ in Studies of Denitrification

J. M. TIEDJE, R. B. FIRESTONE<sup>1</sup>, M. K. FIRESTONE<sup>2</sup>,  
M. R. BETLACH<sup>3</sup>, H. F. KASPAR<sup>4</sup>, and J. SØRENSEN<sup>4</sup>

Departments of Crop and Soil Sciences, Microbiology and Public Health, and  
Cyclotron Laboratory, Michigan State University, East Lansing, MI 48824

*Denitrification results in major losses of fertilizer and native nitrogen from soil, fresh water, and marine habitats. The radioactive isotope,  $^{13}\text{N}$ , allows direct measurement of  $\text{N}_2$ , the principal denitrification product, in any atmosphere and provides a very sensitive measure of denitrification activities. The findings of laboratories that have used  $^{13}\text{N}$  in denitrification studies are summarized in this chapter. Emphasis is placed on the methods for production, purification, and detection of  $^{13}\text{N}$  forms important to denitrification investigations. The summary of research results includes information on the following: measurement of denitrification rates, isotope dilution experiments to investigate denitrification intermediates, factors influencing the proportion of  $\text{N}_2\text{O}$  vs.  $\text{N}_2$  produced, and the partitioning of nitrate between denitrification and dissimilatory nitrate reduction to ammonium for bacterial cultures and natural samples.  $^{13}\text{N}$  and  $^{15}\text{N}$  are considered complementary methods, since each is uniquely suited to certain aspects in the study of denitrification.*

**D**enitrification is the process by which nitrogenous oxides, principally nitrate, are reduced to gaseous nitrogen products, primarily dinitrogen and nitrous oxide. The process is carried out by a diverse group of bacteria that have the unique capability of using nitrogenous oxide as

<sup>1</sup> Current address: Lawrence Berkeley Laboratory, Berkeley, CA 94720.

<sup>2</sup> Current address: University of California, Berkeley, CA 94720.

<sup>3</sup> Current address: NASA Ames Research Center, Moffet Field, CA 94035.

<sup>4</sup> Current address: Cawthron Institute, Nelson, New Zealand.

<sup>4</sup> Current address: University of Aarhus, Aarhus, Denmark.

alternative electron acceptors for their respiratory metabolism when oxygen is limiting. Bacteria capable of this process are widespread. Thus it is not surprising that denitrification is well known in soils and sediments of all types but can also occur in more localized habitats such as food products, animal intestinal tracts, and waste treatment facilities. The pathway of denitrification is generally thought to be  $\text{NO}_3^- \rightarrow \text{NO}_2^- \rightarrow \text{NO} \rightarrow \text{N}_2\text{O} \rightarrow \text{N}_2$  (1) with NO the only intermediate in dispute (2, 3, 4).

Since denitrification produces  $\text{N}_2$  from a nitrogen form available to plants, it represents a loss of this scarce resource for biological growth and productivity. In effect, denitrification is one-half of the nitrogen cycle, the other half being nitrogen fixation, the process that converts  $\text{N}_2$  to nitrogen forms available to organisms. It is estimated that about one-fourth of nitrogen fertilizer is lost by denitrification (5); and on a worldwide basis, estimates of total global denitrification are 200 million metric tons (6, 7). With the projected shortages of food and energy, this loss is one that all would like to reduce. Besides the major concern over the loss of productivity, there are four additional reasons why the denitrification process is of concern: (i) nitrous oxide has been implicated in destruction of the ozone layer (8,9) and in warming of the planet through the greenhouse effect (10); (ii) nitrite, an intermediate in the process reacts with secondary and tertiary amines to form nitrosamines, some of which are among the most potent carcinogens known (11); (iii) nitric oxide, which also seems to be produced during denitrification, is a free radical and can react with heme compounds and other cellular constituents, and thus NO may have some detrimental impact on organisms; and (iv) the denitrification process can be used to remove nitrogen from waste that otherwise would produce an excessive nutrient load in a receiving habitat (12).

Despite the obvious importance of denitrification to human beings and to the environment, it remains the least understood process in the nitrogen cycle. One major reason for this is the absence of methodology to measure the process directly and sensitively, because the product,  $\text{N}_2$ , cannot be measured in the presence of its atmospheric background. The radioisotope,  $^{15}\text{N}$ , therefore provides a major advantage, because it can be sensitively detected in the presence of any atmosphere. A second advantage of  $^{15}\text{N}$  is that its high sensitivity allows one to measure rates of denitrification by addition of the tracer without affecting the natural nitrate concentration. The high sensitivity of  $^{15}\text{N}$  is apparent from Table I, which has a comparison of the  $^{15}\text{N}$  detection limits to those of other isotopes commonly used by biologists. Generally, one need not add more than femtogram quantities of  $^{15}\text{NO}_3^-$  (e.g., 68 fg = 0.1 mCi, which is usually sufficient). Other advantages of  $^{15}\text{N}$  are that kinetics at very low N substrate concentrations can be investigated, that the gamma emission

Table I. Comparison of Sensitivity of <sup>15</sup>N with Other Isotopes

Isotope	Half-life	Maximum Specific Activity Possible (mCi/m atom)	Minimum Detectable Amount (Moles) <sup>a</sup>
<sup>15</sup> N	10 min	$1.4 \times 10^{10}$	$3 \times 10^{-20}$
<sup>15</sup> N	stable	(99 atom % excess)	$7 \times 10^{-9b}$
<sup>14</sup> C	5730 yr	62.4	$7 \times 10^{-12}$
<sup>32</sup> P	14.3 day	$9.1 \times 10^6$	$5 \times 10^{-17}$
<sup>35</sup> S	87.4 day	$1.5 \times 10^6$	$3 \times 10^{-16}$
<sup>3</sup> H	12.35 yr	$2.9 \times 10^4$	$1 \times 10^{-14}$

<sup>a</sup> Assuming 1000 dpm minimum detectable radiation.

<sup>b</sup> Assuming 0.001 atom % excess of <sup>15</sup>N and 1 mg N gas produced in 10 mg N gas sample to be the minimum detectable <sup>15</sup>N enrichment. However, the sensitivity can be increased approximately two orders of magnitude by using the new quadrupole GC mass spectrometers, due to their greater absolute sensitivity (41).

allows nondestructive measurement of biological materials (of special value in studies which include plants), and that one can locate and measure small pools of intermediate N species, as in the isotope dilution experiments discussed later.

We are aware of four groups that have conducted denitrification studies using <sup>15</sup>N: our group at Michigan State University, which uses the sector-focused cyclotron on campus; Gersberg and Goldman cooperating with Krohn and others at the Crocker Nuclear Laboratory at the University of California, Davis; Stout of the New Zealand Soils Bureau cooperating with McNaughton and More using the Van de Graaff accelerator at the DSIR Institute of Nuclear Science near Wellington, New Zealand; and Hollocher of Brandeis University cooperating with Cooper and Tilbury using the cyclotron at the Memorial Sloan-Kettering Cancer Center in New York City. There are many more facilities capable of producing <sup>15</sup>N than are being used for research on the nitrogen cycle. The major discouragement to expansion of <sup>15</sup>N use will probably remain the rather lengthy development phase and the need for collaboration among several people of very different skills.

### Experimental

**The Gas Stripping System.** This system has been the most popular for denitrification studies probably because it provides the most immediate and sensitive measurement of denitrification rates. It was first used by Gersberg et al. (13, 14) to measure denitrification rates in rice paddy soils, sediments, and hypolimnion water, and later by Tiedje et al. (15) and Stout and More (16) to measure denitrification rates in soils. A schematic of the system used by our group is shown in Figure 1.

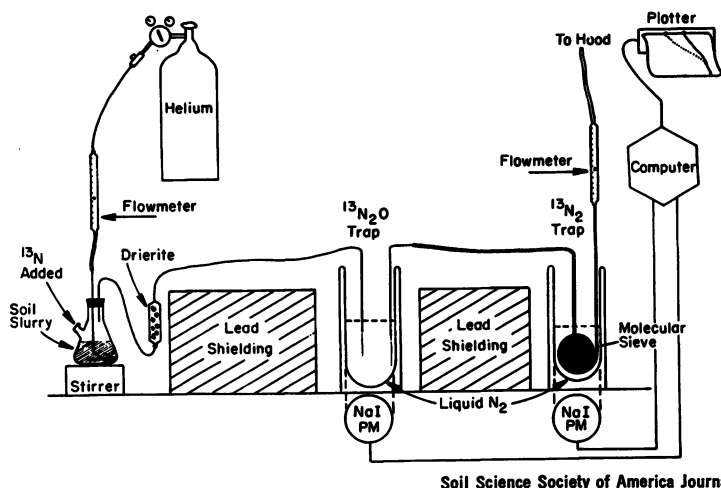


Figure 1. Diagram of gas stripping system used to continuously monitor  $[^{13}\text{N}]-\text{N}_2\text{O}$  and  $[^{13}\text{N}]-\text{N}_2$  produced from denitrification (15).

All three groups used helium to sweep the  $^{13}\text{N}$  gases produced to the traps. Gersberg et al. (13) used a single trap of Molecular Sieve 13 $\times$  immersed in liquid nitrogen to collect all N gases. Tiedje et al. (15) and Stout and More (16) used differential trapping procedures to separate  $\text{N}_2\text{O}$  and  $\text{N}_2$  so that the rate of production of each gas could be measured. We used liquid nitrogen to freeze out the  $\text{N}_2\text{O}$  but not the  $\text{N}_2$  (Figure 1), while Stout and More used a warm molecular sieve trap to retard the  $\text{N}_2\text{O}$  but not the  $\text{N}_2$ . Stout and More had to correct  $\text{N}_2\text{O}$  counts for the transience of  $\text{N}_2$ . We found that the  $^{13}\text{N}_2$  retention in our  $\text{N}_2\text{O}$  trap was less than 3% and thus was considered insignificant. All groups have used NaI(Tl) detectors placed adjacent to the traps and similar electronics to monitor  $^{13}\text{N}$  accumulation in the traps. We also have on-line capability for correction of half-life, background and detector calibration to a standard source ( $^{22}\text{Na}$ ) (15).

The general limitation of the stripping system is that it requires helium as the sweep gas since larger-molecular-weight gases seem to cause channeling in the cold sieve trap, thereby breaking its trapping integrity. Since helium must pass through the sample, the gaseous environment of the sample changes. For naturally anaerobic samples, this is not a concern, but many denitrifying habitats have some oxygen present, for example, most soils and the aerobic-anaerobic interface of sediments. In the latter cases, the oxygen status can not be maintained with a helium sweep gas, and thus one would expect that denitrification would be affected since oxygen is a major environmental regulator of this activity (1). Stout and More (6) have added  $^{13}\text{NO}_3^-$  to natural soil cores and used helium as the sweep gas to pass over the core surface, but they have not completed enough studies nor have they characterized the effect of helium on the soil's gaseous environment to be able to judge the appropriateness of this procedure for measurement of natural denitrification rates.

A stripping system that allowed use of some oxygen and yet trapped all the  $\text{N}_2$  would be much more useful for studies aimed at determining natural denitrification rates.

**<sup>13</sup>N Gas Analysis.** Our laboratory has developed a gas chromatography (GC) system that allows immediate measurement of the radioactivity in each N gas peak by coupling a proportional counter (PC) to the effluent of the microthermister detector cell (15). The output is fed to a computer and the data are later corrected for half-life, background, and the area under the peaks is integrated. Further details on the electronics and the data analysis program are presented in detail elsewhere (17, 18). Measurement of NO is problematic due to its reactivity. Extra <sup>14</sup>NO is added to syringes before taking samples in which <sup>13</sup>NO is to be measured, providing extra carrier to reduce <sup>13</sup>NO loss by adsorption. One gas separation system used was Poropak Q and Molecular Sieve 5A columns in series in which the N<sub>2</sub> and NO were separated on the molecular sieve (15). This system was used successfully, but the NO tailed badly and showed some memory on the column. A second system used a liquid nitrogen cooled loop between the injector and the Poropak Q column (19). N<sub>2</sub>O and NO are retained in the cold loop while N<sub>2</sub> is measured; the loop is then warmed and N<sub>2</sub>O and NO are separated and measured. This seems to be a more accurate system, but it requires more manipulations. An alternative that we used in the NO label exchange experiment was to avoid the difficulty of the NO and N<sub>2</sub> separation by choosing organisms that lacked the capacity to reduce N<sub>2</sub>O to N<sub>2</sub> (4). In this case, only N<sub>2</sub>O and NO gases were present and could be analyzed rapidly on the single Poropak column.

A GC system is essential to verify the identity of the gases and can be used to analyze <sup>13</sup>N in any atmosphere. We have also used it to obtain denitrification rates analogous to those from the stripping system. However, the GC method is more time-consuming, yields fewer points, and is much less sensitive since only a small subsample of gas is taken.

**<sup>13</sup>N Ion Analysis.** A radio high performance liquid chromatograph (R-HPLC) was developed in our laboratory to monitor NH<sub>4</sub><sup>+</sup>, NO<sub>2</sub><sup>-</sup>, and NO<sub>3</sub><sup>-</sup> in studies of dissimilatory nitrate reduction (15). The system was patterned after that of Tilbury and Dahl (20). Separation was accomplished in 5 min on a strong anion-exchange column (Partisil SAX) with a pH 3.0, 0.05M phosphate buffer. Detection was by  $\gamma$  coincidence counting using 2 NaI(Tl) crystals. Data were collected, corrected, and reported as for the gas chromatography-proportional counting system above. An example of a separation is shown in Figure 2 for a <sup>13</sup>N source and for the products following microbial reduction of that substrate.

Our group used the R-HPLC to monitor the N species in each source (since this varied somewhat), to prove purity after a purification procedure, to measure temporal changes in the ions after incubation with bacterial cells or natural samples, and to quantify the ions inside cells. Cells and debris from natural samples were removed by filtration through a 0.22- $\mu$ m filter prior to injection on the R-HPLC column. The internal <sup>13</sup>N species were recovered by extracting washed cells on a filter with hot methanol and by analyzing the methanol extract. The R-HPLC system was more useful in studies in which the dissimilatory fate of nitrate was ammonium rather than dinitrogen and thus sediments, sludge, and rumen contents were those most commonly analyzed.

Although this R-HPLC design was very reliable and useful in our studies, we were sometimes limited by the lower sensitivity of the coincidence circuitry. It may be advantageous to design future systems with a  $\beta^+$  detector to gain sensitivity.

**Measurement of <sup>13</sup>N Uptake by Cells Assimilating Nitrate.** To measure this fate of nitrate, we collected cells incubated with <sup>13</sup>N by passing a portion

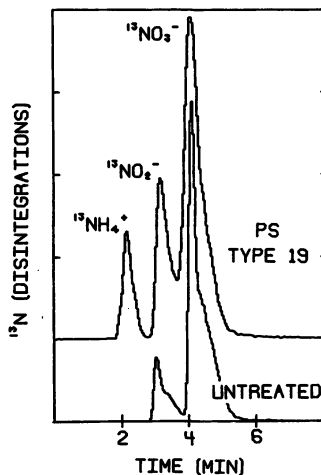


Figure 2. Separation of  $^{13}\text{NH}_4^+$ ,  $^{13}\text{NO}_2^-$ , and  $^{13}\text{NO}_3^-$  by R-HPLC. The components of an untreated  $^{13}\text{N}$  source are compared to the products of the same source after incubation with a culture of *Pseudomonas* (PS type 19).

of the incubation mixture through 0.45- $\mu\text{m}$  cellulose-acetate membrane filters. The collected cells were then washed with buffer and the filters placed in scintillation vials with 10 mL of scintillation cocktail (e.g., FilterSolv, Beckman Instruments). The vials were then shaken 10 min to digest the filters and counted twice in a liquid scintillation counter.

We devised a system to correct for the  $^{13}\text{NO}_3^-$  and  $^{18}\text{F}$  ( $t_{1/2} = 110$  min) bound to the filter, since washing of filters did not remove these counts. To determine the contribution of  $^{18}\text{F}$  to total radioactivity and to correct for  $^{13}\text{N}$  decay, we solved the following pair of simultaneous equations:

$$\text{CPM}(t_1) = N_0 \cdot D_N(t_1) + F_0 \cdot D_F(t_1) \quad (1)$$

$$\text{CPM}(t_2) = N_0 \cdot D_N(t_2) + F_0 \cdot D_F(t_2) \quad (2)$$

In these equations,  $\text{CPM}(t_1)$  represents the total counts in the sample vial recorded at elapsed time,  $t_1$ .  $N_0$  and  $F_0$  refer to the cpm attributable to  $^{13}\text{N}$  and  $^{18}\text{F}$ , respectively, in the sample at the start of counting the sample set.  $D_N(t_1)$  refers to the fraction of  $^{13}\text{N}$  radioactivity remaining at time  $t_1$ . It is determined by evaluating the expression  $\exp(-\ln 2 \cdot t/t_{1/2})$ , where  $t_{1/2}$  is the half-life of  $^{13}\text{N}$ , 9.96 min. A similar expression is represented by  $D_F(t_1)$ , except that the half-life of  $^{18}\text{F}$  is 110 min. Since the counts per minute and the elapsed time (hence fraction remaining) are known for each sample, the equations need only be solved for  $N_0$  and  $F_0$ . This was done using a program (18) written for an IMSAI 8080 microcomputer in our laboratory. This computer was connected to the scintillation counter (via a Beckman RS232C Communications Interface) to receive counting data directly. Such a configuration permitted analysis of an experiment within a few minutes after the last sample had been counted, so that subsequent experiments could be modified as needed.

Since  $^{18}\text{F}$  has a much longer half-life than  $^{13}\text{N}$ , its contribution to total counts increased continuously after bombardment. In all experiments in which cells had incorporated radioactivity, the contribution of fluorine was lower than

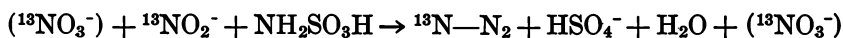


it was in the source used, indicating that there was a selective enrichment for <sup>13</sup>N in the filtered cells. In contrast, filters through which samples of the source were passed to measure nonspecific adsorption always had a higher percentage of counts attributable to fluorine than the source or the filtered cells, indicating <sup>18</sup>F was preferentially bound to the filters. Results of a typical experiment that showed these effects are presented in Table II.

An alternative method for measuring <sup>13</sup>NO<sub>3</sub><sup>-</sup> uptake by bacterial cells is the silicone oil sedimentation method reported on by Thayer and Huffaker in Chapter 17 of this volume.

**Measurement of Total <sup>13</sup>N Counts.** We usually determined total <sup>13</sup>N in samples by placing the sample in NaI(Tl) well counters with data fed to the same computing system as for the above analyses for background and half-life correction (15). Calibration is by a standard <sup>22</sup>Na source dissolved in water and placed in a test tube. The well counters had the most reproducible counting geometry of any of our detection systems and thus were used to obtain total amount of <sup>13</sup>N source added to any experiment. <sup>18</sup>F present in the samples was corrected by using the two-component decay curve analysis.

**Calibration of Detectors, Especially GC-PC Against R-HPLC.** For many experiments, it was useful to calculate a <sup>13</sup>N balance by adding up each fate of the original label. Since the counting systems we used have different geometries and detection methods, an isotope balance was difficult to achieve. We cross-calibrated our detection systems in the following way: The gas stripping system, R-HPLC, and well counters were referenced to <sup>22</sup>Na, the scintillation counter was referenced to the well counter by using the same <sup>13</sup>N source in each, and the GC-PC was referenced to the R-HPLC by conversion of nitrite to dinitrogen according to the following equation:



A standard <sup>13</sup>N source (<1 mL) containing <sup>13</sup>NO<sub>3</sub><sup>-</sup> and <sup>13</sup>NO<sub>2</sub><sup>-</sup> previously analyzed by R-HPLC was reacted with 0.1 mL of 5% sulfamic acid in a sealed

**Table II. Corrected Data for Uptake of 1 μM <sup>13</sup>NO<sub>3</sub><sup>-</sup> by Bacterial Cells Grown on NO<sub>2</sub><sup>-</sup> and WO<sub>4</sub><sup>2-</sup>, Illustrating <sup>18</sup>F Contribution to Total Radioactivity on Filters**

Incubation Time (Min)	Disintegrations per Minute <sup>a</sup>		Percent <sup>18</sup> F	Percent of Possible <sup>13</sup> N Incorporation
	<sup>18</sup> F	<sup>13</sup> N		
0.5	1092	18,667	5.53	4.56
1.0	1432	22,756	5.92	5.56
2.0	1407	35,392	3.82	8.65
3.0	2166	41,253	4.99	10.08
4.0	1024	45,643	2.19	11.15
Adsorption to filter	347	494	41.27	0.12
<sup>13</sup> N solution	144,635	409,303	26.11	100.00

<sup>a</sup> Values reported as disintegrations per minute since they have been calculated back to the time we began counting the sample set.

vial. The vial was shaken for a few minutes and then the gas and liquid products were analyzed by GC-PC and R-HPLC, respectively. The original radioactivity in the  $^{13}\text{NO}_2^-$  should equal the total radioactivity in the  $^{13}\text{N}-\text{N}_2$  produced. The  $\text{NO}_3^-$  is conserved in the reaction and was used to check on the accuracy of the dilution and transfer. The R-HPLC analysis after the reaction also confirmed that total decomposition of the  $\text{NO}_2^-$  had occurred. After accounting for the appropriate dilutions, we obtained an efficiency ratio between the GC-PC and the R-HPLC, thus allowing the nitrogen gases and ions analyzed in an experiment to be evaluated on equivalent terms.

This procedure should be done each day the instruments are used, since the GC-PC particularly can easily vary in sensitivity due to slight changes in gas flow and electronic settings for the proportional counter.

### *Production of $^{13}\text{N}$*

**Production of  $^{13}\text{NO}_3^-$  by the  $^{16}\text{O}(p,\alpha)^{13}\text{N}$  Reaction with an  $\text{H}_2\text{O}$  Target.** Experimenters with access to cyclotrons appear to have settled on this reaction as the most convenient for production of  $^{13}\text{NO}_3^-$ , since the target is easy to prepare and labeled nitrate is produced directly and in solution ready for use (13, 15). Our yields of  $^{13}\text{NO}_3^-$  are 10–20 mCi using a 15-MeV proton beam of 1–3  $\mu\text{A}$  and bombarding for 10–15 min. Others obtained greater than 99% of the  $^{13}\text{N}$  as nitrate (13), whereas we typically found the following distribution of  $^{13}\text{N}$  species: 75–95%  $\text{NO}_3^-$ , 5–10%  $\text{NO}_2^-$ , 0.5–25%  $\text{NH}_4^+$  plus traces of  $\text{N}_2\text{O}$  and  $\text{N}_2$  (15). These differences in products are probably due to differences in current and target environment, though we were not able to increase reproducibly the proportion of  $^{13}\text{N}$  found as nitrate. We could easily remove the contaminating  $\text{NH}_3$ ,  $\text{N}_2\text{O}$ , and  $\text{N}_2$  by flash evaporation (approximately 3 min) under alkaline conditions (15). Nitrite could be converted to nitrate by  $\text{H}_2\text{O}_2$  oxidation (15), but this procedure was cumbersome and was not always reliable.

This method of  $^{13}\text{NO}_3^-$  production does yield some  $^{18}\text{F}$  from the  $^{18}\text{O}(p,n)^{18}\text{F}$  reaction due to the natural abundance of 0.2%  $^{18}\text{O}$  in  $\text{H}_2\text{O}$  (15).  $^{18}\text{O}$  depleted water has been used (21) to reduce the  $^{18}\text{F}$  interference that can be severe after long counting periods. Since no  $^{18}\text{F}$  gases are formed, this contaminant was not a serious problem in denitrification studies.

$^{13}\text{NO}_3^-$  can also be obtained using the  $^{13}\text{C}(p,n)^{13}\text{N}$  reaction with a graphite target developed to produce  $^{13}\text{N}-\text{N}_2$  (22). The advantage of this reaction is that the yield of  $^{13}\text{N}$  is about 10-fold greater. However, the lengthy and complex process of conversion of the  $^{13}\text{N}$  to nitrate makes this reaction less attractive. We have also demonstrated the feasibility of producing  $^{13}\text{N}$  with heavy ion beams and have reported this separately in this volume (Chapter 15).

**Production of  $^{13}\text{NO}_3^-$  by  $^{12}\text{C}(d,n)^{13}\text{N}$  Reaction on a  $\text{LiCO}_3$  Target.** McNaughton and More (23) have produced up to 57  $\mu\text{Ci}$   $^{13}\text{NO}_3^-$  directly

by this reaction using a 2-MeV, 1–1.3- $\mu\text{A}$  deuteron beam from a Van de Graaff accelerator and bombarding a  $\text{LiCO}_3$  pellet for 20 min. They recovered the  $^{13}\text{NO}_3^-$  by mixing the ground pellet with 2.5 mL water and Amberlite 252 ion-exchanger resin in the hydrogen form. The  $\text{Li}^+$  was removed by the resin and the displaced  $\text{H}^+$  formed hydrogen carbonate. The  $\text{CO}_2$  was then driven off by heating. They found traces of  $^{18}\text{F}$ ,  $\text{C}^{13}\text{N}$  and  $^{13}\text{NO}_2^-$  in their product although at least 85% of the original  $^{13}\text{N}$  was in the nitrate form. This  $^{13}\text{NO}_3^-$  source was used by Stout (16) in his studies of soil denitrification.

Although the  $^{13}\text{NO}_3^-$  yields are 100-fold less with this system than with the  $^{16}\text{O}(\text{p},\alpha)^{13}\text{N}$  reaction, these workers have been able to perform denitrification experiments with the gas stripping system. Their success with low-energy accelerators to produce  $^{13}\text{N}$  should be encouraging to others interested in using this isotope, since these machines are more common.

**Production of Other  $^{13}\text{N}$  Species.** Each of the intermediates and products in dissimilatory nitrate reduction can be experimentally useful if labeled with  $^{13}\text{N}$ . Procedures for making each of these species are summarized in Table III. We have demonstrated each. The Cd reduction procedure to produce nitrite worked well when we used the Cd preparation procedure of McElfresh et al. (24). However, we used a small

**Table III. Methods for Production of  $^{13}\text{N}$  Inorganic Species Useful in Studies of Dissimilatory Nitrate Reduction**

<i>Desired <math>^{13}\text{N}</math> Species</i>	<i>Method</i>	<i>Total Elapsed Time (min)</i>
$^{13}\text{NO}_3^-$	Direct production by bombardment (13, 15, 23)	5
$^{13}\text{NO}_2^-$	Reduction of $\text{NO}_3^-$ to $\text{NO}_2^-$ on a copperized cadmium column (19, 24)	10
$^{13}\text{NO}$	Produced by biological reduction of $\text{NO}_2^-$ in the presence of $^{14}\text{NO}$ (see Table IV and Figure 7)	15
$^{13}\text{N}-\text{N}_2\text{O}$	Produced by biological reduction of $\text{NO}_3^-$ by denitrifier species incapable of further $\text{N}_2\text{O}$ reduction (4)	10
$^{13}\text{N}-\text{N}_2$	Produced by biological reduction of $\text{NO}_3^-$ using any active denitrifier species	10
$^{13}\text{N}-\text{N}_2$	Produced by sulfamic acid reduction of $\text{NO}_2^-$ (see section on detector calibration)	12
$^{13}\text{NH}_4^+$	Reduction of $\text{NO}_3^-$ with DeVarda's alloy and distillation to recover the $\text{NH}_4^+$	5

pencil-sized column and gravity flow.  $^{13}\text{NO}_2^-$  was usually the only species detected by R-HPLC if the source was in the column about 3 min and the effluent was treated by alkaline evaporation.

Biological methods are suggested for NO,  $\text{N}_2\text{O}$ , and  $\text{N}_2$  production, since they are the easiest for someone investigating denitrification as the organisms and procedures are standard. In addition, the biological process provides a high-purity, nontoxic product. Chemical methods usually require a much longer development and would be worthwhile only if extensive use of the product is expected. Both  $^{13}\text{NO}$  and  $^{13}\text{N}-\text{N}_2\text{O}$  are readily produced, as indicated in Figure 7. In this experiment, a low cell density was used to examine the kinetics of the reaction, but the density could easily be increased 10-fold or more to get a virtually immediate conversion to product. The  $^{13}\text{NO}$  method may be less useful because it yields a low specific activity product due to the sizeable  $^{14}\text{NO}$  addition.

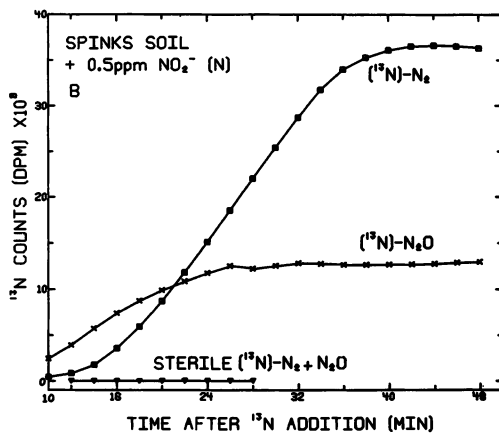
### *Measurement of Rates of Denitrification*

The gas stripping system has been the principal method for assay of denitrification rates by  $^{13}\text{N}$ , since one need only measure the rate of  $^{13}\text{N}$  gas accumulation from a sample in which the native nitrate pool has been amended with tracer quantities of  $^{13}\text{NO}_3^-$ . If the labeled nitrate is truly carrier-free, then the calculated labeled nitrate added is  $10^5$ - to  $10^7$ -fold less than the indigenous nitrate pool and thus will not alter the natural denitrification rate. An example of data obtained by the stripping system is shown in Figure 3. These rates were calculated for the linear portion of these curves by multiplying the  $\Delta d\text{pm}^{13}\text{N gas} \cdot \text{time}^{-1} \cdot \text{g soil}^{-1}$  by the specific activity of the nitrate ( $\mu\text{g NO}_3^- - \text{N present per total } ^{13}\text{NO}_3^- \text{ added}$ ), which is analogous to the equation shown below.

Gersberg et al. (13) first demonstrated the usefulness of this system by measuring denitrification rates using a rice-paddy sediment slurry. They obtained a linear pattern of N gas accumulation for the first 10 min after label addition. They calculated the natural denitrification rate using the following equation:

$$D = \left( \frac{dN}{dt} + \lambda N \right) \frac{^{14}\text{NO}_3^-}{^{13}\text{NO}_3^-}$$

where  $D$  is the rate at which gaseous nitrogen is evolved ( $\mu\text{g min}^{-1}$ );  $dN/dt$  is the rate of  $^{13}\text{N}$  gas accumulation ( $\mu\text{Ci} \cdot \text{min}^{-1}$ );  $N$  is the decay correction, which is the  $\mu\text{Ci}$  multiplied by  $\lambda$  ( $\lambda = 0.0693 \text{ min}^{-1}$ );  $^{13}\text{NO}_3^-$  is the activity of this species in the sample ( $\mu\text{Ci}$ ); and  $^{14}\text{NO}_3^-$  is the amount of unlabeled nitrate ( $\mu\text{g}$ ) in the sample. For rice soils, they obtained reproducible rates of  $1-6 \mu\text{g-N} \cdot \text{L}^{-1} \cdot \text{h}^{-1}$ .



Soil Science Society of America Journal

Figure 3. <sup>13</sup>N gases produced from soil incubated in gas stripping system after adding a mixture of 2.0 ppm <sup>14</sup>NO<sub>3</sub><sup>-</sup>-N (final concentration) and 3.7 mCi <sup>13</sup>NO<sub>3</sub><sup>-</sup>/<sup>13</sup>NO<sub>2</sub><sup>-</sup> (5 × 10<sup>-8</sup> ppm) to a soil slurry (15). Control of autoclaved soil shows no labeled gas was produced.

Gersberg (14) also used this system to help resolve why high concentrations of nitrate persisted in the oxygen-depleted bottom waters of Castle Lake. The denitrification rates he measured for the anaerobic water were only 0.003–0.05 μg-N · L<sup>-1</sup> · h<sup>-1</sup> compared with the sediment rates of 0.3–0.6 μg-N · L<sup>-1</sup> · h<sup>-1</sup>.

We used the stripping system (Figure 1) to obtain denitrification rates in soil slurries and in lake sediments. Slurries were used to obtain rapid mixing of <sup>13</sup>NO<sub>3</sub><sup>-</sup> with the sample and to facilitate efficient stripping of the product gases. This condition probably enhanced the rate of denitrification, especially for soils in which diffusion of nitrate and carbon to denitrifying organisms may have been rate-limiting due to the low moisture tension and the exclusion of oxygen by the helium stripping gas. Hence, we did not use the system to measure natural rates but to determine how various factors altered the rates and ratios of gas products produced. Denitrification rates that we observed ranged from 0.1–2 μg-N · g<sup>-1</sup> · h<sup>-1</sup> for different soils (25, 26). These rates are higher than those Gersberg (14) found for the aquatic environment although the values cannot be directly compared since the aquatic ones are on a volume basis (per liter) and the soil data are on a weight basis (per gram). Furthermore, the higher nitrate pool in soils should yield higher denitrification rates. One striking difference between soils and sediments is that the sediments show immediate <sup>13</sup>N gas production, often with total label conversion to product within 10 min; in soils, a 10–12 min lag is repeatedly observed before a linear rate of gas production is noted (15). We did notice that this lag was reduced when <sup>13</sup>NO<sub>2</sub><sup>-</sup> was used, possibly indicating a lag in the nitrate reductase activity in soils.

Stout and More (16) used natural soil cores amended with  $^{13}\text{NO}_3^-$  but no carrier in 2.5 mL water (*see pp. 303*) and a helium sweep gas to collect  $^{13}\text{N}$  gases emitted from the soil core surface. Cores were freshly collected, adjusted to desired moisture tension, and amended with denitrifying cultures or sterilized by  $^{60}\text{Co}$  irradiation or autoclaving. Autoclaved soil produced some  $^{13}\text{N}-\text{N}_2\text{O}$  but no  $^{13}\text{N}-\text{N}_2$ , whereas irradiated soil produced both gases. Addition of a denitrifying pseudomonad markedly increased the  $^{13}\text{N}-\text{N}_2$  produced by soil sterilized by both methods but generally reduced the amount of  $^{13}\text{N}-\text{N}_2\text{O}$  produced by the sterilized soil. The mechanism responsible for the  $^{13}\text{N}-\text{N}_2\text{O}$  produced in the sterilized soils is not known. We did not observe significant production of this gas in our sterilized soil slurries (Figure 3).

In the published report of Stout and More (16), positive rates of  $^{13}\text{N}-\text{N}_2$  gas production were not discernible from natural soils (without bacterial amendment) over the 30-min assay period. However, in later work Stout and Coleman were able to measure  $^{13}\text{N}-\text{N}_2$  and  $^{13}\text{N}-\text{N}_2\text{O}$  gas production from initially aerobic soil cores and were able to recover up to 50% of the  $^{13}\text{NO}_3^-$ -N as  $^{13}\text{N}$  gas in some cases (J. D. Stout and D. C. Coleman, poster at International Microbial Ecology Symposium, Warwick, England, 1980).

One of the advantages of the stripping system is that it is easy to measure rapid changes in rates of  $\text{N}_2\text{O}$  and  $\text{N}_2$  production in response to a change in environmental conditions. Figure 4 illustrates the effect of lowering the pH of a soil slurry from pH 6.7 to 5.2. The rate of  $\text{N}_2$  production decreased but total denitrification did not. Due to the immediate response, the effect is thought to be on the enzymes already functioning in this process rather than being an adaptive response to the pH change. Other studies on this same soil (26), show that this change

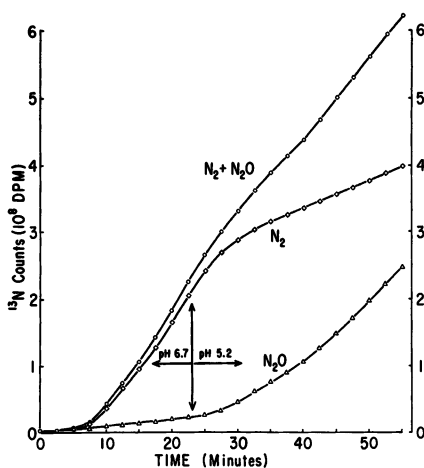


Figure 4. Pattern of  $^{13}\text{N}-\text{N}_2\text{O}$  and  $^{13}\text{N}-\text{N}_2$  production from a Brookston soil amended with  $^{13}\text{NO}_3^-$  plus 2 ppm  $\text{NO}_3^-$ -N carrier at its natural pH (6.7) and after lowering the pH with HCl to 5.2 at 23 min. Data obtained in the gas stripping system.

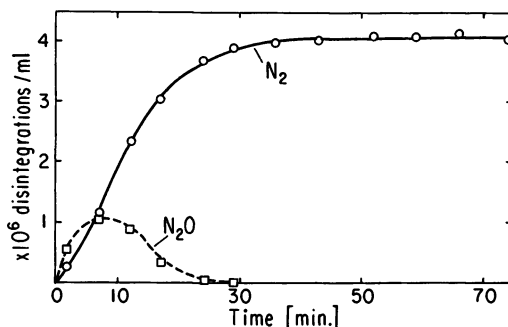


Figure 5. Pattern of <sup>13</sup>N—N<sub>2</sub>O and <sup>13</sup>N—N<sub>2</sub> production from anaerobic digester sludge amended with <sup>13</sup>NO<sub>3</sub><sup>-</sup> plus 10<sup>-4</sup> M NO<sub>3</sub><sup>-</sup> carrier and measured by GC-PC.

in N<sub>2</sub>O production was not due to time of incubation. This pH response was observed in the presence of modern nitrate concentrations (in this case, 2 ppm NO<sub>3</sub><sup>-</sup>—N) but not in the presence of low concentrations of nitrate (27).

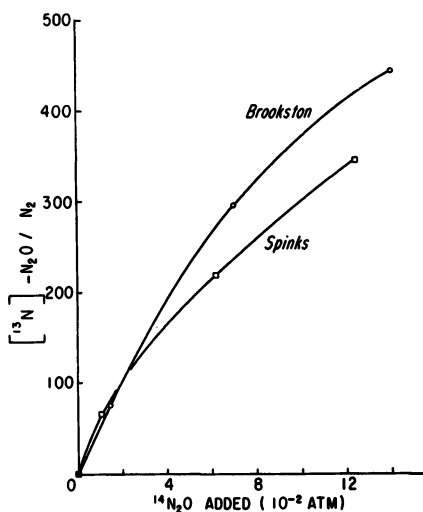
The above studies have all used the stripping system for measurement of denitrification rates. We have also obtained similar data using the GC-PC by repeated gas sampling of the incubation vessel. An example of results obtained by this method is shown in Figure 5. Here, 7 g of anaerobic digester sludge was incubated in a 26-mL serum bottle with <sup>13</sup>NO<sub>3</sub><sup>-</sup> and 10<sup>-4</sup>M NO<sub>3</sub><sup>-</sup> carrier at 22°C on a rotary shaker. Gas samples of 0.1 mL were taken by syringe and analyzed by GC-PC. A linear rate of N<sub>2</sub> production was noted. Initially, N<sub>2</sub>O production was more rapid, but this gas was eventually reduced to N<sub>2</sub>. No lag in <sup>13</sup>N gas production from the sludge was noted in contrast to the lags observed for the soils. (Rates and concentrations in soils literature are expressed as ppm, μg-N · g<sup>-1</sup> soil; for purposes of comparison 1 ppm is roughly equivalent to 80 μM NO<sub>3</sub><sup>-</sup>—N.)

#### **Intermediates of Denitrification: Isotope Dilution Experiments with <sup>13</sup>N**

**N<sub>2</sub>O.** Isotope dilution is a well-known principle used to determine intermediates in metabolic pathways. The suspected intermediate, which is unlabeled, is added to cells that are metabolizing a labeled substrate. If the compound is an intermediate, the subsequent reaction is saturated, causing the labeled material to pool with the added compound. The radioactivity of this pool should increase and that of the terminal product should decrease as the quantity of nonlabeled compound is increased. This method assumes that the intermediate is readily exchanged across the cytoplasmic membrane.

Soil Science Society  
of America Journal

Figure 6. Exchange of  $^{13}\text{N}-\text{N}_2\text{O}$  produced during denitrification of  $^{13}\text{NO}_3^-$  by addition of  $^{14}\text{N}_2\text{O}$  in two soils incubated as anaerobic slurries (26).



We used this principle and  $^{13}\text{NO}_3^-$  and  $^{13}\text{NO}_2^-$  to investigate whether  $\text{N}_2\text{O}$  and  $\text{NO}$  were intermediates in denitrification. The role of both compounds in denitrification has been a matter of controversy although the case for  $\text{N}_2\text{O}$  being an obligate intermediate has recently become much stronger since acetylene was shown to cause stoichiometric  $\text{N}_2\text{O}$  accumulation from nitrate (28, 29) and  $^{15}\text{N}_2\text{O}$  was shown to be trapped by adding  $^{14}\text{N}_2\text{O}$  to *Pseudomonas aeruginosa* cells denitrifying  $^{15}\text{NO}_2^-$  (2). Our studies using  $^{13}\text{NO}_3^-$  have extended the evidence supporting  $\text{N}_2\text{O}$  as an obligate intermediate. We found free exchange of labeled  $\text{N}_2\text{O}$  with added  $^{14}\text{N}_2\text{O}$  in three different denitrifying cultures fed  $^{13}\text{NO}_3^-$  (17). More important, however, we have shown that this exchange occurs with the natural, heterogeneous, denitrifying soil microflora (26). As shown in Figure 6, the ratio of  $^{13}\text{N}_2\text{O}$  to  $^{13}\text{N}_2$  was increased as the quantity of  $^{14}\text{N}_2\text{O}$  was increased.

This means that those organisms in soil active in denitrification have  $\text{N}_2\text{O}$  as a freely diffusable, obligate intermediate of denitrification. Since the cells did not seem to sequester pools of  $\text{N}_2\text{O}$ , factors that stimulate  $\text{N}_2\text{O}$  production or reduce  $\text{N}_2\text{O}$  reduction would be expected to cause an increase in the  $\text{N}_2\text{O}$  emitted from denitrifying cells. This interpretation helps explain why a number of factors affect  $\text{N}_2\text{O}$  production (see the section on factors affecting  $\text{N}_2\text{O}$  production).

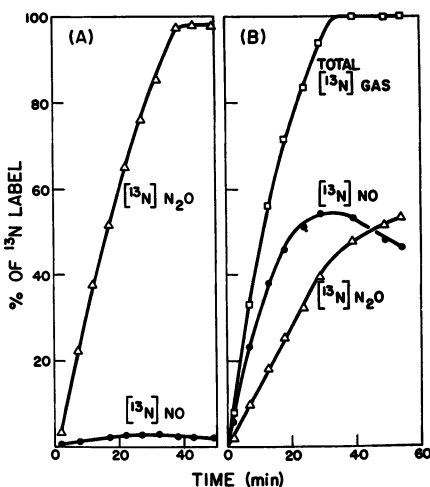
**NO.** The role of  $\text{NO}$  was also examined by the isotope dilution principle. This was technically more difficult than it was for  $\text{N}_2\text{O}$ , because  $\text{NO}$  is formed chemically from  $\text{NO}_2^-$ ,  $\text{NO}$  (a free radical) is very reactive and adsorbs to many materials, and  $\text{NO}$  (which would have to be added in higher concentrations to cells) binds to heme compounds and is toxic



to cells. Sterile controls showed that chemical production of NO was always present but occurred at a slower rate than did the biological production and exchange of NO (4, 17). A range of NO concentrations that caused exchange but was below the toxic level (4) was found. Other methods to analyze this reactive gas are reported under the section on  $^{13}\text{N}$  gas analysis.

Cultures of *Pseudomonas aureofaciens* and *P. chlororaphis* (neither of which reduced  $\text{N}_2\text{O}$  to  $\text{N}_2$ ) were exposed to  $^{13}\text{NO}_2^-$  and several concentrations of  $^{14}\text{NO}$  (4). Increasing  $^{13}\text{NO}$  was noted with increasing concentrations of  $^{14}\text{NO}$ . As shown in Figure 7,  $^{13}\text{NO}$  production occurred at the expense of  $\text{N}_2$  production and continued until  $^{13}\text{NO}_2^-$  was exhausted. At this time,  $^{13}\text{NO}$  consumption began and appeared to give rise to additional  $^{13}\text{N}-\text{N}_2\text{O}$ . We feel this data is evidence that either NO is an intermediate or is in rapid equilibrium with an enzyme-bound species.

We also carried out the isotope dilution experiment with NO on soil (17). Much more  $^{14}\text{NO}$  was added because it was expected that NO would be readily consumed in reactions with soil chemicals. Nonetheless, apparent NO exchange was noted as shown in Table IV. Most of the label was trapped as NO. The sterile controls showed an order of magnitude less gas produced. It was surprising, however, that there was not a trend of more NO with decreasing pH, especially in the sterile control. The data in Table IV seem to support the interpretation of the pure culture data, namely that NO or its enzyme-bound equilibrium species is an intermediate in denitrification.



Biochemical and Biophysical Research Communications

Figure 7.  $^{13}\text{N}$  gas produced by *Pseudomonas aureofaciens* from  $^{13}\text{NO}_2^-$  as influenced by the addition of  $^{14}\text{NO}$  (4): (A) received  $0.4 \times 10^{-3}$  atm NO and (B)  $7.2 \times 10^{-3}$  atm NO.

**Table IV. Apparent NO Exchange from Denitrification in an Anaerobically Incubated Brookston Soil Amended with a  $^{13}\text{NO}_3^-$  Source<sup>a</sup> and 0.12 atm  $^{14}\text{NO}$**

Time of Sample (Min)	Soil pH	$10^2$ Disintegrations <sup>b</sup>			Percent $^{13}\text{N}$ Gas as NO
		$^{13}\text{NO}$	$^{13}\text{N}-\text{N}_2\text{O}$	$^{13}\text{N}-\text{N}_2$	
Brookston <sup>c</sup>					
10	4.5	425	2.1	28.7	93.3
10	6.2	526	19.6	14.1	94.0
10	7.9	169	5.9	26.1	84.1
40	4.5	602	10.8	42.8	91.8
40	6.2	533	7.4	52.9	89.8
40	7.9	639	19.3	56.6	89.4
Autoclaved Brookston <sup>c,d</sup>					
30	4.5	40	0	2.3	94.7
30	6.2	40	0	2.2	95.0
30	7.9	67	0	2.5	96.4

<sup>a</sup>  $^{13}\text{N}$  substrate was predominantly  $^{13}\text{NO}_3^-$ , no carrier  $\text{NO}_3^-$  was added.

<sup>b</sup> Integrated over peak area. Standard deviations of peak area (17) were 1–3 for  $^{13}\text{NO}$  and 0.3–1 for the other two  $^{13}\text{N}$  gases.

<sup>c</sup> Nonautoclaved soil received 56.6  $\mu\text{Ci } ^{13}\text{N}$ ; autoclaved soil received 41.7  $\mu\text{Ci } ^{13}\text{N}$ . All soils received 0.12 atm of NO.

<sup>d</sup> Autoclaved for 30 min 8 h prior to experiment.

**Table V. Summary of Factors That Affect the Proportion of  $\text{N}_2\text{O}$  to  $\text{N}_2$  Produced in Denitrification**

Factor	Response on $\text{N}_2\text{O}/(\text{N}_2\text{O} + \text{N}_2)$	Reference
$\text{NO}_3^-$ concentration	Increasing $\text{NO}_3^-$ increases ratio	25, 26, 33
$\text{NO}_2^-$ concentration	Increasing $\text{NO}_2^-$ increases ratio	26
$\text{O}_2$ concentration	Increasing $\text{O}_2$ increases ratio in soils and most bacterial cultures	18, 26, 34
Length of anaerobic period	The ratio is initially low (0.2–0.4), then increases (0.4–0.9), and after one day drops to 0	31, 32
pH	Decreasing pH increases ratio when $\text{NO}_3^-$ concentrations are moderate or high	27, 34
Sulfide	Increasing sulfide increases ratio	19, 35
Eh	Redox potential changes below 0 mV do not affect ratio	19
Carbon	Increasing carbon decreases ratio	17, 34
Rhizosphere	No consistent effect on ratio	36
$\text{N}_2\text{O}$	Appears to induce synthesis of $\text{N}_2\text{O}$ reductase, which decreases ratio	32

In recent work Hollocher et al. (30) also used <sup>13</sup>N and isotope dilution to determine whether hyponitrite (O—N=N—O) was an intermediate in denitrification. Their results allowed them to conclude that hyponitrite was not a free intermediate.

### **Factors Affecting N<sub>2</sub>O Production**

As noted above, N<sub>2</sub>O is freely diffusable from cells and would be expected to be produced by cells when changes in reaction rates cause an increase in the N<sub>2</sub>O pool. We have examined a number of factors that affect N<sub>2</sub>O production by denitrifiers using <sup>13</sup>N and other methods. The <sup>13</sup>N approach was particularly useful in this investigation, since we were able to use low nitrate concentrations [since it is an effector (26)] and to measure immediate temporal responses [prior to de novo syntheses (31, 32)]; this allowed us to isolate both nitrate concentration and changing enzyme synthesis from the effect of the other factors being studied. Both the gas stripping system and the GC-PC analytical systems were used in these studies. The findings are summarized in Table V. Most factors examined favored N<sub>2</sub>O production over N<sub>2</sub> except for the length of the anaerobic period. When denitrifier cultures or soils were kept anaerobic, additional N<sub>2</sub>O reductase was synthesized, thus increasing the capacity to reduce N<sub>2</sub>O and causing the sample to cease net N<sub>2</sub>O production, and often to become a sink for N<sub>2</sub>O (32).

We did not extensively examine factors that might cause NO production, but during our study of the sulfide and Eh effects we noted that the former caused an increase in NO production, although this increase was much less than noted for N<sub>2</sub>O production (19). It is possible that there are other factors that will stimulate NO production, but this phenomenon is probably not common since NO would be expected to bind much more tightly to its enzyme site than would N<sub>2</sub>O.

### **Fates of Nitrate in Dissimilatory Reduction**

**Dissimilatory Reduction of Nitrate to Ammonium by Microbial Cultures.** We studied nitrate reduction to ammonia by an obligate anaerobe, *Clostridium*, which cannot gain energy from this reduction by electron transport phosphorylation, and by a number of Enterobacteriaceae (known to be nitrate respirers) that can gain energy via the nitrate to nitrite step. All these organisms converted <sup>13</sup>NO<sub>3</sub><sup>-</sup> to <sup>13</sup>NH<sub>4</sub><sup>+</sup> as the major reduced N product. A number of chemicals that are thought to regulate this reduction were added to resting cells of the *Clostridium* together with <sup>13</sup>NO<sub>3</sub><sup>-</sup> to determine their effect on the reduction (37). The only effective chemical was sulfite, which caused some <sup>13</sup>NO<sub>2</sub><sup>-</sup> to accumulate. Since sulfite and nitrite reductases show some reactivity

with the opposite substrate, it is suggested that the  $\text{SO}_3^-$  and  $\text{NO}_2^-$  were competing substrates and thus the reason for the nitrite accumulation (37).

The following nitrate respiring bacteria, which are generally thought to accumulate nitrite, were examined for their ability to reduce  $^{13}\text{NO}_3^-$  to  $\text{NH}_4^+$ : *Escherichia coli*, *Enterobacter*, *Serratia*, *Erwinia*, *Klebsiella*, and *Bacillus*. After a 20-min anaerobic incubation of resting cells of each of these cultures with  $^{13}\text{NO}_3^-$  plus  $10\mu\text{M}$  carrier  $\text{NO}_3^-$ , the R-HPLC analysis showed  $\text{NO}_3^-$  entirely consumed, no  $\text{NO}_2^-$  present, and  $\text{NH}_4^+$  as the only ion detected. Since all of the above cultures were grown in the presence of high concentrations of organic nitrogen and ammonium and readily reduced nitrate to ammonium under these conditions, it is concluded that the reduction is dissimilatory. This eight-electron reduction appears to serve as an electron sink for these organisms that otherwise would have difficulty disposing of the electrons generated during anaerobic metabolism.

**Dissimilatory Reduction of Nitrate to Ammonium in Natural Samples.** In natural samples that experience anaerobiosis, nitrate can have two dissimilatory fates—denitrification to N gas or reduction to ammonium. We examined the partitioning of nitrate among these fates by  $^{13}\text{N}$  and  $^{15}\text{N}$  techniques. These findings are being presented in detail elsewhere by Kaspar and Tiedje (38, 42). The results, however, can be generalized as follows. In a eutrophic lake sediment denitrification was the major fate of the added  $^{13}\text{NO}_3^-$ , whereas in anaerobic digester sludge dissimilatory reduction to ammonium accounted for about 70% of the consumed nitrate. In a bovine rumen (fed a grain ration), no denitrification was noted based on the absence of any detectable  $^{13}\text{N}-\text{N}_2$  (38);  $^{13}\text{N}-\text{N}_2\text{O}$  was detected but in quantities less than 1% of the consumed nitrate. In studies of this type, it is necessary to have the GC-PC, R-HPLC, and well counter (for the original source) accurately calibrated to account for the total label added and to obtain the rates of the conversion.

**$\text{N}_2\text{O}$  Production by Nondenitrifiers.** During the study of nitrate reduction to ammonia by nitrate-respiring organisms, we noted  $\text{N}_2\text{O}$  but not  $\text{N}_2$  production by all of the cultures listed above except *Clostridium*, which produced no gas. We saw no evidence of further consumption of the  $\text{N}_2\text{O}$ . Using  $^{13}\text{NO}_3^-$  as substrate, we evaluated the ratio of  $^{13}\text{N}-\text{N}_2\text{O}:^{13}\text{NH}_4^+$  produced as influenced by incubation conditions. The major effector was the addition of glucose, which reduced the ratio.

Our interpretation is that the  $\text{N}_2\text{O}$  does not arise from denitrification, since these cells are not classical denitrifiers but that it is a product that "leaks" off during the reduction of nitrite to ammonium. It has previously been noted that other nondenitrifying organisms, including

fungi, can produce some  $\text{N}_2\text{O}$  (39, 40). It is not known whether this is an important source of  $\text{N}_2\text{O}$  in nature, but it could be if the phenomenon is widespread among organisms with the  $\text{NO}_3^- \rightarrow \text{NH}_4^+$  pathway. In the study with the rumen contents in which denitrification was not observed, the  $\text{N}_2\text{O}$  produced was thought to have been produced by the dissimilatory ammonia-producing pathway (38), which is well known in rumen anaerobes.

### Summary

The major advantages of  $^{13}\text{N}$  for denitrification studies proved to be the direct measurement of  $\text{N}_2$  and the high sensitivity. Use of  $^{15}\text{N}$  in denitrification studies is limited by its natural abundance of 0.3663% and by the large sample size required, which makes certain types of experiments impossible. On the other hand, the short half-life of  $^{13}\text{N}$  limits the type of experimentation that can be done with this isotope. In the latter case, all data collection must be done within two to three hours from the time of bombardment. This means that the work must be done close to the accelerator, that the  $^{13}\text{N}$  substrate must be mixed rapidly with the sample, and that the subsequent analytical steps prior to detection must not be lengthy. Also, it is usually not technically feasible to analyze many replicates or treatments in an experimental period.

Our experience is that the  $^{13}\text{N}$  and  $^{15}\text{N}$  methods are complimentary rather than redundant. Each allows the investigator to investigate questions with a different class of analytical demands.

One of our original goals was to measure natural denitrification rates especially in soils using tracer  $^{13}\text{NO}_3^-$  additions to the natural nitrate pool. We achieved this with sediments and soil slurries, but the mixed condition does not reflect the natural case. Certainly in field soil the oxygen status and the diffusion rates of nitrate and carbon would be much different and would be expected to affect the denitrification rate. We have not yet attempted to measure denitrification rates with  $^{13}\text{N}$  in natural soil cores due to the perceived difficulty of getting  $^{13}\text{NO}_3^-$  distributed in a core before decay has destroyed the ability to measure  $\text{N}$  gas production. This may yet be possible to achieve, but simple designs will not suffice.

### Acknowledgments

We thank the many colleagues and assistants who have each played important roles in making our  $^{13}\text{N}$  experimentation successful. These are Sam Austin, Peter Miller, Peter Wolk, Jack Meeks, Karel Schubert, Wayne Bentley, Steve Farber, Scott Smith, Alan Sexstone, Bruce Bleakley,

Bill Caskey, Nancy Caskey, Linda McGahen, Joe Robinson, George Coker, Dan Shelton, Duane Berry, and Ami Horowitz. This is published journal article No. 9483 of the Michigan Agricultural Experiment Station. This work was supported by NSF grants DEB-77-19273, PHY-78-01684 and PHY-79-24017, and USDA Regional Research Project NE-39.

### Literature Cited

1. Payne, W. J. *Bacteriol. Rev.* 1973, 37, 409.
2. St. John, R. T.; Hollocher, T. C. *J. Biol. Chem.* 1977, 252, 212.
3. Zumft, W. G. *Naturwissenschaften* 1979, 66, 81.
4. Firestone, M. K.; Firestone, R. B.; Tiedje, J. M. *Biochem. Biophys. Res. Commun.* 1979, 91, 10.
5. Hauck, R. D. *Denitrification Seminar, Fertilizer Institute, Washington, D.C., 1977.*
6. Burns, R. C.; Hardy, R. W. F. "Nitrogen Fixation in Bacteria and Higher Plants"; Springer-Verlag: Berlin, 1975.
7. Pratt, P. F. *Climatic Change* 1977, 1, 109.
8. McElroy, M. B.; Wofsy, S. C.; Yung, Y. L. *Trans. R. Soc.* 1977, 227B, 159.
9. Crutzen, P. J.; Erhault, D. H. *Ambio* 1977, 6, 112.
10. Wang, W. C.; Yung, Y. L.; Lacin, A. A.; Mo, T.; Hanson, J. E. *Science* 1976, 194, 685.
11. Lijinsky, W. *New Scientist* 1977, 73, 216.
12. Francis, C. W.; Callahan, M. W. *J. Environ. Qual.* 1975, 4, 153.
13. Gersberg, R.; Krohn, K.; Peek, N.; Goldman, C. R. *Science* 1976, 192, 1229.
14. Gersberg, R. M., Ph.D. Thesis, Univ. of California, Davis, 1977.
15. Tiedje, J. M.; Firestone, R. B.; Firestone, M. K.; Betlach, M. R.; Smith, M. S.; Caskey, W. H. *Soil Sci. Soc. Am. J.* 1979, 43, 709.
16. Stout, J. D.; More, R. A. In "Biogeochemistry of Ancient and Modern Environments"; Trudinger, P. A.; Walter, M. R.; Ralph, B. J., Eds.; Springer-Verlag: Berlin, 1980; p. 293.
17. Firestone, M. K., Ph.D. Thesis, Michigan State Univ., 1978.
18. Betlach, M. R., Ph.D. Thesis, Michigan State Univ., 1979.
19. Sørensen, J.; Tiedje, J. M.; Firestone, R. B. *Appl. Environ. Microbiol.* 1980, 39, 105.
20. Tilbury, R. S.; Dahl, J. R. *Radiat. Res.* 1979, 79, 22.
21. Skokut, T.; Wolk, C. P.; Thomas, J.; Meeks, J. C.; Shaffer, P. W.; Chien, W.-S. *Plant Physiol.* 1978, 62, 299.
22. Austin, S. M.; Galonsky, A.; Bortins, J.; Wolk, C. P. *Nucl. Instrum. Methods* 1975, 126, 373.
23. McNaughton, G. S.; More, R. D. *Int. J. Appl. Radiat. Isotopes* 1979, 30, 489.
24. McElfresh, M. W.; Meeks, J. W.; Parks, N. J. *J. Radioanal. Chem.* 1979, 53, 345.
25. Smith, M. S.; Firestone, M. K.; Tiedje, J. M. *Soil Sci. Soc. Am. J.* 1978, 42, 611.
26. Firestone, M. K.; Smith, M. S.; Firestone, R. B.; Tiedje, J. M. *Soil Sci. Soc. Am. J.* 1979, 43, 1140.
27. Firestone, M. K.; Firestone, R. B.; Tiedje, J. M. *Science* 1980, 208, 749.
28. Balderston, W. L.; Sherr, B.; Payne, W. J. *Appl. Environ. Microbiol.* 1976, 31, 504.
29. Yoshinari, T.; Knowles, R. *Biochem. Biophys. Res. Commun.* 1976, 69, 705.

30. Hollocher, T. C.; Garber, E.; Cooper, A. J. L.; Reiman, R. E. *J. Biol. Chem.* 1980, 255, 5027.
31. Smith, M. S.; Tiedje, J. M. *Soil Biol. Biochem.* 1978, 11, 261.
32. Firestone, M. K.; Tiedje, J. M. *Appl. Environ. Microbiol.* 1979, 38, 673.
33. Blackmer, A. M.; Bremner, J. M. *Soil Biol. Biochem.* 1978, 10, 187.
34. Nommik, H. *Acta Agric. Scand.* 1956, 6, 195.
35. Tam, T.-Y.; Knowles, R. *Can. J. Microbiol.* 1979, 25, 1133.
36. Smith, M. S.; Tiedje, J. M. *Soil Sci. Soc. Am. J.* 1979, 43, 951.
37. Caskey, W. H.; Tiedje, J. M. *J. Gen. Microbiol.* 1980, 119, 217.
38. Kaspar, H. F.; Tiedje, J. M. *Appl. Environ. Microbiol.* 1981, 41, 705.
39. Yoshida, T.; Alexander, M. *Soil Sci. Soc. Am. Proc.* 1970, 34, 880.
40. Bollag, J.-M.; Tung, G. *Soil Biol. Biochem.* 1972, 4, 271.
41. Focht, D. D., personal communication.
42. Kaspar, H. F.; Tiedje, J. M.; Firestone, R. B. *Can. J. Microbiol.* 1981, in press.

RECEIVED September 4, 1980.

# Nitrogen and Carbon Assimilation in $N_2$ -Fixing Plants

## Short-Term Studies Using $^{13}N$ and $^{11}C$

KAREL R. SCHUBERT and GEORGE T. COKER, III

Department of Biochemistry, Michigan State University,  
East Lansing, MI 48824

*We review the results and interpretations of studies in which the short-lived radionuclides  $^{13}N$  and  $^{11}C$  have been used to examine nitrogen and carbon assimilation and metabolism in roots and nodules of  $N_2$ -fixing leguminous and actinorhizal plants. The labeling pattern after exposure of nodules of Glycine max (soybean) to  $[^{13}N]N_2$  was consistent with the pattern predicted for the assimilation of  $NH_4^+$  via the sequential reactions catalyzed by glutamine synthetase and glutamate synthase. In contrast, the labeling pattern after incubation of roots or nodules of G. max, Vigna unguiculata (cowpea), and Alnus glutinosa (European black alder) with  $^{13}NH_4^+$  was consistent with the assimilation of  $NH_4^+$ , at least in part, via glutamate dehydrogenase in parallel with glutamine synthetase. The reduced carbon compounds required for amino acid synthesis and energy-yielding metabolism associated with the processes of  $N_2$  fixation and  $NH_4^+$  assimilation were provided in part by carboxylation reactions occurring in the roots and nodules.*

Experts predict that the world population will double in the next 20 years (1). To feed this rapidly expanding population, world food production must more than double in the same time period (1). For this reason agricultural scientists are confronted with the task of increasing agricultural productivity.

Aside from water, the availability of an adequate supply of oxidized or reduced nitrogen is the major factor limiting plant growth (2). Consequently, the yield potential of agronomically important crop plants is

0065-2393/81/0197-0317\$05.75/0  
© 1981 American Chemical Society



intimately linked to the processes of nitrogen assimilation and partitioning. Normally plants take up nitrogen in the form of nitrate, which is reduced and assimilated in the roots and leaves. Certain leguminous and non-leguminous angiosperms, however, have the additional ability to form a symbiotic association with specific  $N_2$ -fixing microorganisms. These associations are capable of providing the total nitrogen requirements of the host plant. The ability of these plants to fix  $N_2$  has become increasingly more important as nitrogen fertilizer prices soar and reserves of fossil fuels necessary to produce these fertilizers dwindle.

Unfortunately, symbiotic  $N_2$  fixation is not without cost. The host plant must provide photosynthetically reduced carbon (photosynthate) to support the  $N_2$ -fixing and  $NH_4^+$ -assimilating activities within the nodule, the site of  $N_2$  fixation. In many cases, the photosynthate consumed to support these activities represents from 15–35% of the net photosynthate of the host (3). More than half this amount is utilized for the assimilation of  $NH_4^+$ . Because  $N_2$  fixation is limited by the availability of photosynthate and the amount of photosynthate required to support the assimilation of  $NH_4^+$  is substantial, it is essential to understand the pathways by which nitrogen is assimilated and transported to the host plant as well as the carbon metabolism associated with this process.

Biochemical investigations and tracer studies using the stable isotope  $^{15}N$  have been used to examine possible pathways for the primary assimilation of  $NH_4^+$  in the root nodules of  $N_2$ -fixing plants. The results of these investigations have not, however, been definitive. The use of  $^{13}N$ -labeled tracers has been invaluable in the efforts to substantiate the role of pathways that have been proposed. Similarly,  $^{11}C$  has been used successfully to probe the carbon metabolism associated with nitrogen assimilation in these systems. In this chapter we review the results of studies in which the short-lived radionuclides  $^{15}N$  and  $^{11}C$  have been used to examine nitrogen and carbon assimilation and metabolism in roots and nodules of leguminous and actinorhizal  $N_2$ -fixing plants.

### *An Overview of Nitrogen and Carbon Assimilation and Metabolism in Roots and Nodules of $N_2$ -Fixing Plants*

**Nitrogen Reduction and the Primary Assimilation of Ammonium.** In symbiotic  $N_2$ -fixing plants the reduction of  $N_2$  occurs within the microsymbiont, as shown diagrammatically in Figure 1. Bergersen and Turner (4) demonstrated that after detached soybean nodules were exposed to  $[^{15}N]N_2$  for 1 min, 90% of the  $^{15}N$  was in the form of  $NH_4^+$ . Kennedy (5) reported similar findings for pulse-labeling serradella nodules with  $[^{15}N]N_2$ . On the basis of these results, the authors concluded that the first stable product of  $N_2$  reduction is  $NH_4^+$ .

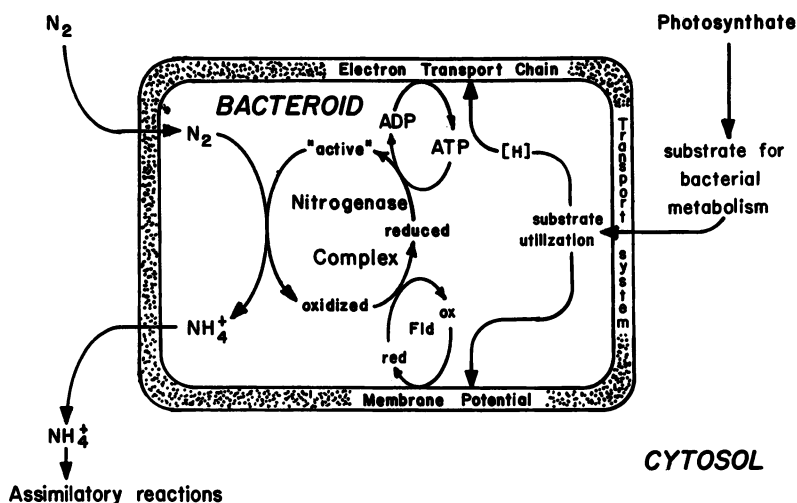
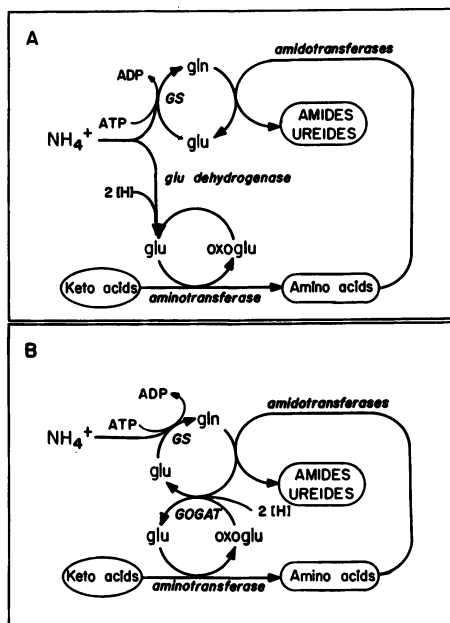


Figure 1. Schematic of the processes of dinitrogen reduction and  $NH_4^+$  assimilation within infected cells of legume nodules

There are conflicting reports, however, concerning the process of  $NH_4^+$  assimilation within the nodule. More recent reports indicate that the enzymes involved in  $NH_4^+$  assimilation within the endophyte are repressed while the levels of assimilatory enzymes are elevated in the plant cytosol (6, 7, 8). These observations have served as the basis for the proposal that the endophyte cannot utilize  $NH_4^+$  effectively and that  $NH_4^+$  is excreted into the cytosol of the host plant, where it is assimilated (Figure 1). This proposal is strengthened by the demonstration that  $N_2$ -fixing cultures of *Rhizobium* or isolated bacteroids (the symbiotic form of *Rhizobium*) do excrete  $NH_4^+$  under certain conditions (9, 10).

The assimilation of  $NH_4^+$  can occur via several mechanisms. The two major assimilatory pathways are presented in Figure 2. In the presence of high concentrations of  $NH_4^+$ , microorganisms assimilate  $NH_4^+$  via the concerted activities of glutamate dehydrogenase and glutamine synthetase. The two enzymes act in parallel to synthesize glutamate and glutamine, the amino- and amide-group donors that are required for the synthesis of other amino acids and nitrogenous components of living cells.

In early tracer studies in which the labeling of amino compounds was examined after detached soybean nodules were exposed to  $[^{15}N]N_2$  for 60 min, Aprison et al. (11) observed that glutamate was the most highly enriched amino acid. In seradella nodules, glutamate and glutamine were the first amino acids labeled after short exposures to  $[^{15}N]N_2$  (5). With longer incubations, aspartate, asparagine, alanine, and homo-



**Figure 2.** Diagram of the alternate pathways for the primary assimilation and metabolism of  $\text{NH}_4^+$  including general amino and amide transfer reactions. The top panel illustrates assimilation via glutamate dehydrogenase in parallel with glutamine synthetase. The lower panel presents the glutamine synthetase and glutamate synthase pathway.

serine were also labeled, although glutamate remained the most highly enriched compound (5). In similar studies with nodules of *Alnus glutinosa* (European black alder), Bond et al. (12) reported that  $^{15}\text{N}$  was incorporated primarily into glutamate and citrulline after incubation with  $^{15}\text{N}_2$ . In the absence of alternative possibilities and on the basis of these labeling studies and the presence of glutamate dehydrogenase activity in the cytosolic fraction of extracts prepared from nodules of certain legumes, many investigators concluded that the reductive amination of oxoglutarate catalyzed by glutamate dehydrogenase was the primary reaction responsible for the assimilation of  $\text{NH}_4^+$  in nodules.

The levels of glutamate dehydrogenase present in nodules of some legumes, however, are quite low (6,8). In addition, the glutamate dehydrogenases examined to date have low affinities for  $\text{NH}_4^+$  and, therefore, presumably do not function efficiently at the low concentrations of  $\text{NH}_4^+$  normally found in living organisms.

The discovery and characterization of glutamate synthase (GOGAT) activity in chemostat cultures of *Aerobacter aerogenes* grown under  $\text{NH}_4^+$ -limiting conditions led Tempest et al. (13) to propose that an alternate

pathway for  $\text{NH}_4^+$  assimilation, which could function at lower concentrations of  $\text{NH}_4^+$ , exists. In this pathway (Figure 2)  $\text{NH}_4^+$  is assimilated sequentially through the reactions catalyzed by glutamine synthetase and glutamate synthase.

The labeling studies described above, however, are not adequate to distinguish between these alternate mechanisms. Based on more recent enzymological evidence and on the results of inhibitor studies, Mifflin and Lea (14) proposed that the glutamine synthetase/glutamate synthase pathway is the primary route for the assimilation of  $\text{NH}_4^+$  by bacteria and plants. The primary role of this pathway in  $\text{NH}_4^+$  assimilation has been substantiated by Wolk and coworkers (15, 16, 17) for a variety of cyanobacteria using  $^{15}\text{N}$ -labeled tracers (see also Chapter 14 in this volume). Of the cyanobacteria examined, *Anacystis nidulans* was the only exception (16, 17). In this latter instance,  $\text{NH}_4^+$  is assimilated through the action of glutamate dehydrogenase in parallel with glutamine synthetase. Nitrogen assimilation has also been studied in cultured tobacco cells grown on  $\text{NO}_3^-$  or  $\text{NH}_4^+$ . Again the glutamine synthetase/glutamate synthase pathway was the major route of assimilation in cells incubated with  $^{15}\text{N}$ -labeled  $\text{NO}_3^-$  or  $\text{NH}_4^+$ , although a lesser activity of glutamate dehydrogenase was also indicated (18).

Meeks et al. (19) initiated similar studies to examine the pathway by which  $\text{NH}_4^+$  derived from  $\text{N}_2$  reduction is assimilated in soybean root nodules. We have continued and extended these investigations to include studies of  $^{15}\text{NH}_4^+$  and  $^{15}\text{NO}_3^-$  assimilation in roots and nodules of  $\text{N}_2$ -fixing leguminous and nonleguminous plants (20).

**Synthesis and Transport of Products of Ammonium Assimilation.** The initial products of  $\text{NH}_4^+$  assimilation, glutamate and glutamine, are required for the synthesis of other nitrogenous compounds needed for nodule metabolism or for export through the xylem to other plant tissues. Effectively nodulated legumes can be classified into amide-exporting or ureide-exporting species based on the predominant form of organic nitrogen being transported from the roots.

The former group includes many of the temperate legumes such as *Lupinus albus* (21), *Pisum sativum* (22), *Trifolium repens* (23), and *Vicia faba* (24). In this group asparagine and other amides such as glutamine or  $\gamma$ -methylene glutamine represent the major products of current  $\text{N}_2$  fixation that are exported from the root system. In contrast, the ureides, allantoin and allantoic acid, are the major products exported in the latter group. In this group, which includes many of the tropical species such as *Glycine max* (25, 26, 27), *Vigna unguiculata* (28, 29), *Psophocarpus tetragonolobus* (28), and *Phaseolus vulgaris* (30, 31), 80–99% of the recently fixed nitrogen is transported as allantoin and allantoic acid.

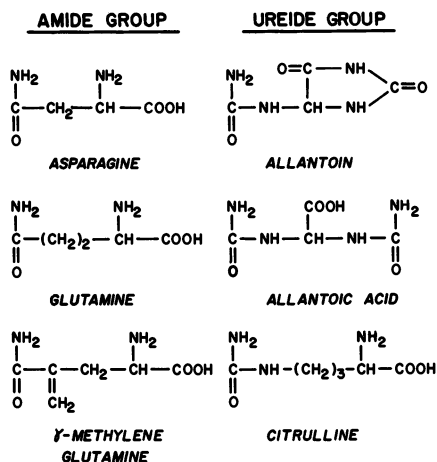


Figure 3. Structures of the major nitrogenous constituents of the xylem sap of  $N_2$ -fixing plants

A similar classification may be appropriate for  $N_2$ -fixing actinorhizal species. Asparagine is the major product of  $N_2$  fixation in *Myrica* species (32), whereas the ureide, citrulline, predominates in *Alnus* species (20, 33). The structures of the different nitrogenous components transported from  $N_2$ -fixing plants are given in Figure 3.

The composition of the xylem sap varies during the development of the plant and with changes in environmental conditions (25, 27, 28, 34, 35, 36). McNeil et al. (37) have presented evidence to suggest that the form of organic nitrogen transported from the root system may serve as the basis for the selective partitioning and utilization of products of nitrogen assimilation within various plant tissues. Thus, changes in the composition of the sap may reflect changes in the metabolic needs of the host plant.

The source of nitrogen utilized by the plant may also affect the composition of the xylem fluid. For instance, in ureide-exporting species such as *Glycine max* (soybeans) or *Vigna unguiculata* (cowpeas), the  $\text{NH}_4^+$  derived from the reduction of  $\text{N}_2$  is apparently used preferentially for the synthesis of ureides (29, 38). In contrast, the  $\text{NH}_4^+$  formed from the reduction of  $\text{NO}_3^-$  or supplied exogenously seems to be selectively incorporated into the amide, asparagine (25, 26, 28). McClure and Israel (39) have shown that the transport of ureides is negatively correlated with increasing concentrations of  $\text{NO}_3^-$ . The molecular mechanism for the selective incorporation of nitrogen from  $\text{N}_2$  or  $\text{NO}_3^-$  into ureides and amides, respectively, is not yet known.

**Carbon Assimilation and Metabolism in Roots and Nodules of  $N_2$ -Fixing Plants.** The assimilation of  $\text{NH}_4^+$  and the biosynthesis of nitrogenous metabolites require a continuous supply of reduced carbon com-

pounds to be used for carbon skeletons and energy sources for biosynthetic reactions. Much of this reduced carbon is derived from recent photosynthesis occurring in the leaves and is transported to nodulated roots in the form of sucrose (29, 40, 41). In addition, the roots and nodules of many  $N_2$ -fixing plants possess an active system for assimilating  $CO_2$ . In legume nodules the carboxylation of phosphoenolpyruvate (PEP) to form oxalacetate catalyzed by PEP carboxylase appears to be the primary reaction of  $CO_2$  fixation, although lesser activities of other carboxylases may be present within nodules (30, 35, 42, 43, 44). A number of investigators (30, 35, 41, 42, 43, 44) have suggested that  $CO_2$  fixation in these tissues may be directly linked to the synthesis of the carbon skeletons required for amino acid biosynthesis, in particular, asparagine biosynthesis. Roots and nodules of actinorhizal species also possess mechanisms for fixing  $CO_2$  (20, 45), although these systems have not been well characterized.

### Experimental

**Production of Labeled Tracers.** All labeled tracers were produced at the Michigan State University Heavy Ion Laboratory using a sector-focused cyclotron. Nitrogen-13 was generated by irradiation of a target for 10 min with a proton beam degraded to 12 MeV. The target consisted of either 18.6 mg of amorphous carbon, 97 atom % of  $^{13}C$  (Monsanto Research Corporation, Mound Laboratory, Miamisburg, Ohio), or 1 mL of  $H_2O$ . The basic methodology has been described in detail previously (46-49) and therefore will not be covered here. The general outline of procedures used for the production of  $N_2$ ,  $NO_3^-$ ,  $NO_2^-$  and  $NH_4^+$  is shown schematically in Figure 4 (see also Chapter 14 in this volume). The purity of preparations of  $^{13}NO_3^-$  and  $^{13}NH_4^+$  were checked for contamination using the high performance liquid chromatography (HPLC) system developed by Firestone et al. (49).

The short-lived isotope of carbon,  $^{14}C$  ( $t_{1/2} = 20$  min), was produced by bombarding pelleted  $B_2O_3$  with a 12-MeV proton beam with a current of  $1 \mu A$

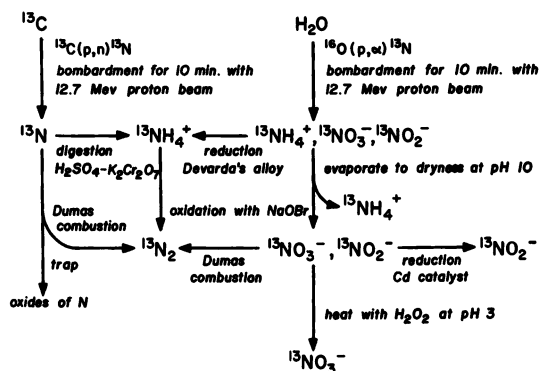


Figure 4. Diagram of the methods used in the production of  $^{13}N$ -labeled tracers

using the  $^{11}\text{B}(\text{p},\text{n})^{11}\text{C}$  nuclear reaction. Pellets of  $\text{B}_2\text{O}_3$  were formed by dipping the end of a heated glass rod (Pyrex) into a crucible containing  $\text{B}_2\text{O}_3$  that had been heated until glasslike. The coated tip of the rod was subsequently heated to the melting point of  $\text{B}_2\text{O}_3$  (approximately  $450^\circ\text{C}$ ) in a methane/oxygen flame. At this point droplets of molten  $\text{B}_2\text{O}_3$  formed and dropped on a cold sheet of aluminum, producing pellets approximately 0.5–1 cm in diameter. Pellets were placed between two layers of aluminum foil and positioned in the "rabbit" carrier used for  $^{13}\text{N}$  production (water target) (49). The rabbit was positioned in the beam line using the rapid retrieval pneumatic system and the target was irradiated.

After bombardment, the pellet was removed and placed in a 25-mL Erlenmeyer flask to which 2 mL of  $\text{H}_2\text{O}$  and a small magnetic stirring bar were added. The flask was sealed with a rubber serum stopper. Carrier (0.04 mL of 0.1M  $\text{NaHCO}_3$ ) was injected into the flask along with 0.1 mL of concentrated HCl. The solution was heated on a magnetic stirrer/hot plate to dissolve the pellet and to release the  $\text{CO}_2$ , which was removed by syringe. Using this technique 50–70% of the total radioactivity could be recovered.

**Exposure of Plants to Labeled Tracers.** Plant material was grown in the greenhouse unless otherwise noted and transferred to the cyclotron laboratory facility prior to conducting experiments. Detached nodules or segments of nodulated roots of intact plants were exposed to  $[^{13}\text{N}]\text{N}_2$  in 1- or 3-mL reaction chambers (19), respectively. Vials were briefly evacuated before  $[^{13}\text{N}]\text{N}_2$  (approximately 0.02 mL at 1 atm) was transferred to the sealed vials using a Toepler pump. The pressure within the vial was adjusted to atmospheric pressure with a mixture of argon/oxygen/carbon dioxide (80:19:1, v/v/v). The reaction was terminated by evacuation or by flushing of the vial to remove  $[^{13}\text{N}]\text{N}_2$  and extraction of the tissue with 80% methanol (v/v). To examine the assimilation of  $\text{NO}_3^-$  or  $\text{NH}_4^+$ , the root systems of intact nodulated or unnodulated plants were trimmed of excess roots, placed into a glass tube to which a solution containing  $^{13}\text{NH}_4^+$  or  $^{13}\text{NO}_3^-$  was added, and incubated. Detached nodules were dipped into a carrier-free solution of the labeled compound and incubated.

Nodulated roots of intact plants were exposed to  $^{11}\text{CO}_2$  or  $^{14}\text{CO}_2$  in the following manner. Plants were gently removed from their pots and shaken to remove excess Perlite. A split rubber stopper was placed around the stem of the plant, and the root system was placed into a 20- or 50-mL flask. Plasticine was used to seal around the stems of the plants. Gases were added or withdrawn by syringe through a serum stopper covering a sidearm of the smaller flasks or a glass tube through a second hole in the rubber stopper of the larger flasks.  $^{14}\text{CO}_2$  was liberated in a sealed vial from  $[^{14}\text{C}]\text{NaHCO}_3$  (Amersham Searle, 59.3 mCi/mmol) according to the procedures described previously (35).

Nodule, root, or stem tissue was extracted by grinding with 1 mL of 80% methanol in a mortar and pestle. Acid-washed sand was added to assist in the grinding of root and stem tissue of soybean and cowpea plants. Nodules and roots from *Alnus* seedlings were frozen in liquid  $\text{N}_2$  to stop further reaction and to facilitate the extraction process. The frozen tissue was subsequently ground and then extracted with 1 mL of 80% methanol.

The extracted material was washed into a 15-mL conical centrifuge tube with an additional 1 mL of 80% methanol. The extract was clarified by centrifugation at  $20,000 \times g$  for 1 min and the supernatant fluid was transferred to another 15-mL tube. The residual material was normally reextracted with 1 mL of 80% methanol, the extract clarified by centrifugation, and the supernatant liquid added to that from the first extraction. The combined

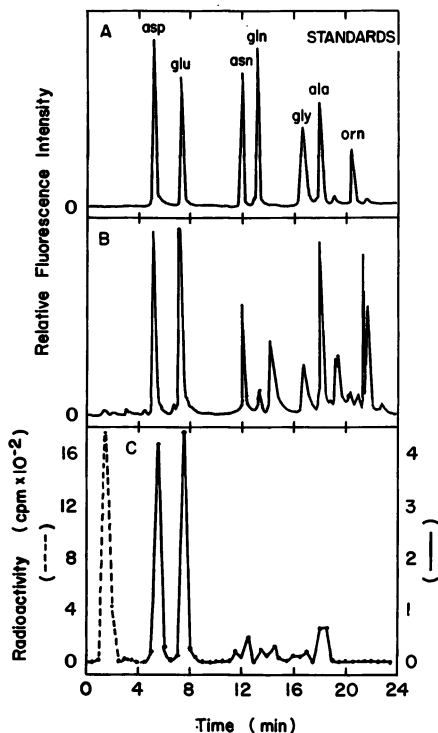
extracts were evaporated to dryness at 50°C in vacuo. The dried material was redissolved in 0.2 mL of 80% methanol and redried. Finally, the dried material was redissolved in 0.1 mL of 80% methanol to which a mixture of standard unlabeled amino acids was added.

Labeled products were analyzed using the procedures described by Meeks et al. (19). Samples were spotted on cellulose thin-layer plates (Brinkman, 0.1-mm thickness of coating) and subjected to high voltage electrophoresis at 3 kV for 8–12 min. The buffer system used was 70mM sodium borate, pH 9.2 (19). Radioactively labeled compounds were localized and quantified by one-dimensional scanning using a gas-flow counter (Berthold). The identity of the radioactive bands was based on comigration with standard amino acids that were detected by reaction with ninhydrin. For experiments in which plants were exposed to  $^{13}\text{NH}_4^+$  and  $^{14}\text{CO}_2$ , radioactivity from  $^{13}\text{N}$  incorporation was measured by covering the thin-layer plate with aluminum foil to mask the  $^{14}\text{C}$  counts during scanning. After the  $^{13}\text{N}$  had decayed, the foil was removed and the plate was rescanned to detect  $^{14}\text{C}$ -labeled compounds.

**Development of a HPLC System for Rapid Analysis of Labeled Compounds.** The electrophoretic procedures used in these studies to identify and quantify labeled products have a number of disadvantages. Many of the amino acids are not completely resolved after electrophoresis. These include aspartate/glutamate and glutamine/alanine/citrulline. To resolve these amino acids from one another, a second chromatographic step and two-dimensional scanning of the plates is required, which adds significantly to the analysis time. Excluding a preliminary chromatographic step to remove lipids, the separation by high voltage electrophoresis and quantification of the labeled products takes 25–40 min. A limited amount of material can be applied to the thin-layer plates, which decreases the detection limit. This is especially important for detecting minor components. Finally, the counting efficiency of the gas-flow counter is less than that possible using other techniques and requires additional time to integrate the peaks.

Therefore, we have been developing an HPLC separation suitable for rapid analysis of labeled compounds. Cooper et al. (50) reported the separation of  $^{13}\text{N}$ -labeled compounds including ammonium, glutamine, glutamate, and aspartate by HPLC using an anion-exchange column. The time required for separation was between 20–30 min, and derivatization was not necessary. This procedure offers the advantage that amino acids can be collected in an underivatized form and used for additional studies. Peaks did have a tendency to trail with this procedure. We have adapted the procedures used by Hill et al. (51) for identification of radiolabeled amino acids. Amino acids were derivatized with *o*-phthalaldehyde for 1 min and separated by reverse phase chromatography on an Ultrasphere column (Beckman Instruments Company) using gradient elution with acetonitrile as described by Hill et al. (51). Elution conditions were modified slightly to improve resolution of certain amino acids (Figure 5). Derivatized amino acids were detected using an Aminco fluorometer. Fractions from the column (0.5–1.0 mL each) were collected using an LKB fraction collector, and radioactivity was measured by scintillation counting (although a flow-cell counting chamber could be utilized to reduce analysis time). The entire separation takes 18–25 min, depending upon whether detection of the basic amino acids and  $\text{NH}_4^+$  is necessary. The advantages of the technique include high resolution, high sensitivity, rapid analysis, and a measurement of the specific activity of the labeled compounds. The major disadvantage of this procedure is that labeled compounds are of no further use for metabolic studies.





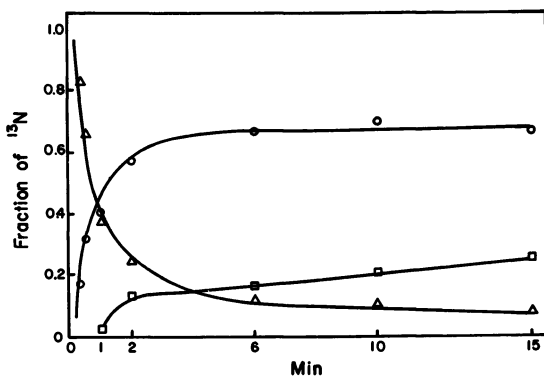
*Figure 5. Separation of amino acids derivatized with o-phthaldialdehyde (OPA) by reverse-phase chromatography. Extracts of nodules were derivatized according to the procedures described by Hill et al. (51), except the final volume was reduced from 5 mL to 0.5 mL or less and the concentrations of OPA and ethanethiol in the derivatizing solution were increased to 60 mg/mL and 0.1 mg/mL, respectively. A sample volume of 20  $\mu$ L was injected on column and the derivatized amino acids were eluted with an increasing gradient of acetonitrile from 12% to 100%.*

## Results and Discussion

**Assimilation of Recently Fixed Nitrogen in Soybean Nodules.** Meeks et al. (19) demonstrated that the initial organic product labeled after exposure of detached soybean nodules to  $[^{15}\text{N}]\text{N}_2$  was glutamine. After 20 s of fixation of  $[^{15}\text{N}]\text{N}_2$  by detached nodules, 82% of the detectable radioactivity was in the form of glutamine with lesser amounts in glutamate (Figure 6). The percent of total label incorporated into glutamine decreased to approximately 11% by 15 min, whereas the percent  $^{15}\text{N}$  in glutamate increased to about 65% by 6 min and then remained approximately constant. The only other organic compound labeled was alanine, which continued to accumulate over the 15-min

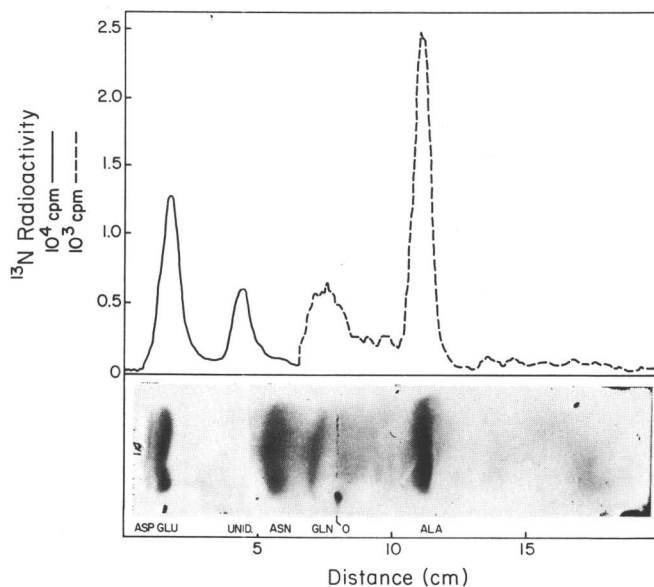
period examined. When extracts of nodules exposed to  $[^{13}\text{N}]\text{N}_2$  for 15 min were subjected to vacuum distillation at pH 10, approximately 5% of the  $^{13}\text{N}$  distilled as amide nitrogen and 6% of the remaining label still electrophoresed with glutamine. These results support the conclusion that  $\text{NH}_4^+$  derived from the reduction of  $\text{N}_2$  in soybean nodules is assimilated via the combined activities of glutamine synthetase and glutamate synthase.

Similar results were obtained when nodules attached to roots of young soybean seedlings were exposed to  $[^{13}\text{N}]\text{N}_2$  for 6 or 15 min (19). Under the conditions used in these studies, the transfer of  $^{13}\text{N}$ -labeled compounds from nodules to other plant parts was not appreciable. Even after a 15-min incubation, only 10% of the  $^{13}\text{N}$  in the organic fraction was detected in stems and leaves of soybean seedlings (19). Asparagine, the predominant amino acid in the xylem exudate and nodule bleeding sap (26, 27) of soybeans, was not labeled significantly within 15 min. There are a number of possible explanations for the failure to observe labeling of asparagine or other nitrogenous compounds and the transport of the labeled compounds to the roots, stems, and leaves. The presence of asparaginase in the extracts is possible, although there is no evidence to support breakdown of exogenously added  $^{14}\text{C}$ -asparagine during extraction (19, 20). The conditions under which nodulated roots were exposed to  $[^{13}\text{N}]\text{N}_2$  were not conducive to  $\text{N}_2$  reduction. The amount of  $[^{13}\text{N}]$  added to the reaction vial (approximately 0.02 mL) resulted in a concentration of  $\text{N}_2$  far below the Michaelis constant ( $K_m$ ) for  $\text{N}_2$ . Mague



Plant Physiology

Figure 6. Time course of distribution of  $^{13}\text{N}$  in amino acids extracted from detached soybean nodules exposed to  $[^{13}\text{N}]\text{N}_2$  (19). The radioactivity was quantified by integration of peaks from radioscan with corrections applied for decay. Values presented are means, from two or three experiments, of the fraction of organic  $^{13}\text{N}$  migrating with stable ( $\Delta$ ) glutamine, ( $\circ$ ) glutamate, and ( $\square$ ) alanine.



Plant Physiology

**Figure 7.** Scan of radioactivity from  $^{13}\text{N}$  in an electrophoretogram of organic compounds extracted from a soybean nodule with 1.5 mL 80% methanol after 6 min of fixation of  $^{13}\text{N}$ -labeled  $\text{N}_2$  by a seedling (19).

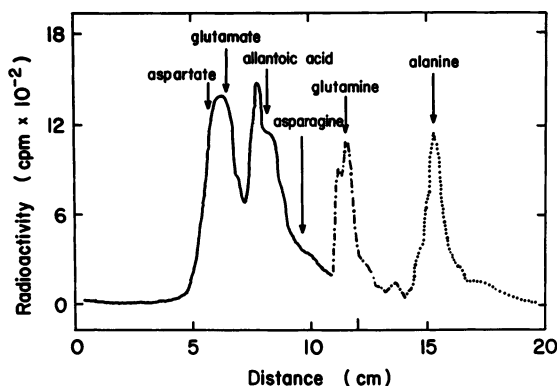
The extract, supplemented with stable aspartate, glutamate, asparagine, glutamine, and alanine as markers, was applied to a cellulose thin-layer plate in a thin strip (origin = 0). After displacement of lipids from the origin by chromatography (19), the extract was subjected to electrophoresis at 3 kV for 11 min in 70mM sodium borate buffer (pH 9.2). The plate was scanned at 2 cm/min ( $\tau = 3$  s) from + (at left) to - and was then dried and sprayed with a solution of ninhydrin to localize the marker amino acids. The  $^{13}\text{N}$ -containing substances detected, which migrated with glutamate, an unidentified compound (unid.), glutamine, and alanine during electrophoresis, were present in a ratio (time-corrected) of 1.00:0.44:0.06:0.19. Less than 3% of the radioactivity was attributable to asparagine.

and Burris (52) reported that the  $K_m$  for soybean nodules was between 0.1–0.15 atm or higher. Under the conditions used (19), the predominant activity of nitrogenase is the ATP-dependent production of hydrogen gas, which may build up in the vial and thereby further inhibit  $\text{N}_2$  reduction (53). The oxygen supply within the vial is limited, and the normal rates of nodule and root respiration measured under similar conditions are high enough to have depleted the available  $\text{O}_2$  significantly. The reduction of the  $p\text{O}_2$  has dramatic effects on  $\text{N}_2$  fixation and the associated processes of  $\text{NH}_4^+$  assimilation as well as on amino acid and ureide biosynthesis. This may be important in these studies, especially during the longer incubations. Because of the biological variability in the  $\text{N}_2$ -fixing capacity of nodules, Meeks et al. (19) determined the  $\text{C}_2\text{H}_2$ -reducing activity of

nodules prior to incubation with  $[^{13}\text{N}]\text{N}_2$ . Although the concentrations of  $\text{C}_2\text{H}_2$  used (0.006%, v/v) were very low and nodules were subjected to evacuation to remove  $\text{C}_2\text{H}_2$ , the results of other experiments suggest that prior exposure to  $\text{C}_2\text{H}_2$  may alter the distribution of amino acids synthesized in nodules (54). Furthermore, evacuation of plant tissues may cause cellular damage as well as disrupt the flow of assimilates from and to nodules and roots (55). Based on more recent experiments, the low incorporation of  $^{13}\text{N}$  into asparagine is consistent with other results that suggest that  $\text{NH}_4^+$  derived from  $\text{N}_2$  may be selectively incorporated into ureides.

The only major difference in labeling observed between detached and attached nodules was the labeling of an unidentified compound in attached nodules (19). This compound migrated between glutamate and asparagine during electrophoresis and accounted for about 30% of the total radioactivity (Figure 7). Meeks et al. (19) suggested that the transfer of a substrate or cofactor from roots might be required for the synthesis of this compound. In subsequent experiments we demonstrated that the unidentified compound was also labeled in detached soybean nodules exposed to  $[^{13}\text{N}]\text{N}_2$  (54). The labeling of this compound in both attached and detached nodules has not been observed consistently, however, which has complicated attempts to identify the compound.

In more recent experiments in which the unidentified compound has been detected, it has coelectrophoresed with the ureide, allantoic acid (Figure 8). Allantoin, which is a precursor of allantoic acid in the purine degradation pathway of ureide synthesis, was not labeled significantly.



**Figure 8.** Scan of radioactivity in an extract of detached soybean nodules exposed to  $[^{13}\text{N}]\text{N}_2$  for 10 min. The products of  $[^{13}\text{N}]\text{N}_2$  fixation were separated and identified by high-voltage electrophoresis. The  $^{13}\text{N}$ -labeled compounds include materials migrating with stable glutamine, glutamate, aspartate, alanine, asparagine, and allantoic acid.

Unfortunately, allantoin breaks down to form allantoic acid under basic conditions such as those used for electrophoresis, and allantoin was not well separated from glutamine and other amino acids using this procedure. For these reasons, it has not been possible to ascertain whether allantoin was labeled, and, therefore, to distinguish between the two proposed pathways for ureide biosynthesis.

The first of these pathways, which has received little experimental support, involves the condensation of 2 mol of urea with 1 mol of a two-carbon compound such as glyoxylate or glycine to form allantoic acid (56). The second and most probable pathway involves the oxidative catabolism of purines (Figure 9). Recent evidence from both biochemical and tracer studies supports the latter pathway (36, 57, 58, 59). Although purines are apparently synthesized *de novo* and then degraded (36, 59), the details of the purine biosynthetic pathway in these tissues have not been elucidated. Recent labeling studies suggest that ImP, the end product of the conventional purine biosynthetic pathway, may not be a direct precursor for the synthesis of ureides in soybean nodules (60). The use of  $^{15}\text{N}$ -labeled tracers along with better analytical procedures provides a potential technique for definitively characterizing the pathway of purine biosynthesis, including the final product of the pathway, and for determining the exact sequence of reactions leading to the production of ureides.

**Assimilation of  $^{15}\text{NH}_4^+$  by Roots and Nodules of *Alnus glutinosa*.** The labeling of nitrogenous compounds in roots and nodules of *A. glutinosa* incubated with  $^{15}\text{NH}_4^+$  has been examined (20). After 30 s of exposure, glutamine and glutamate accounted for 92% and 8% of the total radioactivity in detached nodules. Although the total radioactivity incorporated increased with time, the relative distribution of radioactivity

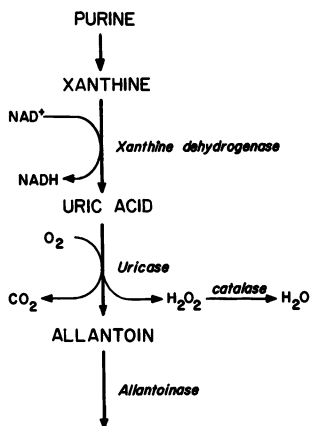


Figure 9. Reactions of purine catabolism implicated in the synthesis of ureides

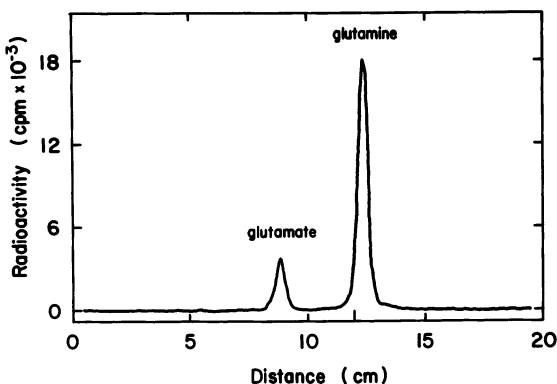


Figure 10. Analysis of labeled products after incubation of nodulated roots of intact *A. glutinosa* plants to  $^{13}\text{NH}_4^+$  for 2.5 min. Nodules were removed and extracted with 80% methanol, and a sample of the extract was subjected to high-voltage electrophoresis. The positions of migration of markers are noted with arrows.

changed little, with [ $^{13}\text{N}$ ]glutamine representing 79% of the total radioactivity after 15 min. Over 90% of the  $^{13}\text{N}$  incorporated into glutamine was still in the amide position after incubation for 14 min. Similar results were obtained using intact seedlings (Figure 10) with less than 8% of the  $^{13}\text{N}$  in the form of other compounds normally present in the xylem exudate or nodule extracts (i.e., citrulline, alanine, aspartate, and asparagine) (20).

The relationship between the incorporation of  $^{13}\text{N}$  into glutamine and glutamate was examined in pulse-labeling experiments and inhibitor studies. In pulse-chase experiments, approximately 70% of the radioactivity migrated with stable glutamine after incubation of nodulated roots with  $^{13}\text{NH}_4^+$  for 5 min followed by a 3-min wash to remove labeled  $\text{NH}_4^+$  and incubation for 10 min with 10mM  $\text{NH}_4\text{OH}$  (20). Azaserine, which inhibits glutamate synthase and other amide-transfer reactions, did not affect the labeling of glutamate significantly, whereas methionine sulfoximine, an irreversible inhibitor of glutamine synthetase, increased the distribution of  $^{13}\text{N}$  in glutamate, aspartate, alanine, and citrulline by a factor of 3–4 (20).

The labeling pattern observed after exposure of nodules and/or roots of *A. glutinosa* to low concentrations of  $^{13}\text{NH}_4^+$  was distinctly different from the pattern observed after exposure of *Anabaena cylindrica* to [ $^{13}\text{N}$ ] $\text{N}_2$  or  $^{13}\text{NH}_4^+$  (16, 17, 47) and was somewhat similar to results reported for cultured tobacco cells incubated with  $^{13}\text{NH}_4^+$  (18). Radioactivity apparently was incorporated independently into the amide position of glutamine and to a lesser extent into glutamate. These results

and the results of inhibitor studies are consistent with those predicted for the assimilation of low concentrations of  $\text{NH}_4^+$  via the reactions catalyzed by glutamine synthetase and glutamate dehydrogenase. Additional studies are necessary to substantiate this possibility and to establish the intracellular site of  $\text{NH}_4^+$  assimilation. Furthermore, these results must be compared to those obtained after exposure to  $[\text{^{13}N}]\text{N}_2$ .

**Assimilation of  $^{13}\text{NH}_4^+$  or  $^{13}\text{NO}_3^-$  by Soybean or Cowpea Roots and Nodules.** Because of the apparent differences between the pattern of incorporation of  $^{13}\text{NH}_4^+$  by *Alnus* and the pattern observed after exposure of soybean nodules to  $[\text{^{13}N}]\text{N}_2$ , the pattern of assimilation of  $^{13}\text{NH}_4^+$  by soybean roots and nodules was examined. As noted in studies with *Alnus*, the distribution of radioactivity after exposure of intact nodulated roots to  $^{13}\text{NH}_4^+$  was distinctly different from the labeling pattern after exposure to  $[\text{^{13}N}]\text{N}_2$ . Glutamine was the most highly labeled amino acid at all times examined with lesser amounts of radioactivity present in glutamate, aspartate, and alanine (20). Similar findings were obtained in studies with roots except the percentage of  $^{13}\text{N}$  in the glutamine peak was even higher (Figure 11). The results after exposure of nodulated roots of cowpea (*V. unguiculata*) plants to  $^{13}\text{NH}_4^+$  were similar with the exception that the compound tentatively identified as allantoic acid was also labeled in this case.

Nitrogen-fixing plants are also capable of reducing  $\text{NO}_3^-$  in the roots and/or leaves of the plant. In soybeans, there is evidence to suggest that reduction may occur in both roots and leaves (26). There has been difficulty, however, in detecting nitrite reductase activity in soybean root or nodule tissue (61). Using  $^{13}\text{NO}_3^-$ , we have demonstrated that both tissues actively assimilate  $^{13}\text{NO}_3^-$  and incorporate  $^{13}\text{N}$  into organic compounds (54). The distribution of label between glutamine and glutamate was similar to that after treatment with  $^{13}\text{NH}_4^+$  and some radioactivity migrated with unlabeled asparagine during electrophoresis. The highest incorporation into asparagine was in root tissue of plants grown in the presence of  $\text{NO}_3^-$ . These findings are consistent with the results of other studies (62), which suggest that root tissue may be the primary site of asparagine synthesis and that  $\text{NH}_4^+$  derived from the reduction of  $\text{NO}_3^-$  may be selectively incorporated into asparagine.

In contrast to the results of studies with  $[\text{^{13}N}]\text{N}_2$ , there was a distinctly different pattern of labeling after incorporation of  $^{13}\text{NH}_4^+$  or  $^{13}\text{NO}_3^-$ . The pattern observed was not the same as the pattern predicted if the assimilation of  $\text{NH}_4^+$  occurred via the reactions catalyzed by glutamine synthetase and glutamate synthase. The results suggest that  $\text{NH}_4^+$  is being assimilated, at least in part, by glutamate dehydrogenase.

Compartmentalization of some of the enzymes involved in the assimilation of  $\text{NH}_4^+$  may provide one possible explanation for the apparent differences in the observed labeling patterns after exposure to different

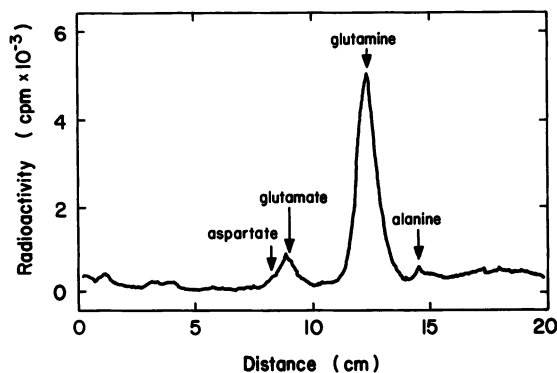


Figure 11. Scan of radioactivity from an extract of detached soybean roots exposed to  $^{13}\text{NH}_4^+$  for 15 min. The extract was subjected to electrophoresis and analysis as described previously (19, 20). The positions of unlabeled amino acid standards are noted.

sources of nitrogen. The compartmentalization of enzymes and metabolites within plant cells including nodule cells has been documented (59, 63, 64). Alternatively, it is possible that  $^{13}\text{NH}_4^+$  or  $^{13}\text{NO}_3^-$  were assimilated only in the outer layers of cells, which may not have an active glutamate synthase. If the latter case is true, the cells are metabolically active since  $^{13}\text{N}$ -labeled compounds were transported from roots or nodules exposed to  $^{13}\text{N}$ -tracers to stem tissue. Compartmentalization may offer certain advantages, such as the ability to maintain the concentrations of metabolites. This may be especially significant in the case of the assimilation of  $\text{NH}_4^+$  via glutamate dehydrogenase, which reportedly has a low affinity for  $\text{NH}_4^+$ .

**Carbon Assimilation in Roots and Nodules: The Role of Dark  $\text{CO}_2$  Fixation.** A number of investigators (30, 35, 41, 42, 43) have proposed that dark  $\text{CO}_2$  fixation, which occurs in roots and nodules of many  $\text{N}_2$ -fixing plants, may play a key role in the synthesis of carbon skeletons for  $\text{NH}_4^+$  assimilation. We have examined the products of  $\text{CO}_2$  fixation in roots and nodules of soybeans, cowpeas, and alters (35, 54, 62, 65, 66).

Plant tissues were incubated with  $^{11}\text{CO}_2$  for varying lengths of time. The initial products of  $^{11}\text{CO}_2$  fixation in soybean nodules were organic acids (primarily malate), which accounted for 83% of the total radioactivity after 2 min of exposure and declined to 61% after 12 min. Aspartate and glutamate were labeled subsequently with lesser amounts of radioactivity associated with alanine, glutamine, and asparagine (Figure 12). Similar results were obtained using cowpea nodules or roots. These observations are consistent with the conclusion that the assimilation of  $\text{CO}_2$  is catalyzed by PEP carboxylase. One interpretation to explain the labeling of glutamate, glutamine, and alanine is that malate is in



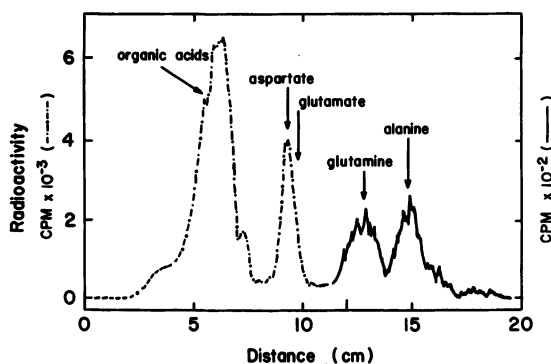


Figure 12. Initial products of  $^{11}\text{CO}_2$  fixation after incubation of a nodulated root system of soybeans with  $^{11}\text{CO}_2$  for 4 min. Labeled products were quantified after high-voltage electrophoresis on thin-layer plates (pH 9.2). The compounds containing  $^{11}\text{C}$  include organic acids, aspartate, glutamate, glutamine, and alanine.

equilibrium with malate within the mitochondria and therefore could be converted into the other tricarboxylic acid cycle intermediates used for the synthesis of these amino acids. If so, these compounds could also be oxidized in energy-yielding reactions. This interpretation is supported by a number of lines of evidence including measurements of respiratory efflux from nodules of recently fixed  $\text{CO}_2$  and results of pulse-chase experiments (35).

One must consider the possibility that recently fixed  $\text{CO}_2$  is reoxidized when estimating rates of  $\text{CO}_2$  fixation in nodulated roots. For instance, in support of their hypothesis that  $\text{N}_2$  fixation and  $\text{CO}_2$  fixation are directly linked, Christeller et al. (43) have reported that  $\text{C}_2\text{H}_2$ , an inhibitor of  $\text{N}_2$  fixation, reduced the rate of  $\text{CO}_2$  fixation in detached lupin nodules. In their analysis, the possibility of reoxidation of fixed  $\text{CO}_2$  was not considered. The experimental procedures used did not distinguish between true inhibition of  $\text{CO}_2$  fixation and an apparent decrease in the rate of fixation as a result of increased reoxidation of fixed  $\text{CO}_2$  in the absence of a demand for carbon skeletons for  $\text{NH}_4^+$  assimilation. To test these two alternatives in soybeans, attached nodules were exposed to  $^{11}\text{CO}_2$  for 2 min, flushed with air, transferred to a new flask, and incubated for an additional 5 min with  $^{14}\text{CO}_2$  in the presence or absence of 10% (v/v)  $\text{C}_2\text{H}_2$  (35). A representative sample of nodules was removed after labeling with  $^{11}\text{C}$ ; the remaining nodules were removed at the end of the treatment with  $^{14}\text{CO}_2$ . The amount of  $^{11}\text{CO}_2$  and  $^{14}\text{CO}_2$  fixed were measured for each sample. In contrast to the results obtained by Christeller et al. (43),  $\text{C}_2\text{H}_2$  had no significant effect on the rates of  $\text{CO}_2$  fixation or on the rates of respiration of recently fixed  $^{11}\text{CO}_2$ . The

rates of  $^{11}\text{CO}_2$  fixation and  $^{14}\text{CO}_2$  fixation were experimentally the same with and without the addition of  $\text{C}_2\text{H}_2$ , and the ratio of  $^{11}\text{C}$  radioactivity per mg nodule fresh weight at the second sampling to that of the first sampling for the control and  $\text{C}_2\text{H}_2$ -treated samples were  $1.12 \pm 0.08$  and  $1.09 \pm 0.12$ , respectively, for eight experiments (35).

To evaluate the relative significance of  $\text{CO}_2$  fixation in the formation of the carbon skeletons for the biosynthesis of different amino acids, nodulated roots of intact plants were simultaneously exposed to  $^{13}\text{NH}_4^+$  and  $^{14}\text{CO}_2$  for 10 min. The results of one such experiment with nodulated cowpea roots are shown in Figure 13. Excluding organic acids, radioactivity from  $^{14}\text{CO}_2$  was preferentially incorporated into aspartate. (Note that glutamate and aspartate are not completely separated by this procedure.) Relatively little  $^{14}\text{C}$  was associated with glutamine. Asparagine and allantoic acid were labeled also. In contrast, glutamine was the predominant  $^{13}\text{N}$ -labeled metabolite. Allantoic acid, glutamate, alanine and aspartate were labeled to some extent. Although not conclusive, these observations strengthen the proposal that  $\text{CO}_2$  fixation in legume nodules supplies oxalacetate for the biosynthesis of aspartate and asparagine.

In addition, the organic acids that are formed may be utilized in energy-yielding reactions within the plant or bacterial cells or as counterions for cation transport (35).

Citrulline as well as organic acids, aspartate, glutamate, alanine, and glutamine were labeled after exposure of nodules of *A. glutinosa* to  $^{14}\text{CO}_2$  for 10 min. Approximately 35% of the total radioactivity was in citrulline. These findings suggest that both PEP carboxylase and carbamyl phos-

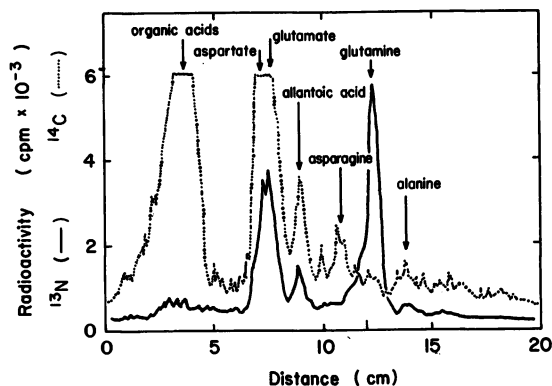


Figure 13. Analysis of labeled products after exposure of attached cowpea nodules to  $^{13}\text{NH}_4^+$  and  $^{14}\text{CO}_2$  for 10 min. Radioactivity from  $^{13}\text{N}$  (—) was measured by covering the plate with aluminum foil to mask the  $^{14}\text{C}$  radioactivity (---), which was measured after the  $^{13}\text{N}$  had decayed. The proposed identification of the products of incorporation of  $^{13}\text{N}$  and  $^{14}\text{C}$  are indicated.

phate synthetase are active in these tissues. Additional experiments are in progress to determine the pathway of citrulline biosynthesis in alder nodules (66).

### Summary

The short-lived radionuclide,  $^{13}\text{N}$ , has been extremely useful in studies of  $\text{N}_2$  fixation and  $\text{NH}_4^+$  assimilation. Wolk and his collaborators have demonstrated that the glutamine synthetase/glutamate synthase pathway is the major assimilatory route for  $\text{NH}_4^+$  in  $\text{N}_2$ -fixing cultures of *Anabaena* and many other cyanobacteria. They have extended these studies to show that the labeling pattern observed after exposure of detached or attached soybean root nodules to  $^{13}\text{N}]\text{N}_2$  was similar to that observed in *Anabaena*. On this basis Meeks et al. (19) concluded that the primary pathway for assimilating  $\text{NH}_4^+$  derived from  $\text{N}_2$  in soybean nodules involves the sequential assimilatory activities of glutamine synthetase and glutamate synthase.

To circumvent some of the technical difficulties encountered in the use of  $^{13}\text{N}]\text{N}_2$ , we have used  $^{13}\text{NH}_4^+$  to continue these investigations of nitrogen assimilation in  $\text{N}_2$ -fixing plants. In direct contrast to the results of studies using  $^{13}\text{N}]\text{N}_2$ , the distribution of radioactivity in organic compounds after incubation of nodules or roots of soybeans, cowpeas, or alders with  $^{13}\text{NH}_4^+$  was distinctly different from the "typical" pattern observed with *Anabaena*. The interpretation presented (20, 67) to explain these observations is that  $\text{NH}_4^+$  supplied exogenously to roots and nodules of these plants is assimilated, at least in part, by glutamate dehydrogenase.

An examination of the biosynthetic route for the synthesis of carbon skeletons necessary for  $\text{NH}_4^+$  assimilation has been conducted. Results of initial studies reviewed here support the conclusion that the fixation of  $\text{CO}_2$ , catalyzed primarily by PEP carboxylase in the roots and nodules of  $\text{N}_2$ -fixing legumes, plays a key role in the synthesis of carbon skeletons. Estimates of the rates of  $\text{CO}_2$  fixation, however, exceed the estimated rates of  $\text{NH}_4^+$  assimilation. Tracer studies using  $^{14}\text{CO}_2$  and/or  $^{13}\text{CO}_2$  indicate that a large portion of the recently fixed carbon is re respired or rapidly transported out of nodules (35, 54). These findings support specific roles for  $\text{CO}_2$  fixation including the synthesis of carbon skeletons for amino acid biosynthesis, for energy-yielding substrates for respiratory activities within the nodule, and for counterions for cation transport.

The concepts that are emerging with respect to the pathways of nitrogen and carbon assimilation in soybean roots and nodules are summarized in Figure 14. The scheme that is shown is based in part on the tracer studies using short-lived isotopes reported here along with published and unpublished observations. The figure is intended to present

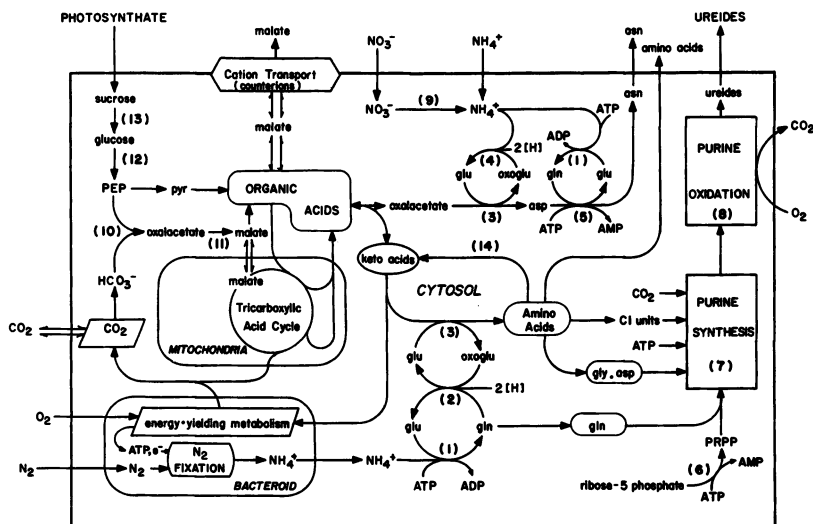


Figure 14. Summary of the proposed reactions and interrelationships of nitrogen and carbon assimilation in soybean roots and nodules.

The major reactions involved, listed by numbers in parentheses, are catalyzed by: (1) glutamine synthetase, (2) glutamate synthase, (3) amino transferase, (4) glutamate dehydrogenase, (5) asparagine synthetase, (6) phosphoribosylpyrophosphate (PRPP) synthetase, (7) enzymes of purine biosynthesis, (8) enzymes of purine oxidation, (9) nitrate and nitrite reductase, (10) phosphoenolpyruvate (PEP) carboxylase, (11) malate dehydrogenase, (12) glycolytic enzymes, (13) invertase, and (14) amino acid deaminases.

an integrated view of results and ideas concerning the interrelationships between carbon and nitrogen metabolism in roots and nodules of  $N_2$ -fixing plants.

### Acknowledgments

This research was supported by grants to K.R.S. from the National Science Foundation (Grant No. PCM 79-24683) and the USDA/SEA Competitive Research Grants Office (Grant No. 5901-0410-9-0248-0). G.T.C. was supported in part by a National Science Foundation National Needs Training Grant. This is publication number 9473 of the Michigan Agricultural Experiment Station. We would like to acknowledge the assistance of Mr. Joe Robinson in the development of some of the methodology used in the production of  $^{11}CO_2$  and the many helpful discussions that we have had with Dr. C. Peter Wolk and Dr. James Tiedje. In addition, we would like to thank Ms. Gay DeShone for her technical assistance and her dedication and willingness to work through the night during cyclotron experiments and to Ms. Julie Doll for her diligence in typing this manuscript.

*Literature Cited*

1. Wortman, S. *Sci. Am.* 1976, 235, 31-39.
2. Date, R. A. *Soil Biol. Biochem.* 1973, 5, 5-18.
3. Schubert, K. R.; Ryle, G. J. A. In "Advances in Legume Science"; Summerfield, R. J.; Bunting, A. H., Eds.; Royal Botanic Gardens: Kew, England, 1980; pp. 85-96.
4. Bergersen, F. J.; Turner, G. L. *Biochim. Biophys. Acta* 1967, 141, 507-515.
5. Kennedy, I. R. *Biochim. Biophys. Acta* 1966, 130, 285-294.
6. Brown, C. M.; Dilworth, M. J. *J. Gen. Microbiol.* 1975, 86, 39-48.
7. O'Gara, F.; Shanmugam, K. T. *Biochim. Biophys. Acta.* 1976, 451, 342-352.
8. Boland, M. J.; Fordyce, A. M.; Greenwood, R. M. *Aust. J. Plant Physiol.* 1978, 5, 553-559.
9. O'Gara, F.; Shanmugam, K. T. *Biochim. Biophys. Acta* 1976, 437, 313-321.
10. Laane, C.; Krone, W.; Konings, W.; Haaker, H.; Veeger, C. *Eur. J. Biochem.* 1980, 103, 39-46.
11. Aprison, M. H.; Magee, W. E.; Burriss, R. H. *J. Biol. Chem.* 1954, 208, 29-39.
12. Bond, G.; Gardner, I.; Leaf, G. *Biochem. J.* 1958, 69, 3P.
13. Tempest, D. W.; Meers, J. L.; Brown, C. M. *Biochem. J.* 1970, 117, 405-407.
14. Miffin, B. J.; Lea, P. J. *Phytochemistry* 1976, 15, 873-855.
15. Thomas, J.; Meeks, J. C.; Wolk, C. P.; Shaffer, P. W.; Austin, S. M.; Chien, W.-S. *J. Bacteriol.* 1977, 129, 1545-1555.
16. Wolk, C. P.; Thomas, J.; Shaffer, P. W.; Austin, S. M.; Chien, W.-S. *J. Biol. Chem.* 1976, 251, 5027-5034.
17. Meeks, J. C.; Wolk, C. P.; Lockau, W.; Schilling, N.; Shaffer, P. W.; Chien, W.-S. *J. Bacteriol.* 1978, 134, 125-130.
18. Skokut, T. A.; Wolk, C. P.; Thomas, J. T.; Meeks, J. C.; Shaffer, P. W.; Chien, W.-S. *Plant Physiol.* 1978, 62, 299-304.
19. Meeks, J. C.; Wolk, C. P.; Schilling, N.; Shaffer, P. W.; Avissar, Y.; Chien, W.-S. *Plant Physiol.* 1978, 61, 980-983.
20. Schubert, K. R.; Coker, G. T., III; Firestone, R. B. *Plant Physiol.* 1981, 67, 662-665.
21. Pate, J. S.; Atkins, C. A.; Hamel, K.; McNeil, D. L.; Layzell, D. B. *Plant Physiol.* 1979, 63, 1082-1088.
22. Gunning, B. E. S.; Pate, T. S.; Minchin, F. R.; Marks, I. *Symp. Soc. Exp. Biol.* 1974, 28, 87-126.
23. Copeland, R.; Pate, J. S. *White Clover Res.* 1970, 6, 71-77.
24. Pate, J. S.; Gunning, B. E. S.; Briarty, L. G. *Planta* 1969, 85, 11-34.
25. Matsumoto, T.; Yatazawa, M.; Yamamoto, Y. *Plant Cell Physiol.* 1977, 18, 613-624.
26. McClure, P. R.; Israel, D. W. *Plant Physiol.* 1979, 64, 411-416.
27. Streeter, J. G. *Plant Physiol.* 1979, 63, 478-480.
28. Pate, J. S.; Atkins, C. A.; White, S. T.; Rainbird, R. M.; Woo, K. C. *Plant Physiol.* 1980, 65, 961-965.
29. Herridge, D. F.; Atkins, C. A.; Pate, J. S.; Rainbird, R. M. *Plant Physiol.* 1978, 62, 495-498.
30. Cookson, C.; Hughes, H.; Coombs, J. *Planta* 1980, 148, 338-345.
31. Pate, J. S. *Soil Biol. Biochem.* 1973, 5, 109-119.
32. Leaf, G.; Gardner, I. C.; Bond, G. *Biochem. J.* 1959, 72, 662-667.
33. Leaf, G.; Gardner, I. C.; Bond, G. *J. Exp. Bot.* 1958, 9, 320-331.
34. Fujihara, S.; Yamamoto, K.; Yamaguchi, M. *Plant Soil* 1977, 48, 233-242.
35. Coker, G. T., III; Schubert, K. R. *Plant Physiol.* 1981, 67, 691-696.
36. Schubert, K. R. *Plant Physiol.*, in press.

37. McNeil, D. L.; Atkins, C. A.; Pate, J. S. *Plant Physiol.* 1979, 63, 1076–1081.
38. Matsumoto, T.; Yatazawa, M.; Yamamoto, Y. *Plant Cell Physiol.* 1977, 18, 459–462.
39. McClure, P. R.; Israel, D. W.; Wolk, R. J. *Plant Physiol.* 1980, 66, 720–725.
40. Lawrie, A. C.; Wheeler, C. T. *New Phytol.* 1975, 74, 429–436.
41. Rawsthorne, S.; Minchin, F. R.; Summerfield, R. J.; Cookson, C.; Coombs, J. *Phytochemistry* 1980, 19, 341–355.
42. Lawrie, A. C.; Wheeler, C. T. *New Phytol.* 1975, 74, 437–445.
43. Christeller, J. T.; Laing, W. A.; Sutton, W. D. *Plant Physiol.* 1977, 60, 47–50.
44. Atkins, C. A.; Pate, J. S.; Layzell, D. B. *Plant Physiol.* 1979, 64, 1078–1082.
45. Gardner, I. C.; Leaf, G. *Plant Physiol.* 1960, 35, 948–950.
46. Austin, S. M.; Galonsky, A.; Bortins, J.; Wolk, C. P. *Nucl. Instrum. Methods* 1975, 126, 373–379.
47. Meeks, J. C.; Wolk, C. P.; Thomas, J.; Lockau, W.; Shaffer, P. W.; Austin, S. M.; Chien, W.-S.; Galonsky, A. *J. Biol. Chem.* 1977, 252, 7894–4900.
48. McElfresh, M. W.; Meeks, J. C.; Parks, N. J. *J. Radioanal. Chem.* 1979, 53, 337–344.
49. Tiedje, J. M.; Firestone, R. B.; Firestone, M. K.; Betlach, M. R.; Smith, M. S.; Caskey, W. H. *Soil Sci. Soc. Am. J.* 1979, 43, 709–716.
50. Cooper, A. J. L.; McDonald, J. M.; Gelbard, A. S.; Gledhill, R. F.; Duffy, T. S. *J. Biol. Chem.* 1979, 254, 4982–4992.
51. Hill, D. W.; Walters, F. H.; Wilson, T. D.; Stuart, J. D. *Anal. Chem.* 1979, 51, 1338–1341.
52. Mague, T. H.; Burris, R. H. *New Phytol.* 1972, 71, 275–286.
53. Schubert, K. R.; Evans, H. J. In "Recent Developments in Nitrogen Fixation"; Newton, W.; Postgate, J. R.; Rodriguez-Barrueco, C., Eds.; Academic: London, 1977; 469–485.
54. Schubert, K. R.; Coker, G.; Firestone, R. B. *Am. Chem. Soc. Symp. Short-Lived Radioisot. Washington, D.C., Sept. 1979.*
55. Pate, J. S., unpublished data.
56. Reinbothe, H.; Mothes, K. *Ann. Rev. Plant Physiol.* 1962, 13, 129–150.
57. Atkins, C. A.; Rainbird, R. M.; Pate, J. S. *Z. Pflanzenphysiol.* 97, 249–260.
58. Triplett, E. W.; Blevins, D. G.; Randall, D. D. *Plant Physiol.* 1980, 65, 1203–1206.
59. Schubert, K. R.; DeShone, G. M. *Plant Physiol.* 1980, 65S, 614.
60. Boland, M.; Schubert, K. R., unpublished data.
61. Randall, D. D.; Russell, W. J.; Johnson, D. R. *Physiol. Plant.* 1978, 44, 325–328.
62. Coker, G. T., III; Schubert, K. R. *Plant Physiol.* 1980, 65S, 610.
63. Mitchell, D. J.; Bidwell, R. G. S. *Can. J. Bot.* 1970, 48, 2001–2007.
64. Hanks, J. F.; Tolbert, N. E.; Schubert, K. R. *Plant Physiol.*, in press.
65. Schubert, K. R.; DeShone, G. M.; Polayls, D. A.; Hanks, J. F. In "Current Perspectives of Nitrogen Fixation"; Gibson, A. H.; Newton, W. E., Eds.; Australian Academy of Sciences: Canberra, Australia, in press.
66. Schubert, K. R.; Tierney, M.; Christensen, A.; McClure, P.; Coker, G. In "Current Perspectives of Nitrogen Fixation"; Gibson, A. H.; Newton, W. E., Eds.; Australian Academy of Sciences: Canberra, Australia, in press.
67. Schubert, K. R. In "Current Perspectives of Nitrogen Fixation"; Gibson, A. H.; Newton, W. E., Eds.; Australian Academy of Sciences: Canberra, Australia, in press.

RECEIVED September 4, 1980.

# Use of $^{13}\text{N}$ -Nitrate to Study Nitrate Transport in *Klebsiella pneumoniae*

J. R. THAYER and R. C. HUFFAKER

Plant Growth Laboratory, and Department of Agronomy and Range Science, University of California, Davis, CA 95616

*Radiolabeled nitrate produced by the proton bombardment of water was purified by high-pressure liquid chromatography (HPLC) over anion exchange media and then used to determine the initial rates of nitrate uptake and nitrite excretion in Klebsiella pneumoniae. Nitrite was transiently excreted when aerobically grown cells were challenged with nitrate. Labeled nitrogen was lost when cells were subjected to vacuum filtration, so an alternative method of separating cells from the radioactive medium, by sedimentation through silicone oil, was adapted. This permitted us to analyze by HPLC the methanolic extracts of the cells after exposure to radiolabeled nitrate, confirming that  $\text{NO}_3^-$  was indeed the compound transported. Initial rate data indicated the presence of at least one and perhaps two nitrate transport systems.*

The goal of our study is to understand the steps involved in the conversion of  $\text{NO}_3^-$  to  $\text{NH}_4^+$  in soil bacteria. Since transport is the first step in this process, results are presented describing  $\text{NO}_3^-$  transport.

The organism chosen for study is *Klebsiella pneumoniae*, a soil and enteric bacterium capable of anaerobic nitrogen fixation, which harbors two  $\text{NO}_3^-$  reductase systems. An assimilatory system is synthesized under conditions of nitrogen starvation (1), when  $\text{NO}_3^-$  alone or when  $\text{NO}_3^-$  and  $\text{N}_2$  gas are present as the sole sources of nitrogen (2). The presence of  $\text{NO}_3^-$  under conditions in which nitrogen fixation may occur represses the synthesis of nitrogenase, apparently through the presence of the second nitrate reductase system, which permits  $\text{NO}_3^-$  to replace oxygen

0065-2393/81/0197-0341\$05.00/0  
© 1981 American Chemical Society

as the terminal electron acceptor in the electron transport chain (2). In that case, the oxidation-reduction potential of the cell is altered such that a nitrogenase redox control fails to permit its synthesis. Under anaerobic or semianaerobic conditions the respiratory nitrate reductase system (RNR) is expressed, allowing a respiratory, rather than a less efficient fermentative, metabolism to occur. The activity of the RNR is one or more orders of magnitude greater than that of the assimilatory nitrate reductase (ANR) and, as a consequence, high levels of nitrite are produced and excreted into the medium. The respiratory system is inactivated by oxygen, so it is present only when the cellular oxygen tension is low (1).

The assimilatory system is inactivated by pure oxygen but not by air, and it may be present under either aerobic or anaerobic conditions, where it can coexist with the RNR (1).

Controversy exists regarding the site of  $\text{NO}_3^-$  reduction in enteric and denitrifying bacteria. The RNR clearly resides in the cell membrane, as preparations of lysed cells, cleared of cytoplasmic constituents, produce  $\text{NO}_2^-$  when incubated with a suitable electron donor under anaerobic conditions (1). Thus,  $\text{NO}_3^-$  may be reduced on either the inside or outside of the cell membrane. Garland and others have presented evidence that  $\text{NO}_3^-$  is reduced on the outside of the cell membrane, which results in proton translocation and release of  $\text{NO}_2^-$  back into the medium (3, 4, 5). Kristajansson et al. have evidence that  $\text{NO}_3^-$  may be transported and hence reduced inside the cells (6) and that the site of proton translocation need not be the RNR itself (7).  $\text{NO}_2^-$  is toxic to bacteria, so the internal reduction of  $\text{NO}_3^-$  must not exceed the reduction of  $\text{NO}_2^-$  or  $\text{NO}_2^-$  will accumulate inside the cells. If  $\text{NO}_3^-$  reduction is internal, a  $\text{NO}_2^-$  export system must be present under anaerobic conditions (since  $\text{NO}_2^-$  appears in the medium when the cells are grown in the presence of  $\text{NO}_3^-$ ). The demonstration that  $\text{NO}_3^-$  transport occurs would have a significant impact on the status of this controversy in addition to further elucidating the process of nitrate assimilation.

Definitive transport experiments in bacteria require that initial uptake rates be obtained. This is most accurately done using radioactive isotopes. The longest lived radioisotope of nitrogen,  $^{13}\text{N}$ , has a half-life of 10 min and releases positrons that annihilate to produce gamma emissions with a 511-keV energy (8). The short half-life of  $^{13}\text{N}$  requires that it be used very soon after generation, but the nature of transport in bacteria is such that most experiments can be performed in a few minutes. Using  $^{13}\text{N}$ -labeled  $\text{NO}_3^-$ , we present evidence that  $\text{NO}_3^-$  is transported into *Klebsiella pneumoniae*, is reduced to  $\text{NO}_2^-$ , which is transiently excreted, and is subsequently reabsorbed.



## Experimental

**Microbiology.** *Klebsiella pneumoniae* strain M5a1 was obtained from R. C. Valentine. The medium used for growth was that used by Cohen-Bazire et al. (9), with glucose as the carbon source and  $\text{KNO}_3$  as the nitrogen source. Semiaerobic growth was obtained in 50-mL cultures placed in 250-mL flasks and shaken at 100 rpm in a New Brunswick Scientific Incorporated Model G76 shaking water bath. Aerobic growth was obtained by spreading 125  $\mu\text{g}$  dry wt of exponentially growing cells on agar plates containing the same medium and incubating them at 30°C for 3–4 h. The plate-grown cells were harvested in agar-free growth medium containing 15  $\mu\text{g}$  chloramphenicol/mL to prevent induction of the RNR. After centrifugation at  $15,000 \times g$  for 15 min, the supernatant was tested for  $\text{NO}_2^-$  (the absence of  $\text{NO}_2^-$  ensures the absence of significant RNR activity) by the methods of Schrader et al. (10) or Thayer and Huffaker (11). The cultures were then washed and resuspended twice in 0.1M phosphate buffer, pH 7.0, without a nitrogen source, containing 15  $\mu\text{g}$  chloramphenicol/mL, and kept on ice until used.

**Transport Assays.** Cells obtained as described above were diluted to 0.05–0.5 mg dry wt/mL as desired, and  $^{14}\text{NO}_3^-$  was added with the radiolabeled  $\text{NO}_3^-$ . At appropriate time intervals (10–150 s) after the addition of radiolabeled nitrate, 1.0 mL of cell suspension was filtered through 0.45- $\mu\text{m}$  pore size, 25-mm-diameter Millipore filters, and washed with 5–10 mL of 50mM phosphate buffer containing 10mM  $\text{KNO}_3$ . Alternatively 0.5 mL of the cells were layered over 0.5 mL of silicone oil [Dow Corning; 75% 550, 25% 510–100 cs (v/v)] in Eppendorf 1.5-mL microfuge tubes in the microfuge (12).  $^{13}\text{NO}_3^-$  was added using a Gilson Pipetteman micropipet to the indicated concentrations at 15-s intervals. The microfuge was started, reaching 12,000 g's in 5 s and stopped 25 s later. The aqueous layer was sampled for HPLC analysis, and the remaining liquid was aspirated off. The pellet was extracted with methanol and counted with constant geometry in a well  $\gamma$  counter equipped with a sodium iodide crystal. Corrections were made for elapsed time (half-life) and for  $^{13}\text{N}$  binding to filters (when used) or dead cells on filters.

Preparation of  $^{13}\text{NO}_3^-$  was as described by Parks and Krohn (13), and purification of  $^{13}\text{NO}_3^-$  from other products by anion-exchange HPLC was as described by Tiedje et al. (14) except that the purified  $^{13}\text{NO}_3^-$  was harvested by hand. The radiochemical purity of  $^{13}\text{N}$  determined by analytical anion-exchange HPLC was greater than or equal to 99.5% as  $\text{NO}_3^-$  (Figure 1). The acidic eluate from the HPLC was neutralized with 10N NaOH prior to addition to cells.

**Chemicals.** All chemicals were of analytical grade and no further purification was performed. Chloramphenicol was from Sigma Chemical Company.

## Results

Initial studies with nitrate concentrations from 10  $\mu\text{M}$ –10mM using a 2.5-min incubation suggested the presence of two uptake systems with  $K_m$ s of about 15–20  $\mu\text{M}$  and 1–2mM. That experiment was repeated with semiaerobically grown cells with  $\text{NO}_3^-$  concentrations bracketing those two values (Table I). What appeared initially to be two uptake systems

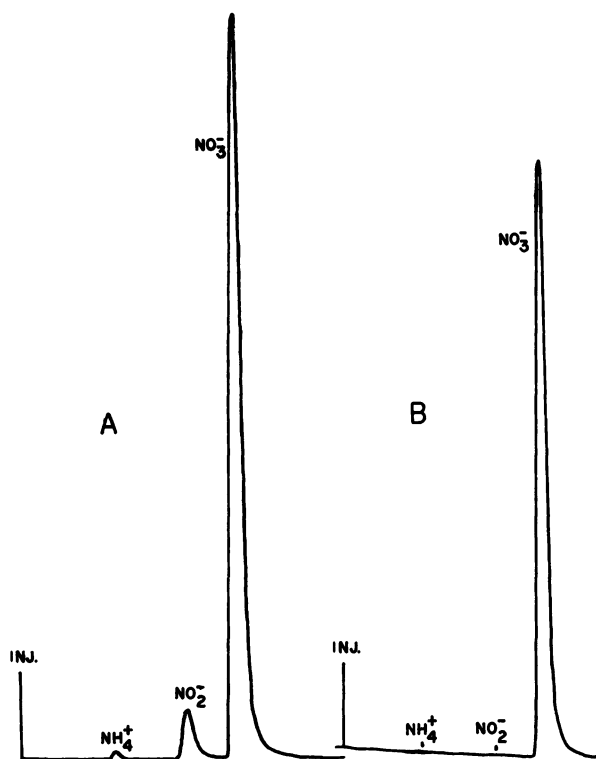


Figure 1. Analysis of  $^{13}\text{N}$ -labeled compounds (A) in target solution and (B) in nitrate sample purified by high-pressure anion exchange-liquid chromatography.

Conditions: 50mM sodium phosphate buffer pH 2.9 was pumped at 1.5 mL/min through a Whatman Partisil-10 SAX column ( $0.46 \times 25$  cm). Detection was by gamma counting using a well-type sodium iodide crystal. In (A) 350  $\mu\text{L}$  of the target solution was chromatographed 1 h after production. In (B) 50  $\mu\text{L}$  of purified  $\text{NO}_3^-$  was chromatographed 40 min after production of  $^{13}\text{N}$ .

upon correction yielded a single system for  $\text{NO}_3^-$  uptake with a  $K_m$  of about  $8\mu\text{M}$  and a second uptake capability that was not saturated at the  $\text{NO}_3^-$  concentrations used. The latter capability may reflect either the ability of  $\text{NO}_3^-$  to cross the cell membrane as a permeant anion (4) or the possibility that  $\text{NO}_3^-$  is reduced outside the cell membrane and that  $\text{NO}_2^-$  or  $\text{NH}_4^+$  are the transported compounds. To test the latter hypothesis, the pattern of initial  $\text{NO}_3^-$  transport at  $\text{NO}_3^-$  concentrations from  $10\text{--}80\mu\text{M}$  and from  $0.67\text{--}5\text{mM}$  were determined. In this experiment the semiaerobically grown cells were kept aerobic prior to and during incubation with  $^{13}\text{NO}_3^-$  by bubbling the culture with  $\text{O}_2$ . Label was taken up rapidly but was subsequently lost (Figure 2). Several such experiments using incubations from 5–60 s yielded similar results. We interpret

Table I. Uptake Rates of  $^{15}\text{NO}_3^-$  in Semiaerobically Grown Cells<sup>a</sup>

$[\text{NO}_3^-]$	$\frac{\mu\text{Mol}/\text{min}}{\text{mg dry wt}}$	Uncorrected Apparent $K_m$	$K_m$ After Corrections (3 Cycles) <sup>b</sup>
10 $\mu\text{M}$	2.46	9.5 $\mu\text{M}$	8 $\mu\text{M}$
15 $\mu\text{M}$	3.16		
25 $\mu\text{M}$	3.38		
80 $\mu\text{M}$	4.38		
0.67 mM	5.72	7.3 mM	not saturating
1.0 mM	9.44		
1.5 mM	12.1		
5 mM	33.2		

<sup>a</sup> 0.2 mg dry wt of cells was incubated with  $^{15}\text{NO}_3^-$  for 2.5 min, vacuum-filtered over 0.45- $\mu\text{m}$  Millipore filters, and washed with 10 mL HMB + 10 mM  $\text{KNO}_3$  prior to counting.

<sup>b</sup> Corrections for the contribution of each apparent system to the other were made using sequential approximations of the  $K_m$  and  $V_{\text{max}}$  values and substituting them in the Lineweaver-Burk equation,  $1/V = K_m/V_{\text{max}} (1/s) + 1/V_{\text{max}}$ . After 3 cycles the values did not change significantly.

this pattern to mean that a product of  $\text{NO}_3^-$  metabolism may be released. If the ANR is located in the cell membrane, then  $\text{NO}_2^-$  may be released directly back into the medium; and if ANR is cytoplasmic, then  $\text{NO}_2^-$  may be rapidly exported. Alternatively,  $\text{NH}_4^+$  as  $\text{NH}_3$  gas may be washed from the cells during filtration. [Interestingly, Sawada and Satoh (15) have shown that  $\text{NO}_3^-$  reductase from *Rhodopseudomonas sphaeroides* forma sp. *denitrificans* can be released by removing the cell wall during spheroplast formation.]

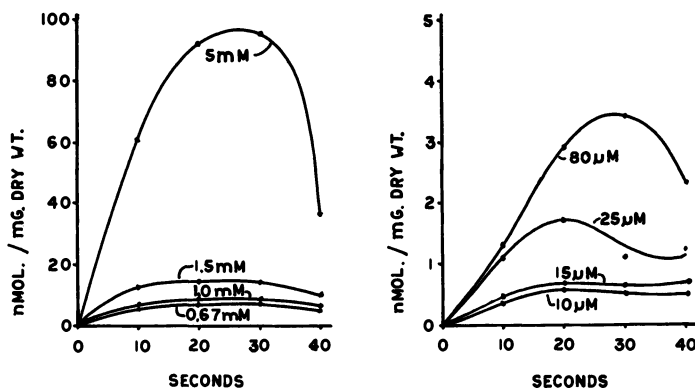


Figure 2. Initial  $\text{NO}_3^-$  transport rate studies in *Klebsiella pneumoniae* using the membrane filtration technique, showing the binding of  $^{15}\text{N}$ -labeled nitrate and the subsequent release of it or its metabolic products

**Table II.  $\text{NO}_2^-$  Excretion and Disappearance by Aerobic *Klebsiella* Cultures Incubated with  $0.5\text{mM } ^{13}\text{NO}_3^-$**

Time (s)	External [ $\text{NO}_2^-$ ]
0 (radiochemical purity $\geq 99.5\%$ )	$\leq 2.5\mu\text{M}$
10	$8.1\mu\text{M}$
30	$6.5\mu\text{M}$
60	$< 5.0\mu\text{M}$

<sup>a</sup>  $0.6\text{ mg dry wt}$  of cells in  $2.0\text{ mL}$  of medium was incubated with  $^{13}\text{NO}_3^-$  and at the indicated times  $0.5\text{ mL}$  was withdrawn through a  $0.45\text{-}\mu\text{m}$  pore size filter into a syringe. This filtrate was analyzed by HPLC to determine the  $\text{NO}_2^-$  concentration.

If  $\text{NO}_2^-$  or  $\text{NH}_4^+$  are released during filtration of the cells, they should be detected in the filtrates. However, under aerobic conditions no  $^{14}\text{NO}_2^-$  or  $^{14}\text{NH}_4^+$  accumulated in cultures of growing cells. So if  $\text{NO}_2^-$  or  $\text{NH}_4^+$  is released, then it either represents an artifact of filtration or is an oscillation in the metabolism of  $\text{NO}_3^-$  that is later stabilized. To distinguish between these possibilities, aerobic cultures were incubated with  $^{13}\text{NO}_3^-$  at  $0.5\text{mM}$ , filtered at various times thereafter, and the filtrate analyzed by HPLC (Table II). The appearance of  $^{13}\text{NO}_2^-$  (but not  $^{13}\text{NH}_4^+$ ) at 10 and 30 s followed by its disappearance at 60 s suggests that  $\text{NO}_3^-$  is rapidly reduced to  $\text{NO}_2^-$ , which is released or excreted back into the medium and is then taken up again. This suggests that the release of label from filtered cells represents an oscillation in metabolism rather than an artifact of filtration. The transient external appearance of  $\text{NO}_2^-$  also indicates that NiR and/or  $\text{NO}_2^-$  transport activation may occur. Nitrite is toxic, so the relatively high intracellular  $\text{NO}_2^-$  concentration potentially resulting from  $\text{NO}_3^-$  reduction supplies a rationale for either an external site for  $\text{NO}_3^-$  reduction or the presence of a nitrite export system.

Nitrite appears to be released from the cells; therefore the transport systems described earlier (using 2.5-min incubations) may reflect either

**Table III. Initial Rates of  $^{13}\text{NO}_3^-$  Transport in *K. pneumoniae* Assayed by Sedimentation Through Silicone Oil<sup>a</sup>**

[ $\text{NO}_3^-$ ]	Initial Rate ( $\mu\text{mol}/\text{min mg dry wt}$ )	$r^2$
$1\mu\text{M}$	0.232	0.998
$3\mu\text{M}$	0.477	0.998
$10\mu\text{M}$	0.854	0.999
$30\mu\text{M}$	1.199	0.982

<sup>a</sup> Linear regression analysis on 0–45-s time points was used to determine initial rates.

$K_m$  and  $V_{\text{max}}$  determination from the data above.  $1/V = K_m/V_{\text{max}} (1/s) + 1/V_{\text{max}}$  is the equation used to determine  $K_m$  and  $V_{\text{max}}$ :  $K_m = 4.4\mu\text{M}$ ,  $V_{\text{max}} = 1.24\text{ nM}/\text{min} \cdot \text{mg dry wt}$ ,  $r^2$  of Lineweaver–Burk plot = 0.997. Assays are as described in the Experimental section.

**Table IV. HPLC Analysis of Radioactivity Taken Up by and Cosedimenting with Cells of *K. pneumoniae* in Initial Rate Experiments**

Initial [NO <sub>3</sub> <sup>-</sup> ]	Incubation Time (s)	Percentage of Pellet Counts Found as:		
		NO <sub>3</sub> <sup>-</sup>	NO <sub>2</sub> <sup>-</sup>	NH <sub>4</sub> <sup>+</sup>
1 μM	15	> 99	< 0.2	< 0.2
1 μM	45	> 93	< 0.2	5.2
3 μM	15	> 99	< 0.2	< 0.2

NO<sub>2</sub><sup>-</sup> uptake, occurring after NO<sub>3</sub><sup>-</sup> reduction and NO<sub>2</sub><sup>-</sup> export, or may result from the activity(ies) of some other step(s) involved in NO<sub>3</sub><sup>-</sup> assimilation. To address this question, another method was adapted to separate cells rapidly from the suspending medium.

Use of an Eppendorf microfuge to centrifuge cells layered over a silicone oil of appropriate density permits a very rapid separation of cells from the aqueous suspending medium. The addition of radiolabeled NO<sub>3</sub><sup>-</sup> at 15-s intervals to cells suspended over silicone oil followed by sedimentation established initial rates of transport, and HPLC analysis of methanolic extracts of the pellets identified the transported compound. Using NO<sub>3</sub><sup>-</sup> concentrations from 1–30 μM and incubation times of 0, 15, 30, and 45 s, we established the presence of the high-affinity transport system (Table III) obtained earlier (see Table I). The *K<sub>m</sub>* of that system when assayed in this manner was about half that obtained by filtration assays. Selected pellets thus obtained were extracted and analyzed by HPLC to determine whether NO<sub>3</sub><sup>-</sup> or NO<sub>2</sub><sup>-</sup> was the transported compound (Table IV). Since no NO<sub>2</sub><sup>-</sup> or NH<sub>4</sub><sup>+</sup> appear in the pellet in 15-s incubations and no NO<sub>2</sub><sup>-</sup> appears after 45 s, we conclude that NO<sub>3</sub><sup>-</sup> is the transported compound.

### Discussion

While the goal in this study was to demonstrate the presence of one or more transport system(s) for NO<sub>3</sub><sup>-</sup>, our initial rate studies were hampered by the uptake, then loss, of counts bound to filters in filtration assays. This suggested that NO<sub>3</sub><sup>-</sup> was bound to the cells in some fashion, then released, perhaps as NO<sub>2</sub><sup>-</sup>, or reduced nitrogen (see also Ref. 15). By collecting the filtrates in these experiments and analyzing them by anion exchange HPLC, we demonstrated that in aerobic cultures NO<sub>2</sub><sup>-</sup> is released into the medium transiently and then is taken back up. Since NO<sub>3</sub><sup>-</sup> may be reduced on the outside of the cell membrane, the transport capability identified in 2.5-min experiments may have reflected the subsequent uptake of NO<sub>2</sub><sup>-</sup> or the assimilation of NO<sub>3</sub><sup>-</sup> after reduction to NH<sub>4</sub><sup>+</sup> (16). On the other hand, NO<sub>3</sub><sup>-</sup> may be transported and reduced intracellularly to NO<sub>2</sub><sup>-</sup>, which is transiently excreted as a toxic compound

before nitrite reduction occurs. If  $\text{NO}_3^-$  reduction were intracellular, an internal  $\text{NO}_2^-$  concentration in excess of 6 or 7mM would have been generated if no  $\text{NO}_2^-$  export mechanism were present.

By sedimenting cells exposed to  $^{13}\text{NO}_3^-$  for 0–45 s through silicone oil, we demonstrated the presence of a high-affinity transport system. The time course of the experiment was potentially slow enough to permit  $\text{NO}_3^-$  reduction and  $\text{NO}_2^-$  release, followed by  $\text{NO}_2^-$  uptake. Therefore we were required to identify the form of  $^{13}\text{N}$  transported. By subjecting the pelleted cells to a rapid methanolic extraction after sedimentation away from  $^{13}\text{NO}_3^-$  and analyzing that extract by anion-exchange HPLC, it was shown that  $\text{NO}_3^-$  was the transported compound. Furthermore,  $\text{NO}_2^-$  failed to appear in the pelleted cells at 15–45 s. Thus, if any  $\text{NO}_3^-$  were reduced to  $\text{NO}_2^-$  in the 30–60 s required to aspirate off the silicone oil and aqueous layers in the tube prior to extraction with methanol, that  $\text{NO}_2^-$  was further reduced to  $\text{NH}_4^+$ .

This study shows that *K. pneumoniae*, when growing under aerobic or semiaerobic conditions, transports  $\text{NO}_3^-$  into the cells. Therefore “assimilatory” or aerobic  $\text{NO}_3^-$  reduction probably occurs inside the cells. The observation that  $\text{NO}_2^-$  is transiently excreted into the medium from which it then disappears suggests the presence of both a  $\text{NO}_2^-$  export system (possibly a consequence of  $\text{NO}_3^-$  reduction by a membrane-associated enzyme) and a  $\text{NO}_2^-$  uptake system. The presence of a  $\text{NO}_2^-$  uptake capability may simply reflect the permeability of membranes to weak acids in the presence of a transmembrane pH gradient (19–23) or may indicate the presence of carrier-mediated transport systems. If the  $\text{NO}_2^-$  uptake is carrier-mediated, the transient nature of the accumulation of  $\text{NO}_2^-$  outside the cells suggests that uptake and/or reduction may be activated shortly after the cells are exposed to  $\text{NO}_3^-$ . It may also be possible that simultaneous transport of nitrite across the cell membrane and reduction are mediated by one enzyme system. While we have not attempted to demonstrate a membrane-associated nitrite reductase, Jones and Garland (3) and Coleman et al. (22) have found such activities in other enteric bacteria.

### Acknowledgments

We acknowledge the support of the National Science Foundation (Grants NSF-PFR 77-07301 and NSF-DEB 77-01199). We are indebted to Drs. Krohn, J. C. Meeks, N. J. Parks, and N. Peek for providing labeled  $\text{NO}_3^-$  and encouragement. We also thank Dr. N. Peek and J. H. Chasko for help with our radiochromatographic analyses.

### Literature Cited

1. Van't Riet, J.; Stouthammer, A. H.; Planta, R. J. *J. Bacteriol.* 1968, 96, 1455.

2. Hom, S. S.-M.; Hennecke, H.; Shanmugam, K. T. *J. Gen. Microbiol.* 1980, 117, 169.
3. Jones, R. W.; Garland, P. B. *Biochem. J.* 1977, 164, 199.
4. Boonstra, J.; Konings, W. N. *Eur. J. Biochem.* 1977, 78, 361.
5. Garland, P. B.; Downie, J. A.; Haddock, B. A. *Biochem. J.* 1975, 152, 547.
6. Kristajansson, J. K.; Walter, B.; Hollocher, T. C. *Biochemistry* 1978, 17, 5014.
7. Kristajansson, J. K.; Hollocher, T. C. *J. Bacteriol.* 1979, 137, 1227.
8. Gersberg, R.; Krohn, K.; Peek, N.; Goldman, C. R. *Science* 1976, 192, 1229.
9. Cohen-Bazire, C.; Siström, W. R.; Stanier, R. Y. *J. Cell. Comp. Physiol.* 1957, 49, 25.
10. Schrader, L. E.; Ritenour, G. L.; Elrich, G. L.; Hageman, R. H. *Plant Physiol.* 1968, 43, 930.
11. Thayer, J. R.; Huffaker, R. C. *Anal. Biochem.* 1980, 102, 110.
12. Kashket, E. R.; Barker, S. L. *J. Bacteriol.* 1977, 130, 1017.
13. Parks, N. J.; Krohn, K. A. *Int. J. Appl. Radiat. Isotopes* 1978, 29, 754.
14. Tiedje, J. M.; Firestone, R. B.; Firestone, M. K.; Betlach, M. R.; Smith, M. S.; Caskey, W. H. *Soil Sci. Soc. Am. J.* 1979, 43, 709.
15. Sawada, E.; Satoh, T. *Plant Cell Physiol.*, in press.
16. Tempest, D. W.; Meers, J. L.; Brown, C. M. In "The Enzymes of Glutamine Metabolism"; Academic: New York; 1973; p. 167.
17. Rottenberg, H. *J. Bioenerg.* 1975, 7, 61.
18. Padan, E.; Zilberstein, D.; Rottenberg, H. *Eur. J. Biochem.* 1976, 63, 533.
19. Ramos, S.; Schuldiner, S.; Kaback, H. R. *Proc. Natl. Acad. Sci. USA* 1976, 73, 1892.
20. Ramos, S.; Kaback, H. R. *Biochemistry* 1977, 16, 848.
21. *Ibid.*, 854.
22. Coleman, K. J.; Cornish-Bowden, A. J.; Cole, J. A. *Proc. Soc. Gen. Micro.* 1976, 3, 84.

RECEIVED September 4, 1980.

# $^{13}\text{N}$ -Labeling of a Substituted Nitrosourea, Its Carbamate, and Nitrosocarbaryl: In Vivo and In Vitro Studies

G. A. DIGENIS, Y. C. CHENG, and R. L. McQUINN

Division of Medicinal Chemistry, College of Pharmacy, University of Kentucky, Lexington, KY 40506

B. R. FREED and R. S. TILBURY

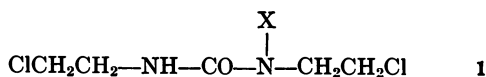
Biophysics Laboratory, Memorial Sloan Kettering Cancer Center, New York, NY 10021

*A procedure for the preparation of mCi quantities of 1,3-bis(2-chloroethyl)-1-nitrosourea (BCNU), its carbamate analog N-nitroso-N-chloroethyl-1-chloroethyl carbamate (BCNC), and nitrosocarbaryl (NC), labeled in the nitroso position with  $^{13}\text{N}$ , is described. Whole body retention measurements of  $^{13}\text{N}$  after iv injection of BCNU( $^{13}\text{NO}$ ) in rats showed volatilization of 19–30% dose in 40 min. For iv BCNC( $^{13}\text{NO}$ ) and NC( $^{13}\text{NO}$ ), volatilization was much more rapid: 50% in 30–70 s, 90% in 5–11 min. More than 90% of iv BCNU was cleared from blood by 5 min. A  $^{13}\text{N}$ -containing urinary metabolite, amounting to 10% dose at 60–70 min, demonstrated a non- $\text{N}_2$ -producing pathway of BCNU metabolism. Label from intragastric NC( $^{13}\text{NO}$ ) was about 50% volatilized in 90–100 min. In vitro aqueous decomposition rates of all three compounds, as measured by net loss of  $^{13}\text{N}$  from solution, did not show the expected steady increase with pH, for  $\text{pH} > 9$ . The relative decomposition rates of the three compounds were not predictive of their relative fates in vivo.*

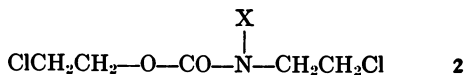
In 1961 Skipper and coworkers originally demonstrated that administration of 1-methyl-1-nitrosourea increased the lifespan of mice intracerebrally inoculated with L1210 leukemic cells (1). This demonstration launched extensive research into the synthesis and testing of N-nitrosoureas for antitumor activity (2), a line of research that continues to the

0065-2393/81/0197-0351\$05.00/0  
© 1981 American Chemical Society

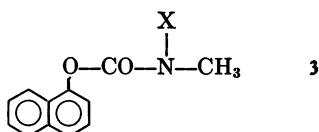




- a x = H = BCU  
b x = \*NO = BCNU



- a x = H  
b x = \*NO = BCNC



- a x = H = Carbaryl  
b x = \*NO = NC

Figure 1. Formulas for compounds studied: a, urea or carbamate precursor; b, N-nitroso derivative; \* denotes position of  $^{13}\text{N}$  label

present. One of the first compounds so developed was 1,3-bis(2-chloroethyl)-1-nitrosourea or BCNU (1b, Figure 1). Of particular importance was the fact that it was found to be more effective in the treatment of brain tumors than any previously known drug. BCNU is still in wide use and has become commercially available. Although a great deal of effort has been devoted to defining the modes of action of this and other therapeutic nitrosoureas, their metabolic fates are still not well understood.

Of more general concern is the question of the magnitude of carcinogenic hazard posed by several classes of N-nitroso compounds, including those formed in the environment, in foodstuffs, and, potentially, in vivo. One such class is the nitrosocarbamates. Carbamate insecticides are currently among the most heavily used agricultural chemicals. It is thought that residues of these compounds, ingested in food or directly, by those occupationally exposed, can react in vivo with dietary or endogenously produced nitrite to form nitrosocarbamates, many of which are proven carcinogens (3). An example is the insecticide carbaryl (1-naphthyl-N-methylcarbamate, 3a) whose nitrosation product, nitrosocarbaryl (3b), has been shown to be a potent mutagen (4, 5) and carcinogen (3, 6, 7, 8).

Despite the fact that the nitroso moiety is indispensable to the biological activity (both carcinogenic and carcinocidal) of the aforementioned N-nitroso compounds, very little is known of its metabolic fate, a situation perhaps related to the difficulties associated with use of the

stable isotopic tracer <sup>15</sup>N. Although not yet widely available and despite the evident time limitations its use imposes, the cyclotron-produced positron emitter, <sup>13</sup>N, the longest-lived radioisotope of nitrogen ( $t_{1/2} = 10$  min), offers several distinct advantages over <sup>15</sup>N: (i) convenient assay (by detection of the 511-keV gamma rays its decay produces); (ii) lack of interference from isotope naturally present in all nitrogenous material; and (iii) ability to monitor metabolic processes in vivo by external scintigraphic techniques.

This chapter describes the labeling of the nitroso nitrogen of BCNU, nitrosocarbaryl (NC), and the carbamate analog of BCNU, *N*-nitroso-*N*-chloroethyl-1-chloroethyl carbamate or BCNC (2b) with cyclotron-produced <sup>13</sup>N. The fate of the nitroso moiety in vivo was investigated following injection of the labeled compound in rats. Studies of the decomposition rates of these compounds in aqueous media are also described.

### Experimental

**Preparation of <sup>13</sup>N-Labeled *N*-Nitroso Compounds.** The precursor urea, 1,3-bis(2-chloroethyl) urea (1a, BCU), was prepared in 40% yield by the method of Bestian (9). Its carbamate analog, *N*-chloroethyl-1-chloroethyl carbamate (2a), was prepared by the method of McQuinn et al. (10). Carbaryl (3a) was purchased from Aldrich Chemical Company (Milwaukee, WI) and was recrystallized from ethanol.

Nitrogen-13 was produced via the <sup>16</sup>O(p,α)<sup>13</sup>N reaction by the irradiation of water with 14.5-MeV protons from the Memorial Sloan-Kettering Cancer Center cyclotron (model CS-15, Cyclotron Corporation, Berkeley, California). A typical irradiation of 25-μA beam current for 20 min yielded 375 mCi of <sup>13</sup>N, mostly in the form of nitrate ion (11).

Details of the synthesis of BCNU(<sup>13</sup>NO) have been published (12). The technique for synthesis of the *N*-nitrosocarbamates was a modification of that procedure, as follows. The target water (~20 mL) was transferred by helium pressure through Teflon tubing to a beaker in a shielded "hot cell." About 1 mg Na<sub>2</sub>CO<sub>3</sub> was added and the water evaporated to dryness on a hot plate. After cooling, the <sup>13</sup>N activity was dissolved in 1–1.5 mL of nitrate carrier solution (69mM HNO<sub>3</sub> in glacial acetic acid) and transferred to a mixture of 30 mg copper dust and 8 mg carbamate precursor (2a or 3a). This was vortex mixed and allowed to react for 6–8 min. One mL water was added and the mixture extracted with 1.5 mL methylene chloride. The organic layer was removed, washed with 1 mL 2% Na<sub>2</sub>CO<sub>3</sub>, dried by passage through granular, anhydrous Na<sub>2</sub>SO<sub>4</sub>, and evaporated to a dry residue under a stream of N<sub>2</sub>. This procedure was usually completed in 25–30 min from the end of bombardment.

Radiochemical yields, corrected for physical decay of <sup>13</sup>N, were 20–40% for BCNU (<sup>13</sup>NO), 20–35% for NC(<sup>13</sup>NO) and 4–11% for BCNC (<sup>13</sup>NO). The radiochemical purity of all three compounds as determined by autoradiographic scanning of TLC plates (Silica Gel) was found to be greater than 98%. The R<sub>f</sub> values using CHCl<sub>3</sub> as eluting solvent for BCNU, NC, and BCNC were 0.47, 0.62, and 0.58, respectively.

**Animal Studies.** Normal male Sprague-Dawley rats (Charles River Labs, South Wilmington, Massachusetts), ranging in weight from 250 to 450 g were used for all in vivo studies. For injection, the <sup>13</sup>N-labeled com-

pound (dry residue) was dissolved in ethanol, diluted with 3 vol (for BCNU) or 1/4–1/3 vol (for BCNC) of saline and taken up in a 1 mL syringe with 26-gauge needle. In the case of NC, the addition of more than a few drops of water caused formation of precipitates. For injection of BCNU ( $^{13}\text{N}$ ) and for intragastric injection of NC ( $^{13}\text{N}$ ), rats were anesthetized with I.P. sodium pentobarbital (ca. 50 mg/kg). For intravenous injection of BCNC ( $^{13}\text{N}$ ) or NC ( $^{13}\text{N}$ ), it was necessary to use light, intermittent ether anesthesia. This was a consequence of the low aqueous solubility of these compounds and the need to use a minimum of 0.1–0.15 mL of ethanol to take up sufficient  $^{13}\text{N}$  activity for external scintigraphy. In pentobarbital-anesthetized rats, such injections (iv) were invariably fatal, causing cessation of breathing followed by cardiac arrest. Even under light ether anesthesia, a number of fatalities resulted. (Separate experiments showed that the quantity of ethanol injected, without dissolved nitrosocarbamate, was sufficient to incur the observed mortality). Carrier doses injected were of the order of 1–10 mg/kg.

**Whole Body Retention of  $^{13}\text{N}$  After iv Injection.** These measurements were carried out on one head of the TOKIM, a dual-head, Anger-type scintillation camera system designed and constructed at the Biophysics Laboratory, MSKCC. Each head contains a 13-in. diameter, one-half-in. thick NaI(Tl) crystal viewed by 19 phototubes. A 65-mm-thick, parallel-hole tungsten collimator (hole diameter 5 mm, distance between centers 8 mm), which provides a large region of uniform detection efficiency, was used to image the distribution of  $^{13}\text{N}$  in the rat. With an energy band of approximately 400–600 keV, 1 mCi of  $^{13}\text{N}$  distributed in the body of a rat gave approximately 3700 counts/s. Following energy and position analysis, detected events, as ( $x,y$ ) coordinate pairs, were transferred to buffered storage arrays in a PDP 11/70 computer and stored on magnetic tape in time-notated data records of 1024 events each. Overall system dead-time was 15  $\mu\text{s}/\text{event}$ .

For study, a rat was immobilized over the inverted upper head of the TOKIM. An incision was made in the inguinal region and the  $^{13}\text{N}$ -labeled compound injected into the femoral vein. From 0.1–1 mCi were injected for the three compounds. Data were accumulated until count rates became prohibitively low. A ventilation duct near the apparatus provided sufficient air flow to remove quickly any volatile  $^{13}\text{N}$  activity evolved from the rat. No loss of urine or feces occurred during imaging.

Analysis of the TOKIM data used a program package developed by R. E. Reiman of the Biophysics Laboratory. Magnetic tape data records were used to construct time frames with one or more records per frame. The image contained in any frame could be displayed in either a gray scale or alphabetic mode, using linear or logarithmic level spacing, on hard copy from a Gould 5005 printer/plotter. Regions of interest were defined by providing the computer with the appropriate perimeters. Decay and dead-time corrected counts/s for the regions were computed for each time frame and the results produced on a line printer. The whole body count rate obtained upon completion of the injection, minus any residual activity remaining in the syringe or at the injection site, was taken to be 100% dose. That the whole body count rate was quite insensitive to the distribution of  $^{13}\text{N}$ -activity in the rat was determined previously in studies with the positron-emitter  $^{18}\text{F}$ , injected as fluoride ion. Considerable redistribution of activity over a period of several hours following iv injection (including concentration of 20–30% dose in the bladder) produced changes of only a few percent in the corrected whole body count rate (13).

**<sup>13</sup>N Content of Blood and Urine Following iv Injection of BCNU(<sup>13</sup>NO).** Rats anesthetized with pentobarbital were injected with 0.01–3 mCi of BCNU-(<sup>13</sup>NO) in the femoral vein. At specified time intervals the chest was opened and blood was drawn into a syringe from the left ventricle and transferred to a preweighed glass counting vial with screw cap. (The vials were reweighed for net weight determination). The abdomen was then opened, the urinary ducts clamped with a hemostat, the intact bladder removed, and its contents emptied into a counting vial. Standards were prepared from weighed aliquots of the injection solution, diluted with ethanol to volumes comparable to the blood and urine samples. The samples and standards were assayed for <sup>13</sup>N activity in a Packard model 5986 gamma spectrometer/automatic sample changer equipped with a line printer and digital elapsed timer. Detection efficiency for <sup>13</sup>N using a wide energy band of 10–1150 keV was approximately 24000 counts/s/μCi. Net counts were decay-corrected to a common time and percent dose calculations were based on dilution by weight. Blood <sup>13</sup>N content was expressed as relative concentration, which is defined, for either a specimen of tissue or whole organ, as percent dose/percent body weight (14).

**High-Pressure Liquid Chromatography.** A high-pressure liquid chromatograph (Laboratory Data Control, Riviera Beach, Florida), consisted of a pump, pulse dampener, sample injection valve, 25 × 0.4 cm (i.d.) stainless steel column filled with Partisil SAX (Whatman, Incorporated, Boonton, New Jersey) anion-exchange medium, variable wavelength spectrophotometer (LDC) and a shielded well-type 5 × 5 cm NaI(Tl) gamma scintillation detector connected to a rate meter. The effluent of the column passed through a spiral loop of stainless steel tubing in the detector well and then through the spectrophotometer. The count rate and UV absorbance were recorded by a dual-pen strip chart recorder. The column was eluted with 50mM KH<sub>2</sub>PO<sub>4</sub> buffer, pH 3.0, at an inlet pressure of about 800 psi and flow rate of approx. 1 mL/min. For determination of radiopurity, <sup>13</sup>N-labeled *N*-nitroso compounds were injected into the system in 10-μL amounts, dissolved in ethanol. In addition, urine samples collected from rats after iv injection of BCNU(<sup>13</sup>NO) were filtered by passage through a 50-μm filter and 100-μL aliquots were injected into the HPLC. Absorbance was measured at 254 nm.

**Intragastric Injection of Nitrosocarbaryl(<sup>13</sup>NO).** Fed rats were anesthetized with pentobarbital, an incision was made in the upper abdomen, and the stomach was exteriorized. In one group of rats, both ends of the stomach were tightly ligated with 2-0 silk suture. NC(<sup>13</sup>NO) in ethanol was injected directly into the stomach through a 26-gauge needle. There was no fluid leakage from the site of injection. The stomach was returned to the abdominal cavity and the wound closed with surgical clips. At sacrifice, the entire gut tract and whole liver were removed for radioassay. Ligated stomachs were counted with sutures intact. They were then carefully cleaned of their contents, and the stomach wall and contents were counted separately.

**In Vitro Aqueous Decomposition Measurements.** Buffered aqueous solutions covering a wide pH range were prepared. Phosphate (0.05M KH<sub>2</sub>PO<sub>4</sub>) solutions were utilized for the preparation of buffers covering pH 1.28–8.25 and borate (0.05M) buffers were used for pH > 9.0. Heparinized whole rat blood was also studied. Ten-mL aliquots of these solutions were placed in 20-mL glass counting vials. About 1 μCi of BCNU(<sup>13</sup>NO), BCNC(<sup>13</sup>NO), or NC(<sup>13</sup>NO) in approximately 0.1 mL of ethanol was added to each test solution. The contents were gently agitated, and the vials were placed uncapped in the

gamma spectrometer and counted in the automatic mode. Depending on the number of samples studied, the activity added, and the rate of decomposition, the number of usable count measurements obtained for a given sample varied from a minimum of 3 to a maximum of 14. For each sample, the net counts vs. time were fitted to a single negative exponential function by means of a Poisson-weighted linear least-squares fit to the logarithm of the net counts. The gross  $^{13}\text{N}$  loss rate constant thus obtained minus the physical decay constant of  $^{13}\text{N}$  gave the rate constant of net loss of  $^{13}\text{N}$  from solution. The underlying assumptions of this method are that the aqueous decomposition of the *N*-nitroso compounds studied results in the equimolar liberation of the  $^{13}\text{N}$  label as molecular nitrogen (see Discussion) and that the rate of loss of this  $^{13}\text{N} \cdot \text{N}$  into ambient air is much faster than the rate of decomposition. The physical decay constant of  $^{13}\text{N}$  was separately measured with this system (as  $^{13}\text{NO}_3^-$  in a capped vial) and found to be  $4.158 \pm .005$  ( $\text{h}^{-1}$ ). The variance of the net loss rate constants was estimated from the maximum-likelihood equations for the fit to the count data (using Poisson statistics) plus the variance in our measurement for the decay constant of  $^{13}\text{N}$ .

## Results

**Whole Body Retention of  $^{13}\text{N}$  After iv Injection.** The results of these measurements for the three compounds studied are shown in Figure 2. For BCNU( $^{13}\text{NO}$ ), a smooth curve has been drawn through the mean whole body retention (WBR) at 10, 20, 30, and 40 min after injection (5 rats/point to 30 min, 4 rats/point to 40 min), followed by individual retention curves for 2 rats (dotted lines). The vertical bars denote the range of measured retention at the four time points. Individual WBR curves for 2 rats per compound are shown for BCNC( $^{13}\text{NO}$ ) and NC( $^{13}\text{NO}$ ).

It is seen that for both the nitrosourea and the nitrosocarbamates, nitrogen-13, labeled in the nitroso moiety of these compounds, was evolved from the body of the rat, but at rates that differed markedly. At 40 min after injection of BCNU( $^{13}\text{NO}$ ), an average of 24% of the administered  $^{13}\text{N}$  was lost in expired air. Extrapolation of the mean WBR curve to 1 h indicates a mean loss of at most 30% dose in this time period. In the four rats injected with nitrosocarbamates, this amount was lost within 30 s. Fifty percent was liberated from the rats in 30–70 s and 80% in 2–4.3 min. At 10 min, WBR ranged from 6% to less than 12% dose. Even in those rats that succumbed to the large doses of iv ethanol administered (data not shown), substantial amounts of  $^{13}\text{N}$  (up to 60% dose of either nitrosocarbamate) were evolved in periods up to 100 s before pulmonary arrest. Analysis of the time course of  $^{13}\text{N}$  activity in the lung region on the  $\gamma$ -camera images indicated a first-pass extraction of the order of 20–30% for all three compounds. In one rat that stopped breathing at about 20 s after injection of NC( $^{13}\text{NO}$ ), dissection and

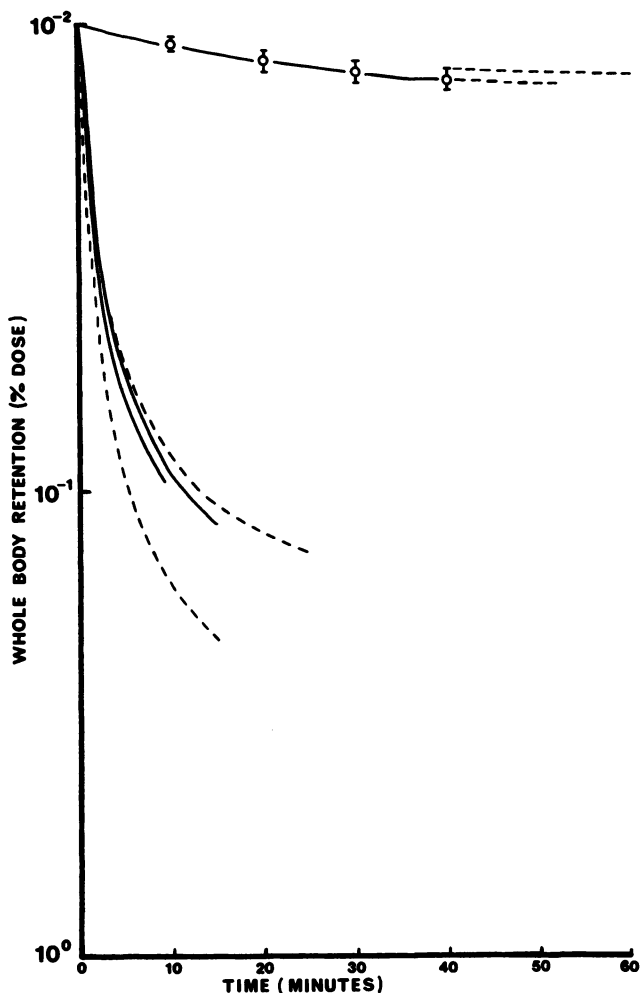


Figure 2. Whole body retention of  $^{13}\text{N}$  (corrected for decay) after iv injection of N-nitroso compounds in rats: (O) BCNU( $^{13}\text{NO}$ ); (—) BCNC( $^{13}\text{NO}$ ); (---) NC ( $^{13}\text{NO}$ )

radioassay of several tissues revealed 25% dose in the lungs and 10% in the liver. Twenty-two percent of injected  $^{13}\text{N}$  had been lost in expired air.

**$^{13}\text{N}$  Content of Blood and Urine Following iv Injection of BCNU ( $^{13}\text{NO}$ ) in Rats.** The mean values ( $\pm$  standard error of the mean, 3–7 rats/point) of  $^{13}\text{N}$  relative concentration in the blood and percent dose in the urine at each of eight time points from 5 to 70 min after

**Table I.  $^{13}\text{N}$  Content of Blood and Urine Following  
iv Injection of BCNU( $^{13}\text{NO}$ ) in Rats**

Time (min):	<i>(Mean <math>\pm</math> s.e.m.)</i>							
	5	10	20	30	40	50	60	70
	<i>Blood: Relative Concentration<sup>a</sup></i>							
	0.908 $\pm$ .018	0.702 $\pm$ .014	0.528 $\pm$ .049	0.472 $\pm$ .011	0.418 $\pm$ .020	0.445 $\pm$ .062	0.387 $\pm$ .025	0.386 $\pm$ .018
(n)	(7)	(5)	(6)	(5)	(5)	(7)	(3)	(3)
	<i>Urine: Percent Dose</i>							
	0.178 $\pm$ .022	1.49 $\pm$ .30	3.6 $\pm$ 1.4	4.70 $\pm$ .71	6.80 $\pm$ .94	7.91 $\pm$ .73	8.7 $\pm$ 2.0	11.1 $\pm$ 2.0
(n)	(7)	(5)	(5)	(6)	(6)	(7)	(4)	(3)
	<sup>a</sup> $\frac{\% \text{ Dose}}{\% \text{ Body Weight}}$							

injection are shown in Table I. Taking rat blood weight to be 6% of body weight (15), we see that only 5.4% of the injected  $^{13}\text{N}$  remained in circulation at 5 min. The net clearance of  $^{13}\text{N}$  from blood slowed considerably thereafter and relative concentration of label was essentially constant from 40 to 70 min after injection. Urinary excretion of  $^{13}\text{N}$  amounted to about 10% dose in 60–70 min.

**High-Pressure Liquid Chromatography.** The radiochemical purity of freshly prepared BCNU( $^{13}\text{NO}$ ) was found to be greater than 98% by radiomonitored high-pressure liquid chromatography (HPLC). Nitrogen-13 excreted in the urine (samples collected at 15, 30, and 40 min) was shown to be contained in a single peak, with retention time longer than that of BCNU. Any  $^{13}\text{N}$  present in the form of molecular nitrogen would have appeared at the solvent front. No such activity was observed.

**Intragastric Injection of Nitrosocarbaryl( $^{13}\text{NO}$ ).** Measurements of  $^{13}\text{N}$  recovered in the gastrointestinal tracts (with contents, unless otherwise noted) and livers of individual rats are given in Table II. Patency of the ligations was demonstrated by the grossly distended state of the ligated stomachs at dissection. In both groups, the  $^{13}\text{N}$  content of the remainder of the body was less than 1% of the administered dose. Thus, in each rat studied, some portion of the injected  $^{13}\text{N}$  was volatilized, the amount increasing with time after administration. The results for rats with ligated stomachs show clearly that volatilization of the  $^{13}\text{N}$ -nitroso label took place in the stomach itself. Significant amounts of  $^{13}\text{N}$  were also found in the stomach wall.

**In Vitro Aqueous Decomposition Measurements.** The decomposition rate constants of BCNU in buffers of various pH as measured by

the net rate of loss of <sup>13</sup>N from solution ( $T = 25.5^\circ\text{C}$ ) are plotted against pH in Figure 3. Rate constants reported by Loo and coworkers (16), obtained by a colorimetric assay of intact BCNU in solution (and by UV absorbance, for  $\text{pH} > 8.0$ ), for several types of buffers, at  $25^\circ\text{C}$  and  $37^\circ\text{C}$ , are also shown for comparison. The precision of the <sup>13</sup>N method is greatest for rapid decomposition rates. Its lower limit of detection is of the order of  $2 \times 10^{-4} \text{ min}^{-1}$ . The values obtained by us for  $\text{pH} < 8$ , when combined with those of Loo et al., for  $25^\circ\text{C}$ , appear to vary with pH in a manner similar to their results for  $37^\circ\text{C}$ . The pH dependence in this range is also similar in form to that reported for *N,N'*-dimethyl-*N*-nitrosourea by Garrett and Goto (UV absorbance measurements) (17). (The data from their Table 1 for acetate, phosphate, and borate buffers in overlapping pH ranges are plotted in Figure 4). The three rate constants found in the present study for  $\text{pH} > 9$ , however, do not exhibit the expected increase with increasing pH. An anomalous set of results for  $\text{pH} > 9$  was also obtained for NC(<sup>13</sup>NO) and BCNC(<sup>13</sup>NO) as shown in Figure 5. For  $\text{pH} \leq 8.25$ , the pH dependence of nitroso-carbaryl decomposition resembles that of the aforementioned nitroso-ureas, with the possible exception of a shallower rise at low pH. From pH 9.5 to 12, however, there is little, if any, increase in the rate of decomposition. No points are shown for BCNC for  $\text{pH} < 8$  because, in seven buffers ranging in pH from 1.28 to 7.57, there was no detectable volatilization of <sup>13</sup>N. The results, for two measurements each, of rate of

**Table II.** <sup>13</sup>N Content of Rat Organs Following Intra-gastric Administration of Nitrosocarbaryl(<sup>13</sup>NO)<sup>a</sup>

	<i>Stomach Not Ligated</i>			
	<i>40 min</i>	<i>50 min</i>	<i>50 min</i>	
Stomach	95.7	93.0	83.5	
Small intestine	0.12	0.39	2.3	
Colon and caecum	0.02	0.02	0.03	
Liver	0.12	0.15	0.24	
	<i>Stomach Ligated</i>			
	<i>59 min</i>	<i>62 min</i>	<i>94 min</i>	<i>97 min</i>
Stomach (intact)	67.8	83.8	54.4	47.3
Stomach wall	4.5	2.7	4.2	6.8
Stomach contents	23.4	52.4	46.2	31.3
(Gas phase) <sup>b</sup>	39.8	28.7	4.1	9.2
Small intestine	0.03	0.03	0.07	0.05
Colon and caecum	0.02	0.004	0.03	0.08
Liver	0.25	0.14	0.34	—

<sup>a</sup> Data reported as percent dose (individual cases).

<sup>b</sup> Intact Stomach - (Wall + Stomach Contents).



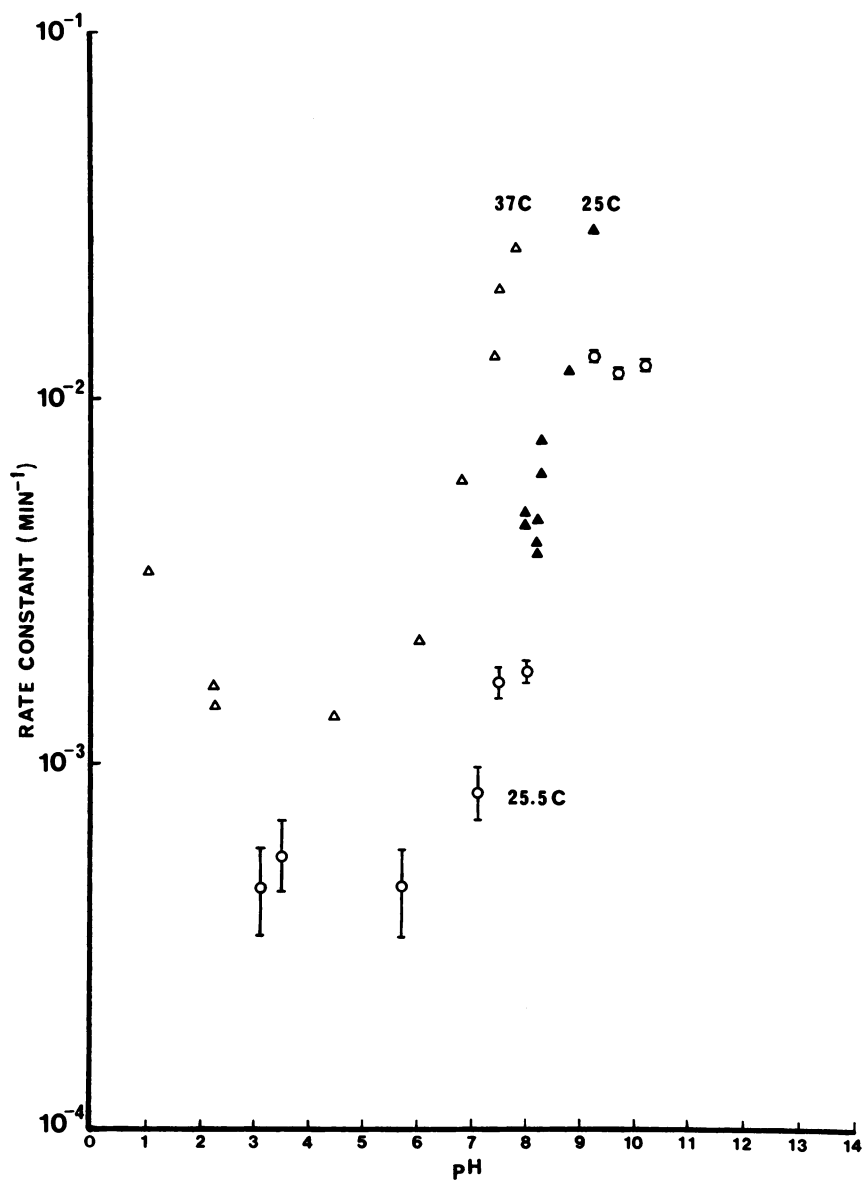


Figure 3. Decomposition rate constants of BCNU in aqueous media vs. pH: (○) values obtained in this study; (▲, △) values reported by Loo et al. (16)

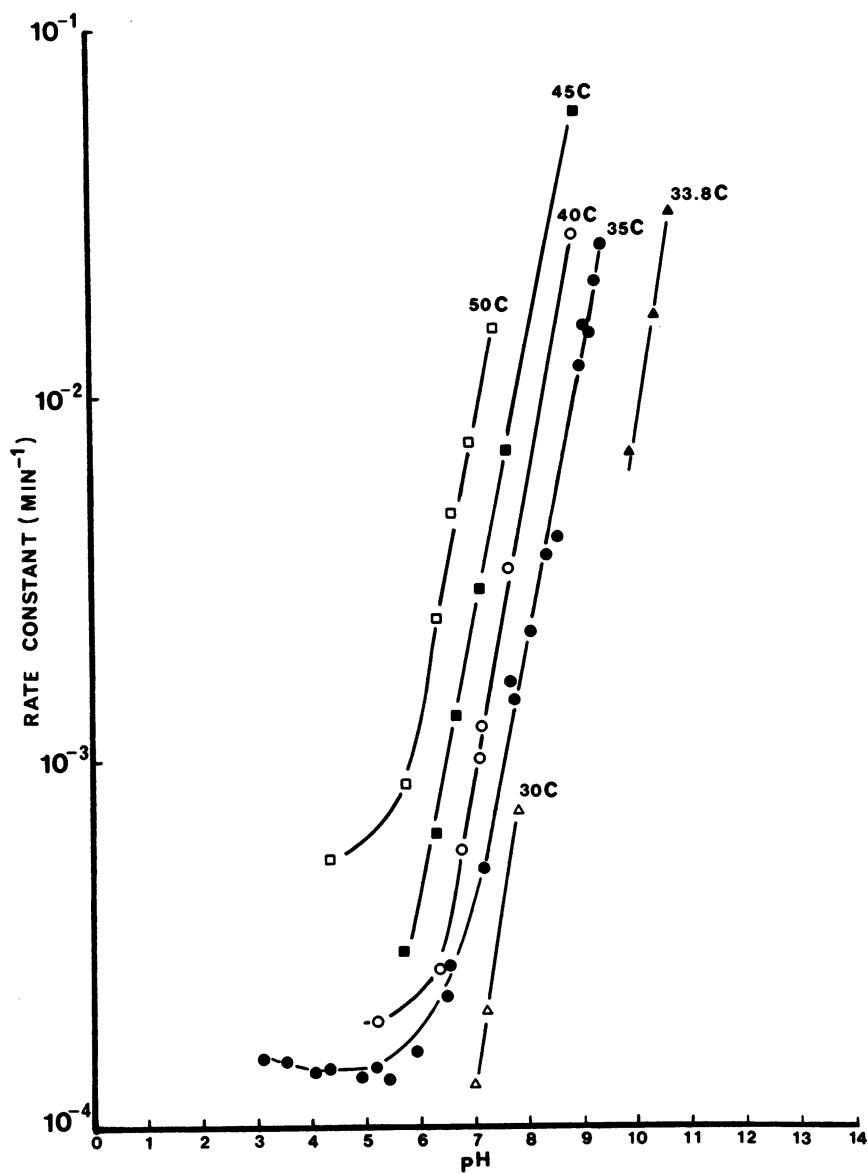


Figure 4. Decomposition rate constants of N,N'-dimethyl-N-nitrosourea in aqueous media vs. pH at various temperatures; values from Garrett and Goto (17)

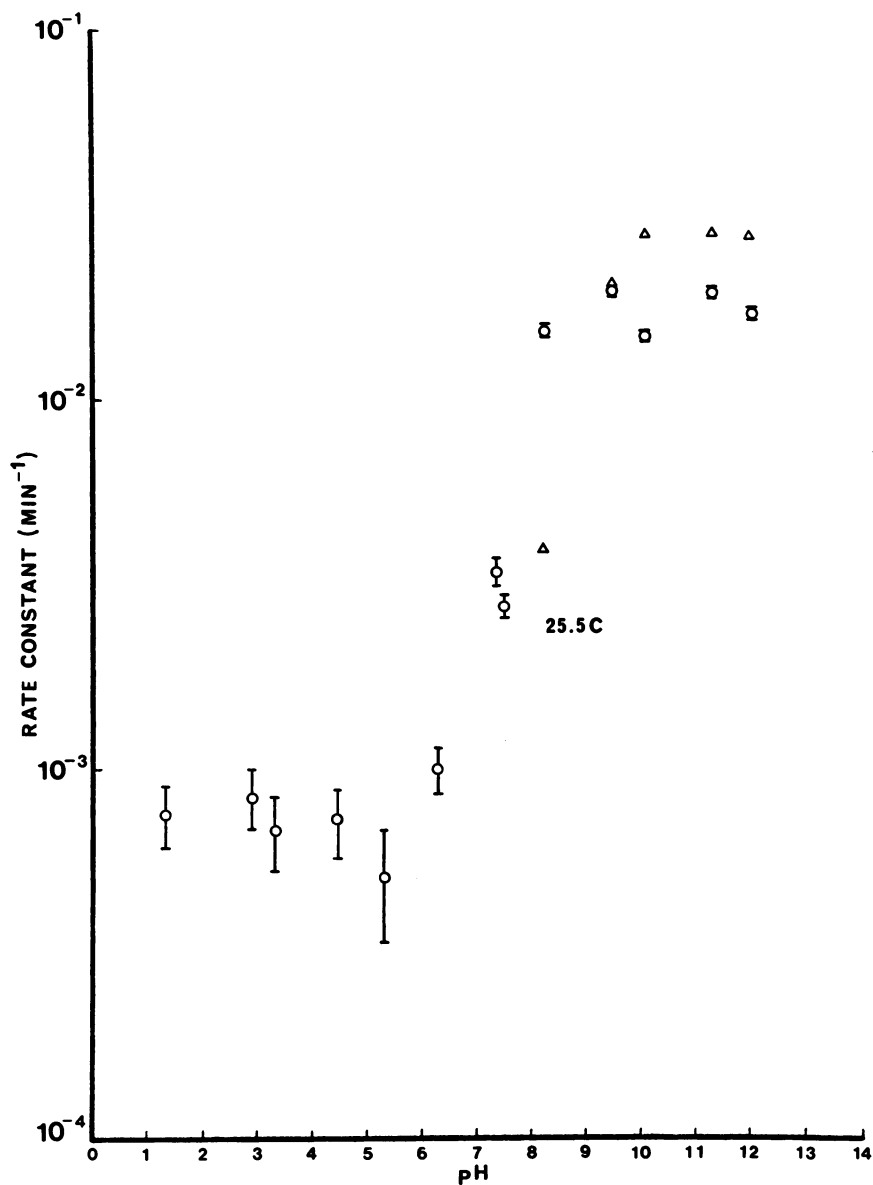


Figure 5. Decomposition rate constants of ( $\Delta$ ) BCNC and (O) nitrosocarbaryl in aqueous media vs. pH

breakdown in heparinized rat blood ( $T = 25.5^{\circ}\text{C}$ ), in units of  $10^{-3} \text{ min}^{-1}$  were: BCNU(<sup>13</sup>NO): 3.26, 3.53; NC(<sup>13</sup>NO): 16.6, 17.5; BCNC(<sup>13</sup>NO): 19.5, 23.5.

### Discussion

These experiments are, to our knowledge, the first investigations of the in vivo fate of the nitroso-nitrogen of an *N*-nitrosoourea or carbamate. The results obtained for BCNU(<sup>13</sup>NO) are clearly at variance with some generally held concepts of the metabolism of this chemotherapeutic agent.

Several investigators have measured the disappearance of intact BCNU from plasma after intravenous injection in dogs (16), humans (18), and rats (19) and have estimated "half-times" of 15–20 min for this process. [De Vita et al. did not detect BCNU in the plasma of humans or monkeys as early as 5 min after iv injection (20), but their method of assay was apparently the limiting factor]. Other investigators have determined the duration of effective (carcinostatic) drug levels (in mice), and have obtained half-times of similar magnitude, by following a dose of BCNU with an inoculation of tumor cells and demonstrating a falloff of therapeutic effect (survival time) with increase of time between the two administrations (21, 22, 23).

Judging by the frequent references to several of these studies in the BCNU literature in connection with the "biological half-life" of the drug, they appear to have been widely interpreted as providing a measure of the rate of breakdown of BCNU in the body as a whole.

Extensive study has been made of the modes of aqueous decomposition of BCNU, at least in part for the purpose of elucidating its mechanism of antitumor activity (24–28). Montgomery and coworkers found that N<sub>2</sub> was quantitatively evolved during aqueous decomposition of the drug and used nitrogen production as the measure of rate of reaction (24). Furthermore, all aqueous decomposition schemes proposed to date for BCNU place the *N*-nitroso group in unstable intermediates (e.g., diazohydroxides) from which N<sub>2</sub> is promptly evolved (16, 24–30).

As pointed out by Levin et al., it has been generally assumed that breakdown of BCNU in vivo is essentially a chemical, rather than metabolic, process (19), that is, that it follows the modes of decomposition observed in vitro. Thus, combining this assumption with the widely held notion of the rate of in vivo degradation, one would expect the iv injection of BCNU in a rat to result in the equimolar production of molecular nitrogen, with a half-time of 15–20 min. That most nitrogen so produced would be lost within minutes in expired air follows from the known kinetics of N<sub>2</sub> elimination in humans (31, 32, 33) and the more than threefold greater resting specific cardiac output (mL/min/kg body weight) of rats (34).

Instead, a more modest degree of volatilization was observed (Figure 2), amounting to 19–30% dose at 40 min (four rats). Moreover, the rather gradual slopes of the WBR curves beyond 40 min indicate that a considerable fraction of the injected nitroso-nitrogen may remain in the body for many hours. It should be noted that this rate of volatilization is considerably slower than the reported *in vitro* decomposition rates for BCNU at 37°C in phosphate buffer ( $t_{1/2} = 50\text{--}57$  min) (16, 19, 24) and in rat serum, liver supernatant, and liver microsomes ( $t_{1/2} = 24\text{--}27$  min) (19). Thus, the  $^{13}\text{N}$  WBR measurements imply that either the rate of breakdown of BCNU *in vivo* is slower than is generally thought or that a large portion of the dose is metabolized in a manner that does not convert the  $^{13}\text{N}$  label to gaseous nitrogen.

That at least one metabolic pathway exists that does not involve evolution of  $\text{N}_2$  has been demonstrated by Hill, Kirk, and Struck, who found that BCNU was denitrosated to BCU by mouse liver microsomes and lung homogenates (35). Our finding of an  $^{13}\text{N}$ -containing urinary metabolite (which, although not identified, was clearly not molecular nitrogen) in the amount of 10% dose at 60–70 min after injection, at which time the urinary excretion curve was apparently still rising, shows that one or more non- $\text{N}_2$ -producing pathways represent a significant part of BCNU metabolism. The lack of appearance of a peak corresponding to intact BCNU agrees with the reports of several investigators that, at most, tenths of a percent of administered BCNU are found in the urine of dogs (18), humans (20), monkeys (20), or rats (36).

Combining our  $^{13}\text{N}$  respiratory loss and urinary excretion measurements provides a minimum value for the rate of BCNU degradation in the rat: about 40% in 1 h. It is of interest here to consider the data of Levin, Kabra, and Freeman-Dove (37) for the intact BCNU concentrations of six rat tissues after *iv* injection of 40  $\mu\text{mol/kg}$  BCNU (chloroethyl- $^{14}\text{C}$ ) (37). Conversion of their data for 40 min after injection to units of relative concentration gives values between 0.1 and 0.2 for striated muscle, omental fat, liver, lung, and brain and a value of 0.8 for the kidney. If the concentrations of the first five tissues were typical of the body as a whole, then only 10–20% of the injected BCNU was intact at 40 min. If this estimate is correct, then most of the breakdown of BCNU in the rat does not involve the production of  $\text{N}_2$ .

Determining whether the carcinostatic activity of BCNU is associated with  $\text{N}_2$ -producing or non- $\text{N}_2$ -producing modes of metabolism represents a potentially fruitful area for further study. The former eventuality would permit the monitoring of such activity *in vivo* by following the washout of  $^{13}\text{N} \cdot \text{N}$  from the region of interest, utilizing external scintigraphic techniques. The latter eventuality might permit the identification of  $^{13}\text{N}$ -containing metabolites in the tumor tissue, which would yield valuable information on the drug's mechanism of action.

In contrast to the results for BCNU(<sup>13</sup>NO), iv injection of the two labeled nitrosocarbamates yielded a remarkably rapid evolution of <sup>13</sup>N, one that may conceivably have been limited by blood flow and breathing rate rather than by the rate of reaction. It appears that the lungs, which extracted a substantial portion of the injected dose, either by virtue of the high lipid solubility of the nitrosocarbamates or by trapping of precipitates formed in the blood upon injection, were an important site of metabolism of these compounds.

Since the structures of BCNU and its carbamate analog are identical except for the O-for-NH substitution, this position is clearly the key to the extreme biological reactivity of the latter compound. This point is reinforced by the quite similar in vivo elimination rates of the nitroso-nitrogen of BCNC and nitrosocarbaryl despite the differences in their end groups. The observed reactivity of these compounds may result from the hydrolytic action of esterases, which are known to attack the C—O bond in carbamate insecticides (38).

The fate of intragastric NC(<sup>13</sup>NO) was somewhat less dramatic than that given intravenously, perhaps due to lack of suitable enzymes in the environment of the stomach, to its relative stability at acid pH, or both. Nevertheless, considerable breakdown occurred in the stomach itself, as evidenced by the appearance of 30–40% of the label in the gas phase at 1 h. Since absorption of intact NC(<sup>13</sup>NO) into the bloodstream would be expected to produce rapid, quantitative volatilization of the label, as for iv injection, it cannot be excluded that some portion of the <sup>13</sup>N evolved from the rat in each case took this route. However, the low aqueous solubility of nitrosocarbaryl and the strictly local nature of its carcinogenic action when administered subcutaneously (6) or intragastrically (3, 7, 8) suggest that absorption of the intact compound was minimal. In light of the results noted above, it would be interesting, although evidently technically difficult, to study the carcinogenicity of nitrosocarbaryl by iv injection.

Examination of the in vitro decomposition measurements for BCNU, BCNC, and nitrosocarbaryl shows that they are poor predictors of the relative in vivo fates of these compounds. For example, while the rate constant (at 25.5°C) for NC is about 1.8 times that for BCNU in aqueous buffer pH 7.4 and 5 times that for BCNU in whole rat blood, these values barely hint at the radically different results produced by iv injection of these compounds in rats. For BCNC, the rates of decomposition at acid and neutral pH appear to be lower than those of BCNU, in contrast to the far greater in vivo reactivity of the former vs. the latter compound.

Unlike the case with BCNU, there do not appear to be any published reports of N<sub>2</sub> production from the aqueous decomposition of nitrosocarbamates. We have demonstrated volatilization of the <sup>13</sup>N-labeled nitroso-nitrogen of BCNC and nitrosocarbaryl, both in vivo and

in vitro. Although we did not identify the volatile species, a theoretical analysis of the possible modes of decomposition as well as the rapidity of in vivo loss strongly suggest that it was molecular nitrogen.

As noted in the experimental section, it was assumed that  $^{13}\text{N}$  label evolved by the aqueous decomposition of the compounds studied would be rapidly lost from solution into ambient air. The failure of our measurements to exhibit the expected rate vs. pH dependence for  $\text{pH} > 9$  may indicate that at high decomposition rates the rate of loss of evolved  $^{13}\text{N}$  from solution represents a significant limitation on the accuracy of the method.

In summary, we believe this chapter illustrates the wide range of investigative possibilities that use of the short-lived radionuclide  $^{13}\text{N}$  offers in the study of *N*-nitroso compounds.

### Acknowledgment

The authors wish to acknowledge the support and guidance of Dr. John S. Laughlin of the Biophysics Laboratory during the course of this investigation. Thanks are also extended to R. Lee for operation of the cyclotron. This work was supported in part by NCI Grant CA-18153-03, DOE Contract. EE-77-S-4268, NCI Core Grant CA-08748-14, NCI Grant CA-17786, and the University of Kentucky Tobacco and Health Institute Grant No. 22011.

### Literature Cited

1. Skipper, H. E.; Schabel, F. M.; Trader, M. W.; Thompson, J. R. *Cancer Res.* **1961**, *21*, 1154.
2. Schabel, F. M.; Johnston, T. P.; McCaleb, G. S.; Montgomery, J. A.; Laster, W. R.; Skipper, H. E. *Cancer Res.* **1963**, *23*, 725.
3. Lijinsky, W.; Schmahl, D. *Ecotox. Environ. Safety* **1978**, *2*, 413.
4. Elespuru, R.; Lijinsky, W.; Setlow, J. K. *Nature* **1974**, *247*, 386.
5. Seiler, J. P. *Mutation Res.* **1977**, *48*, 225.
6. Eisenbrand, G.; Ungerer, O.; Preussman, R. *Food Cosmet. Toxicol.* **1975**, *13*, 365.
7. Eisenbrand, G.; Schmahl, D.; Preussman, R. *Cancer Lett.* **1976**, *1*, 281.
8. Lijinsky, W.; Taylor, H. W. *Cancer Lett.* **1976**, *1*, 275.
9. Bestian, H. *Ann. Chem.* **1950**, *566*, 210.
10. McQuinn, R. L.; Cheng, Y. C.; Digenis, G. A. *Synth. Commun.* **1979**, *9*(1), 25.
11. Tilbury, R. S.; Dahl, J. R. *Radiat. Res.* **1979**, *79*, 22.
12. Pettit, W. A.; Tilbury, R. S.; Digenis, G. A.; Mortara, R. H. *J. Lab. Comp. Radiopharm.* **1977**, *13*, 119.
13. Freed, B. R.; Reiman, R. E., unpublished data.
14. Woodard, H. O.; Bigler, R. E.; Freed, B. R.; Russ, G. A. *J. Nucl. Med.* **1975**, *16*, 958.
15. Everett, N. B.; Simmons, B.; Lasher, E. P. *Circ. Res.* **1956**, *4*, 419.
16. Loo, T. L.; Dion, R. L.; Dixon, R. L.; Rall, D. P. *J. Pharm. Sci.* **1966**, *55*, 492.

17. Garrett, E. R.; Goto, S. *Chem. Pharm. Bull.* **1973**, *21*, 1811.
18. Levin, V. A.; Hoffman, W.; Weinkam, R. J. *Cancer Treat. Rep.* **1978**, *62*, 1305.
19. Levin, V. A.; Stearns, J.; Byrd, A.; Finn, A.; Weinkam, R. J. *J. Pharmacol. Exp. Ther.* **1979**, *208*, 1.
20. De Vita, V. T.; Denham, C.; Davidson, J. D.; Oliverio, V. T. *Clin. Pharmacol. Ther.* **1967**, *8*, 566.
21. Chirigos, M. A.; Humphreys, S. R.; Goldin, A. *Cancer Chem. Rep.* **1965**, *49*, 15.
22. Schabel, F. M. *Proc. Chemother. Conf. Chemother. Sol. Tumors, An Appraisal of 5-Fluorouracil and BCNU, N.C.I., Bethesda, 1970*, p. 159-180.
23. Connors, T. A.; Hare, J. R. *Biochem. Pharmacol.* **1975**, *24*, 2133.
24. Montgomery, J. A.; James, R.; McCaleb, G. S.; Johnston, T. P. *J. Med. Chem.* **1967**, *10*, 668.
25. Colvin, M.; Cowens, J. W.; Brundrett, R. B.; Kramer, B. S.; Ludlum, D. B. *Biochem. Biophys. Res. Comm.* **1974**, *60*, 515.
26. Montgomery, J. A.; James, R.; McCaleb, G. S.; Kirk, M. C.; Johnston, T. P. *J. Med. Chem.* **1975**, *18*, 568.
27. Brundrett, R. B.; Cowens, J. W.; Colvin, M. *J. Med. Chem.* **1976**, *19*, 958.
28. Colvin, M.; Brundrett, R. B.; Cowens, W.; Jardine, I.; Ludlum, D. B. *Biochem. Pharmacol.* **1976**, *25*, 695.
29. Reed, D. J.; May, H. E.; Boose, R. B.; Gregory, K. M.; Beilstein, M. A. *Cancer Res.* **1975**, *35*, 568.
30. Brundrett, R. B.; Colvin, M. *J. Org. Chem.* **1977**, *42*, 3538.
31. Boothby, W. M.; Lundin, G.; Helmholz, H. F. *Proc. Soc. Exp. Biol. Med.* **1948**, *67*, 558.
32. Jones, H. B. In "Medical Physics", 2nd ed.; Glasser, O., Ed.; Yearb. Med.: Chicago, 1950; pp. 885-871.
33. Matthews, C. M. E.; Dollery, C. T. *Clin. Sci.* **1965**, *28*, 573.
34. Guyton, A. C.; Jones, C. E.; Coleman, T. G. "Circulatory Physiology: Cardiac Output and Its Regulation", 2nd ed.; W. B. Saunders: Philadelphia, 1973; p. 6-11.
35. Hill, D. L.; Kirk, M. C.; Struck, R. F. *Cancer Res.* **1975**, *35*, 296.
36. McQuinn, R. L., Ph.D. Dissertation, Univ. Kentucky, 1978.
37. Levin, V. A.; Kabra, P. A.; Freeman-Dove, M. A. *Cancer Chem. Pharmacol.* **1978**, *1*, 233.
38. Kuhr, R. J.; Dorough, H. W. "Carbamate Insecticides: Chemistry, Biochemistry and Toxicology"; C. R. C.: Cleveland, 1976; Chap. 3.

RECEIVED September 4, 1980.



# $^{13}\text{N}$ as a Tracer for Studying Ammonia Uptake and Metabolism in the Brain

ARTHUR J. L. COOPER and THOMAS E. DUFFY

Departments of Neurology and Biochemistry, Cornell University Medical College, New York, NY 10021

JOSEPH M. McDONALD and ALAN S. GELBARD

Biophysics Laboratory, Memorial Sloan-Kettering Cancer Center, New York, NY 10021

*The uptake and metabolism of [ $^{13}\text{N}$ ]ammonia in the rat brain have been investigated. The results show that blood-borne ammonia (and cerebrospinal fluid ammonia) enters the brain largely by diffusion of the free base. On entering the brain much of the [ $^{13}\text{N}$ ]ammonia is rapidly metabolized ( $t_{1/2} = 1-3$  s); 99% is incorporated into glutamine and only a small fraction appears in glutamate (1%). Specific activity measurements of metabolites, following infusion of [ $^{13}\text{N}$ ]ammonia, confirm the hypothesis that the brain contains at least two separate compartments of glutamate metabolism. A computer model that simulates the flow of  $^{13}\text{N}$  into various compartments and metabolites following either a bolus injection or continuous infusion of [ $^{13}\text{N}$ ]ammonia has been devised, and the results of this simulation agree with experimental observations.*

In recent years there has been a great deal of interest in understanding the mechanisms involved in ammonia metabolism in brain. The reasons for this interest are twofold: ammonia is thought to be a major toxin contributing to the symptoms of encephalopathy associated with liver disease (1, 2) and of Reye's disease (3); and earlier experiments with  $^{15}\text{N}$ -labeled ammonia suggested the existence of at least two distinct metabolic pools in brain (4).

**Ammonia as a Neurotoxin.** Several compelling reasons underlie the belief that ammonia is a major toxin contributing to the symptoms of hepatic encephalopathy (1, 2, 5, 6, 7). Ammonia is toxic to the brain in

0065-2393/81/0197-0369\$05.00/0

© 1981 American Chemical Society

hereditary hyperammonemia (congenital defects of the urea cycle) (8). Electroencephalographic changes and neuropathological abnormalities that resemble those of human hepatic encephalopathy can be induced in alert monkeys by chronic infusions of ammonium salts (9). Ammonia concentrations in blood and cerebrospinal fluid (CSF) show a high correlation with hepatic encephalopathy in patients (10). Rats made chronically hyperammonemic, by the surgical construction of a portacaval anastomosis, are extremely sensitive to a small ammonia challenge (11). The currently most effective treatments for patients with hepatic coma are those directed toward reducing the plasma ammonia concentration (12).

**The Two-Pool Hypothesis Based on Studies of Brain Ammonia Metabolism.** Schoenheimer and colleagues, in a series of classical experiments, administered [ $^{15}\text{N}$ ]ammonia or  $^{15}\text{N}$ -labeled amino acids to rats and were the first to demonstrate that nitrogen derived from ammonia was incorporated into urea, the amide group of glutamine, other amino acids, and creatine (cf. 13). It had originally been assumed that deamination of L-amino acids in vivo was accomplished by the consecutive action of a specific  $\alpha$ -ketoglutarate-dependent transaminase and glutamate dehydrogenase (14) and that incorporation of  $^{15}\text{N}$ , derived from [ $^{15}\text{N}$ ]ammonia, into amino acids occurred by the reversal of this reaction. However, Duda and Handler showed that, in the brain and other organs, the major fate of  $^{15}\text{N}$ , whether administered intravenously as [ $^{15}\text{N}$ ]ammonia or derived from endogenously produced [ $^{15}\text{N}$ ]ammonia (as in the breakdown of D- [ $^{15}\text{N}$ ]leucine), was incorporation into the amide group of glutamine (15). Later Waelsch and coworkers carried out a number of investigations in which they determined the metabolic fate of  $^{14}\text{C}$ -labeled glutamate in the brain (16, 17). Comparison of the specific activities of glutamate vs. glutamine led to the conclusion that glutamate metabolism was compartmentalized in the brain. In later experiments,  $^{15}\text{N}$ -labeled ammonia was infused into the right common carotid artery of cats (4) and the incorporation of the label into the  $\alpha$ -amino group of glutamine, the amide group of glutamine, and the  $\alpha$ -amino group of glutamate was determined for the brain and liver. Analysis of the results indicated that blood-borne ammonia was converted to glutamine in the brain in a rapidly turning over compartment of glutamate; this compartment was metabolically distinct from a more slowly turning over, larger glutamate compartment (4). In contrast to the brain, the liver was shown to contain only one pool of glutamate (4). These early experiments were the starting point for a large number of metabolic studies designed to characterize further the nature of the two cerebral compartments. Thus,  $^{14}\text{C}$ -labeling patterns obtained after administration of  $^{14}\text{C}$ -acetate indicated the existence of separate TCA cycles in the small and large pools (18, 19, 20, 21).

A criticism of the early studies with  $^{15}\text{N}$ -labeled ammonia and ammonia precursors is that they were often carried out under nonphysiological conditions. We reinvestigated the metabolic fate of blood-borne ammonia at physiological concentrations of ammonia in awake rats, using  $^{13}\text{N}$  as a tracer (22). The findings confirm the existence of the two pools for brain glutamate metabolism and emphasize the importance of glutamine synthetase in the brain for ammonia detoxification. These tracer studies also showed that the metabolic compartmentation was lost after inhibition of brain glutamine synthetase by methionine sulfoximine (22).

**Use of  $^{13}\text{N}$  as a Tracer for Ammonia in the Brain.** With the introduction of newer, more sensitive, and more accurate detection techniques, minute quantities of  $^{15}\text{N}$  can be analyzed. However, limitations to the use of  $^{15}\text{N}$  as a tracer would seem to be its natural abundance (0.37%) and the small variation of  $^{15}\text{N}$ -content in nature. A small amount of metabolite of high  $^{15}\text{N}$ -content, entering a large unlabeled pool might raise the  $^{15}\text{N}$ -content of endogenous metabolite only slightly above background. Such a small increase of  $^{15}\text{N}$  would be difficult to quantitate accurately. In contrast, because there is no natural  $^{13}\text{N}$ , relatively small amounts of high-specific-activity [ $^{13}\text{N}$ ]ammonia can be administered to experimental animals without disruption of the physiological steady state. Furthermore, because  $^{13}\text{N}$  gives rise to gamma radiation via positron annihilation, it is easier to quantitate than  $^{15}\text{N}$  and has the added advantage that it can be detected in vivo by external imaging devices.

$^{13}\text{N}$  has two major drawbacks as a biological tracer: its use is limited to those institutions that possess a cyclotron; and since it has a short half-life (10 min), it can only be used in experiments of relatively short duration. Although few studies have been carried out using  $^{13}\text{N}$  as a tracer for uptake and metabolism of ammonia by the brain (e.g., 22, 23, 24, 25), initial findings indicate that  $^{13}\text{N}$ , despite its short half-life, is eminently suitable for this purpose.

### *Production of [ $^{13}\text{N}$ ]Ammonia*

$^{13}\text{N}$ -Labeled ammonia has been generated by the bombardment of methane gas (26) or metal carbides (27) with high-energy deuterons. The method that is now used at the Memorial Sloan-Kettering Cancer Center is to bombard water with protons. The chemical form of the generated  $^{13}\text{N}$  is mostly nitrate, with smaller amounts of nitrite and very small amounts of ammonia (28). However, the [ $^{13}\text{N}$ ]nitrate and [ $^{13}\text{N}$ ]nitrite are readily converted to [ $^{13}\text{N}$ ]ammonia with a Devarda's alloy-NaOH mixture (29). The [ $^{13}\text{N}$ ]ammonia produced by the reduction reaction is flushed into 3 mL of physiological saline or buffer. Theoretically, the label should be carrier-free. However, it is impossible to exclude ammonia completely. Some unlabeled ammonia apparently arises from the De-

varda's alloy-sodium hydroxide mixture, so that dilution of the specific activity always occurs (22). Typically, after flushing into buffer the concentration of ammonia is in the range 80–200  $\mu\text{M}$  and the total  $^{13}\text{N}$ -radioactivity is in the range 20–100 mCi (22, 25).

### *Dynamics of [ $^{13}\text{N}$ ]Ammonia Uptake and Metabolism by the Brain as Assessed by External Imaging*

**Studies on the Whole Brain.** The dynamics of uptake of label by the brain in vivo following a bolus injection of [ $^{13}\text{N}$ ]ammonia have been investigated in animals and in human beings (23, 24, 25). Phelps et al. found that the single-pass extraction of [ $^{13}\text{N}$ ]ammonia by cerebral capillaries (internal carotid artery injection) was inversely related to blood flow and was limited by the permeability of the blood-brain barrier to ammonia (23, 24). In a comparable experiment in which [ $^{13}\text{N}$ ]ammonia was administered intravenously, Lockwood et al. determined that the single-pass extraction of ammonia in the human brain was 47% (25). Moreover, Lockwood et al. showed that: In 5 normal subjects and in 17 patients with liver disease, the rate of [ $^{13}\text{N}$ ]ammonia clearance from the vascular compartment and the brain ammonia utilization rate were linear functions of the arterial ammonia concentration, at least over the range of 50–250  $\mu\text{M}$ ; the ammonia utilization reaction(s) appeared to take place in a compartment that included <20% of all brain ammonia.

The fraction of [ $^{13}\text{N}$ ]ammonia extracted by the rhesus monkey brain was found to be independent of ammonia concentration over an 18-fold range in the arterial blood (24), indicating that ammonia enters the brain largely by diffusion of the free base and not by an active transport system (see also the discussion on the brain uptake index that follows). In the human and the monkey studies,  $^{13}\text{N}$ -activity rapidly approached a maximum in the brain soon after injection of the isotope and thereafter remained fairly constant despite the rapid clearance of the label from the blood (24, 25). It was concluded that [ $^{13}\text{N}$ ]ammonia, upon entering the brain, was rapidly metabolized.

**Localization of Tumors and Infarcted Regions of the Brain.**  $^{13}\text{N}$ -Labeled ammonia has been used as a means of producing tomographic images of the human brain (23, 24, 30, 31, 32, 33) and to delineate infarcted regions of the brain (23, 24). Phelps et al. showed that the magnitude of the uptake of label in different brain structures was in good agreement with the magnitude of the relative capillary density and/or blood flows through these structures. These investigators suggested that [ $^{13}\text{N}$ ]ammonia may be of use in the early detection of cerebral perfusion defects (23, 24). However, caution is necessary in interpreting brain images obtained with [ $^{13}\text{N}$ ]ammonia, because its usefulness as a blood-flow marker depends on its rapid chemical fixation

(presumably as glutamine) in the brain. Since glutamine synthetase is ATP-dependent and ATP is depleted during ischemia (34), failure of the brain tissue to fix the label could result from impaired metabolic trapping rather than from decreased blood flow.

Other investigators have attempted to use [ $^{13}\text{N}$ ]ammonia to image human brain tumors, with varying success (33). Thus it was found that uptake in a meningioma was greater than that of surrounding tissue, the same in an acoustic neuroma, and depressed in a metastatic adenocarcinoma and a glioma (33). The results emphasize that although [ $^{13}\text{N}$ ]ammonia shows promise as a brain-imaging agent, its use for diagnostic purposes is still empirical.

### *Mechanism of Uptake of Blood-Borne [ $^{13}\text{N}$ ]Ammonia by Brain*

Ammonia ( $\text{NH}_3$ ) is thought to be diffusible across biological membranes, whereas ammonium ion ( $\text{NH}_4^+$ ) is relatively impermeable (35). The  $\text{pK}_a$  of ammonia is 9.15 (36), so that under physiological conditions approximately 1% of ammonia will be un-ionized. Cerebral uptake of blood-borne [ $^{13}\text{N}$ ]ammonia will be a complex function of blood pH, brain pH, lipid solubility of  $\text{NH}_3$ , and cerebral blood flow (CBF). To investigate some of these factors on the cerebral uptake of blood-borne [ $^{13}\text{N}$ ]ammonia in rats, we made use of the brain uptake index, or (BUI), technique. Oldendorf has introduced the term BUI to describe the uptake, following a carotid bolus injection, of a  $^{14}\text{C}$ -labeled test substance by the brain relative to a diffusible marker, such as  $^3\text{H}_2\text{O}$  (e.g., 37, 38, 39). Ideally, the diffusible marker should be 100% extracted by the brain, but as pointed out by Oldendorf and others, this is not the case for  $^3\text{H}_2\text{O}$  (38, 39). Raichle et al. have shown that  $n$ - $^{14}\text{C}$ -butyl alcohol is 99% extracted by the brain and have suggested that  $n$ -butyl alcohol may be used as the freely diffusible reference marker for BUI measurements (40). Following this suggestion, we measured the BUI of [ $^{13}\text{N}$ ]ammonia relative to  $n$ - $^{14}\text{C}$ -butyl alcohol; indium-111 diethylenetriaminepentaacetate ( $^{111}\text{In}$ -DTPA) was used as a blood marker to correct for incomplete washout (22). Briefly, a 0.2-mL bolus containing [ $^{13}\text{N}$ ]ammonia,  $^{111}\text{In}$ -DTPA, and  $n$ -[ $^{14}\text{C}$ ]butyl alcohol in physiological saline, pH 7.2–7.4, was injected rapidly via a cannula in the right common carotid artery of an awake rat. Five seconds later the animal was killed by decapitation, and the brain content of the three isotopes was determined by standard methods. The BUI for [ $^{13}\text{N}$ ]ammonia was calculated according to the equation

$$\text{BUI} = \left[ \frac{^{13}\text{N-tissue}/^{14}\text{C-tissue}}{^{13}\text{N-bolus}/^{14}\text{C-bolus}} - \frac{^{111}\text{In-tissue}/^{14}\text{C-tissue}}{^{111}\text{In-bolus}/^{14}\text{C-bolus}} \right] \times 100$$

and was found to be  $24\% \pm 1\%$  (SEM,  $n = 10$ ) (22). This value is lower than that obtained by Lockwood et al. (41). However, Lockwood et al. used rats anesthetized with phenobarbital at a concentration expected to almost halve the CBF (34). This lowered CBF would be expected to greatly increase the BUI relative to that obtained for unanesthetized animals. The values for the BUI of [ $^{13}\text{N}$ ]ammonia in the rat brain are lower than the single-pass extraction calculated for the monkey brain (43%, Ref. 24) and the human brain (47%, Ref. 25). However, as shown by Phelps et al. (24), the single-pass extraction is inversely proportional to blood flow; CBF is higher in the rat than in human beings (42).

Since the brain is relatively permeable to  $\text{NH}_3$  but not to  $\text{NH}_4^+$  (35), one would predict that the cerebral uptake of blood-borne ammonia would increase with increasing pH of the blood (an increase in pH will result in proportionally more of the un-ionized form of ammonia) (cf. 43, 44). Carter et al. (45) have shown that there is a positive correlation between blood pH and cerebral uptake of [ $^{13}\text{N}$ ]ammonia in the dog. We have found that the BUI for [ $^{13}\text{N}$ ]ammonia in normal and chronically hyperammonemic (portacaval shunt for eight weeks) rats is greatly increased by raising the pH of the injectate (Table I). Similar findings have been reported by Lockwood et al. for phenobarbital-anesthetized rats (41). The data for the BUI in normal and eight-week portacaval rats, although similar, cannot be compared directly, because the CBF is increased in rats that have been shunted for eight weeks (42; Duffy and Cruz, unpublished observation), and there is evidence that the blood-brain barrier is altered in such animals (11).

Although  $\text{NH}_4^+$  is relatively impermeable to biological membranes, it is conceivable that some  $\text{NH}_4^+$  enters the brain by a carrier system. However, the available evidence does not support such a hypothesis. Thus, the single-pass extraction by the monkey brain is independent of

**Table I. Brain Uptake Index of [ $^{13}\text{N}$ ]Ammonia Relative to  $n$ -[1- $^{14}\text{C}$ ]Butyl Alcohol at Two pH Values\***

	<i>pH of Bolus</i>	<i>n</i>	<i>BUI (%)</i>
Control	7.2	6	$23.7 \pm 4.1$
Portacaval shunt	7.2	6	$21.3 \pm 3.1$
Control	8.6	5	$53.0 \pm 4.0$
Portacaval shunt	8.6	6	$57.2 \pm 2.5$

\*The injected bolus (0.2 mL) contained  $100\mu\text{M}$  ammonium chloride (20–100 mCi/mL) in  $10\text{mM}$  potassium phosphate buffer, pH 7.2, or in  $10\text{mM}$  HEPES-HCl buffer, pH 8.6. The values are the means  $\pm$  SEM;  $n$  = number of determinations. Controls were normal awake male Wistar rats weighing approximately 300 g. Portacaval shunts were animals in which a portacaval anastomosis had been surgically constructed according to the method of Lee and Fisher (46) eight weeks prior to the BUI determination.

**Table II. Brain Uptake Index for [<sup>13</sup>N]Ammonia Relative to *n*-[1-<sup>14</sup>C]Butyl Alcohol<sup>a</sup>**

<i>Concentration of Ammonia in Bolus (mM)</i>	<i>n</i>	<i>BUI (%)</i>
0.025	2	22.5, 20.1
0.59	2	20.1, 26.1
2.50	4	24.5 ± 0.4
26.0	2	25.1, 20.0

<sup>a</sup> From Cooper et al. (22).

arterial ammonia concentration over a 17-fold range (24) and in the human brain, over a 5-fold range (25). In addition, Carter et al. (45) showed that prior loading of the blood with unlabeled ammonia (at a constant blood pH) had no effect on the uptake of blood-borne [<sup>13</sup>N]-ammonia in the dog brain. In awake rats, the BUI for [<sup>13</sup>N]ammonia relative to *n*-<sup>14</sup>C-butyl alcohol was independent of ammonia concentration over a 1000-fold range (Table II). The concentration of ammonia within the bolus at the upper limit was approximately 300 times greater than the blood concentration (22). Taken together these data show that ammonia enters the brain largely by diffusion and that there is no saturable carrier system for ammonia (22).

The finding that the uptake of [<sup>13</sup>N]ammonia was only about 25% that of butyl alcohol suggests a diffusion limitation to the passage of the free base into the brain. The rate constant for the conversion of NH<sub>3</sub> + H<sup>+</sup> to NH<sub>4</sub><sup>+</sup> is  $4.3 \times 10^{10} \text{M}^{-1}\text{s}^{-1}$  (47). Compared with the brain capillary transit time in the rat (2–3 s, Ref. 39), the rate of interconversion between the ammonia base and the ammonium ion is far too rapid to be rate-determining for passage of ammonia into the brain (cf. 22, 23, 24). Therefore, the blood–brain barrier must be less permeable to the ammonia base than to *n*-butyl alcohol.

Assuming that ammonia enters and leaves the brain largely by diffusion of the free base, the expected brain ammonia concentration can be calculated from the Henderson–Hasselback equation (48). In fact, the concentration in the rat brain is in accord with the known values of blood ammonia, blood pH, brain pH, and pK<sub>a</sub> of ammonia (48). However, since diffusion of ammonia across the blood–brain barrier appears to be impeded (see above) and since ammonia entering the brain is, at least in part, rapidly converted to glutamine (see the section that follows), the equilibrium between blood and brain cannot be attributable to rapid mixing of blood and brain ammonia pools. This is borne out by the findings that whenever the normal blood/brain ammonia ratio is perturbed by administration of ammonium salts or by methionine sulfoximine poisoning, there is a delay in the reestablishment of the normal ratio (e.g., 11, 22, 43, 49). Kelley and Kazemi (49) have argued

that CNS ammonia production is an important buffer mechanism for controlling brain and CSF pH, implying that some of the brain ammonia is generated *de novo*. On the other hand, Hindfelt and Siesjö have proposed that during cerebral lactic acidosis, associated with ammonium acetate infusion, intracellular pH is maintained by a passive influx of ammonia from the blood (50). The relative importance of blood ammonia uptake vs. endogenous ammonia production in controlling brain pH is debatable. However, there is no doubt that the potential of the brain to generate ammonia *de novo* is considerable (51, 52).

### *Metabolism of [<sup>13</sup>N]Ammonia by the Brain*

**The Roles of Glutamine Synthetase and Glutamate Dehydrogenase.** Imaging experiments on the human and the monkey brain, following an injection of [<sup>13</sup>N]ammonia, have indicated that [<sup>13</sup>N]ammonia upon entering the brain is rapidly metabolized (23, 24, 25). To ascertain the nature of this fixation, we studied the cerebral uptake and metabolism of [<sup>13</sup>N]ammonia in rats. A bolus of [<sup>13</sup>N]ammonia was injected into awake restrained rats via a cannula placed in the right common carotid artery. The animals were killed 5 s later by a "freeze-blowing" technique (53) and the frozen brain tissue samples were analyzed for various <sup>13</sup>N-metabolites. Freeze-blowing ensures that postmortem ischemic changes of metabolites will be minimal. With this technique it was found that approximately 57% of the label recovered in the brain 5 s after a bolus injection was in a metabolized form (22), setting a maximum  $t_{1/2}$  for metabolism of blood-borne ammonia by the brain at approximately 3 s.

At 5 s following the bolus injection, more than 99% of the metabolized label was recovered in glutamine ( $\alpha$ -amine plus amide); <1% was in glutamate and aspartate (22). Thus, the major route for the metabolism (detoxification) of blood-borne ammonia by the brain is via the glutamine synthetase reaction. The glutamate dehydrogenase reaction, despite reports in the literature to the contrary (e.g., 54), appears to be a minor pathway for the detoxification of blood-borne ammonia by the brain. Although under ideal conditions glutamate dehydrogenase activity is greater than glutamine synthetase activity in crude brain homogenates (cf. 22), the concentration of ammonia in the whole brain is low ( $\sim 180 \mu\text{M}$ ) and the affinity of glutamine synthetase for ammonia is much greater than that exhibited by glutamate dehydrogenase [the apparent  $K_m$  values for ammonia exhibited by sheep brain glutamine synthetase and rat brain glutamate dehydrogenase are 0.18 and 10mM, respectively (55, 56)]. Therefore, the *in vivo* metabolism of blood-borne ammonia by glutamine synthetase will be favored over that by glutamate



dehydrogenase. A similar kinetic argument has been put forward by Dennis and Clarke (57), who concluded that "under most circumstances most  $\text{NH}_3$  fixation in the brain will occur by glutamine formation in the 'small compartment' and it is only under high ammonia concentrations that glutamate formation occurs via glutamate dehydrogenase in the 'large compartment'." Moreover, it seems probable that most, if not all, the glutamine synthetase activity is in a single compartment (small pool), whereas glutamate dehydrogenase activity is present both in small and large compartments (see the section beginning p. 378).

**Distribution of Label Among Various Brain Metabolites After Carotid Artery Infusion of [ $^{15}\text{N}$ ]Ammonia.** Compartmentation of glutamate metabolism in the brain has been inferred from specific activity measurements following the administration of a variety of  $^{14}\text{C}$ -labeled glutamate precursors (16, 17) and [ $^{15}\text{N}$ ]ammonia (4). Thus, Berl et al. found that after 20 min of continuous infusion of high concentrations of [ $^{15}\text{N}$ ]ammonia via the carotid artery of paralyzed and artificially ventilated cats, the relative incorporation of label into brain metabolites was of the order glutamate <  $\alpha$ -amino group of glutamine < amide group of glutamine (4). Since glutamate is the only known precursor of glutamine, the findings prompted Berl et al. (4) to put forward the hypothesis that cerebral glutamine was being synthesized (from blood-borne ammonia) in a compartment of glutamic acid that did not exchange readily with the remainder of brain glutamic acid.

By measuring the specific activity of various brain metabolites after 10 min of continuous infusion of physiological concentrations of [ $^{15}\text{N}$ ]ammonia into awake restrained rats, we were able to confirm the hypothesis of Berl, Waelsch, and coworkers. Thus, the order of the specific activity of various brain metabolites was: glutamate <  $\alpha$ -amino group of glutamine < amide group of glutamine. However, there were quantitative differences between our results (22) and those of Berl et al. (4). The major route for the metabolism of continuously infused [ $^{15}\text{N}$ ]ammonia was via the glutamine synthetase reaction; the glutamate dehydrogenase reaction was negligible ( $\sim 1\%$ ) (22). In contrast, in the experiments of Berl et al., approximately 30% of the label derived from [ $^{15}\text{N}$ ]ammonia was metabolized via the glutamate dehydrogenase reaction. Most likely, the difference is attributable to the unphysiologically high concentrations of ammonia used by Berl et al. At high concentrations of ammonia, such as may occur in disease, the brain glutamine synthetase reaction is likely to become saturated, and the glutamate dehydrogenase activity relative to the glutamine synthetase activity would be expected to increase, provided  $\alpha$ -ketoglutarate levels do not fall. [High ammonia has been shown to stimulate  $\text{CO}_2$  fixation, thereby replenishing Krebs cycle intermediates lost by increased reductive amination of  $\alpha$ -ketoglutarate (58)].

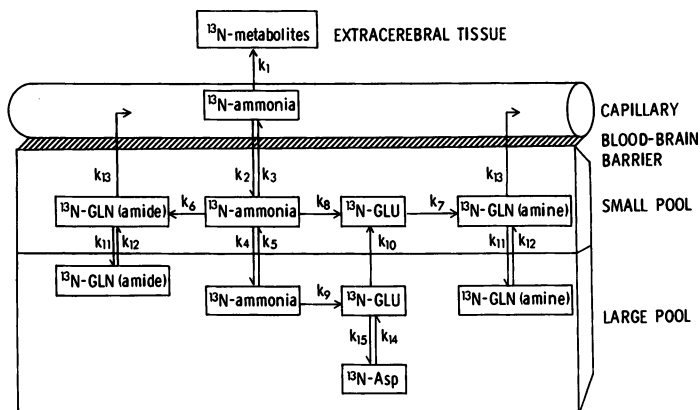
**Distribution of Label Among Various Brain Metabolites After Ventricular Infusion of [ $^{13}\text{N}$ ]Ammonia.** Analysis of brain metabolites following administration of [ $^{13}\text{N}$ ]ammonia via the CSF have indicated that CSF-borne ammonia is also metabolized in a small glutamate pool (22). Thus, after infusion of [ $^{13}\text{N}$ ]ammonia into the right lateral cerebral ventricle for 14 min, the relative incorporation of label into glutamate,  $\alpha$ -amino group of glutamine, and amide group of glutamine was found to be 1:2:59 (22). The observation, that of the  $^{13}\text{N}$ -activity recovered in the brain and CSF (61%), most (66%) was in a metabolized form, suggests an active removal of ammonia from CSF. Ammonia concentrations in the CSF are lower than those of the brain as a whole or of the blood (48, 50, 59). Hindfelt pointed out that the differences in ammonia concentration between the brain and cisternal CSF cannot be entirely accounted for by the higher pH of CSF relative to the brain, and he postulated that the brain can actively remove ammonia from the CSF, presumably via the glutamine synthetase reaction (48). Our findings are consistent with this hypothesis (22).

**Distribution of Label Among Various Brain Metabolites After Carotid Artery Infusion of [ $^{13}\text{N}$ ]Ammonia into Methionine-Sulfoximine-Treated Rats.** The biochemical and pathological effects on the brain of methionine sulfoximine (MSO), a convulsant and strong inhibitor of glutamine synthetase, have been studied for a number of years. To determine the effect of inhibition of glutamine synthetase on the distribution of  $^{13}\text{N}$ -metabolites derived from [ $^{13}\text{N}$ ]ammonia, we pretreated rats with a subconvulsive dose of MSO and 3 h later infused [ $^{13}\text{N}$ ]ammonia via the internal carotid artery (22). Compared with normal controls, less of the infused activity was recovered in the brain and, of the label recovered, a greater percentage was in an unmetabolized form. These findings were thought to reflect the less efficient trapping of ammonia as glutamine and the subsequent greater egress of unmetabolized [ $^{13}\text{N}$ ]ammonia from the brain. Nevertheless, of the label recovered in a metabolized form, a substantial amount was still found in the amide group of glutamine, despite the fact that the glutamine synthetase activity of the whole brain was 86% inactivated and the specific activity of the whole brain [ $^{13}\text{N}$ ]ammonia must have been lower than in the controls (22). A striking finding was, that of the label recovered, the percentage incorporation into glutamate was considerably greater than that in the control animals, and this difference could not be accounted for by a change in glutamate dehydrogenase activity. Moreover, the specific activity of the  $\alpha$ -amino group of glutamate was found to be greater than that of the  $\alpha$ -amino group of glutamine, that is, a true precursor-product relationship for these metabolites was obtained. This relationship indicated that the small and large pools of glutamate

metabolism were no longer metabolically distinct 3 h after MSO administration. The apparent explanation for this finding is that glutamine synthetase activity was so reduced by MSO treatment that the small compartment glutamine synthetase could no longer efficiently metabolize blood-borne [ $^{13}\text{N}$ ]ammonia. Thus, [ $^{13}\text{N}$ ]ammonia equilibrated across both the small and large metabolic compartments of the brain. Although some [ $^{13}\text{N}$ ]glutamate would still be produced in the small pool, MSO treatment made conditions favorable for increased synthesis of [ $^{13}\text{N}$ ]glutamate in the large pool via the glutamate dehydrogenase reaction.

### *Model of Blood-Borne [ $^{13}\text{N}$ ]Ammonia Uptake and Metabolism by the Brain*

Illustrated in Figure 1 is a model that describes the passage of  $^{13}\text{N}$  into various brain compartments and metabolites after administration of [ $^{13}\text{N}$ ]ammonia to rats under physiological conditions. The model is similar to that published previously (22) except that rate constants are included and all the brain glutamine synthetase is assumed to be in the small pool. The latter assumption is based on the recent findings of Norenberg et al. (60, 61), who found that brain glutamine synthetase was located in a single cell type (see the section that follows). From this present model we have assigned various rate constants and other parameters (Table III) to simulate the cerebral uptake and metabolism of blood-borne [ $^{13}\text{N}$ ]ammonia in normal awake rats.



**Figure 1.** Flow diagram of the cerebral distribution of label derived from [ $^{13}\text{N}$ ]ammonia used in the computer simulation study. The rate constants  $k_1$ ,  $k_2$ , etc. are defined in the text.  $^{13}\text{N}$ -GLU,  $^{13}\text{N}$ -ASP,  $^{13}\text{N}$ -GLN (amine), and  $^{13}\text{N}$ -GLN (amide) refer to label in glutamate, aspartate, amino group of glutamine, and amide group of glutamine, respectively.

**Table III. Kinetic Constants Used in a Computer Simulation Study for the Uptake and Metabolism of Blood-Borne [ $^{13}\text{N}$ ]Ammonia by the Rat Brain<sup>a</sup>**

Rate Constant	Definition	Magnitude ( $\text{s}^{-1}$ )
$k_1$	Clearance of ammonia from blood	0.2
$k_2$	Ammonia diffusion into brain	0.6
$k_3$	Ammonia diffusion from brain to blood	0.3
$k_4$	Ammonia diffusion from small pool to large pool	0.3
$k_5$	Ammonia diffusion from large pool to small pool	0.3
$k_6$	Ammonia incorporation into glutamine (amide) in small pool	0.4
$k_7$	Ammonia incorporation into glutamine (amine) in small pool	0.4
$k_8$	Ammonia incorporation into glutamate in small pool	0.001
$k_9$	Ammonia incorporation into glutamate in large pool	0.005
$k_{10}$	Glutamate exchange from large to small pool	0.025
$k_{11}$	Glutamine exchange from small to large pool	0.1
$k_{12}$	Glutamine exchange from large to small pool	0.01
$k_{13}$	Glutamine release from small pool to blood	0.01
$k_{14}$	Aspartate conversion to glutamate in large pool	0.079
$k_{15}$	Glutamate conversion to aspartate in large pool	0.024

<sup>a</sup> Two types of experiments were simulated: (i) *Bolus Injection*. A 0.2-mL bolus of [ $^{13}\text{N}$ ]ammonia was injected rapidly (0.2 s) into the right common carotid artery. Based on previously determined recoveries of a diffusible marker, only 8.5% of the dose was assumed to have reached the brain (22). (ii) *Continuous Infusion*. [ $^{13}\text{N}$ ]Ammonia dissolved in physiological saline was infused at a rate of 0.2 mL/min via the common carotid artery. The external carotid artery was ligated so that 80% of the dose was assumed to have reached the brain via the internal carotid artery; it was assumed that the remainder was lost via the pterygopalatine artery.

Rate constants were determined as follows:  $k_1$  was determined from the rate of clearance of [ $^{13}\text{N}$ ]ammonia from rat blood (Freed, B. R., and Cooper, A. J. L., unpublished results).  $k_2$  was deduced by determining the best fit necessary to yield a BUI of 24% given a CBF of 100 mL/100 g/min (42) and a brain transit time of 3 s (39).  $k_3$  was assumed to be one-half  $k_2$  based on the known pH difference between the brain and the blood (48).  $k_4$  and  $k_5$  were assumed to equal  $k_3$  (i.e., no pH difference between small and large pools was assumed).  $k_6$  (and  $k_7$ ) were calculated from the known activity of whole brain glutamine synthetase

(22); all the glutamine synthetase of the brain was assumed to be in the small pool, and the small pool was assumed to occupy 20% of the brain (25). Cerebral blood volume of the unanesthetized rat was taken to be 2.5% of total brain volume (62, 63).  $k_8$  was assigned a value of one-fifth  $k_9$  (i.e., glutamate dehydrogenase activity was assumed to be evenly spread throughout the brain).  $k_{10}$ ,  $k_{11}$ , and  $k_{12}$  were determined by introspection.  $k_{13}$  was calculated from published values for the arterio-venous (A-V) difference across the rat brain for glutamine (42), the cerebral blood flow for the rat (42) and total brain glutamine (22).  $k_{14}$  and  $k_{15}$  were calculated as follows: Rat brain was homogenized in five volumes of ice-cold 100mM potassium phosphate buffer, pH 7.4, and 1–2  $\mu$ L samples of the crude homogenate were added to a system containing the glutamate–aspartate transaminase reaction components at equilibrium. A small aliquot of high-specific-activity [ $^{13}$ N]glutamate was then added and the rate of conversion of [ $^{13}$ N]glutamate to [ $^{13}$ N]-aspartate at 37°C was determined. Whole brain concentrations ( $\sim$  large pool) of ammonia, glutamate, transaminase glutamine, and blood ammonia were assumed to be as in (22).

The computer model was used to simulate the uptake and loss of label from the rat brain following a bolus injection of [ $^{13}$ N]ammonia via the right internal carotid artery (Figure 2). The simulation predicts rapid loss of unmetabolized [ $^{13}$ N]ammonia from the rat brain over the first 10 s followed by a much slower loss of [ $^{13}$ N]glutamine. The simula-

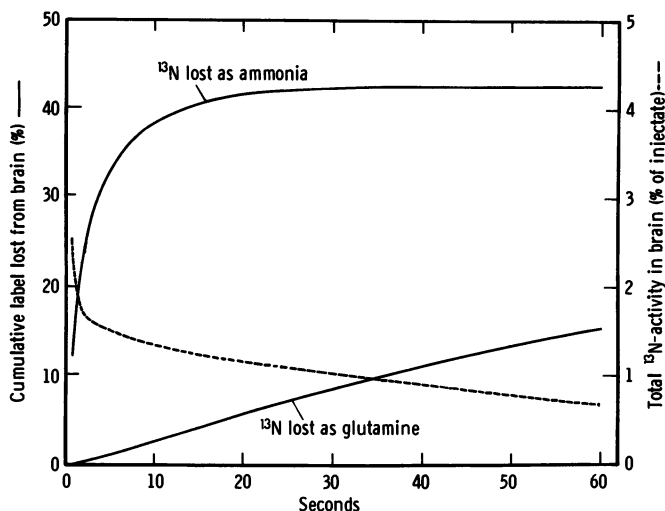


Figure 2. Computer simulation of uptake and loss of label from the rat brain following a bolus injection of [ $^{13}$ N]ammonia via the right common carotid artery. For details see the footnote to Table III.

tion (Figure 2) may be compared with the scanning experiments of Phelps et al. (23, 24) in which the time course of radioactivity in the rhesus monkey brain following a bolus injection of [ $^{13}\text{N}$ ]ammonia was described by three components: a rapidly clearing component with a mean transit time of 2.9 s, which is consistent with clearance from a vascular compartment; a slow component with a  $t_{1/2}$  of about 40–50 min that results from loss of label derived from [ $^{13}\text{N}$ ]ammonia extracted into the brain tissue; and a third small component that was attributed to recirculation of the tracer (23, 24). The predicted total  $^{13}\text{N}$ -activity in the rat brain as a function of time after a bolus injection of [ $^{13}\text{N}$ ]ammonia (Figure 2) can also be broken down into three components: a rapid component from 1–3 s attributable to loss of [ $^{13}\text{N}$ ]ammonia by washout from the vascular compartment; an intermediate component from 3–20 s attributable to uptake of recirculating metabolites; and a slow component from 20 s onward reflecting loss of  $^{13}\text{N}$ -glutamine to the blood.

Although the present model predicts bidirectional movement of [ $^{13}\text{N}$ ]ammonia across the blood–brain barrier, loss of label by back-diffusion of [ $^{13}\text{N}$ ]ammonia is likely to be small and not easily separable from a washout component. From the data given in Table III on the relative sizes of cerebral blood volume and small pool, and the rate constants  $k_2$  and  $k_3$ , we estimate a back-flow of [ $^{13}\text{N}$ ]ammonia of no more than 3% of the [ $^{13}\text{N}$ ]ammonia that enters the brain.

The computer model was also used to simulate the cerebral uptake of label during continuous (carotid) infusion of [ $^{13}\text{N}$ ]ammonia over a

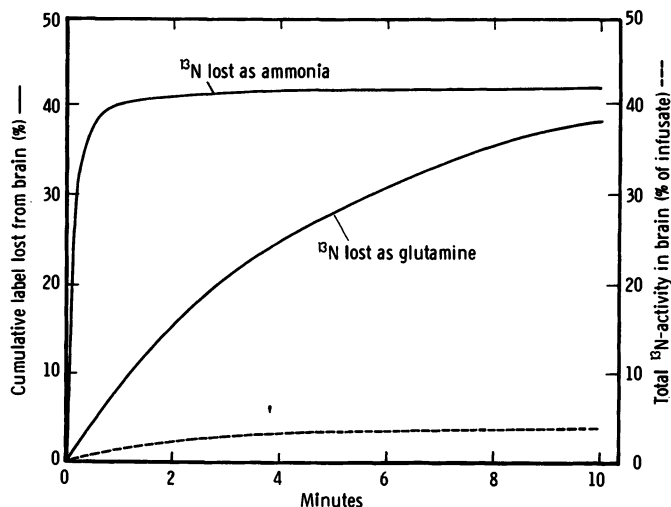


Figure 3. Computer simulation of uptake and loss of label from the rat brain during continuous infusion of [ $^{13}\text{N}$ ]ammonia via the right common carotid artery. For details see the footnote to Table III.

**Table IV. Test of the Simulation Model After Administration of [<sup>15</sup>N]Ammonia**

<i>Parameter Measured in Brain</i>	<i>Calculated<sup>a</sup></i>	<i>Observed<sup>b</sup></i>
<b>A. Five seconds after a bolus injection</b>		
Percent of dose remaining as ammonia	35.4	41.5 ± 1.0
Percent of dose incorporated into glutamine	63.6	57.0 ± 1.0
Percent of dose incorporated into glutamate plus aspartate	0.8	0.5 ± 0.2
Brain uptake index (percent)	19.0	24.0 ± 1.0
<b>B. Ten minutes after continuous infusion</b>		
Percent of total label recovered	3.9	4.8 ± 1.8
Percent of label found in glutamine (amide)	93.4	80.4 ± 1.9
Percent of label found in glutamine (amine)	2.3	1.0 ± 0.2
Percent of label found in ammonia	4.0	[15.7 ± 2.2] <sup>c</sup>
Percent of label found as glutamate	0.2	0.3 ± 0.1
Percent of label found as aspartate	0.05	0.2 ± 0.1

<sup>a</sup> Calculated from the rate constants given in Table III.

<sup>b</sup> Data of Cooper et al. (22).

<sup>c</sup> Includes [<sup>15</sup>N]ammonia in cerebral blood as well as in brain sample. Since [<sup>15</sup>N]ammonia is continuously infused into the cerebral circulation until the moment of sacrifice, an indeterminate amount of [<sup>15</sup>N]ammonia will necessarily be trapped with the vascular component of the brain sample.

10-min period (Figure 3). The model predicts that total <sup>15</sup>N-activity accumulated in the brain at 10 min would be 3.9%, a value comparable with that determined experimentally (4.8% ± 1.8%, Ref. 22). The reason for the low recovery is postulated to be attributable to continuous and substantial loss of <sup>15</sup>N-glutamine to venous blood and to a small loss of [<sup>15</sup>N]ammonia by back-diffusion.

The distribution of <sup>15</sup>N among various brain metabolites predicted by computer simulation agrees moderately well with the observed values both for the bolus injection and continuous infusion studies (Table IV). However, the computer simulation is somewhat artificial in that: many of the rate constants are estimates derived from total brain enzyme and metabolite levels; four constants were assigned by introspection and manipulated to give the best fit; the flow of label into some metabolites, such as  $\gamma$ -aminobutyrate, glutathione, and other amino acids has been ignored; and the effect of recirculating metabolites other than [<sup>15</sup>N]-ammonia has not been taken into account. Nevertheless, the model describes adequately the previous findings (22).

The most controversial aspect of the model is the proposed rapid loss of  $^{13}\text{N}$  as glutamine from the rat brain. Evidently, if the model is correct, the loss is much more rapid than that from the monkey brain. [The slow component for loss of  $^{13}\text{N}$  from the monkey brain, following a bolus injection of [ $^{13}\text{N}$ ]ammonia, has a  $t_{1/2}$  of 40–50 min (24)]. This difference may be attributable to species variation, that is, to differences in cerebral metabolic rate, CBF, and enzymatic activities. The concept that  $^{13}\text{N}$ -glutamine leaves the brain following a carotid bolus injection of [ $^{13}\text{N}$ ]ammonia is not unreasonable, since several groups of workers have shown that in the rat (42, 64) and cat (65) there is a negative A-V difference for glutamine across the brain. Clearly, to test the hypothesis, the rate at which  $^{13}\text{N}$ -glutamine leaves the rat brain must be determined.

#### *Location of the Small and Large Glutamate Compartments in the Brain*

It has been customary, on the basis of experiments using radioactively ( $^{14}\text{C}$  and  $^3\text{H}$ ) labeled precursors, to assign the large glutamate compartment to neuronal perikarya and some nerve endings and the small glutamate compartment to glial cells and their processes (e.g., 66, 67, 68). This idea is consistent with  $^{13}\text{N}$ -labeling patterns in brain metabolites following administration of [ $^{13}\text{N}$ ]ammonia (22). We have proposed that the small glutamine-synthesizing compartment is cellular and interposed between blood capillaries and the large compartment. The small compartment also appears to be arranged between the large pool and the CSF (22). The glia fulfill these positional requirements for the small pool.

Astrocytic foot processes surround the blood capillaries and distally abut onto neurons; they also underlie the ependyma (e.g., 69, 70). This anatomical relationship has prompted Bradbury (71) and others to suggest that the astrocytes act as a physical and metabolic link between capillary and neuron. Apparently, the ependymal and subjacent glial cells constitute a brain-CSF barrier (70). Perhaps the most compelling evidence that the glia represent the small compartment are the findings of Norenberg et al. (60, 61) on the distribution of brain glutamine synthetase. Using an ultrastructural immunocytochemical technique, these investigators found that, except for trace amounts in a rare indeterminate glial cell, all the reaction product was located in astrocytes (61). Specifically, no activity was observed in neurons, synaptic endings, oligodendrocytes, microglial cells, pericytes, endothelial cells, or other mesenchymal vascular elements (61). Hertz has proposed that the small pool is actually comprised of metabolically interacting astrocytes and synaptic



parts of the neuron, whereas the large pool is represented by noninteracting parts of the astrocyte and nerve endings, neuronal perikarya, and oligodendrocytes (72). Hertz makes the distinction between compartments defined anatomically and those defined kinetically (72). For instance, it is known from *in vitro* studies that uptake of glutamate by glia is extremely rapid (73, 74), so that a transfer of glutamate from nerve endings to astrocytes may not be detectable kinetically, that is, the glutamate in the interacting nerve endings and the glutamate in the astrocytes may behave as a single glutamate (small) pool. Whether the small pool is kinetically represented by the nerve endings in addition to the astrocytes remains to be verified.

### *Nitrogen Balance in the Brain*

Since there is an output of glutamine from the brain (42, 64, 65), there must be a mechanism for maintenance of the nitrogen balance in the brain. Part of this balance may be made up by a net uptake of ammonia, but at the present time a significant A-V difference for ammonia across the rat brain has not been demonstrated. However, a positive A-V for ammonia across the hyperammonemic rat brain (42) and across the human brain has been demonstrated (75). Since very little glutamate is made in the small pool from blood-borne ammonia (22), it appears that the  $\alpha$ -amino nitrogen of virtually all glutamine lost to the blood must be derived from a source other than ammonia. Such a source could, in part, be blood-borne amino acids. Indeed, Felig et al. measured a significant A-V difference for eleven amino acids across the brains of fasted healthy volunteers; unfortunately no data for glutamine were included (76). The A-V differences ranged from 5–12% of the corresponding plasma amino acid concentration. We have been unable to demonstrate consistent A-V differences for the same amino acids across the normal rat brain (77). It is likely, therefore, that if such differences occur, they are much smaller than those across the human brain. In fact, after continuous infusion of [ $^{13}\text{N}$ ]valine for 10 min via the common carotid artery, less than 1% of the administered activity was recovered in the rat brain (78). Experiments are in progress to determine the efficiency with which the brain can take up [ $^{13}\text{N}$ ]valine and to what extent an amino acid such as valine can contribute to the synthesis of glutamate in the small pool.

### *Acknowledgments*

The work from the authors' laboratory was supported, in part, by the National Institute of Health Grant AM 16739 and the Department of Energy, contract number EE-77-S-4268. AJLC is a recipient of a

United States Public Health Service Career Development Award NS 00343. TED is an Established Investigator of the American Heart Association.

### Literature Cited

1. Schenker, S.; Breen, K. J.; Hoyumpa, Jr., A. M. *Gastroenterology* 1974, 66, 121-151.
2. Walker, C. O.; Schenker, S. *Am. J. Clin. Nutr.* 1970, 23, 619-633.
3. Huttenlocher, P. R.; Schwartz, A. D.; Klatskin, G. *Pediatrics* 1969, 43, 443-454.
4. Berl, S.; Takagaki, G.; Clarke, D. D.; Waelsch, H. *J. Biol. Chem.* 1962, 237, 2562-2569.
5. Zieve, L.; Nicoloff, D. M. *Annu. Rev. Med.* 1975, 26, 143-157.
6. Plum, F.; Hindfelt, B. In "Handbook of Clinical Neurology"; Vinken, P. J.; Bruyn, G. W., Eds.; North-Holland: Amsterdam, 1976; Vol. 27, pp. 349-377.
7. Ansley, J. D.; Isaacs, J. W.; Rikkers, L. F.; Kutner, M. H.; Nordlinger, B. M.; Rudman, D. *Gastroenterology* 1978, 75, 570-579.
8. Bruton, C. J.; Corsellis, J. A. N.; Russell, A. *Brain* 1970, 93, 423-434.
9. Cole, M.; Rutherford, R. B.; Smith, F. O. *Arch. Neurol.* 1972, 26, 130-136.
10. Plum, F. *Exp. Biol. Med.* 1971, 4, 34-41.
11. Ehrlich, M.; Plum, F.; Duffy, T. E. *J. Neurochem.* 1980, 34, 1538-1542.
12. Breen, K. J.; Schenker, S. In "Progress in Liver Disease"; Popper, H.; Schaffner, F., Eds.; Grune and Stratton: New York, 1972; Vol. 4, pp. 301-332.
13. Schoenheimer, R. "The Dynamic State of Body Constituents"; Harvard University Press: Cambridge, 1942.
14. Braunstein, A. E.; Bychkov, S. M. *Nature (London)* 1939, 144, 751-752.
15. Duda, G. D.; Handler, P. *J. Biol. Chem.* 1959, 232, 303-314.
16. Lajtha, A.; Berl, S.; Waelsch, H. *J. Neurochem.* 1959, 3, 322-332.
17. Berl, S.; Lajtha, A.; Waelsch, H. *J. Neurochem.* 1961, 7, 186-197.
18. Van den Berg, C. J.; Mela, P.; Waelsch, H. *Biochem. Biophys. Res. Commun.* 1966, 23, 479-484.
19. Clarke, D. D.; Nicklas, W. J.; Berl, S. *Biochem. J.* 1970, 120, 345-351.
20. Lai, J. C. K.; Walsh, J. M.; Dennis, S. C.; Clarke, J. B. In "Metabolic Compartmentation and Neurotransmission"; Berl, S.; Clarke, D. D.; Schneider, D., Eds.; Plenum: New York, 1975; pp. 487-496.
21. Van den Berg, C. J. In "Metabolic Compartmentation in the Brain"; Balázs, R.; Cremer, J. E., Eds.; Macmillan: London, 1973; pp. 137-166.
22. Cooper, A. J. L.; McDonald, J. M.; Gelbard, A. S.; Gledhill, R. F.; Duffy, T. E. *J. Biol. Chem.* 1979, 254, 4982-4992.
23. Phelps, M. E.; Hoffman, E. J.; Coleman, R. E.; Welch, M. J.; Raichle, M. E.; Weiss, E. S.; Sobel, B. E.; Ter-Pogossian, M. M. *J. Nucl. Med.* 1976, 17, 603-612.
24. Phelps, M. E.; Hoffman, E. J.; Raybaud, C. *Stroke* 1977, 8, 694-702.
25. Lockwood, A. H.; McDonald, J. M.; Reiman, R. E.; Gelbard, A. S.; Laughlin, J. S.; Duffy, T. E.; Plum, F. *J. Clin. Invest.* 1979, 63, 449-460.
26. Tilbury, R. S.; Dahl, J. R.; Monahan, W. G.; Laughlin, J. S. *Radiochem. Radioanal. Lett.* 1971, 8, 317-323.
27. Welch, M. J.; Lifton, J. F. *J. Am. Chem. Soc.* 1971, 93, 3385-3388.
28. Tilbury, R. S.; Dahl, J. R. *Radiat. Res.* 1979, 79, 22-33.
29. Gelbard, A. S.; Clarke, L. P.; McDonald, J. M.; Monahan, W. G.; Tilbury, R. S.; Kuo, T. Y. T.; Laughlin, J. S. *Radiology* 1975, 116, 127-132.

30. Phelps, M. E.; Hoffman, E. J.; Mullani, N. A.; Ter-Pogossian, M. M. *J. Nucl. Med.* 1975, 16, 210-224.
31. Hoffman, E. J.; Phelps, M. E.; Mullani, N. A.; Higgins, C. S.; Ter-Pogossian, M. M. *J. Nucl. Med.* 1976, 17, 493-502.
32. Phelps, M. E.; Hoffman, E. J.; Huang, S.-C.; Kuhl, D. E. *J. Nucl. Med.* 1978, 19, 635-647.
33. Hoop, B.; Hnatowich, D. J.; Brownell, G. L.; Jones, T.; McKusick, K. A.; Ojemann, R. G.; Parker, J. A.; Subramanyam, R.; Traveras, J. M. *J. Nucl. Med.* 1976, 17, 473-479.
34. Siesjö, B. K. "Brain Energy Metabolism"; John Wiley & Sons: New York, 1978.
35. Milne, M. D.; Scribner, B. H.; Crawford, M. A. *Am. J. Med.* 1958, 24, 709-729.
36. Bromberg, P. A.; Robin, E. D.; Forkner, Jr., C. E. *J. Clin. Invest.* 1960, 39, 332-341.
37. Oldendorf, W. H. *Am. J. Physiol.* 1973, 221, 1629-1639.
38. Oldendorf, W. H.; Szabo, J. *Am. J. Physiol.* 1976, 230, 94-98.
39. Oldendorf, W. H.; Braun, L. D. *Brain Res.* 1976, 113, 219-224.
40. Raichle, M. E.; Eichling, J. O.; Straatman, M. G.; Welch, M. J.; Larson, K. B.; Ter-Pogossian, M. M. In "Blood Flow and Metabolism in the Brain"; Harper, M. et al., Eds.; Churchill Livingstone: London, 1975; pp. 7.11-7.14.
41. Lockwood, A. H.; Finn, R. D.; Campbell, J. A.; Richman, T. B. *Brain Res.* 1980, 181, 259-266.
42. Gjedde, A.; Lockwood, A. H.; Duffy, T. E.; Plum, F. *Ann. Neurol.* 1978, 3, 325-330.
43. Warren, K. S.; Nathan, D. G. *J. Clin. Invest.* 1958, 37, 1724-1728.
44. Stabenau, J. R.; Warren, K. S.; Rall, D. P. *J. Clin. Invest.* 1959, 38, 373-383.
45. Carter, C. C.; Lifton, J. F.; Welch, M. J. *Neurology* 1973, 23, 204-213.
46. Lee, S. H.; Fisher, B. *Surgery* 1961, 50, 668-672.
47. Eigen, M.; DeMaeyer, L. In "Technique of Organic Chemistry: Rates and Mechanisms of Reactions"; Friess, S. L. et al., Eds.; John Wiley & Sons: New York, 1963; Vol. 8, Part 2, p. 1035.
48. Hindfelt, B. *Clin. Sci. Mol. Med.* 1975, 48, 33-37.
49. Kelley, M. A.; Kazemi, H. *Respir. Physiol.* 1974, 22, 345-359.
50. Hindfelt, B.; Siesjö, B. K. *Scand. J. Clin. Lab. Invest.* 1971, 28, 353-364.
51. Schultz, V.; Lowenstein, J. M. *J. Biol. Chem.* 1976, 251, 485-492.
52. Schultz, V.; Lowenstein, J. M. *J. Biol. Chem.* 1978, 253, 1938-1943.
53. Veech, R. L.; Harris, R. L.; Veloso, D.; Veech, E. H. *J. Neurochem.* 1973, 20, 183-188.
54. Colombo, J. P.; Bachmann, C.; Peheim, E.; Berüter, J. *Enzyme* 1977, 22, 399-406.
55. Pamiljans, V.; Krishnaswamy, P. R.; Dumville, G.; Meister, A. *Biochemistry* 1962, 1, 153-158.
56. Chee, P. Y.; Dahl, J. L.; Fahien, L. A. *J. Neurochem.* 1979, 33, 53-60.
57. Dennis, S. G. C.; Clarke, J. B. *J. Neurochem.* 1978, 31, 673-680.
58. Berl, S. In "Experimental Biology and Medicine"; Wechsler, W.; Zilliken, F., Eds.; S. Karger: New York, 1971; Vol. 4, pp. 71-84.
59. Hindfelt, B.; Plum, F.; Duffy, T. E. *J. Clin. Invest.* 1977, 59, 386-396.
60. Martinez-Hernandez, A.; Bell, K. P.; Norenberg, M. D. *Science (Wash. D.C.)* 1977, 195, 1356-1358.
61. Norenberg, M. D.; Martinez-Hernandez, A. *Brain Res.* 1979, 161, 303-310.
62. Ohno, K.; Pettigrew, K. D.; Rapoport, S. I. *Am. J. Physiol.* 1978, 235, H299-H307.
63. Rapoport, S. I.; Fredericks, W. R.; Ohno, K.; Pettigrew, K. D. *Am. J. Physiol.* 1980, 238, R421-R431.

64. Lund, P. *Biochem. J.* 1971, 124, 653-660.
65. Abdul-Ghani, A.-S.; Marton, M.; Dobkin, J. *J. Neurochem.* 1978, 31, 541-546.
66. Nicklas, W. J.; Nunez, R.; Berl, S.; Duvoisin, R. *J. Neurochem.* 1979, 33, 838-844.
67. Balázs, R.; Patel, A. J.; Richter, D. In "Metabolic Compartments in the Brain"; Balázs, R.; Cremer, J. E.; Eds.; Macmillan: London, 1973; pp. 167-184.
68. Berl, S.; Nicklas, W. J.; Clarke, D. D. In "Dynamic Properties of Glial Cells"; Schoffeniels, E., et al., Eds.; Pergamon: Oxford, 1978; pp. 143-149.
69. Oldendorf, W. H. In "The Nervous System. The Basic Neurosciences"; Tower, D. B., Ed.; Raven: New York, 1975; Vol. 1, pp. 279-289.
70. Carpenter, M. B. "Human Neuroanatomy"; 7th ed.; Williams and Wilkins: Baltimore, 1976; pp. 17-21.
71. Bradbury, M. W. B. In "Fluid Environment of the Brain"; Cserr, H. F.; Fenstermacher, J. D.; Fencl, V., Eds.; Academic: New York, 1975; pp. 81-103.
72. Hertz, L. *Prog. Neurobiol.* 1979, 13, 277-323.
73. Schousboe, A.; Svenneby, G.; Hertz, L. *J. Neurochem.* 1977, 29, 999-1005.
74. Hertz, L.; Schousboe, A.; Boechler, N.; Mukerji, S.; Federoff, S. *Neurochem. Res.* 1978, 3, 1-14.
75. Fazekas, J. F.; Ticktin, H. E.; Ehrmantraut, W. R.; Alman, R. W. *Am. J. Med.* 1956, 21, 843-849.
76. Felig, P.; Wahren, J.; Ahlborg, G. *Proc. Soc. Exp. Biol. Med.* 1973, 142, 230-231.
77. Sage, J. I.; Duffy, T. E., unpublished data.
78. Cooper, A. J. L.; Gelbard, A. S., unpublished results.

RECEIVED September 4, 1980.

# <sup>13</sup>N-Labeled L-Amino Acids: Enzymatic Syntheses and Metabolic Studies

ALAN S. GELBARD, BARRY R. FREED, and ROBERT E. REIMAN  
Biophysics Laboratory, Memorial Sloan Kettering Cancer Center,  
New York, NY 10021

ARTHUR J. L. COOPER

Departments of Neurology and Biochemistry, Cornell University  
Medical College, New York, NY 10021

*The synthesis of L-amino acids, labeled with short-lived, positron-emitting radionuclides, is reviewed. Five L-amino acids (methionine, phenylalanine, aspartic acid, alanine, and glutamic acid) have been labeled with <sup>11</sup>C. In addition, L-[<sup>18</sup>F]-p-fluorophenylalanine has been prepared. The synthesis procedures were organic, enzymatic, or a combination of the two methods. L-<sup>13</sup>N-Amino acids have been enzymatically synthesized from [<sup>13</sup>N]ammonia by (i) the reductive amination of  $\alpha$ -keto acids with glutamate dehydrogenase; (ii) ATP-dependent amidation of L-glutamate and L-aspartate via reactions catalyzed by glutamine synthetase and asparagine synthetase, respectively; and (iii) the coupling of glutamate dehydrogenase and glutamate-utilizing aminotransferases. Tissue distribution studies with L-<sup>13</sup>N-amino acids have shown species differences in uptake of label in some organs, notably the heart. Some biomedical applications of <sup>13</sup>N-labeled amino acids are described.*

**D**uring the past decade a number of research laboratories have developed procedures for the rapid synthesis of amino acids labeled with short-lived, positron-emitting radionuclides. These tracers make possible the study of regional amino-acid metabolism in the living organism by external detection of the  $\gamma$  photons produced by positron annihilation. This decay mode also permits the determination of label distribution in transverse sections through the body by means of positron emission

0065-2393/81/0197-0389\$05.00/0  
© 1981 American Chemical Society

tomography. Although much of the motivation for developing these compounds has come from medical scientists who are primarily interested in using radiopharmaceuticals to image tumors or organs such as the pancreas, amino acids labeled with positron emitters are becoming more generally recognized as useful tracers in the study of such fundamental biological processes as amino-acid transport, intermediary metabolism, and protein synthesis.

The radionuclides that are of primary interest for labeling amino acids are two isotopes of elements naturally present, that is, nitrogen-13 ( $t_{1/2} = 10$  min) and carbon-11 ( $t_{1/2} = 20$  min). Fluorine-18 ( $t_{1/2} = 110$  min) has also been used to label some amino acids. Although fluorine is not normally present in naturally occurring amino acids, the rationale for synthesizing and using  $^{18}\text{F}$ -analogs of amino acids for metabolic studies is that: (i) covalently bonded hydrogen and fluorine are of similar size; (ii) the C—F bond is not easily ruptured; and (iii) longer-term studies than those with  $^{13}\text{N}$  or  $^{11}\text{C}$  are possible.

Most of the published syntheses for labeling of amino acids with  $^{11}\text{C}$  and  $^{18}\text{F}$  have been organic procedures, whereas those for labeling with  $^{13}\text{N}$  have been enzymatic processes. Unlike most organic chemical reactions, enzymatic labeling results in formation of only one stereospecific amino-acid isomer. Although racemic mixtures of labeled amino acids have been used satisfactorily for imaging such organs as the pancreas, quantitative measurements of amino-acid metabolism are likely to be complicated by the presence of label derived from the D-isomer. In this connection, tissue distribution studies in rats have shown substantial differences in the concentration of label in the pancreas at 15 min after injection of L- as compared with DL-[*side chain-3- $^{14}\text{C}$* ]tryptophan (1). Differences were also noted in pancreas uptake for L-[*carboxyl- $^{14}\text{C}$* ]tryptophan vs. DL-[*carboxyl- $^{14}\text{C}$* ]tryptophan (2). Significantly greater pancreatic  $^{11}\text{C}$ -concentrations were found in rats 30 and 60 min after injection of L-[*carboxyl- $^{11}\text{C}$* ]phenylalanine than with the D-isomer (3).

The latter study illustrates the labeling of stereospecific amino acids by a combination of organic and enzymatic procedures. DL-[*carboxyl- $^{11}\text{C}$* ]Phenylalanine, synthesized from [ $^{11}\text{C}$ ]cyanide by the Bucherer modification of the Strecker synthesis, was resolved into its L- and D-isomers by the action of the D- and L-amino acid oxidases, respectively. The optically active amino acid was separated from phenylpyruvic acid by cation exchange chromatography (3). Similarly, DL-[ $^{18}\text{F}$ ]acyl-*p*-fluorophenylalanine has been subjected to stereospecific deacylation with the fungal enzyme, L-amino acylase; enzymatically generated L-[ $^{18}\text{F}$ ]p-fluorophenylalanine was separated from the D-acyl amino acid by column chromatography (4).

An example of the synthesis of a  $^{11}\text{C}$ -labeled L-amino acid solely by organic chemical means is the preparation of L-[*methyL- $^{11}\text{C}$* ]methionine

by the methylation of L-homocysteine thiolactone with [<sup>11</sup>C]methyl iodide in basic solution in the presence of acetone (5). The radiochemical yield was found to be about 50%, and the specific activity of labeled methionine was estimated to be  $5 \times 10^4$  Ci/mol.

Three L-amino acids, namely aspartic acid, glutamic acid, and alanine, have been labeled with <sup>11</sup>C solely by enzymatic means. Aspartic acid labeled in the carboxyl position was synthesized from <sup>11</sup>CO<sub>2</sub> in a series of enzymatic reactions (6). First, <sup>11</sup>CO<sub>2</sub> was converted to H<sup>11</sup>CO<sub>3</sub><sup>-</sup> by the action of carbonic anhydrase. [1-<sup>11</sup>C]Oxaloacetate was then prepared by the enzymatic action of oxaloacetate decarboxylase. Finally, [1-<sup>11</sup>C]-oxaloacetate was transaminated to labeled aspartate by the action of glutamate-oxaloacetate transaminase. L-[1-<sup>11</sup>C]Glutamic acid has also been prepared from [1-<sup>11</sup>C]oxaloacetate (7). In a series of reactions catalyzed by citrate synthase, aconitase, and isocitrate dehydrogenase, [1-<sup>11</sup>C]-α-ketoglutarate was formed from labeled oxaloacetate. This α-keto acid was then transaminated to L-[1-<sup>11</sup>C]glutamic acid, with alanine as the amino donor, by the action of glutamate-pyruvate transaminase (7). L-[1-<sup>11</sup>C]Alanine was also labeled by procedures involving coupled enzymatic reactions (8). First, [1-<sup>11</sup>C]pyruvate was synthesized by reacting <sup>11</sup>CO<sub>2</sub> and acetyl CoA in the presence of pyruvate-ferredoxin oxidoreductase extracted from *Clostridium acidii urici*. [1-<sup>11</sup>C]Pyruvate was then converted to L-[1-<sup>11</sup>C]alanine by transamination with glutamate in a reaction catalyzed by glutamate-pyruvate transaminase.

### Syntheses of <sup>13</sup>N-Labeled Amino Acids

The recent development of methods for the production of [<sup>13</sup>N]-ammonia has created the possibility of enzymatic synthesis of L-<sup>13</sup>N-amino acids of high specific activity. One of the first methods for the production of [<sup>13</sup>N]ammonia used the irradiation of metallic carbides, particularly aluminum carbide, with deuterons, the <sup>13</sup>N being produced by a (d,n) reaction on <sup>12</sup>C (9). By dissolving the aluminum carbide target at the end of bombardment in either acid or alkali, [<sup>13</sup>N]ammonia was produced and recovered by distillation. A disadvantage of this method was that about 16 times as much <sup>28</sup>Al as <sup>13</sup>N was produced at the end of irradiation, a situation that constituted a radiation hazard in handling and processing the target. This problem was subsequently bypassed by producing [<sup>13</sup>N]ammonia via irradiating methane gas with deuterons (10). The first reported syntheses of L-[amide-<sup>13</sup>N]glutamine (11) and L-[<sup>13</sup>N]glutamate (12) involved [<sup>13</sup>N]ammonia generated in this manner. However, labeled and unlabeled impurities, as well as large amounts of carrier ammonia, were found in solutions of [<sup>13</sup>N]ammonia produced by the methane irradiation procedure (13). These impurities were removed by distillation, yielding [<sup>13</sup>N]ammonia more suitable for enzymatic syn-

theses; however, the total amount of [ $^{13}\text{N}$ ]ammonia produced in this two-step procedure was low. The present method of choice for [ $^{13}\text{N}$ ]ammonia production utilizes the (p, $\alpha$ ) reaction on the  $^{16}\text{O}$  of water to yield  $^{13}\text{N}$ -labeled nitrate and nitrite, which are then reduced to [ $^{13}\text{N}$ ]ammonia by titanous chloride (14) or by Devarda's alloy in basic solution (15, 16). Yields of 0.2–0.5 Ci of [ $^{13}\text{N}$ ]ammonia have been reported by this method. The concentration of unlabeled ammonia found in preparations of [ $^{13}\text{N}$ ]ammonia after reaction with Devarda's alloy was 80–200  $\mu\text{M}$  (17, 18). Unlabeled ammonia arises from the Devarda's alloy–sodium hydroxide mixture so that dilution of specific activity always occurs with this reduction procedure.

With high yields of [ $^{13}\text{N}$ ]ammonia, it may be possible to label many naturally occurring L-amino acids with  $^{13}\text{N}$  by enzymatic incorporation of [ $^{13}\text{N}$ ]ammonia into appropriate precursors. Some amino acids can be directly labeled by the reductive amination of the corresponding  $\alpha$ -keto acid with such enzymes as glutamate dehydrogenase. Glutamine and asparagine, labeled in the amide position with  $^{13}\text{N}$ , can be prepared from the corresponding dicarboxylic acid and [ $^{13}\text{N}$ ]ammonia, by the action of glutamine synthetase and asparagine synthetase, respectively. Other amino acids, such as alanine and aspartic acid, can be labeled by coupling two enzymatic reactions, a process that involves the labeling of glutamate and then the transfer of the amino group of glutamate to the corresponding  $\alpha$ -keto acid by reactions catalyzed by appropriate glutamate- $\alpha$ -keto acid transaminases. Other amino acids and nitrogen-containing metabolites such as amino sugars, purines, pyrimidines, and nicotinamide nucleotides could be labeled by using L-[amide- $^{13}\text{N}$ ]glutamine as the amide donor in reactions catalyzed by glutamine amidotransferases.

While the number of potential  $^{13}\text{N}$ -labeled physiological tracers is large, to date very few have been synthesized and an even smaller number have been used in metabolic and clinical studies. A principal reason is that most of the enzymes that are required for syntheses are not available from commercial sources and, with few exceptions, labeling has been restricted to amino acids that can be prepared by methods using commercially available enzymes. Another problem with enzymatic syntheses is that the protein catalyst is potentially antigenic or pyrogenic and must be removed from the solution containing the labeled product before clinical studies can be initiated. This problem of pyrogenic effects of enzyme protein can, in principle, be overcome by immobilizing the desired enzyme(s) to a solid support and passing a solution containing [ $^{13}\text{N}$ ]ammonia, substrate, and cofactors through a column containing the bound enzyme(s). The use of immobilized enzymes also offers the advantage that the same enzyme preparation may be used for several syntheses.



Detailed descriptions of the synthesis of L-[amide-<sup>13</sup>N]glutamine and L-[<sup>13</sup>N]glutamate have been published (13, 15, 19, 20). The enzymes used in these studies were commercially available sheep brain glutamine synthetase and bovine liver glutamate dehydrogenase. L-[amide-<sup>13</sup>N]-Glutamine has been prepared by a batch method in yields exceeding 100 mCi. Glutamine synthetase has recently been immobilized on CNBr-activated Sepharose and has been used to prepare L-[amide-<sup>13</sup>N]glutamine and L-[α-<sup>13</sup>N]glutamine (21). L-[<sup>13</sup>N]Glutamate has been prepared by a batch method and by immobilizing glutamate dehydrogenase on porous derivatized (*N*-hydroxysuccinimide) silica beads (22) or CNBr-activated Sepharose (23). Clinical studies are carried out in our laboratory with L-[<sup>13</sup>N]glutamate prepared from glutamate dehydrogenase immobilized on CNBr-activated Sepharose. Labeled glutamate, in yields of 70–140 mCi, are produced from 120–200 mCi of [<sup>13</sup>N]ammonia. Briefly, the procedure is as follows. Five μmol of α-ketoglutarate and 3 μmol of reduced nicotinamide adenine dinucleotide are added to the labeled ammonia that has been collected in 3 mL of phosphate buffer, pH 8.0. The solution is allowed to pass through a column packed with 0.5 g of Sepharose to which glutamate dehydrogenase has been immobilized. Labeled glutamate is separated from unreacted [<sup>13</sup>N]ammonia by passage through an AG-50 cation-exchange column that has previously been equilibrated with 0.01M Tris-acetate buffer, pH 4.0. The eluate from the ion-exchange column is passed through a Millex filter (0.22-μm pore size) into a sterile vial, at which point it is ready for clinical studies. Preparation of the labeled amino acid takes 8 min from the end of cyclotron bombardment of the water target. The radiochemical purity of the product, as determined by high-pressure liquid chromatography on a Whatman SAX anion exchange column (17), is very high (>99%).

A number of α-keto acids other than α-ketoglutarate are known to be substrates for glutamate dehydrogenase (e.g., References 24, 25). The feasibility of using this enzyme to incorporate <sup>13</sup>N into amino acids other than glutamate was originally demonstrated by Straatman and Welch (13), who synthesized L-[<sup>13</sup>N]valine from α-ketonsovalerate, L-[<sup>13</sup>N]alanine from pyruvate, and L-[<sup>13</sup>N]leucine from α-ketoisocaproate, in yields varying from 6.8% to 26%. However, total activities produced were not reported and the enzyme catalyst was not immobilized.

The amino acid specificity of glutamate dehydrogenase is known to be broad (e.g., References 26, 27). Since the reaction is reversible, the α-keto acid specificity should also be correspondingly broad. Indeed, Table I shows that glutamate dehydrogenase can catalyze the reductive amination of at least 10 α-keto acids. It should be noted that kinetic data were determined in the presence of a low ammonia concentration (5mM) in order to obtain realistic parameters for the design of optimal

**Table I. Specificity of Beef Liver Glutamate Dehydrogenase for  $\alpha$ -Keto Acids<sup>a</sup>**

$\alpha$ -Keto Acid Substrate <sup>b</sup>	Corresponding L-Amino Acid	$K_m$ (mM)	$V_{max}$ ( $\mu$ mol/ min/ mg)
Pyruvate <sup>c</sup>	alanine	26	0.015
$\alpha$ -Ketobutyrate	$\alpha$ -aminobutyrate	50	0.13
$\alpha$ -Ketovalerate <sup>d</sup>	norleucine	40	0.15
$\alpha$ -Ketoisovalerate	valine	83	0.11
$\alpha$ -Ketoisocaproate	leucine	52	0.036
$\alpha$ -Keto- $\gamma$ -methiolbutyrate	methionine	17	0.12
D- $\alpha$ -Keto- $\beta$ -methylvalerate <sup>e</sup>	isoleucine	13	0.036
$\beta$ -Hydroxypyruvate <sup>f</sup>	serine	1.8	0.012
D- $\alpha$ -Keto- $\beta$ -hydroxybutyrate	threonine	3	0.005
$\alpha$ -Ketoglutarate <sup>g</sup>	glutamate	1.2	15.9

<sup>a</sup>The reaction mixture (1.0 mL) contained variable concentrations of  $\alpha$ -keto acid, 5mM ammonium acetate, 0.1mM NADH, and enzyme (1–1000  $\mu$ g) in 50mM Tris-HCl buffer, pH 8.5. The rate of disappearance of NADH was determined by continuous monitoring of absorbance at 340 nm; 25°C. Data from Reference 28.

<sup>b</sup>No activity was detected with the  $\alpha$ -keto acid analogs of glycine, glutamine, asparagine, phenylalanine, tyrosine, tryptophan, arginine, citrulline, and aspartate.

<sup>c</sup>Paper chromatography of the reaction products after 1 h of incubation revealed the presence of both alanine and  $\gamma$ -hydroxyglutamate. The latter compound presumably arises via dimerization of pyruvate to  $\alpha$ -keto- $\gamma$ -hydroxyglutarate.

<sup>d</sup>The  $K_m$  has previously been reported as 6.6mM and the  $V_{max}$  as 25% that obtained with  $\alpha$ -ketoglutarate (24).

<sup>e</sup>Not available commercially.

<sup>f</sup>The  $K_m$  for  $\alpha$ -ketoglutarate has previously been reported as 0.7mM; pH 7.6, 22°C (26).

conditions for the synthesis of <sup>13</sup>N-amino acids. Although the  $V_{max}$  values are two to four orders of magnitude greater for  $\alpha$ -ketoglutarate than for other  $\alpha$ -keto acids, the turnover number is such that significant amounts of a number of <sup>13</sup>N-amino acids can be generated via glutamate dehydrogenase-catalyzed reductive amination of the corresponding  $\alpha$ -keto acid with [<sup>13</sup>N]ammonia. Using the parameters listed in Table I as a guide, we have been able to devise strategies for the synthesis of apyrogenic solutions of L-[<sup>13</sup>N]valine, L-[<sup>13</sup>N]methionine, L-[<sup>13</sup>N]leucine, and L-[<sup>13</sup>N] $\alpha$ -aminobutyrate. For example, L-[<sup>13</sup>N]valine was synthesized as follows: Three mL of glycine-potassium hydroxide buffer, pH 9.0, containing 72  $\mu$ mol of  $\alpha$ -ketoisovalerate, 2  $\mu$ mol of reduced nicotinamide adenine dinucleotide, and 100–200 mCi of [<sup>13</sup>N]ammonia, was added to

a column consisting of 1 g of CNBr-activated Sepharose onto which glutamate dehydrogenase had been immobilized. This solution, whose volume was equal to the void volume of the Sepharose column, was kept in contact with the bound enzyme for 10 min before being washed through the column with 3 mL of buffer. A yield exceeding 50% conversion of [<sup>13</sup>N]ammonia to L-[<sup>13</sup>N]valine was obtained in this manner, with final yields of 15–30 mCi (28).

L-[amide-<sup>13</sup>N]Asparagine has been prepared in radiochemical yields of 10–20%, in a reaction catalyzed by asparagine synthetase purified from extracts of rat Novikoff hepatoma (29) or from *Escherichia coli* (30). Neither enzyme preparation is presently available from commercial sources.

Higher yields of L-[amide-<sup>13</sup>N]asparagine have been obtained by a rapid, nonenzymatic method. The free  $\beta$ -carboxyl group of L- $\alpha$ -N-t-Boc- $\alpha$ -t-Bu-aspartic acid is activated with N-hydroxysuccinimide to yield L- $\alpha$ -N-t-Boc- $\alpha$ -t-Bu- $\beta$ -N-hydroxysuccinimidyl aspartic ester, which is refluxed for 10 min with [<sup>13</sup>N]ammonia. Hydrolysis for 1 min in 1N HCl yields up to 30–40% of L-[amide-<sup>13</sup>N]asparagine, which is then purified by cation-exchange column chromatography (31).

L-[<sup>13</sup>N]Aspartate has recently been prepared, in low yield, in a reaction catalyzed by aspartase immobilized on CNBr-activated Sepharose (21).

L-[<sup>13</sup>N]Alanine has been prepared by coupling the glutamate dehydrogenase and glutamate-pyruvate transaminase reactions. In this procedure both enzymes were immobilized in sequence onto porous derivatized (N-hydroxysuccinimide) silica beads with glutamate dehydrogenase bound onto the top half of the column and glutamate-pyruvate transaminase onto the lower half. The reaction solution, containing  $\alpha$ -ketoglutarate, pyruvate and [<sup>13</sup>N]ammonia is first passed through the bound enzyme column, then through a cation-exchange column to remove unreacted [<sup>13</sup>N]ammonia, and finally through an anion-exchange column to remove [<sup>13</sup>N]glutamate. The solution containing the purified [<sup>13</sup>N]-alanine was shown to be pyrogen-free (22).

Commercial preparations of pig heart glutamate-oxaloacetate transaminase have been screened for their ability to transaminate various  $\alpha$ -keto acids with L-[<sup>13</sup>N]glutamate (32). In addition to L-[<sup>13</sup>N]aspartate, enzyme preparations were able to catalyze the formation of labeled tyrosine, phenylalanine, leucine, and dihydroxyphenylalanine, as demonstrated by HPLC (17). However, these amino acids have not yet been obtained in radiopure form by this method. The  $\alpha$ -keto acid analogs of valine and tryptophan were not transaminated by the enzyme preparations. Glutamate-oxaloacetate transaminases obtained from several commercial sources have varying abilities to transaminate the  $\alpha$ -keto acid

analogs of the aromatic amino acids, suggesting that tyrosine aminotransferase activity is due to a contaminating enzyme. Although they all effectively convert oxaloacetate to aspartate, some preparations of glutamate-oxaloacetate transaminase have catalyzed up to 40% transfer of label from L-[ $^{13}\text{N}$ ]glutamate to *p*-hydroxyphenylpyruvate; other preparations have yielded less than 10% transfer of label.

### *Metabolic Studies with $^{13}\text{N}$ -Labeled Amino Acids*

To date, studies of the gross tissue distribution of label following intravenous injection in several mammalian species, either by external scintigraphy or by dissection and tissue radioassay, have been reported for five  $^{13}\text{N}$ -labeled L-amino acids: glutamate, glutamine, asparagine, alanine, and valine. While many of these observations are semi-quantitative or qualitative in nature and while the detailed metabolic fate in tissue has not yet been reported for these compounds, a number of valuable empirical observations have been obtained, providing clues for further research. In particular, unexpectedly high (or in some cases, low) concentrations of  $^{13}\text{N}$  in certain organs and a considerable degree of species-related variation in the patterns of  $^{13}\text{N}$ -distribution have been observed following administration of these  $^{13}\text{N}$ -labeled compounds.

In the following discussion, tissue  $^{13}\text{N}$  content is expressed as % injected dose/whole organ, where such data are available. In some cases, reported values of % dose/g tissue have been converted to units of relative concentration (% injected dose/% body weight) (33), by means of reported or estimated body weights. The use of relative concentration, which expresses the ratio of radionuclide concentration found in a given tissue to that which would result from a uniform distribution of label throughout the body, facilitates comparison of results among subjects of varying body size.

The most extensively studied of the  $^{13}\text{N}$ -labeled L-amino acids is glutamic acid. The first reported distribution studies, in rabbits killed at 20 min after injection, showed 1.3% dose in the heart, 11% in the liver, and 2.4% in the kidneys (12). From the reported % dose/g data, using an estimated body weight of 3 kg, we calculate relative concentrations of 4.5 (heart), 3.0 (liver), 9.3 (pancreas), and 3.3 (kidneys). Data subsequently reported by Lathrop et al. (19) for mice yield relative concentration values (for 25-g body weight) of 1.2 and 1.3 (heart), 2.2 and 1.9 (liver), 4.0 and 4.8 (pancreas), and 2.8 and 2.6 (kidneys) at 10 and 30 min, respectively. Gamma camera-imaging of a baboon (10–20 min after injection) revealed "marked"  $^{13}\text{N}$  concentrations in the liver and kidneys and the suggestion of a pancreatic image. In a normal human subject, an indication of pancreatic imaging and large  $^{13}\text{N}$ -concentrations in the liver and the heart were noted (19). These findings

have been confirmed and extended in our laboratory. Quantitative whole-body rectilinear scanning, starting at 5 min after injection, in normal human subjects and cancer patients with no known heart involvement, yielded a range of 3.6–7.7% dose in the heart (mean 5.7% for 10 subjects), (23). Similar studies in dogs and rhesus monkeys demonstrated myocardial <sup>13</sup>N to be less than 0.5% dose in the dog and 3% in the rhesus monkey (34). Tissue distribution measurements in rats showed 0.4–0.5% dose and relative concentrations of 1.4–1.7 in the heart over the interval 5–30 min after injection (35). Thus, accumulation of <sup>13</sup>N in the heart following intravenous injection of L-[<sup>13</sup>N]glutamate shows the following species dependence: human > rhesus monkey > rabbit > dog, rat, mouse, with the overall range a factor of 10 or more. By contrast, the fraction of dose taken up by the liver in the same time period for all of these species has a much narrower range, about 8–15% dose.

L-[<sup>13</sup>N]Glutamate also gives rise to remarkable concentrations of <sup>13</sup>N in the normal human pancreas. We have found an average of 9% in the pancreases of five individuals by means of quantitative scanning (36). Considering that the weight of the pancreas for a "standard reference man" of 70 kg is 100 g (37), or 0.14% body weight, a relative concentration of 63 is indicated. This may be compared with the value of 9.3 quoted above for the rabbit, 4–4.8 for the mouse, and our own measurements of 5–7.5 for the rat (5–30 min; Reference 35). Notable concentrations of label are also observed in the salivary glands (chiefly parotids) of humans and dogs (15, 23). About 1% dose, or a relative concentration of 4.8 is found in the submaxillary salivary glands of rats at 5 min after injection (35). In accordance with the measurements of Oldendorf of an extremely low brain uptake index for glutamate (38), little <sup>13</sup>N is observed in the brains of humans, rhesus monkeys, dogs or rats.

Early reports suggested selective concentration of label derived from L-[<sup>13</sup>N]glutamate into transplanted tumors of rats (39) and mice (40). Following this lead, an extensive study was undertaken in our laboratory to assess the tumor-imaging capability of <sup>13</sup>N-labeled ammonia, glutamate, and glutamine in spontaneous tumors of dogs. While all three agents provided images of tumors, L-glutamate appeared to be the most consistently useful, particularly for bone tumors (41, 42). This observation led to a clinical research program, currently in progress at the Memorial Sloan Kettering Cancer Center, in which the efficacy of various modes of cancer therapy is monitored by observing changes in tumor <sup>13</sup>N-concentration when L-[<sup>13</sup>N]glutamate is administered intravenously before, and at intervals after, the onset of treatment. Thus far, in over 50 individuals studied, this method has been very successful in assessing tumor response to chemotherapy. Good correlation between changes in uptake of activity in the tumor and clinical response has been noted (43).

Studies with L-[amide- $^{13}\text{N}$ ]glutamine in rabbits, dogs, and rhesus monkeys have generally found  $^{13}\text{N}$ -concentrations in the liver to exceed those of other tissues, although a somewhat higher concentration in the pancreases of mice was noted at 5 min after injection (20). Quantitative whole-body scans beginning at 5 min after injection yielded fractional dose measurements of 2% in the heart and 25% in the liver of rhesus monkeys (34), and in dogs less than 0.5% in the heart, 20% in the liver, 1% in the parotids, and about 4% in the bladder (15). Label derived from L-[amide- $^{13}\text{N}$ ]glutamine was selectively taken up in transplanted tumors of mice and spontaneous tumors of dogs (40, 42). Studies have not yet been carried out in humans with labeled glutamine. It is thought that this agent may be useful in detecting glutaminase-sensitive tumors.

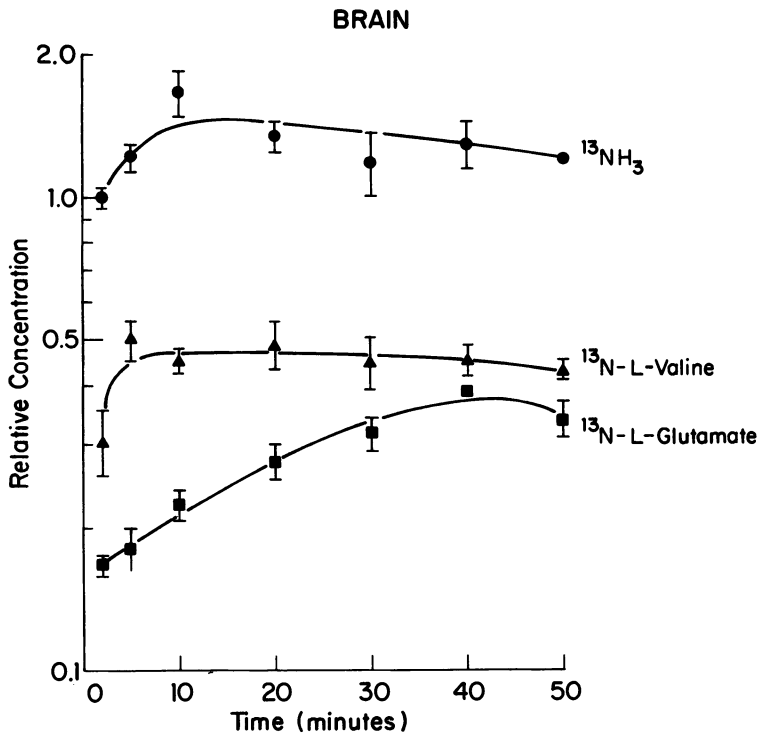
L-[amide- $^{13}\text{N}$ ]Asparagine has been prepared in this laboratory and administered to dogs that were scanned at 5 min after injection. An extraordinary  $^{13}\text{N}$  concentration of nearly 14% dose in the heart was observed in two dogs, an amount equal to the  $^{13}\text{N}$  content of the entire liver in these animals (29). Majumdar and coworkers have reported confirmation of these results (44). These investigators also reported quantitative in vivo measurements of 6–9% dose in the baboon heart and 2.5% in the human heart after administration of L-[amide- $^{13}\text{N}$ ]-asparagine. A 1:10 heart/liver percent dose ratio was found for the rabbit, but the liver content was not reported. Thus, as with L-[ $^{13}\text{N}$ ]-glutamate, a substantial species variation has been demonstrated for the myocardial accumulation of  $^{13}\text{N}$  from L-[amide- $^{13}\text{N}$ ]asparagine, although with a species specificity markedly different from that obtained with L-[ $^{13}\text{N}$ ]glutamate.

L-[ $^{13}\text{N}$ ]Alanine has been administered to rabbits, which were killed 5 min after injection. Pancreas/liver  $^{13}\text{N}$  concentration ratios of 1.8 and 2.3 were reported for barbiturate-anesthetized and unanesthetized animals, respectively. The kidneys contained about 20% higher  $^{13}\text{N}$  concentrations than did the liver (45). Label content of the liver itself was not reported. In gamma camera studies of humans, imaging of the heart and pancreas was reported with L-[ $^{13}\text{N}$ ]alanine (46). L-[ $^{13}\text{N}$ ]alanine has also been used to image the human myocardium and pancreas by positron emission tomography (47). It should be noted, however, that radioactivity derived from DL-[1- $^{14}\text{C}$ ]alanine did not localize in either organ in human subjects (48).

The fraction of dose in the liver following administration of L-[ $^{13}\text{N}$ ]-valine to dogs and rhesus monkeys was 13% and 11%, respectively (34). Neither species accumulated significant amounts of label in the heart or pancreas. Tissue distribution studies in rats with L-[ $^{13}\text{N}$ ]valine yielded pancreatic relative concentrations of about 10 from 10–50 min after injection. Liver  $^{13}\text{N}$  relative concentration in this interval was 1.9–2.6.

Label concentrations in the heart and submaxillary salivary glands were similar to those for L- $^{13}\text{N}$ glutamate (35).

While the above discussion has focused, in part, on several instances of rather striking species-related variations in organ  $^{13}\text{N}$  accumulation after administration of labeled L-amino acids, it must be pointed out that these variations have not yet been studied in a highly systematic fashion. The time course of the radionuclide content of a given organ or tissue following administration of a labeled compound reflects the contributions of several distinct modes of label movement: the rate of delivery of the injected compound to the tissue (which is, in turn, a function of the magnitude and distribution of cardiac output and the rate of systemic clearance of the compound from the blood); the fractional extraction of the compound by the tissue (which may depend, in part, on the rate of perfusion); the rate of release of the compound and of labeled metabolites from the tissue; secondary extraction and retention



*Figure 1. Relative concentration of  $^{13}\text{N}$  in rat brain as a function of time following intravenous injection of L- $^{13}\text{N}$ glutamate, L- $^{13}\text{N}$ valine, and  $^{13}\text{N}$ ammonia. Each entry represents the mean  $\pm$  standard error of the mean for four rats.*

of labeled products recirculated from other organs/tissues (involving all of the factors noted above). Observed differences in organ tracer content among species may result from variations in only one or several of these factors. Determination of the source of these differences requires, at the very least, a knowledge of their time dependence.

At the present time, there are no instruments capable of carrying out rapid time sequence ("dynamic"), high resolution, quantitative, whole-body distribution measurements of positron-emitting radionuclides in humans or in large animals. Dynamic studies are usually restricted to limited regions of the body, while quantitative whole-body measurements, performed with scanners, do not follow organ tracer content as a function of time. Thus, most of the available quantitative, *in vivo* tracer distribution data for humans or large animals have not been associated with specific times after injection, but are reported for periods during which a quasi-steady state is thought to exist.

Quantitative distribution measurements for positron-emitting radionuclides in a wide selection of organs and tissues as a function of time after injection can, at present, best be obtained by dissection studies. We are currently carrying out such studies in rats, in which the  $^{13}\text{N}$ -concentrations of 14 major organs and tissues are measured at a series of time points up to 50 min after intravenous injection of  $^{13}\text{N}$ -labeled L-amino acids or [ $^{13}\text{N}$ ]ammonia. As an example of the data obtained in these studies,  $^{13}\text{N}$  relative concentrations of the brain, heart, and pancreas of pentobarbital-anesthetized adult male Sprague-Dawley rats are plotted

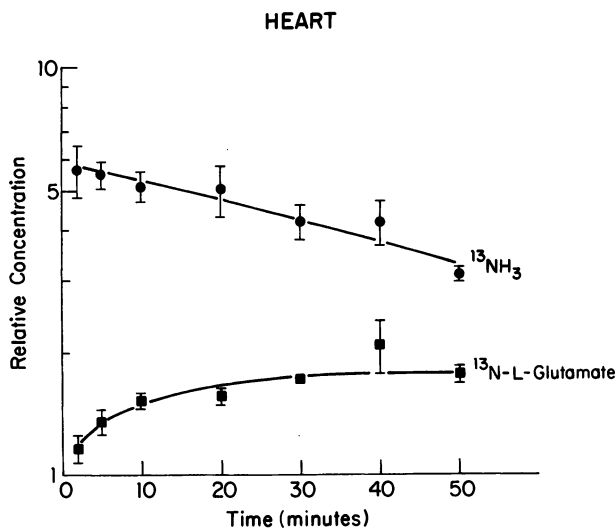


Figure 2. Relative concentration of  $^{13}\text{N}$  in rat heart as a function of time. Conditions are as in the legend to Figure 1.



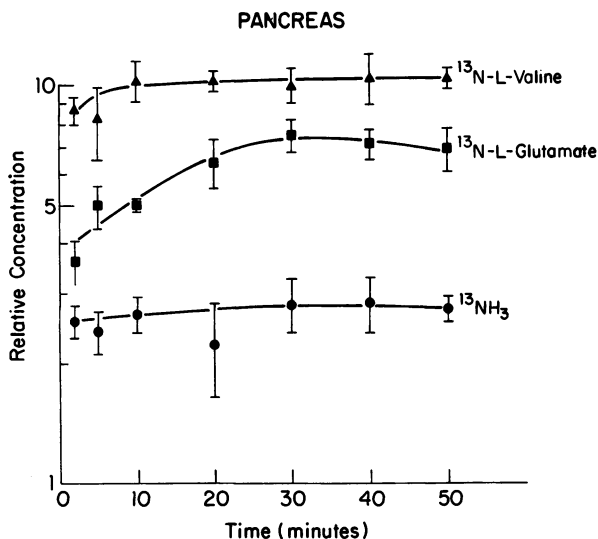


Figure 3. Relative concentration of <sup>13</sup>N in rat pancreas as a function of time. Conditions are as in the legend to Figure 1.

semilogarithmically against time after injection of L-[<sup>13</sup>N]glutamate, L-[<sup>13</sup>N]valine, or [<sup>13</sup>N]ammonia (Figures 1–3). (Results for L-[<sup>13</sup>N]valine in the heart are quite similar to those for L-[<sup>13</sup>N]glutamate and have been omitted for the sake of clarity).

We regard these organ distribution measurements as a necessary first step in the quantitative study of the metabolic fate of nitrogen derived from amino acids, providing useful information on the role of the various organs in the metabolism of these compounds. These distribution measurements are to be followed by the separation of labeled products from organs of interest by chromatographic means, as has already been done for the rat brain following administration of [<sup>13</sup>N]-ammonia (17).

### Conclusion

The number of radiochemically pure L-amino acids that have been synthesized with a short-lived positron-emitting radionuclide is limited at the present time. However, with the further development of rapid organic synthetic procedures and enzyme immobilization techniques it is expected that this number will increase. Such labeled amino acids will be useful for (i) basic research in determining the metabolic fate of a given amino acid in vivo; and (ii) imaging of physiological processes in human organs in various disease states.

### Acknowledgments

The work that was reviewed from the authors' laboratory was supported in part by D.O.E. Contract No. EE-77-S-4268, by Grant CA-18153-03, Core Grant CA-08748-14 awarded by the National Cancer Institute, DHEW, and the National Institute of Health Grant AM 16373. AJLC is a recipient of a United States Public Health Service Career Development Award NS 00343.

### Literature Cited

1. Matolo, N. M.; Stadalnik, R. C.; Krohn, K. A. *Am. J. Surgery* 1978, 136, 735-739.
2. Washburn, L. C.; Sun, T. T.; Byrd, B. L.; Hayes, R. L.; Butler, T. A. *J. Nucl. Med.* 1979, 20, 857-864.
3. Digenis, G. A.; Casey, D. L.; Wesner, D. A.; Washburn, L. C.; Hayes, R. L. *J. Nucl. Med.* 1979, 20, 662.
4. Goulding, R. W.; Gunasekera, S. W. *Int. J. Appl. Radiat. Isot.* 1975, 26, 561-564.
5. Comar, D.; Cartron, J.-C.; Maziere, M.; Marazano, C. *Eur. J. Nucl. Med.* 1976, 1, 11-14.
6. Hara, T.; Taylor, C.; Lembares, N.; Lathrop, K. A.; Harper, P. V. *J. Nucl. Med.* 1971, 12, 361-362.
7. Cohen, M. B.; Spolter, L.; Chang, C. C.; MacDonald, N. S. *Clin. Nucl. Med.* 1980, 5, S15.
8. Cohen, M. B.; Spolter, L.; Chang, C. C.; MacDonald, N. S. *J. Nucl. Med.* 1978, 19, 701.
9. Welch, M. J.; Lifton, J. F. *J. Am. Chem. Soc.* 1971, 93, 3385-3388.
10. Tilbury, R. S.; Dahl, J. R.; Monahan, W. G.; Laughlin, J. S. *Radiochem. Radioanal. Lett.* 1971, 8, 317-323.
11. Cohen, M. B.; Spolter, L.; MacDonald, N. S.; Cassen, B. *J. Nucl. Med.* 1972, 13, 433.
12. Lembares, N.; Dinwoodie, R.; Gloria, I.; Harper, P.; Lathrop, K. *J. Nucl. Med.* 1972, 13, 786.
13. Straatman, M. G.; Welch, M. J. *Radiat. Res.* 1973 56, 48-56.
14. Krizek, H.; Lembares, N.; Dinwoodie, R.; Gloria, I.; Lathrop, K. A.; Harper, P. V. *J. Nucl. Med.* 1973, 14, 629-630.
15. Gelbard, A. S.; Clarke, L. P.; McDonald, J. M.; Monahan, W. G.; Tilbury, R. S.; Kuo, T. Y. T.; Laughlin, J. S. *Radiology* 1975, 116, 127-132.
16. Vaalberg, W.; Kamphuis, J. A. A.; Beerling-van der Molen, H. D.; Reiffers, S.; Rijskamp, A.; Woldring, M. G. *Int. J. Appl. Radiat. Isot.* 1975, 26, 316-318.
17. Cooper, A. J. L.; McDonald, J. M.; Gelbard, A. S.; Gledhill, R. F.; Duffy, T. E. *J. Biol. Chem.* 1979, 254, 4982-4992.
18. Lockwood, A. H.; Finn, R. D.; Campbell, J. A.; Richman, T. B. *Brain Res.* 1980, 181, 259-266.
19. Lathrop, K. A.; Harper, P. V.; Rich, B. H.; Dinwoodie, R.; Krizek, H.; Lembares, N.; Gloria, I. In "Radiopharmaceuticals and Labelled Compounds"; I.A.E.A.: Vienna, 1973; Vol. 1, pp. 471-481.
20. Cohen, M. B.; Spolter, L.; MacDonald, N. S.; Masuoka, D. T.; Laws, S.; Neely, H. H.; Takahashi, J. In "Radiopharmaceuticals and Labelled Compounds"; I.A.E.A.: Vienna, 1973; Vol. 1, pp. 483-490.
21. Baumgartner, F. J.; Barrio, J. R.; Henze, E.; Schelbert, H.; MacDonald, N. S.; Kuhl, D. E. *Clin. Nucl. Med.* 1980, S16.

22. Cohen, M. B.; Spolter, L.; Chang, C. C.; MacDonald, N. S.; Takahashi, J.; Bobinet, D. D. *J. Nucl. Med.* 1974, 15, 1192-1195.
23. Gelbard, A. S.; Benua, R. S.; Reiman, R. E.; McDonald, J. M.; Vomero, J. J.; Laughlin, J. S. *J. Nucl. Med.* 1980, 21, 998-991.
24. Bässler, K. H.; Hammer, C. H. *Biochem. Z.* 1958, 330, 446-451.
25. Fisher, H. F.; McGregor, L. L. *J. Biol. Chem.* 1961, 236, 791-794.
26. Frieden, C. *J. Biol. Chem.* 1959, 234, 2891-2896.
27. Tomkins, G. M.; Yielding, K. L.; Curran, J. F.; Summers, M. R.; Bitensky, M. W. *J. Biol. Chem.* 1965, 240, 3793-3798.
28. Cooper, A. J. L.; Gelbard, A. S. *Anal. Biochem.* 1981, 111, 42-48.
29. Gelbard, A. S.; Clarke, L. P.; Laughlin, J. S. *J. Nucl. Med.* 1974, 15, 1223-1225.
30. Majumdar, C.; Lathrop, K. A.; Harper, P. V. *J. Labelled Compd. Radiopharm.* 1977, 13, 206.
31. Elmaleh, D. R.; Hnatowich, D. J.; Kulprathipanja, S. *J. Labelled Compd. Radiopharm.* 1979, 16, 92-93.
32. Gelbard, A. S.; Cooper, A. J. L. *J. Labelled Compd. Radiopharm.* 1979, 16, 94.
33. Woodard, H. Q.; Bigler, R. E.; Freed, B. R.; Russ, G. A. *J. Nucl. Med.* 1975, 16, 958-959.
34. Gelbard, A. S.; McDonald, J. M.; Reiman, R. E.; Laughlin, J. S. *J. Nucl. Med.* 1975, 16, 529.
35. Freed, B. R., unpublished data.
36. Gelbard, A. S.; Benua, R. S.; McDonald, J. M.; Reiman, R. E.; Vomero, J. J.; Laughlin, J. S. *J. Nucl. Med.* 1979, 20, 663.
37. Snyder, W. S.; Cook, M. J.; Nasset, E. S.; Karhausen, L. R.; Howells, G. D.; Tipton, I. H. "Report of the Task Group on Reference Man," ICRP Publication #23; Pergamon: Oxford, 1974; p. 151.
38. Oldendorf, W. H. *Am. J. Physiol.* 1971, 221, 1629-1639.
39. Lembares, N.; Dinwoodie, R.; Gloria, I.; Lathrop, K. A.; Bautovich, G.; Harper, P. V. *J. Nucl. Med.* 1973, 14, 630.
40. Spolter, L. S.; Cohen, M. B.; MacDonald, N. S.; Troulman, B.; Chang, C. C. *J. Nucl. Med.* 1973, 14, 456.
41. McDonald, J. M.; Gelbard, A. S.; Clarke, L. P.; Christie, T. R.; Laughlin, J. S. *Radiology* 1976, 120, 623-626.
42. Gelbard, A. S.; Christie, T. R.; Clarke, L. P.; Laughlin, J. S. *J. Nucl. Med.* 1977, 18, 718-723.
43. Rosen, G.; Gelbard, A. S.; Benua, R. S.; Laughlin, J. S.; Reiman, R. E.; McDonald, J. M. *Proc. Am. Assoc. Cancer Res.* 1979, 20, 189.
44. Majumdar, C.; Stark, V.; Lathrop, K.; Harper, P. V. *J. Nucl. Med.* 1978, 19, 701.
45. Cohen, M. B.; Spolter, L.; MacDonald, N.; Chang, C. C.; Takahashi, J. In "Radiopharmaceuticals"; Society of Nuclear Medicine: New York, 1975; pp. 185-188.
46. Cohen, M. B. *Int. J. Nucl. Med. Biol.* 1978, 5, 201.
47. Cho, Z. H.; Cohen, M. B.; Singh, M.; Eriksson, L.; Chan, J.; MacDonald, N. S.; Spolter, L. In "Medical Radionuclide Imaging"; I.A.E.A.: Vienna, 1977; Vol. 1, pp. 269-290.
48. Harper, P. V.; Wu, J.; Lathrop, K. A.; Wickland, T.; Moosa, A. *J. Nucl. Med.* 1980, 21, P77.

RECEIVED September 4, 1980.

# Radiopharmaceuticals Labeled with $^{11}\text{C}$ and $^{18}\text{F}$

## Considerations Related to the Preparation of $^{11}\text{C}$ -Palmitate

MICHAEL J. WELCH, STEPHEN L. WITTMER, CARMEN S. DENCE, and TIMOTHY J. TEWSON<sup>1</sup>

The Edward Mallinckrodt Institute of Radiology, Washington University School of Medicine, 510 South Kingshighway, St. Louis, MO 63110

*A general introduction to the problems associated with the use of C-11 and F-18 as radiotracers in the production of diagnostic compounds in a clinical setting is presented. The systematic development of a useful radiopharmaceutical,  $^{11}\text{C}$ -palmitic acid, is discussed in detail, from the production of the radionuclide to the final delivery of the product for clinical and animal studies. Steps in the procedure in which technical and chemical problems might arise are emphasized.*

Compounds labeled with 20-min half-lived carbon-11 were first introduced into biomedical research over 40 years ago (1-6). Before the discovery of carbon-14, compounds such as propionic acid (3) and lactic acid (2) labeled with carbon-11 were synthesized and utilized in biochemical research. After the introduction of carbon-14 as a biomedical tracer, interest in the shorter-lived carbon-11 decreased, and only in the past decade has there been renewed interest in labeling compounds with carbon-11 as well as with other short-lived positron-emitters such as oxygen-15, nitrogen-13, and fluorine-18.

The list of compounds that have been labeled with carbon-11 and fluorine-18 is extensive. Several recent reviews (7-15) have outlined methods of synthesizing compounds labeled with carbon-11 and fluorine-18 and have discussed some of the problems associated with such syntheses. In this chapter we will not attempt to list these syntheses. Instead, by using  $^{11}\text{C}$ -palmitic acid as a specific example, we will

<sup>1</sup> Current address: Division of Cardiology, University of Texas Medical School, Houston, TX 77025.

illustrate some of the problems associated with the development of a production technique that yields a routinely available radiopharmaceutical.

Unlike the  $\beta$ -particle emitted by carbon-14, the two 511-keV photons emitted when a positron/electron annihilation occurs following the decay of carbon-11 can be detected from outside the body of a human being or an animal. This, in turn, allows noninvasive tracer studies to be carried out using short-lived positron-emitting radionuclides. Recently, further emphasis has been added to the application of positron-emitting radionuclides in medicine by the introduction of positron-emission tomographs (PET) (16, 17), devices that allow the distribution of positron-emitting radionuclides in vivo to be quantified in three dimensions. The application of positron emission tomography to the measurement of brain flow and metabolism is discussed elsewhere in this volume (18). One of the most exciting potential applications of positron emission tomography is the mapping of receptors (19-21) such as the dopamine or opiate receptors (22) in the brain or the estrogen receptors in breast tumors (23). Receptor concentrations in tissues tend to be very low (commonly picomoles/gram of tissue); thus radiolabeled ligands with high specific activity are essential to enable the mapping of receptors in vivo.

One problem of great concern is the difficulty of preparing compounds of high specific activity with these radionuclides. Carbon-11 is generally produced by the  $^{14}\text{N}(p,\alpha)^{11}\text{C}$  and the  $^{10}\text{B}(d,n)^{11}\text{C}$  nuclear reactions; fluorine-18 is usually produced by the  $^{20}\text{Ne}(d,\alpha)^{18}\text{F}$  reaction but also has been produced by the  $^{16}\text{O}(^3\text{He},n)^{18}\text{F}$  and the  $^{18}\text{O}(p,n)^{18}\text{F}$  reactions. One might expect to be able to prepare these radionuclides at close to their carrier-free specific activities, which are  $9.2 \times 10^6$  Ci/mmol for carbon-11 and  $1.7 \times 10^6$  Ci/mmol for fluorine-18. In practice, however, the specific activities of carbon-11 compounds that have been prepared have a dilution of at least a factor of  $10^4$  from the theoretical maximum, while fluorine-18 compounds are diluted at least one order of magnitude. Because  $^{18}\text{F}$  can be produced in higher specific activity than  $^{11}\text{C}$ , compounds such as 3-fluoro-3-deoxyglucose (24), fluoroethanol (25), haloperidol (20), and spiroperidol (26) labeled with fluorine-18 have been produced closer to their theoretical maximum specific activity than compounds labeled with carbon-11. These compounds have all been synthesized using the starting material  $\text{H}^{18}\text{F}$ , which can be prepared in a no-carrier-added state by using the  $^{20}\text{Ne}(d,\alpha)^{18}\text{F}$  nuclear reaction to produce  $^{18}\text{F}$  and adding 10%  $\text{H}_2$  to the neon target. With the use of a circulating system, one can remove the  $\text{H}^{18}\text{F}$  from the reaction chamber and trap it on a silver wool plug coated with cesium hydroxide or cesium carbonate to produce  $^{18}\text{F}$ -labeled cesium fluoride. In the preparation of 3-fluoro-3-deoxyglucose, 1-fluoroethanol, haloperidol, and spiroperidol,  $\text{Cs}^{18}\text{F}$  prepared in this manner is used as the fluorine source.

Stable fluorine present in fluorine-18 preparations appears to originate from reagents used in later synthetic steps. In the case of carbon-11, the stable carbon comes from traces of carbon dioxide in the target and sweep gas, radiolysis of pump oil left in the chamber, radiolysis of O-rings used in the construction of the chamber, and impurities in reagents used in subsequent synthetic steps (13–15). The reduction of the amount of stable carbon in carbon-11 preparations is one of the major challenges to workers in this field. In many applications, specifically in metabolic studies utilizing <sup>11</sup>C-labeled glucose (18), such dilutions may not be important. Another major challenge is to develop rapid techniques for the routine production of compounds labeled with these short-lived radionuclides. Only a few compounds labeled with short-lived radionuclides have been synthesized in a manner simple enough to be useful in a clinical setting. Some examples include <sup>18</sup>F-labeled 2-fluoro-2-deoxyglucose (27), and <sup>11</sup>C-labeled methionine, imipramine, and flunitrazepam (28).

During the past five years, we have been preparing <sup>11</sup>C-palmitic acid in the Washington University Medical School cyclotron for use in myocardial studies by the Cardiovascular Division of Washington University School of Medicine. In the clinical setting, the <sup>11</sup>C-labeled fatty acid is used in patients in conjunction with the PETT IV system to assess the extent of myocardial infarction (29–31). Several animal studies have been completed using <sup>11</sup>C-palmitic acid to investigate its usefulness in determining the rate of myocardial metabolism (32–34).

One of the inherent problems in the production of short-lived radio-pharmaceuticals is the consistent delivery of usable amounts of labeled product. In a clinical cardiac study using the PETT system and <sup>11</sup>C-labeled palmitic acid, 20–25 mCi is normally injected into a patient. The amount of activity injected depends on the patient's physical characteristics and the desired scan time. The lower limit of usable amount of activity is 15–17 mCi; however, this amount of <sup>11</sup>C-palmitate often produces borderline statistical information and makes determination of the infarct size difficult. Animal studies usually require lower amounts of labeled product; however, in the case of some dog studies, the amount of activity required is the same as for a human preparation. In our experience covering over 220 syntheses for patient and animal studies during the past two years, <sup>11</sup>C-palmitic acid has been prepared in usable amounts in over 85% of the cases. Several modifications and additional quality control tests have been added to the previously described synthesis to increase the reliability of the procedure (32–34).

For a researcher who wishes to use <sup>11</sup>C-palmitic acid in a human or animal study, an unsuccessful preparation is one that does not yield enough activity. Causes for this can often be assigned to: operator errors, such as the incorrect manipulation of valves; mechanical problems,

such as leaks in the cyclotron vacuum system (which can allow air into the reaction vessel and thereby destroy the Grignard reagent); and chemical problems, such as incomplete reaction of the Grignard reagent with  $^{11}\text{CO}_2$ .

In principle, the addition of a Grignard reagent to  $\text{CO}_2$ , the decomposition of the complex with acid, and the binding of the product to albumin should be a simple task. However, there are several steps in the reaction sequence that may create problems, and often these difficulties become apparent only at the end of the preparation. For example, one potential hazard is denaturation of the albumin, which is commonly caused by high temperatures and trace amounts of HCl or ether (35, 36). Extreme care must be taken to prevent such an occurrence. The activity present at various stages in the synthesis of  $^{11}\text{C}$ -palmitic acid is monitored by an ionization chamber; this is done after the  $^{11}\text{CO}_2$  is trapped, when the Grignard addition is completed, after evaporation of the ether, and after the final filtration. These measurements serve as checks on how the synthesis is proceeding. Under normal circumstances, 60 mCi of  $^{11}\text{CO}_2$  are trapped after a 16  $\mu\text{Ah}$  bombardment at approximately 35- $\mu\text{A}$  beam current. After the Grignard reaction, 50 mCi are measured; after ether evaporation, 40 mCi; and following the final filtration, 20–25 mCi. Average values for actual amounts of activity trapped and delivered are given in Table I.

Despite the quality control procedures that are carried out, the failure rate in the production of  $^{11}\text{C}$ -palmitic acid is still significant. It is hoped that the number of preparations containing less than 15 mCi of radioactivity can be reduced by producing greater amounts of  $^{11}\text{CO}_2$  using the  $^{14}\text{N}(p,\alpha)^{11}\text{C}$  nuclear reaction instead of the  $^{10}\text{B}(d,n)^{11}\text{C}$  reaction currently used. However, the handling of considerably greater amounts of activity will increase the radiation dose to the chemist performing the synthesis. The ultimate aim in this synthesis and in the preparation of other labeled compounds discussed here and elsewhere for routine clinical use is the automation of the procedure. This has been done for the

**Table I. Average of  $^{11}\text{C}$ -Activity Measured During Various Stages in  $^{11}\text{C}$ -Palmitic Acid Preparation**

	<i>Time Elapsed</i> ( $\mu\text{Ah}$ )	<i>mCi <math>^{11}\text{CO}_2</math> Trapped</i> (5 min)	<i>mCi After Grignard Reaction</i> (8 min)	<i>mCi After Ether Evaporation</i> (13 min)	<i>mCi Delivered <math>^{11}\text{C}</math>-Palmitic Acid</i> (18 min)
Patient	23.7	75.0	62.2	55.3	21.5
Animal	14.9	61.6	45.9	39.3	15.8
Total	16.6	63.4	49.7	40.8	16.5

production of <sup>13</sup>NH<sub>3</sub> (37), and hopefully it will be accomplished for other more complex molecules in the near future. As can be seen from the example given here, the initial development of the synthesis of a compound labeled with a short-lived radionuclide is only part of an overall development program. A collaborative effort among chemists, chemical engineers, electrical engineers, and physicists is needed before compounds labeled with carbon-11 and fluorine-18 can be used for routine clinical studies.

A flow diagram for the production of <sup>11</sup>C-palmitic acid is given in Figure 1. We will proceed to describe in detail the synthesis of <sup>11</sup>C-palmitic acid, starting with its precursor, the Grignard reagent of 1-bromopentadecane.

### *Synthesis of the Grignard Reagent of 1-Bromopentadecane*

The Grignard reagent is synthesized in the following manner. About 100–120 mL ether, previously dried by heating under reflux in an argon atmosphere with LiAlH<sub>4</sub> for about one hour, is distilled directly into a 250-mL round-bottomed flask containing 0.34 g (14.0 mmol) magnesium turnings. All the glassware is dried in a vacuum oven and assembled hot; Teflon sleeves are used to seal all the ground joints, thus avoiding any contamination arising from vacuum grease. The entire system is kept under an inert atmosphere of argon; any traces of CO<sub>2</sub>, O<sub>2</sub>, or H<sub>2</sub>O are eliminated by bubbling the inert gas first through concentrated sulfuric acid and finally through a U-shaped tube containing potassium hydroxide pellets.

After the required volume of ether is collected, 3.64 g (12.5 mmol) of 1-bromopentadecane freshly distilled under reduced pressure is added dropwise from the addition funnel at a rate of one drop every four seconds while maintaining vigorous stirring. The onset of the reaction occurs when about one-third to one-half of the alkyl bromide has been added, and it is characterized by turbidity and a grayish color of the contents. After all the alkyl bromide has been added, the reaction mixture is stirred for an additional 2–3 h at room temperature. The Grignard solution (about 0.1M) is stored in evacuated vials and is kept at –5°C in a desiccator for a period of no longer than one month.

### *Qualitative Tests*

The Gilman test (38), a color test for the detection of a Grignard reagent, is performed on each preparation prior to its use in the synthesis of <sup>11</sup>C-palmitic acid. First, 0.5 mL of the Grignard solution is treated at room temperature with an equal volume of a 1% solution of 4,4'-bis(dimethylamino)benzophenone (Michler's ketone) while shaking. The



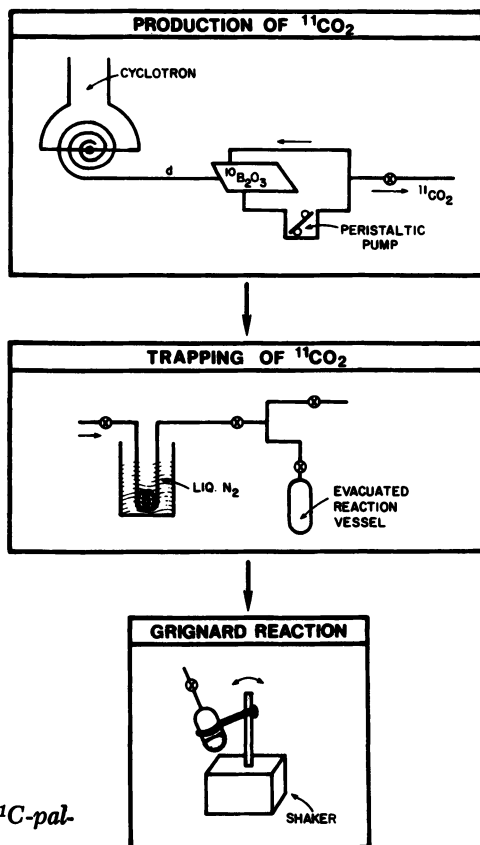
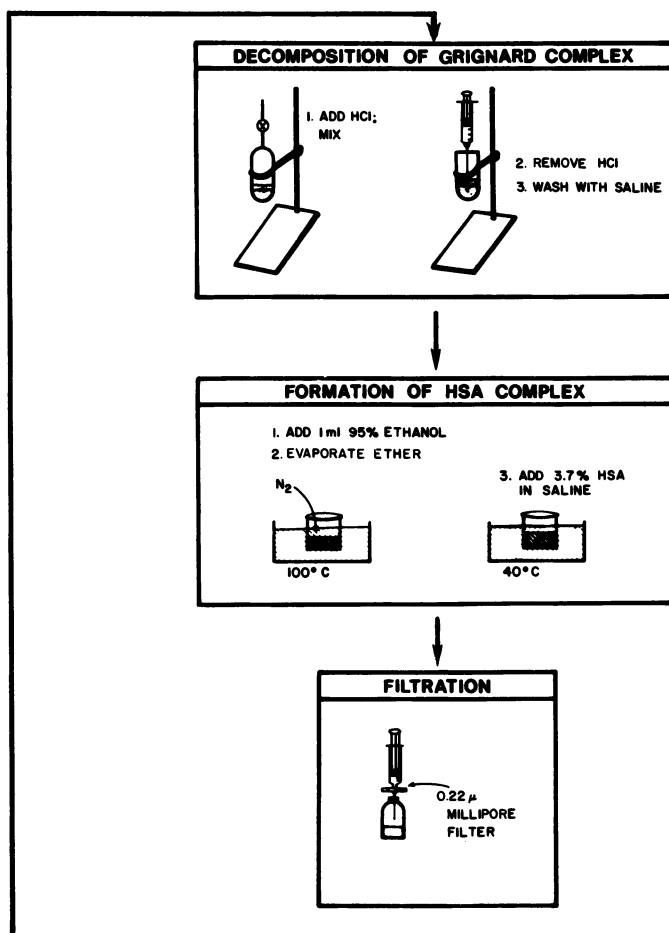


Figure 1. Schematic of  $^{11}\text{C}$ -palmitic acid preparation

yellow product is hydrolyzed by the slow addition of 1 mL  $\text{H}_2\text{O}$ . Upon addition of a few drops of a 0.2% solution of iodine in glacial acetic acid, the contents of the tube develop a greenish-blue color, indicating the presence of a Grignard reagent.

Gas-liquid chromatographic (GC) analysis is used to confirm the absence of any unreacted starting material, 1-bromopentadecane. About 1 mL of the Grignard solution is transferred to a test tube and slowly decomposed by addition of 0.1N HCl. The clear ether layer is separated and 1–2  $\mu\text{L}$  is analyzed via GC separation [column: 10% carbowax on 20 M chromosorb W 60/80, 5 ft  $\times$   $\frac{1}{4}$  in. SS; program: 150°C (3 min) to 210°C (3 min) at 14°/min; injector block and FID detector at 270°C; carrier gas helium at 60 mL/min]. Under these conditions, pentadecane elutes at about 2 min, while the starting material, 1-bromopentadecane, elutes at 8.6 min. In a few preparations we found a small percentage of



an impurity with a retention time of 10 min. The presence of this impurity does not have a detrimental effect on the  $^{11}\text{C}$ -palmitic acid preparation, but its identity has not yet been established.

A second GC separation has been developed on a column containing 20% OV-1 on chromosorb W 45/60 programmed from 220°C (1 min) to 270°C (2 min) at 6°/min; injector block and FID detector at 280°C, carrier gas helium at 60 mL/min. The retention time for pentadecane is about 1.3 min; 1-bromopentadecane elutes at about 4.2 min, with the impurity (if present) eluting at about 2.4 min.

### *Synthesis of $^{11}\text{C}$ -Palmitic Acid*

The  $^{11}\text{CO}_2$  is produced in situ at the Washington University Medical School cyclotron (Allis Chalmers) by the  $^{10}\text{B}(\text{d},\text{n})^{11}\text{C}$  reaction. The  $^{11}\text{CO}_2$  is swept from the target with a carrier gas mixture of 98:2 helium:

oxygen, yielding better than 96% of the isotope as the desired  $^{11}\text{CO}_2$ . The  $^{11}\text{CO}_2$  is trapped in a coiled glass tube containing a plug of glass wool and immersed in liquid nitrogen.

After warming the trap in a water bath, the  $^{11}\text{CO}_2$  is quickly transferred to an evacuated vessel using a flow of helium. Two mL of the Grignard solution are added and the vessel is shaken for about 3–4 min. The palmitic acid–MgBr complex is decomposed with 2 mL of 1N HCl while shaking the vessel to clarify the ether layer. The contents are transferred to a  $1.5 \times 12$  cm test tube, the acidic layer removed by means of a syringe, and the ether freed of any traces of acid by washing twice with 2-mL portions of normal saline solution (0.9% NaCl). The ethereal solution is then transferred to a 50-mL beaker, 1 mL 95% ethanol is added, and the ether is evaporated in a hot water bath under  $\text{N}_2$  to yield a final volume of approximately 1 mL. The resulting solution is warmed to  $40^\circ\text{C}$  and combined with about 8 mL of 3.7% human serum albumin in normal saline, also at  $40^\circ\text{C}$ . After warming for about 3 min to allow for binding of the palmitic acid to the albumin (39–40), the mixture is filtered through a  $0.45\text{-}\mu\text{m}$  Millipore filter, and the filter and beaker are rinsed with approximately 1 mL of saline. The solution is finally passed through a  $0.22\text{-}\mu\text{m}$  disposable Millipore filter and the activity measured prior to injection. The total preparation time, including the initial trapping of  $^{11}\text{CO}_2$ , is about 15–20 min.

### *High-Pressure Liquid Chromatography of $^{11}\text{C}$ -Palmitic Acid and Pentadecane*

To verify the formation of  $^{11}\text{C}$ -palmitic acid and to detect any pentadecane or other impurities that may be present, the final solution is analyzed by high-pressure liquid chromatography (HPLC) under the following conditions:

Instrument: Waters LC; M-6000 solvent delivery system  
Column: Fatty acid analysis column,  $10\ \mu\text{m}$  particle size;  
 $3.9\ \text{mm i.d.} \times 30\ \text{cm long}$   
Solvent: THF:CH<sub>3</sub>CN:H<sub>2</sub>O 35:30:40 (v/v)  
Flow Rate: 2 mL/min ( $\sim 2300$  psi)  
Refractive Index and NaI(Tl) Detectors

$^{11}\text{C}$ -Palmitic acid elutes at about 5.0 min, and the hydrocarbon at about 10.0 min. Analyses of  $^{11}\text{C}$ -palmitic acid preparations, as expected, have not shown a mass peak corresponding to the pentadecane, which precipitates out into the alcoholic solution upon evaporation of ether and is later filtered out of the final preparation. Radiochromatograms consistently show a single peak with a retention corresponding to that time of unlabeled palmitic acid; the radiochemical yield is calculated to be higher than 99%. An example of a typical chromatogram is shown in Figure 2.

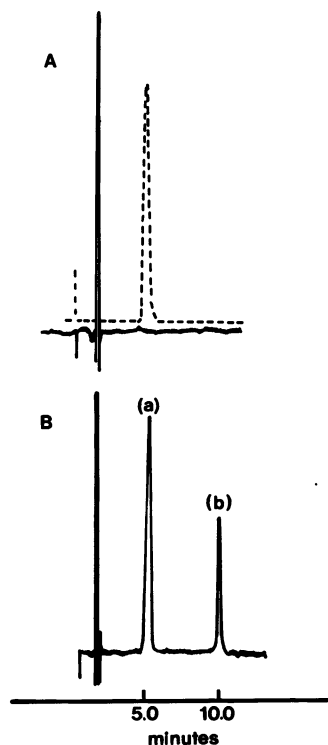


Figure 2. (A) HPLC separation of a typical  $^{11}\text{C}$ -palmitic acid preparation: (---) radioactivity detector; (—) refractive index detector. (B) HPLC of a mixture of (a) palmitic acid and (b) n-pentadecane standards.

Last, the  $^{11}\text{C}$ -palmitic acid is regularly checked for apyrogenicity and sterility using standard U.S.P. methods. Elemental analyses of two random preparations have shown no significant contribution from the Grignard reagent to the percentages of bromine and magnesium, as compared to a blank made up of 3.7% human serum albumin in normal saline (0.9% NaCl).

### Acknowledgments

The work described here was supported by NIH Grants HL13851, HL17646, and NS06833.

### Literature Cited

1. Tobias, C. A.; Lawrence, J. H.; Roughton, F. J. W.; Root, W. S.; Gregersen, M. I. *Am. J. Physiol.* **1945**, *145*, 253.
2. Cramer, R. D.; Kistiakowsky, G. B. *J. Biol. Chem.* **1941**, *137*, 549.
3. Buchanan, J. M.; Hastings, A. B.; Nesbitt, F. B. *J. Biol. Chem.* **1943**, *150*, 415.
4. Long, F. A. *J. Am. Chem. Soc.* **1939**, *61*, 570.
5. Allen, M. B.; Ruben, S. *J. Am. Chem. Soc.* **1942**, *64*, 949.

6. Nahinsky, P.; Rice, C. S.; Ruben, S.; Kamen, M. D. *J. Am. Chem. Soc.* **1942**, *64*, 2299.
7. Wolf, A. P.; Christman, D. R.; Fowler, J. S.; Lambrecht, R. M. In "Radiopharmaceuticals and Labeled Compounds"; IAEA: Vienna, 1976; pp. 345-380.
8. Robinson, G. D. In "Radiopharmaceuticals"; Subramanian, G., et al., Eds.; Society of Nuclear Medicine: New York, 1975; pp. 141-148.
9. Wolf, A. P.; Redvanly, C. S. *Int. J. Appl. Radiat. Isot.* **1977**, *28*, 29-48.
10. Palmer, A. J.; Clark, J. C.; Goulding, R. W. *Int. J. Appl. Radiat. Isot.* **1977**, *28*, 53-65.
11. Welch, M. J.; Eichling, J. O.; Straatmann, M. G.; Raichle, M. E.; Ter-Pogossian, M. M. In "Non-Invasive Brain Imaging: Computed Tomography and Radionuclides"; DeBlanc, Jr., J. H.; Sorenson, J. A., Eds.; Society of Nuclear Medicine: New York, 1975; pp. 25-44.
12. Welch, M. J.; Wagner, S. J. In "Recent Advances in Nuclear Medicine"; Lawrence, J. H.; Budinger, T. F., Eds.; Grune and Stratton: New York, 1978; Vol. 5, pp. 51-69.
13. Wolf, A. P.; Fowler, J. S. In "Radiopharmaceuticals II"; Society of Nuclear Medicine: New York, 1979; pp. 73-92.
14. Welch, M. J.; Tewson, T. J. In "Radiopharmaceuticals II"; Society of Nuclear Medicine: New York, 1978; pp. 201-217.
15. Welch, M. J.; McElvany, K. D.; Tewson, T. J. In "Radiotracers in Biology and Medicine, Vol. 10—Receptor Binding Radiotracers"; Eckelman, W. C., Ed.; CRC: Boca Raton, in press.
16. Ter-Pogossian, M. M. *Semin. Nucl. Med.* **1977**, *7*, 109-128.
17. Budinger, T. F. *Semin. Nucl. Med.* **1977**, *7*, 285-298.
18. Raichle, M. E., Chap. 22 in this book.
19. Comar, D.; Mazière, M.; Godot, J. M.; Berger, G.; Minini, C. L.; Artel, G.; Naquet, K. *Nature (London)* **1979**, *280*, 329-381.
20. Tewson, T. J.; Raichle, M. E.; Welch, M. J. *Brain Res.* **1980**, *192*, 291.
21. Hochberg, R. B. *Science* **1979**, *205*, 1138.
22. Young, W. S.; Kuhar, M. J. *Brain Res.* **1979**, *179*, 255-270.
23. Katzenellenbogen, J. A.; Heiman, D. F.; Carlson, K. E.; Lloyd, J. E. In "Radiotracers in Biology and Medicine, Vol. 10—Receptor Binding Radiotracers"; Eckelman, W. C., Ed.; CRC: Boca Raton, in press.
24. Tewson, T. J.; Raichle, M. E.; Welch, M. J. *J. Nucl. Med.* **1978**, *19*, 1339.
25. Tewson, T. J.; Welch, M. J. *J. Nucl. Med.* **1980**, *21*, 559.
26. Maeda, M.; Tewson, T. J.; Welch, M. J. *J. Labelled Compd. Radiopharm.*, in press.
27. Ido, T.; Won, C. N.; Casella, V.; Fowler, J.; Wolf, A. P. *J. Labelled Compd. Radiopharm.* **1978**, *14*, 175.
28. Mazière, M.; Berger, G.; Prenant, C.; Sastre, J.; Comar, D. *J. Labelled Compd. Radiopharm.*, in press.
29. Ter-Pogossian, M. M.; Klein, M. S.; Markham, J.; Roberts, R.; Sobel, B. E. *Circulation* **1980**, *61*, 242-255.
30. Sobel, B. E.; Weiss, E. S.; Welch, M. J.; Siegel, B. A.; Ter-Pogossian, M. M. *Circulation* **1977**, *55*, 853-857.
31. Ter-Pogossian, M. M.; Weiss, E. S.; Coleman, R. E.; Sobel, B. E. *Am. J. Roentgenol.* **1976**, *127*, 79-90.
32. Klein, M. S.; Goldstein, R. A.; Welch, M. J.; Sobel, B. E. *Am. J. Physiol.* **1979**, *273*, H51-H57.
33. Weiss, E. S.; Ahmed, S. A.; Welch, M. J.; Williamson, J. R.; Ter-Pogossian, M. M.; Sobel, B. E. *Circulation* **1977**, *55*, 66-73.
34. Weiss, E. S.; Hoffman, E. J.; Phelps, M. E.; Welch, M. J.; Henry, P. D.; Ter-Pogossian, M. M.; Sobel, B. E. *Circ. Res.* **1976**, *39*, 24-32.
35. Peters, Jr., T. *Adv. Clin. Chem.* **1970**, *13*, 37-111.
36. Watson, D. *Adv. Clin. Chem.* **1965**, *8*, 237-303.

37. Ido, T.; Iwata, R. *J. Labelled Compd. Radiopharm.*, in press.
38. Gilman, H.; Schulze, F. *J. Am. Chem. Soc.* **1925**, *47*, 2002–2005.
39. Goodman, D. S. *J. Am. Chem. Soc.* **1958**, *80*, 3892–3898.
40. Evans, J. R.; Opie, L. H.; Shipp, J. C. *Am. J. Physiol* **1963**, *205*, 766–770.

RECEIVED September 29, 1980.

# Positron Emission Tomography Tracer Techniques

MARCUS E. RAICHLE

Edward Mallinckrodt Institute of Radiology, and Department of Neurology and Neurological Surgery, Washington University School of Medicine, St. Louis, MO 63110

*Short-lived, positron-emitting radionuclides such as  $^{15}\text{O}$ ,  $^{13}\text{N}$ ,  $^{11}\text{C}$ , and  $^{18}\text{F}$  have provided the basis for many unique in vivo tracer strategies for the study of specific metabolic and biochemical processes, regionally and quantitatively in laboratory animals and, to some extent, in humans. By labeling specific compounds with these radionuclides, it is possible to measure not only the regional kinetics, distribution, and metabolism of such compounds as glucose labeled with either  $^{11}\text{C}$  or  $^{18}\text{F}$ , but also regional oxygen utilization and blood flow. A variety of studies employing compounds such as  $^{15}\text{O}$ -labeled water and  $^{11}\text{C}$ -labeled alcohols have also permitted a unique exploration of the permeability characteristics of the brain in vivo in a manner never before possible. The development of positron emission tomography (PET) has greatly expanded the employment of such strategies in humans. This new imaging technique permits quantitative tissue autoradiography to be performed safely in vivo in humans. When combined with extant tracer strategies and positron-emitting radionuclides, PET offers a very important new tool for clinical investigation. It is the purpose of this chapter to review tracer strategies currently being employed with PET for studies in humans.*

Although biochemists have developed a very sophisticated understanding of in vivo chemical events occurring in various organs of the body, their work has been hampered by difficulty in making direct measurements of dynamic events in living tissue, especially that of human beings. It is obvious that simplified test tube systems may not always

0065-2393/81/0197-0419\$05.00/0  
© 1981 American Chemical Society

accurately represent the situation *in vivo*. Great advances have been made over the past thirty years in the development of techniques for the measurement, *in vivo*, of the circulation, biochemistry, and metabolism of various organs of the human body.

Exemplifying progress toward the development of a satisfactory means of obtaining dynamic *in vivo*, biochemical, and hemodynamic information is the work on the human brain begun by Kety and Schmidt in 1948. Their introduction of the nitrous oxide technique for the measurement of cerebral blood flow (1) when combined with the measurement of brain arteriovenous differences of various substrates and metabolites provided our first clear *in vivo* information on the relationship between substrate delivery and utilization in human beings. Although this technique was widely utilized and provided much valuable information, it suffered from the obvious flaw of not providing regional information. Dynamic regional differences in both circulation and metabolism were obscured, if not lost completely, by this approach. The introduction of a method for the measurement of regional cerebral blood flow based on the external detection of the clearance of freely diffusible radioactive gases such as xenon-133 from the brain (2) provided much additional information on regional hemodynamics in the human brain, and demonstrated for the first time the dynamic interplay between localized functional events in the brain and its circulation (3). However, this technique precluded the measurement of regional metabolism, thus significantly reducing its capacity to provide the type of information desired. The introduction of cyclotron-produced, positron-emitting radiopharmaceuticals into the medical environment for the measurement of brain hemodynamics and metabolism partially fulfilled this need for regional metabolic and biochemical information. *In vivo* techniques were developed for the measurement of regional blood flow (4), glucose (5), and oxygen utilization (6) as well as regional cerebral blood volume (7) and vascular permeability (8). These techniques, however, have received limited application because they require the intracarotid injection of the radiopharmaceutical as well as the presence of a cyclotron in the immediate medical environment. Thus, until recently we have been unable to obtain more than a quasi-regional assessment of cerebral blood flow in the human brain and only limited metabolic information.

Three significant developments move us closer to the capability of safely acquiring regional *in vivo* biochemical information in the human brain. First, the appearance within the medical environment of apparatus for nuclear bombardment, such as cyclotrons and linear accelerators, coupled with ingenious techniques for rapid synthesis of radiopharmaceuticals, have provided many radiopharmaceuticals suitable for *in vivo* regional hemodynamic and metabolic studies (9). Second, the parallel development of appropriate mathematical models has provided



the basis for practical algorithms that allow parameters of biochemicals and physiological significance to be estimated from data obtained by monitoring the fate of these radiopharmaceuticals in vivo. Third, the more recent development of detection systems employing the concept of positron emission tomography (PET) permits us to monitor the fate of these radiopharmaceuticals in vivo in a truly regional and quantitative manner.

Emission tomography is a visualization technique in nuclear medicine that yields an image of the distribution of a previously administered radionuclide in any desired transverse section of the body. PET utilizes the unique properties of the annihilation radiation generated when positrons are absorbed in matter. It is characterized by the fact that an image reconstructed from the radioactive counting data is an accurate and quantitative representation of the spatial distribution of a radionuclide in the chosen section. This approach is analogous to quantitative autoradiography but has the added advantage of allowing in vivo studies. It is the purpose of this chapter to present an introduction to the tracer techniques involved in the actual measurement of tissue hemodynamics, metabolism, and biochemistry. Although much of the work to be reviewed focuses on the brain it must be kept in mind that these are general techniques applicable to other organs as well.

### ***Blood Volume***

The measurement of regional cerebral blood volume (rCBV) in transverse sections of the human brain was one of the first measurements accomplished with PET. The early introduction of this measurement was, in part, the result of its simplicity and accuracy. The most satisfactory way to measure rCBV using PET is to label the circulating blood pool of the body with the vascular tracer  $^{11}\text{C}$ -labeled carboxyhemoglobin. This is achieved by causing the subject to inhale air which contains trace amounts of carbon monoxide labeled with carbon-11. The rCBV is then computed from data obtained from the equilibrium tomographic image of  $^{11}\text{C}$ -carboxyhemoglobin in the brain [counts  $\text{sec}^{-1}$  (mL tissue) $^{-1}$ ] and venous blood samples [counts  $\text{sec}^{-1}$  (gm blood) $^{-1}$ ] obtained during the time of the emission scan.

Measurements of rCBV in man by PET not only reveal the expected regional differences due to differences in vascular density between grey and white matter, but also provide a clear delineation of the major vascular structures, primarily venous, surrounding the brain. Furthermore, the responsiveness of the cerebral blood volume to changes in arterial carbon dioxide tension observed with emission tomography compare favorably with such measurements obtained by a variety of other such techniques (10).

The ability to measure rCBV by PET is important for three reasons. First, it provides in a simple and accurate manner an assessment of regional perfusion within the brain. Changes in rCBV have been correlated with changes in regional cerebral blood flow (rCBF) (11), and as such provide a potential index of blood flow. However, it must be remembered that blood volume is a relatively insensitive index of blood flow, changing little in relation to large changes in blood flow (11), and further, that blood volume may at times change quite independent of blood flow due to the phenomenon of blood flow autoregulation (12). Second, the technique employed for measurement of rCBV, when combined with other tracer strategies, can provide a variety of measurements in addition to that of blood volume alone. For example, a measurement of the equilibrium distribution of the plasma tracer  $^{11}\text{C}$ -labeled methyl albumin when combined sequentially with a measurement of erythrocyte tracer  $^{11}\text{C}$ -labeled carboxyhemoglobin allows the measurement of the tissue hematocrit. Finally, the measurement of rCBV assumes major importance in the other measurements possible with PET. It provides the only means of determining the concentration of a radiopharmaceutical in the vascular compartment as compared to the extravascular compartment of tissue. The ability to make this distinction accurately is a unique feature of PET and of critical importance in the measurement of metabolism and tissue chemical composition.

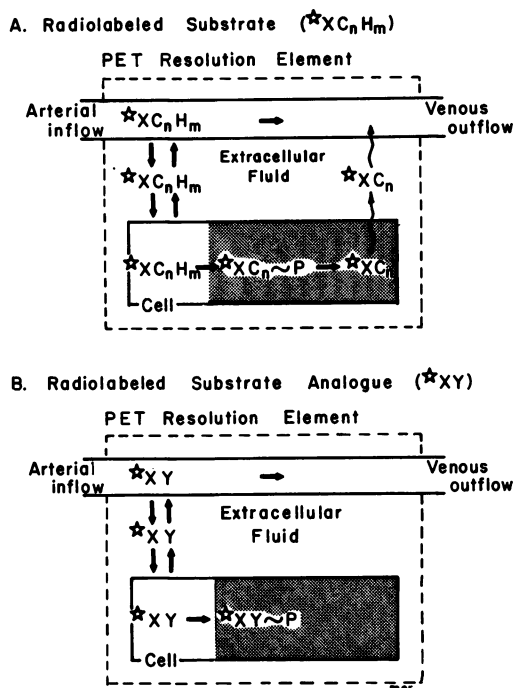
### ***Metabolism***

**Substrate Utilization.** Quantitative measurement of regional substrate utilization *in vivo* is well within the capability of PET, but is of somewhat greater conceptual complexity than the measurement of regional blood volume. Such measurements are exemplified by the quantitative studies of cerebral glucose utilization using  $^{11}\text{C}$ -labeled glucose (13) and  $^{18}\text{F}$ -labeled 2-deoxy-D-glucose (14).

To understand the tracer strategy employed in these measurements of metabolism by PET, it is first important to understand the behavior of a labeled substrate such as  $^{11}\text{C}$ -glucose or a labeled substrate analogue such as [ $^{18}\text{F}$ ]2-deoxy-D-glucose. These are illustrated in Figure 1.

Because of the complex behavior of the tracers employed in metabolic studies with PET, rather sophisticated mathematical models and data acquisition schemes have been developed to extract metabolic rates from the data provided by the quantitative PET images and samples of arterial blood specific activity. These are illustrated in Figure 2.

From the material presented in Figures 1 and 2, it should be apparent that several important assumptions must be addressed in the application of these techniques. First, we assume that the tracer is transported and metabolized in the same manner and at the same rate as the compound being traced (i.e., tracee). This requirement is clearly met when



**Figure 1.** A representation of the fate of (A) a radiolabeled substrate ( $^*X C_n H_m$ ) such as  $^{11}C$ -glucose or (B) a radiolabeled substrate analogue ( $^*X Y$ ) such as  $[^{18}F]2$ -deoxy-D-glucose (41).

Both are introduced into the vascular compartment from a peripheral site such as a vein. They traverse the vasculature in the region of interest usually entering brain tissue by a highly specific mechanism of carrier mediated, facilitated diffusion. Because a significant pool of the substance being traced (e.g., glucose) usually exists in the tissue the radiolabeled tracer moves back and forth across the blood tissue barrier in response to the local concentration gradients. Within the cell the tracer must be transformed, through metabolism, to a chemical species that does not readily leave the cell in order to permit satisfactory measurement of its metabolism. In the case of radiolabeled glucose (A) or a glucose analogue (B) phosphorylation through the action of hexokinase irreversibly transforms the tracer into an impermeable compound. Analogues (B) are so designed to remain irreversibly trapped by resisting further metabolic breakdown whereas a tracer such as radiolabeled glucose (A) will eventually be metabolized to labeled substances, such as carbon dioxide, that readily pass from the cell and the tissue. Mathematical models and data acquisition schemes must account for these complexities to achieve an accurate measurement of metabolism.

a substrate such as glucose is labeled with  $^{11}C$ .  $^{11}C$ -Glucose is biologically indistinguishable from unlabeled D-glucose. This requirement is not met in the case of substrate analogue tracers such as  $[^{18}F]2$ -deoxy-D-glucose, thus requiring appropriate correction factors (Figure 2C).

Second, we assume that the metabolized tracer is retained within the area of interest during the measurement period. In the case of a radiolabeled substrate such as  $^{11}C$ -glucose, achievement of this require-



**Figure 2.** A general approach to data acquisition and analysis in the measurement of metabolism by PET is shown (41).

(A) The data resulting from the intravenous administration of a tracer such as  $^{14}\text{C}$ -glucose or  $^{18}\text{F}$ ]2-deoxy-D-glucose consists of time varying blood specific activity  $[a_b(t)]$  measured by repeated sampling of blood from a peripheral artery and local tissue activity  $[q(t)]$  determined at discrete points in time by PET after tracer administration. At early times after tracer administration ( $T < 5$  min) activity in blood contributes significantly to the PET image, whereas at late times ( $T' > 30$  min) blood activity contributes little to the image. The basic step in determining the metabolic rate from these data generated either by a radiolabeled substrate or a substrate analogue is to divide the tissue activity by the integral of the blood specific activity. (B) In the case of a radiolabeled substrate such as  $^{14}\text{C}$ -glucose the data are analyzed at early times to avoid egress of metabolized tracer from the tissue. As a result a correction must be made for unmetabolized tracer in the blood as well as the tissue. These corrections require a prior knowledge of the blood volume ( $V_b$ ), which can be measured by PET using  $^{14}\text{C}$ -carboxyhemoglobin and the concentration of tracee in blood ( $C_b$ ). Additionally, two parameters,  $\alpha$  and  $\kappa$ , must be determined by separate experimentation.  $\alpha$  denotes the ratio of forward to reverse unidirectional systemic tracee fluxes across the blood-brain barrier and  $\kappa$ , the sum of the two compartmental rate constants for egress of tracee and tracer from tissue to blood and into the metabolic pathways. Details of the derivation of this model are found in the work of Raichle et al. (24, 26). (C) In the case of a radiolabeled substrate analogue such as  $^{18}\text{F}$ ]2-deoxy-D-glucose the data are analyzed at late times ( $T' > 30$  min) when blood activity is negligible. Corrections for the presence and behavior of unmetabolized tracer in the tissue must still be made and are based upon a prior knowledge of  $\kappa$ , the compartmental rate constant for tracee movement from blood to tissue ( $K_p^*$ ) and the concentration of tracer in plasma at the time of the measurement ( $C_p^*$ ). The other correction accounts for the difference between tracer and tracee that occurs when radiolabeled analogues are used. Here  $\lambda$  equals the ratio of the distribution volume of tracer to that of tracee;  $\phi$  is the fraction of tracee, in this case, glucose, that once phosphorylated continues down the glycolytic pathway; and  $k_m^*$ ,  $V_{max}^*$ ,  $k_m$ , and  $V_{max}$  are the familiar Michaelis-Menten kinetic constants for tracer and tracee. Further details of this model are found in the work of Sokoloff et al. (31).

tion step (16). Further metabolism is blocked because of the structure of the molecule. Thus,  $^{18}\text{F}$ -labeled 2-deoxy-D-glucose-6-phosphate is theoretically retained within the cells of the central nervous system for the period of the measurement.

Third, we assume that the amount of tracer not metabolized, that is, free tracer in blood and extracellular fluid, is either negligible or accounted for at the time of the measurement. This requirement is most easily met when radiolabeled analogues are employed. Because they are irreversibly trapped within the cells of the region of interest (16) it is possible to delay the actual measurement until free tracer in tissue and blood has fallen to insignificant levels thus minimizing the errors in estimating the free tracer in the tissue. In the case of glucose analogues, this usually requires 30–60 min (16). This type of delay is not possible when radiolabeled substrates such as  $^{14}\text{C}$ -glucose are employed, because, as pointed out above, significant egress of radiolabeled metabolites from the tissue begins within 5 min of the time of injection (5). Thus, in the case of radiolabeled substrates, the tracer strategy employed must ex-

PLICITLY account for the free tracer in blood and tissues. This is accomplished, in part, by measuring the rCBV in association with the measurement of regional metabolism. By knowing the rCBV, it is then possible to compute not only the free tracer in blood, but also the free tracer within the tissue itself (13).

It should be clear from the foregoing that tracers in the form of radiolabeled substrates (e.g.,  $^{14}\text{C}$ -glucose) and radiolabeled substrate analogues (e.g., [ $^{18}\text{F}$ ]2-deoxy-D-glucose) each have their special advantages and disadvantages. It is important that these should be specifically noted.

There are several advantages to the use of a radiolabeled substrate such as  $^{14}\text{C}$ -glucose. First, the tracer is biochemically identical to the compound being traced. Thus, corrections need not be made in the tracer model for differences in transport properties and enzyme affinities that vary among species (Figure 2C) (16). Such corrections may present an added difficulty when the organ of interest is diseased. Second, the measurement requires, by necessity, a relatively short time. This permits repeated measurements to be made during the course of one experiment should they be required for the evaluation of transient phenomena. Finally, there are currently available a large number of substrates labeled with positron-emitting radioisotopes (17), thus affording the opportunity of making a wide variety of metabolic measurements. These advantages of radiolabeled substrates such as  $^{14}\text{C}$ -glucose are tempered by several clear disadvantages. First, these tracers are not efficiently trapped as radiolabeled metabolites in the tissue (5, 13). Thus the measurement strategy must be designed to permit measurement within the first few minutes following injection, or properly account for tracer egress from the tissue. One possible and rather simple means of accounting for this egress of metabolized tracer from the tissue in each subject is to repeat the measurement of metabolism several times within the first 5 min following the injection of the tracer. The computed metabolic rate from these data would obviously fall as a function of time. The rate of its decline could be obtained from the data. Knowledge of this rate of decline as a function of time after injection allows an estimate of the true metabolic rate prior to egress of metabolized tracer. Preliminary data in our laboratory (unpublished) suggest that this is a very workable solution to this problem (see below).

Second, because the measurement must be made shortly after the injection of the tracer, it is necessary to couple the measurement of metabolism with the measurement of rCBV, thus adding to the logistical and computational complexity of the measurement.

Finally, specific descriptors ( $\alpha$  and  $\kappa$ , Figure 2B) (5) of the behavior of free tracer in the tissue must be predetermined to compute the amount

of tracer within the tissue that remains unmetabolized. With the advent of rapid, multislice PET imaging devices (18, 19, 20) it should be possible to determine such parameters on-line by obtaining, rapidly, sequential PET images of regional tissue activity as a function of time during the course of a slow intravenous infusion of tracer. These data, coupled with a knowledge of the time activity history of tracer in arterial blood, should allow the application of statistical procedures previously described and validated (5) to estimate these parameters, as well as the metabolic rate. Successful implementation of such a strategy would not only circumvent the risk of assuming arbitrary values for such parameters, but would also greatly expand the information available from such a study. Thus, in addition to a measurement of the local utilization rate of glucose, one would be able to obtain such important measurements as the brain-to-blood glucose concentration ratio, relative free-glucose space in tissue, brain free-glucose concentration, and brain free-glucose turnover time (5) in humans for the first time.

Radiolabeled substrate analogues have a number of unique advantages. First, these compounds are so designed as to remain irreversibly trapped within the tissue once they have been metabolized (16). Thus we are not concerned with the egress of metabolites when employing them to measure regional metabolic rates. Second, because these compounds remain irreversibly trapped within tissue, it is possible to minimize the impact of corrections for free tracer in tissue and blood such as is done when radiolabeled substrates are employed. By reducing or eliminating the necessity for making such a correction, the accuracy of the measurement of metabolism obviously is enhanced. However, radiolabeled substrate analogues do have a number of noteworthy disadvantages. First and most importantly, they are not biochemically identical to the compound being traced. When radiolabeled substrate analogues are employed, it is necessary to correct for differences in transport properties and enzyme affinities that have been shown to vary among species (16). Such corrections may present an added difficulty when the organ of interest is diseased. Second, because the strategy employed relies on time ( $\sim 30$ – $60$  min) for unmetabolized tracer to clear from blood and tissue, measurement time tends to preclude the examination of transient phenomenon, and repeat measurements. In fact, because presently employed mathematical models for radiolabeled substrate analogues ignore altogether a blood contribution to the observed tissue signal [cf. Figure 2B and 2C, (6)] measurements at early times are prohibited. This time requirement also necessitates the administration of larger quantities of the radionuclide and/or the use of radionuclides with longer half lives (e.g.,  $^{18}\text{F}$  rather than  $^{11}\text{C}$ ) to achieve adequate counting statistics in the PET image. This results in a higher dose to the patient.

Third, substrate analogues are capable of disrupting normal metabolism if they enter the cell in sufficiently high concentration. Although this is not a problem when tracer quantities of radiolabeled substrate analogues are employed, it is important that synthesis techniques employed in the production of such tracers assure very low concentrations of unlabeled carrier.

**Oxygen Utilization.** The strategies outlined above for the measurement of substrate utilization using as tracers radiolabeled substrates or substrate analogues do not permit, in their present form, the measurement of tissue oxygen consumption. This is not a problem of tracer labeling, as the positron-emitting radionuclide  $^{15}\text{O}$  is readily available from most cyclotrons in the form of a gas (17) which can then be used to label the subject's blood as  $^{15}\text{O}$ -oxyhemoglobin. Rather it is the prompt conversion of  $^{15}\text{O}$ -labeled oxygen to  $^{15}\text{O}$ -labeled water of metabolism in the brain and its rapid egress from the tissue that precludes the direct application of the methods outlined above. Quite simply, the egress of metabolized tracer from the tissue occurs immediately and in significant quantities.

In response to the clear need for a means of measuring tissue oxygen consumption Jones and his colleagues (21, 22), and, later, Subramanyam et al. (23) proposed a technique for the measurement of the regional fractional extraction of oxygen by the brain. This measurement is accomplished by the sequential inhalation to equilibrium of trace amounts of  $^{15}\text{O}$ -oxygen and  $^{15}\text{O}$ -labeled carbon dioxide. The inhalation of  $^{15}\text{O}$ -labeled oxygen to equilibrium produces a brain image that results from the accumulation of molecular oxygen and water of metabolism within brain tissue. To obtain the fractional extraction of oxygen by the brain, it is necessary to correct this image for the egress of water of metabolism labeled with  $^{15}\text{O}$  from the brain and its recirculation back to the brain. This is accomplished by inhaling  $^{15}\text{O}$ -labeled carbon dioxide to equilibrium. Inhalation of  $^{15}\text{O}$ -labeled carbon dioxide immediately labels the circulating water pool in blood because of the presence of carbonic anhydrase in the red cell (24). The resulting brain image simulates the egress as well as the recirculation of metabolic water to the brain. The regional oxygen fractional extraction can then be computed by dividing the equilibrium image of metabolic water ( $\text{H}_2^{15}\text{O}_{\text{met}}$ ) by the image of circulating water ( $\text{H}_2^{15}\text{O}_{\text{circ}}$ ). Thus

$$\frac{\text{H}_2^{15}\text{O}_{\text{met}}}{\text{H}_2^{15}\text{O}_{\text{circ}}} = \frac{(\text{Ca} - \text{Cv})}{(\text{Ca})} \cdot \text{C}_{\text{O}_2}/\text{C}_{\text{H}_2\text{O}}$$

where Ca and Cv represent the arterial and cerebral venous oxygen contents respectively and  $(\text{Ca} - \text{Cv})/(\text{Ca})$ , the oxygen fractional extraction;  $\text{C}_{\text{O}_2}$  represents the arterial concentration of radioactive oxygen



and  $C_{H_2O}$  the arterial concentration of circulating  $H_2^{15}O$ . This ratio will be a constant for all regions of the tissue, and hence this "normalization" (22) procedure will produce a distribution of activity that represents the local fractional extraction of oxygen.

Employing this technique, these investigators have demonstrated regional differences in the fractional extraction of oxygen in the brain of man under normal circumstances and in a number of disease states. Their data clearly demonstrate the usefulness of this technique in assessing regional metabolism in the brain. However, it must always be borne in mind that the fractional extraction of oxygen is not only influenced by the local oxygen utilization rate in brain, but also by the regional blood flow as can be seen from the following expression.

$$\text{Fractional extraction of } O_2 = \frac{\text{oxygen consumption}}{\text{blood flow} \times \text{arterial } O_2 \text{ content}}$$

Thus, where oxygen utilization and blood flow move in parallel, for example, during functional activation (25) or during a seizure (26), a significant change in the local fractional extraction of oxygen will not be observed. Thus a significant change in local oxygen utilization under such circumstances will not be appreciated with this tracer technique. On the other hand, where blood flow is altered independently of metabolism, for example, during acute changes in arterial carbon dioxide tension (27) a significant change in the local fractional extraction of oxygen will merely reflect the change in blood flow. Without a knowledge of the latter, it is not possible to arrive at a correct interpretation of a change in the regional fractional extraction of oxygen. Clearly, this technique has promise, but only if it can be employed with an accurate measure of regional blood flow.

An alternative approach to the measurement of brain oxygen utilization, made possible by the development of fast, multislice PET imaging devices (19), employs a modification of the tracer model depicted in Figure 2B (5, 13). The adaptation of this model for the measurement of local tissue oxygen consumption with PET requires, first, an understanding of the model parameters  $\alpha$  and  $\kappa$  as they apply to the kinetics of oxygen in brain tissue and, second, a practical strategy to correct on line for the rapid egress of tracer from the tissue that occur in the form of  $^{15}O$ -labeled water. These two issues are briefly dealt with below.

As originally formulated (5) the parameter  $\alpha$  represents the ratio of unidirectional fluxes of a compound across the blood-brain barrier. In the case of a compound like glucose, which passes the blood-brain barrier by carrier mediated facilitated diffusion,  $\alpha = (1 + K_m/C_t)/(1 + K_m/C_b)$ ,

where  $K_m$  is the Michaelis-Menten constant for the system.  $C_t$  and  $C_b$  are the tissue and blood concentration respectively. However, when  $K_m$  becomes large with respect to  $C_t$  and  $C_b$ , as in the case for the simple diffusion of a gas such as oxygen,  $\alpha = C_b/C_t$ . An approximate value for  $\alpha$  can be estimated from the oxygen tension measurements made in vivo across the cerebral vasculature by Duling et al. (28) and the known solubility of oxygen in blood and brain (29) of approximately  $0.023 \text{ mL} \cdot \text{mL}^{-1} \cdot \text{atm}^{-1}$ . The value obtained for  $\alpha$  in this manner is approximately 1.3. Such a rough estimate of  $\alpha$  might at first seem hazardous if one hopes to achieve an acceptable degree of accuracy in the measurement of local oxygen consumption with PET. However, the term containing  $\alpha$  (see Figure 2B) is virtually eliminated because of the large value of  $\kappa$  (see below).

The parameter  $\kappa$  represents the sum of the fractional rate constants for the clearance of tracer or tracee from the tissue extracellular fluid compartment (5). In the case of oxygen,  $\kappa$  can be represented as

$$\kappa = \frac{(PS)_v}{V_e} + \frac{(PS)_t}{V_e}$$

where PS represents the permeability-coefficient-surface-area product for oxygen;  $V_e$ , the volume of the extracellular fluid space; and the subscripts v and t, the blood vessels and tissue, respectively. Although experimental complexities preclude a direct measurement of the brain vascular or tissue PS for oxygen at this time, an acceptable lower bound can be established from the following relationships and extant literature data. Thus from Fick's law for diffusion,  $\phi = (PS)_v (C_b - C_t)$ , which, on rearranging becomes  $(PS)_v = \phi / (C_b - C_t)$ . A lower bound for  $(PS)_v$  is then  $(PS)_v = \phi / C_b$ . In the above equation  $\phi$  is the net flux of oxygen between blood and tissue (i.e., oxygen utilization rate). Letting  $\phi$  be  $5.8 \times 10^{-4} \text{ mL} \cdot \text{s}^{-1} \cdot \text{g}^{-1}$  (30), the mean capillary oxygen partial pressure be 60 Torr [estimated as the simple average of arterial and cerebral venous oxygen tensions (30)], together with a plasma oxygen solubility of  $0.023 \text{ mL} \cdot \text{mL}^{-1} \cdot \text{atm}^{-1}$  yields an acceptable lower bound for  $(PS)_v$  of approximately  $0.32 \text{ s}^{-1}$ . Making the not unreasonable assumption that  $(PS)_v$  and  $(PS)_t$  are similar and that the volume of the brain extracellular fluid space of  $0.15 \text{ mL/mL}$ , the lower bound of  $\kappa$  is approximately  $4.3 \text{ s}^{-1}$ . The significance of the magnitude of  $\kappa$  should be immediately apparent on inspection of the equation in Figure 2B. For values greater than  $1 \text{ s}^{-1}$  and measurement times greater than a few seconds, the equation reduces to the very simple form

$$\phi = \frac{q [T] - C_b V_b a_b (t)}{\int_0 T_{ab} (t) dt}$$

The rapid egress of  $^{15}\text{O}$ -labeled water of metabolism can be satisfactorily characterized by serial measurements of oxygen consumption following a single breath of  $^{15}\text{O}$ -labeled oxygen in air. Because the true oxygen utilization rate is assumed to remain constant, a time dependent decline in the oxygen utilization rate computed on the basis of the above equation will occur as the sole function of this egress of labeled metabolic water from the tissue. The true metabolic rate can be estimated from these data by back extrapolation of these data to early times when no egress has occurred. Using a simple graphical extrapolation procedure we have directly compared estimates based on this approach to actual measurements of the cerebral metabolic rate for oxygen consumption ( $\text{CMRO}_2$ ) in monkeys (unpublished observation) using an established procedure (6). The agreement was excellent ( $n = 6$ ,  $r = 0.90$ ), lending strong support to the use of this procedure with PET. An example is shown in Figure 3A.

Three important advantages exist in this alternative approach to the measurement of local tissue oxygen consumption with PET. First, the measurement requires a short time to accomplish; that is, approximately 1 min. This allows repeat measurements in the same setting and the more accurate measurement of transient metabolic phenomenon. Second, unknown model parameters have virtually no effect on the computed metabolic rate; thus eliminating concern about the study of diseased tissue where model parameters and corrections for tracee-tracer difference for compounds such as glucose and deoxyglucose may vary unpredictably. Finally, a more detailed model of the fate of the  $\text{O}^{15}\text{O}$  label in tissue and a more sophisticated parameter estimation scheme, currently under development in our laboratory, are likely to permit the simultaneous measurement of oxygen consumption and blood flow from a single inhaled breath of air labeled with  $\text{O}^{15}\text{O}$ . Such an approach should have broad application in the study of the relationship between blood flow and metabolism in the brain and other organs of the body.

### ***Tissue Chemical Composition***

PET can be used to measure quantitatively the chemical composition of tissues of the body by using appropriately selected compounds labeled with positron-emitting radioisotopes that rapidly distribute between the blood and the tissue of interest. The measurement is based on the determination of the tissue-to-blood partition coefficient of the tracer at equilibrium. Knowledge of the tissue-to-blood partition coefficient plus the concentration of the compound of interest in the vascular compartment permits the calculation of the actual tissue concentration. This concept has been tested by measuring brain carbon dioxide content using  $^{14}\text{C}$ -labeled carbon dioxide as a tracer (31). These measurements were

performed in adult rhesus monkeys at different levels of arterial carbon dioxide tension, which were adjusted by varying the partial pressure of carbon dioxide in the inspired air. The resulting data compare favorably with direct measurements of tissue carbon dioxide content and show the expected relationship between arterial carbon dioxide tension and tissue carbon dioxide content. Such data illustrate the unique potential of PET specifically to explore, *in vivo* and quantitatively, brain tissue acid–base chemistry. The ability to obtain this information in humans should provide valuable new insights with regard to the regulation of acid–base chemistry in normal and diseased states of the brain.

It is important to emphasize the general applicability of this type of measurement. It is not restricted to the measurement of tissue carbon dioxide content and acid–base status with  $^{14}\text{C}$ -carbon dioxide. The approach may be employed with a variety of radiopharmaceuticals to explore the chemical properties of the brain or any other organ of the body. One of the most obvious applications of this method is its potential to measure tissue drug levels. The study of tissue drug levels with PET will not only refine our appraisal of the therapeutic efficacy of specific drugs (i.e., anticonvulsants), but also will permit, for the first time, a study of specific brain receptors, *in vivo* and regionally, in humans when employed using drugs with specific receptor binding characteristics. This approach to the study of specific brain receptors is analogous in all respects to studies in laboratory animals (32) except that it can be conducted *in vivo* and, thus, in humans. The ability to make such measurements in humans may assume special importance in the study of certain conditions for which a satisfactory animal model does not exist (e.g., schizophrenia, Parkinson's disease). Preliminary studies suggest that it is entirely feasible.

### ***Blood Flow***

The development of a completely satisfactory measurement of regional cerebral blood flow (rCBF) employing PET has lagged behind developments in other areas of PET tracer methodology. This is somewhat ironic in that prior to the advent of PET, blood flow was the primary parameter available to the clinical investigator interested in hemodynamic and metabolic data on the human brain. All other measurements, including blood volume, metabolism, and tissue chemical composition, were obtained, at best, with great difficulty. The reason for this state of affairs is that techniques for the measurement of blood flow have, to date, depended upon the analysis of dynamic tracer data. This requires data sampling times of 1 s or less. Most PET units currently in operation have not been able to collect sufficient data for an adequate reconstruction of a tissue slice in less than 1–2 min, although

units currently being tested (19, 20) offer the temporal resolution necessary for such measurements (see below). As a result methods for the measurement of blood flow have focused on techniques that require equilibrium imaging.

One approach relates the equilibrium image of  $^{15}\text{O}$ -labeled water, obtained by the continuous inhalation of  $^{15}\text{O}$ -labeled carbon dioxide, to rCBF. As Lenzi and his colleagues (22) and others have shown (23) the amount of the tracer  $^{15}\text{O}$ -water in a region of the brain or other organ under these circumstances is proportional to rCBF. Thus, an equation can be presented in the following manner to permit calculation of the cerebral blood flow (CBF):

$$\text{CBF} = \frac{K_D}{C_a/C_t - \lambda^{-1}}$$

where  $K_D$  is the physical decay constant of oxygen-15 ( $\sim 0.335 \text{ min}^{-1}$ ),  $\lambda$  the tissue-to-blood equilibrium partition coefficient for water [grey matter  $\simeq 1.04$ ; white matter  $\simeq 0.88$ ; whole brain = 0.95 (4)], and  $C_a$  and  $C_t$  are the arterial blood and tissue concentration of circulating  $\text{H}_2^{15}\text{O}$ , respectively. Although superficially appealing, this approach has two significant problems. First, the relationship between blood flow and the measured parameters  $C_a$  and  $C_t$  is nonlinear (22). For example, it can be shown that starting at a CBF of  $50 \text{ mL}/(100 \text{ g} \cdot \text{min})$ , a normal resting blood flow in man (30), a 40% increase in blood flow is accompanied by only a 12% increase in the  $C_a/C_t$  ratio, whereas a 40% decrease in blood flow is accompanied by a 22% decrease in  $C_a/C_t$ . Thus as blood flow increases the measured parameters become less sensitive to change, whereas with a decrease in blood flow they become more sensitive. Second, the estimate of blood flow by this method is very sensitive to errors in the measurement of  $C_a$  and  $C_t$ . For example, at a blood flow of  $50 \text{ mL}/(100 \text{ g} \cdot \text{min})$ , letting  $K_D$  be  $0.35 \text{ min}^{-1}$  and  $\lambda$  be 0.95, it can be shown that measurement errors leading to a 10% overestimation of  $C_a/C_t$  produce a 20% underestimation of blood flow. As blood flow increases, error magnification becomes greater because the value of  $C_a/C_t$  approaches the value of  $\lambda^{-1}$ . The converse is also true. In considering the likelihood of errors in the determination of  $C_a/C_t$  it should be noted that this measurement actually involves several measurements, including: (i) the response of the PET imaging system to radioactivity in the region of interest, (ii) arterial blood radioactivity, and (iii) the relationship between (i) and (ii) as determined by PET imaging of appropriately designed and calibrated phantoms (33). Thus the opportunity for errors to occur is high.

A second approach to the estimation of rCBF with PET is analogous to the radiolabeled microsphere method employed in laboratory animals

(34). While the microsphere method employed in animals depends upon mechanical trapping of the tracer in the microcirculation of the organ of interest, PET studies have employed the concept of metabolic trapping. Specifically,  $^{13}\text{N}$ -labeled ammonia has been employed as a tracer to map perfusion in the brain (35) and other organs (36) because of its ability to be efficiently trapped, presumably by immediate incorporation into amino acids. Although conceptually sound, this approach is not likely to succeed in the case of  $^{13}\text{N}$ -ammonia because this tracer is not freely permeable (35) because some of the tracer in blood always exists in the impermeable form of ammonium ion ( $^{13}\text{NH}_4^+$ ). Because of this it can be shown that the amount deposited in the tissue as a function of blood flow will progressively deviate from the expected. Thus, as blood flow increases, estimated flow based on  $^{13}\text{N}$ -ammonia deposition will be increasingly underestimated. The particular case of  $^{13}\text{N}$ -ammonia is further complicated by the fact that the ratio of the diffusible species ( $^{13}\text{NH}_3$ ) to the nondiffusible ( $^{13}\text{NH}_4^+$ ) in blood is a function of blood pH. Therefore, PET images of  $^{13}\text{N}$ -ammonia purporting to depict a map of brain perfusion or blood flow must be viewed with caution. Clearly what is needed is a freely permeable radiopharmaceutical that is completely trapped within tissue during a single pass through the microcirculation. Although no such radiopharmaceutical labeled with a positron-emitting radionuclide has yet emerged, several candidates are being considered by a number of laboratories.

Finally, it now seems reasonable to propose that rCBF can be measured by PET in a manner analagous to the tissue autoradiographic method originally proposed by Landau and his colleagues (37) and later refined by Reivich (38), Sakurada (39), and their associates. In this technique as originally applied to animals, a freely diffusible radiolabeled tracer is infused intravenously for 1 min followed immediately by decapitation. Quantitative autoradiograms of brain slices and the time activity curve of arterial blood radioactivity form the data base from which rCBF is calculated. The PET image can substitute for the tissue autoradiogram provided that the image is obtained in a relatively short period of time ( $\sim 5\text{--}10$  s). Recent developments in PET technology (19, 20, 40) now permit such a measurement to be accomplished as illustrated by the study in Figure 3 using  $^{15}\text{O}$ -labeled water as the diffusible tracer. A number of freely diffusible tracers labeled with positron-emitting radionuclides could serve satisfactorily as the tracer for such measurements (9).

### **Conclusion**

The emergence of PET in the biomedical environment provides a unique new tool for sophisticated clinical investigation. The potential of the technique is obvious. PET should provide unique new information

on the biochemistry and physiology of the human central nervous system in health and disease. Such information can provide a valuable interface between basic science studies in simple systems and the in vivo condition in man, which most investigators, whatever their tools, are striving to understand. The requirements for the successful implementation of PET may not be so obvious. It may be clear to most that expensive and complicated machinery including cyclotrons, imaging devices, and computers are a necessary foundation but not so clear that a critical mass of diverse human talents must be closely coordinated to make the full potential of PET a reality in the biochemical environment. Successful implementation of PET, if achieved, will represent a truly collaborative effort among physicists, chemists, mathematicians, and neurobiologists who share in common the desire to develop and implement quantitative techniques for the study of brain biochemistry and physiology in man.

### *Literature Cited*

1. Kety, S. S.; Schmidt, C. F. *J. Clin. Invest.* **1948**, *27*, 476–483.
2. Hoedt-Rasmussen, K.; Sveinsdottir, E.; Lassen, N. A. *Circ. Res.* **1966**, *18*, 237–247.
3. Olesen, J. *Brain* **1971**, *94*, 635–646.
4. Ter-Pogossian, M. M.; Eichling, J. O.; Davis, D. O.; Welch, M. J. *Radiology*, **1969**, *93*, 31–40.
5. Raichle, M. E.; Larson, K. B.; Phelps, M. E.; Grubb, R. L., Jr.; Welch, M. J.; Ter-Pogossian, M. M. *Am. J. Physiol.* **1975**, *228*, 1936–1948.
6. Ter-Pogossian, M. M.; Eichling, J. O.; Davis, D. O.; Welch, M. J. *J. Clin. Invest.* **1970**, *49*, 381–391.
7. Eichling, J. O.; Raichle, M. E.; Grubb, R. L., Jr.; Larson, K. B.; Ter-Pogossian, M. M. *Circ. Res.* **1975**, *37*, 707–714.
8. Raichle, M. E.; Eichling, J. O.; Straatmann, M. G.; Welch, M. J.; Larson, K. B.; Ter-Pogossian, M. M. *Am. J. Physiol.* **1976**, *320*, 543–552.
9. Welch, M. J., Ed. "Radiopharmaceuticals and Other Compounds Labelled with Short-Lived Radionuclides"; Pergamon: New York, 1977.
10. Greenberg, J. H.; Alavi, A.; Reivich, M.; Kuhl, D.; Uzell, B. *Circ. Res.* **1978**, *43*, 324–330.
11. Grubb, R. L., Jr.; Raichle, M. E.; Eichling, J. O.; Ter-Pogossian, M. M. *Stroke* **1974**, *5*, 630–639.
12. Grubb, R. L., Jr.; Raichle, M. E.; Phelps, M. E.; Ratcheson, R. A. *J. Neurosurg.* **1975**, *43*, 385–398.
13. Raichle, M. E.; Welch, M. J.; Grubb, R. L., Jr.; Higgins, C. S. *Science* **1978**, *199*, 986–987.
14. Reivich, M.; Kuhl, D.; Wolf, A.; Greenberg, J.; Phelps, M.; Ido, T.; Cosella, N.; Fowler, J.; Hoffman, E.; Alavi, A.; Som, P.; Sokoloff, L. *Circ. Res.* **1979**, *44*, 127–137.
15. Phelps, M. E.; Huang, S. C.; Hoffman, E. J.; Selvi, C.; Sokoloff, L.; Kuhl, D. E. *Ann. Neurol.* **1979**, *6*, 371–388.
16. Sokoloff, L.; Reivich, M.; Kennedy, C.; deRosiers, M. H.; Pattak, C. S.; Pettigrew, K. C.; Sakurada, O.; Shinohara, M. *J. Neurochem.* **1977**, *28*, 897–916.
17. Welch, M. J.; Ter-Pogossian, M. M. *Radiat. Res.* **1968**, *36*, 580–587.
18. Ter-Pogossian, M. M.; Mullani, N. A.; Hood, J. T.; Higgins, C. S.; Currie, C. M. *Radiology* **1978**, *128*, 477–484.
19. Ter-Pogossian, M. M.; Mullani, N. A.; Hood, J. T.; Higgins, C. S.; Ficke, D. C. *J. Comp. Assisted Tom.* **1978**, *2*, 539–544.

20. Thompson, C. J.; Yamamoto, Y. L.; Meyer, E. *J. Comp. Assisted Tom.* 1978, 2, 650-651.
21. Jones, T.; Chesler, D. A.; Ter-Pogossian, M. M. *J. Radiol.* 1976, 49, 339-343.
22. Lenzi, G. L.; Jones, T.; McKenzie, C. G.; Buckingham, P. D.; Clark, J. C.; Moss, S. *J. Neurol., Neurosurg., Psych.* 1978, 41, 1-10.
23. Subramanyam, R.; Alpert, N. M.; Hoop, B., Jr.; Brownell, G. L.; Taveras, J. M. *J. Nucl. Med.* 1978, 19, 48-53.
24. West, J. B.; Dollery, C. T. *J. Appl. Physiol.* 1962, 17, 9-13.
25. Raichle, M. E.; Grubb, R. L., Jr.; Gado, M. H.; Eichling, J. O.; Ter-Pogossian, M. M. *Arch. Neurol.* 1976, 33, 523-526.
26. Plum, F.; Posner, J. B.; Troy, B. *Arch. Neurol.* 1968, 18, 1-13.
27. Raichle, M. E.; Posner, J. B.; Plum, F. *Arch. Neurol.* 1970, 23, 394-403.
28. Duling, B. R.; Kurchinsky, W.; Wahl, M. *Eur. J. Physiol.* 1979, 383, 29-34.
29. Thews, G. *Pflügers Arch.* 1960, 217, 197-226.
30. Cohen, P. J.; Alexander, S. C.; Smith, F. C.; Reivich, M.; Wollman, H. *J. Appl. Physiol.* 1967, 23, 183-189.
31. Raichle, M. E.; Grubb, R. L., Jr.; Higgins, C. S. *Brain Res.* 1979, 166, 413-417.
32. Kuhar, M. J.; Murrin, L. C.; Malouf, A. T.; Klumm, N. *Life Sci.* 1978, 22, 203-210.
33. Eichling, J. O.; Higgins, C. S.; Ter-Pogossian, M. M. *J. Nucl. Med.* 1977, 18, 845-847.
34. Marcus, M. L.; Heistad, D. D.; Ehrhardt, J. E.; Abboud, F. M. *J. Appl. Physiol.* 1976, 40, 501-507.
35. Phelps, M. E.; Hoffman, E. J.; Raybaud, C. *Stroke* 1977, 8, 694-702.
36. Harper, P. V.; Lathrop, K. A.; Frizek, H.; Lembarer, N.; Stark, V.; Hoffer, P. B. *J. Nucl. Med.* 1972, 13, 278-280.
37. Landau, W. M.; Freygang, W. H., Jr.; Rowland, L. P.; Sokoloff, L.; Kety, S. S. *Trans. Am. Neurol. Assoc.* 1955, 80, 125-129.
38. Reivich, M.; Jehle, J.; Sokoloff, L.; Kety, S. S. *J. Appl. Physiol.* 1969, 27, 296-300.
39. Sakurada, O.; Kennedy, C.; Jehle, J.; Brown, J. D.; Carbin, G. L.; Sokoloff, L. *Am. J. Physiol.* 1978, 234, H59-H66.
40. Budinger, T. F.; Derenzo, S. E.; Greenberg, W. L.; Gullberg, G. T.; Huesman, R. H. *J. Nucl. Med.* 1978, 19, 309-315.
41. Raichle, M. E. *Brain Res. Rev.* 1979, 1, 47-68.

RECEIVED September 4, 1980.



# In Vivo Tracers for Studies of Myocardial Metabolism

G. D. ROBINSON, JR.<sup>1</sup>

Division of Nuclear Medicine, University of California at Los Angeles, School of Medicine and the Laboratory of Nuclear Medicine and Radiation Biology, Los Angeles, CA 90024

*Labeled molecules have been used to assess many aspects of myocardial physiology but recent attention has focused on the development of tracers and techniques for measuring the metabolic rates of such substances as glucose, fatty acids, ammonia, and amino acids. A variety of labeled fatty acids have been evaluated as tracers of perfusion and metabolism. Labeled glucose analogs, such as <sup>18</sup>F-labeled 2-deoxy-2-fluoro-D-glucose, have been used to measure glucose utilization. Nitrogen labeled ammonia and amino acids are taken up by the heart and a substantial fraction of the label is rapidly incorporated into diverse chemical forms. The multiple biochemical pathways that are usually available to the label severely complicate the use of labeled substrates and analogs in quantitative studies of myocardial metabolism.*

A great deal of work has gone into the development of suitable radioactive agents for use as tracers in a variety of types of myocardial studies. Excluding the important area of myocardial mechanics (wall motion, ejection fraction), such studies can be placed into one of three general categories. These are: (i) studies of regional myocardial perfusion, (ii) evaluation of damage to myocardial tissue, and (iii) measurement of myocardial metabolism.

<sup>1</sup> Current address: Room 556, Dulles Building (G1), 3600 Spruce Street, Hospital of the University of Pennsylvania, Philadelphia, PA 19104.

0065-2393/81/0197-0437\$05.00/0  
© 1981 American Chemical Society

### *Tracers of Regional Myocardial Perfusion*

The regional distribution of blood flow in the heart (or any organ) can be determined by arterial injection of suitably labeled particles in the 10–20  $\mu\text{m}$  size range (1, 2, 3). With the provision that adequate mixing with the blood occurs, the particulate agent is delivered to and becomes trapped in the various tissue regions in proportion to regional perfusion. This is a commonly used research tool for the relative measurement of regional myocardial blood flow. With appropriate arterial sampling, the method can be used to measure regional perfusion in absolute terms (4).

The monovalent cations including  $\text{K}^+$ ,  $\text{Rb}^+$ ,  $\text{Cs}^+$ , and  $\text{Tl}^+$  are known to be taken up by myocardial tissue in proportion to blood flow (5, 6, 7). Using a conventional scintillation camera, normally perfused myocardium shows good uptake while ischemic regions have decreased concentrations of these tracers. Uptake is absent in regions of myocardial infarction. In the clinical setting the use of the other monovalent cation tracers has been largely displaced by the use of  $^{201}\text{Tl}$ , which is used in combined rest/exercise studies to demonstrate regional coronary artery disease (8, 9). The uptake of  $^{13}\text{NH}_4^+$  in myocardium may be related to its monovalent character, although this is not clear because of its metabolic activity within the heart (10, 11).

Since fatty acids are the primary substrate for aerobic metabolism within the heart, they are also of interest as potentially useful tracers of myocardial perfusion (12–18). This class of compounds labeled with the positron emitter  $^{11}\text{C}$  is being used with specially designed positron imaging (ECT) systems to quantitatively measure the regional distribution of myocardial blood flow in three dimensions (12, 13, 14). Carbon-11 labeled palmitic acid is also being evaluated as a tracer for studies of myocardial metabolism. Likewise, the  $\omega$ -iodofatty acids, which are structural analogs of the physiologic substrates, have been shown to be taken up by myocardial tissue in proportion to blood flow (15). Iodine-123 labeled 16-iodo-9-hexadecenoic acid (16, 17) and 17-iodo-heptadecanoic acid (18) have been used in conjunction with conventional scintillation cameras for in vivo studies in humans. In all cases with this class of compounds, turnover of the label within the tissue is related to some aspect of metabolism (17, 18).

Glucose and several of its analogs are being investigated for use as myocardial perfusion agents (19–24) because glucose is the primary substrate for anaerobic myocardial metabolism. Carbon-11 labeled glucose (19) and  $^{18}\text{F}$  labeled 2-deoxy-2-fluoro-D-glucose (2-FDG) and 3-deoxy-3-fluoro-D-glucose (3-FDG) have been utilized for this purpose (20, 21, 22) and  $^{11}\text{C}$  labeled 2-deoxy-D-glucose has been proposed (23, 24). With each of these molecules, however, most attention has been focused on their use as tracers of anaerobic metabolism.

### *Tracers of Damaged Myocardial Tissues*

The ability to demonstrate the presence and extent of damaged myocardial tissue is an important medical concern, particularly when the conventional diagnostic tests are equivocal. Early work with radioiodine labeled fluorescein and tetracycline derivatives demonstrated slow diffusion of such tracers into the sites of experimentally induced myocardial infarction in animals (25, 26). However, results of clinical trials were unconvincing. Subsequently,  $^{99m}\text{Tc}$  labeled tetracycline was found to exhibit a high ratio of uptake in damaged myocardium compared with normal tissue (27, 28). This agent was used successfully to delineate zones of damaged heart tissue in clinical studies of myocardial infarction (29). Other chelates labeled with  $^{99m}\text{Tc}$  were eventually found to have similar behavior in respect to damaged tissue (30–35). This property was particularly striking for the phosphorus-containing chelating agents used for bone scanning (32, 33, 34, 35) and  $^{99m}\text{Tc}$  pyrophosphate has now become the agent of choice for such studies (34, 35). The mechanism for damaged tissue uptake is not clearly understood but it is presumably dependent upon altered permeability of cellular membranes in the damaged tissue (36, 37). Calcium influx into regions of tissue damage have been implicated by some investigators (38, 39). Most recently, radioiodinated molecules that can bind to receptor sites within damaged tissue have been proposed for use as tracers in this application (40). Since the receptor binding mechanism has frequently been proposed, but never been successfully used for imaging studies in nuclear medicine, the true potential of this approach remains uncertain.

### *Tracers of Myocardial Metabolism*

Metabolism, of course, depends upon perfusion. The delivery of substrates in the blood to the various tissues, including the heart, is a primary requirement if metabolic activity is to occur. Damaged tissue usually exhibits some type of abnormal metabolism and, thus, markers for damaged tissues can also be tracers for abnormal metabolic activity. Oxygen utilization is one of the most basic aspects of aerobic metabolism of tissues. Although some interesting studies of oxygen metabolism in the brain of humans has been done using  $^{14}\text{O}$  or  $^{15}\text{O}$  (41, 42), the oxygen utilization measurements in the heart have generally been confined to relatively complex animal models (43, 44).

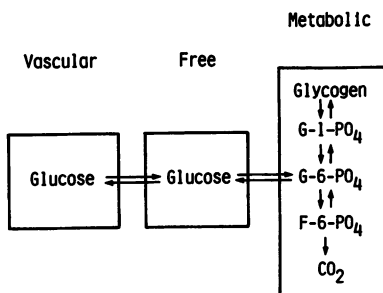
Measurement of myocardial metabolism using three types of metabolic substrates has been the focus of a great deal of recent research activity. The use of glucose and its analogs, fatty acids and their analogs, and ammonia and amino acids illustrates the general approach taken in this work and the principles involved. These examples can also be used

to emphasize some of the difficulties encountered and limitations imposed, and to call attention to some strategic options for unraveling the complexities involved.

### *Glucose Analogs for Metabolic Studies in the Brain*

Perhaps the most recent example of an extensively studied tracer for use *in vivo* as a probe for measuring metabolism is the glucose analog 2-deoxy-2-fluoro-D-glucose (2-FDG) labeled with  $^{18}\text{F}$  (20, 45–50). An intensive effort has gone into developing methods for using this tracer molecule for monitoring regional glucose utilization. A brief summary of the use of this and other glucose analogs in quantitatively measuring regional glucose metabolic rates in the brain is instructive, since this illustrates a nearly ideal situation in application of the newly developed techniques.

The relevant glucose biochemical pathways (51) are illustrated in a schematic compartmental model in Figure 1. Like glucose itself, after intravenous administration, 2-FDG is actively transported across the blood-brain-barrier (BBB) by the glucose transport mechanism. It then moves in a reversible fashion into a metabolic compartment where it is converted to 2-FDG-6-phosphate (2-FDG-6- $\text{PO}_4$ ) by brain hexokinase. Since there is little glucose storage capacity in the brain, conversion to 2-FDG-1- $\text{PO}_4$  followed by incorporation into glycogen is minimal in brain tissue. Similarly, since the C2–OH group on glucose is required for metabolic utilization of glucose, and this is absent in the 2-deoxyglucose analogs, metabolic utilization of the labeled analogs is not possible. As a result, except for a very slow conversion of 2-FDG-6- $\text{PO}_4$  back to free 2-FDG in the extracellular compartment, once the labeled 2-FDG has entered the brain metabolic compartment and has been phosphorylated, the label becomes trapped within the brain tissue. Since uptake of 2-FDG is via the glucose metabolic route, its rate and amount of accumulation within various tissues, though not identical to that for glucose itself, is directly related to glucose influx. Since no storage of glucose occurs



*Figure 1. Simplified, three-compartment model of glucose metabolic pathways (51)*

within the brain, influx must equal glucose metabolic rate. Using appropriate mathematical models, quantitative measurement of absolute glucose metabolic rate in the brain becomes possible (52, 53). The key elements in the use of 2-FDG in this application are that it becomes locked into an intermediate metabolic step in a biochemical system where only a single metabolic pathway is available. Detailed accounts of the development and use of 2-FDG for regional brain metabolic studies are available in a variety of references (52, 53, 54, 55).

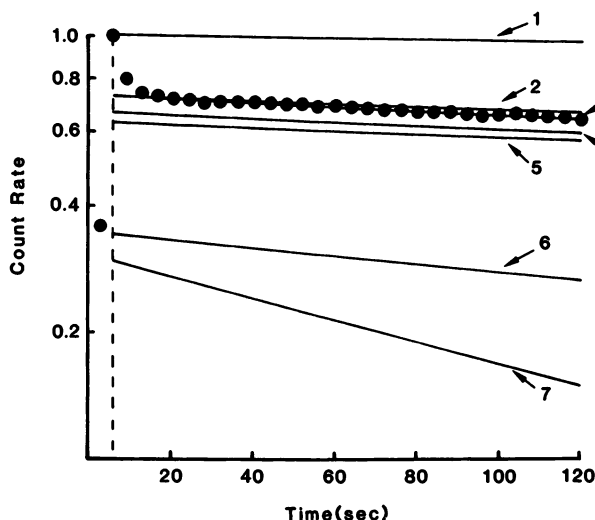
### *Labeled Glucose Analogs for Myocardial Studies*

As was indicated previously, glucose is the primary substrate for anaerobic myocardial metabolism. The heart uptake of various glucose analogs has been demonstrated by several investigators in a variety of animal models and in humans. The use of  $^{18}\text{F}$  labeled 2-FDG as a tracer for monitoring myocardial glucose utilization in a manner analogous to its use in the brain appears attractive (20, 21). Unfortunately, the situation in the heart is more complex than in the brain, and the use of 2-FDG, or the other glucose analogs, is not as straightforward.

Presumably, 2-FDG is transported into the myocardial tissue via the glucose pathway, as it is in the brain. It enters the myocardial metabolic compartment where it is converted to 2-FDG-6- $\text{PO}_4$  by heart hexokinase. The enzymatic conversion of 2-FDG-6- $\text{PO}_4$  to a form suitable for metabolic utilization is blocked, as in the brain. However, the heart has the capacity for glucose storage as glycogen (56), and conversion of 2-FDG-6- $\text{PO}_4$  to 2-FDG-1- $\text{PO}_4$  with subsequent storage as glycogen can proceed in myocardial tissue. Thus, in this case, though 2-FDG uptake is related to glucose influx, it is not necessarily a measure of glucose utilization. Uptake is simply related to glucose influx, which can result in either storage as glycogen or metabolic utilization. Since there is no noninvasive method for determining the actual chemical form of  $^{18}\text{F}$  labeled 2-FDG within the myocardial cells, the fraction of glucose being stored as opposed to being utilized for energy production remains uncertain. The label, in essence, becomes metabolically lost, since it is not possible to differentiate between the multiple metabolic pathways involved. As a result, quantitative measurement of absolute glucose metabolic rates becomes much more difficult in the heart than when 2-FDG is used for this purpose in the brain.

### *Labeled Fatty Acids for Myocardial Studies*

Since free fatty acids are the major source of metabolic energy under aerobic conditions in the myocardium, it is not surprising that this class of compounds has received considerable attention for use as tracers in heart



**Figure 2.** Myocardial extraction of labeled tracers following intracoronary administration in the dog: 1, particles (15–20  $\mu\text{m}$ ); 2,  $^{13}\text{N}$ -ammonia; 3,  $^{131}\text{I}$ -16-iodo-9-hexadecenoic acid; 4,  $^{43}\text{K}$ -potassium; 5,  $^{11}\text{C}$ -octadecanoic (stearic) acid; 6,  $^{131}\text{I}$ -oleic acid (ICI addition); 7,  $^{18}\text{F}$ -2-fluorotetradecanoic acid

studies. Initial interest was focused on their potential use as indicators of regional myocardial perfusion (12, 18). The results of some of our previously reported myocardial extraction measurements on a variety of labeled fatty acids is shown in Figure 2. Although, as can be seen in Figure 2, severe alterations of the normal fatty acid molecular architecture result in lowered uptake, several tracers in this class have been used in metabolic studies of the myocardium.

Sobel et al. have published a series of reports on the use of  $^{14}\text{C}$  labeled palmitic acid for metabolic studies using ECT techniques in animals and humans (12, 13, 14, 57, 58, 59). Robinson et al. (16, 17), Machulla et al. (18), and a few other investigators, have demonstrated the use of  $\omega$ -iodofatty acids, labeled with  $^{123}\text{I}$ , for perfusion studies and limited metabolic applications using conventional scintillation camera imaging systems. Myocardial uptake of similar compounds labeled with  $^{18}\text{F}$  and  $^{123\text{m}}\text{Te}$  have also been reported (60, 61, 62). The many attempts to prepare fatty acid analog molecules labeled with  $^{99\text{m}}\text{Tc}$  have met with uniform lack of success (63, 64, 65).

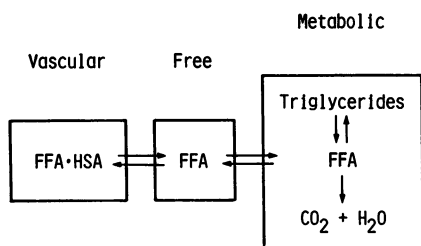
Unfortunately, results derived from application of these labeled molecules to the measurement of absolute metabolic rates in the heart are even more difficult to interpret than when glucose analogs are used. This is so because the use of labeled fatty acids or fatty acid analogs as

tracers of myocardial free fatty acid (FFA) metabolism is complicated not only by the multiple metabolic pathways that the fatty acid substrates can follow, but also by lack of metabolic trapping of the label at an intermediate point along the biochemical routes. These points are illustrated in Figure 3, which outlines the essentials of myocardial FFA metabolism (66).

After the fatty acids, or their suitably labeled analogs, are taken up by myocardial tissue, they are transported into the myocardial metabolic cycle via the acyl carnitine transport system. Once they are within the metabolic compartment, the FFA substrates may either be metabolized through the citric acid cycle or they may be stored as triglycerides. There have been no reports of metabolic trapping of labeled fatty acids or their analogs within either of these pathways. Thus, after the labeled fatty acids are taken up by the myocardium and are transported into the metabolic compartment, the label may be either liberated through metabolism, or stored as triglyceride. In the latter case the stored label may be subsequently liberated by metabolic mobilization of triglyceride stores. As was the case for myocardial studies using glucose and its analogs, the complexities of multiple metabolic pathways confuse the detailed monitoring of the metabolic process because FFA cannot be easily distinguished from triglycerides within the intact tissue. Metabolic liberation of tracer can easily be followed by monitoring washout of radioactivity from the myocardial tissue. However, because of the multiple sources from which substrate can be drawn, it becomes extremely difficult to determine in absolute terms what fraction of the total fatty acid metabolism is being monitored without using complex, highly invasive procedures.

### *Nitrogen-13 Labeled Ammonia for Myocardial Studies*

The avid accumulation of  $^{13}\text{N}$ -radioactivity within the myocardium following intravenous administration of  $^{13}\text{N}$ -labeled ammonia has been well documented (10, 11, 67, 68). From the known complexity of ammo-



*Figure 3. Simplified, three-compartment model of FFA metabolic pathways (66)*

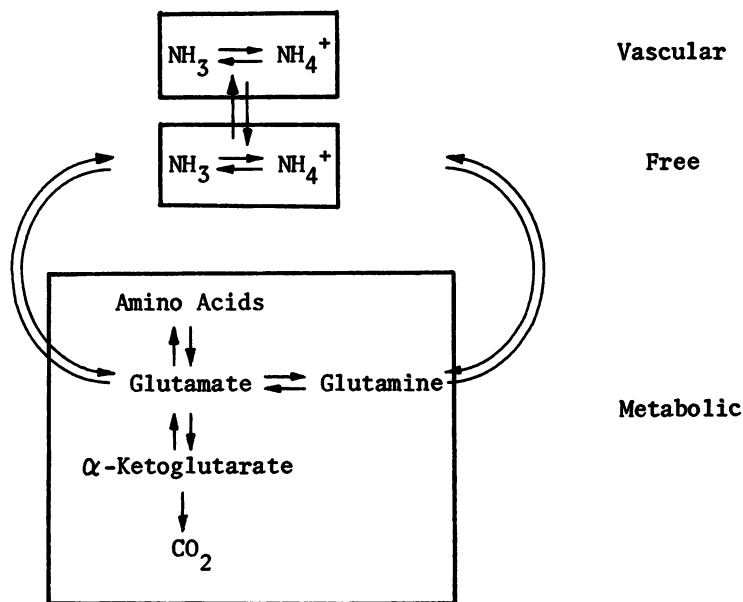


Figure 4. Simplified, three-compartment model of ammonia and amino acid metabolic pathways

nia and amino acid metabolism in the heart it was soon apparent that, while the initial distribution of uptake may be related to regional blood flow, subsequent redistribution of radioactivity into various metabolic pools was likely. This is illustrated in a simplified manner in Figure 4 (69).

Labeled ammonia, which is in equilibrium with ammonium ion, readily diffuses or is transported out of vascular compartment and equilibrates within the free space in the myocardial tissue. The label can enter the myocardial metabolic compartment in at least two ways. Glutamic dehydrogenase can couple the labeled ammonia with  $\alpha$ -keto-glutarate to form labeled glutamic acid. Alternatively, glutamine synthetase can couple the labeled ammonia with nonradioactive glutamate to produce labeled glutamine. The transaminating enzymes can act upon labeled glutamate to produce a spectrum of labeled amino acids. Glutamate dehydrogenase can split off ammonia from glutamate to regenerate  $\alpha$ -ketoglutarate.

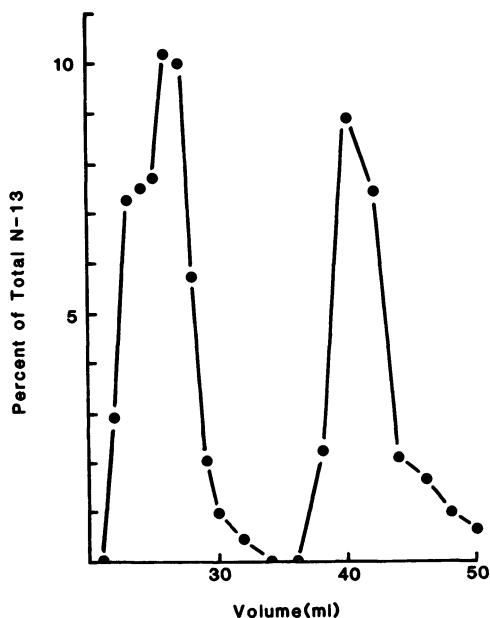
Thus, once again, while it is relatively trivial to monitor the influx and washout of  $^{15}\text{N}$  activity in the myocardial tissue, the tracer itself is rapidly lost within a complex metabolic pool.

To study this rapid metabolic fixing of  $^{15}\text{N}$  ammonia we used anion exchange chromatography to isolate the various chemical forms of  $^{15}\text{N}$



present in plasma at different times after intravenous injection of  $^{13}\text{N}$ -labeled ammonia in the dog. Using 0.005M ammonium acetate buffer (pH = 6.0) and a 30 cm  $\times$  1.5 cm diameter anion exchange column (Dowex 1-X4, 200–400 mesh, acetate form) eluted at 2.0 mL/min, a rapid separation of ammonia and several amino acids was obtained. The results from the analysis of a sample taken 3.5 min after injection are shown in Figure 5.

The early shoulder is due to ammonia itself while the initial large peak is glutamine. The second large peak has been tentatively identified as glutamic acid, although some other amino acids behave similarly in this analytical system. The data, though admittedly crude, suggest two relevant points: (i) even at this short time interval after administration most of the circulating radioactivity is not due to  $^{13}\text{N}$ -labeled ammonia, and (ii) this distribution reflects the results of metabolic fixing of the label in the total body, and is not limited to myocardial metabolism. These results may be compared with those obtained following a similar analysis of effluent collected from an isolated perfused rabbit heart septum. The development of this *in vitro* biological model is described in detail elsewhere (70). The results shown in Figure 6 are from the analysis of effluent which was collected between 9.5 and 10.5 min after addition of  $^{13}\text{N}$ -labeled ammonia to the perfusate.



**Figure 5.** Anion exchange radiochromatographic analysis of  $^{13}\text{N}$  in plasma 3.5 min after iv injection of  $^{13}\text{N}$ -labeled ammonia in the dog

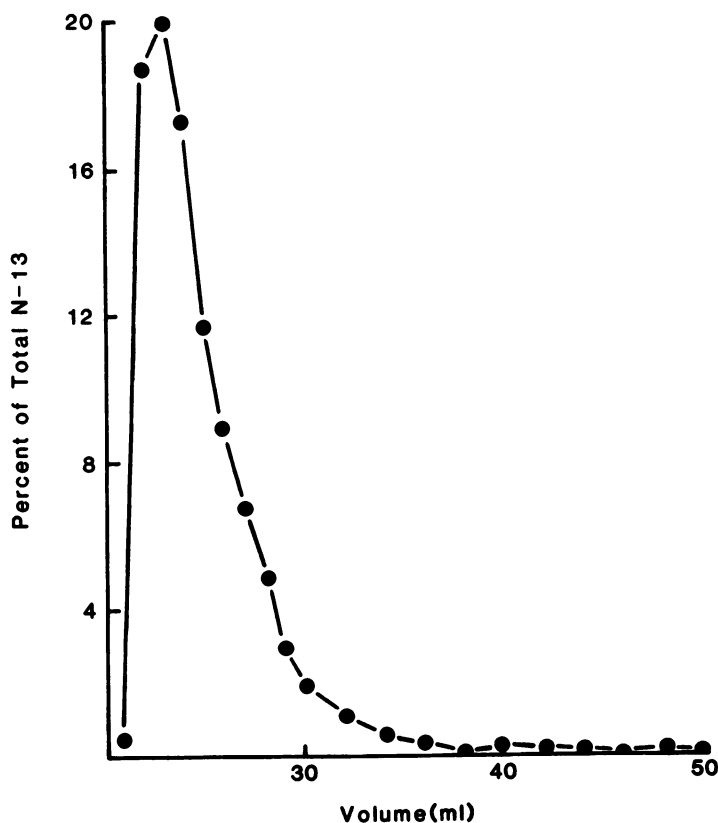


Figure 6. Anion exchange radiochromatographic analysis of  $^{13}\text{N}$  in rabbit septum effluent collected from 9.5 to 10.5 min after addition of labeled ammonia to perfusate

In this case the major peak is due to free ammonia while glutamine appears as a shoulder on the ammonia peak. The second metabolite peak, which was attributed to glutamate, was not observed in any sample up to 20 min. The growth of the glutamine peak as a fraction of total plasma  $^{13}\text{N}$  was studied using cation exchange chromatography. The effluent sample was applied to the top of a 20 cm  $\times$  0.7 cm diameter cation exchange column (BioRad AG-50W-X8, 200–400 mesh, ammonium form), which was eluted with 0.005M ammonium acetate buffer (pH = 6.0). In this system, the amino acids are recovered from the column while the cationic species, including ammonium ion are retained. The results of these studies are shown in Figure 7 and illustrate a progressive accumulation of glutamine in the effluent. This clearly indicates the formation of a labeled pool of metabolites within the myocardial tissue.

These results also suggest that the  $^{13}\text{N}$ -labeled glutamate that was observed in the plasma samples is not formed as a result of myocardial metabolism. Further studies to clarify this point are underway.

As a final point, it should be noted that amino acids themselves exhibit some myocardial specificity (71, 72, 73) and, thus, the metabolically generated labeled amino acids contribute to total heart uptake and further confuse the issue. One can readily see that this use of  $^{13}\text{N}$ -labeled ammonia as a tracer for myocardial metabolism presents a very complex situation in which determination of even relative metabolic rates is difficult at best; and absolute measurements become virtually impossible.

### *Strategies for Resolving Current Limitations*

As has been adequately illustrated, there are substantial difficulties involved in directly applying the techniques that have been so successfully used to monitor brain metabolism to the measurement of myocardial

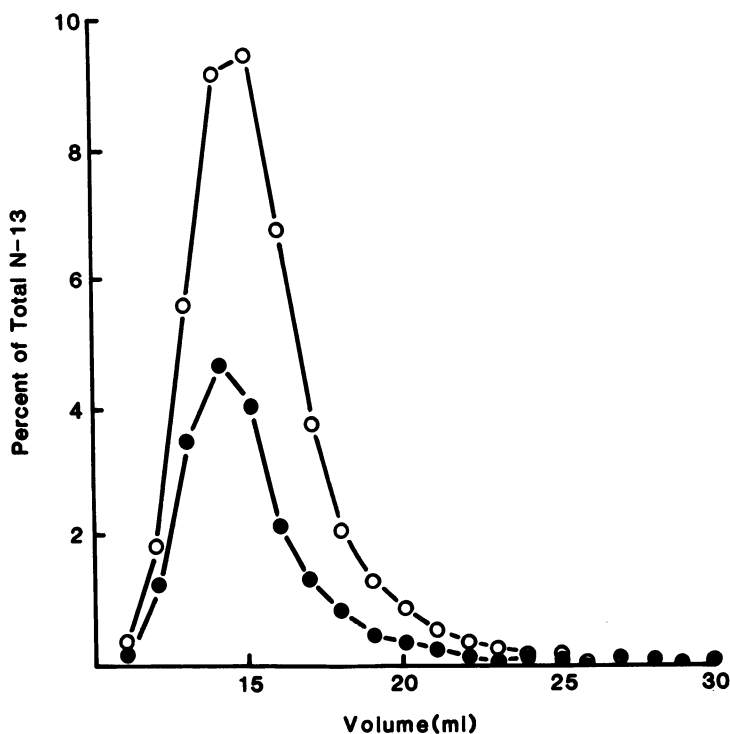


Figure 7. Cation exchange radiochromatographic analysis of  $^{13}\text{N}$  in rabbit septum effluent collected (●) 5 min and (○) 15 min after addition of labeled ammonia to perfusate

American Chemical  
Society Library  
1155 16th St., N.W.

metabolic rates in vivo in humans. There are, however, several options that represent attractive strategies for resolving, or at least minimizing, these inherent difficulties. Since the major present limitations are derived from the multiple metabolic pathways available to labeled substrates within the myocardium and from the rapid turnover of the label within the various metabolic pools, the development of new classes of substrate analogs that are irreversibly trapped metabolically, or that participate in only a single metabolic pathway would be helpful.

An example of this type of new agent may be found in the fluorinated fatty acids, which have been shown to be taken up by the myocardium (60, 61). When these compounds are labeled with  $^{18}\text{F}$  attached to an even-numbered carbon atom they are highly toxic because of their ability to be converted to fluorocitrate, which is a "suicide" inhibitor of aconitase (73). The label thus becomes locked into an intermediate step of the citric acid cycle. When  $^{18}\text{F}$  is attached to an odd-numbered carbon, toxicity is dramatically reduced, and  $\beta$ -oxidation and subsequent metabolism proceeds as with the physiologic FFA substrates. A more detailed understanding of the behavior of such tracer molecules in altered and normal states of myocardial metabolism may provide considerable insight into applying them to the in vivo measurement of metabolic rates.

A second method is to develop pharmacologic methods that would selectively channel substrates, which would usually be available to participate in multiple metabolic pathways, into a specific, selected route. This approach is similar to that reported by Cooper et al. (75), who used methionine sulfoxamine in studies of metabolic fixing of  $^{13}\text{N}$ -labeled ammonia in the rat brain. Prior administration of methionine sulfoximine largely inhibits the glutamine-synthetase-catalyzed production of labeled glutamine. At the same time, however, glutamate dehydrogenase activity is essentially unaffected, although overall metabolic incorporation of intracarotid infused  $^{13}\text{N}$  ammonia into brain tissue was reduced. The relationship between the multiple competing biochemical processes can be clarified in this way. A complementary study by Phelps et al. (21) reported the use of fasting followed by glucose and insulin infusion to facilitate myocardial glucose utilization; this procedure selectively "shuts down" myocardial FFA metabolism.

It is apparent that a great amount of preliminary work of this type in animals is needed to probe and clarify the behavior of labeled substrates in physiologic models of normal and disease states. The recently discovered role of amino acids in protecting ischemic myocardial tissue from the deleterious effects of hypoxia (76) is an example of the type of processes that may be at work but whose effects on the metabolism of myocardial tissue are not yet fully understood.

The development of these kinds of techniques for measuring fundamental aspects of human physiology in vivo is just beginning. Over the

next several years the procedures and measurements that now seem so difficult, tedious, and totally impractical in the clinical setting, will undoubtedly be developed to the point where the study of nuclear physiology will be as routine as nuclear medicine is today.

### *Acknowledgments*

The author wishes to acknowledge the important assistance of several colleagues who have contributed to the development of the viewpoints and concepts presented in this work. They include: J. R. Barrio, E. J. Hoffman, S. C. Huang, J. Krivokapich, D. E. Kuhl, N. S. MacDonald, M. E. Phelps, N. D. Poe, and F. W. Zielinski. This work was supported in part by Contract D.E.-AM06-76-SF000012 between the U.S. Department of Energy, Washington, D.C., and the University of California at Los Angeles, California.

### *Literature Cited*

1. Yipintosi, T.; Dobbs, W. A., Jr.; Scanlon, P. D.; Knapp, T. J.; Bassingthwaighte, J. B. *Circ. Res.* **1973**, *33*, 573.
2. Utley, J. A.; Carlson, E. L.; Hoffman, J. I. E.; Marinez, H. M.; Buckberg, C. D. *Circ. Res.* **1974**, *34*, 391.
3. Ashburn, W. L.; Braunwald, E.; Simon, A. L.; Peterson, K. L.; Gault, J. H. *Circulation* **1971**, *44*, 851.
4. Bassingthwaighte, J. B.; Holloway, G. A., Jr. *Semin. Nucl. Med.* **1976**, *6*, 141.
5. Poe, N. D. *J. Nucl. Med.* **1972**, *13*, 557.
6. Prokop, E. K.; Strauss, H. W.; Shaw, J.; Pitt, B.; Wagner, H. N., Jr. *Circulation* **1974**, *50*, 978.
7. Love, W. D.; Ishihara, Y.; Lyon, L. D.; Smith, R. O. *Am. Heart J.* **1968**, *76*, 353.
8. Strauss, H. W.; Pitt, B. *Semin. Nucl. Med.* **1977**, *7*, 49.
9. Meade, R. C.; Bamrah, V. S.; Horgan, J. D.; Ruetz, P. P.; Kronenwetter, C.; Yeh, E. L. *J. Nucl. Med.* **1978**, *19*, 1175.
10. Hunter, W. W., Jr.; Monahan, W. G. *J. Nucl. Med.* **1971**, *12*, 368.
11. Harper, P. V.; Schwartz, J.; Beck, R. N. *Radiology* **1973**, *108*, 613.
12. Hoffman, E. J.; Phelps, M. E.; Weiss, E. S.; Welch, M. J.; Coleman, R. E.; Sobel, B. E.; Ter-Pogossian, M. M. *J. Nucl. Med.* **1977**, *18*, 57.
13. Weiss, E. S.; Ahmed, S. A.; Welch, M. J.; Williamson, J. R.; Ter-Pogossian, M. M.; Sobel, B. E. *Circulation* **1977**, *55*, 66.
14. Poe, N. D.; Robinson, G. D., Jr.; MacDonald, N. S. *Proc. Soc. Exp. Biol. Med.* **1975**, *148*, 215.
15. Poe, N. D.; Robinson, G. D., Jr.; Graham, L. S.; MacDonald, N. S. *J. Nucl. Med.* **1976**, *17*, 1077.
16. Robinson, G. D., Jr. *Int. J. Appl. Radiat. Isot.* **1977**, *28*, 149.
17. Poe, N. D.; Robinson, G. D., Jr.; Zielinski, F. W.; Cabeen, W. R., Jr.; Smith, J. W.; Gomes, A. S. *Radiology* **1977**, *124*, 419.
18. Machulla, J. H.; Stocklin, G.; Kupfernagel, C.; Freundlieb, C.; Hock, A.; Vyska, K.; Feinendegen, L. E. *J. Nucl. Med.* **1978**, *19*, 298.
19. Lifton, J. F.; Welch, M. J. *Radiat. Res.* **1971**, *45*, 35.
20. Gallagher, B. M.; Ansari, A.; Atkins, H. L.; Casella, V.; Christman, D. R.; Fowler, J. S.; Ido, T.; MacGregor, R. R.; Som, P.; Wan, C. N.; Wolf, A. P.; Kuhl, D. E.; Reivich, M. *J. Nucl. Med.* **1977**, *18*, 990.

21. Phelps, M. E.; Hoffman, E. J.; Selin, C.; Huang, S. C.; Robinson, G. D., Jr.; Schelbert, H. R.; Kuhl, D. E. *J. Nucl. Med.* 1978, 19, 1311.
22. Tewson, T. J.; Welch, M. J.; Raichle, M. E. *J. Nucl. Med.* 1978, 19, 1339.
23. Shiu, C. Y.; MacGregor, R. R.; Lade, R. E.; Wan, C. N.; Wolf, A. P. *J. Nucl. Med.* 1978, 19, 676.
24. Mestelan, G.; Aubert, F.; Beaucourt, J. P.; Comar, D.; Pichat, L. *J. Labelled Compd. Radiopharm.* 1979, 16, 661.
25. Huber, P. F. B. *Cardiovasc. Res.* 1970, 4, 509.
26. Malek, P.; Kole, J.; Zastava, V. L.; Zak, F.; Peleska, B. *Cardiologica* 1963, 42, 303.
27. Holman, B. L.; Dewanjee, M. K.; Idoine, J.; Fliegel, C. P.; Davis, M. A.; Treves, S.; Eldh, P. *J. Nucl. Med.* 1973, 14, 595.
28. Robinson, G. D., Jr.; Battaglia, D. J. *Int. J. Appl. Radiat. Isot.* 1975, 26, 147.
29. Holman, B. L.; Lesch, M.; Zweiman, F. G.; Temte, J.; Lown, B.; Gorlin, R. *N. Engl. J. Med.* 1974, 291, 159.
30. Rossman, D. J.; Rouleau, J.; Strauss, H. W.; Pitt, B. *J. Nucl. Med.* 1975, 16, 980.
31. Bonte, F. J.; Parkey, R. W.; Graham, K. D.; Moore, J. G. *J. Nucl. Med.* 1975, 16, 132.
32. Davis, M. A.; Holman, B. L.; Carmel, A. N. *J. Nucl. Med.* 1976, 17, 911.
33. Kung, H. F.; Ackerhelt, R.; Blau, M. *J. Nucl. Med.* 1978, 19, 1027.
34. Perez, L. *Clin. Nucl. Med.* 1976, 1, 2.
35. Parkey, R. W.; Bonte, F. J.; Stokeley, E. M.; Lewis, S. E.; Graham, K. D.; Buja, L. M.; Willerson, J. T. *J. Nucl. Med.* 1976, 17, 771.
36. Dewanjee, M. K.; Kahn, P. C.; Dewanjee, U.; Connolly, R. J. *J. Nucl. Med.* 1975, 16, 525.
37. Holman, B. L.; Davis, M. A.; Hanson, R. N. *Semin. Nucl. Med.* 1977, 7, 29.
38. Parkey, R. W.; Bonte, F. J.; Buja, L. M.; Stokeley, E. M.; Willerson, J. T. *Semin. Nucl. Med.* 1977, 7, 15.
39. Shen, A. C.; Jennings, R. B. *Am. J. Pathol.* 1972, 67, 441.
40. Dewanjee, M. K.; Kahn, P. *J. Nucl. Med.* 1976, 17, 639.
41. Subramanyam, R.; Alpert, N. M.; Hoop, B., Jr.; Bromwell, G. L.; Taveras, J. M. *J. Nucl. Med.* 1978, 19, 48.
42. Jones, T.; Chesler, D. A.; Ter-Pogossian, M. M. *Br. J. Radiol.* 1976, 49, 339.
43. Metzger, J. M.; MacDonald, N. S.; MacDonald, C.; Takahashi, J. M. *J. Nucl. Med.* 1975, 16, 550.
44. Ter-Pogossian, M. M.; Eichling, J. O.; Davis, D. O.; Welch, M. J. *J. Clin. Invest.* 1970, 49, 381.
45. Ido, T.; Wan, C. N.; Casella, V.; Fowler, J. S.; Wolf, A. P. *J. Labelled Compd. Radiopharm.* 1978, 14, 174.
46. Robinson, G. D., Jr.; MacDonald, N. S.; Easton, M. P.; Cook, J. S. *J. Nucl. Med.* 1978, 19, 701.
47. Reivich, M.; Kuhl, D.; Wolf, A.; Greenberg, J.; Phelps, M.; Ido, T.; Casella, V.; Fowler, J.; Callaher, B.; Hoffman, E.; Alavi, A.; Sokoloff, L. *Acta. Neurol. Scand.* 1977, 56 (64), 190.
48. Kuhl, D. E.; Phelps, M. E.; Engel, J., Jr.; Hoffman, E. J.; Robinson, G. D., Jr.; MacDonald, N. S.; Kowell, A. P.; Winter, J. *J. Compt. Assist. Tomogr.* 1978, 2, 655.
49. Welch, M. J.; Eichling, J. O.; Straatman, M. G.; Raichle, M. E.; Ter-Pogossian, M. M. In "Noninvasive Brain Imaging"; DeBlanc, H. J., Jr.; Sorenson, J. A., Eds., Society of Nuclear Medicine: New York, 1975; p. 33.
50. Gallagher, B. M.; Fowler, J. S.; Gutterson, N. I.; MacGregor, R. R.; Wan, C. N.; Wolf, A. P. *J. Nucl. Med.* 1978, 19, 1154.

51. Baldwin, E. "The Nature of Biochemistry"; Cambridge, 1962; pp. 65-72.
52. Phelps, M. E.; Huang, S. C.; Hoffman, E. J.; Selin, C.; Sokoloff, L.; Kuhl, D. *Ann. Neurol.* 1979, 6, 371.
53. Kuhl, D. E.; Phelps, M. E.; Hoffman, E. J.; Robinson, G. D., Jr.; MacDonald, N. S. *Acta. Neurol. Scand.* 1977, 56 (64), 192.
54. Sokoloff, L.; Reivich, M.; Kennedy, C.; Des Rosiers, M. H.; Patlak, C. S.; Pettigrew, K. D.; Sakurada, O.; Shinohara, M. *J. Neurochem.* 1977, 28, 897.
55. Huang, S. C.; Phelps, M. E.; Hoffman, E. J.; Sideris, K.; Selin, C. J.; Kuhl, D. E. *Am. J. Physiol.* 1980, 238, E69.
56. Olson, R. E. In "Handbook of Physiology: Circulation"; Hamilton, W. F.; Phillips, D., Eds.; Williams & Wilkins: Baltimore, 1962; pp. 199-237.
57. Weiss, E. S.; Hoffman, E. J.; Phelps, M. E.; Welch, M. J.; Henry, P. D.; Ter-Pogossian, M. M.; Sobel, B. E. *Circ. Res.* 1976, 39, 24.
58. Ter-Pogossian, M. M.; Klein, M. S.; Markham, J.; Robert, R.; Sobel, B. E. *Circulation* 1980, 61, 342.
59. Goldstein, R. A.; Klein, M. S.; Welch, M. J.; Sobel, B. E. *J. Nucl. Med.* 1980, 21, 342.
60. Robinson, G. D., Jr. In "Radiopharmaceuticals and Labelled Compounds, Vol. I"; IAEA: Vienna, 1973; pp. 423-432.
61. Knust, E. J.; Kupfernagel, C.; Stocklin, G. *J. Labelled Compd. Radio-pharm.* 1979, 16, 143.
62. Knapp, F. F., Jr.; Ambrose, K. R.; Callahan, A. P. In "Radiopharmaceuticals II"; Sodd, V. J.; Allen, D. R.; Hoogland, D. R.; Ice, R. D., Eds.; Society of Nuclear Medicine: New York, 1979; pp. 101-108.
63. Bonte, J. F.; Graham, K. D.; Moore, J. G.; Parkey, R. W.; Curry, G. C. *J. Nucl. Med.* 1973, 14, 381.
64. Loberg, M. D.; Fields, A. T.; Porter, D. W. *J. Nucl. Med.* 1978, 19, 717.
65. Livni, E.; Davis, M. A.; Warner, V. D. In "Radiopharmaceuticals II"; Sodd, V. J.; Allen, D. R.; Hoogland, D. R.; Ice, R. D., Eds.; Society of Nuclear Medicine: New York, 1979; pp. 487-495.
66. Banks, P.; Bartley, W.; Birt, L. M. In "The Biochemistry of the Tissues"; John Wiley & Sons: New York, 1976; pp. 230-235.
67. Walsh, W. F.; Fill, H. R.; Harper, P. V. *Semin. Nucl. Med.* 1977, 7, 59.
68. Monahan, W. G.; Tilbury, R. S.; Laughlin, J. S. *J. Nucl. Med.* 1972, 13, 274.
69. Banks, P.; Bartley, W.; Birt, L. M. In "The Biochemistry of the Tissues"; John Wiley & Sons: New York, 1976; pp. 325-330.
70. Shine, K. I.; Douglas, A. M.; Ricchiuti, N. V. *Am. J. Physiol.* 1977, 232, H564.
71. Cohen, M. B.; Spolter, L.; MacDonald, N.; Chang, C. C.; Takahashi, J. In "Radiopharmaceuticals"; Society of Nuclear Medicine: New York, 1975; pp. 184-188.
72. Gelbard, A. S.; Benua, R. S.; McDonald, J. M.; Rerman, R. E.; Vomero, J. J.; Laughlin, J. S. *J. Nucl. Med.* 1979, 20, 663.
73. Cohen, M. B.; Spolter, L.; MacDonald, N.; Masuoka, D. T.; Laws, S.; Neely, H.; Takahashi, J. In "Radiopharmaceuticals and Labelled Compounds I"; IAEA: Vienna, 1973; pp. 483-490.
74. Pattison, F. L. M. "Toxic Aliphatic Fluorine Compounds"; Elsevier: Amsterdam, 1959.
75. Cooper, A. J. L.; McDonald, J. M.; Gelbard, A. S.; Gledhill, R. F.; Duffy, T. E. *J. Biol. Chem.* 1979, 254, 4982.
76. Rau, E. E.; Shine, K. E.; Douglas, A. M.; Amos, E. C., III. *Am. J. Physiol.*, in press.

RECEIVED September 4, 1980.

# Tracer Studies with $^{13}\text{NH}_4^+$ , $^{42}\text{K}^+$ , and $^{28}\text{Mg}^{2+}$

## A Bug's Eye View of the Periodic Table

SIMON SILVER and ROBERT D. PERRY

Division of Biology and Biomedical Sciences, Washington University,  
St. Louis, MO 63130

*Free-living cells must accumulate needed inorganic nutrients by uphill energy-dependent transport processes, exclude those normally found cations and anions that are not utilized intracellularly, and regulate the equilibrium ratios and osmotic pressures due to both. Studies with short half-lived  $^{42}\text{K}^+$  and  $^{28}\text{Mg}^{2+}$  have allowed characterization of highly substrate-specific and energy-dependent transport systems for these inorganic nutrients. Evidence supports the separate existence of one or more bacterial systems for both cations (and for other required intracellular cations and anions) and shows differences in uptake and retention of the "natural" substrates (in kinetic constants and other characteristics) from those that would be deduced primarily from studies with longer half-lived analogues  $^{86}\text{Rb}^+$  or  $^{137}\text{Cs}^+$  (for  $\text{K}^+$ ) and  $^{54}\text{Mn}^{2+}$  or  $^{60}\text{Co}^{2+}$  (for  $\text{Mg}^{2+}$ ). Transport studies using  $^{14}\text{CH}_3\text{NH}_3^+$  as an analogue of  $\text{NH}_4^+$  suggest that free-living cells discriminate between this analogue and  $\text{NH}_4^+$ . A realistic understanding of the manner in which free-living cells regulate and govern their intracellular inorganic milieu requires use of the radionuclides of the normal environmental ion.*

**I**n this volume, with several chapters devoted to the assimilation and metabolism of  $^{13}\text{N}$ -labeled ammonia and nitrate into amino acids, purines, and pyrimidines that are the building units of cellular macromolecules, it is perhaps worthwhile to consider the larger context of basic inorganic biochemistry, or how cells view and utilize the elements of the periodic table (1, 2, 3).

0065-2393/81/0197-0453\$05.00/0  
© 1981 American Chemical Society



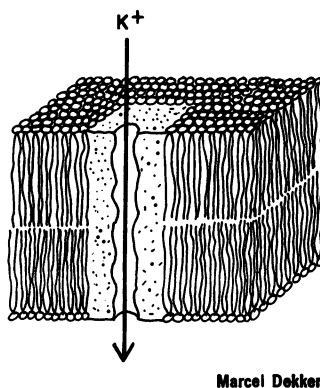


Figure 1. Hypothetical model for a cation-specific channel through a membrane-spanning transport protein (3)

Marcel Dekker

Although this report concerns bacterial cells ("bugs," but not the six-legged kind), and most frequently experiments with that most-studied of microbes, *Escherichia coli*, it is our experience that conclusions reached with specific bacteria will generalize to all bacteria, to free-living cells of higher organisms, and often to the cells and intracellular mitochondria and chloroplasts of animal and plant cells. Clearly, such generalizations do not always hold and must be made with caution; however, the existence and general properties of many cation and anion transport systems are quite universal for cellular membranes.

This has been the primary interest of our laboratory for the last decade and has been summarized in several recent reviews (3-6). Our general conclusion is that quite separate and specific membrane transport systems exist for each and every inorganic cation or anion that is needed for cellular metabolism. The specificity of these systems is indicative of membrane-embedded proteins (Figure 1), which we picture as serving as channels or as pumps. In a few cases, such as the mammalian  $\text{Na}^+/\text{K}^+$  ATPase (7) and the sarcoplasmic reticulum  $\text{Ca}^{2+}$  ATPase (5, 8, 9), the basic properties of these systems are being investigated with purified membrane proteins reconstituted into artificial membranes. At least for charged molecules, nothing crosses the membrane by bulk diffusion.

In addition to our general thesis that quite separate membrane transport systems exist in free-living cells for each and every inorganic cation or anion required for growth, cations and anions that are not normally accumulated are excreted by similar transport systems of opposite polarity. Figure 2 summarizes many of these systems.  $\text{K}^+$  and  $\text{Mg}^{2+}$  are the major intracellular cations required for growth of all cells. These are actively accumulated by two separate  $\text{K}^+$  transport systems (10, 11, 12) and two separate  $\text{Mg}^{2+}$  transport systems (13, 14, 15) in *E. coli*, as will be described in greater detail below. A  $\text{K}^+$  efflux system (16) has been identified, which probably serves as a  $\text{K}^+/\text{H}^+$  exchange system that regulates intra-

cellular pH.  $\text{Na}^+$  and  $\text{Ca}^{2+}$  are the major monovalent and divalent cations that are not accumulated or found in significant intracellular concentrations. These cations are excreted by one or more outwardly oriented transport systems (17–20).  $\text{Mn}^{2+}$  (6, 21, 22) and  $\text{Zn}^{2+}$  (23) are essential intracellular divalent cations required at levels much lower than that needed for  $\text{Mg}^{2+}$ . They are accumulated by separate and distinct transport systems (Figure 1; Reference 3). All cells require  $\text{Fe}^{3+}$  for growth and metabolism; *E. coli* has at least four distinct iron transport systems, whose regulation and function have been extensively studied (3).

Inorganic anions are accumulated by separate, carefully regulated transport systems. There are at least two such systems for phosphate in *E. coli* (24) and a separate one for sulfate (25). Chloride, the major inorganic anion found in growth environments but not generally used for metabolism, is probably governed by a separate, outwardly oriented transport system, whose function is to regulate osmotic pressure. In this volume the first direct evidence is presented for  $\text{NO}_3^-$  transport systems in bacteria (26). We hypothesized the existence of such systems three years ago (3). Bacteria contain two types of nitrate reductase enzymes: (i) a low level assimilatory reductase synthesized during nitrate-dependent growth; and (ii) a dissimilatory nitrate reductase that functions as an electron sink in anaerobic respiration. In the first case, either the  $\text{NO}_3^-$  must be transported across the membrane prior to reduction or, less likely, the product ( $\text{NO}_2^-$ ) must be transported subsequently to continue the enzymatic reduction to  $\text{NH}_4^+$  and incorporation into amino acids. Since

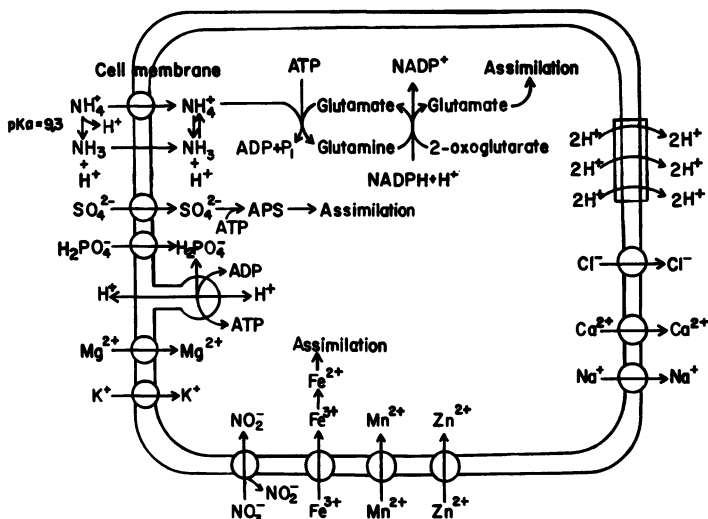


Figure 2. Some known membrane transport systems for cations and anions

$\text{NO}_2^-$  is toxic, it is likely (27, 28) that the dissimilatory nitrate reductase functions at the membrane surface (as diagrammed in Figure 2) so that the  $\text{NO}_2^-$  never enters the cell. Eucaryotic microbes also have  $\text{NO}_3^-$  and  $\text{NO}_2^-$  transport systems (29, 30) whose function is regulated by the availability of  $\text{NH}_4^+$  (31).

That leaves the two more complicated situations in Figure 2: Proton movement outward across the membrane is carried out by the respiratory chain (where each of the classic coupling sites is now pictured as a site of proton translocation) and by the reversible proton-translocating ATPase. This is the coupling factor, essentially identical in bacterial cells, mitochondria, and chloroplasts (32). The protons that have been excreted pass back into the cell through many paths including the anion transport systems and  $\text{Na}^+$ /proton and  $\text{Ca}^{2+}$ /proton "antiport" exchange systems (17–20) shown in Figure 2, the reversible ATPase (resulting in "coupled" oxidative phosphorylation or photophosphorylation), or "symport" with neutral organic substrates (providing the driving force in these transport systems). The proton excretion sets up a transmembrane electrical potential ( $\Delta\psi$ ) and pH gradient ( $\Delta\text{pH}$ ) that constitute the "energized" membrane state available for osmotic and chemical work (32).

Finally, there is the still-open question of ammonium transport pictured in the upper-left portion of Figure 2. Two likely routes for ammonium uptake are envisaged: (i) passive diffusion of the relatively lipid-soluble and uncharged  $\text{NH}_3$  and (ii) active carrier-mediated uptake of charged  $\text{NH}_4^+$  through a membrane protein. Both mechanisms are diagrammed in Figure 2 because, in spite of considerable efforts to distinguish between these mechanisms, we are unfortunately unable, at this time, to rule out either. The  $\text{pK}_a$  for the transition from  $\text{NH}_4^+$  to  $\text{NH}_3$  is 9.3; therefore at pH 7.0, 99.5% of the available ammonium will be in the  $\text{NH}_4^+$  form. The arguments in favor of an  $\text{NH}_4^+$  transport system and  $^{13}\text{NH}_4^+$  uptake experiments designed to test this hypothesis are described in detail below.

This volume is concerned with the use of short-lived radioisotopes (half-lives of minutes). We will expand this "short" range to include  $^{42}\text{K}$  ( $t_{1/2} = 12.4$  h) and  $^{29}\text{Mg}$  ( $t_{1/2} = 21.3$  h), as well as  $^{13}\text{NH}_4^+$ , since many biologists would consider these radioisotopes "short-lived." Although differences exist between the three systems, the general conclusion that studies on the accumulation of these cations must utilize the radioisotopes of "natural" substrates can be made. Analogues such as  $^{86}\text{Rb}^+$  and  $^{137}\text{Cs}^+$  for  $\text{K}^+$ ,  $^{54}\text{Mn}^{2+}$  and  $^{60}\text{Co}^{2+}$  for  $\text{Mg}^{2+}$ , and  $^{14}\text{CH}_3\text{NH}_3^+$  for  $\text{NH}_4^+$  are imperfect and can lead to inaccurate conclusions.

### **Potassium Transport**

Because procaryotic and eucaryotic  $\text{K}^+$  transport systems are the best understood of all cation transport systems, we shall start with an exami-

nation of the use of  $^{42}\text{K}^+$  vs.  $^{86}\text{Rb}^+$  in such studies. With a 12.4-h half-life  $^{42}\text{K}^+$  is much less convenient for experimentation than is the frequently used  $\text{K}^+$  analogue  $^{86}\text{Rb}^+$  with a 18.7-day half-life. Nevertheless, 12.4 h translates into about 1% loss in 10 min, and we have found that  $^{42}\text{K}^+$  can be handled and used in transport studies essentially as would  $^{14}\text{C}$ - or  $^3\text{H}$ -labeled compounds.  $^{42}\text{K}^+$  emits strong  $\beta$  particles that can be conveniently counted on a Geiger counter or in a liquid scintillation counter either in organic scintillation fluid or in water via Cerenkov radiation (33); we have used all three methods with essentially equal ease and high efficiencies. With a shipment of a few mCi of  $^{42}\text{K}^+$  arriving at the airport in the evening from a commercial source, we can experimentally process and count around 1000 samples (one minute each with no repeat counting) during the 5 half-lives or so of useful activity. Radioisotope decay corrections may be made by normalization either from control samples counted every 10 min and/or from recorded elapsed counting times, as explained below for  $^{13}\text{NH}_4^+$ .

Much biological information has been obtained from studies of transport of  $\text{K}^+$  and its analogues. The general conclusion is that cells of higher animals (7, 34) and plants (35) do not discriminate effectively between  $^{42}\text{K}^+$  and  $^{86}\text{Rb}^+$  for transport. Therefore experiments with  $^{86}\text{Rb}^+$  yield biologically interesting and valid results. Some microorganisms, of which *Rhodospseudomonas capsulata* is the best studied example (36), discriminate somewhat between  $\text{K}^+$  and  $\text{Rb}^+$  (and even more so against  $\text{Cs}^+$ ) (Table I). Other microbes, notably *Escherichia coli* (Table I; Reference 12) discriminate so strongly against  $\text{Rb}^+$  that its use as a  $\text{K}^+$  analogue is precluded. Note from Table I that the two  $\text{K}^+$  transport systems of *E. coli* have different degrees of discrimination against  $\text{Rb}^+$ .

**Table I. Kinetic Parameters of Bacterial Potassium Transport Systems\***

Bacterium	Cation Transported	$K_m$ (mM)	$V_{max}$ ( $\mu\text{mol}/\text{min per g}$ )	Competitive Inhibitors or Discrimination Against $\text{Rb}^+$
<i>R. capsulata</i>	$\text{K}^+$	0.20	8.0	$K_i = 0.56\text{mM Rb}^+$ $K_i = 2.8\text{mM Cs}^+$
	$\text{Rb}^+$	0.52	5.9	$K_i = 0.2\text{mM K}^+$ $K_i = 2.6\text{mM Cs}^+$
	$\text{Cs}^+$	3	2	
<i>E. coli</i> Kdp TrkA	$\text{K}^+$	0.002	150	$>1000 \times \text{K}^+/\text{Rb}^+$
	$\text{K}^+$	1.5	550	$10 \times \text{K}^+/\text{Rb}^+$

\* Kinetic parameters for *R. capsulata* (for photosynthetically grown cells) and the  $K_m$ s and  $V_{max}$ s for *E. coli* are from previously published reports (10, 12, 36). The  $K_i$ s for *R. capsulata* are kinetically determined values from experiments such as Reference 36. The ratios for the *E. coli* systems are not accurately determined  $K_i$  values but rather calculated discrimination ratios of Reference 12.

The "trace-scavenging" Kdp system (which is responsible for accumulating  $K^+_{in}/K^+_{out}$  gradients of greater than  $10^6:1$ ; Reference 10, 12) has a discrimination ratio ( $K^+/Rb^+$ ) of 1000, while the major TrkA system (which functions under conditions of abundant extracellular  $K^+$ ) has a ratio of only 10. The high affinity Kdp system includes a transport ATPase (11, 37), which is in fact the first example of a cation-specific transport ATPase in bacteria. Very recently, Epstein and Laimins (10) have reevaluated  $K^+$  transport in *E. coli* and concluded that there are two, rather than four, separate transport systems for  $K^+$ . The two deleted transport systems were actually the TrkA system with mutationally altered kinetic parameters.

These results are as might be expected and represent another generalization from studies of the last 10 years: the specificity of a transport system is tailored to meet cellular needs with systems that function under conditions of nutrient starvation having the highest degree of specificity. For the monovalent cation systems, discrimination is greatest against the related abundant cation ( $Na^+$ ) and lesser for rarer analogues ( $Rb^+$  or  $Cs^+$ ). Organisms such as *E. coli* (which sometimes grows in very dilute fresh water) or *Halobacter halobrium* (which grows in supersaturated NaCl ponds) require systems that have specificity characteristics that will sustain the universal need for very high internal  $K^+$  levels. Cells growing in better  $K^+$ -buffered environments do not require such great specificity (except against abundant  $Na^+$ ), and therefore animal cells need not discriminate against  $Rb^+$  at all. Even among the free-living bacteria, *R. capsulata* can grow with intracellular  $K^+$  replaced with  $Rb^+$  (36), whereas *E. coli* cannot (38).

As the major intracellular inorganic cation,  $K^+$  levels are carefully regulated (38). The regulation is primarily in response to extracellular osmolarity (10, 12, 38). However,  $K^+$  transport is also regulated during the cell cycle in exponentially growing cells (39) and during developmental cycles such as bacterial sporulation and spore germination (40).

Among the Group Ia elements of the Periodic Table, living cells accumulate  $K^+$  and exclude  $Na^+$ —in fact,  $Na^+$  is universally excreted by a pump of reversed polarity from inside to out (3, 19, 32). While some organisms utilize  $Na^+$  entry in a symport mechanism to accumulate amino acids and carbohydrates, they also have  $Na^+$  efflux systems (41, 42, 43).  $Li^+$  is a  $Na^+$  analogue and does not function as a  $K^+$  substitute. Although ionic radius is undoubtedly the primary factor utilized by the membrane transport proteins to distinguish between cations of similar charge, there is no direct evidence as to how the presumed negatively charged chemical groups lining the transmembrane channel (Figure 1) accomplish this task. With the lipid-soluble 1100 molecular weight depsipeptide valinomycin (44, 45), discrimination between transmembrane movement

of  $\text{K}^+$  and of  $\text{Na}^+$  is governed by the stability of the complex, which is in turn dependent on ionic radius [ $\text{K}^+$  ( $r = 0.169 \text{ nm}$ );  $\text{Na}^+$  ( $r = 0.095 \text{ nm}$ )]. Whether membrane transport proteins (Figure 1) utilize a mechanism similar to this model compound (46, 47) to discriminate between  $\text{K}^+$  and  $\text{Rb}^+$  is an open question.

### ***Magnesium Transport***

It is precisely because of the absence of a long half-lived radioisotope of  $\text{Mg}^{2+}$  that there have been few studies of  $\text{Mg}^{2+}$  transport in biological systems.  $^{28}\text{Mg}$  has a 21.3-h half-life and emits a 0.45-meV  $\beta$  particle as well as  $\gamma$  radiation (33). It is not available from commercial sources, but it has been made on a fixed schedule of every two or three weeks from the Hot Laboratory Division, Brookhaven National Laboratory in the United States and was available on request from the Radiochemical Centre, Amersham, Great Britain. Jasper and Silver (4) summarized all known single-cell and subcellular studies on  $^{28}\text{Mg}^{2+}$  and biological materials (animal, plant, and microbial) in 1977. We are not aware of newer studies with  $^{28}\text{Mg}^{2+}$  at the cellular or subcellular levels.

Transport of  $^{28}\text{Mg}^{2+}$  by a variety of bacteria has been studied in our laboratory (15, 48, 49, 50). The most thoroughly studied example for  $\text{Mg}^{2+}$  transport is *E. coli*, where  $\text{Mg}^{2+}$  transport was first reported in 1969 (50, 51). The eucaryotic microbe *Euglena* and human KB cells in tissue culture also have  $\text{Mg}^{2+}$  transport systems (4, 52). In fact, all tested cells have active transport systems for  $^{28}\text{Mg}^{2+}$  (4) with the one exception of mature human red blood cells (unpublished data). It is possible that this transport process is lost during red blood cell maturation just as  $\text{Na}^+/\text{K}^+$  ATPase activity decreases during red blood cell maturation (53). *E. coli* has two  $\text{Mg}^{2+}$  transport systems (13, 14). Competitive inhibitors and alternative substrates for *E. coli*  $\text{Mg}^{2+}$  transport include  $\text{Co}^{2+}$  and  $\text{Mn}^{2+}$ , two cations for which longer-lived, more convenient radioisotopes exist. Indeed  $^{60}\text{Co}^{2+}$ ,  $^{63}\text{Ni}^{2+}$ , and  $^{54}\text{Mn}^{2+}$  have been used in these studies (4, 14). Nevertheless, the existence of mutants with altered discrimination against  $\text{Co}^{2+}$  and  $\text{Mn}^{2+}$  (14, 15) and the ratio of the  $K_m$ s for  $\text{Mg}^{2+}$  and for other divalent cations (often 10:1 in favor of  $\text{Mg}^{2+}$ ) point out the essential requirement that studies of magnesium transport and metabolism utilize the short half-life radioisotope  $^{28}\text{Mg}^{2+}$ . Faulty conclusions can be drawn from overreliance on imperfect analogues.

### ***Ammonium (a) Uptake***

There are several alternative mechanisms for movement of  $\text{NH}_3/\text{NH}_4^+$  across biological membranes (Table II). Indeed, more than one mechanism may occur in nature, and different organisms may utilize different

**Table II. Possible Mechanisms for Ammonia Uptake\***

<i>Mechanisms</i>	<i>Predicted Characteristics</i>
Likely	
Passive diffusion of $\text{NH}_3$	$\Delta\text{pH}$ dependent and unsaturable
Carrier-mediated transport of $\text{NH}_4^+$	$\Delta\text{pH}$ and $\Delta\psi$ dependent; saturable
Unlikely	
Passive diffusion of $\text{NH}_4^+$	$\Delta\text{pH}$ and $\Delta\psi$ dependent; unsaturable
Carrier-mediated diffusion of $\text{NH}_3$	$\Delta\text{pH}$ dependent and saturable

\* All mechanisms would be followed by the "pull" from ATP-dependent saturable assimilation into amino acids.

mechanisms. The two mechanisms that are considered most likely to occur are (i) the passive diffusion of lipid-soluble un-ionized  $\text{NH}_3$  across the lipid bilayer regions of membranes, and (ii) the protein-carrier mediated energy-dependent transport of ionized  $\text{NH}_4^+$ . The primary characteristics of the former mechanism is an absence of saturation kinetics—bulk solubility parameters of lipid surfaces would govern the rate of uptake, rather than a small number of specific sites—and a dependence on the pH gradient across the membrane for the final equilibrium ratio. With a  $\text{pK}_a$  of 9.3, essentially all the ammonia will occur as  $\text{NH}_4^+$  at physiological pH, and a difference in pH (internal alkaline) will result in an equilibrium concentration of a factor of  $10\times$  less ammonia internally for every pH difference across the membrane. An internal pH more acidic than the external pH would be required for net accumulation of ammonia by this mechanism. Yet, the Mitchell chemiosmotic theory for chloroplasts, mitochondria, and bacterial membranes predicts an internal pH alkaline relative to the outside pH; this has indeed been found repeatedly by direct experiment (e.g., see Reference 32 for review). Nevertheless, passive diffusion of  $\text{NH}_3$  appears to be the actual mechanism of ammonia uptake in mammalian cells and across membranes such as the blood-brain barrier (54, 55, 67). Perhaps with the stable low  $\text{NH}_4^+$  levels in blood serum (about  $5\ \mu\text{M}$ ; Reference 55) and the use of organic rather than inorganic compounds as nitrogen sources within animals, there is no need for an ammonium transport system in animal cells comparable to that required for growth by free-living cells dependent on inorganic nitrogen for nutrient supply.

There have been several reports of passive diffusion of  $\text{NH}_3$  in free-living microbial cells as well: Suzuki et al. (56) measured the effect of pH on whole-cell oxidation rates of  $\text{NH}_4^+$  to  $\text{NO}_2^-$  by *Nitrosomonas europaea* and concluded that  $\text{NH}_3$  was the form that moved across the cellular membrane to the intracellular oxidation site. This conclusion was based on the questionable assumptions of equal concentrations across

the cell membrane and no pH gradient. More recently, Bhandari and Nicholas (57), using the same organism, came to the opposite conclusion, that is, that *N. europaea* utilizes a specific  $\text{NH}_4^+$  translocase for ammonia uptake. Subsequent extrusion of protons leads to a net  $\text{NH}_3$  uptake, but the initial  $\text{NH}_4^+$  uptake process was inhibited more completely by energy inhibitors than were subsequent oxygen-dependent stages (57).

Zarlengo and Abrams (58) measured the entry of  $\text{NH}_3$  to aged (for days at  $4^\circ\text{C}$ ) stationary phase *Streptococcus fecalis*. With cells starting with an internal pH of near 5, entry of un-ionized  $\text{NH}_3$  was rapid. Under these physiologically nonactive conditions, bacterial cells were indeed rapidly penetrable to  $\text{NH}_3$ , with a decrease in the pH gradient across the membrane an immediate result of the process. Uptake led to a net accumulation of ammonia, starting with cells that were acidic inside relative to the incubation medium.

Stevenson and Silver (59) used the radioactive  $\text{NH}_4^+$  analogue  $^{14}\text{CH}_3\text{NH}_3^+$  in transport studies with *E. coli*. Methylamine had been previously used as an  $\text{NH}_4^+$  analogue in studies with nonbacterial microbes (see below). Energy-dependent uptake of methylamine was demonstrated. The pH dependence of this uptake was complex, but optimum uptake was obtained at pH 9, well below the  $\text{pK}_a$  of  $\text{CH}_3\text{NH}_3^+$  to  $\text{CH}_3\text{NH}_2$  of 10.9. Stevenson and Silver (59) postulated the existence of one or possibly two specific  $\text{NH}_4^+$  transport systems in *E. coli*. Subsequently, *Clostridium pasteurianum* cells (60) were shown to accumulate  $\text{NH}_4^+$  (and  $\text{CH}_3\text{NH}_3^+$ ) by physiologically active processes that were interpreted to occur across a membrane essentially impermeable to un-ionized  $\text{NH}_3$ . *C. pasteurianum* cells maintained a gradient of  $\text{NH}_3 + \text{NH}_4^+$  of 100:1 inside to outside while growing on  $\text{N}_2$  as nitrogen source (60). This result is consistent with a basically impermeable membrane. Valinomycin released cellular  $\text{NH}_4^+$  by functioning as a membrane carrier of  $\text{NH}_4^+$ . *C. pasteurianum* reduces  $\text{N}_2$  to  $\text{NH}_4^+$  only when there is no alternative nitrogen source available;  $\text{NH}_4^+$  in the environment is scavenged down to traces below  $1\mu\text{M}$ . The transport system utilized for scavenging was studied with  $^{14}\text{CH}_3\text{NH}_3^+$  as an analogue substrate for the  $\text{NH}_4^+$  transport system; concentration gradients of 70:1 (internal:external  $\text{CH}_3\text{NH}_3^+$ ) were established. This gradient was almost completely eliminated by addition of low levels of  $\text{NH}_4^+$ , indicating a preference for the natural substrate over the analogue.

Laane et al. (61) demonstrated energy-dependent  $\text{NH}_4^+$  uptake in another  $\text{N}_2$ -fixing bacterial species, *Azotobacter vinelandii*. This uptake was in response to the cellular membrane potential (internal negative).  $^{14}\text{CH}_3\text{NH}_3^+$  was used again as a radioactive analogue of  $\text{NH}_4^+$ . Whereas intact cells of free-living  $\text{N}_2$ -fixing *A. vinelandii* accumulated  $\text{CH}_3\text{NH}_3^+$ , bacteroids of *Rhizobium leguminosarum* (which is symbiotic in plant



root nodules and which fixes nitrogen only in association with the leguminous host plant) did not accumulate  $^{14}\text{CH}_3\text{NH}_3^+$ , as if they lacked an  $\text{NH}_4^+$  uptake system. *Rhizobium* bacteroids in fact excreted  $^{14}\text{CH}_3\text{NH}_3^+$  in response to the pH gradient (0.45 pH units internal alkaline; Reference 61). *Pseudomonas sp.* MA actively transports  $^{14}\text{CH}_3\text{NH}_3^+$ . However, this transport system was inducible only under conditions where methylamine served as carbon source. That and the absence of inhibition of methylamine uptake by ammonia indicate that this methylamine transport system was not an ammonia transport system (62).

In summary, there appears to be evidence for both mechanisms of  $\text{NH}_3/\text{NH}_4^+$  transport in bacterial cells. Passive diffusion of  $\text{NH}_3$  would not generally lead to net accumulation by cells with an alkaline interior pH relative to the medium pH. Passive diffusion would be rate-limited by the low level of  $\text{NH}_3$  available at physiological pH and by the solubility properties of the cell membrane.  $\text{NH}_4^+$  active transport would be required for net ammonium uptake. However, net nitrogen accumulation could be accomplished by rapid assimilation of internal ammonia into amino acids. Net accumulation might be limited by the balance of the two processes: uptake by active transport vs. loss by passive diffusion.

More extensive studies characterizing  $\text{NH}_4^+$  accumulation have been carried out in free-living eucaryotic organisms using  $^{14}\text{CH}_3\text{NH}_3^+$  as an analogue for  $\text{NH}_4^+$ . In *Aspergillus nidulans*, an active methylamine transport system ( $K_m = 20\mu\text{M}$ ), which was repressed by growth on high  $\text{NH}_4^+$ , has been characterized (63). Competitive inhibition of  $^{14}\text{CH}_3\text{NH}_3^+$  uptake by  $\text{NH}_4^+$  was not tested, but mutants were identified with phenotypic characteristics, which include poor growth on  $\text{NH}_4^+$  and altered methylamine transport activities. A repressible methylamine active transport system ( $K_m = 220\mu\text{M}$  with ammonia as a strong competitive inhibitor) was identified in *Saccharomyces cerevisiae* (64, 65). *Penicillium chrysogenum* also has a repressible active  $^{14}\text{CH}_3\text{NH}_3^+$  transport system ( $K_m = 10\mu\text{M}$ ). Both  $\text{NH}_4^+$  and  $\text{C}_2\text{H}_5\text{NH}_3^+$  were competitive inhibitors of the system, with  $K_i$ s of  $0.25\mu\text{M}$  and  $100\mu\text{M}$  respectively (66).

### ***<sup>13</sup>N-Ammonium Accumulation***

Although the use of methylamine as an  $\text{NH}_4^+$  analogue has been moderately successful with the above organisms, its similar application to many bacterial systems may lead to erroneous conclusions. Accordingly, we have started  $^{13}\text{NH}_4^+$  uptake experiments designed to characterize bacterial  $\text{NH}_4^+$  accumulation.

The Mallinckrodt Institute of Radiology at Washington University School of Medicine produces  $^{13}\text{NH}_4^+$ .  $^{13}\text{NH}_4^+$  can be conveniently counted in a standard commercial liquid scintillation spectrophotometer,

obviating the need for special counting equipment. Approximately 100 samples can be processed and counted (0.5–1.0 min each with no repeat counting) before decay precludes further analysis. With a half-life of 9.96 min, it is necessary periodically to record the “clock time” on the counter printout. Decay corrections for each sample may then be calculated by the equation: Decay correction factor =  $\text{antilog}(0.0302 \times \text{elapsed time in minutes})$  either by computer or by hand calculator.

Our experiments have used primarily *S. typhimurium* strains with wild-type and mutant phenotypes for ammonia assimilation. Figure 3 illustrates the pH profiles for [ $^{13}\text{N}$ ]ammonia accumulation of *S. typhimurium* strains JL907 (wild-type) and JB801, which lacks glutamate dehydrogenase (GDH) and glutamate synthase (GOGAT). L-Methionine-DL-sulfoximine is an inhibitor of the first steps of the ammonia assimilatory process depicted in Figure 2. The pH profile for strain JB801 showed a

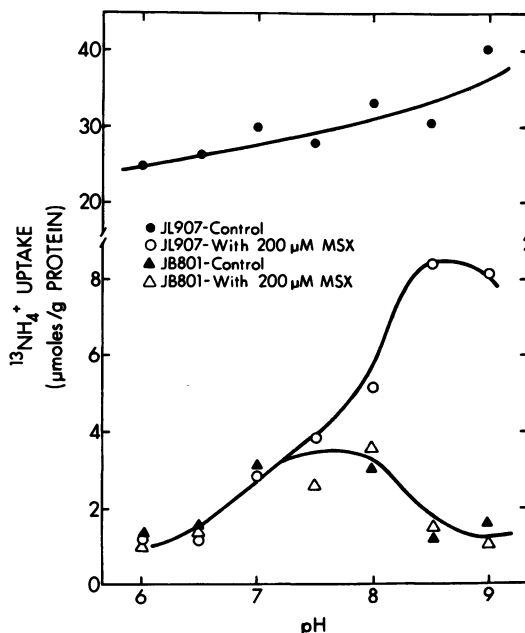


Figure 3. pH profile of  $^{13}\text{NH}_4^+/\text{NH}_3$  accumulation by *S. typhimurium* strains JL907 (wild-type) and JB801 (GDH<sup>-</sup>, GOGAT<sup>-</sup>).

The cells were grown to mid-log phase in a minimal medium (M9) with 2mM  $\text{NH}_4\text{Cl}$  (JL907) or 10mM L-glutamate (JB801). The cells were then washed and resuspended in M9 medium without a N-source. After 4 h of incubation at 42°C, the cells were washed and resuspended in 50mM Tris–72.5mM NaCl–0.4% glucose of the appropriate pH. After equilibration at 37°C,  $71\mu\text{M } ^{13}\text{NH}_4^+/\text{NH}_3$  was added; 0.5-mL samples were filtered after 30 s of incubation and washed twice with 5-mL volumes of appropriate pH buffer (without  $\text{NH}_4\text{Cl}$ ). 200 $\mu\text{M}$  L-methionine-DL-sulfoximine (MSX) was added where indicated.

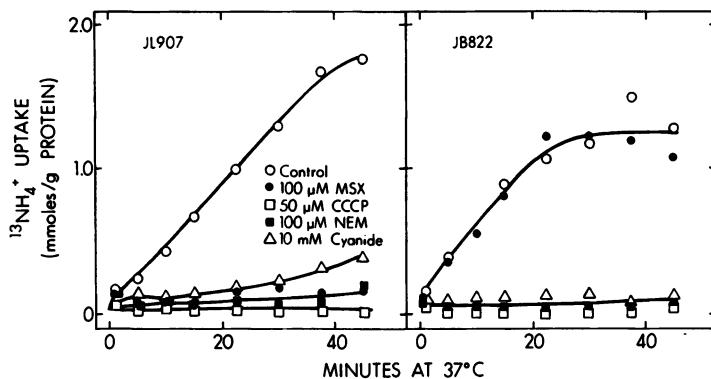


Figure 4. The effects of inhibitors on  $^{13}\text{NH}_4^+/\text{NH}_3$  accumulation by strains JL907 (wild-type) and JB822 (GDH<sup>-</sup>).

The cells were grown to mid-log phase in M9 medium with 2mM  $\text{NH}_4\text{Cl}$ , washed and resuspended in 50mM Tris-72.5mM NaCl-0.4% glucose (pH 6.5 at 37°C). The cells were incubated for 1 h at 37°C before the addition of 480  $\mu\text{M}$   $^{13}\text{NH}_4^+/\text{NH}_3$ . Samples were filtered as described in Figure 3. Abbreviations: CCCP, carbonyl cyanide, *m*-chlorophenylhydrazone; and NEM, *N*-ethylmaleimide.

peak around pH 7.5 (Figure 3), well below the  $\text{pK}_a$  of 9.3. For strain JL907 the uptake of  $^{13}\text{NH}_4^+/\text{NH}_3$  continued to increase to pH 8.5. The absence of a pH profile that mimics the titration of  $\text{NH}_4^+$  to  $\text{NH}_3$  indicates that the actual  $\text{NH}_3$  concentration in the incubation medium is not rate-limiting. With the wild-type strain in the absence of the inhibitor, uptake was more than 10 $\times$  as rapid as with the inhibitor and it was essentially independent of pH.

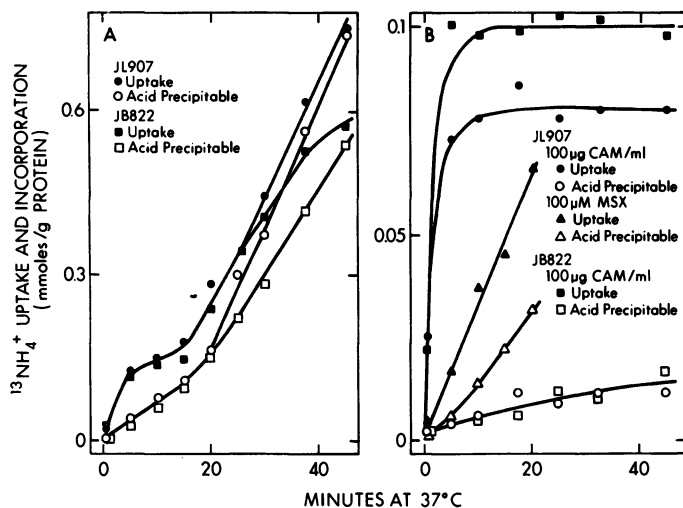
Inhibition patterns of [ $^{13}\text{N}$ ]ammonia accumulation by strains JL907 and JB822 (GDH<sup>-</sup>) are shown in Figure 4. It is clear that assimilation plays an important role in [ $^{13}\text{N}$ ]ammonia accumulation in these strains. Strain JB822 is resistant to methionine sulfoximine due to a defect in methionine transport (data not shown). The inhibition by metabolic inhibitors (Figure 4) was not unexpected, since assimilation and all possible accumulation mechanisms (Table II) are energy-dependent. It is presently unclear whether *N*-ethylmaleimide inhibition was due to inactivation of a sulfhydryl-containing surface receptor or to inhibition of electron transport.

Figure 5 illustrates several other characteristics of  $^{13}\text{NH}_4^+/\text{NH}_3$  uptake and assimilation by these strains. A reproducible initial lag in [ $^{13}\text{N}$ ]ammonia incorporation into protein (acid precipitable radioactivity) may be the cause of the apparent biphasic uptake curve (Figure 5A). When protein synthesis was inhibited by chloramphenicol, ammonia accumulation reached a steady-state level after 5 min of incubation (Figure 5B). In the presence of methionine sulfoximine, accumulation

and incorporation of  $^{13}\text{N}$  into protein continued although at reduced rates. A few explanations for the incomplete inhibition of  $^{13}\text{NH}_4^+/\text{NH}_3$  assimilation are possible: (i) inhibition of glutamine synthetase and glutamate synthase by MSX may be less than 100%; or (ii) under these conditions, glutamate dehydrogenase may play an assimilatory role.

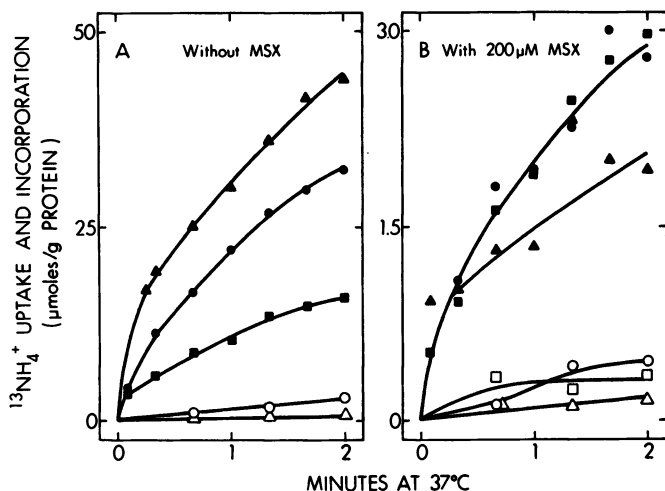
Assimilation into protein initially lagged behind accumulation (Figure 5), indicating that short time-course experiments might yield better information on uptake mechanisms. Figure 6 depicts an initial rate experiment with strain JL907. Clearly assimilation plays a vital role even during the first seconds of [ $^{13}\text{N}$ ]ammonia accumulation. The differences between N-sufficient cells (growth with 10mM  $\text{NH}_4^+$ ) and N-starved cells (4 h incubation without N-source) may be due to regulatory changes in ammonia assimilatory enzymes.

With whole-cell studies, we have unfortunately been unable to elucidate the [ $^{13}\text{N}$ ]ammonia uptake mechanism. The incomplete inhibition of assimilatory processes both by mutation and by inhibitors is the major obstacle. Valid transport studies require that the accumulated substrate be unmodified by subsequent metabolism. However, these preliminary experiments have yielded interesting conclusions about the



**Figure 5.** The effects of L-methionine-DL-sulfoximine (MSX) and chloramphenicol (CAM) on  $^{13}\text{NH}_4^+/\text{NH}_3$  accumulation and incorporation into protein by strains JL907 (wild-type) and JB822 ( $\text{GDH}^-$ ).

The cells were grown to mid-log phase in M9 medium with 10mM  $\text{NH}_4\text{Cl}$ , washed and resuspended in 50mM Tris-72.5mM NaCl-0.4% glucose (pH 6.5 at 37°C).  $^{13}\text{NH}_4^+/\text{NH}_3$  (190 $\mu\text{M}$ ) was added and samples filtered and processed as described in Figure 3. Acid precipitable refers to  $^{13}\text{NH}_4^+/\text{NH}_3$  retained by filtration after treatment with cold 10% trichloroacetic acid.



**Figure 6.** Effects of L-methionine-DL-sulfoximine (MSX) and chloramphenicol (CAM) on  $^{13}\text{NH}_4^+/\text{NH}_3$  accumulation and protein synthesis by N-sufficient and N-starved cells of strain JL907.

The cells were grown to mid-log phase in M9 medium with 10mM  $\text{NH}_4\text{Cl}$  (N-sufficient) or 2mM  $\text{NH}_4\text{Cl}$  (N-starved). N-starved cells were washed, re-suspended in medium M9 without a N-source, and incubated at 42°C for 4 h. Both cell cultures were subsequently washed and resuspended in 50mM Tris-72.5mM NaCl-0.4% glucose (pH 6.5 at 37°C)  $^{13}\text{NH}_4^+/\text{NH}_3$  (80 $\mu\text{M}$ ) was added, samples filtered and processed as described in Figure 3. Symbols: (●) uptake and (○) incorporation by N-sufficient cells; (■) uptake and (□) incorporation in the presence of 200  $\mu\text{g}$  CAM/mL by N-sufficient cells; (▲) uptake and (△) incorporation by N-starved cells.

overall process of nitrogen uptake and assimilation. First, assimilation of  $\text{NH}_4^+$  into amino acids and subsequently into protein is rapid, with only a few minutes (Figure 5A) between initial passage across the cell membrane and appearance in protein. Since inhibition of  $^{13}\text{NH}_4^+$  uptake by MSX occurred within 15 s at 37°C and was 95% effective within the first minute of uptake (compare Figures 6A and B), it is not currently possible to state whether: (i) that 95% represents assimilation into amino acids and the remaining 5% uptake as  $\text{NH}_4^+$ ; (ii) the MSX block was only 95% effective and 5% residual incorporation into amino acids continued; or (iii) a  $\text{NH}_4^+$  transport system is rate-limiting for uptake plus accumulation but inhibited by MSX or regulated rapidly by some intermediate that is itself sensitive to MSX inhibition.

### Acknowledgments

Research in our laboratory on cation transport is currently supported by National Science Foundation grant PCM79-03986 and over the years has been supported by previous National Science Foundation and

National Institutes of Health grants. RDP was supported by a National Research Service award from the NIH. Jean E. Brenchley provided the *Salmonella* mutant strains for the  $^{13}\text{NH}_4^+$  experiments.

### Literature Cited

1. Frieden, E. *Sci. Am.* 1972, 227, 52-60.
2. Hutner, S. H. *Ann. Rev. Microbiol.* 1972, 26, 313-346.
3. Silver, S. In "Bacterial Transport"; Rosen, B. P., Ed.; Marcel Dekker: New York, 1978; p. 221-324.
4. Jasper, P.; Silver, S. In "Microorganisms and Minerals"; Weinberg, E. D., Ed.; Marcel Dekker: New York, 1977; p. 7-47.
5. Silver, S. In "Microorganisms and Minerals"; Weinberg, E. D., Ed.; Marcel Dekker: New York, 1977; p. 49-103.
6. Silver, S.; Jasper, P. In "Microorganisms and Minerals"; Weinberg, E. D., Ed.; Marcel Dekker: New York, 1977; p. 105-149.
7. Hilden, S.; Hokin, L. E. *J. Biol. Chem.* 1975, 250, 6296-6303.
8. Jilka, R. L.; Martonosi, A. N.; Tillack, T. W. *J. Biol. Chem.* 1975, 250, 7511-7524.
9. MacLennan, D. H.; Holland, P. C. In "The Enzymes of Biological Membranes"; Martonosi, A., Ed.; Plenum: New York, 1976; Vol. 3, p. 221-259.
10. Epstein, W.; Laimins, L. *Trends Biochem. Sci.* 1980, 5, 21-23.
11. Epstein, W.; Whitelaw, V.; Hesse, J. *J. Biol. Chem.* 1978, 253, 6666-6668.
12. Rhoads, D. B.; Woo, A.; Epstein, W. *Biochim. Biophys. Acta* 1977, 469, 45-51.
13. Nelson, D. L.; Kennedy, E. P. *Proc. Natl. Acad. Sci. U.S.A.* 1972, 69, 1091-1093.
14. Park, M. H.; Wong, B. B.; Lusk, J. E. *J. Bacteriol.* 1976, 126, 1096-1103.
15. Silver, S.; Clark, D. *J. Biol. Chem.* 1971, 246, 569-576.
16. Brey, R. N.; Rosen, B. P.; Sorensen, E. N. *J. Biol. Chem.* 1980, 255, 39-44.
17. Beck, J. C.; Rosen, B. P. *Arch. Biochem. Biophys.* 1979, 194, 208-214.
18. Brey, R. N.; Rosen, B. P. *J. Biol. Chem.* 1979, 254, 1957-1963.
19. Lindley, E. V.; MacDonald, R. E. *Biochem. Biophys. Res. Commun.* 1979, 88, 491-499.
20. Rosen, B. P.; McClees, J. S. *Proc. Natl. Acad. Sci. U.S.A.* 1974, 71, 5042-5046.
21. Eisenstadt, E.; Fisher, S.; Der, C.-L.; Silver, S. *J. Bacteriol.* 1973, 113, 1363-1372.
22. Fisher, S.; Buxbaum, L.; Toth, K.; Eisenstadt, E.; Silver, S. *J. Bacteriol.* 1973, 113, 1373-1380.
23. Failla, M. L. In "Microorganisms and Minerals"; Weinberg, E. D., Ed.; Marcel Dekker: New York, 1977; p. 151-214.
24. Rosenberg, H.; Gerdes, R. G.; Chegwidan, K. *J. Bacteriol.* 1977, 131, 505-511.
25. Springer, S. E.; Huber, R. E. *FEBS Lett.* 1972, 27, 13-15.
26. Chapter 17 in this book.
27. Garland, P. B.; Downie, J. A.; Haddock, B. A. *Biochem. J.* 1975, 152, 547-559.
28. MacGregor, C. H.; Christopher, A. R. *Arch. Biochem. Biophys.* 1978, 185, 204-213.
29. Schloemer, R. H.; Garrett, R. H. *J. Bacteriol.* 1974, 118, 259-269.
30. *Ibid.*, 270-274.
31. Goldsmith, J.; Livoni, J. P.; Norberg, C. L.; Segel, I. H. *Plant Physiol.* 1973, 52, 362-367.
32. Harold, F. M.; Altendorf, K. In "Current Topics in Membranes and Transport"; Bronner, F.; Kleinzeller, A., Eds.; Academic: New York, 1974; Vol. 5, p. 1-50.

33. Silver, S.; Bhattacharyya, P. *Methods Enzymol.* 1974, 32, 881-893.
34. Mills, B.; Tupper, J. T. *J. Membr. Biol.* 1975, 20, 75-97.
35. Polley, L. D.; Hopkins, J. W. *Plant Physiol.* 1979, 64, 374-378.
36. Jasper, P. J. *Bacteriol.* 1978, 133, 1314-1322.
37. Laimins, L. A.; Rhoads, D. B.; Altendorf, K.; Epstein, W. *Proc. Natl. Acad. Sci. U.S.A.* 1978, 75, 3216-3219.
38. Nakajima, H.; Yamato, I.; Anraku, Y. *J. Biochem.* 1979, 85, 303-310.
39. Kubitschek, H. E.; Freedman, M. L.; Silver, S. *Biophys. J.* 1971, 11, 787-797.
40. Eisenstadt, E. *J. Bacteriol.* 1972, 112, 264-267.
41. Lanyi, J. K.; MacDonald, R. E. *Biochemistry* 1976, 15, 4608-4614.
42. Lanyi, J. K.; Renthal, R.; MacDonald, R. E. *Biochemistry* 1976, 15, 1603-1610.
43. Tokuda, H.; Kaback, H. R. *Biochemistry* 1977, 16, 2130-2136.
44. Andreoli, T. E.; Tieffenberg, M.; Tosteson, D. C. *J. Gen. Physiol.* 1967, 50, 2527-2545.
45. Pressman, B. C. *Annu. Rev. Biochem.* 1976, 45, 501-530.
46. Bhattacharyya, P.; Epstein, W.; Silver, S. *Proc. Natl. Acad. Sci. U.S.A.* 1971, 68, 1488-1492.
47. Lombardi, F. J.; Reeves, J. P.; Kaback, H. R. *J. Biol. Chem.* 1973, 248, 3551-3565.
48. Jasper, P.; Silver, S. *J. Bacteriol.* 1978, 133, 1323-1328.
49. Scribner, H.; Eisenstadt, E.; Silver, S. *J. Bacteriol.* 1974, 117, 1224-1230.
50. Silver, S. *Proc. Natl. Acad. Sci. U.S.A.* 1969, 62, 764-771.
51. Lusk, J. E.; Kennedy, E. P. *J. Biol. Chem.* 1969, 244, 1653-1655.
52. Beauchamp, R. S.; Silver, S.; Hopkins, J. W. *Biochim. Biophys. Acta* 1971, 225, 71-76.
53. Joiner, C. H.; Lauf, P. K. *Membrane Biochem.* 1978, 1, 187-202.
54. Chapter 19 in this book.
55. Subcommittee on Ammonia, National Research Council "Ammonia"; University Park Press: Baltimore, 1979.
56. Suzuki, I.; Dular, U.; Kwok, S. C. *J. Bacteriol.* 1974, 120, 556-558.
57. Bhandari, B.; Nicholas, D. J. D. *Arch. Microbiol.* 1979, 122, 249-255.
58. Zarlengo, M.; Abrams, A. *Biochim. Biophys. Acta* 1963, 71, 65-77.
59. Stevenson, R.; Silver, S. *Biochem. Biophys. Res. Commun.* 1977, 75, 1133-1139.
60. Kleiner, D.; Fitzke, E. *Biochem. Biophys. Res. Commun.* 1979, 86, 211-217.
61. Laane, C.; Krone, W.; Konings, W.; Haaker, H.; Veeger, C. *Eur. J. Biochem.* 1980, 103, 39-46.
62. Bellion, E.; Ali Khan, M. Y.; Romano, M. J. *J. Bacteriol.* 1980, 142, 786-790.
63. Pateman, J. A.; Dunn, E.; Kinghorn, J. R.; Forbes, E. C. *Mol. Gen. Genet.* 1974, 133, 225-236.
64. Roon, R. J.; Even, H. L.; Dunlop, P.; Larimore, F. L. *J. Bacteriol.* 1975, 122, 502-509.
65. Roon, R. J.; Levy, J. S.; Larimore, F. *J. Biol. Chem.* 1977, 252, 3599-3604.
66. Hackette, S. L.; Skye, G. E.; Burton, C.; Segel, I. H. *J. Biol. Chem.* 1970, 245, 4241-4250.
67. Thayer, J. R. *J. Bacteriol.* 1981, 148, in press.

RECEIVED September 4, 1980.

# Radiometric Microbiologic Assays for the Measurement of Vitamin B<sub>12</sub>, Folate, and Niacin in Human Blood and Food

MARIANNE F. CHEN and PATRICIA A. McINTYRE

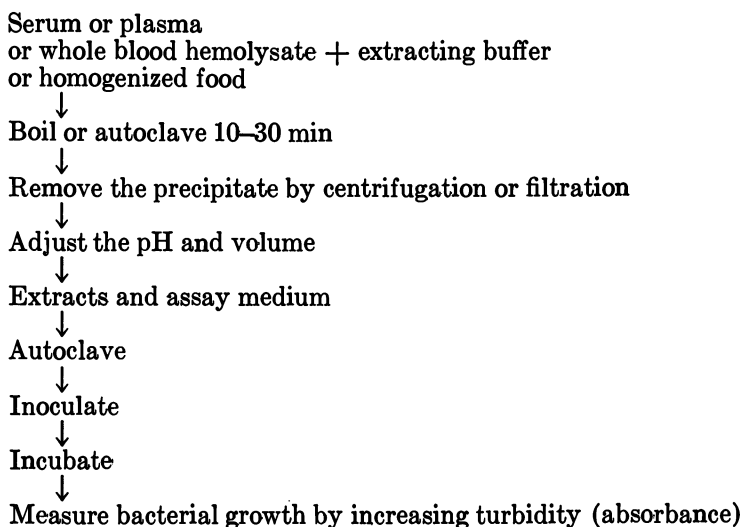
The Johns Hopkins Medical Institutions, 615 North Wolfe Street,  
Baltimore, MD 21205

*Radiometric microbiological assays (RMA) for measuring the levels of vitamin B<sub>12</sub>, folate, and niacin in biological fluids and food were developed using Lactobacillus leichmannii, casei, and plantarum, respectively. In the presence of the appropriate <sup>14</sup>C-labeled substrate, these organisms readily produce <sup>14</sup>CO<sub>2</sub> directly proportional to the amount of the respective vitamin present. Sensitivity for the RMA was 10 pg for vitamin B<sub>12</sub>, 0.1 ng for folic acid, and 0.05 μg for niacin. Direct comparison of RMA with standard turbidimetric microbiological assays gave r = 0.94 for serum vitamin B<sub>12</sub>, r = 0.98 for red-cell folate, r = 0.93 for red-cell niacin, and r = 0.988 for vitamin-B<sub>12</sub> content of 22 foods. Recovery and reproducibility studies gave satisfactory results. The niacin RMA was equally responsive to NAD, NADH, NADP, and NADPH. Biologically inactive forms of niacin gave little or no <sup>14</sup>CO<sub>2</sub> output but showed detectable growth by the conventional assay. These radiometric microbiological assays were found applicable for measuring vitamin B<sub>12</sub>, folate, and niacin levels in biological fluids and also in food.*

The need for simple, sensitive, and specific assays for measuring the level of B vitamins such as vitamin B<sub>12</sub>, folate, and niacin in the blood of normal subjects and patients with various disease conditions has long been recognized (1-9). The past methods for determining the biologically active forms of these vitamins were either animal or microbiological

0065-2393/81/0197-0471\$05.75/0  
© 1981 American Chemical Society



**Table I. Comparison of the Standard and the***Standard Turbidimetric Assay*

assays. Animal assays such as rats or chicks growth assay for vitamin B<sub>12</sub> (10, 11), chicks, monkeys, guinea pigs, or rats assay for folate (12, 13, 14), and chicks, dogs, or rats assay for niacin (15, 16) were all so expensive and time-consuming that they were prohibitive for routine use. Microbiological assays introduced in the 1940s and 1950s depended on measuring increasing turbidity as an index of growth in the presence of the vitamin. Turbidimetric microbiological assays (TMA) were found to be sensitive and inexpensive and became the standard methods of assay for these essential nutrients. However, TMA were time-consuming and tedious, with many requiring special dedicated laboratory facilities (17), and in the case of niacin assays, they lacked specificity (18, 19).

Elucidation of the structure of the B vitamins resulted in the development of analytical chemical methods. Such methods are useful in industries manufacturing vitamins in which measurements of microgram to milligram quantities are routine, but these same methods are often not applicable to biological fluids that contain as little as picogram quantities. Colorimetric and fluorometric techniques have been developed for niacin and folate, but these techniques require complicated extraction procedures and blank determinations. They also suffer from lack of specificity, and the results are often altered by interference from biologically inactive materials that occur naturally or are produced during extraction (16, 20).

In an attempt to overcome some of the difficulties mentioned above, radioisotopic competitive protein binding assays (CPBA) were devel-

**Radiometric Microbiological Assays General Procedure***Radiometric Assay*

Serum or plasma  
or whole blood hemolysate + extracting buffer + assay medium  
or homogenized food



Autoclave 3–5 min



Inoculate



Incubate



Measure bacterial response by the <sup>14</sup>CO<sub>2</sub> produced

oped. Some of these have become commercially available in kit form. However, an inherent disadvantage of such assays is that the binder may “recognize” a chemically similar substance that is devoid of metabolic activity in human beings, thus providing falsely normal test results. This was shown to be the case in the commercial vitamin B<sub>12</sub> kits (21, 22).

After repeated failures to obtain comparable results with the CPBA and the TMA for vitamin B<sub>12</sub> (23, 24), we decided to approach the microbiological assay in a new way. Our studies have led to the development of RMA for the essential nutrients vitamin B<sub>12</sub>, folate, and niacin.

These RMA utilize the same organisms as the TMA but incorporate a <sup>14</sup>C-labeled compound. Instead of measuring net cell growth by turbidity, the response of the microorganism to the minute quantities of vitamin present is measured by quantifying the amount of <sup>14</sup>CO<sub>2</sub> produced. Thus the advantages of this technique over the TMA are: (i) it is sensitive and simple; (ii) there is no interference from colored or turbid materials; (iii) only small amounts of material are required; and most important (iv) it combines the biological specificity of the microorganisms with the precision of measuring radioactive decay as the endpoint.

The methods for each of these RMA are detailed in Refs. 19, 25, 26. The general procedure for the TMA (Table I) requires that the vitamin in a plasma, blood, or food sample first be freed from any binding proteins by boiling or autoclaving it for 30 min in the presence of an “extracting” buffer (and in the case of the folate assay, in the presence

of a reducing compound such as ascorbic acid to prevent degradation of the folates present). Next, the sample is cooled, and the precipitated proteins are removed by either centrifugation or filtration. The clear extract is then adjusted for pH and volume. Varying amounts of the extract are added to the assay medium in tubes, and the volume is adjusted with either water or a buffer. The tubes are then capped, autoclaved, cooled, inoculated with the test organism, incubated for 20–24 h, and net bacterial growth is measured using turbidity as an index.

With the radiometric microbiological technique, the assay is simplified since colored, turbid, or precipitated debris do not interfere with the output or detection of  $^{14}\text{CO}_2$ . Thus the extract and precipitated material from the original sample need not be separated. Extraction of vitamin B<sub>12</sub>, folate, and niacin from serum, plasma, or whole blood can be accomplished by autoclaving in sealed 20-mL vials with the assay medium for 3–5 min at 15 psi. After autoclaving, the vials are cooled, inoculated with the appropriate  $^{14}\text{C}$ -labeled compound, the bacterial suspension, and then incubated for 16–20 h at 37°C. The amount of  $^{14}\text{CO}_2$  generated by the test organism is then automatically quantified in an ionization chamber (BACTEC Model 460, shown in Figure 1, or R301), which samples and records the amount of  $^{14}\text{CO}_2$  produced at a rate of one sample per minute. The  $^{14}\text{CO}_2$  is then automatically trapped in an absorbent-filled chamber for safe and easy disposal at a later date.

General principles apply to each of the RMA we have developed and on which we have performed standard quality control tests.



**Figure 1.** BACTEC model 460; an automated ionization chamber, which samples and records the amount of  $^{14}\text{CO}_2$  produced at a rate of one sample per minute.

1. A microorganism (species of *Lactobacillus*) whose growth was known to be proportional to the amount of each specific nutrient to be assayed was chosen. This organism had already been well characterized and was readily available from the American Type Culture Collection.
2. Assay media that had been characterized as ideal for the growth of that particular strain and that could also be obtained lacking a specific nutrient were commercially available.
3. It was then necessary for us to undertake a lengthy search in each instance to identify the ideal <sup>14</sup>C-labeled compound that would be metabolized to <sup>14</sup>CO<sub>2</sub> during growth of the organism with direct proportionality to the amount of the essential nutrient added.

### *Radiometric Microbiological Assay for Vitamin B<sub>12</sub>*

To search for the potential <sup>14</sup>C-labeled substrate, several <sup>14</sup>C compounds that were known to be metabolized by the microorganism were tested in the presence and absence of the essential nutrient in question. For the vitamin B<sub>12</sub>, we found that in the presence of guanido-<sup>14</sup>C-arginine and cyanocobalamin (CN—Cbl) (27) *Lactobacillus leichmannii* produced the most significant amount of <sup>14</sup>CO<sub>2</sub> within 16 h (Table II). Not every <sup>14</sup>C-labeled compound tested was metabolized to <sup>14</sup>CO<sub>2</sub> by *L. leichmannii*. On the other hand, U-<sup>14</sup>C and 1-<sup>14</sup>C glucose were metabolized even in the absence of CN—Cbl (Table II).

A typical dose-response curve for CN—Cbl is shown in Figure 2. The amount of <sup>14</sup>CO<sub>2</sub> produced was found to be proportional to the amount of CN—Cbl present, from 10–100 pg.

Arginine is one of the amino acids essential for growth of this organism. The guanido carbon of arginine provides the basic structures of carbamyl phosphate (28). The latter compound is involved in two major pathways: pyrimidine biosynthesis; and the production of ATP through the arginine dihydrolase pathway, in which carbamyl phosphate is coupled to ADP, producing CO<sub>2</sub>, ATP, and NH<sub>3</sub> (29). The <sup>14</sup>CO<sub>2</sub> that we are measuring from guanido-<sup>14</sup>C-arginine is probably evolved through this latter pathway. In the presence of vitamin B<sub>12</sub>, the actively growing *L. leichmannii* utilizes its supply of carbamyl phosphate for the more rapid biosynthesis of both pyrimidines and ATP.

Next, we compared this RMA to the standard microbiological method for measuring the vitamin B<sub>12</sub> levels on 48 serum samples. We obtained a very good correlation between the two methods ( $r = 0.98$ ) over the entire range of CN—Cbl tested (65–1530 pg/mL), as shown in Figure 3.

The recovery of added CN—Cbl to serum samples was examined using this new RMA. One volume of aqueous solution containing 100–

Table II. Production of  $^{14}\text{CO}_2$  by *L. leichmannii* in the Presence and Absence of CN—Cbl (25)

Substrate	Radio-activity Added ( $\mu\text{Ci}$ )	$^{14}\text{CO}_2$ Pro-duction Control	(Meta-bolic Index Units) <sup>a</sup> 200 pg CN—Cbl Added <sup>b</sup>	Net $^{14}\text{CO}_2$ Production in Presence of Added CN—Cbl (Metabolic Index Units)
D-(U- $^{14}\text{C}$ )-glucose	5	400	459	59
D-(1- $^{14}\text{C}$ )-glucose	1	305	350	45
(2- $^{14}\text{C}$ )-propionate	1	0	0	0
DL-(1- $^{14}\text{C}$ )-ornithine	1	0	7	7
(1,5- $^{14}\text{C}$ )-citric acid monohydrate	1	0	0	0
(1- $^{14}\text{C}$ )-acetate	1	0	0	0
(1- $^{14}\text{C}$ )-glutamic acid	1	0	0	0
(U- $^{14}\text{C}$ )-glycine	1	0	0	0
L-(U- $^{14}\text{C}$ )-arginine	1	0	900	900
L-(guanido- $^{14}\text{C}$ )-arginine	1	0	2080	2080
L-(U- $^{14}\text{C}$ )-histidine	1	0	0	0
L-(U- $^{14}\text{C}$ )-valine	1	0	0	0
L-(U- $^{14}\text{C}$ )-aspartic acid	1	0	0	0
L-(U- $^{14}\text{C}$ )-isoleucine	1	0	0	0
$^{14}\text{C}$ -formate	1	220	230	10

<sup>a</sup> 100 metabolic index units is equivalent to 0.031  $\mu\text{Ci}$  of  $^{14}\text{CO}_2$ .

<sup>b</sup> 100 pg CN—Cbl added for  $^{14}\text{C}$ -labeled glucose.

Journal of Nuclear Medicine

500 pg amounts of CN—Cbl was added to nine volumes of serum. The mixture was vortexed and allowed to stand at room temperature for 10–15 min before assay. Triplicate or quadruplicate vials were used for each determination. The mean percent recovery on seven different sera was  $-0.17 \pm 5.6\%$  (1 SD) (Table III). The reproducibility of this assay was evaluated by assaying three different sera on seven different occasions over a period of several months. The coefficient of variation of the vitamin  $\text{B}_{12}$  ranged from 6.8%–18.7% (Table IV).

There is a very real need for a simple assay for vitamin  $\text{B}_{12}$  analysis of food. Since colored, turbid, or precipitated debris do not interfere with this RMA, we were hopeful that it might prove applicable to this problem and undertook an evaluation of this technique for food analysis (30). Comparison of 22 foods of varying matrices that were high, moderate, and low in vitamin  $\text{B}_{12}$  levels (egg yolk, whole milk, nonfat dry milk, canned salmon, canned sardines, canned tuna, fresh rockfish, chicken, pork, veal, beef sirloin, lamb, ground beef, liverwurst, oatmeal, and various baby foods) by the RMA and the TMA gave an excellent

correlation ( $r = 0.988$ ) (Figure 4). Values obtained by the RMA compared well with published values.

Reproducibility of the RMA for vitamin B<sub>12</sub> in food was studied using a powdered nonfat dry milk and three different baby foods; each was analyzed in duplicate or triplicate five to seven times within a period of two months. As shown in Table V, the variance between repeated assays was small. Furthermore, the reproducibility of results obtained when different subsamples of the same lot were assayed was satisfactory (Table VI).

Recovery studies done using different baby foods as the food matrix gave a mean recovery of  $106.0 \pm 8.8\%$  (1 SD) with a range of 95.0% to 115.0% from five foods of animal origin and a mean recovery of  $66.3 \pm 2.1\%$  (1 SD) with a range of 63.6% to 68.6% from four foods of vegetable or grain origin. The poor recovery obtained from the latter

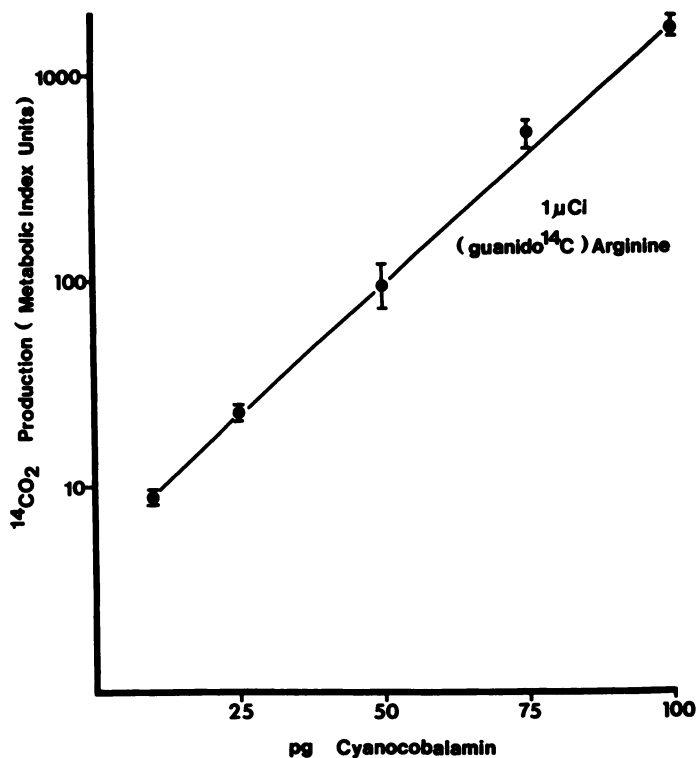
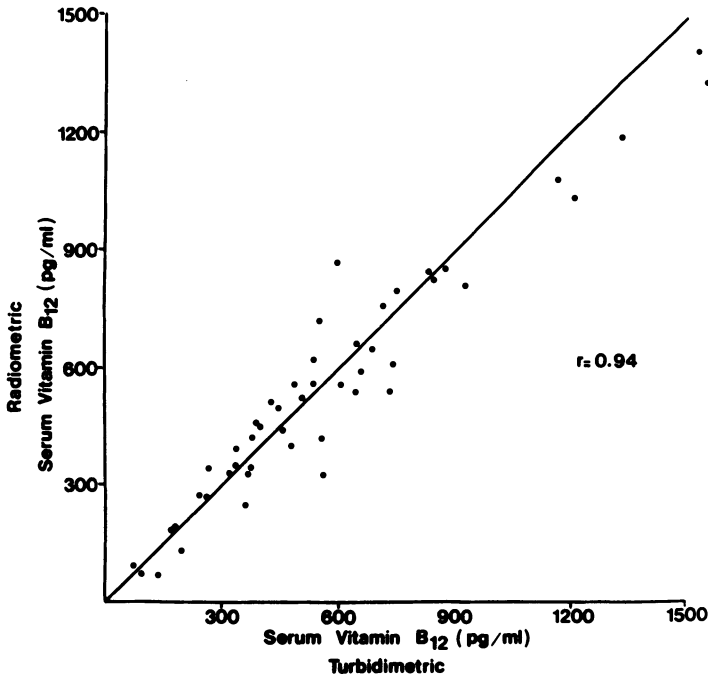


Figure 2. Response of *L. leichmannii* to increasing concentration of cyanocobalamin in the presence of  $1 \mu\text{Ci}$  guanido-<sup>14</sup>C-arginine; incubation time, 16 h. Each point represents the mean and 1 SD of five experiments, each in duplicate.



Journal of Nuclear Medicine

Figure 3. Comparison of 48 serum vitamin B<sub>12</sub> levels assayed by L. leichmannii radiometric procedure and turbidimetric procedure. Line drawn through origin represents line of identity for two results on the same serum (25).

Table III. Radiometric Microbiological Method: The Recovery of Added Vitamin B<sub>12</sub> from Serum

Serum Number	Initial B <sub>12</sub> Concentration (pg/mL)	B <sub>12</sub> Added (pg/mL)	Final B <sub>12</sub> Concentration (pg/mL) Mean ± SD	Recovery (%)
1	358	400	793 ± 46	104.6
2	563	400	965 ± 37	100.2
3	597	500	1150 ± 4	104.8
4	680	500	1150 ± 1	97.5
5	503	500	1040 ± 10	103.7
6	212	300	558 ± 4	109.0
7	166	100	245 ± 3	92.1
Mean Recovery			101.7 ± 5.6% (1 SD)	

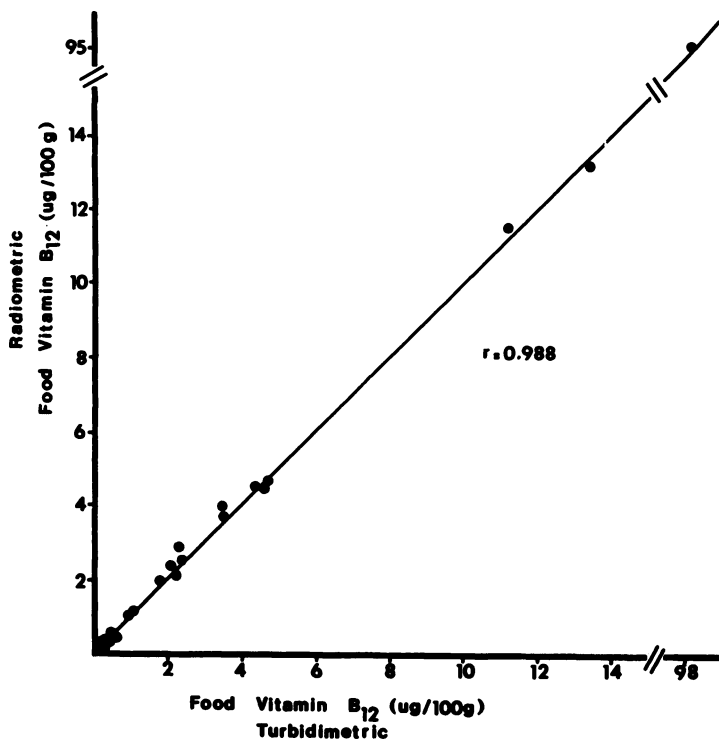


Figure 4. Comparison of the vitamin B<sub>12</sub> content of 22 varieties of food by the radiometric and turbidimetric microbiological assays; correlation coefficient,  $r = 0.988$ . Foods include various milks, baby food, fish, poultry, meat, and cereal. Each point represents the mean of five experiments.

Table IV. Radiometric Microbiological Assay: Reproducibility of Serum Vitamin B<sub>12</sub> Levels (pg/mL)

	Sample I	Sample II	Sample III
	333	745	355
	327	733	395
	313	785	357
	230	860	435
	263	809	390
	205	751	343
	242	865	363
Mean $\pm$ 1 SD	273 $\pm$ 51	792.6 $\pm$ 54	376.9 $\pm$ 32
C.V.	18.7	6.8	8.5



**Table VI. Radiometric**

<i>Food</i>	<i>Vitamin B<sub>12</sub> Content (<math>\mu\text{g}/100\text{ g}</math>) Samples of Same Lot Number</i>
	<i>No. 1</i>
Nonfat powdered milk	4.2300 $\pm$ 0.390
Evaporated milk	0.2980 $\pm$ 0.050
Beef, strained	1.6300 $\pm$ 0.450
Chicken, strained	0.9700 $\pm$ 0.190
Egg yolks, strained	2.2700 $\pm$ 0.080
Cereal and egg yolk	0.2030 $\pm$ 0.016
Oatmeal with applesauce and banana	0.0069 $\pm$ 0.003
Rice with applesauce and banana	0.0
Plums with tapioca	0.0

may be due either to the presence of some factor(s) that may bind the vitamin B<sub>12</sub> or to the presence of ascorbic acid added to the baby food. Ascorbic acid has been shown to destroy vitamin B<sub>12</sub> in food (31, 32).

#### *Radiometric Microbiologic Assay for Folate*

For the determination of the folate levels of plasma or whole blood, *Lactobacillus casei* is the microorganism that has been most widely used. This organism utilizes the widest spectrum of folates for growth; these include the mono-, di-, and triglutamates of pteroylglutamic acid and reduced derivatives.

**Table V. Radiometric Microbiological Assay: Reproducibility  
Study of Vitamin B<sub>12</sub> Content in Food (30)**

<i>Assay Number</i>	<i>Sample I: Milk (Powdered)*</i>	<i>Sample II: Beef (Strained)<sup>b</sup></i>	<i>Sample III: Oatmeal (Strained)<sup>b</sup></i>	<i>Sample IV: Chicken (Strained)<sup>b</sup></i>
1	4.15	1.525	0.01125	1.235
2	4.25	1.325	0.006	1.30
3	3.53	1.340	0.006	1.14
4	4.50	1.265	0.006	1.125
5	4.57	1.215	0.013	0.775
6	—	1.9375	0.0135	0.70
7	—	—	—	0.825
Mean $\pm$ SD	3.79 $\pm$ 0.35	1.43 $\pm$ 0.27	0.0093 $\pm$ 0.004	0.956 $\pm$ 0.28

\* Data given as  $\mu\text{g}/3.2\text{ oz. package}$ .

<sup>b</sup> Data given as  $\mu\text{g}/\text{jar}$ .

National Bureau of Standards

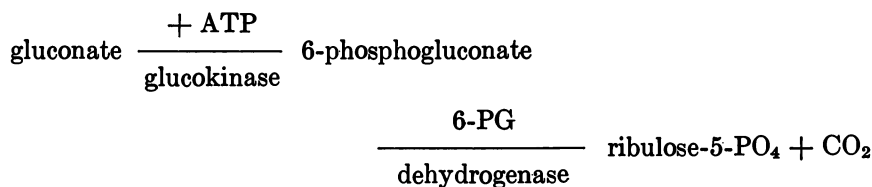
## Microbiological Assay (30)

Vitamin B <sub>12</sub> Content ( $\mu\text{g}/100\text{ g}$ ) Samples of Same Lot Number				Total Subsamples
No. 2	No. 3	No. 4	No. 5	
4.7000 $\pm$ 0.460	4.600 $\pm$ 0.540	4.80 $\pm$ 1.20	—	19
0.2960 $\pm$ 0.020	—	—	—	7
1.4400 $\pm$ 0.270	—	—	—	12
0.9600 $\pm$ 0.280	0.8800 $\pm$ 0.260	—	—	20
2.5900 $\pm$ 0.850	2.6900 $\pm$ 0.420	2.28 $\pm$ 0.55	2.05 $\pm$ 0.57	17
0.2100 $\pm$ 0.030	0.1930 $\pm$ 0.016	—	—	11
0.0069 $\pm$ 0.004	0.0069 $\pm$ 0.003	—	—	16
0.0	0.0	—	—	9
0.0	0.0	—	—	9

National Bureau of Standards

Guanido-<sup>14</sup>C-arginine was the first radiolabeled compound tested for the development of the radiometric assay for folate. *L. casei* was found not to produce <sup>14</sup>CO<sub>2</sub> from the labeled arginine in the presence of folic acid (PteGlu). We therefore had to identify another radiolabeled compound whose metabolism to <sup>14</sup>CO<sub>2</sub> during growth of this organism was proportional to the amount of folic acid added. After trying numerous substrates (Table VII), we found that in the presence of 1-<sup>14</sup>C-gluconate and PteGlu *L. casei* yielded <sup>14</sup>CO<sub>2</sub> in proportion to the amount of folic acid present, from 0.1 ng–1.2 ng of PteGlu. This organism was found to respond equally to both the nonreduced (PteGlu) and the reduced form of folate, 5-methyltetrahydrofolate (5-methyl-H<sub>4</sub>PteGlu), in equimolar concentrations (Figure 5).

The metabolism of gluconate by *L. casei* has been shown by Buyze et al. (33) to be via the hexosemonophosphate shunt. *L. casei* was found to possess the enzyme 6-phosphogluconate dehydrogenase (6-PG); when this organism was grown with gluconate as the sole carbon source, the compound was metabolized through this pathway with the release of CO<sub>2</sub>.



This pathway has been shown to exist also in other microorganisms (34, 35, 36).

Table VII. Production of  $^{14}\text{CO}_2$  by *L. casei* in the Presence and Absence of PGA (26)

Substrate	Radio-activity Added ( $\mu\text{Ci}$ )	$^{14}\text{CO}_2$ Production (Metabolic Index Units) <sup>a</sup>		Net $^{14}\text{CO}_2$ Production (Metabolic Index Units)
		0 ng PGA	1 ng PGA	
L-(U- $^{14}\text{C}$ )-arginine	1	2	2	0
L-(guanido- $^{14}\text{C}$ )-arginine	1	0	0	0
(L- $^{14}\text{C}$ )-glycine	1	0	2	2
L-(U- $^{14}\text{C}$ )-histidine	1	2	4	2
DL-(carboxyl- $^{14}\text{C}$ )-histidine	1	0	0	0
L-(U- $^{14}\text{C}$ )-valine	1	2	2	0
(2- $^{14}\text{C}$ )-propionate	1	0	1	1
L-(U- $^{14}\text{C}$ )-glutamic acid	1	0	0	0
L-(U- $^{14}\text{C}$ )-isoleucine	1	0	0	0
L-(U- $^{14}\text{C}$ )-aspartic acid	1	0	0	0
L-(U- $^{14}\text{C}$ )-malic acid	1	16	30	14
(1,5- $^{14}\text{C}$ )-citric acid	1	10	15	5
(U- $^{14}\text{C}$ )-glycerol	1	0	0	0
D-(1- $^{14}\text{C}$ )-glucose	2	0	47	47
D-(U- $^{14}\text{C}$ )-gluconate	1	8	60	52
D-(1- $^{14}\text{C}$ )-gluconate	1	0	234	234

<sup>a</sup> 100 Metabolic index units are equivalent to 0.031  $\mu\text{Ci}$  of  $^{14}\text{CO}_2$ .

Journal of Nuclear Medicine

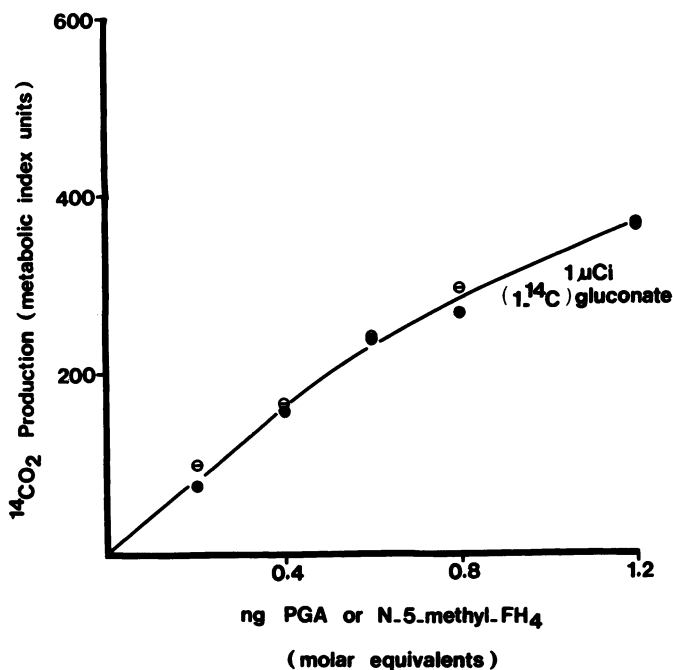
The importance of red cell folate determinations in certain diagnoses of folate deficiency has been clearly established. Erythrocyte folate levels are good indicators of tissue folate stores, whereas serum folate levels are poor indicators since they reflect recent dietary intake and often provide little useful clinical information (37-34). For example, serum folate levels fall promptly after transient periods of dietary deprivation and remain abnormally low for weeks or months before red cell folate levels fall. In contrast, the fall in red cell folate immediately precedes the clinical and hematologic manifestation of folate deficiency (42).

To determine erythrocyte folate levels by the RMA, one volume of heparinized blood was hemolyzed in nine volumes of deionized water. An equal volume of 0.05M phosphate buffer, pH 6.1, containing 200 mg % of ascorbic acid was added to the hemolyzed blood. Since erythrocyte folate is mainly reduced polyglutamates, this hemolysate was incubated at 37°C for 20-30 min in order for plasma conjugase to reduce the glutamic acid residues to the extent necessary for their utilization by *L. casei* (44). After incubation, the hemolysate was further diluted and assayed as described (26).

When the red cell folate levels from 57 normal volunteers were determined by both the radiometric and the standard microbiological methods, the values obtained had a correlation coefficient of  $r = 0.98$  (Figure 6). The mean red cell folate value obtained by the RMA was 270.0 ng/mL with a range of 149.4–769.2 ng/mL, using 5-methyl-H<sub>4</sub>PteGlu as the standard. By the turbidimetric assay, the mean red cell folate value was 281.7 ng/mL with a range of 142.7–707.1 ng/mL.

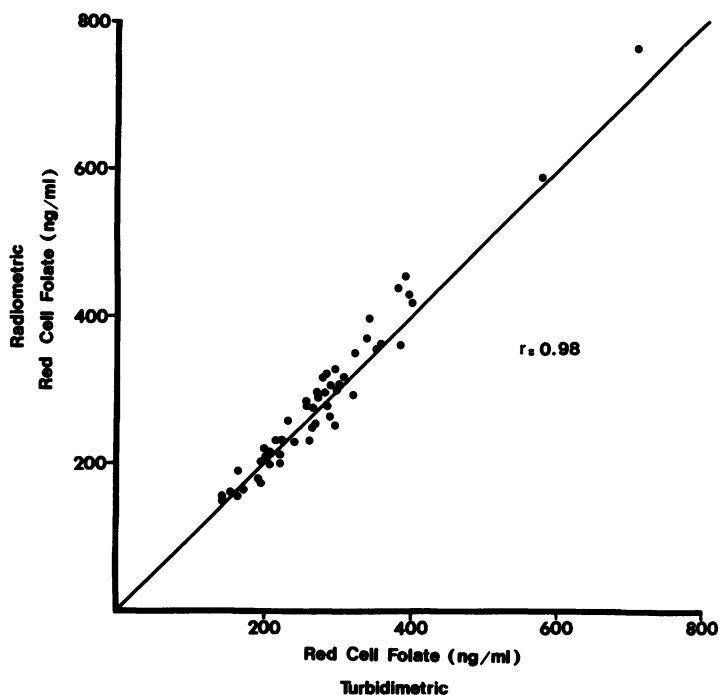
To evaluate the accuracy of the RMA for folate, both the reproducibility and the recovery of this assay were determined. For the reproducibility study, four hemolysates were assayed eight to ten times over a period of six months, and the coefficients of variation were 8.6%, 12.9%, 11.5%, and 8.5% (Table VIII).

Recovery studies were performed by adding 5 ng of 5-methyl-H<sub>4</sub>PteGlu to seven plasma samples, and 50 ng and 100 ng of 5-methyl-H<sub>4</sub>PteGlu to seven hemolysates (Table IX). The mean percent recovery for the seven plasma samples was  $102.7 \pm 8.7\%$  (1 SD). The mean percent



Journal of Nuclear Medicine

Figure 5. Response of *L. casei* to (⊖) PGA and (●) 5-methyl-H<sub>4</sub>PteGlu on equimolar basis in the presence of 1 μCi of D-(1-<sup>14</sup>C) gluconate; incubation time, 16–17 h. Each point represents the mean of triplicate determinations (26).



Journal of Nuclear Medicine

Figure 6. Comparison of 57 hemolysate samples assayed by the radiometric and turbidimetric procedures using *L. casei*; correlation coefficient,  $r = 0.98$ . Each point represents mean of duplicate determinations. Line of identity is drawn in (26).

Table VIII. Radiometric Microbiological Assay Reproducibility of Erythrocytic Folate Levels (26)

Assay	Folate (ng/mL)			
	Sample I	Sample II	Sample III	Sample IV
1	217.7	76.9	226.1	200.0
2	232.9	92.3	261.1	181.7
3	201.5	67.1	263.1	170.4
4	234.8	72.1	223.5	195.4
5	227.5	70.4	223.5	188.1
6	206.1	62.3	189.6	172.1
7	194.9	71.0	210.6	180.6
8	185.4	83.8	193.4	188.8
9	—	—	218.4 <sup>r</sup>	223.3
10	—	—	—	171.5
Mean $\pm$ 1 SD	219.6 $\pm$ 18.4	74.5 $\pm$ 9.6	223.3 $\pm$ 25.6	187.2 $\pm$ 16.2
C.V. (%)	8.6%	12.9%	11.5%	8.5%

Journal of Nuclear Medicine

Table IX. Recovery of N-5-Methyl-FH<sub>4</sub> Added to Plasma and Hemolysates (26)

Sample Number	Percent Recovery		
	Plasma	Hemolysate	
	5 ng	50 ng	100 ng
1	102.5	92.1	112.6
2	110.8	103.0	110.2
3	110.8	116.3	102.8
4	86.2	119.7	108.2
5	99.2	126.7	104.6
6	109.0	92.4	100.1
7	100.5	102.8	103.3
Mean ± 1 SD	102.7 ± 8.7	107.5 ± 13.5	106.0 ± 4.5

Journal of Nuclear Medicine

recovery for the hemolysates was  $107.5 \pm 13.5\%$  (1 SD) when 50 ng was added, and  $106.0 \pm 4.5\%$  (1 SD) when 100 ng was added.

There is an urgent need for a simple assay for measuring the folacin level in food. To date, we have successfully determined various levels of folacin content in different types of food (45). The folacin levels obtained by the RMA compared well with the TMA. Recovery studies performed with added folate (PteGlu) were excellent.

Further simplifications and a significant reduction of the time required for these radiometric microbiological techniques can be achieved by lyophilization of the test organisms. *Lactobacillus* has been successfully lyophilized for use in other microbiological assays (46, 47, 48). Lyophilization eliminates the need for much of the routine maintenance of the organism (Table X). On the day of the assay the lyophilized culture can be simply resuspended, diluted, and inoculated into the assay vials. Comparison of the lyophilized culture with the standard culture of *L. leichmannii* on 20 serum samples by the RMA gave a correlation of 0.98 (Figure 7). Comparison of the lyophilized culture with the standard culture of *L. casei* on 26 hemolysates by the RMA gave a correlation of 0.94 (Figure 8).

#### Radiometric Microbiological Assay for Niacin

The microbiological method using *Lactobacillus plantarum*, originally described by Snell and Wright (49), has been widely used for the determination of niacin in urine, serum, blood, foods, and tissues (16, 48, 50, 51, 52). This organism is able to detect minute amounts of niacin (1–30 ng/mL) using a turbidimetric or titrimetric assay.

Table X. Lyophilization as Method

*Standard Technique*

Stock cultures of *Lactobacillus casei* are kept as stab inoculum in microassay culture agar. These are subcultured monthly in microassay culture agar.



Prior to day of assay, subculture into microinoculum broth and grow for 16–18 h at 37°C.



On morning of assay, subculture from 16-h grow to fresh microinoculum broth. Grow for 6–7 h at 37°C.



Centrifuge bacteria. Wash three times with assay medium. →



Resuspend, dilute, and inoculate assay tubes or vials.

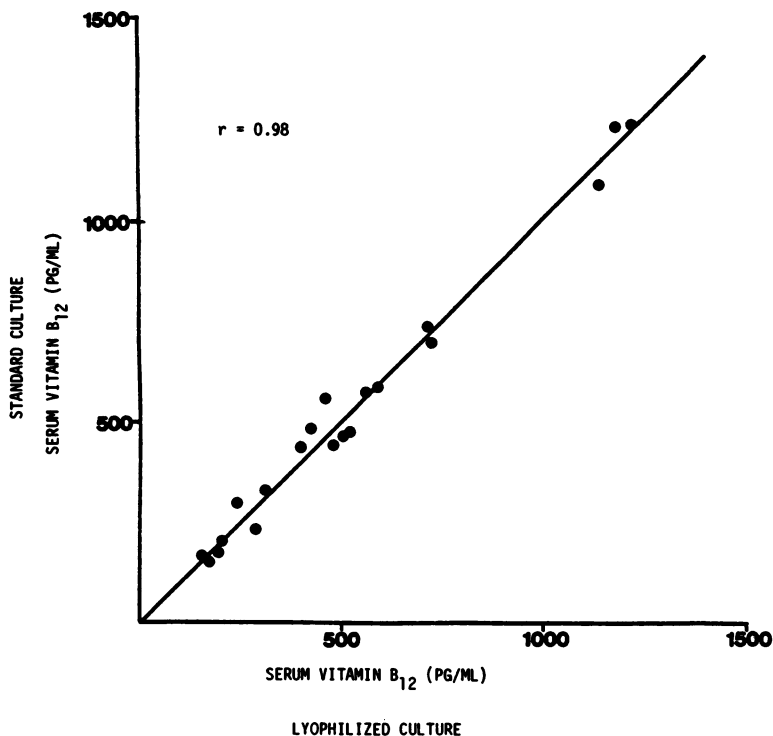


Figure 7. Comparison of 20 serum samples assayed by the RMA using standard and lyophilized cultures of *L. leichmannii*; correlation coefficient,  $r = 0.98$ . Each point represents mean of duplicate determinations. Line of identity is drawn in.

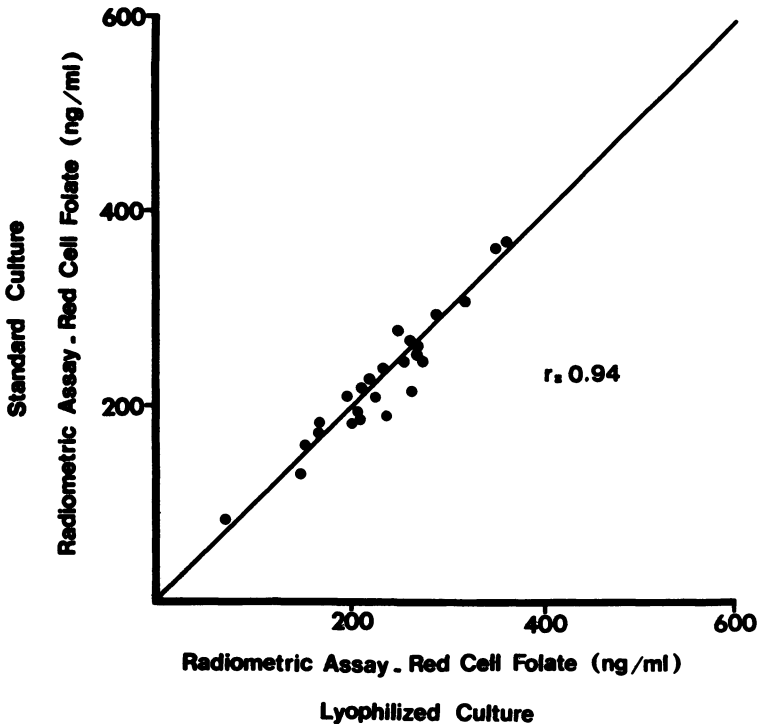
of Shortening Assay Time (26)

*Lyophilization Technique*

Lyophilize bacteria and seal the ampoules. Store at 4°C.

On day of assay, break open ampoule, resuspend, dilute, and immediately inoculate assay vials.

Journal of Nuclear Medicine



Journal of Nuclear Medicine

Figure 8. Comparison of 26 hemolysate samples assayed by the RMA using standard and lyophilized cultures of *L. casei*; correlation coefficient,  $r = 0.94$ . Each point represents mean of duplicate determinations. Line of identity is drawn in (26).



Table XI. Production of  $^{14}\text{CO}_2$  by *Plantarum* in the Presence and Absence of Nicotinic Acid (19)

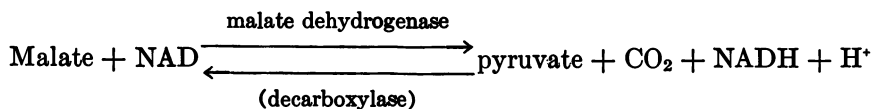
Substrate <sup>b</sup>	$^{14}\text{CO}_2$ Production (Metabolic Index Units) <sup>a</sup>		Net $^{14}\text{CO}_2$ Production (Metabolic Index Units)
	Nicotinic Acid ( $\mu\text{g}$ )		
	0	0.5	
L-(U- $^{14}\text{C}$ )-histidine	0	2	2
L-(U- $^{14}\text{C}$ )-isoleucine	0	0	0
( $^{14}\text{C}$ )-formate	0	22	22
L-(U- $^{14}\text{C}$ )-arginine	0	0	0
L-(guanido- $^{14}\text{C}$ )-arginine	0	0	0
D-(U- $^{14}\text{C}$ )-glucose	65	82	17
(1- $^{14}\text{C}$ )-glycine	0	2	2
L-(U- $^{14}\text{C}$ )-glutamic acid	0	0	0
L-(U- $^{14}\text{C}$ )-aspartic acid	0	5	5
L-(U- $^{14}\text{C}$ )-valine	0	0	0
DL-(1- $^{14}\text{C}$ )-ornithine	0	0	0
L-(U- $^{14}\text{C}$ )-malic acid	0	268	268

<sup>a</sup> Expressed in metabolic index units (miu) where 100 miu are equivalent to 0.031  $\mu\text{Ci}$  of  $^{14}\text{CO}_2$ .

<sup>b</sup> 2  $\mu\text{Ci}$  radioactivity (0.2 mL).

Journal of Nuclear Medicine

To extend the radiometric microbiological methodology to niacin, we first sought an appropriate  $^{14}\text{C}$ -labeled substrate (Table XI). After considerable effort we were able to identify that the evolution of  $^{14}\text{CO}_2$  from U- $^{14}\text{C}$  malate by *L. plantarum* was proportional to the amount of niacin present in the assay medium (Figure 9). This organism is known to be able to convert malate to pyruvate through the following reaction (53):



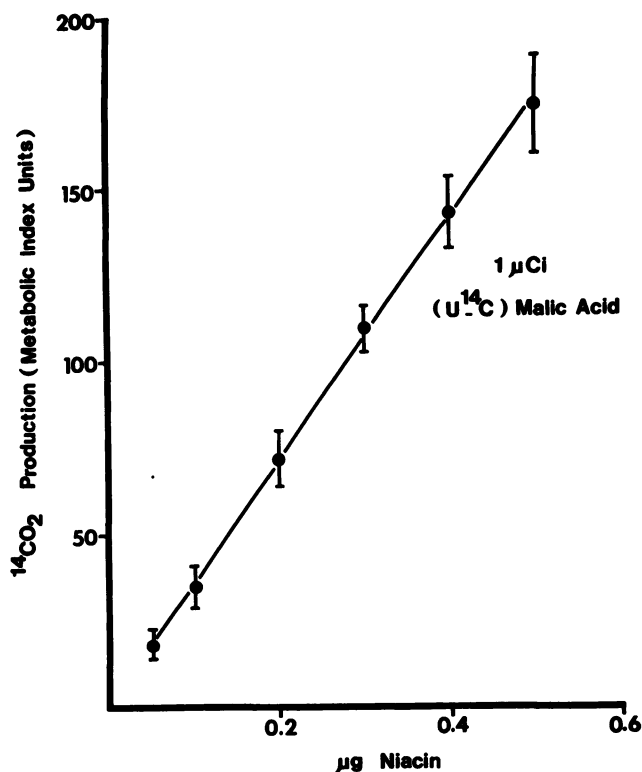
Presumably the  $^{14}\text{CO}_2$  evolved from U- $^{14}\text{C}$  malate by *L. plantarum* in this assay is coming from this "niacin" coenzyme-dependent pathway.

In human beings niacin is rapidly converted to its biologically active forms: NAD, NADP, NADH, and NADPH. To test the validity of using niacin as our standard, we assayed the response of *L. plantarum* to those five forms in equimolar concentration (Figure 10). The difference in the  $^{14}\text{CO}_2$  output was not statistically significant ( $p \leq 0.05$ ), and we concluded that niacin was a valid indicator of the biologically active forms of this vitamin.

The specificity of the NAD-dependent malate dehydrogenase (decarboxylase) as used in this radiometric assay was evaluated using

nicotinic acid and nicotinamide (biologically active in humans) and the following two chemically very similar structures and two metabolites of niacin: trigonelline and nicotinuric acid, and *N*'-methylnicotinamide and 2-pyridone, all of which are known to be biologically inactive in humans (5, 54). When these compounds were assayed on a molar basis by the standard microbiological method that measures turbidity as cell growth, they supported the growth of *L. plantarum* (Figure 11). When these compounds were assayed by the RMA, there was no <sup>14</sup>CO<sub>2</sub> output from the same organism except in the case of nicotinuric acid, which produced less than 10% of the amount of <sup>14</sup>CO<sub>2</sub> at the highest concentration tested. These experiments seem to indicate an increased specificity of the niacin-dependent step for the biologically active forms of niacin with the radiometric assay.

Like the RMA for vitamin B<sub>12</sub> and folate, the RMA for niacin also gave good reproducibility and recovery studies. Since the ratio of niacin



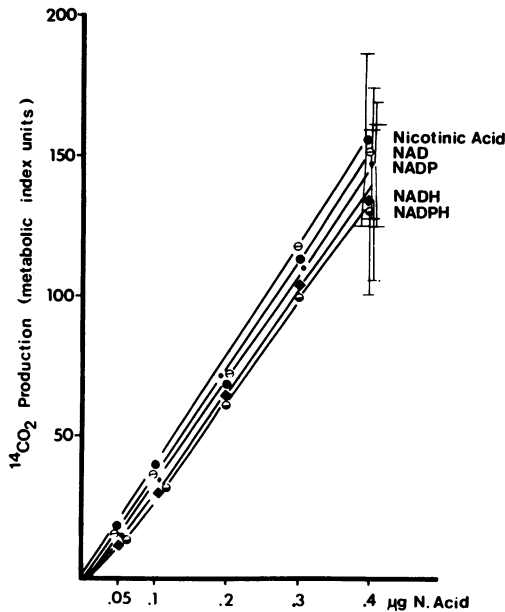
Journal of Nuclear Medicine

Figure 9. Response of *L. plantarum* to increasing concentration of nicotinic acid in the presence of 1 µCi of L-(U-<sup>14</sup>C) malate; incubation time, 19–20 h. Each point represents the mean and 1 SD of five experiments, each in triplicate (19).

level in whole blood to that of serum is 100:1, we elected to assay the niacin levels in red cells (55, 56, 57). A good correlation between this technique and the standard turbidimetric assay on 30 normal hemolysates were obtained with a correlation coefficient  $r = 0.91$ .

### Conclusion

The RMA have been shown to be simple, sensitive, and specific for the measurement of vitamin B<sub>12</sub>, folate, and niacin in the blood and for the measurement of vitamin B<sub>12</sub> and folate in food. Further work will be carried out for the measurement of niacin in food. For the determination of the biologically active forms of niacin, the RMA is more specific than the TMA. The RMA is also more specific than the CPBA for the measurement of vitamin B<sub>12</sub>. The advantages of the RMA over the TMA are: (i) it is sensitive and simple; (ii) the colored or turbid materials do not interfere with the assay; (iii) only small amounts of material are required; and most important, (iv) RMA combines the biological specificity of the microorganisms with the precision of measuring radioactive decay as the endpoint.



Journal of Nuclear Medicine

**Figure 10.** Comparison of biologically active forms of niacin in equimolar amounts. Shown are mean and 1 SD for three experiments, each in duplicate. Biologically active forms were compared with nicotinic acid, and no difference was significant at  $p \leq 0.05$  (19).

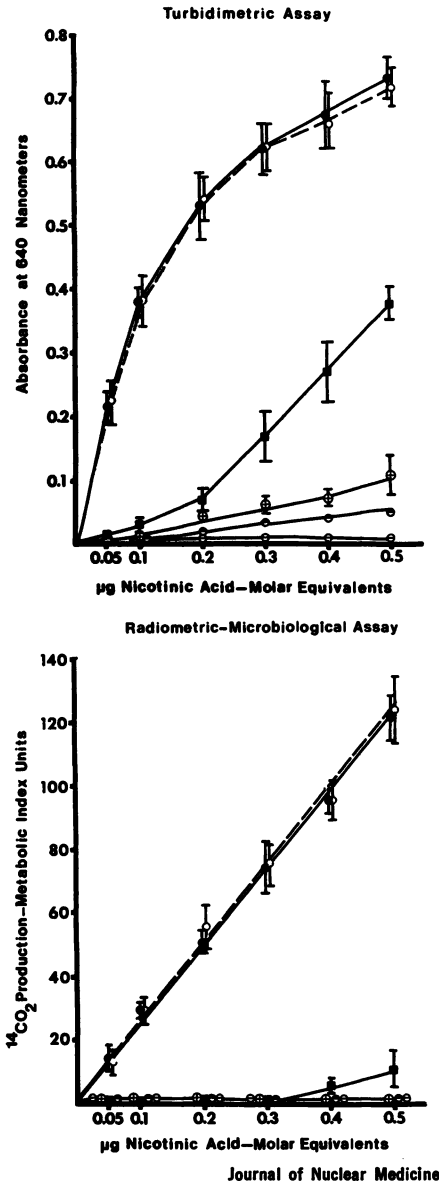


Figure 11. Response of *L. plantarum* to (●—●) nicotinic acid, (○—○) nicotinamide, (■—■) nicotinic acid, (⊕—⊕) trigonelline, (●—●) N'-methylnicotinamide, and (⊖—⊖) 2-pyridone on a molar basis (in the presence of 1  $\mu\text{Ci}$  L-(U-<sup>14</sup>C) malic acid for radiometric assay). Each point represents mean of six determinations  $\pm$  1 SD. Top graph represents net growth of organism to metabolites added. Bottom graph indicates ability of organism to metabolize the <sup>14</sup>C-substrate to metabolites added (19).

### Acknowledgments

This work was supported by the Science and Education Administration of the U.S. Department of Agriculture under Grant No. 5901-0410-8-0013-0 from the Competitive Research Grants Office, and Contract No. 53-32U4-8-56 from the Human Nutrition Center (Consumer and Food Economics Institute); by a Broad Form Cooperative Research Agreement

No. 12-14-1001-1222 between the Department of Environmental Health Sciences, Division of Radiation Health Sciences, of The Johns Hopkins University School of Hygiene and Public Health, Baltimore, Maryland, and the Nutrient Composition Laboratory of the Nutrition Institute, Beltsville, Maryland; and U.S.P.H.S. Grant GM 10548.

The authors are indebted to Tom Guilarte, Ph.D., for his work on the niacin RMA and TMA specificity studies (Figure 11).

The authors are also indebted to Donna M. Lea for her superb secretarial support.

### Literature Cited

1. Williams, W. J.; Beutler, E.; Erslev, A. J. "Hematology"; Rundles, R. W., Ed.; McGraw-Hill: New York, 1977; pp. 307-362.
2. Goodhart, R. "Modern Nutrition in Health and Disease"; Shills, M. H., Ed.; Lea-Febiger: Philadelphia, 1976; pp. 198-202, 221-244, 535-546.
3. Burton, B. T., Ed. "Human Nutrition"; McGraw-Hill: New York, 1976; pp. 101-126, 260-264.
4. Darby, W. J.; McNutt, P. W.; Todhunter, E. N. *Nutr. Rev.* 1975, 33, 289.
5. Sauberlich, H. E.; Dowdy R. P.; Skala, J. H., Ed. "Laboratory Tests for the Assessment of Nutritional Status"; CRC: Cleveland, 1974; pp. 49-74.
6. Pearson, W. N. *J. Am. Med. Assoc.* 1962, 180, 49.
7. Spivak, J. L.; Jackson, D. L. *Johns Hopkins Med. J.* 1977, 140, 295.
8. Colman, N.; Barber, E. A.; Baker, M.; Green, R.; Metz, J. *Am. J. Clin. Nutr.* 1975, 28, 471.
9. McIntyre, P. A.; Sachs, M. V.; Krevans, J. R.; Conley, C. L. *Arch. Intern. Med.* 1956, 98, 541.
10. Scheid, H. E.; Andrews, M. M.; Schweigert, B. S. *J. Nutr.* 1952, 47, 601.
11. Tappan, D. V.; Lewis, V. J.; Register, U. D.; Elvehjem, D. V. *Arch. Biochem.* 1950, 29, 408.
12. Howard, L.; Wagner, C.; Schenker, S. *J. Nutr.* 1974, 104, 1024.
13. Albanese, A. A., Ed. "Newer Methods of Nutritional Biochemistry"; Academic: New York, 1965; Vol. 2, p. 286.
14. Draft, F. S.; McDaniel, E. G.; Herman, L. G.; Romine, M. K.; Hegner, J. R. *Fed. Proc., Fed. Am. Soc. Exp. Biol.* 1963, 22, 129.
15. György, P., Ed. "Vitamin Methods"; Academic: New York, 1951; Vol. 2, pp. 210-214.
16. György, P.; Pearson, G., Ed. "The Vitamins"; Academic: New York, 1967; Vol. 7, pp. 164-167, 144-156, 243-250, 258-263.
17. Horwitz, W., Ed. "Official Methods of Analysis"; Assoc. Official Anal. Chem.: Washington, D.C., 1975; pp. 839-845.
18. Baker, H. et al. *Clin. Chem.* 1960, 6, 572.
19. Kertcher, J. A.; Guilarte, T. R.; Chen, M. F.; Rider, A. A.; McIntyre, P. A. *J. Nucl. Med.* 1979, 20, 419.
20. Brunink, H.; Wessels, E. J. *Analyst* 1972, 97, 258.
21. Kolhouse, J. F.; Kondo, H.; Allen, N. C.; Podell, E.; Allen, R. H. *N. Engl. J. Med.* 1978, 299, 785.
22. Cooper, B. A.; Whitehead, M. V. *N. Engl. J. Med.* 1978, 299, 816.
23. Buchanan, J. W.; McIntyre, P. A.; Scheffel, U.; Wagner, H. N., Jr. *J. Nucl. Med.* 1977, 18, 394.
24. Brown, E. B., Ed. "Progress in Hematology"; Grune & Stratton: New York, 1977; Vol. 10, p. 361-409.

25. Chen, M. F.; McIntyre, P. A.; Wagner, H. N., Jr. *J. Nucl. Med.* 1977, 18, 388.
26. Chen, M. F.; McIntyre, P. A.; Kertcher, J. A. *J. Nucl. Med.* 1978, 19, 906.
27. Babior, D. M., Ed. "Cobalamin Biochemistry and Pathophysiology"; John Wiley & Sons: New York, 1975; p. 466.
28. Hutson, J. Y.; Downing, M. *J. Bacteriol.* 1968, 96, 1259.
29. Greenberg, D. M., Ed. "Metabolic Pathways"; Academic: New York, 1969; Vol. 3, p. 206.
30. Chen, M.; McIntyre, P. A. *Natl. Bur. Stand., Spec. Publ.* 1979, 519, 257.
31. Herbert, V.; Jacobs, E. *J. Am. Med. Assoc.* 1974, 230, 241.
32. Hogenkamp, H. P. C. *Am. J. Clin. Nutr.* 1980, 33, 1.
33. Buyze, G.; Van Den Hamer, C. J. A., De Haan, P. G. *Antonie van Leeuwenhoek* 1957, 23, 345.
34. Gary, N. D.; Bard, R. C. *J. Bacteriol.* 1952, 64, 501.
35. Cohen, S. S.; Roth, L. *J. Bacteriol.* 1953, 65, 490.
36. Deley, J.; Stouthamer, A. J. *Biochim. Biophys. Acta.* 1959, 34, 171.
37. Rothenberg, S. P.; DaCosta, M., Lawson, J.; Rosenberg, Z. *Blood* 1974, 43, 437.
38. Liu, Y. *Am. J. Clin. Path.* 1974, 63, 688.
39. Hoffbrant, A. V.; Newcombe, B. F. A.; Mollin, D. L. *J. Clin. Path.* 1966, 19, 17.
40. Mincey, E.; Wilcox, E.; Morrison, R. *Clin. Biochem.* 1973, 6, 274.
41. Scheiber, C., Waxman, S. *Br. J. Haematol.* 1974, 27, 551.
42. Herbert, V. *Trans. Assoc. Am. Phys.* 1962, 75, 307.
43. Tisman, G. *N. Engl. J. Med.* 1972, 287, 466.
44. Toennies, G.; Frank, H. G.; Callant, D. L. *J. Biol. Chem.* 1953, 200, 23.
45. Chen, M. F.; Walsh, J. A.; McIntyre, P. A., unpublished data.
46. Volz, F. E.; Gortner, W. A. *Arch. Biochem.* 1948, 17, 141.
47. Nymon, M. C.; Gunsalus, I. C.; Gortner, W. A. *Science* 1945, 102, 125.
48. Gorin, N.; Meulenhoff, E. J. S.; Yarrow, D. *Appl. Microbiol.* 1970, 20, 641.
49. Snell, E. E.; Wright, L. D. *J. Biol. Chem.* 1941, 139, 675.
50. Hutner, S. H.; Cury, A.; Baker, H. *Anal. Chem.* 1958, 30, 849.
51. Barton-Wright, E. C. *Clin. Chem.* 1944, 38, 316.
52. Barton-Wright, E. C. *Analyst* 1972, 97, 300.
53. Nathan, H. A. *J. Gen. Microbiol.* 1961, 25, 415.
54. Baker, H.; Frank, O.; Pasher, I.; Hutner, S. H.; Sobotka, H. *Clin. Chem.* 1960, 6, 572.
55. Burch, H. B.; Storvick, C. A.; Bickness, R. L.; Kung, H. C.; Alejo, L. G.; Everhart, W. A.; Lowry, O. H.; King, C. G.; Bessy, O. A. *J. Biol. Chem.* 1955, 212, 897.
56. Preiss, J.; Handler, P. *J. Biol. Chem.* 1958, 233, 488.
57. *Ibid.*, 493.

RECEIVED September 4, 1980.

# Environmental and Geochemical Applications of Mössbauer Spectroscopy

TAKESHI TOMINAGA

Department of Chemistry, Faculty of Science, The University of Tokyo, Hongo, Tokyo, Japan

*Mössbauer spectroscopy is a useful probe for analyzing chemical states of iron (or tin) and has been used to characterize environmental and geochemical samples and to study the chemical changes occurring in such systems. Recent progress in Mössbauer applications in geochemistry are reviewed with emphasis on characterizing amorphous minerals and environmental samples such as airborne particles, sediments, and archaeological artifacts, and on monitoring chemical processes in the environment such as alteration, weathering, oxidation of minerals, and corrosion of metals. The use of the scattered-electron Mössbauer technique is also discussed.*

While a number of techniques are now available for elementary analyses of environmental and geochemical samples, very few can characterize the chemical states of elements in such systems. However, it is obvious that knowledge of the chemical states rather than the mere contents of particular elements is often indispensable for a complete understanding of their behaviors and roles in the environment or in the mechanisms of environmental and geochemical processes.

Mössbauer spectroscopy is one of the most useful nuclear probes for studying chemical states and has been used successfully in geochemistry to characterize minerals since they commonly contain iron, which is a typical Mössbauer element (1). Very recently, this technique has also been applied to characterizing environmental samples and to monitoring chemical changes occurring in the environment. It is a very promising means for nondestructive characterization of iron-containing environ-

0065-2393/81/0197-0495\$05.00/0  
© 1981 American Chemical Society

mental samples, because it can provide useful information about even poorly crystallized materials or very fine particles to which the x-ray diffraction method cannot be applied.

This chapter will review recent progress in geochemical and environmental applications of Mössbauer spectroscopy with emphasis on characterizing amorphous minerals and environmental samples such as airborne particles and lake and ocean sediments and on monitoring chemical changes in the environment such as alteration and weathering, corrosion, and redox processes. Due to limited space, I have confined myself to discussing only typical works suitable for demonstrating the usefulness of this technique, rather than to providing a nearly complete bibliography.

### *Experimental*

Mössbauer spectroscopy is based on the phenomenon of recoil-free resonant absorption of  $\gamma$  rays by atomic nuclei, and the spectrum reflects the perturbation induced in the nuclear levels due to the interaction of the Mössbauer atom with its chemical environment. The Mössbauer elements, iron and tin, can be used conveniently as in situ probes in environmental and geochemical applications. Since Mössbauer spectroscopy has now become relatively familiar to chemists, I present here only a brief description of typical experimental techniques used in Mössbauer measurements. There are two types of Mössbauer measurements: transmission method and scattering method.

**The Transmission Method.** In transmission measurements finely powdered samples are used as absorbers, with thickness corresponding to 6–7 mg iron/cm<sup>2</sup> or 0.5–0.9 mg tin/cm<sup>2</sup>. For <sup>57</sup>Fe Mössbauer measurements of iron-containing materials, a 10–30 mCi <sup>57</sup>Co source diffused into a copper or rhodium foil is driven electromagnetically by a transducer so that the energy of the emitted  $\gamma$  rays can be altered very slightly by the Doppler effect resulting from the relative motion of the source to absorber. A Ba<sup>119m</sup>SnO<sub>3</sub> source is employed in measurements of tin-containing materials. The transmission (absorption) Mössbauer spectrum is obtained by measuring the transmitted  $\gamma$ -ray intensity as a function of the source velocity, using a Mössbauer spectrometer in conjunction with a multichannel analyzer.

**The Scattering Method.** The Mössbauer scattering spectrum can be obtained by measuring the intensity of  $\gamma$  rays or electrons scattered by Mössbauer atoms as a function of the source velocity. This technique is especially useful for completely nondestructive analysis of samples. In particular, the scattered-electron Mössbauer technique (or conversion-electron Mössbauer technique), in which conversion and Auger electrons from Mössbauer atoms are measured, provides a promising means for studying surface conditions because there are shorter average ranges of the scattered electrons. For example, this technique has been applied to characterize corrosion products on metal surfaces or weathering products on surfaces of rocks and minerals. For scattered-electron Mössbauer measurements we usually count back-scattered electrons from the sample placed inside of a gas-flow proportional counter.

**Mössbauer Parameters.** The parameters derived from the peak positions in the Mössbauer spectrum include isomer shift  $\delta$ , quadrupole splitting  $\Delta E_Q$ , and effective internal magnetic field  $H_i$ . The isomer shift (shift of the centroid



of peak(s) of a component with respect to a standard reference material) and the quadrupole splitting (separation between the two component peaks of a quadrupole doublet) represent the oxidation state and chemical environment of the Mössbauer atom. If the iron atom experiences a magnetic field, a six-line structure (magnetic hyperfine splitting) appears in the Mössbauer spectrum. The effective internal magnetic field can then be estimated from the positions of the magnetically split peaks and can characterize the magnetic iron, such as iron oxides and oxyhydroxides.

The relative abundances of the Mössbauer atoms (e.g., iron) distributed in various chemical states can be determined on the basis of the areas of the corresponding absorption or scattering peaks.

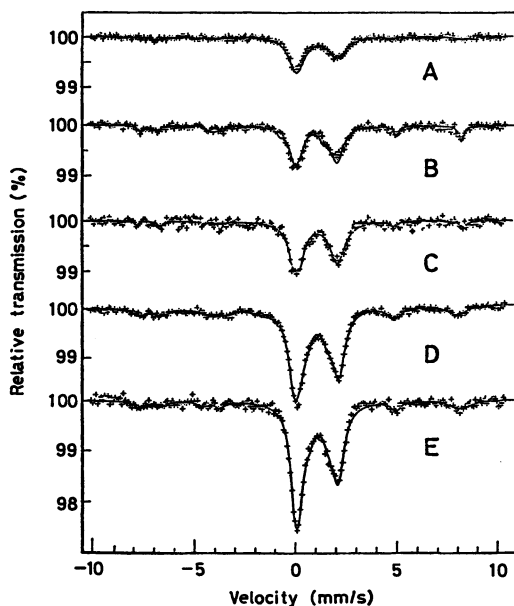
### *Characterization of Environmental and Geochemical Samples*

Mössbauer spectroscopy can provide a variety of useful information regarding the in situ probe atoms (e.g., iron) in geochemical systems (1). Such information includes valence (oxidation state), spin state, coordination number, site symmetry, electric field gradient, and internal magnetic field in minerals. Mössbauer spectra of igneous and metamorphic rocks and soils have been measured to characterize the mineral phases constituting such systems. We can analyze semiquantitatively the total percentage of the Mössbauer elements and the relative abundances in different chemical states or mineral phases. Since iron is the most typical Mössbauer element commonly existing in the earth's crust, most geochemical applications have been limited to iron-containing materials. However, Mössbauer studies with other elements such as  $^{119}\text{Sn}$  and  $^{121}\text{Sb}$  have also been reported recently on tin-containing minerals such as cassiterite, stannite, and stannoidate (2, 3) and on antimony sulfide minerals (4, 5, 6). If the minerals contain magnetically ordered iron, Mössbauer spectra can be used conveniently for detecting and identifying the magnetic phases. The grain-size distribution of ultrafine particles of magnetic minerals can also be determined on the basis of superparamagnetic relaxation observed in the spectra.

I shall not discuss in further detail general applications of Mössbauer spectroscopy in geochemistry since relevant books, review articles, and original papers are available (1, 7, 8, 9, 10). The following sections are devoted to a few selected topics in this field, that is, Mössbauer studies of amorphous minerals and environmental samples.

**Amorphous Minerals.** Mössbauer spectroscopy is useful for studying the structure and bonding of amorphous materials, because it is only sensitive to the configuration of the nearest neighbors and the oxidation states of the probe atoms in those systems (11).

While a number of works have contributed to Mössbauer spectra of synthetic glasses (12–17), only a few studies have been reported on obsidians, which constitute a typical amorphous mineral of terrestrial origin. Although the  $\text{Fe}^{3+}/\text{Fe}^{2+}$  ratios (0.32–0.45) in obsidians from



Gauthier-Villars

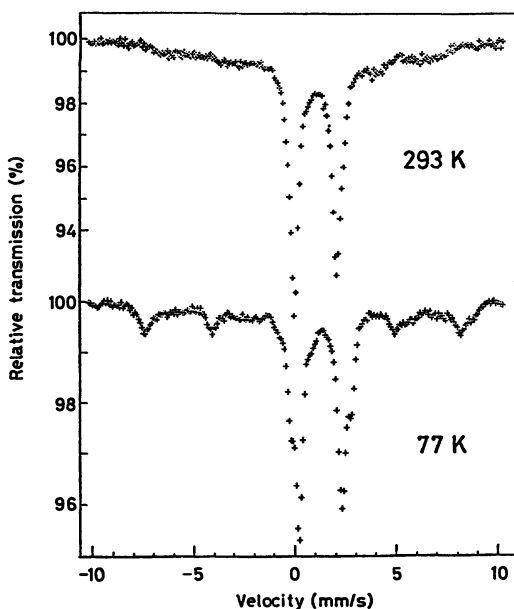
**Figure 1.** Mössbauer spectra of Japanese obsidians at 293 K: (A) Wada pass, Nagano; (B) Arasaki pumice fall deposit, Kagoshima; (C) Mifune, Kagoshima; (D) Hotoke-iwa lava, Asama, Nagano; and (E) Ibusuki, Kagoshima (20)

North America have been estimated by Mössbauer technique (18, 19), no Mössbauer parameters (isomer shift and quadrupole splitting) have been reported to characterize them. We have recently studied Mössbauer spectra of several obsidian samples from different areas in Japan to obtain structural information (20). Such studies of obsidians may also contribute to understanding the structure of molten systems in magma. The Mössbauer spectra are essentially alike regardless of the locality, and they consist of paramagnetic  $\text{Fe}^{2+}$ ,  $\text{Fe}^{3+}$  (center doublet peaks), and magnetic iron (six-line peaks in the background) components with relative peak areas of 60–77%, 0–13%, and 15–40%, respectively (Figure 1). The magnetic component can be identified as magnetite (based on the effective internal magnetic field), which is likely contained as inclusion in the obsidians. The spectrum of the obsidian from Hōei Crater (Mt. Fuji) shows appreciable superparamagnetic relaxation, indicating the presence of extremely fine magnetic particles as small as 60 Å in diameter (Figure 2). The comparison of the Mössbauer parameters of the  $\text{Fe}^{2+}$  ions in the obsidians with those of silicate minerals with known structures suggests that the oxygen environments around the  $\text{Fe}^{2+}$  ions may be similar to those in M(2) sites in pyroxenes (i.e., highly distorted octahedra similar to those of M(2) sites in orthopyroxenes and/or eight-

fold coordination similar to  $M(2)$  sites in clinopyroxenes). Similarity in the  $\text{Fe}^{2+}$  environments has also been observed between the obsidians and synthetic silicate glasses.

Allophane is another amorphous mineral composed mainly of silica, alumina, and water. Natural allophane generally contains iron. Since the atomic configuration of allophane was not known, we have investigated the  $^{57}\text{Fe}$  Mössbauer spectra of synthetic allophane with the varying iron content,  $1.8 \text{ SiO}_2 \cdot (\text{Al}_{1-x}\text{Fe}_x)_2\text{O}_3 \cdot 8\text{H}_2\text{O}$  ( $x = 0-0.15$ ). In this way we were able to acquire structural information regarding the synthetic allophane, which may also reflect the characteristics of natural allophane (21). The Mössbauer spectra at 293 K reveal broad absorption peaks due to magnetic relaxation, which are characterized as octahedral  $\text{Fe}^{3+}$ . The comparison of line width of component peaks of the quadrupole doublet suggests that the  $\text{Fe}^{3+}$  octahedron is possibly elongated along the principal axis.

**Environmental Samples.** Since environmental samples such as airborne particles and sediments originate mainly from constituents of the crust (soils and rocks) and generally contain a high percentage of iron, they can be characterized by  $^{57}\text{Fe}$  Mössbauer spectroscopy. A fairly comprehensive review article has been published recently on iron oxides and hydroxides in soils (22).



Gauthier-Villars

**Figure 2.** Mössbauer spectra of a Japanese obsidian from Hō-ēi crater, Mt. Fuji at 293 K and 77 K (20)

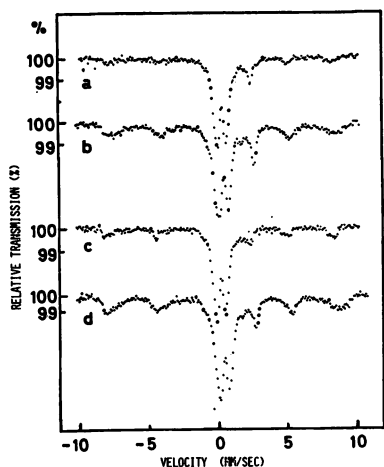


Figure 3. Mössbauer spectra of typical airborne particles collected in Tokyo (urban area) and at Tokai (remote area): (a) Tokai sample measured at 293 K; (b) Tokai, 77 K; and (c) Tokyo, 293 K; (d) Tokyo, 77 K (23)

**AIRBORNE PARTICLES.** The Mössbauer studies of airborne particles from remote, urban, and industrial areas have revealed that the local mineralogical features and the effects of human activities can be recognized by characterizing chemical states of iron (23, 24). The oxidation state of iron in airborne particles is also an important probe for redox processes involving trace materials in the atmosphere.

As is shown in Figure 3, Mössbauer spectra of typical airborne particles collected in Tokyo (urban area) and at Tokai (remote area) indicate the presence of paramagnetic  $\text{Fe}^{2+}$  (iron in common silicate minerals),  $\text{Fe}^{3+}$ , and magnetic components (hematite and magnetite) (23). Since the relative abundances of the magnetic iron components were increased appreciably at the cost of paramagnetic  $\text{Fe}^{3+}$  at lower temperatures (superparamagnetism), ultrafine particles of the iron oxides should be contained in addition to paramagnetic iron hydroxides and oxyhydroxides. Comparison of the samples from these two areas reveals that the urban (Tokyo) sample contains more hematite and less  $\text{Fe}^{2+}$ ; hematite may possibly originate from human activities in the urban area. The relative abundances of the iron components collected at different times of the year showed considerable seasonal variations, suggesting that meteorological factors may also affect the behavior and composition of the airborne particles.

Similar results about the airborne particles collected in urban and remote locations in Europe and the United States have been reported (24). Iron was distributed in paramagnetic  $\text{Fe}^{2+}$ ,  $\text{Fe}^{3+}$ , metallic iron, and iron oxides ( $\text{Fe}_2\text{O}_3$ ,  $\text{Fe}_3\text{O}_4$ ), and their relative abundances were altered remarkably according to the sampling location: samples from remote areas contain paramagnetic  $\text{Fe}^{2+}$  and  $\text{Fe}^{3+}$  alone, whereas urban samples

are rich in iron oxides, and some samples from the industrial areas even contain metallic iron (Figure 4). It is assumed that metallic iron and iron oxides are mainly anthropogenic.

The above assumption has been confirmed by a recent work on automobile pollution. The iron compounds emitted into the atmosphere as exhaust were determined with the Mössbauer technique (25). The Mössbauer spectra of the deposit from the car exhaust revealed that the iron compounds were mainly composed of hematite ( $\alpha\text{-Fe}_2\text{O}_3$ ) in the form of ultrafine particles  $\sim 120$  Å in diameter. In general, we should

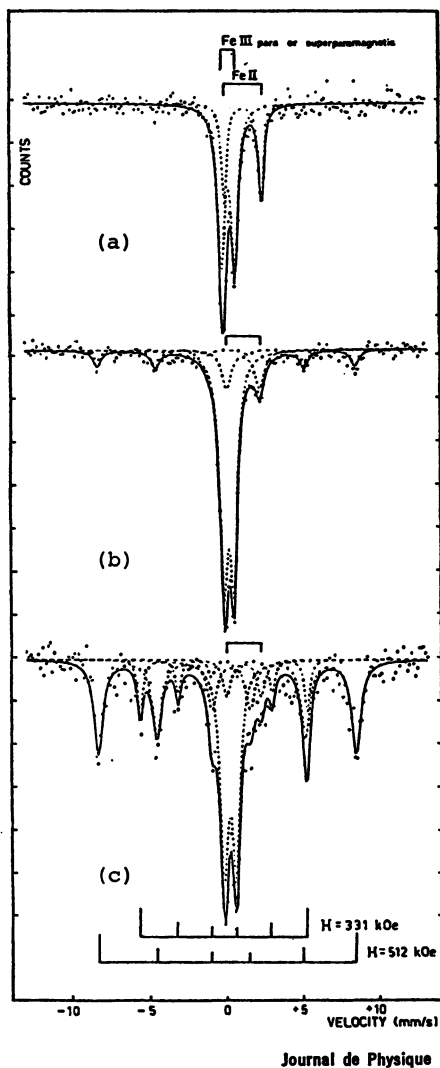
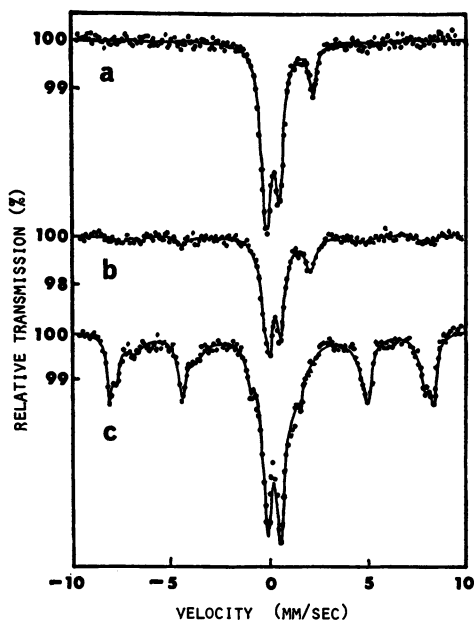


Figure 4. Mössbauer spectra of airborne particles collected at (a) Saint-Malo (remote area); (b) Antwerp (urban area); and (c) La Louvière (industrial area) (24).



Journal de Physique

Figure 5. Mössbauer spectra of sediments at 293 K: (a) Lake Kasumiga-ura (remote area); (b) Pond Sanshiro-ike (urban area); and (c) NBS river sediment (28)

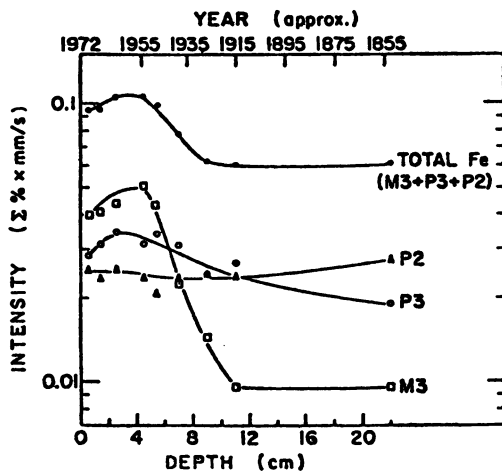
be careful in our evaluation of the sources of iron in the atmosphere, since iron of extraterrestrial origin (e.g., meteorites) has also been observed in the samples collected on high mountains (26, 27). However, hematite particles as large as 120 Å in diameter are probably due to anthropogenic emission (25).

**SEDIMENTS.** Lake, river, and ocean sediments can also be characterized by their Mössbauer spectra. Figure 5 illustrates Mössbauer spectra of typical lake and pond sediments from remote and urban areas in Japan and of an NBS river sediment reference sample distributed for intercomparison (28). The spectrum of the lake sediment from remote areas (Figure 5a) consists mainly of paramagnetic  $\text{Fe}^{2+}$  and  $\text{Fe}^{3+}$  peaks, but no magnetic components are observed even at lower temperatures. However, Mössbauer spectra of the sediment from urban areas (Figure 5b) suggests the presence of various iron oxides besides the paramagnetic  $\text{Fe}^{2+}$  and  $\text{Fe}^{3+}$ . The NBS river sediment is extremely rich in iron oxides (hematite, etc.), indicating the presence of a nearby iron source (Figure 5c).

A  $^{57}\text{Fe}$  Mössbauer study of the serial sections taken from a core at Lake Michigan has demonstrated the presence of anthropogenic iron in the sediments (29). Their Mössbauer spectra are essentially similar to

Figure 5b, with more magnetic fractions especially in the samples taken from near the surface. Figure 6 shows a striking depth dependence of iron components: both total iron content and magnetic  $\text{Fe}^{3+}$  fractions display a maximum at 4 cm below the surface and then decrease with the depth. After the exponential drop, the magnetic  $\text{Fe}^{3+}$  fraction levels off at 11 cm depth (corresponding to about the year 1915). Such observation has been ascribed to the effect of air pollution from the steel mills at the southern shores of the lake, and the growth of steel industry appears to be recorded historically in the sediment (29). Lake sediments in Europe and Canada have been characterized on the basis of their Mössbauer spectra in connection with the chemical environments (30, 31, 32, 33).

Deep ocean sediments have also been studied by means of the Mössbauer technique (7, 34, 35). Figure 7 illustrates a typical Mössbauer spectra of a greenish-gray clay collected at Japan Trench and a spectra of a reddish-brown clay at Philippine Basin (34). The  $\text{Fe}^{2+}/\text{Fe}^{3+}$  ratio in the former is apparently larger than it is in the latter, indicating that the color of deep ocean sediments is related to the iron oxidation state, which reflects the chemical environment. A Mössbauer study on the  $\text{Fe}^{2+}/\text{Fe}^{3+}$  ratio in sediments collected at different depths on the Rumanian shore of the Black Sea has revealed the presence of  $\text{Fe}^{3+}$  only to 100-m depth and the coexistence of  $\text{Fe}^{2+}$  and  $\text{Fe}^{3+}$  at about 200-m depth, where the redox process involving  $\text{H}_2\text{S}$  takes place (35). The presence of goethite ( $\alpha\text{-FeOOH}$ ) and ferric polymer gel (possibly precursor to



Journal de Physique

Figure 6. Depth dependence of the intensities of iron components: M3 (magnetic  $\text{Fe}^{3+}$ ); P3 (paramagnetic  $\text{Fe}^{3+}$ ); and P2 (paramagnetic  $\text{Fe}^{2+}$ ) (29)

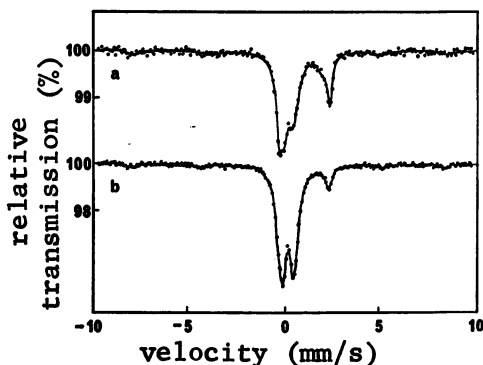


Figure 7. Mössbauer spectra of typical deep ocean sediments at 293 K: (a) greenish-gray clay from Japan Trench; and (b) reddish-brown clay from Philippine Basin (34)

goethite) has been observed in the spectrum of a Red Sea core sediment, while the presence of  $\gamma\text{-Fe}_2\text{O}_3$  has been observed in an Atlantic red clay (7). A systematic survey of Mössbauer spectra may help characterize marine sediments and provide a clue for inferring their origins.

Considerable attention has been directed to Mössbauer spectra of iron-manganese nodules, which are marine mineral deposits with fine-grained structure (36-41).

**ARCHAEOLOGICAL ARTIFACTS.** Archaeological artifacts such as earthenware (e.g., pottery, terra-cotta, and roofing tiles) and metalware (iron and bronze artifacts) can be characterized by means of  $^{57}\text{Fe}$  or  $^{119}\text{Sn}$  Mössbauer spectroscopy (42-45). We have investigated a number of ancient roofing tiles excavated in eastern Japan (ancient site of Taga Castle, 8-10th century), and we noted a correlation between the color and the chemical state of iron determined from their Mössbauer spectra (44, 46). Based on the comparison of Mössbauer parameters of such ancient earthenware with those of products obtained by firing the clay (as starting material) at varied temperatures in various atmospheres, we may be able to infer the ancient technology (e.g., firing temperature and kiln atmosphere) used for manufacturing of such artifacts. It is likely that the roofing tiles in Figure 8 were fired at 800-1000°C under a reducing kiln atmosphere (46, 47). Keisch developed a detector for Mössbauer scattered  $\gamma$  rays convenient for nondestructive characterization of paintings as well as iron-containing pigments (42, 48). The scattering technique has also been used in analyzing glazes applied on the surface of pottery (49).

Gold ( $^{197}\text{Au}$ ) is another Mössbauer element that can possibly be employed in archaeological applications. However,  $^{197}\text{Au}$  studies will be fairly limited in practice, since samples must be cooled down to very low temperatures.



**Monitoring of Chemical Changes in the Environment**

Mössbauer spectroscopy has been established already as a very useful tool for studying reaction mechanisms in a number of solid systems (50, 51). The geochemical and environmental applications include monitoring of alterations, weathering, and oxidation processes in minerals and monitoring of corrosion processes in metals. The chemistry of the environmental processes, such as oxidation and reduction in sediments, can also be followed by characterizing the chemical states of iron contained as in situ probes in such systems.

**Alteration, Weathering, and Oxidation of Minerals.** Weathering of micas (e.g., biotites) and oxidation of other silicate minerals have been investigated by  $^{57}\text{Fe}$  transmission Mössbauer technique (52–57). Conversion-electron Mössbauer spectroscopy has also been used to study the initial stages of oxidation of biotite (58). Biotite single crystals were subjected to heat treatment at 620 K for various periods ranging from 24 h to 114 h in air. The conversion-electron Mössbauer spectra indicate that the  $\text{Fe}^{3+}/\text{Fe}^{2+}$  ratio increases from 0.60 (24-h heating) to 1.03 (114-h heating) due to mild oxidation (possibly oxygenation reaction,  $4\text{Fe}^{2+} + \text{O}_2 \rightarrow 4\text{Fe}^{3+} + 2\text{O}^{2-}$ ) in thin ( $\sim 300$  nm) surface region (Figure 9). These slight changes in the surface cannot be detected by the conventional transmission Mössbauer measurements of bulk samples. Hence, the conversion-electron Mössbauer technique has proved to be valuable in understanding the early stages of solid-phase reactions taking place only in the surface regions.

Recently we have conducted Mössbauer studies of core-to-rim alteration of a deep sea basalt and a continental basalt (59, 60). The ocean basalt from the Mariana deep was altered by seawater, and several concentric layers with different colors could be recognized from core to rim. Based on the Mössbauer spectra and petrographic observation of these layers, chemical states of iron were characterized as ilmenite, titanomagnetite, and silicate minerals (59). The enhanced superparamagnetic effect in the rim demonstrates that the rim of the sample pre-

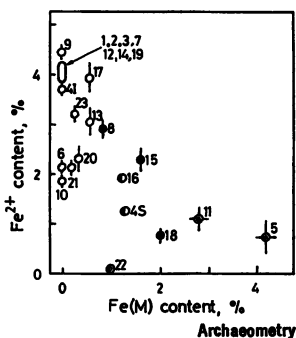
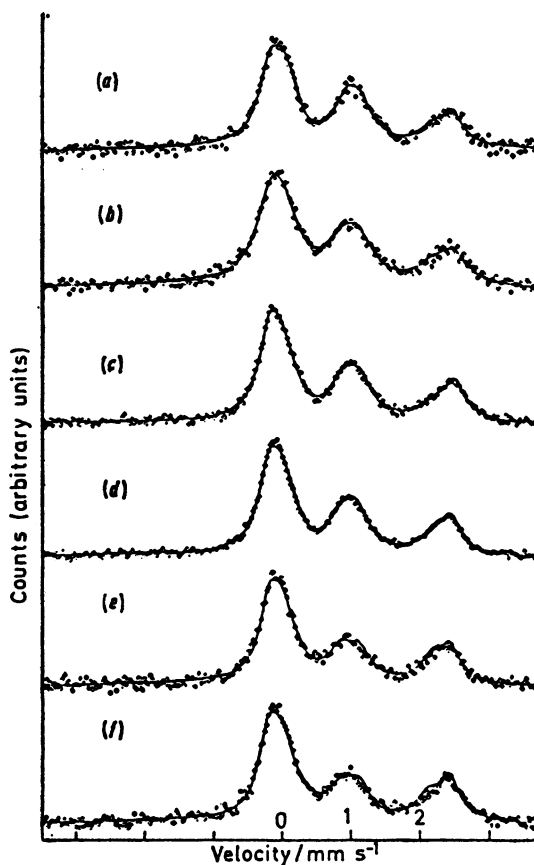


Figure 8. Relation between the paramagnetic  $\text{Fe}^{2+}$  and magnetic iron contents, and the color of the Hinodeyama (numbers 1–20) and Taga (numbers 21–23) roofing tiles. The color of the samples: (⊙) reddish-brown; (●) dark gray; (⊖) reddish dark gray; (○) gray, greenish-gray, greenish-gray with a slightly brown tint, and grayish-white (46).

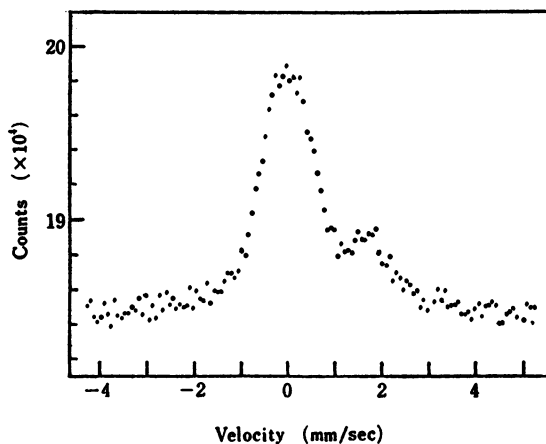
sumably suffered more alteration than the core. The alteration caused by meteoric water in the continental basalt from Oregon was also studied by means of layer-by-layer Mössbauer measurements: in the altered region (rim), intensities of the paramagnetic  $\text{Fe}^{3+}$  and magnetic  $\text{Fe}(M)$  peaks were increased at the cost of the  $\text{Fe}^{2+}$  components, suggesting that  $\text{Fe}^{2+}$  ions were oxidized to paramagnetic or magnetic  $\text{Fe}^{3+}$  in the course of alteration (60).

**Corrosion of Metals.** Corrosion phenomena of iron, cobalt, tin, and their alloys have been investigated by a variety of Mössbauer techniques: by the transmission and scattering methods and by the emission technique in which the specimen under study is doped with a Mössbauer source isotope (e.g.,  $^{57}\text{Co}$ ) and measured against a single-line resonant



Journal of the Chemical Society

**Figure 9.** Conversion-electron Mössbauer spectra of biotite heated at 620 K. The total time of heat treatment (h): (a) 114; (b) 90; (c) 78; (d) 60; (e) 43; and (f) 24 (58).



Cultural Property and Analytical Chemistry

Figure 10. Conversion-electron Mössbauer spectrum (293 K) of a Chinese bronze coin, Hsiang-fu Yüan-pao (65)

absorber (51, 61). These techniques are quite useful for characterizing corrosion products (chemical identities and particle sizes) and for studying the kinetics and mechanisms of corrosion processes. A number of experiments have been attempted with  $^{57}\text{Co}$  or  $^{57}\text{Fe}$ , but there are relatively few  $^{119}\text{Sn}$  corrosion studies (62, 63, 64). Figure 10 illustrates the conversion-electron Mössbauer spectrum of a Chinese bronze coin, Hsiang-fu Yüan-pao, subjected to oxidation in air (65). The spectrum clearly indicates that Sn(IV) oxide (the peak at  $\sim 0$  mm/s) is formed as the major corrosion product in the surface region (the shoulder at  $\sim 2$  mm/s corresponds to Sn(0) in the alloy phase), but it provides no information about the bulk sample at further depth.

**Probe for Environmental Processes.** Chemical states of iron in the environment (in sediments, for example) may be sensitive to environmental and geochemical processes and can possibly serve as a probe for such processes. In lake sediments the distribution of iron among different chemical states or mineral phases (e.g.,  $\text{Fe}^{3+}/\text{Fe}^{2+}$  ratio) has been correlated with water chemistry (oxidizing conditions of the overlying water) or biological activity (30, 31). However, wet or frozen-wet sediments should be recommended for Mössbauer measurements, since they are often susceptible to oxidation in air (23).

### Conclusions

The applications of Mössbauer spectroscopy in environmental systems have started only recently. Further progress will be expected in future, especially in its applications to the study of the kinetics and

mechanisms of environmental and geochemical processes such as the alteration of deep sea rocks, the redox processes in sediments involving organic materials, and the corrosion of metals in the environment. Coupled with other methods of elementary analysis, this technique provides a powerful tool for understanding what is happening in the environment. The development of electron spectrometry coupled with the conversion-electron Mössbauer technique may facilitate depth-selective characterization of the surface regions that play an important role in the environmental processes.

### Literature Cited

1. Bancroft, G. M. "Mössbauer Spectroscopy"; McGraw-Hill: London, 1973.
2. Clark, A. M.; Fejer, E. E.; Donaldson, J. D.; Silver, J. *Mineral. Mag.* **1976**, *40*, 895.
3. Yamanaka, T.; Kato, A. *Am. Mineral.* **1976**, *61*, 260.
4. Baker, R. J.; Stevens, J. G. *Rev. Chim. Mineral.* **1977**, *14*, 339.
5. Hedges, S. W.; Stevens, J. G. *Rev. Chim. Mineral.* **1977**, *14*, 331.
6. Stevens, J. G.; Macintosh, J. R. *Inorg. Nucl. Chem. Lett.* **1977**, *13*, 595.
7. Herzenberg, C. L.; Riley, D. L. "Developments in Applied Spectroscopy"; Plenum: New York, 1970; Vol. 8, p. 277.
8. Greenwood, N. N.; Gibb, T. C. "Mössbauer Spectroscopy"; Chapman Hall: London, 1973.
9. Bancroft, G. M.; Maddock, A. G.; Burns, R. G. *Geochim. Cosmochim. Acta* **1967**, *31*, 2219.
10. Bancroft, G. M. *J. Phys. Colloq.* **1979**, *40*, C2-464.
11. Coey, J. M. D. *J. Phys. Colloq.* **1974**, *35*, C6-89.
12. Belyustin, A. A.; Ostanevich, Yu. M.; Pisarevskii, A. M.; Tomilov, S. V.; Bai-Shi, U.; Cher, L. *Sov. Phys. Solid State* **1965**, *7*, 1163.
13. Gosselin, J. P.; Shimony, U.; Grodzins, L.; Cooper, A. R. *Phys. Chem. Glasses* **1967**, *8*, 56.
14. Labar, Ch.; Gielen, P. *J. Non-Cryst. Solids* **1973**, *13*, 107.
15. Iwamoto, N.; Tsunawaki, Y.; Nakagawa, H.; Yoshimura, T.; Wakabayashi, N. *J. Non-Cryst. Solids* **1978**, *29*, 347.
16. Kurkjian, C. R.; Buchanan, D. N. E. *Phys. Chem. Glasses* **1964**, *5*, 63.
17. Boon, J. A. *Chem. Geol.* **1971**, *7*, 153.
18. Herzenberg, C. L. "Mössbauer Effect Methodology"; Gruverman, I. J., Ed.; Plenum: New York, 1970; Vol. 5, p. 209.
19. Ericson, J. E.; Makishima, A.; Mackenzie, J. D.; Berger, R. *J. Non-Cryst. Solids* **1975**, *17*, 129.
20. Takeda, M.; Sato, K.; Sato, J.; Tominaga, T. *Rev. Chim. Mineral.* **1979**, *16*, 400.
21. Takeda, M.; Matsuo, M.; Tominaga, T. *Radiochem. Radioanal. Lett.* **1979**, *41*, 1.
22. Bowen, L. H. *Mössbauer Effect Ref. Data J.* **1979**, *2*, 76.
23. Minai, Y.; Tominaga, T. *Radiochem. Radioanal. Lett.* **1979**, *37*, 125.
24. Mahieu, B.; Ladrière, J.; Desaedeleer, G. *J. Phys. Colloq.* **1976**, *37*, C6-837.
25. Eymery, J. P.; Raju, S. B.; Moine, P. *J. Phys. D: Appl. Phys.* **1978**, *11*, 2147.
26. Kopcewicz, B.; Kopcewicz, M. *J. Phys. Colloq.* **1976**, *37*, C6-841.
27. Kopcewicz, B.; Kopcewicz, M. *Tellus* **1978**, *30*, 562.
28. Minai, Y.; Tominaga, T., unpublished data.
29. Perlow, G. J.; Potzel, W.; Edgington, D. *J. Phys. Colloq.* **1974**, *35*, C6-547.

30. Coey, J. M. D.; Schindler, D. W.; Wever, F. *Can. J. Earth Sci.* 1974, 11, 1489.
31. Coey, J. M. D. *Geochim. Cosmochim. Acta* 1975, 39, 401.
32. Readman, P. W.; Coey, J. M. D.; Mosser, Ch.; Wever, F. *J. Phys. Colloq.* 1976, 37, C6-845.
33. Manning, P. G.; Ash, L. A. *Can. Mineral.* 1979, 17, 111.
34. Minai, Y.; Wakita, H.; Kobayashi, K.; Tominaga, T., unpublished data.
35. Barb, D.; Diamandescu, L.; Morariu, M.; Georgescu, I. I. *J. Phys. Colloq.* 1979, 40, C2-445.
36. Gager, H. M. *Nature* 1968, 220, 1021.
37. Johnson, C. E.; Glasby, G. P. *Nature* 1968, 222, 376.
38. Hryniewicz, A. Z.; Sawicka, B. D.; Sawicki, J. A. *Phys. Status Solidi A* 1970, 3, 1039.
39. Hryniewicz, A. Z.; Pustowka, A. J.; Sawicka, B. D.; Sawicki, J. A. *Phys. Status Solidi A* 1972, 10, 281.
40. Georgescu, I. I.; Morariu, M.; Diamandescu, L. *Rev. Roum. Phys.* 1973, 18, 401.
41. Eissa, N. A.; Sallam, H. A.; El-Kerdani, H. A.; Tael, F. M. *J. Phys. Colloq.* 1976, 37, C6-857.
42. Keisch, B. "Applications of Mössbauer Spectroscopy"; Cohen, R. L., Ed.; Academic: New York, 1976; Vol. 1, p. 263.
43. Kostikas, A.; Simopoulos, A.; Gangas, N. H. "Applications of Mössbauer Spectroscopy"; Cohen, R. L., Ed.; Academic: New York; Vol. 1, p. 241.
44. Tominaga, T.; Takeda, M.; Mabuchi, H.; Emoto, Y. *Radiochem. Radioanal. Lett.* 1977, 28, 221.
45. Takeda, M.; Mabuchi, H.; Tominaga, T. *Radiochem. Radioanal. Lett.* 1977, 29, 191.
46. Tominaga, T.; Takeda, M.; Mabuchi, H.; Emoto, Y. *Archaeometry* 1978, 20, 135.
47. Takeda, M.; Kawakami, O.; Kobayashi, H.; Tominaga, T. *J. Phys. Colloq.* 1979, 40, C2-483.
48. Keisch, B. *Archaeometry* 1973, 15, 1.
49. Longworth, G.; Warren, S. E. *Nature* 1975, 255, 625.
50. Gallagher, P. K. "Applications of Mössbauer Spectroscopy"; Cohen, R. L., Ed.; Academic: New York, 1976; Vol. 1, p. 199.
51. Güllich, P.; Link, R.; Trautwein, A. "Mössbauer Spectroscopy and Transition Metal Chemistry"; Springer: Heidelberg, 1978.
52. Bowen, L. H.; Weed, S. B.; Stevens, J. G. *Am. Mineral.* 1976, 54, 72.
53. Rice, C. M.; Williams, J. M. *Mineral. Mag.* 1969, 37, 210.
54. Taylor, C. L.; Ruotsala, A. P.; Keeling, Jr., R. O. *Clays Clay Mineral.* 1968, 16, 301.
55. Gibb, T. C.; Greenwood, N. N. *Trans. Faraday Soc.* 1965, 61, 1317.
56. Whitfield, H. J.; Freeman, A. G. *J. Inorg. Nucl. Chem.* 1967, 29, 903.
57. Hogg, C. S.; Meads, R. E. *Mineral. Mag.* 1975, 40, 79.
58. Tricker, M. J.; Winterbottom, A. P. *J. Chem. Soc. Dalton* 1976, 1289.
59. Minai, Y.; Takeda, M.; Wakita, H.; Tominaga, T. *Radiochem. Radioanal. Lett.* 1978, 36, 199.
60. Minai, Y.; Takeda, M.; Wakita, H.; Tominaga, T. *Radiochem. Radioanal. Lett.* 1979, 39, 279.
61. Simmons, G. W.; Leidheiser, Jr., H. "Applications of Mössbauer Spectroscopy"; Cohen, R. L., Ed.; Academic: New York, 1976; Vol. 1, p. 85.
62. Bonchev, Zw.; Jordanov, A.; Ninkova, A. *Nucl. Instrum. Methods* 1969, 70, 36.
63. Pella, P. A.; DeVoe, J. R. *Anal. Chem.* 1970, 42, 1833.
64. Pella, P. A.; DeVoe, J. R. *Appl. Spectrosc.* 1971, 25, 472.
65. Tominaga, T. *Proc. 2nd ISCRCP, Cultural Property and Anal. Chem., Tokyo*, 1979, p. 195.

RECEIVED September 4, 1980.

# Ion Beam Analysis of Environmental Samples

THOMAS A. CAHILL

Department of Physics and Crocker Nuclear Laboratory,  
University of California, Davis, CA 95616

*Use of energetic (MeV) ions for analytical purposes continues to diversify and expand into areas of application ill-served by more conventional techniques. Early programs in Rutherford backscattering (RBS), generally associated with analysis of layered structures in materials science, have been joined by particle induced x-ray emission (PIXE) and charged particle activation analysis (CPAA) based groups. Very active programs have recently evolved around proton microprobes, capable of nondestructive multielemental analyses to  $10^{-6}$ -m dimensions and  $10^{-21}$ -kg masses, and radioactive dating such as  $^{14}\text{C}$  by accelerators. While all these programs have environmental components, major environmental activity centers on PIXE programs, often using CPAA and scattering techniques to extend their range into the elements hydrogen through fluorine.*

**A**t first glance, the thought of using MeV-energy ion beams from accelerators for analyses of environmental samples seems improbable. At such energies, only elemental determinations are generally accessible, and direct information on chemical species can only be inferred, for example, via elemental ratios, or correlations. The analyses are usually done in vacuum, requiring reductions to solid targets that may pose problems. The radiation and temperature environment of the analyses are severe, and loss of some species has been documented. Finally, access to accelerators and/or cost factors discourage routine use of ion beams for analytical purposes; yet, most environmental problems require large numbers of analyses for statistical reasons. Thus, for these reasons, and others, large-scale analytical use of ion beams appears unlikely.

Yet, such large-scale use has become common in the past decade. Despite an almost explosive growth of capability in analytical chemistry, informational needs have grown even more rapidly. One rationale for

0065-2393/81/0197-0511\$05.00/0  
© 1981 American Chemical Society

use of ion beams, and one that surmounts any barrier stated above, is that no other method is capable of delivering information of prime importance. Here, the nature of the unmet need is the primary factor, not ion beam capabilities.

Quasi-random development of analytical capability, no matter how clever, usually fails to achieve any impact as the need can be met by other methods or the need is not important enough to generate the impulse (fund time) to surmount barriers to ion beam use. There exist other situations in which ion beam methodologies may not be uniquely capable but still be widely used. Probably the best example involves most applications of particle induced x-ray emission (PIXE). Circumstances may reduce the importance of the barriers; a relatively inexpensive accelerator may be underused; samples may be enormously chemically complicated, so that less detailed elemental analyses may still be useful; the techniques may be widely known and inexpensive to initiate; personnel may be available, and other such factors. Then, if there is an important need, ion beam methodologies may become established despite the barriers.

This review will examine both types of rationales, using a historical ordering to follow expansion of ion beam techniques into areas of application. The first important analytical use of ion beams involves Rutherford backscattering for studies of layered materials.

### ***Ion Beam Methodologies***

**Scattering of Ions.** The earliest major use of MeV ions for analytical purposes was in studies of layered materials in materials sciences via Rutherford backscattering (RBS), largely in the United States and Great Britain. In this technique, ions (generally alpha particles) of a few MeV are scattered at back angles by the coulomb field of the target nuclei. Separation of elemental species is accomplished by the kinematic energy lost in the nuclear recoil, as shown in Figure 1 from the excellent review by Ziegler (1). The method is absolute and nondestructive, which plays a large part in its popularity. Even more important is that consideration of that energy lost as the incident and scattered ions traverse the layered structures allow accurate measurements of the locations and thicknesses of layers, especially heavy element layers on light substrates such as silicon. (Figure 2). This information is vital to the behavior of these structures. The limitations of the method, such as in distinguishing adjacent elements and lack of trace sensitivity, are not very important in materials sciences, but they limit use of the method for environmental samples.

Nevertheless, persistent efforts have been made to develop alternative scattering techniques, largely because of the inability of x-ray based

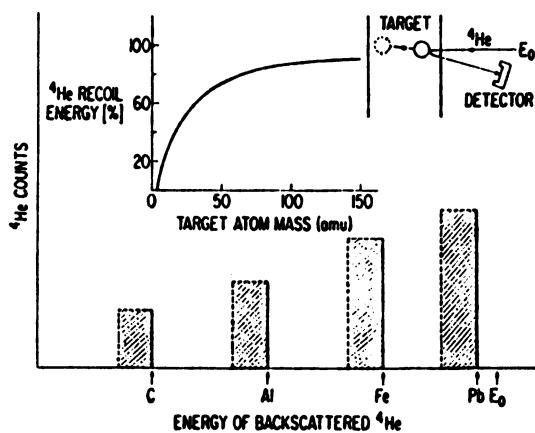


Figure 1. Schematic of a RBS measurement (1)

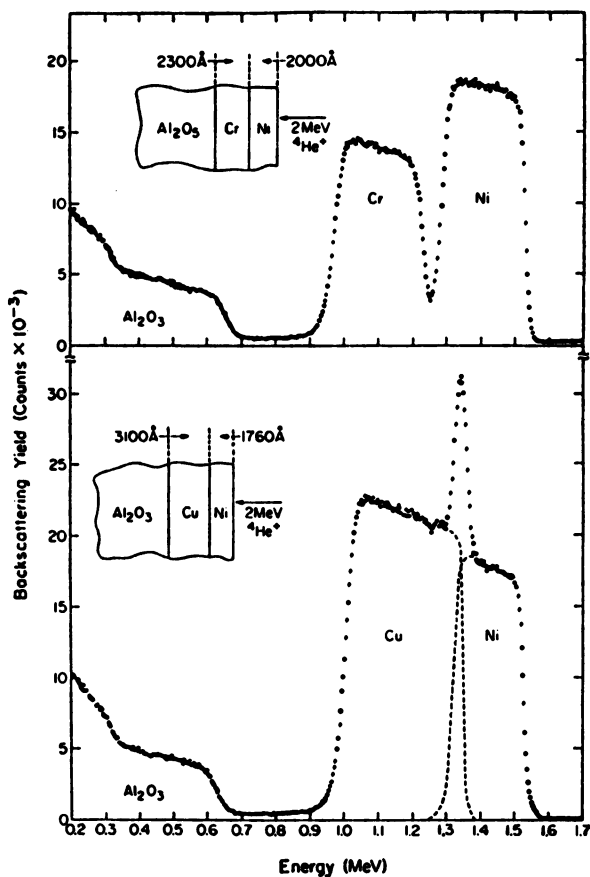


Figure 2. Spectra from metal layers on  $\text{Al}_2\text{O}_3$  substrates (1)



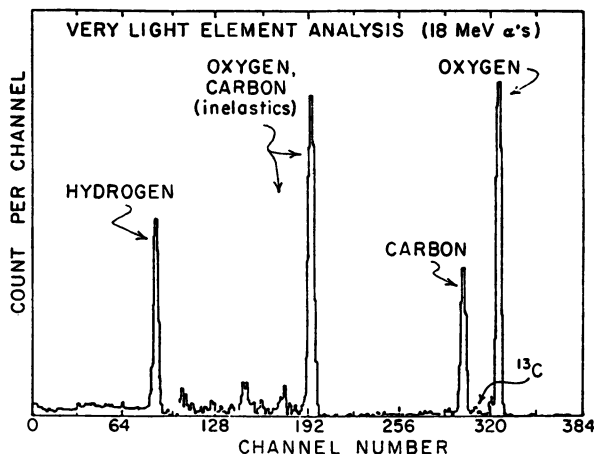


Figure 3. Energy spectra of 18-MeV alpha particles scattered from mylar-based target at  $55^\circ$

methods to detect quantitatively very light elements, hydrogen through fluorine. Since such elements make up about two-thirds of most materials, lack of information on them hampers programs in atmospheric chemistry and other areas. Thus, for environmental samples, the problem is reversed in that we are looking for very light elements in the presence of heavier elements, although now considering gross components, not traces. Active programs exist at about a dozen laboratories, mainly those with atmospheric chemistry programs and PIXE capabilities. An example of one such analysis is shown in Figure 3. Here, alpha particles are used, but at a forward angle of  $55^\circ$ . Energies are now higher to avoid range straggling, such as the 18-MeV alphas used in the Davis program. The use of alphas at forward angles allows detection of the knock-on proton from hydrogen, thus allowing all elements  $Z = 1$  and up to be detected. Beyond sodium, however, separation of adjacent elements becomes more difficult, although the Florida State group has resolved up to calcium using 16-MeV protons at back angles (2). At such energies, scattering processes now involve nuclear interactions, not coulomb, and inelastic states, reaction products, and variable cross sections make calibrations less obvious than in RBS. A serious problem in such studies is that if we have the capability to see all elements, we must handle a severe interference problem in the sampling substrate. This can be handled via parallel collection devices with different substrates, as we shall see in nuclear reaction methods, or by careful subtraction by analyzing a blank portion of the substrate, but a more elegant answer has become available through improved filter technology. Recent development of

very thin, "stretched," Teflon filters allows accurate scattering measurements to be made from such filters. Then, if we assume negligible fluorine in the air (which could be checked via more conventional filters), we can use the Teflon C/F ratio, stable to  $\pm 0.7\%$ , to ascertain the carbon content of the filter (3, 4). This, then, allows excellent subtraction from carbon in the air, since the stoichiometry of the filters is so good. Rapid increase in the use of scattering now appears assured, giving total elemental range to a combined PIXE-scattering system.

**Prompt Nuclear Reactions.** Use of nuclear reactions in analytical chemistry has a long history, with strong programs in geological and materials studies especially in Great Britain, Australia, and South Africa. In many such uses, a single element was studied, or information on very light elements was needed to extend neutron activation analyses. Energies were generally below 10 MeV, and a variety of ions were used to enhance the probability for the chosen reaction. For instance, common reactions used for light elements include (5):  $^1\text{H}$  ( $^{11}\text{B}, \alpha$ ) $2\alpha$ ,  $^2\text{H}$  ( $^3\text{He}, p$ ),  $^7\text{Li}$  ( $p, \alpha$ )  $\alpha$ ,  $^9\text{Be}$  ( $\alpha, u$ ),  $^9\text{Be}$  ( $d, p$ ), and a variety of ( $p, p'\gamma$ ), ( $p, d$ ), ( $d, p$ ), ( $d, p\gamma$ ), ( $d, \alpha$ ), ( $\alpha, p$ ) reactions, giving results such as those shown in Figure 4, reproduced from (1). The method is absolute and quantitative, but tends to be applied for gross or minor constituents (as opposed to trace). To achieve such energy resolutions with relatively low energy beams, thin, uniform targets must be prepared.

**Nuclear Activation.** Activation of light elements with ions generally results in positron decays. Often only use of selective ions and energies, maximizing probabilities for the element of choice, and measurements of half-life allows positive identification to be made. While heavier elements can be activated by ions to give gamma ray spectra suitable for Ge(Li) detectors, surmounting the coulomb barrier requires higher energies and larger accelerators, reducing the attractiveness. In addition, well established and successful programs in neutron activation analysis (NAA) compete with such uses.

In terms of environmental samples, several programs exist based upon charged particle activation, generally to detect the very light elements not seen by x-ray methods. A good example is the program in gamma ray activation for light elements (GRALE) of Macias and coworkers at Washington University, St. Louis (6). Substrate interferences are handled for carbon by special quartz filters, and sensitivities are excellent. Generally, the ion beam is optimized for each element under study. Such activation programs are used for environmental purposes in about 15 laboratories around the world, according to a recent survey (7).

A new approach to charged particle activation has been reported by Schweihert at Texas A & M. In his technique, relatively thick samples

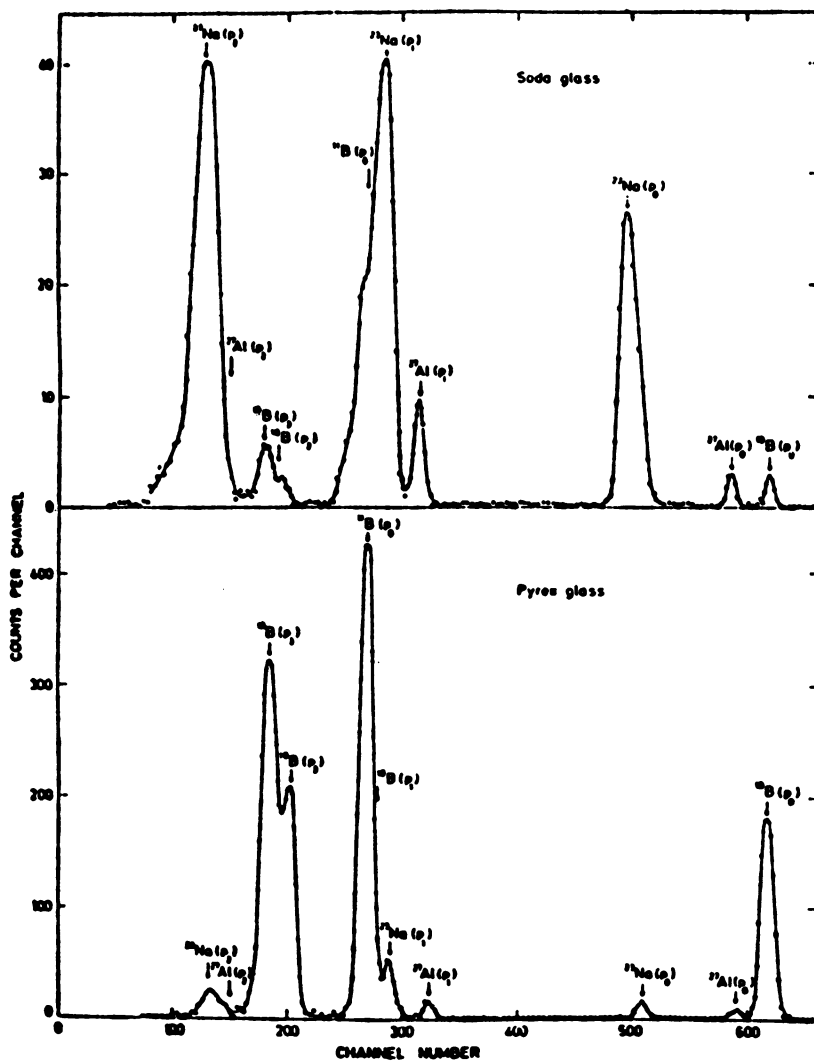


Figure 4. Proton spectra obtained by  $(\alpha,p)$  reactions on glass samples (1)

are activated in high fluxes of low energy protons. Detection of the activated materials is made via x-rays rather than the more common gamma rays. A number of counts are made at increasing time intervals, allowing half-lives to be measured. Advantages include easy identification of x-ray peaks, high detector efficiencies, and sensitive detection of intermediate mass elements poorly done by PIXE. Whether this method will find a permanent place in ion beam methodologies is yet to be seen, but it illustrates the potentialities.

**Particle Induced X-ray Emission.** The most widely used analytical method based on MeV ions is particle induced x-ray emission (PIXE). In this technique, ions of a few MeV, generally protons, ionize atoms, and the subsequent x-ray emission is detected, generally with Si(Li) energy dispersive detectors. It was the development of such detectors around 1970 capable of resolving characteristic x-rays of adjacent elements that lead to the wide application of the method. In addition, the atomic cross sections are large compared with nuclear cross sections, while the physics of inner-shell ionization allows absolute measurements of high sensitivity and precision. A recent review article (7) lists 83 PIXE labs in 30 countries, not including the 24 proton microprobes with PIXE detection schemes. The details of PIXE systems can be found in the extensive literature cited in this article and Johansson and Johansson (8). Johansson et al. (9) and Johansson et al. (10) are the proceedings of the first and second PIXE conferences in Lund, Sweden, and are highly recommended.

Why has PIXE become so widely used? The survey showed that atmospheric particulate matter was the most important application of PIXE. The reasons for this are based both in the capabilities of PIXE and the nature of fine particles in the air. The key lies in the importance of information on both composition and particle size. Particle size governs transport and removal mechanisms, lung capture and light scattering, acidic rainfall, dust soiling, and other effects, as well as serving as an effective way to pinpoint pollution sources (11). However, simultaneous measurements of size and chemistry require particle collection by size through impactors and filters. Such devices, however, can rarely collect more than a few monolayers of particles before sizing errors occur due to clogging or particle bounce. A few monolayers of 1- $\mu$  particles only delivers a few hundred micrograms per square centimeter, which often results in less than 10  $\mu$ g of total mass per size range. This poses serious problems to most chemical methods, and only special methods such as electron beam or neutron activation analyses provide alternatives to PIXE in such cases. X-ray fluorescence, especially with modern energy dispersive detectors, is a valuable method if larger areas of deposit are available, but this is not often the case for multiple size fractions from impactors.

The nature of PIXE also matches the analytical needs of atmospheric particles as well. Many elements in an enormous variety of chemical states are important, so that even elemental analyses are most useful. For example, only five elements deliver over 99% of the mass for gaseous pollutants, but 22 elements are required to describe an equivalent fraction of particulate matter (12) (Figure 5). The relatively uniform sensitivity of PIXE from sodium to uranium in a single, quick analysis delivers the

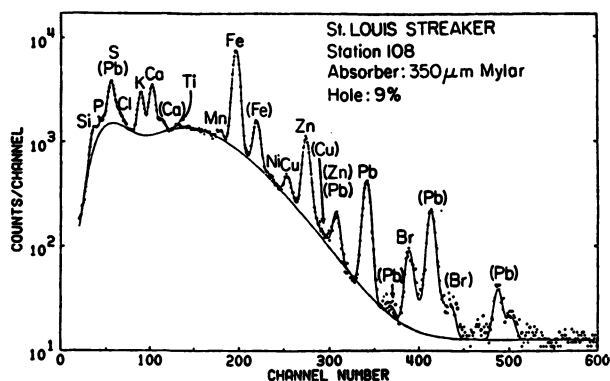


Figure 5. Spectrum of a particulate sample analyzed by PIXE. The fit is by the program HEX written by H. Kaufmann (9)

required information at low cost, and in the final accounting, this explains why over 90% of all simultaneous composition-size analyses of three (or more) stage impactors has been done through this method.

Many other PIXE analyses of aerosols do not have any real advantage over x-ray fluorescence (XRF), but a number of vigorous programs have prospered when access to an accelerator is available. Generally, studies involving only medium and heavy elements collected on filters can be handled well by XRF, and if loadings are reasonable ( $> 100 \mu\text{g}/\text{cm}^2$ ) sensitivities via XRF may be superior by a factor of four or so than for PIXE (13). However, most programs in air chemistry need detailed information on the elements sodium through calcium—elements that make up about one-fourth of all atmospheric particulate mass. These elements, especially sulfur and chlorine, are chemically active and very important in air chemistry. PIXE does very well for these elements, while XRF must use multiple anodes in x-ray tubes to get adequate excitation, slowing analysis rates. Thus, there is an extraordinarily good match between PIXE capabilities and the needs of atmospheric aerosol research, which helps explain the heavy use of ion beams in this work. It might also be mentioned that one of the most attractive features of ion beams is that nuclear processes—scattering and reactions—are available that allow detection of any element. Thus, the two-thirds of particulate mass in the light elements hydrogen through fluorine can be measured in the same laboratory when the need arises. Many PIXE-based programs are using such methods more widely, as it improves the quality of the research programs and helps justify the choice of ion-beam based analytical techniques.

Moving from atmospheric sciences into other environmental fields, use of ion beam analyses falls off sharply. Analyses of fluids is probably

the next most active area, but the problems of reduction of a sample into an accurate, representative target capable of ion beam analysis are severe (7). Active responses to these problems lie in a variety of methods for removing the fluid matrix (drying, vapor filtration, lyophilizing), and in bringing the ion beam into air (or helium) and analyzing the fluid in a cell, dish, or liquid jet (14). The problem of water quality, however, often involves questions about the chemical states of pollutants, which reduces the attractiveness of elemental methods. In addition, there are many optical methods well suited to samples already present in fluid form (atomic absorption and emission spectrography, polarography), and if only a few elements are of interest, these methods are often simpler and cheaper to use. Nevertheless, for surveys of many metals to ppb levels, PIXE is competitive, and a large survey of U.S. drinking water is handled entirely by PIXE at Purdue University on samples prepared by vapor filtration (15). Very little work has been reported on seawater.

Biological tissue presents many of the same problems as fluids, plus some new aspects (16). The major barrier to ion beam analyses in such samples appears to be the need for information on elemental species at sub-ppm levels. The major ion beam technique—PIXE—does not easily achieve such levels, and thus, we are faced with sample preparation problems to reduce the light element matrix. Brutal methods such as ashing achieve such reductions, but at the expense of loss of volatiles. Wet ashing methods are not very effective, and they add new contaminants in the process. The best results achieved to date appear from groups using plasma ashing devices, which result in a reduction of 20 or so in sample mass with minimal loss of volatiles (17). An increase in the use of ion beams is to be expected for biological materials as such units become more common, as multielement surveys are expensive by alternate techniques. The relative lack of interest in the elements sodium through chlorine may favor XRF, however, if mass of sample is adequate.

The final type of environmental sample considered is dusts, be they soil, fly ash, or industrial waste. In some ways, multielemental surveys of such dusts appear easy, as samples can be easily prepared that will stand vacuum and irradiation, while a wide range of elements are to be expected. Only rather recently has the problem of size-chemistry shifts in dusts been appreciated, and almost any attempt to prepare a small aliquot of a bulk dust sample for analysis will produce varying results depending on the method used. The solution lies in separating dusts into size categories, measuring the composition of each category, and then calculating the gross composition (18). Even this technique runs into the problems of severe x-ray attenuation corrections for particles above about 15  $\mu\text{m}$  diameter. Nuclear methods have no such problems, but a different reaction is needed for each element, and surveys are

difficult. Nevertheless, more and more work is appearing on dusts, often in response to program in air chemistry that need source term analyses of soils and such seen in the air.

**The Proton Microprobe.** No discussion of ion beam analytical systems would be complete without mention of the "ultimate" ion beam system—the proton microprobe. As shown in the excellent review articles by Cookson (5) and Martin and Nobile (19), ion beams can be prepared with dimensions of a micron or so. Such finely focussed ion beams can be supported by the nuclear or atomic analytical methodologies mentioned above, with PIXE being the most widely used. Since the PIXE system's fractional mass sensitivity is not changed by beam area, one can have a 1-ppm measurement made over an area of  $10^{-8}$  cm<sup>2</sup>, yielding mass sensitivities of  $10^{-18}$  g or so in a nondestructive multielemental analysis as shown in Figure 6. No other method exists that can obtain such data, so the role of ion beams is well founded. Explosive growth of these expensive systems has occurred in the past five years, but the cost has limited applications to most environmental samples.

**Radioisotope Dating with Accelerators.** Another area that has recently gained considerable attention involves use of an accelerator to perform measurements of radioactive atoms (20). In such cases, the

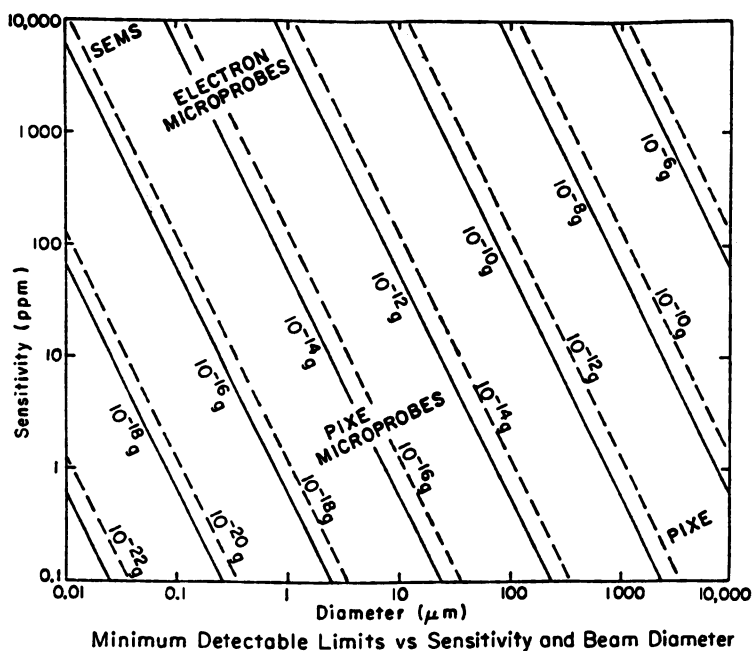


Figure 6. Mass sensitivity achieved by scanning electron microscopes (SEMS), PIXE systems, and PIXE microprobes (7)

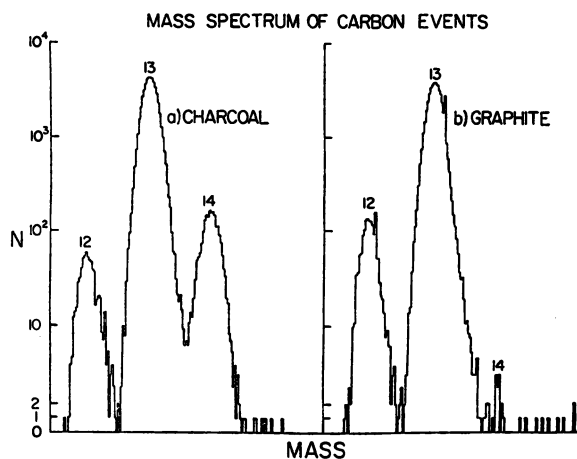


Figure 7. Measurement of  $^{14}\text{C}$  in charcoal and graphite samples by a Tandem van de Graaff accelerator

atoms are accelerated to high velocity by a cyclotron or a potential drop accelerator. In the case of the cyclotron, such acceleration yields particles of identical charge-to-mass ratios (such as  $^{14}\text{N}^{8+}$  and  $^{14}\text{C}^{3+}$ ) and identical velocities. A relatively simple range chamber will then separate the abundant  $^{14}\text{N}$  from rare  $^{14}\text{C}$ , since the ions are soon stripped to bare nuclei, and the higher nitrogen charge will slow it down faster than carbon. Tandem van de Graaffs can use the fact that nitrogen forms no negative atomic ion while carbon does, allowing separation in the acceleration process. The energetic ions can then be conclusively identified by standard nuclear  $\Delta E$  and  $E$  detection schemes (Figure 7). Masses required for detection are very low, and many radioactive species are under study.

**Other Techniques.** There exist other areas of potential application of ion beams. Ion beams can excite transitions in outer electron shells, with information in the optical wavelengths. Beam foil spectroscopy has used such methods for years, but no regular analytical use has been made. Nevertheless, samples irradiated under ion bombardment glow with characteristic radiation visible to the eye or television camera. Certain chemical or physical properties could be inferred by analyzing this radiation, perhaps including the physical condition of carbon atoms in graphitic or organic states. Certainly opportunities exist.

### Conclusions

Ion beams have become well established in a number of analytical methodologies, despite the barriers present in any accelerator-based



system. In addition, many opportunities exist for new techniques, assuming that there is a significant need not well met by other (nonaccelerator) options. These other options, however, have become much more expensive in the past decade, so that the cost barrier for both acquisition and operation of an accelerator are not as great a negative factor as in the past. If, however, the facility already has an accelerator, perhaps associated with short-lived isotopes, then accelerator-based techniques may be able to fill a major role with relatively little developmental effort.

### Literature Cited

1. Ziegler, J., Ed. "New Uses of Ion Accelerators", Plenum: New York; 1975.
2. Nelson, J. W.; Courtney, W. J., *Nucl. Instrum. Methods* 1977, 142, 127-132.
3. Nelson, J. W.; Hudson, G. M.; Kaufmann, H. C.; Courtney, W. J.; Williams, I.; Akselsson, K. R.; Meinert, D.; Winchester, J. W. Technical Report, United States Environmental Protection Agency, Jan., 1978.
4. Andreae, M. O.; Barnard, W. R.; "Light Element Composition of the Atmospheric Aerosol at Cape Grim (Tasmania) and Townsville (Queensland) by PIXE and PESA", *Nucl. Instrum. Methods*; to be published.
5. Cookson, J. A.; *Nucl. Instrum. Methods* 1979, 165, 477-508.
6. Macias, E. S.; Radcliffe, C. D.; Lewis, C. W.; Sawicki, C. R. *Anal. Chem.* 1978, 50, 1120-1124.
7. Cahill, T. A. *Annu. Rev. Nucl. Part. Sci.* 1980, 30, 211-252.
8. Johansson, S. A. E.; Johansson, T. B. *Nucl. Instrum. Methods* 1976, 137, 473-516.
9. Johansson, S. A. E. *Nucl. Instrum. Methods* 1977, 142, 1-338.
10. Johansson, S. A. E. "Proceedings of the Second International Conference on Partical Induced X-Ray Emission and Its Analytical Application", *Nucl. Instrum. Methods*, to be published.
11. Butcher, S. K.; Charlson, R. J. "Introduction to Air Chemistry", John Wiley & Sons: New York; 1975.
12. Cahill, T. A. In "New Uses of Ion Accelerators", Ziegler, J., Ed.; Plenum: New York, 1975; 1-72.
13. Perry, S. K.; Brady, F. P.; *Nucl. Instrum. Methods* 1973, 108, 389.
14. Deconninck, G. *Nucl. Instrum. Methods* 1977, 142, 609-614.
15. Rickey, F. A.; Mueller, K.; Simms, P. C.; Michael, B. D.; In "X-Ray Fluorescence Analysis of Environmental Samples", Dzubay, T., Ed.; Ann Arbor Sci.: Ann Arbor, Mich., 1977; pp. 135-143.
16. Campbell, J. L. *Nucl. Instrum. Methods* 1977, 142, 263-273.
17. Mangelson, N. F.; Hill, M. W.; Nielson, K. K.; Eatough, D. J.; Christensen, J. J.; Izatt, R. M.; Richards, D. O.; *Anal. Chem.* 1979, 51, 133-142.
18. Cahill, T. A.; Ashbaugh, L. L. In "Environmental and Climactic Impact of Coal Utilization", Deepak, A., Ed.; Academic: New York, 1980; pp. 569-572.
19. Martin, B.; Nobiling, R. In "Applied Charged Particle Optics", Septier, A., Ed.; Academic: New York, to be published.
20. Bennet, C. L.; Beukens, R. P.; Clover, M. R.; Elmore, D.; Goue, H. E.; Kilius, L.; Litherland, A. E.; Purser, K. H. *Science* 1978, 201, 345-347.

RECEIVED March 16, 1981.

# The Use of Stable Activable Tracers in Environmental Science

WALTER LOVELAND

Department of Chemistry, Oregon State University, Corvallis, OR 97330

*Stable activable tracers are powerful tools for the study of many environmental problems. Compared with fluorescent dyes or radiotracers, they offer many advantages that are reviewed herein. Our research group has emphasized the use of rare earth nuclides with short-lived activation products as stable activable tracers. Use of rare earth nuclides is cost-competitive with conventional tracers and allows rare earth "fingerprints" to mark individual sources with subsequent simultaneous tracing of effluents from several sources. We present results from the application of these tracers to monitor pollutant dispersal from multiple industrial stacks, monitor fluid-bound pollutant dispersal in estuarine and fresh-water systems, monitor herbicide dispersal, and trace toxic organic chemicals in the marine environment.*

## **Introduction**

**Conventional Tracers.** A survey of the history of environmental science will show that tracers are important tools for the environmental scientist. They have been used to measure flow rates and dispersion coefficients, to follow the movement of materials through the atmosphere, hydrosphere, and biosphere, and to characterize pollutant sources. Three principal types of tracer have been used in environmental science: chemical tracers, such as NaCl, KHSO<sub>4</sub>, and K<sub>2</sub>CO<sub>3</sub>; radioactive tracers, such as <sup>3</sup>H, <sup>32</sup>P, and <sup>82</sup>Br; and fluorescent dyes, such as fluorescein, Rhodamine B, and Rhodamine WT.

Use of each of these tracer types has been beset by certain problems. The chemical tracers are difficult to detect except in the highest concentrations, at which point their use leads to a modification of the system

0065-2393/81/0197-0523\$05.00/0  
© 1981 American Chemical Society

under study. The uncontrolled use of the radiotracer in the environment poses real or imagined safety problems, definite regulatory problems (with their associated delays), and, in the case of short-lived radionuclides, an effective limit to the duration of the experiment (because of the tracer half-life). The use of fluorescent dyes may lead to aesthetically objectionable modifications of water or air color (the red tide syndrome) and significant alterations of the tracer concentrations by photochemical decay. Furthermore, fluorescent tracers are inapplicable in highly colored media.

**Stable Activable Tracers.** To overcome many of these problems and to open new possibilities of tracer use for the environmental scientist, there has been renewed interest in developing stable activable tracer technologies that will be attractive alternatives to conventional tracers. This chapter reviews some of these developments with illustrative examples from the author's published and unpublished work.

A stable activable tracer (SAT) is a stable material that is injected into a system under study and whose concentration in the system is measured by a post sampling activation analysis. The advantages of such "artificial" tracers as compared with the "naturally occurring" trace elements in various systems (which act as "natural" tracers) are as follows: artificial tracers have a controlled emission rate (either pulse or continuous injection) and control of the amount injected, both of which are valuable in model validation studies; they can be injected in amounts sufficient to ensure easy detection in the system under study; and they lend themselves better to simultaneous tracing of several similar pollutant sources.

**Advantages of SATs.** What advantages do stable activable tracers possess in general? When compared in specific situations with fluorescent dyes, radiotracers, or conventional chemical tracers, what advantages do they have? The advantages are listed below.

1. The tracers are nontoxic at concentrations encountered in environmental studies (1, 2, 3, 4).
2. The detection sensitivity of these tracers is very good. For example, Dy can be readily detected in amounts down to  $10^{-12}$  g. This allows pollutant tracing over very long distances. Stable activable tracers can be chosen such that their naturally occurring concentrations are very small.
3. The tracers can be bound as EDTA or DTPA complexes and thus do not suffer any adsorption by sediments, etc.
4. The detection of SATs is not affected by the presence of water, color, or the occurrence of photochemical or radioactive decay of the tracer.
5. According to our estimates (*see* Table II), the rare earth SAT is cost-competitive with the use of radiotracers and fluorescent dyes.

6. Effluents from specific pollutant sources can be marked with a given "fingerprint" (fixed ratio of tracer elements), making it possible to trace the effluent from several sources simultaneously. By carefully selecting the elements and their ratio for any one fingerprint, results that can be analyzed in the laboratory in one day or less can be obtained. This avoids the traditional problem of activation analysis-based methods, that is, one of long analysis times.

**Choice of SATs.** What elements should one choose as stable activable tracers? Probably no universal tracer suitable for all applications exists, but certain general criteria can be stated for the choice of suitable SATs. These criteria include: a good detection sensitivity (which for neutron activation analysis translates into a high neutron capture cross section and/or a short half-life for the activation product); a reasonable cost (as measured by the sum of analysis and tracer cost); a low natural concentration; the fact that it is nonhazardous at environmentally useful concentrations; and an equivalence in behavior to the material being traced.

**Non Rare Earth SATs.** Several candidates that meet these criteria have been found, and some of their applications are discussed by Kruger (5). Kruger's discussion also contains an excellent account of the early history of this field. In a series of experiments at the Pennsylvania State University, Jester and coworkers (6,7) have used  $\text{Br}^-$  and  $\text{I}^-$  to mimic the movement of soluble species in natural waters. In-EDTA complexes have been used by Behrens et al. (8) to monitor groundwater movement, while Dahl (9) has shown that  $\text{In}(\text{NO}_3)_2$  could be used to trace water stream patterns and pollutant dispersal in and around the harbor of a Norwegian town. Indium and scandium were used as stable activable tracers for monitoring in-plant movements of water in waste water treatment plants by Craft and Eicholz (10). The entire subject of industrial uses of activable tracers has been reviewed recently by Van Dalen and Wijkstra (11).

**Rare Earth SATs.** One class of elements that are especially appealing as stable activable tracers is the class of rare earth elements. They admirably fulfill the criteria for stable activable tracers, especially those of low environmental concentration and ease of detection. These qualities were first recognized by Channell and Kruger (12), who used the lanthanides as estuarine tracers.

In an unpublished work Hansen (13) actually compared the behavior of long-lived Eu, Tb, and In activable tracers with the fluorescent dye Rhodamine B in a small (0.5-mi long) stream. Hansen showed the conservative nature of the tracers over this distance, but he did not demonstrate the economic viability of these tracers or their use in large-scale experiments. In a preliminary study Schmitt (14) showed that the

**Table I. Properties of Some Rare Earth Stable Activable**

<i>Element</i>	<i>Cost</i> (\$/kg) <sup>a</sup>	<i>Target</i> <i>Nuclide</i> <sup>b</sup>	<i>E<sub>γ</sub></i> (% Abundance)
Ce	45	Ce-136	446.0 (2.3%)
Pr	236	Pr-141	1575.5 (3.7%)
Nd	176	Nd-148	211.3 (27%)
Sm	320	Sm-154	104.3 (73%)
Eu	3960	Eu-151	121.8 (37%)
Gd	3720	Gd-158	363.6 (9%)
Dy	920	Dy-164	94.7 (4%)
Ho	1100	Ho-165	80.6 (54%)
Er	420	Er-170	112.0 (25%)
Yb	860	Yb-176	151.0 (16%)
Lu	18000	Lu-175	88.4 (10%)
In <sup>c</sup>	1760	In-115	1097.2 (80%)

<sup>a</sup> Alfa Catalog, Ventron Corp., Danvers, MA, 1977-1978. (Large quantities can be purchased at significantly lower cost).

<sup>b</sup> Lederer, C. M.; Hollander, J. M.; Perlman, I. "Table of Isotopes", 6th ed.; Wiley: New York, 1967; Binder, T.; Kraus, R.; Xlein, R.; Lee, D.; Fowler, M. M. "A Chemist's Gamma Ray Table," Lawrence Berkeley Laboratory Report, LBL-6515, June 1977.

dispersal of La and Sm could be followed in rivers, but they made no attempts to study the use of these elements as tracers systematically. Shum et al. (15) demonstrated that the rare earth elements could be used to monitor dispersal of airborne pollutants and simultaneously to trace emissions from multiple pollutant sources. Kuhn et al. (16) demonstrated the use of rare earths, such as Dy, in atmospheric pollutant removal studies. Loveland (17) showed that those rare earths with short-lived activation products could be used to monitor the dispersal of fluid-bound pollutants in fresh waters. Most recently, McCown (18) demonstrated the use of Dy and Sm to trace the dispersal of oily waste in fresh waters.

The rare earth tracers, especially those with short-lived activation products, are cost-competitive with other types of tracers. Tables I and II show typical rare earth stable activable tracers and the total cost of using them in tracing water pollutants. These cost estimates are, of course, rough approximations and are intended to demonstrate that the costs associated with different tracer technologies are similar. Also note, as shown in Table I, the small amounts of tracer that can be easily detected (give  $10^4$  counts). These detection sensitivities are emphasized further when one notes that the natural concentrations of the rare earths in fresh water are (17) in the ppt-ppb range and the atmospheric concentrations (19) are around  $10^{-2}$  ng/m<sup>3</sup>.

**Tracers with Short-Lived ( $t_{1/2} < 1$  day) Activation Products**

$t_{1/2}^b$	$g/10^4$ cts	Cost (\$/10 <sup>4</sup> cts)
9.0 h	0.085	$3.8 \times 10^{-3}$
19.2 h	0.018	$4.27 \times 10^{-3}$
1.8 h	$5.93 \times 10^{-4}$	$1.04 \times 10^{-4}$
22.997 min	$3.31 \times 10^{-5}$	$1.05 \times 10^{-5}$
9.30 h	$1.32 \times 10^{-7}$	$5.24 \times 10^{-7}$
18.706 min	$1.11 \times 10^{-4}$	$4.13 \times 10^{-4}$
2.334 h	$1.56 \times 10^{-6}$	$1.44 \times 10^{-6}$
66.78 min	$2.42 \times 10^{-6}$	$2.67 \times 10^{-6}$
7.519 min	$3.61 \times 10^{-4}$	$1.51 \times 10^{-4}$
1.900 h	$1.77 \times 10^{-4}$	$1.52 \times 10^{-4}$
3.679 h	$2.04 \times 10^{-5}$	$3.67 \times 10^{-4}$
54 min	$6.80 \times 10^{-7}$	$1.21 \times 10^{-6}$

<sup>a</sup> Assume 1-min irradiation at a flux of  $10^{13}$  n/cm<sup>2</sup> s. Delay of 5 m, count 3 m. Sample positioned 1 cm away from a 40 cm<sup>3</sup> Ge(Li) detector.

<sup>b</sup> In is not a member of the rare-earth family. It is a well known stable activable tracer and is therefore included here for comparison.

**Experimental**

There are certain experimental decisions that must be made either explicitly or implicitly in the use of stable activable tracers in environmental science. In this section I shall review some of these factors.

**The Choice of Tracer and Its Chemical Form.** As stated previously, the tracer should be easy to detect, inexpensive, nontoxic at environmentally useful concentrations, have low environmental abundance, and, most important, exhibit similar behavior to the material being traced. Among the elements used for their ease of detection (in the absence of other elements) by neutron activation analysis are Sc, V, Mn, Cu, As, Br, Y, Pd, In, Sb, I, the rare earths, Ta, W, Re, Ir, Au, and U. In particular matrix, some of these may become much more difficult to detect. For example, in marine samples, the high levels of 15-h <sup>24</sup>Na produced by activation may necessitate pre- (or post-) irradiation removal of the Na or use of trace elements with long half-lives ( $t_{1/2} > 5$  days).

The chemical form of the tracer may be exceedingly important. In Figure 1, we show the behavior of a Ce tracer in a marine environment. Without chelation by DTPA, the tracer is quickly absorbed from the solution; with chelation it remains stable over a period of time and can act as a tracer for fluid-bound materials. Proper "packaging" of the tracer element in an organic matrix can allow the tracer to mimic the behavior of toxic organic materials. Ghannam and Loveland (20) have shown the bioaccumulation behavior of a number of toxic organic compounds in oysters and some organometallic stable activable tracers to be similar.

A low environmental concentration of the tracer element allows the use of smaller quantities of tracer, reducing possibilities of injury to the environment from the tracer and less interference from fluctuations in the background

**Table II. Cost Analysis of Tracer Method**

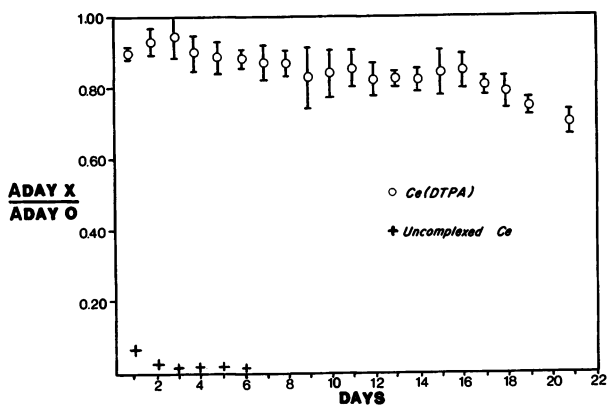
Volume of water tagged	$5 \times 10^{10}$ liters
Duration of experiment	1 day
Number of samples taken	100 samples
<i>Rhodamine WT</i> <sup>a</sup>	
Weight needed	110 lb
Tracer cost	\$ 457
Analysis cost <sup>b</sup>	\$ 200
Total	\$ 657
<i>Tritium</i> <sup>c</sup>	
Activity needed	81 Ci
Tracer cost	\$ 243
Analysis cost <sup>b</sup>	\$3000
Total	\$3243
<i>Dysprosium</i> <sup>d</sup>	
Weight needed	10 lb
Tracer cost	\$ 250
Analysis cost <sup>b</sup>	\$ 600
Total	\$ 850

<sup>a</sup> Tracer cost is based on an average minimum concentration of  $1.3 \times 10^{-5}$  g/m<sup>3</sup> and a tracer cost of \$4.15/lb.

<sup>b</sup> All charges for analysis of samples are based on current charges of Oregon State University's in-house service analysis groups. The tritium analysis charge includes cost of preconcentration.

<sup>c</sup> Tracer cost is based on an average concentration of 1.622 nCi/L and a cost of \$3/Ci for tritium.

<sup>d</sup> Tracer cost is based on an average concentration of 100 ng/L and a cost for Dy of \$25/lb.



**Figure 1.** The fraction of tracer remaining in solution after contact with sediments in estuarine water for uncomplexed Ce and Ce DTPA

levels. Frequently the first step in choosing a tracer is to verify or measure the background level of the tracer element. Generally, the heavier the element, the lower its environmental concentration (and unfortunately, the greater the cost of the tracer material).

**Dispersal, Collection, and Analysis of the Tracer.** The dispersal of the stable activable tracer is similar to that of a chemical tracer, radiotracer, etc. Tracer aerosols can be produced by, for example, pyrotechnic flares, acetone burners, or spraying water solutions. Dispersal in water should cause little problems other than concern that the initial tracer concentration near the point(s) of dispersal may be high. Collection and analysis of the tracer species proceed like the analysis of the trace element content of any matrix, except that the tracer should be present at a level high enough to ensure easy detection.

**Tests of Tracer Behavior.** Any use of a tracer to derive quantitative information about environmental processes should be preceded by tests that show the tracer to behave like the material being traced or by evidence that the tracer exhibits the desired physical or chemical properties. Generally, this testing procedure involves laboratory tests to show the conservative nature of the tracer in environmental matrices followed by field tests to show the same properties. When using tracers like the rare earths for simultaneous multiple source tracing, it is important to verify that each tracer behaves identically and that they can be detected in the presence of one another.

### *Applications*

To gain an appreciation for some of the unique ways in which stable activable tracers may contribute to environmental investigations, let us review some of the applications of these tracers in environmental science.

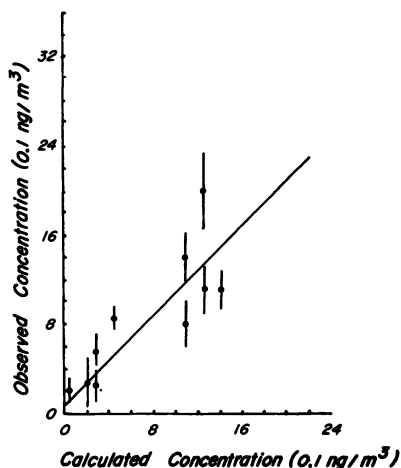
**Air Pollutant Tracing.** Shum, Loveland, and Hewson (15) investigated the dispersal of pollutants from a closely spaced group of paper mills, plywood companies, and metallurgical processors using the SATs La, Ce, Sm, and Dy. Tracer solutions were sprayed into the hot exhaust gases in the stacks of these plants, and aerosol samples of the stable emissions were taken using ground-level samplers over distances of 0–4 km from the sources. Standard meteorological models, such as the Gaussian plume model, were found to account satisfactorily for the pollutant dispersion for cases involving moderately intense turbulence fields (stability types B, C, and D), including cases in which the pollution was trapped by an inversion layer aloft. In Figure 2 we show a comparison of the observed tracer concentrations and those calculated using the standard Gaussian plume model, that is,

$$X(x, y, z) = \frac{Q}{\pi \sigma_y \sigma_z u} \exp \left[ -\frac{1}{2} \left( \frac{y}{\sigma_y} \right)^2 - \frac{1}{2} \left( \frac{z - h_e}{\sigma_z} \right)^2 \right]$$

where the symbols have their customary meanings. A statistically significant agreement between calculated and observed tracer concentrations



Figure 2. Scatter diagram comparing observed and calculated concentrations obtained from the standard Gaussian plume model under neutral conditions (stability type D): number of observations, 18; correlation coefficient  $R = 0.89$ , at the 95% confidence level,  $R = 0.48$ ; observed  $= 1.0 \pm 0.1$ , calculated  $= (0.6 \pm 0.2) \times 10^{-10}$



was obtained. Using different tracers to fingerprint several individual stacks, Shum et al. (15) found they were able to trace the emissions from these multiple sources at several kilometers from the sources.

One of the most appropriate uses of stable activable tracers is in measuring removal of pollutants from the atmosphere. The concentrations of species are extremely low even in tracer experiments ( $\sim\text{ng/L}$ ), and the good detection sensitivity of activation analysis is a necessity along with the controlled emission of the tracer. Much of this work has been carried out by the Battelle Pacific Northwest Laboratories and is summarized in annual reports of that laboratory from 1972–1976.

**Hydrospheric Applications.** Most applications of stable activable tracers have been to trace pollutant movement in water systems. In one example of such an application, Loveland (17) used DTPA anionic complexes of the rare earth elements to trace the movement of fluid-bound pollutants in fresh waters. Figure 3 shows a comparison of the dispersal pattern of a Dy tracer injected into a municipal sewage outfall and the dispersal pattern of Zn, a naturally occurring trace element in

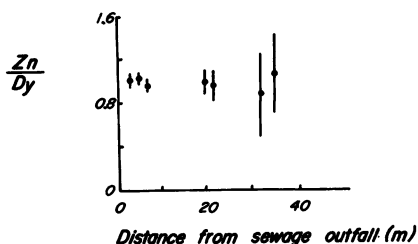


Figure 3. The ratio of naturally occurring Zn to artificially injected Dy tracer as a function of distance from the sewage outfall

the sewage material. One can see that the Zn and Dy behave similarly enough to allow the use of the tracer to monitor the dispersal at large distances where the Zn becomes very difficult to detect. (The increase in uncertainties of the Zn/Dy ratios as the distance increases is attributable primarily to difficulties in detecting the Zn, not the Dy, tracer).

An unusual application of stable activable tracers in the marine environment was reported recently by Ghannam and Loveland (20). They used SATs to mimic the physical and chemical behavior of toxic, biologically significant organic molecules in the marine environment. To

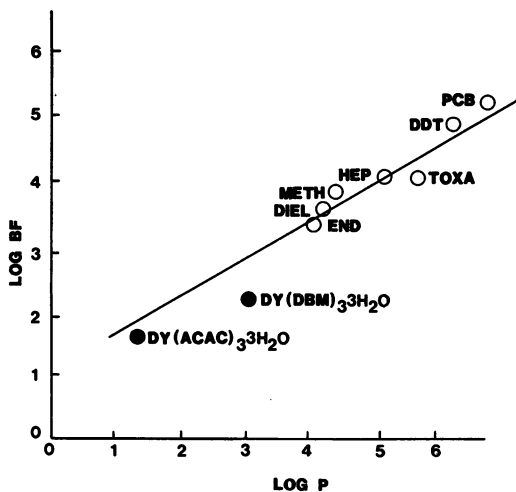


Figure 4. The relationship between the bioconcentration factor BF for various species in the oyster, *Ostrea edulis*, and the 1-octanol/water partition coefficient, P, for the same species. The best fit relationship is  $\log BF = 0.9906 + 0.5978 \log P$ .

mimic these molecules, they synthesized similarly structured metal chelates whose central metal atoms could be easily detected by neutron activation analysis. As analogs to the lower chlorinated pesticides, they used the dysprosium  $\beta$ -diketonates, dysprosium(III) trisdibenzoylmethane monohydrate,  $Dy(dbm_3) \cdot H_2O$  and dysprosium(III) trisacetylacetonate trihydrate,  $Dy(acac)_3 \cdot 3H_2O$ . The tracers were shown to be stable and conservative in seawater solutions for periods of a week. To test their bioaccumulation behavior, the European oyster *Ostrea edulis* was chosen as a model system. Figure 4 shows the relationship between the biocon-

centration factor,  $BF$ , and the 1-octanol/water partition coefficient,  $P$ , for the tracer species and a number of environmentally significant organic molecules. While the bioconcentration factors and partition coefficients are lower for the tracer species than the organic molecules considered in Figure 4, the tracers appear to show the same functional relationship between  $BF$  and  $P$  as the organic species. Experiments are now underway to measure  $BF$  for the lower chlorinated pesticides, whose partition coefficients are known to be similar to those of the tracers.

**Biospheric Applications.** The current controversies about the dispersal of herbicides used in forestry have demanded the immediate implementation of tracer techniques that can be used in connection with herbicide dispersal. As a result, we have developed a "quick and dirty" tracer technology. The success of our effort has certain consequences concerning strategies for monitoring herbicide dispersal and for establishing legal responsibility for its consequences.

The activable tracer we chose to monitor herbicide dispersal was Dy (DTPA). In an initial test, seven common herbicides and insecticides were purchased, prepared in their recommended concentrations, and spiked with 150  $\mu\text{g/L}$  Dy (DTPA). The products involved were (i) a 20.2% solution of monosodium acid methanearsenate; (ii) sodium cacodylate (1.98%); (iii) amitrole (21.1%); (iv) prometon (3.3%); (v) 2,4-D (6.3%); (vi) carbaryl (23.4%); (vii) malathion (50.0%); and (viii) diazinon (12.5%). INAA of the samples revealed the tracer to be easily detected in the concentrations given above. Two arsenic-based herbicides [(i) and (ii) above] were chosen for further study and spiked with 150  $\mu\text{g/L}$  Dy (DTPA). Plots of grass of area 300  $\text{ft}^2$  were treated with the spiked herbicides in a manner recommended by the manufacturer, and grass clippings were collected over a one-week period. Analysis of the clippings revealed the As/Dy ratio in the clippings remained constant over this period of time, indicating that the tracer and herbicide were behaving similarly. In a second experiment, runoff water from the sprayed grass was collected for over a week and was analyzed. Once again we found the As/Dy ratio to be constant in the runoff water, with the absolute values indicating approximately 3% removal of the herbicide/tracer by rainwater.

It is true that to trace the movement of the herbicides studied in this work in the environment, one would need only to measure the As content of various samples. However, the results do have potential usefulness in monitoring herbicide dispersal. Quite frequently, the problem is not to establish whether or not herbicides were present but to establish who was responsible for the herbicide. Thus, drawing on this work and previous work involving multiple source tracing in fresh water (17), one should be able simply to mark a given application of herbicide with a

unique fingerprint of rare earth (DTPA) tracers (spiking at the levels used here and with concentrations of the elements in the fingerprint differing by a factor of 3).

### ***Future Directions***

Most of the applications of stable activable tracers in environmental science have involved mimicking environmental behavior of a physical nature, that is, phenomena in which chemical reactions were not playing an important role in defining the property under study. Examples of this type of behavior involve pollutant diffusion, precipitation scavenging, etc. But there are many environmental processes in which chemical reactions contribute to pollutant concentrations, act to remove pollutants, or affect the accumulation of pollutants in biological systems. I look forward to further developments of stable activable tracer technologies in which the chemical state of the tracer is carefully controlled by the experimenter to allow tracing and modeling of chemical and biological behavior of pollutants in the environment.

The environmental use of radiotracers poses many regulatory and safety problems whose occurrence has spurred the use of stable activable tracers. One cannot help but wonder whether similar problems may occur in the extensive use of radiotracers in medicine. Difficulties in the production, transport, and handling of radionuclides along with the sometimes appreciable radiation doses received by patients in diagnostic procedures may impel attention to the use of more benign technologies. If the problems associated with detecting the tracers can be solved (i.e., easily accessible activation facilities or the use of tracers that are detected by x-ray fluorescence), stable activable tracers may play a more important role in medical diagnostic procedures.

The use of stable activable tracers is an important alternative for today's environmental science. With proper future development, this use can expand. Hopefully, such developments will lead to an increased understanding of the many complex problems facing the environmental scientist.

### ***Acknowledgments***

I wish to acknowledge the cooperation and assistance of a number of my graduate students, past and present, whose experimental work forms the basis of this report. They include Y. S. Shum (air-pollutant tracers); S. W. K. Chick, K. M. Keasler (fluid-bound pollutants); A. Borovik (herbicide dispersal); and L. Channam (toxic organic chemicals). I would gratefully acknowledge financial support for these efforts

by the U.S. Department of the Interior, the Water Resources Research Institute of Oregon State University, and the Sea Grant College Program of Oregon State University. Some support, advice, and encouragement for our work with tracers for toxic organic chemicals was furnished by Dr. D. J. Baumgartner and the staff of the Corvallis Environmental Research Laboratory of the USEPA.

### *Literature Cited*

1. Haley, T. J. *J. Pharm. Sci.* **1965**, *54*, 683.
2. Kyker, G. C.; Cress, E. A. *A.M.A. Arch. Ind. Health* **1957**, *16*, 475.
3. Graca, J. G.; Davison, F. C.; Feavel, J. B. *Arch. Environ. Health* **1962**, *5*, 437.
4. Dzata, F., M.S. Thesis, Oregon State Univ., 1981.
5. Kruger, P. "Principles of Activation Analysis"; Wiley-Interscience: New York, 1971; pp. 482-503.
6. Schmotzer, K.; Jester, W.; Parizek, K. *J. Hydrol.* **1973**, *20*, 217.
7. Jester, W. A.; Uhler, K. A. "Identification and Evaluation of Water Tracers Amenable to Post-Sampling Neutron Activation Analysis"; Pennsylvania Univ.: Philadelphia, 1974; Vol. 85.
8. Behrens, H.; Moser, H.; Wildner, E. *J. Radioanal. Chem.* **1977**, *38*, 491.
9. Dahl, J. B. "Water Pollution Studies by Means of Inactive Indium Tracer and Activation Analysis," *Isot. Hydrol.* **1970**.
10. Craft, T. F.; Eicholz, G. C. *Environ. Lett.* **1975**, *9*, 307.
11. Van Dalen, A.; Wijkstra, J. *J. Radioanal. Chem.* **1977**, *38*, 223.
12. Channell, J. K.; Kruger, P. "Modern Trends in Activation Analysis," *Natl. Bur. Stand. (U.S.), Spec. Publ.* **1968**.
13. Hansen, P. J. Ph.D. Thesis, Oregon State Univ., 1970.
14. Schmitt, R. A. "A Study of Pollutant Flow in the Willamette River and Its Tributaries Using the Rare-Earth Spiking Method," Oregon State Environmental Health Science Center Project No. 9, 1968.
15. Shum, Y. S.; Loveland, W. D.; Hewson, E. W. *JAPCA.* **1975**, *25*, 1123.
16. Kuhn, W. K. G.; Alps, W.; Korn, D. In "Measurement, Detection and Control of Environmental Pollutants"; IAEA: Vienna, 1976.
17. Loveland, W. "Hydrospheric Trace Elements and Their Application in Tracing Water Pollutants," Oregon State University Report, WRR1-59, 1978.
18. McCown, D. L. *Water Res.* **1979**, *13*, 1065.
19. Shum, Y. S.; Loveland, W. D. *Atmos. Environ.* **1974**, *8*, 645.
20. Ghannam, L.; Loveland, W. to be published.

RECEIVED September 4, 1980.

- A**
- Accelerator, drop . . . . . 521
- Accelerators, radioisotope dating  
with . . . . . 520–521
- Acetate, aminoxy . . . . . 281
- Acetylation of ethanol . . . . . 40
- Acetylene formation . . . . . 8–9
- Acetylene reduction technique . . . . . 235
- Aconitase . . . . . 391
- Activation, nuclear recoil chemical . . . . . 147
- Acyl carnitine transport system . . . . . 443
- Addition–elimination of thermal Cl  
atoms . . . . . 141
- Adenocarcinoma, metastatic . . . . . 373
- Adenosine triphosphate (ATP) production . . . . . 475
- Aerobacter aerogenes* . . . . . 320
- Aerobacter glutinosa* . . . . . 335
- Aerosols, PIXE analyses . . . . . 518
- Air pollutant tracing . . . . . 529–530
- Airborne particles . . . . . 500–502
- Mössbauer spectra . . . . . 501f
- Alanine . . . . . 326, 332–336, 391, 392, 396
- dehydrogenase . . . . . 285
- formation . . . . . 285
- radioactive . . . . . 278–279
- Albumin, denaturation . . . . . 410
- Algae, blue–green . . . . . 237, 239
- ALICE, particle evaporation code . . . . . 252
- Alkali halides, surface ionization for  
detection . . . . . 180
- Alkyl replacement . . . . . 107, 109f
- Alkylation of *t*-butylbenzene with  $CT_3^+$ ,  
decay ions . . . . . 45–48
- Allantoic acid . . . . . 321, 329–330
- Allantoin . . . . . 321, 329–330
- Allene formation . . . . . 16–17
- Allophane . . . . . 499
- Alnus glutinosa* . . . . . 320, 332
- assimilation of  $^{13}NH_4^+$  by roots and  
    nodules . . . . . 330–332
- Alpha particles . . . . . 514
- spectra of 18-MeV . . . . . 514f
- Aluminum oxide substrates, spectra  
from metal layers . . . . . 513f
- L-[Amide- $^{13}N$ ]asparagine . . . . . 395, 398
- L-[Amide- $^{13}N$ ]Glutamine . . . . . 391, 392, 393, 398
- Amide nitrogen . . . . . 278, 284
- $NH_4^+$  . . . . . 275f
- Amino acids . . . . . 439
- derivatized with *o*-phthaldialdehyde . . . . . 326f
- distribution of  $^{13}N$  . . . . . 276f–278f, 280f, 281f
- enzymatic synthesis . . . . . 263
- identification of radioactive . . . . . 272–274
- isomer . . . . . 390
- metabolic pathways, ammonia . . . . . 444f
- Amino acids (*continued*) . . . . . 246
- $^{13}N$ - . . . . . 390
- transport . . . . . 390
- L-Amino acids,  $^{13}N$ -labeled . . . . . 389–402
- Amino sugars . . . . . 392
- Aminoxy acetate . . . . . 281
- Ammonia . . . . . 263, 439, 444
- and amino acid metabolic pathways . . . . . 444f
- in the brain,  $^{13}N$  tracer . . . . . 371
- uptake and metabolism . . . . . 369–386
- lipid solubility . . . . . 373
- metabolism, two-pool hypothesis . . . . . 370–371
- methylamine uptake . . . . . 462
- for myocardial studies, labeled . . . . . 443–447
- $^{13}N$  . . . . . 244
- as neurotoxin . . . . . 369–370
- uptake, possible mechanisms . . . . . 460f
- Ammonium acetate infusion . . . . . 376
- and amide nitrogen . . . . . 275f
- assimilation, dinitrogen reduction . . . . . 319f
- assimilation, synthesis, and  
    transport . . . . . 321–322
- fluoride . . . . . 264
- initial metabolism . . . . . 286f, 291f
- $N_2$ -derived, metabolism . . . . . 287–292
- nitrogen reduction and primary  
    assimilation . . . . . 318–321
- primary assimilation and metabolism . . . . . 320f
- reduction of nitrate by microbial  
    cultures . . . . . 311–312
- reduction of nitrate in natural samples . . . . . 312
- salts . . . . . 370, 375
- transport . . . . . 456
- uptake . . . . . 459–462
- Amorphous minerals . . . . . 497–499
- Anabaena cylindrica* . . . . . 331
- assimilation of  $^{13}NO_2^-$  and  $^{13}NO_3^-$  . . . . . 283
- $N_2$ -grown . . . . . 270f
- Anacystis nidulans* . . . . . 321
- Angle, velocity, contour diagram . . . . . 199f
- Angular distributions . . . . . 200f
- Anhydrase, carbonic . . . . . 428
- Animal studies . . . . . 353–354
- Anions and cations membrane  
transport systems . . . . . 455f
- Anticonvulsants . . . . . 432
- Antimony sulfide minerals . . . . . 497
- Antitumor activity . . . . . 351
- mechanism . . . . . 363
- Arenes reaction with  $CT_3^+$  decay ions . . . . . 44
- Arginine . . . . . 475
- labeling . . . . . 285–286
- radioactive . . . . . 279
- Artifacts, archaeological . . . . . 504
- Ascorbic acid . . . . . 264

- Asparagine . . . . . 332-336, 392, 396  
 biosynthesis . . . . . 323  
 Aspartate . . . . . 332-336, 376  
 formation . . . . . 285  
 radioactive . . . . . 278  
 Aspartic acid . . . . . 391, 392  
*Aspergillus nidulans* . . . . . 462  
 Assimilation (of)  
<sup>13</sup>N by intact cyanobacteria . . . . . 274-286  
<sup>13</sup>N, metabolic routes . . . . . 283-286  
<sup>13</sup>NH<sub>4</sub><sup>+</sup> . . . . . 272, 278-281  
 by cyanobacteria, radioactive  
 constituents . . . . . 282*t*, 283*t*  
 by heterocysts . . . . . 286-288  
<sup>13</sup>NO<sub>3</sub><sup>-</sup> and <sup>13</sup>NO<sub>2</sub><sup>-</sup> . . . . . 281-283  
 Atomic absorption . . . . . 519  
 Atoms, free, chemical generation . . . . . 21-26  
 Australia . . . . . 515  
 Autoclaving . . . . . 306  
 Azaserine . . . . . 278, 281, 284  
*Azotobacter vinelandii* . . . . . 461

## B

- Bacillus* . . . . . 312  
 Bacteria . . . . . 235, 296  
 NO<sub>3</sub><sup>-</sup> transport systems . . . . . 455  
 Bacterial membranes . . . . . 460  
 Bacterial sporulation . . . . . 458  
 Barley plants . . . . . 234  
 Basalt continental . . . . . 505, 506  
 Basalt, deep sea . . . . . 505  
 BCNU (*see*  
 1,3-bis(2-Chloroethyl)-1-nitrosourea)  
 Beam foil spectroscopy . . . . . 521  
 Beam studies using radiotracer techniques,  
 crossed . . . . . 179-205  
 Benzene, multitritiated . . . . . 35-36  
 Biotite, Mössbauer spectra . . . . . 506  
 Biotite oxidation . . . . . 505  
 Black Sea . . . . . 503  
 Blood  
 -brain barrier . . . . . 460  
 cell maturation, red . . . . . 459  
 flow . . . . . 432  
 autoregulation . . . . . 422  
 cerebral . . . . . 373, 420  
 volume . . . . . 421-422  
 Bone scanning . . . . . 439  
 Boron nitride . . . . . 234  
 Brain . . . . . 400  
 blood-, barrier . . . . . 460  
 CO content . . . . . 431  
 computer simulation of uptake and loss  
 of label . . . . . 381*f*, 382*f*  
 -CSF barrier . . . . . 384  
 glucose analogs for metabolic  
 studies . . . . . 440-441  
 glutamate compartments . . . . . 384-385  
 glutamine synthetase . . . . . 379, 384  
 sheep . . . . . 393  
 hexokinase . . . . . 440  
 localization of tumors and  
 infarcted regions . . . . . 372-373  
 metabolic pools . . . . . 369

Brain (*continued*)

- NH<sub>3</sub> metabolism,  
 two-pool hypothesis . . . . . 370-371  
<sup>13</sup>N as tracer for NH<sub>3</sub> . . . . . 369-386  
 [<sup>13</sup>N]ammonia  
 mechanism of uptake . . . . . 373-376  
 metabolism . . . . . 376-379  
 model of uptake . . . . . 379-384  
 uptake index . . . . . 374*t*-375*t*  
 uptake and metabolism by . . . . . 372-373  
 nitrogen balance . . . . . 385  
 rhesus monkey . . . . . 372  
 radioactivity . . . . . 382  
 whole, studies . . . . . 372  
 Bromine atom velocity . . . . . 201  
 Bromine, trace quantities . . . . . 180  
 1-Bromopentadecane . . . . . 411, 412  
 Bronze coin, Mössbauer spectrum . . . . . 507*f*  
 1,3-Butadiene, reactions with recoil  
<sup>11</sup>C atoms . . . . . 60-61  
 1,3-Butadiene, reactions with recoil  
<sup>31</sup>Si atoms . . . . . 14, 62-63  
*t*-Butylbenzene alkylation with CT<sub>3</sub><sup>+</sup>  
 decay ions . . . . . 45-48  
*t*-Butyltoluenes . . . . . 48

## C

- <sup>11</sup>C (*see* Carbon-11)  
<sup>12</sup>C (*see* Carbon-12)  
<sup>14</sup>C (*see* Carbon-14)  
 Cadmium reduction procedure . . . . . 303-304  
 Caging density threshold . . . . . 91  
 Calcium . . . . . 514  
 Calculation  
 classical trajectory . . . . . 195  
 distorted-wave Born approximation . . . . . 195  
 theoretical, in recoil chemistry . . . . . 19-21  
 CAM (*see* Chloramphenicol)  
 Canada, lake sediments . . . . . 503  
 Carbamate analog of BCNU . . . . . 353  
 Carbamyl phosphate . . . . . 475  
 Carbenes . . . . . 55  
 trapping . . . . . 82  
 Carbides, inorganic . . . . . 262  
 Carbides, metallic . . . . . 391  
 Carbon . . . . . 237  
 assimilation  
 and metabolism in N<sub>2</sub>-fixing  
 plants . . . . . 322-323  
 in N<sub>2</sub>-fixing plants, nitrogen . . . . . 317-337  
 in roots and nodules . . . . . 322-323, 333-336  
 in soybean . . . . . 337*f*  
 containing compounds, deuterons 261-263  
 dioxide . . . . . 262  
 fixation . . . . . 333-336  
<sup>15</sup>O-labeled . . . . . 433  
 disulfide, exchange reactions with sulfur  
 atoms . . . . . 22  
<sup>18</sup>F dissociation . . . . . 105  
 ground state atoms, collisional removal 23*t*  
 hydrogen insertion . . . . . 16  
 monoxide formation from carbon  
 atoms . . . . . 17-18  
 target thickness vs. <sup>13</sup>N recoil  
 charge fractions . . . . . 71*f*

- Carbon-11..... 390  
 atom, recoil, reactions with  
   1,3-butadiene..... 60-61  
 -carboxyhemoglobin..... 421  
 and  $^{18}\text{F}$ , radiopharmaceuticals labeled  
   with..... 407-415  
 -glucose..... 422, 423f, 438  
 glucose-6-phosphate..... 424  
 -labeled  
   carboxyhemoglobin..... 422  
   2-deoxy-D-glucose..... 438  
   methyl albumin..... 422  
   palmitate..... 407-415  
   palmitic acid..... 411, 438, 442  
     high-pressure liquid  
     chromatography..... 414-415  
     synthesis..... 410-414  
 short-term studies using  $^{13}\text{N}$ ..... 317-337
- Carbon-12  
 bombardments, isotope yields..... 254f  
 (d,n)  $^{13}\text{N}$ , reaction parameters..... 69t  
 (n,2n)  $^{11}\text{C}$  transformation..... 61
- Carbon-14  
 arginine, guanido-..... 481  
 carbon dioxide..... 473  
 in charcoal and graphite..... 521f  
 labeled products after exposure to  
    $^{13}\text{NH}_4^+$ ..... 335f  
   by plantarum and nicotinic acid..... 488t  
   production by *L. casei*..... 482t  
   production by *L. leichmannii*..... 476t  
 Carboxylation of phosphoenol-pyruvate..... 323  
 Carotid artery infusion of  $^{13}\text{N}$   $\text{NH}_3$  into  
   rats..... 378-379
- Cascading collision sequence..... 159  
 Cascading falloff simulation, hot atom.. 116f  
 Cassiterite..... 497  
 Catabolism, oxidative, of purines..... 330
- Cation(s)  
 and anions, membrane transport  
   systems..... 455f  
 exchange chromatography..... 390  
 gaseous multitruncated..... 36-38  
 gaseous phenylum..... 39-40  
 multitruncated decay, liquid-phase  
   reactivity..... 43-50  
 multitruncated free methyl, gas-phase  
   reactivity..... 40-43  
 systems, monovalent..... 458
- Caustic soda..... 234
- Cerebral  
 blood flow..... 373, 433  
 distribution of label derived from  
    $^{13}\text{N}$   $\text{NH}_3$ ..... 379f  
 glucose utilization..... 422  
 lactic acidosis..... 376  
 metabolic rate..... 384
- Cerebrospinal fluid..... 370
- Cesium atoms reactions with  
   TBr molecules..... 183-187
- Charcoal..... 234  
 and graphite, measurement of  $^{14}\text{C}$ ... 521f
- Charge distribution in  $^{13}\text{N}$  ions..... 67-75
- Charge equilibrium and target  
 thickness..... 72-73
- Chemiluminescence relative rate  
 coefficients vs.  $\text{H}^{18}\text{F}$  product  
 analysis..... 218t
- Chloramphenicol..... 464-466f
- Chloride..... 455
- Chlorine  
 atoms, thermal, addition-elimination.. 141  
 -for-Cl replacement reaction..... 140  
 and hydrogen donors, nonthermal  
   reactivities..... 212t  
 reactivity to hot  $^{18}\text{F}$  atoms..... 209-212  
 -scavenged  $\text{CF}_4$  and  $\text{C}_2\text{F}_6$ ..... 86-88  
 scavenger..... 83
- 1,3-bis(2-Chloroethyl)-1-nitrosourea. 351-366  
 carbamate analog..... 353  
 decomposition rate constants..... 360f  
 metabolism..... 364
- Chloroform..... 262
- 2-Chloro-4-methylvaleryl chloride..... 140
- Chloroplasts..... 460
- Chromatograms of  $^{13}\text{N}$ -labeled  
 radiochemicals..... 240f
- Chromatography, cation exchange..... 390
- Citrate synthase..... 391
- Citric acid cycle..... 448
- Citrulline..... 322, 335  
 labeling..... 285-286  
 radioactive..... 279
- Classical trajectory studies..... 202, 203
- Clostridium*  
*acidum*..... 391  
*pasteurianum*..... 461
- Cobalt..... 506
- Cobalt-60 irradiation..... 306
- Collision(s)  
 cascading, sequence..... 159  
 dynamics..... 132-133, 182  
 energy(ies)..... 194f, 201  
 fraction law..... 211  
 momentum transferring..... 208
- Collisional dissociation..... 133
- Collisional transfer..... 126
- Computer simulation of label  
 in rat brain..... 381f, 382f
- Configuration geometries, critical..... 149
- Contamination, nonthermal..... 221
- Coronary artery disease..... 438
- Correlation diagrams  
 C +  $\text{O}_2$  and  $\text{CO} + \text{O}$  via  $\text{CO}_2$ ..... 19f
- Cross-section mapping..... 134-135
- Crossed beam  
 apparatus..... 190f  
 mass spectrometric experiments..... 182  
 studies..... 202
- Curvature differences..... 173
- Curvature matching..... 177t
- Cyanobacteria, intact, assimilation of  
 $^{13}\text{N}$ ..... 274-286
- Cyanobacteria, nitrogen metabolism 269-293
- Cyanocobalamin..... 475  
 response of *L. leichmannii*..... 477f
- Cyclobutane  
 chemical activation..... 127-128  
 excited, collisional energy transfer... 130t  
 multitruncated..... 35-36
- Cyclopropylidene intermediate..... 16



- Cyclopropylmethylene ..... 8  
 Cyclotron(s) ..... 238, 521
- D**
- Deactivation  
 behavior, unit ..... 160  
 mechanism, heterogeneous ..... 164  
 process, cascade ..... 160f
- Decay  
 $\beta^-$ , of tritium ..... 34  
 $\beta^-$ , of  $CT_4$  ..... 58  
 correction factor ..... 463  
 of  $CT_4$  ..... 42-43
- Ions  
 $CT_3^+$ , reaction with arenes ..... 44  
 $CT_3^+$ , reactions with  
 halobenzenes ..... 42t-43t  
 $C_4X_7^+$ , gas-phase reactions ..... 38t-39t  
 of multitritiated cyclobutane ..... 37  
 positron ..... 515  
 radioactive, of multitritiated  
 molecules ..... 33-50  
 reactions of multitritiated cations ..... 43-50  
 synthesis of multitritiated compounds ..... 58
- Decomposition  
 branching ratios, substitution  
 product ..... 106t-107t  
 ethane ..... 149  
 measurements, in vitro  
 aqueous ..... 355, 358-363  
 rate constants  
 of BCNU ..... 360f  
 of *N,N'*-dimethyl-*N*-nitrosourea ..... 361f  
 of nitrosocarbaryl ..... 362f  
 sequential, of excited  
 fluoromethane ..... 126-127  
 threshold, critical ..... 129  
 unimolecular  
 labeled fluoroethane ..... 92-94  
 rate constant ..... 130, 155  
 rotational excitation ..... 147, 152-155  
 statistical models ..... 148
- Degenerate rearrangement of  
 multitritiated ions ..... 38-40
- Dehydrogenase, glutamic ..... 444
- Denitrification  
 intermediates ..... 307-311  
 kinetics ..... 236  
 NO exchange from ..... 310t  
 $N_2O$  and  $N_2$  produced ..... 310t  
 rates ..... 304-307  
 studies, use of  $^{15}N$  ..... 295-314
- 2-Deoxy-2-fluoro-D-glucose ..... 440  
 -1-phosphate ..... 441  
 -6-phosphate ..... 440
- 3-Deoxy-3-fluoro-D-glucose ..... 438
- Detectors, calibration ..... 301-302  
 Detectors and ovens, geometry ..... 185f
- Deuteron(s)  
 on carbon-containing compounds ..... 261-263  
 8-MeV ..... 234  
 reaction with  $T_2$  molecules ..... 187-196  
 stripping ..... 195
- Devarda's alloy-NaOH mixture ..... 371-372, 392
- Diatomic molecules as diagnostic reagents 18
- Dichloroethylene,  $^{36}Cl$ -labeled ..... 56  
 Diffusion, Fick's law ..... 430  
*N,N'*-dimethyl-*N*-nitrosourea,  
 decomposition  
 rate constants ..... 361f
- Dinitrogen fixation ..... 270
- Dinitrogen reduction and  $NH_4^+$   
 assimilation ..... 319f
- Dispersion coefficients ..... 523
- Dissociation, collisional ..... 204
- Dissociation, reverse ..... 165
- Distorted-wave Born approximation ..... 195
- Divalent atoms reactions ..... 3-7
- Dopamine-receptors ..... 408
- DWBA (Distorted-wave Born  
 approximation) ..... 195
- Dyes, fluorescent ..... 523
- Dyprosium  $\beta$ -diketonates ..... 531
- Dyprosium(III) trisacetylacetonate  
 trihydrate ..... 531
- Dyprosium(III) trisdibenzoylmethane  
 monohydrate ..... 531
- E**
- Earthenware ..... 504
- Elastic collision diameters, realistic  
 potential ..... 167
- Electric discharge, generation ..... 22-24
- Electrophoretograms of *A. cylindrica*,  
 radioactivity from  $^{15}N$  ..... 273f, 274f
- Elimination, HF, critical configuration  
 models ..... 165
- Emission spectrography ..... 519
- Encephalopathy ..... 369
- End-on attack ..... 17
- Energy  
 collision ..... 194f  
 dependence ..... 171  
 distribution(s) ..... 107, 109f  
 for F-for-F activated labeled  
 fluoromethane ..... 102-105  
 for fluoroethane primary  
 reactions ..... 106-110  
 recoil ..... 200f  
 internal, of excited molecules ..... 127  
 levels for atomic nitrogen ..... 266t  
 potential, surfaces ..... 182  
 randomization, intramolecular ..... 153  
 rotational ..... 203  
 transfer  
 calculations, theoretical ..... 115-118  
 collisional, from excited  
 cyclobutane ..... 130t  
 from F-for-X activated  
 molecules ..... 110-115  
 intramolecular, in excited molecules 131  
 phenomenological approach ..... 110-115  
 unimolecular, radiotracer  
 studies ..... 157-178  
 vibrational ..... 157, 160, 203
- Enterobacter* ..... 312
- Enterobacteriaceae* ..... 311
- Environment, monitoring of chemical  
 changes ..... 505-507

- Environmental applications of Mössbauer spectroscopy . . . . . 495–508  
 control . . . . . 234  
 samples, characterization . . . . . 497–504  
 samples, ion beam analysis . . . . . 511–522  
 science, stable activable tracers . . . . . 523–534
- Epithermal nonequilibrium model . . . . . 221
- Equation, Henderson–Hasselback . . . . . 375
- Equation, steady-state stochastic master . . . . . 164
- Erwinia* . . . . . 312
- Erythrocytic folate levels, reproducibility . . . . . 484*t*
- Escherichia coli* . . . . . 312, 395, 459–460
- Esterases, hydrolytic action . . . . . 365
- Estrogen receptors . . . . . 408
- Estuarine tracers, lanthanides . . . . . 525
- Ethane  
 bath gas . . . . . 172*f*, 173*f*, 176*f*  
 high-pressure rate constants . . . . . 168*t*  
 decomposition . . . . . 149  
 molecules . . . . . 149*t*
- Ethanol . . . . . 262, 264  
 acetylation . . . . . 40
- Ethylene formation . . . . . 13–14
- N-Ethylmaleimide inhibition . . . . . 464
- Euglena* . . . . . 459
- Europe and Canada lake sediments . . . . . 503
- Evaporation, bulk element, metal vapors by . . . . . 24–26
- Exchange reactions of atoms with CS . . . . . 22
- Excitation  
 product internal . . . . . 203  
 product translational . . . . . 203  
 rotational, in unimolecular decomposition . . . . . 147–155
- Excited molecule(s)  
 dynamics . . . . . 125–133  
 intramolecular energy transfer . . . . . 131  
 polyatomic . . . . . 132
- Exponential model . . . . . 171*f*, 173*f*, 175*f*, 176*f*
- F**
- F (See Fluorine)
- <sup>19</sup>F (see Fluorine-18)
- Fatty acids . . . . . 438, 439  
 fluorinated . . . . . 448  
 for myocardial studies, labeled . . . . . 441–443
- 2-FDG (2-Deoxy-2-fluoro-D-glucose) . . . . . 440
- Ferric polymer gel . . . . . 503
- Fiber production . . . . . 234
- Fick's law for diffusion . . . . . 430
- Flow rates . . . . . 523
- Flunitrazepam . . . . . 409
- Fluorine . . . . . 514  
 -abstraction . . . . . 64  
 atoms, thermal abstraction reactions . . . . . 135–136  
 -for-βH substitution . . . . . 94  
 for fluorine  
 excitation distributions . . . . . 104*f*–106*f*  
 substitution . . . . . 99–100  
 in fluoroethane . . . . . 91, 93*f*  
 -to-HF reactions . . . . . 88  
 yields, nonthermal . . . . . 213*t*, 214*f*
- Flourine (continued)  
 -for-hydrogen substitutions . . . . . 107, 108*f*  
 thermal hydrogen abstraction and olefinic addition reactions by atomic . . . . . 223*t*, 228–230*t*  
 -for-X activated molecules, energy transfer . . . . . 110–115
- Fluorine-18 . . . . . 390, 442  
 atoms, reactivity of Cl<sub>2</sub> toward . . . . . 209–212  
 atoms, recoil reactions with gas-phase halocarbons . . . . . 79–119  
 contribution to filter radioactivity . . . . . 301*t*  
 labeled 2-deoxy-2-fluoro-D-glucose . . . . . 422, 423*f*, 438  
 -labeled superexcited molecules . . . . . 102–118  
 loss relative rate coefficients vs. H<sup>18</sup>F product analysis . . . . . 219*t*  
 radiopharmaceuticals labeled with <sup>11</sup>C . . . . . 407–415
- Fluorocyclopropanes, substituted, synthesis . . . . . 58–60
- 3-Fluoro-3-deoxyglucose . . . . . 408, 409
- Fluoroethane  
 C<sub>1</sub> and C<sub>2</sub> product distributions . . . . . 84*t*–85*t*  
 double substitution . . . . . 96  
 F-for-F substitution . . . . . 91, 93*f*  
 scavenged, H<sub>2</sub>S . . . . . 88, 89*t*  
 labeled, unimolecular decomposition . . . . . 92–94  
 mass-balance testing . . . . . 95*t*  
 primary reaction, energy distributions . . . . . 106–110  
 reaction mechanism . . . . . 88, 97–99
- Fluoroethanol . . . . . 408
- Fluoromethane  
 excited, sequential decomposition . . . . . 126–127  
 labeled, energy distribution for F-for-F substituted . . . . . 102–105  
 reaction mechanism . . . . . 99–102
- Fluoroscein and tetracycline derivatives, radioiodine labeled . . . . . 439
- 1-Fluorosilacyclopenta-3-ene . . . . . 63–64
- Folacin level in food . . . . . 485
- Folate . . . . . 471–492  
 levels, erythrocyte . . . . . 482, 484*t*  
 levels, serum . . . . . 482  
 radiometric microbiologic assay . . . . . 480–485
- Folic acid (PGA) . . . . . 481, 483*f*
- Food production . . . . . 234
- Forestry, herbicides used . . . . . 532
- Formic acid . . . . . 264
- Free fatty acid, myocardial . . . . . 443
- G**
- Gamma ray activation for light elements . . . . . 515
- Gas analysis, <sup>13</sup>N . . . . . 299
- Gas stripping system . . . . . 297–298
- Gaussian model (s) . . . . . 171*f*–176*f*, 530*f*
- Geochemical applications of Mössbauer spectroscopy . . . . . 495–508
- Geochemical samples, characterization . . . . . 497–504
- Germanium, ground state atoms, collisional removal . . . . . 23*t*
- Germanium vapor . . . . . 24

- Germylenes ..... 25  
 Glass samples, proton spectra ..... 516f  
 Glial cells ..... 384  
 Glioma ..... 373  
 Glucose ..... 438, 439  
   analogs for brain metabolic studies ..... 440-441  
   analogs for myocardial studies, labeled ..... 441  
   metabolic pathways, model ..... 440f  
   utilization, cerebral ..... 422  
 Glutamate ..... 321, 326, 332-336, 376, 396  
   compartments in the brain ..... 384-385  
   dehydrogenase ..... 320, 376-378, 392, 463  
   metabolism ..... 370  
   -oxaloacetate transaminase ..... 396  
   -pyruvate transaminase ..... 391  
   radioactive ..... 276-278, 284  
   synthetase ..... 284, 463  
     cellular localization ..... 289-291  
 Glutamic acid ..... 391, 444  
   dehydrogenase ..... 285  
 Glutamine ..... 321, 326, 332-336, 370, 375, 392, 396, 444  
   amidotransferases ..... 392  
   radioactive ..... 276-278, 284  
   synthetase ..... 284, 288, 376-377, 444, 465  
     cellular localization ..... 289-291  
     glutamate synthetase pathway ..... 321  
     reaction ..... 376-378  
 Glycine max ..... 321, 322  
 Glycogen ..... 441  
 Goethite ..... 503  
 Gold ..... 504  
 Graphite ..... 234  
   measurement of  $^{14}\text{C}$  ..... 521f  
 Greenhouse effect ..... 296  
 Grignard reagent of  
   1-bromopentadecane, synthesis ..... 411  
 Guanido- $^{14}\text{C}$ -arginine ..... 475, 481
- H**
- Halobacter halobrium* ..... 458  
 Halobenzene(s)  
   methylation with toluene ..... 46t-47t  
   reactions with  $\text{CT}_3^+$  ..... 42t-43t, 48t-49t  
   tritiated ..... 42  
 Halocarbons, reactions with recoil  $^{18}\text{F}$   
   atoms ..... 79-119  
 Haloperidol ..... 408  
 Heart ..... 398, 400  
   hexokinase ..... 441  
    $^{13}\text{N}$  in rat ..... 400f  
 Helium stripping gas ..... 305  
 Helium 3 bombardment(s) ..... 255-257  
   isotope yields ..... 254f  
 Hematite ..... 501  
 Hematocrit ..... 422  
 Hemolysate samples assayed by  
   RMA ..... 484f, 487f  
 Hemolysate samples assayed  
   turbidimetrically ..... 484f  
 Herbicide dispersal ..... 532  
 Herbicides used in forestry ..... 532  
 Heterocysts ..... 269, 270f
- Heterocysts (*continued*)  
   assimilation of  $^{13}\text{NH}_4^+$  ..... 286-288  
   destruction ..... 290f  
   fixation of  $^{13}\text{N}_2$  ..... 286-288  
 Hexafluoroethane bath  
   gas ..... 168f, 170f, 171f, 175f  
   high-pressure rate constants ..... 167t  
 Hexane formation ..... 7-8  
 Hö-ei Crater ..... 498  
   Mössbauer spectra of obsidian from ..... 499f  
 Hot atom cascading falloff simulation ..... 116  
 Hydrazine ..... 266  
 Hydrocarbons,  $\text{C}_1$ - $\text{C}_6$ , nonthermal  
   reactivities ..... 213  
 Hydrogen  
   -abstracton ..... 64, 88, 142  
   thermal ..... 207-230  
     by atomic fluorine ..... 223t, 228-230t  
   donors, nonthermal reactivities ..... 212t  
   -exchange reaction ..... 181, 182, 187-196  
   fluoride  
     -eliminations ..... 95  
     labeled product  
       analysis ..... 218t, 219t, 220t  
     reaction with  $\text{T}_2$  molecules ..... 187-196  
     sulfide-scavenged  
       fluoroethane. 81t, 82t, 84t, 85t, 88, 89t  
 Hyperammonemia, hereditary ..... 370
- I**
- Ianthanides as estuarine tracers ..... 525  
 Igneous rocks ..... 497  
 Imipramine ..... 409  
 Indium ..... 525  
 Infrared chemiluminescence studies ..... 182, 202  
 Insecticides, carbamate ..... 352, 365  
 Insecticides, carbaryl ..... 352  
 Interaction processes, distributions for  
   direct ..... 194f  
 Intermediates  
   via nuclear recoil methods ..... 54-56  
   reactive, formation ..... 4-6  
   recoil reaction ..... 7-15  
 Iodine atoms and ions, recoil ..... 143  
 Iodine-123 labeled 16-iodo-9-hexadecenoic  
   acid ..... 438  
 $\omega$ -Iodofatty acids ..... 442  
 17-Iodo-heptadecanoic acid ..... 438  
 Ion(s)  
   analysis,  $^{13}\text{N}$  ..... 299  
   beam(s)  
     analysis of environmental  
     samples ..... 511-522  
     methodologies ..... 512-521  
     producing  $^{11}\text{C}$ ,  $^{13}\text{N}$ ,  $^{15}\text{O}$ , and  
      $^{18}\text{F}$  ..... 251-259  
   gaseous multitritiated, degenerate  
   rearrangement ..... 38-40  
   scattering ..... 512-513  
   thermal reactions ..... 142-144  
 Ionization chamber, automated ..... 474f  
 Ionization, surface, for alkali halides  
   detection ..... 180  
 Iron ..... 495, 497  
   chemical states ..... 500  
   components intensities ..... 503f

- Iron (continued)**  
 magnetic..... 498  
 metallic..... 501  
 oxidation state..... 500  
 oxides..... 501, 502  
 and hydroxides in soils..... 499  
**Iron(II), paramagnetic**..... 498, 500, 502  
 and magnetic contents..... 505*f*  
**Iron(III)**..... 455, 498, 500, 502  
**Ischemia**..... 373  
**Isocitrate dehydrogenase**..... 391  
**Isomer shift**..... 498  
**Isotope(s)**  
 dilution experiments with <sup>13</sup>N..... 307-311  
 radioactive..... 342  
 yields  
 for beams on H<sub>2</sub>O targets..... 253*t*  
 from <sup>12</sup>C bombardments..... 254*f*  
 from <sup>3</sup>He bombardments..... 254*f*  
 from proton bombardments..... 253*f*
- K**
- α-Keto acids**..... 394  
 beef liver glutamate dehydrogenase.. 394*t*  
**α-Ketoglutarate**..... 394, 444  
**Kidneys**..... 398  
**Kinetic(s)**  
 behavior for abstraction..... 136*f*  
 denitrification..... 236  
 falloff, bimodal..... 114-115  
 of high energy recoil reactions... 138-139  
 recoil parameter characterization . 133-139  
 theory, steady-state hot atom..... 216  
**Klebsiella**..... 312  
*pneumoniae*, nitrate transport... 341-348  
*pneumoniae* radioactivity..... 347*t*
- L**
- Label migration**..... 39  
**Labeled**  
 compounds, HPLC system..... 325  
 tracers, exposure of plants..... 324-325  
 tracers, production..... 323-324  
**Lactic acid**..... 407  
**Lactobacillus**..... 475, 485  
*casei*..... 80  
 production of <sup>14</sup>CO<sub>2</sub>..... 482*t*  
*leichmannii*..... 475  
 production of <sup>14</sup>CO<sub>2</sub>..... 476*t*  
 response to CN-Cbl..... 477*f*  
 vitamin-B<sub>12</sub> levels assayed..... 478*f*  
*plantarum*..... 485  
 response to nicotinic acid..... 489*f*
- Lake**  
 Castle..... 305  
 Michigan..... 502  
 sediment(s)  
 in Europe and Canada..... 503  
 eutrophic..... 312  
**Legume nodules**..... 319*f*  
**Lipid solubility of NH<sub>3</sub>**..... 373  
**Lithium carbonate target**..... 302-303  
**Liver**..... 370, 398
- Liver (continued)**  
 bovine, glutamate dehydrogenase ... 393, 394*t*  
 disease..... 369  
 microsomes..... 364  
**Lung homogenates**..... 364  
**Lupinus albus**..... 321  
**Lyophilization to shorten assay**  
 time..... 486*t*-487*t*  
**Lyophilization of test organisms**..... 485
- M**
- Magma, molten systems**..... 498  
**Magnesium**  
 dianion..... 454, 455  
 tracer studies..... 453-467  
 nitride, <sup>14</sup>N(n,p)<sup>14</sup>C transmutation . 61-62  
 transport..... 459  
**Magnesium-28**..... 456  
**Magnetic components**..... 500  
**Malate**..... 488  
**Manganese dication**..... 455  
**Marine environment, stable activable tracers**..... 531  
**Mass**  
 -balance testing of fluoroethane..... 95*t*  
 -spectrometric detection..... 188  
 spectrometry, crossed beam..... 182  
**Mechanistic studies with polyvalent atoms**..... 3-28  
**Mechanistic studies with radioactive decay of multitruncated molecules**..... 33-50  
**Melamine plastic powder**..... 235  
**Metabolic pathways**..... 234  
**Metabolic routes of <sup>13</sup>N assimilation**..... 283-286  
**Metal**  
 carbides..... 371  
 chelates..... 531  
 corrosion..... 506-507  
 evaporation-cocondensation..... 24-26  
 layers on Al<sub>2</sub>O<sub>3</sub> substrates, spectra... 513*f*  
 vapors by bulk element evaporation. 24-26  
**Metallurgical processors**..... 529  
**Metalware**..... 504  
**Metamorphic rocks**..... 497  
**Methane**..... 262, 371  
 irradiation procedure..... 391  
 -T<sub>1</sub>, radioactive decay..... 33  
**Methanol**..... 262  
**Methionine**..... 409  
**Methionine sulfoximine** . 278, 281, 284, 371, 378, 448, 464  
 poisoning..... 375  
 L-Methionine-DL-sulfoximine 463, 465*f*, 466*f*  
**Methyl bromide**..... 262  
**Methyl chloride**..... 262  
**2-Methyl-3-chloropropene**..... 143  
**5-Methyl-H<sub>4</sub>PteGlu**..... 483*f*  
**N-5-Methyl-FH<sub>4</sub> added to plasma and hemolysates, recovery**..... 485*t*  
**Methylamine**..... 461  
 active transport system..... 462  
 uptake by ammonia..... 462  
**Methylating reagent**..... 50  
**Methylation of toluene**..... 48  
 with halobenzenes..... 46*t*-47*t*

- Methylene formation . . . . . 7  
 Methylenimine, formation . . . . . 61-62  
 Methylhaloareonium ions . . . . . 49  
*N*'-Methylnicotinamide . . . . . 489, 491*f*  
 Methylphenyl halonium ions . . . . . 49  
 5-Methyltetrahydrofolate . . . . . 481  
 Methyne . . . . . 55  
   mechanism of ethylene formation . . . . . 13  
 Micas . . . . . 505  
 Microbes, eucaryotic . . . . . 456  
 Microorganisms . . . . . 235  
 Microprobe proton . . . . . 520  
 Migration label . . . . . 39  
 Minerals, alteration, weathering, and  
   oxidation . . . . . 505-506  
 Mitchell chemiosmotic theory . . . . . 460  
 Mitochondria . . . . . 460  
 Moderated Nuclear Recoil (MNR)  
   Arrhenius parameters, relative . . . . . 228*t*  
   equilibrium hypothesis, bimolecular  
     reaction tests . . . . . 217-226  
   equilibrium hypothesis, unimolecular  
     reaction tests . . . . . 221  
     experiments, nonthermal yields . . . . . 216-217  
     experiments RH-C<sub>3</sub>F<sub>6</sub>/C<sub>2</sub>F<sub>6</sub><sup>18</sup>F . . . . . 227*t*  
 Molecular beam studies . . . . . 203  
 Molecular dynamics studies . . . . . 123-144  
 Monkey(s) . . . . . 363, 364  
   brain, radioactivity in the rhesus . . . . . 382  
   oxygen consumption (CMRO<sub>2</sub>) . . . . . 431  
 Monovalent atoms reactions . . . . . 3-7  
 Mössbauer spectra  
   of airborne particles . . . . . 500*f*, 501*f*  
   of biotite . . . . . 506  
   of a bronze coin . . . . . 507*f*  
   of a obsidian from  
     Hö-ei Crater . . . . . 499*f*  
   of sediments . . . . . 502*f*  
   of typical deep ocean . . . . . 504*f*  
 Mössbauer spectroscopy,  
   applications . . . . . 495-508  
 Myocardial  
   extraction of labeled tracers . . . . . 442*f*  
   imaging agent . . . . . 235  
   metabolism . . . . . 409  
   in vivo tracers . . . . . 437-449  
   regional perfusion, tracers . . . . . 438  
   studies, labeled fatty acids . . . . . 441-443  
   studies, labeled glucose analogs . . . . . 441  
   tissues, tracers of damaged . . . . . 439
- N
- Neuronal perikarya . . . . . 384  
 Neurotoxin, ammonia as . . . . . 369-370  
 Niacin . . . . . 471-492  
   biologically active forms . . . . . 490*f*  
   radiometric microbiological assay . . . . . 485-490  
 Nicotinamide . . . . . 489, 491*f*  
   nucleotides . . . . . 392  
 Nicotinic acid . . . . . 489, 491*f*  
   effect on production of <sup>14</sup>CO<sub>2</sub> by  
     plantarum . . . . . 488*t*, 489*f*  
 Nitrate  
   dissimilatory reduction . . . . . 303*t*, 311  
   measurement of <sup>13</sup>N uptake by  
     cells . . . . . 299-301  
 Nitrate (*continued*)  
<sup>13</sup>N . . . . . 241-243  
   to NH<sub>4</sub><sup>+</sup> by microbial cultures . . . . . 311-312  
   to NH<sub>4</sub><sup>+</sup> in natural samples . . . . . 312  
   reductase enzymes . . . . . 455  
   transport in *pneumoniae* . . . . . 341-348  
 Nitric oxide  
   exchange from denitrification . . . . . 310*t*  
 Nitrite reductase activity . . . . . 332  
 Nitrogen . . . . . 237, 263  
   assimilation in N<sub>2</sub>-fixing plants . . . . . 317-337  
   assimilation in soybean roots and  
     nodules . . . . . 337*f*  
   atoms reactions . . . . . 73*t*  
   balance in the brain . . . . . 385  
   cation reactions . . . . . 73*t*  
   cellular sites of metabolism . . . . . 291-293  
   compounds, fast neutrons . . . . . 264  
   dioxide, <sup>13</sup>N labeled . . . . . 246  
   energy levels for atomic . . . . . 266*t*  
   fixation . . . . . 296  
   -fixing plants  
     carbon assimilation and  
       metabolism . . . . . 322-323  
       nitrogen assimilation . . . . . 317-337  
     nitrogenous constituents of xylem  
       sap . . . . . 322*f*  
     isotopic, as biochemical tracer . . . . . 233-247  
     metabolism in cyanobacteria . . . . . 269-293  
     and N<sub>2</sub>O produced in denitrification . . . . . 310*t*  
     <sup>13</sup>N . . . . . 244-245, 306*f*-307*f*  
     reduction and primary assimilation of  
       NH<sub>4</sub><sup>+</sup> . . . . . 318-321  
     in soybean nodules . . . . . 326-330  
 Nitrogen-13 . . . . . 390  
   amino acids . . . . . 246  
   distribution . . . . . 276*f*, -278*f*, 280*f*  
     281*f*, 327*f*  
   ammonia . . . . . 234, 244, 401  
   by brain  
     mechanism of uptake . . . . . 372-376,  
     379-384  
     metabolism . . . . . 372-373, 376-384  
   carotid artery infusion . . . . . 377-379  
   cerebral distribution of label . . . . . 379*f*  
   kinetics for uptake and metabolism of  
     blood-borne . . . . . 380*t*  
   production . . . . . 371-372  
   uptake index . . . . . 374*t*, 375*t*  
   ventricular infusion . . . . . 378  
 ammonium . . . . . 456  
   accumulation . . . . . 462-466  
   assimilation . . . . . 272, 278-281, 286-288  
   by *Alnus glutinosa* roots and  
     nodules . . . . . 330-332  
   by cyanobacteria, radioactive  
     constituents . . . . . 283*t*  
   by soybean or cowpea roots and  
     nodules . . . . . 332  
   labeled products after exposure . . . . . 335*f*  
   in myocardium, uptake . . . . . 438  
   NH<sub>3</sub> accumulation . . . . . 463*f*-466*f*  
   tracer studies with . . . . . 453-467  
   anion exchange radiochromatographic  
     analysis . . . . . 446*f*, 465*f*  
   assimilation by cyanobacteria . . . . . 274-286

Nitrogen-13 (*continued*)

- cation exchange radiochromatographic analysis ..... 447f  
 chemical form ..... 261-266  
 content of blood and urine after injection of BCNU ( $^{13}\text{N}$ ) ..... 355, 357-358  
 counts, measurement ..... 301  
 denitrification studies ..... 295-314  
 distribution among brain metabolites ..... 383  
 $\text{N}_2$  fixation ..... 274-278, 286-288  
 gases  
   analysis ..... 299  
   from *pseudomonas aureofaciens* ..... 309f  
   from soil ..... 305f  
 generation ..... 271-274  
 glutamine formation ..... 288  
 incorporation ..... 275f  
   after injection, whole body retention ..... 354, 356-357
- ion  
 analysis ..... 299  
 from  $^{12}\text{C}(\text{d},\text{n})^{13}\text{N}$  reaction ..... 67-75  
 charge distribution ..... 67-75  
 isotope dilution experiments ..... 307-311  
 labeled  
   L-amino acids ..... 389-402  
   ammonia for myocardial studies ..... 443-447  
   BCNU, BCNC, and nitrosocarbyl ..... 351-366  
   glutamate ..... 447  
   metabolite ..... 335  
   N-nitroso compounds, preparation ..... 353  
   radiochemicals ..... 240-247  
   radiopharmaceuticals ..... 235  
   tracers production ..... 323f  
 radiobiochemistry, experimental methods ..... 237-247  
 in rat organs ..... 359t, 399f-401f  
 recoil charge  
   vs. recoil velocity ..... 72f  
   state distributions ..... 70f  
   state fractions vs. target thickness .. 71f  
 recoiling, products ..... 74t  
 short-term studies ..... 317-337  
 tracer studies, history ..... 234-237  
 uptake by cells assimilating nitrate ..... 299-301
- Nitrogen-14(*n,p*) $^{14}\text{C}$  transmutation ..... 61-62  
 Nitrosamines ..... 296  
 N-Nitroso  
   compounds, preparation of labeled ... 353  
   derivative ..... 352f  
   N-chloroethyl-chloroethyl carbamate. 353  
 Nitrosocarbamates ..... 352, 356  
 Nitrosocarbyl ..... 352, 353  
   decomposition rate constants ..... 362f  
   intra-gastric injection ..... 355, 358  
*Nitrosomonas europaea* ..... 460-461  
 Nitrosobromine of BCNU ..... 353  
 Nitrosourea ..... 356  
 N-Nitrosoureas ..... 351  
 Nitrous oxide ..... 307  
   anion ..... 342, 346t, 455  
   labeled ..... 246, 306f-308f  
   and  $\text{N}_2$  produced in denitrification ... 310t

Nitrous oxide (*continued*)

- production, factors affecting ..... 311  
 production by nondenitrifiers .... 312-313  
 technique ..... 420  
 Novikoff hepatoma, rat ..... 395  
 Nozzles, arc-heated ..... 196  
 Nuclear  
   activation ..... 515-516  
   reactions for producing  $^{13}\text{N}$  ..... 237-238  
   reactions, prompt ..... 515  
   recoil methods, synthesis via ..... 53-64  
   recoil technique, moderated ..... 207-230

## O

- Obsidians ..... 497  
 Ocean sediments, Mössbauer spectra .. 504f  
 Olefinic addition reactions ..... 223t, 228-230t  
 Opiate receptors ..... 408  
 Organic acids ..... 333-336  
 Organs, imaging with radiopharmaceuticals ..... 390  
 Oregon, continental basalt ..... 506  
 Orthopyroxenes ..... 498  
 Osmolarity, extracellular ..... 458  
*Ostrea edulis* ..... 531f  
 Ovens and detectors, geometry ..... 185f  
 Oxalacetate ..... 335  
 Oxidation of biotite ..... 505  
 Oxidation state of iron ..... 500  
 Oxygen ..... 237  
   consumption (CMRO<sub>2</sub>) in monkeys ... 431  
   consumption, tissue ..... 428  
   -containing compounds, protons .. 263-264  
   fractional extraction ..... 429  
   -hydrogen insertion ..... 25  
   -scavenged fluoroethane ..... 81t, 82t, 84t, 85t  
   utilization ..... 428-431  
 Oxygen-15-oxyhemoglobin ..... 428  
 Oyster ..... 531f  
 Ozone layer ..... 296

## P

## P-Z

- dependence of substitution product decomposition branching ratios ..... 106t-107t  
 falloff data, stepladder simulation .... 117f, 118f  
 -limiting falloff ..... 112, 113f, 114t  
 Palmitic acid,  $^{11}\text{C}$  labeled ..... 438, 442  
 Pancreas ..... 398, 400  
 $^{13}\text{N}$  in rat ..... 401f  
 Paper mills ..... 529  
 Parkinson's disease ..... 432  
 Particle evaporation code ALICE ..... 252  
 Particle induced X-ray emission ..... 512, 517-520  
   analyses of aerosols ..... 518  
   microprobes ..... 520f  
   spectrum of particulate sample ..... 518f  
   systems ..... 520f  
*Penicillium chrysogenum* ..... 462  
 Pentadecane, HPLC of  $^{11}\text{C}$ -palmitic acid ..... 414-415

1,2,3-Pentatriene	60-61
1,2,4-Pentatriene	61
1-Penten-3-yne	61
1-Penten-4-yne	61
3-Penten-1-yne	61
Pesticides, chlorinated	531
PET (Positron emission tomography)	408, 419-435
pH	
blood	373
brain	373
profile of $^{13}\text{NH}_4^+ - \text{NH}_3$ accumulation	463f
<i>Phaseolus vulgaris</i>	321
Phenomenological approach to energy transfer	110-115
Phenylum cation, gaseous	39-40
Phenylum ion condensation with methanol	41t
Phosphate	455
Phosphine-butadiene, recoiling reactions of Si atoms in	15f
Phosphine-silane systems	9-12
6-Phosphogluconate dehydrogenase	481
Phosphorus-31 (n,p) $^{31}\text{Si}$ transmutation with 1,3-butadiene	62
Phosphorylation, oxidative	456
Photochemical conversion	163
Photofragmentation	182, 204
Photolysis, flash, generation	22-24
$\gamma$ -Photons	389
Photophosphorylation	456
Phytoplankton	236
<i>Pisum sativum</i>	321
PIXE (see Particle induced X-ray emission)	
Plants, exposure to labeled tracers	324-325
Plasma ashing devices	519
Polarography	519
Pollutants, airborne	526
Pollutant movement in water systems	530-532
Pollution sources	517
Polyatomics, highly excited	148
Polyglutamates	482
Polyvalent atom recoil reactions	7-21
Porter-Karplus surface	196
Positron emission tomography (PET)	408, 418-435
Positron-emitting radioisotopes	426
Potassium	
atoms reactions with TB	
molecules	183-187
cation	454
tracer studies with	453-467
transport	456-459
systems, kinetic parameters of bacterial	457t
Potassium-42	456
Pressure falloff curves, comparison	169-174
Pressure, osmotic	455
Primary reactions of polyvalent recoiling atoms	15-21
Probability, models, transition	165-166
Propane, multitritiated	35-36
Propionic acid	407
Protein	
binding assays, radioisotopic competitive	472

Protein (continued)	
bombardment	255
cation-specific channel	454
membrane-embedded	454
synthesis	390
$^{13}\text{NH}_4^+ - \text{NH}_3$ accumulation	466f
Proton(s)	
bombardments, isotope yields	253f
microprobe	520
on oxygen-containing compounds	263-264
spectra obtained by ( $\alpha,\rho$ reactions on glass samples	516f
<i>Pseudomonas</i>	
<i>aeruginosa</i>	308
<i>aureofaciens</i> , $^{13}\text{N}$ gas produced	309f
<i>chlororaphis</i>	309
<i>Psophocarpus tetragonolobus</i>	321
Purine(s)	392
catabolism reactions	330f
oxidative catabolism	330
2-Pyridone	489, 491f
Pyrimidines	392
biosynthesis	475
Pyruvate	488
glutamate-, transaminase	391

## Q

Quenching problem	174
Quadrupole splitting	498

## R

Radioactive isotopes	342
Radioactive labeling and detection, crossed-beam	197f
Radioactivity	
<i>A. cylindrica</i> extracts	273f, 274f
after heteroyst fixation of [ $^{13}\text{N}$ ]N <sub>2</sub>	288t
of <i>K. pneumoniae</i>	347t
from $^{13}\text{N}$ in organic compounds	328f
in rhesus monkey brain	382
in soybean nodules extract	329f
in soybean roots extract	333f
Radioiodine labeled fluorescein and tetracycline derivatives	439
Radioisotope(s)	
dating with accelerators	520-521
experiments using long-lived	183-203, 456
positron-emitting	426
Radioisotopic competitive protein binding assays	472
Radiolabeled microsphere method	433
Radiometric microbiologic assay(s)	471-492
for folate	480-485
for niacin	485-490
standard	472t-473t
for vitamin B <sub>12</sub>	475-480
Radiometric procedure and turbidimetric procedure	478-479
Radiopharmaceuticals to image tumors or organs	390
Radiopharmaceuticals labeled with $^{11}\text{C}$ and $^{18}\text{F}$	407-415
Radiotracer(s)	
environmental use	533

- Radiotracer(s) (*continued*)  
 recoil generated. . . . . 123-144  
 studies on unimolecular energy  
 transfer . . . . . 157-178  
 techniques, crossed beam . . . . . 179-205  
 Rare earth elements . . . . . 526  
 Rare earth stable activable tracers . . . . . 525-527  
 Rate constant(s)  
 high-pressure  
 for C<sub>2</sub>F<sub>6</sub> bath gas . . . . . 167*t*, 168*t*  
 unimolecular . . . . . 168*f*  
 ratios, thermal . . . . . 137*f*  
 unimolecular . . . . . 149*t*  
 decomposition . . . . . 155  
 Rates of denitrification . . . . . 304-307  
 Rats . . . . . 363, 364  
 carotid artery infusion of [<sup>15</sup>N] NH<sub>3</sub>  
 into . . . . . 378-379  
 organs, <sup>15</sup>N content . . . . . 359*t*  
 phenobarbital-anesthetized . . . . . 374  
 RBS (Rutherford backscattering) . . . . . 517  
 Reaction(s)  
 alkali . . . . . 195  
 divalent atoms . . . . . 3-7  
 H and D atoms with T<sub>2</sub> molecules 187-196  
 hydrogen-exchange . . . . . 181, 182, 187-196  
 of K and Cs atoms with TBr  
 molecules . . . . . 183-187  
 kinematics, comparison . 183-185, 189-191  
 of monovalent atoms . . . . . 3-7  
 nuclear . . . . . 195  
 TiCl<sub>3</sub> . . . . . 244  
 Reactive collision . . . . . 204  
 Reactivities, significance of  
 nonthermal . . . . . 214-216  
 Reactivity, gas-phase, of multitritiated free  
 methyl cations . . . . . 40-43  
 Rearrangement, degenerate, of gaseous  
 multitritiated ions . . . . . 38-40  
 Receptors  
 dopamine . . . . . 408  
 estrogen . . . . . 408  
 opiate . . . . . 408  
 Recoil  
 chemistry with polyvalent atoms . . . . . 3-28  
 generated radiotracers . . . . . 123-144  
 labeling with monovalent hot atoms . . . . . 57  
 parameter characterization,  
 kinetic . . . . . 133-139  
 reaction(s)  
 high energy, kinetics . . . . . 138-139  
 intermediates . . . . . 7-15  
 mechanisms . . . . . 139-144  
 stereochemistry . . . . . 139-144  
 velocity vs. <sup>15</sup>N recoil charge . . . . . 72*f*  
 Red Sea . . . . . 504  
 Respiratory nitrate reductase system . . . . . 342  
 Rey's disease . . . . . 369  
*Rhizobium*  
*leguminosarum* . . . . . 461-462  
*Rhodospseudomonas capsulata* . . . . . 457-460  
 Rice-Ramsperger-Kassel-Marcus  
 unimolecular rate theory . . . . . 108-110,  
 125-126  
 Ring scission in spiropentane . . . . . 131-132  
 Rotational  
 effects in hot atom activated  
 systems . . . . . 148-152  
 effects, unimolecular . . . . . 110  
 excitation on unimolecular  
 decomposition . . . . . 152-155  
 Rutherford backscattering (RBS) . . . . . 512  
 Rutherford measurement . . . . . 513*f*
- S**
- Saccharomyces cerevisiae* . . . . . 462  
 SATs (*see* Stable activable tracers) . . . . . 169  
 Scaling factors . . . . . 525  
 Scandium . . . . . 520*f*  
 Scanning electron microscopes . . . . . 520*f*  
 Scattering calculations . . . . . 196  
 Schizophrenia . . . . . 432  
 Sediment(s) . . . . . 502-504  
 Mössbauer spectra . . . . . 502*f*  
 slurry, rice-paddy . . . . . 304  
*Serratia* . . . . . 312  
 Serum samples assayed by RMA . . . . . 486*f*  
 Silacyclopentadiene . . . . . 14-15  
 1-Silacyclopenta-2,4-diene formation . . . . . 62  
 Silicate minerals . . . . . 498, 505  
 Silicon . . . . . 512  
 difluoride, monomeric . . . . . 6  
 ground state atoms, collisional removal 23*t*  
 -hydrogen bonds, silylene insertion . . . . . 12  
 -hydrogen insertion . . . . . 25  
 recoiling atoms  
 reaction scheme . . . . . 4-6  
 reactions with butadiene . . . . . 14  
 reactions in phosphine-butadiene . . . . . 15*f*  
 vapor . . . . . 24  
 Silicon-31  
 atom recoil reactions with  
 1,3-butadiene . . . . . 62-63  
 recoiling atoms, product yields vs.  
 substrate ratio . . . . . 13*f*  
 insertion into Si-H bond . . . . . 63  
 oil . . . . . 346*t*  
 Silylene(s) . . . . . 55  
 insertion in Si-H bonds . . . . . 12  
 -to-silylene interconversion . . . . . 11  
 Sodium . . . . . 514, 517  
 cation efflux systems . . . . . 458  
 hydroxide mixture, Devarda's  
 alloy . . . . . 371-372  
 nitrate . . . . . 264  
 Soil(s)  
 iron oxides and hydroxides . . . . . 499  
<sup>15</sup>N gases from . . . . . 305*f*  
 slurries . . . . . 305  
 Solvent molecules and stereochemistry of  
 hot substitution reactions . . . . . 140-141  
 Soybean nodules . . . . . 318  
 assimilation of fixed nitrogen . . . . . 326-330  
 extract radioactivity in . . . . . 329*f*  
 Soybean roots extract, radioactivity in . . . . . 333*f*  
 Spiroonadiene . . . . . 14  
 Spiropentane ring scission . . . . . 131-132  
 Spiroperidol . . . . . 408  
 Spore germination . . . . . 458  
 Stabilization, collisional . . . . . 45, 49



Stabilization-decomposition energy, competitive .....	128
Stable activable tracers	
in environmental science .....	523-534
in marine environment .....	531
rare earth .....	525-527
Stannite .....	497
Stannoidate .....	497
States and pathways for C + H <sub>2</sub> system ..	21f
Steady-state stochastic master equation ..	164
Stepladder model .... 170f, 172f, 174, 175f, 176f	
Stepladder simulation of falloff data ....	117f, 118f
Stereochemistry of high-energy substitution reactions .....	140
Stereochemistry, recoil .....	139-144
Strecker synthesis .....	390
<i>Streptococcus fecalis</i> .....	461
Stripping, deuteron .....	195
Stripping mechanism .....	195
Substitution	
hot atom .....	147-155
isotropic .....	181, 182
reactions, stereochemistry of high energy .....	140
Sucrose .....	323
Sulfate .....	455
Sulfur atoms exchange reactions with CS <sub>2</sub>	22
Superexcited molecules, <sup>19</sup> F-labeled	102-118
Superparamagnetism .....	500

## T

Target thickness and charge	
equilibrium .....	72-73
Technetium-99m pyrophosphate .....	439
Tellurium-123m .....	442
Tetracycline derivatives, radioiodine	
labeled .....	439
1,1,1,2-Tetramethylsilane formation ....	63
Tetratritiated methane, β <sup>-</sup> decay .....	58
Thermal abstraction reactions by FI atoms .....	135-136
Thermal rate constants, absolute .....	222
Thermochemical excitation energy	
distribution .....	102-110
Time decay curves .....	256f, 258f
Time resolved kinetic spectroscopy ..	22-24
Tin .....	506
Tin-119 .....	497
Tissue chemical composition .....	431-432
Toluene, methylation .....	48
Toluene, reaction with CT <sub>3</sub> <sup>+</sup> decay ions .....	48t-49t
Tomography, positron emission ....	419-435
Tracer(s)	
artificial .....	524
chemical .....	523
conventional .....	523-524
method of cost analysis .....	528t
of myocardial	
metabolism, in vivo .....	437-449
perfusion, regional .....	438
tissues, damaged .....	439
radioactive .....	523

Tracer(s) ( <i>continued</i> )	
stable activable, in environmental science .....	523-534
studies with <sup>13</sup> NH <sub>4</sub> <sup>+</sup> , <sup>42</sup> K <sup>+</sup> , and <sup>22</sup> Mg <sup>2+</sup> .....	453-467
Trajectory calculations, classical .....	182
Transition probability models .....	165-166
Transaminations .....	292
<i>Trifolium repens</i> .....	321
Triglycerides .....	443
Trigonelline .....	491f
Tritiated monofluorocarbene formation	58-60
Tritium	
atom(s)	
detection scheme .....	188
distribution for K + TBr .....	186f
distribution of reactively scattered .....	192f, 193f
bromide reactions with K and Cs atoms .....	183-187
-for-H replacement reactions .....	126
labeling .....	180-183
molecules reaction with H and D atoms .....	187-196
Tritritiated methyl cation decay ions	
alkylation of <i>t</i> -butylbenzene .....	45-48
with halobenzenes reaction .....	48t-49t
gas-phase .....	48t-43t
with toluene, reaction .....	48t-49t
Tryptophan .....	395
Tumors	
bone .....	397
brain, localization .....	372-373
glutaminase-sensitive .....	398
or organs, radiopharmaceuticals .....	390
Turbidimetric microbiological assays ....	472
Turbidity procedure, radiometric procedure .....	478-479

## U

Unimolecular	
decomposition rate constant .....	130
rate theory, RRKM .....	108-110
reaction tests of MNR equilibrium hypothesis .....	221
rotational effects .....	110
Uranium .....	517
Urea .....	352f
cycle .....	370
Ureide(s) .....	321, 322
synthesis .....	330f

## V

Valine .....	395, 396
Van de Graaff accelerators .....	238
Velocity	
-angle contour diagram .....	199f
distributions .....	200f
vector diagram .....	184f, 189f, 199f
Vessel size, photolysis .....	165t
<i>Vicia faba</i> .....	321
<i>Vigna unguiculata</i> .....	321, 322
Vinyl radical mechanism of ethylene formation .....	13

Vitamin B<sub>12</sub> ..... 471-492  
 Volatiles, loss ..... 519

## W

Water  
 chemistry ..... 507  
<sup>15</sup>O-labeled ..... 433  
 quality ..... 519  
 systems, pollutant movement .... 530-532  
 target ..... 253f, 302  
 Weathering ..... 505  
 Wet ashing methods ..... 519  
 Wolfgang's Adiabatic Theory ..... 265

## X

x-ray fluorescence ..... 517, 518  
 Xenon-133 ..... 420  
 Xylem sap ..... 322  
 of N<sub>2</sub>-fixing plants, nitrogenous  
 constituents ..... 322f

## Z

Zinc  
 dication ..... 455  
 dispersal pattern ..... 530